Guangli Huang · Victor F. Melnikov
Haisheng Ji · Zongjun Ning

Solar Flare Loops: Observations and Interpretations

Science Press
Beijing

Springer

Solar Flare Loops: Observations and Interpretations

Guangli Huang · Victor F. Melnikov
Haisheng Ji · Zongjun Ning

Solar Flare Loops: Observations and Interpretations

Science Press
Beijing

Springer

Guangli Huang
Purple Mountain Observatory
Nanjing
China

Haisheng Ji
Purple Mountain Observatory
Nanjing
China

Victor F. Melnikov
Pulkovo Observatory
Russian Academy of Sciences
Saint-Petersburg
Russia

Zongjun Ning
Purple Mountain Observatory
Nanjing
China

ISBN 978-981-10-2868-7 ISBN 978-981-10-2869-4 (eBook)
https://doi.org/10.1007/978-981-10-2869-4

Jointly published with Science Press Ltd., Beijing, China

The print edition is not for sale in China Mainland. Customers from China Mainland please order the print book from: Science Press.
ISBN of the China Mainland edition: 978-7-03-056483-2

Library of Congress Control Number: 2017960910

Printed on acid-free paper

This Springer imprint is published by Springer Nature
The registered company is Springer Nature Singapore Pte Ltd.
The registered company address is: 152 Beach Road, #21-01/04 Gateway East, Singapore 189721, Singapore

Foreword

Solar flares are among the most spectacular eruptive phenomena in the solar system as well as in the universe. Flares can produce a large number of high-energy particles and intense emissions into the interplanetary space which may affect the solar-terrestrial environment. Solar flares involve diverse physical processes like magnetic reconnection, particle acceleration, bremsstrahlung, gyrosynchrotron emission, radiative transfer, and so on, each of which is an important topic and has generic applications to other eruptive phenomena in the universe. Although solar flares have been intensively studied for more than half a century, there are still many unresolved questions regarding the eruption mechanisms, emission processes at various wavelengths, and dynamics of the flaring plasma. Therefore, studies on solar flares have always been and will continue to be an attractive topic in astrophysics.

During the past decades, people witnessed a major progress in the understanding of solar flares thanks to a series of spacecrafts like RHESSI, Hinode, SDO, and IRIS, and ground-based solar telescopes and radio heliographs. Many new observational discoveries and theoretical models have been achieved in the recent years. Therefore, it is highly desirable to publish a monograph which provides a comprehensive review on recent advances and prospects for future research. One year ago, when Prof. Guangli Huang told me that he and his collaborators planned to write a book on solar flares, I felt very excited and full of expectation. As a researcher in this field, I strongly support their plan and hope this book can bring readers a new horizon in the related research field.

This book focuses on a specific topic, flare loops, which are an important component in the whole flare process. Flare loops are the creatures of magnetic reconnection and the sites where most flare emissions originate. The plasma in flare loops undergoes violent dynamic evolution with a rapid energy input from, most likely, energetic electron beams. The book introduces in detail the recent advances in the study of the microwave emissions and hard X-ray emissions from flare loops, both of which are thought to be produced by energetic electrons. More importantly, the book describes the major topics from two aspects, both basic theories and observations. This makes it easy for the readers to get a comprehensive view of the

topics of interest. The book also introduces the diagnostics of physical parameters and the dynamics of flare loops, which are also important research topics with the advent of various high-resolution observations in recent years. The authors of the book are all active researchers on solar flares. Therefore, the book provides the frontier of the studies on flare loops with a unique depth.

I would like to recommend this book to researchers and graduate students working on solar physics, space physics, and related fields.

Nanjing, China
October 2016

Mingde Ding
Nanjing University

Preface

Regarding the publication of this book, I should mention Qian Jun, a sunny boy, and the editor of Science Press for my first book in 2009, "Plasma kinetic theory and application in solar physics", he visited my institute in 2013, and suggested me to consider a new publication. In the first book, the plasma theories (70%) are well combined with observations (30%), and of course, I want to keep this characteristic, but to increase the proportion of observations properly to attract much attention of astronomers. Thus, I should thank my coauthor, Victor F. Melnikov (in Central Astronomical Observatory at Pulkovo of Russian Academy of Sciences, Saint-Petersburg, Russia), to contribute greatly to the second book, "Physics in flaring loops", especially in the theoretical development of gyrosynchrotron radiation and particle propagation, and distinctive studies on observations. The main topic of this book that is different from the other numerous solar monographs is concentrated in the microwave theories and observations of flaring loops, which is expected to be attractive for the studies of solar physics. And I also would like to thank the other two coauthors, Dr. Ji Hai-sheng and Dr. Ning Zong-jun (my colleague in Purple Mountain Observatory (PMO) of Chinese Academy of Sciences, Nanjing, China) to extend this book from microwave and X-ray to optical and EUV bands. Another characteristic of the second book is that it covers all representative studies of the authors in recent years, even the most papers that have been published in English, but the authors have reorganized the material and deepened it to be a systematical monograph (including theories and observations, case study and statistics, forward and backward diagnostics, and micro and global processes), and helpful particularly for the Chinese solar people and graduate students to understand this book.

After the second book was published by Science Press in 2015, it was a bit surprising that the editor of Springer, Li Jian suggested me to publish an English version of this book, and which is actually cooperated with Science Press, and the editor Qian Jun as well. Probably a specific monograph in the field of solar microwave theories and observations was rare in recent years, and definitely, it is a great honor for Chinese scientists to publish a book by a famous publisher in the world. In this case, I don't want to simply translate the Chinese version to English,

but keep about 80% of the original material, and increase some new contents in the recent 2 years given by all of the authors, and here I should thank Prof. Mingde Ding of Nanjing University, Nanjing, China and Dr. Zhang Qing-min of PMO (jointed by Dr. Ning Zong-jun) to add the recent theoretical and observational studies on chromospheric evaporation to this book, which make it to face more solar physicists of the world, and Prof. Mingde Ding has also kindly provided a graceful foreword for this book as given before. The other authors have also added their new results published in 2015–2016 to the English version, to make an update rate over 20% in comparison with the Chinese version.

The feature of English version is somehow similar to the Chinese one, both focused in the microwave and relevant X-ray emissions in flaring loops. The English version is composed of seven chapters. A general review is given in Chap. 1 to summarize the main contents and new results of this book. Chapters 2 and 4 respectively introduce the radiation mechanisms in microwave (gyrosynchrotron) and X-ray bands (bremsstrahlung), as the theoretical basis of this book, while Chaps. 3 and 5 respectively show the observational studies in these two bands, including intensity, time profiles, spectral evolution, polarization, etc., and theoretical explanations for these observations. Chapter 6 pays particular attention to the radio and X-ray diagnostics for flaring parameters from the observations and theories, especially for coronal magnetic field and energetic electrons. At last, some large-scaled or global variations of flaring loops based on the microwave and X-ray data and relevant theories are discussed in Chap. 7.

Moreover, an important motivation of this book is based on the newly developed radio heliographs in China (Inner Mongolia, MUSER), Russia (Irkutsk, SSRT), and USA (Owens-Valley, FASR), etc., from which we can expect a 3-D radio image of solar corona, as well as coronal magnetic field and energetic particles with high spatial, temporal, and spectral resolutions, to open a new window to explore and answer the key mysteries of solar physics, as well as to develop and protect our Earth. The content of this book is closely associated with the scientific objective of the instruments as mentioned above, and it is expected to play a definite role to analyze the released data from these instruments in near future. This is my dream and expectation to the young generation of solar physicists as a retired person.

Finally, I also would like to thank my colleagues of PMO, Dr. Li Jian-ping and Dr. Song Qi-wu, for supporting the publication of this book effectively. Furthermore, I should thank all of the coauthors who participated in the main references of the authors for their contribution to this book, especially, Dr. Hiroshi Nakajima (Nobeyama Radio Observatory, NAOJ, Minamimaki, Minamisaku, Nagano 384-1305, Japan), Dr. Gregory Fleishman (Center For Solar-Terrestrial Research, New Jersey Institute of Technology, Newark, NJ 07102, USA), etc. I'd like to share all my happiness and hardship about this book with my wife Gu Li-min, as well as my Ph.D. supervisor Wang De-yu in PMO.

Nanjing, China Guangli Huang
February 2016

Contents

Acronyms

AIA	Atmospheric Imaging Assembly
AR	Active Regions
CME	Coronal Mass Ejection
ECM	Electron Cyclotron Maser
EIT	Extreme Ultraviolet Imaging Telescope
EM	Electromagnetic
EUV	Extreme Ultraviolet
EVE	Extreme Ultraviolet Variability Experiment
FP	Foot-Point
GS	Gyro-Synchrotron
HMI	Helioseismic and Magnetic Imager
HSH	Hard-Soft-Hard
HXR	Hard X-ray
HXT	Hard X-ray Telescope
LCP	Left Circular Polarization
LOS	Line-of-Sight
LT	Loop-Top
MDI	Michelson Doppler Imager
MHD	Magnetohydrodynamics
MW	Microwave
NoRH	Nobeyama Radio Heliograph
NoRP	Nobeyama Radio Polarimeters
NT	Non-Thermal
OVSA	Owens-Valley Solar Arrays
PIL	Polarity Inversion Line
QPP	Quasi-Periodic Pulsation
RCP	Right Circular Polarization
RHESSI	Reuven Ramaty High Energy Solar Spectroscopic Imager
SDO	Solar Dynamics Observatory
SEP	Solar Energetic Particle

SHH	Soft-Hard-Harder
SHS	Soft-Hard-Soft
SNR	Signal-Noise-Ratio
SOHO	Solar and Heliospheric Observatory
SST	Solar Sub-mm Telescope
SSW	Solar Software
SXR	Soft X-ray
SXT	Soft X-ray Telescope
Trace	Transition Region and Coronal Explorer

Chapter 1
Introduction

Solar flares are the most powerful events in our solar system. Normally the range of their energy release is $10^{30} - 10^{32}$ erg. Most of this energy comes in the form of heated plasma (up to 2×10^7 K), accelerated particles (electrons, protons, and ions) in the energy range from some keV up to several GeV, and strong plasma motions [1]. Accelerated particles and heated plasma manifest themselves through their electromagnetic (EM) emission in all the EM spectrum: radio, optical, ultraviolet, soft and hard X-ray, and gamma-ray. Flares are often accompanied with so-called solar energetic particle events (SEPs) and coronal mass ejections (CMEs), which propagate through interplanetary space, reach the Earth, and be capable to disrupt the operation of satellites, navigation and communication systems, and power grids [2].

The most interesting and informative element of the solar flares is a flaring loop. We can call it as an elementary structure of solar flares. Most of the processes and effects taking place in this hot and dense magnetic tube are common throughout the entire astrophysics, plasma physics, and physics of solar-terrestrial relationship. Among them there are strong energy release, acceleration of charged particles, formation and evolution of large- and small-scale magnetohydrodynamics (MHD) waves and plasma turbulence, and generation and propagation of nonthermal (NT) radiation. Thus, the study of the solar flaring loops is of great fundamental and practical importance.

In recent years, the problem of flares is especially topical in connection with an abrupt jump of spatial, temporal, and spectral resolution of ground-based and space solar telescopes. Huge flows and high quality of the modern solar data offer an opportunity to develop very detailed physical mechanisms and models, which may be applied to stars and other space objects.

Nowadays, we have the following important ground-based facilities in microwave (MW) band that allow us receiving data about flaring loops with high spatial, temporal, and spectral resolution:

(*a*) Nobeyama Radioheliograph (NoRH) [3, 4], a synthetic radio telescope composed of 84 paraboloid dishes as a T-type array of 490 m in east-west baseline and

G. Huang et al., *Solar Flare Loops: Observations and Interpretations*,
https://doi.org/10.1007/978-981-10-2869-4_1

220 m in north-south baseline, with the first image in April 1994, working 6 hours per day from June 1994, and the simultaneous imaging at 17 and 34 GHz from April 1996, with the angular resolution respectively of 7 and 14 arcsec in respect to the summer noon along the east-west baseline, while 8 and 16 arcsec along the south-north baseline, and time resolution of 1 and 0.1 s for a stable observation and burst event, respectively.

(*b*) Expanded Owens Valley Solar Array, a multifrequency 18 antenna array operating in the frequency range 1–9 GHz, is the test facility of prospective Frequency Agile Solar Radio Telescope (FASR) [5].

(*c*) Siberian Radioheliograph (SRH) [6, 7], a T-shaped 48-antennas array operating from July 2016 at 5 frequencies in the range 4–8 GHz with time resolution 0.3 s. At the second stage, after its upcoming upgrade to 96 dishes (baselines 622 m and 311 m), its spatial resolution will be 15 arcsec at 8 GHz;

(*d*) Mingantu Ultrawide Spectral Radioheliograph (MUSER) [8], composed of 40 and 60 dishes at 0.4–2 and 2–15 GHz, respectively, to be operated in the near future for simultaneous imaging at multiple frequencies of decimeter and centimeter band.

Furthermore, there are a lot of solar satellites working at multiple wavebands, such as

(*a*) Reuven Ramaty High Energy Solar Spectroscopic Imager (RHESSI) [9] in 3 keV $\sim$ 20 MeV, and to construct a photon spectrum at each pixel of X-ray and γ-ray images;

(*b*) Transition Region and Coronal Explorer (Trace) [10], simultaneously imaging in solar photosphere, transition region, and corona with different temperatures, with the spatial resolution up to 1 arcsec;

(*c*) Solar and Heliospheric Observatory (SOHO) [11], observing solar structure, chemical composition, dynamics in solar interior, the structure (density, temperature, and velocity) and dynamics of solar atmosphere, and solar wind as well as its relation with solar atmosphere;

(*d*) Solar Dynamics Observatory (SDO) [12], with Extreme Ultraviolet Variability Experiment (EVE), Atmospheric Imaging Assembly (AIA), Helioseismic and Magnetic Imager (HMI) to observe solar interior, magnetic field, high-temperature plasma in corona, and caused emission in the Earth's ionosphere;

(*e*) Hinode satellite [13], with a 50 cm optical telescope (SOT), a vector magnetogram (spatial resolution of 0.2 arcsec), and a 34 cm X-ray telescope (XRT);

(*f*) Stereo satellites [14], composed of two space-based observatories, one ahead of Earth in its orbit, and the other trailing behind, to realize a 3-D observation of speed, shape, and trajectory of CMEs.

There is quite a wide variety of acceleration mechanisms in solar flares [15–17], which can be divided into four groups:

(*1*) electric DC-field acceleration (in current sheets or in twisted loops);

(*2*) stochastic acceleration (wave turbulence, micro-flares);

(*3*) shock acceleration (propagating MHD shocks; standing MHD shocks in reconnection outflows);

(*4*) betatron acceleration (in collapsing magnetic traps).

They may act and inject accelerated electrons in different places inside a flaring loop, for example, near one loop-top (LT) or near two foot-points (FPs). Moreover, different acceleration models may produce electrons with different types of pitch-angle distributions (isotropic, with transverse or parallel anisotropy). Possibly, all of the mentioned mechanisms may operate in solar flares. Only observations can tell us which mechanism is dominant in a specific flare configuration.

Analysis of spatially resolved MW observations of NoRH has already allowed us to discover very interesting and unexpected phenomena. One of them is the presence of the strong optically thin MW source in the LT of some single flaring loops [18, 19]. Gyrosynchrotron (GS) emission that is generated by mildly relativistic electrons has a very strong dependence on the strength of magnetic field in an MW source. The problem arises: how is it possible to generate more intensive GS emission from the LT than from the regions close to the FPs if the magnetic field in the LT has to be weaker? The solution for this problem was found by the assumption of the enhanced concentration of mildly relativistic electrons in the upper part of MW flaring loops [19]. Such an accumulation of electrons in LT is really possible, if particle acceleration/injection takes place near the LT, and electrons are distributed isotropically or have the transverse pitch-angle anisotropy. It was proved by solving the nonstationary spatially resolved relativistic Fokker-Planck kinetic equation [20]. For the first time, a strong influence of different types of the electron pitch-angle anisotropy on spectral and polarization properties of GS emission was shown [21], and new methods of flaring loop diagnostics were developed for studies of spatial distributions of mildly relativistic electrons [20, 22]. It is shown in series of papers [22–25] that the position of the acceleration site and the pitch-angle anisotropy of emitting electrons strongly influence the intensity, polarization, and spectral characteristics of GS emissions in different parts of a magnetic loop. Spatially resolved observations of the corresponding microwave characteristics can be used for diagnostics of the position of the acceleration site in flaring loops as well as for diagnostics of the type and level of pitch-angle anisotropy of accelerated electrons. Using the mentioned methods, ample evidence have been found for the existence of the pitch-angle anisotropy parallel to the magnetic field in specific flaring loops [22, 26, 27].

A problem with the explanation of the LT source exists not only in the microwave range. A similar problem appears in hard X-ray (HXR) studies of flaring loops. Observations with the Yohkoh and RHESSI space vehicles showed that HXR brightness maxima can be located not only at the FPs but also at the LT of flare loops [28]. The HXR and γ-ray radiation models meet difficulties in interpreting of coronal sources [29] that are first of all associated with an insufficiently high plasma density at the LT. To overcome this problem, some assumptions were proposed:

(*a*) an extremely high plasma density at the LT [28];

(*b*) acceleration and trapping of electrons in a region with a high level of plasma turbulence [30–32];

(*c*) inverse Compton scattering of mildly relativistic electrons on photons of soft X-ray and extreme ultraviolet radiation [20];

(*d*) trapping of electrons injected into the loop perpendicular to the magnetic field lines [33].

The latter idea of the trapping and accumulation of energetic electrons at the top of an inhomogeneous magnetic loop seems to be fruitful. Recently, it was further developed [34] on the basis of software and results obtained in studies of the dynamics of spatial distributions of mildly relativistic electrons and GS radiation of flare loops mentioned above.

Besides new theoretical studies, a series of statistical results have been obtained from spatial distributions of the brightness temperature, polarization, and optically thin index for *24* events with a loop-like structure observed with NoRH, in comparison with calculated magnetic field and column density of NT electrons [35–37]. Some interesting results have been obtained, such as:

(*1*) the LT source is brighter than the loop FPs in a considerable proportion of events [35],

(*2*) a new hard-soft-hard (HSH) pattern appears in each peak of a complicated event, while the common soft-hard-soft (SHS) or soft-hard-harder (SHH) pattern exists in overall spectral evolution [36],

(*3*) the asymmetry of two FPs associated with the pitch-angle anisotropy rather than mirroring effect [37].

Meanwhile, the HXR emissions in LT and FPs were studied statistically in 13 RHESSI sources with a loop-like structure [38]. Both negative and positive correlations have been found between the spectral indices in the LT and FPs, which can be explained respectively by the thick-target model and thin-target model with a large low-energy cutoff. Moreover, the spectral evolution in different energies has been studied, the hard-soft-hard (HSH) pattern is found only in the high-energy band and may be explained by return current [39], while the spectral evolution in MW bursts also depends on frequencies [40, 41]. The co-analysis on HXR and MW bursts has confirmed that the HSH pattern appears mainly in LT, which can be well explained by the magnetic trapping effect [42, 43].

Another hot topic of solar flare physics is physics of arcade flares, or, in other words, two-ribbon flares, which may be accompanied by CMEs and prominence eruptions [44, 45]. The basic model for such flares is well known as the "CSHKP" [46–49] reconnection model, in which a flare occurs in an arcade containing a prominence presumably due to the onset of reconnection below the rising arcade. A rapid eruption at the flare onset leads to the stretching of arcade field lines and the formation of the vertical current sheet above the magnetic inversion line where a production of high-energy particles and flare loops via reconnection occurs [50–55], which predicts such morphological features as an expansion of the flare ribbons/footpoint distance and growth of a flare loop system.

In the past decade, special attention was paid to a new observational phenomenon: the contraction of flaring loops on the flare rising phase, which is not predicted by the standard model. The usual expansion of flaring loops occurs only after the contraction, which consists of three observational factors: converging motion of FPs measured using HXR data [56–60], downward motion of the LT observed in SXR [61–64], and shrinkage of the loop length [65, 66].

One of the most remarkable achievements of solar physics in the last decade is the discovery of spatially resolved MHD wave and oscillatory activity of the corona [67], and now there are abundant evidence of MHD waves of various kinds in the corona. Several theoretically predicted wave modes (transverse kink and sausage, and longitudinal) have been identified in the imaging and spectral data with high temporal and spatial resolution in the visible light, EUV, soft X-ray, and microwave bands [67, 68]. Characteristic periods of the MHD waves were directly detected in imaging observations in solar coronal loops, plumes, and other structures ranging from several seconds to several minutes. The interest to coronal waves and oscillations is mainly connected with the possible role played by them in the coronal heating [1, 69], and with the use of them as natural probes for the plasma diagnostics [67, 68, 70].

The study of coronal MHD waves stimulated the application of this gained knowledge to another example of oscillatory processes in the corona, the quasiperiodic pulsations (QPPs) in flaring energy releases. QPPs, with periods ranging from fractions of seconds [71–73] to several minutes [74, 75] are often observed in the light curves of solar flares. QPP can be present in both two ribbon and compact types of flares. The modulation depth can reach 100% of the emission trend and can often be well recognized without data processing. The most pronounced QPPs are seen in the emission associated with flare-accelerated NT electrons in the MW, HXR, and white light bands [68], and QPPs can be found in all stages of flares, from pre-flaring to decaying phases [76], thus, the flare can be seen as a sequence of periodically separated bursts. Often, QPPs are seen to be simultaneous and in phase in different bands, *e.g.*,, in HXRs and in MWs [77–79].

The interest in flaring QPPs has several motivations. First of all, QPPs are an intrinsic part of flares, and hence carry information about the mechanisms responsible for the energy releases, processes operating in them, and their triggering. For a high observational cadence time, down to fractions of a second, it allows for resolution of the wave transit time *e.g.,* across magnetic plasma structures, which is important for various techniques of MHD coronal seismology. Moreover, the nearest vicinity of flare epicenters is the region of the corona where the likelihood of the excitation of waves and oscillations is highest. In addition, understanding of the relationship between QPPs and the parameters of flaring plasma structures can contribute to the stellar coronal seismology, exploiting the similarity in structure and dynamics of the solar and Sun-like stellar coronae [80].

With in-depth studies on flaring loops, an important topic is how to use a mature theory and observations to inverse some unmeasurable plasma parameters, especially, the local magnetic field in coronal loops. For instance, it was reviewed about the radio diagnostics of coronal magnetic field [81], including that in AR above chromosphere estimated by the polarization at centimeter band, that above AR calculated by the gyro-resonant radiation at centimeter band, and that measured by cyclotron line emission etc. Some authors also used the GS emission in a nonuniform magnetic loop to calculate the local magnetic distribution [82–84], used the free-free emission to measure the magnetic field in corona and chromosphere [85], and used the variation of polarization when the GS emission travels the transverse magnetic field to deduce

a magnetogram in corona [86]. There were a lot of studies on coronal magnetic field from various fine structures and theories (see an earlier review [87]).

Regarding the magnetic field in the sources of MW bursts, an analytical expression of the local magnetic field (depending on the radio flux, optically thin spectral index, turnover frequency) was derived [88] based on the approximated GS formula [89], and the view-angle between GS emission and local magnetic field can be calculated uniquely, if the polarization of GS emission is taken into consideration [90], thus to obtain two magnetic components transverse and perpendicular to the direction of LOS, and a violent variation of transverse component has been found near the magnetic neutral line in one flare [91]. More recently, a continuous attenuation of transverse magnetic field was calculated comparable with relevant optical observations [92], and an extremely flattened spectrum at centimeter and millimeter bands has been studied in several events, which are well explained by a very high magnetic field strength and turnover frequency in these events [93].

Recent success in developing the fast GS code [94] allows one to apply the automated forward fitting method for diagnostics of solar flare MW sources [95]. Provided that the good spatially resolved MW emission characteristics at several frequencies are available, this method can give us various information not only on the magnetic field strength and electron spectrum, but also on such intrinsic properties of flaring loops as its magnetic field orientation, plasma density, the type of electron pitch-angle anisotropy, etc. [96]. Also very useful for flaring loop diagnostics is a new Solar Software (SSW) tool called GX-Simulator [97]. The tool allows one to simulate 3D images of MW and HXR emission characteristics of model flare loops. The model loops are built on the basis of a linear force free magnetic field (LFFMF) extrapolation of the photosphere magnetic field obtained from SOHO/MDI or SDO/HMI magnetograms.

The flattened HXR spectra may be caused by the low-energy cutoff of NT electrons, and albedo by photosphere etc. [98–107]. Some authors suggested that when the albedo effect is discounted from the HXR emission observed by RHESSI satellite, the flattened spectra can be well fitted, so it is not necessary to consider the low-energy cutoff, which may be an unphysical effect [106, 108]. However, recent statistics showed that even the albedo effect is removed from the RHESSI data, the flattened spectra still exist in a part of events, so that the effect of low-energy cutoff cannot simply be neglected [107]. Actually, both the low-energy and high-energy cutoffs are predicted in any acceleration processes with an electric field (direct field or wave field), because a given electric field can only accelerate the electrons larger than a critical speed [108]. A recent study showed that the relation between photon and electron spectral indices strongly depends on the magnitude of low-energy cutoff in both HXR and MW emission, some common relations can be used only when the low-energy cutoff is close to zero [109], and it probably has a large varied range [98].

There are also a lot of diagnostics of other plasma parameters, such as the pitch-angle distribution. The ratio of trapping and precipitating electrons in flaring loops is determined jointly by mirroring effect and initial pitch-angle of NT electrons, and the measured ratios of brightness temperatures and magnetic fields in two FPs can

be used to calculated the ratio of initial pitch-angles in two FPs, which plays an important role for explaining the asymmetry of two FP emissions [37, 110].

In the strongly coupled solar atmosphere where the temperature and density change by several orders of magnitude from the chromosphere to the corona, chromospheric evaporation is one of the most important processes in solar flares and plays a key role in the flare dynamics. Many processes are involved, such as the release, transport, and deposition of energy. Chromospheric evaporation is characterized by high-speed plasma upflows (blueshifts) in the spectroscopic observations. They are sometimes accompanied by chromospheric condensation, which is characterized by plasma downflows (redshifts). The study of chromospheric evaporation from the theoretical and observational perspectives has achieved great progress and is still one of the hot topics in modern solar physics (e.g.,, see the references [111–114]). The numerical models and results of observations from ground-based and space-borne solar telescopes are described briefly in this book.

The contents of this book were selected from the studies of authors in recent years about flaring loops (mainly in MW and HXR bands, but also in optical and other bands), which are closely associated with both theory and observations in MW and HXR bands, including analytical and numerical models, case studies, and statistical studies. The authors hope this book to be useful for solar researchers, especially for the graduate students. Even if its contents have been published already, a systematic monograph may be more helpful than separated papers.

References

1. Aschwanden, M.J.: Physics of the Solar Corona. An Introduction. Praxis Publishing Ltd., Chichester, Springer, Berlin (2004)
2. Miroshnichenko, L.I.: Solar Cosmic Rays. Astrophysics and Space Science Library, vol. 260. Springer, Berlin (2010)
3. Nakajima, H., Nishio, M., Enome, S., Shibasaki, K., Takano, T., et al.: The Nobeyama radioheliograph. Proc. IEEE **82**, 705–713 (1994)
4. Takano, T., Nakajima, H., Enome, S., Shibasaki, K., Nishio, M., et al.: An upgrade of nobeyama radioheliograph to a dual-frequency (17 and 34 GHz) system. In: Trottet G. Coronal Physics from Radio and Space Observations; Proceedings of the CESRA Workshop held in Nouan le Fuzelier, France 3–7 June 1996, p. 183. Springer, Berlin (1997)
5. Gary, D.E., Nita, G.M., Sane, N.: Expanded Owens Valley Solar Array (EOVSA) Testbed and Prototype, American Astronomical Society, AAS Meeting 220, id.204.30
6. Lesovoi, S.V., Altyntsev, A.T., Ivanov, E.F., Gubin, A.V.: A 96-antenna radioheliograph. Res. Astron. Astrophys. **14**, 864–868 (2014)
7. Lesovoi, S.V., Altyntsev, A.T., Kochanov, A.A., Grechnev, V.V., Gubin, A.V., et al.: Siberian radioheliograph: first results. Solnechno-zemnaya fizika [Solar-Terrestrial Phys.] **3**, 3–16 (2017)
8. Yan, Y., Zhang, J., Chen, Z., Wang, W., Liu, F., Geng, L.: On solar radio imaging-spectroscopy. Science with large solar telescopes. In: Proceedings of IAU Special Session 6, held 22–24 August (2012)
9. Lin, R., 65 colleagues: The Reuven Ramaty high-energy solar spectroscopic imager (RHESSI). Sol. Phys. **210**, 3–32 (2002)

10. Handy, B.N., Acton, L.W., Kankelborg, C.C., Wolfson, C.J., Akin, D.J., et al.: The transition region and coronal explorer. Sol. Phys. **187**, 229–260 (1999)
11. Domingo, V., Fleck, B., Poland, A.I.: The SOHO mission: an overview. Sol. Phys. **162**, 1–37 (1995)
12. Dean, P.W., Thompson, B.J., Chamberlin, P.C.: The solar dynamics observatory (SDO). Sol. Phys. **275**, 3–15 (2012)
13. Kosugi, T., Matsuzaki, K., Sakao, T., Shimizu, T., Sone, Y., et al.: The Hinode (Solar-B) mission: an overview. Sol. Phys. **243**, 3–17 (2007)
14. Luhmann, J.G., Curtis, D.W., Lin, R.P., Larson, D., Schroeder, P., et al.: IMPACT: science goals and firsts with STEREO. Adv. Space Res. **36**, 1534–1543 (2005)
15. Aschwanden, M.J.: Particle acceleration and kinematics in solar flares - a synthesis of recent observations and theoretical concepts (Invited Review). Space Sci. Rev. **101**, 1–227 (2002)
16. Vlahos, L.: Magnetic complexity, fragmentation, particle acceleration and radio emission from the sun. The High Energy Solar Corona: Waves, Eruptions, Particles. Lecture Notes in Physics, vol. 725, p. 15. Springer, Berlin (2007)
17. Zaitsev, V.V., Stepanov, A.V.: Reviews of topical problems: coronal magnetic loops. Phys. Uspekhi **51**, 1123–1160 (2008)
18. White, S.M., Kundu, M.R., Garaimov, V.I., Yokoyama, T., Sato, J.: The physical properties of a flaring loop. Astrophys. J. **576**, 505–518 (2002)
19. Melnikov, V.F., Shibasaki, K., Reznikova, V.E.: Loop-top nonthermal microwave source in extended solar flaring loops. Astrophys. J. **580**, L185–L188 (2002)
20. Melnikov, V.F., Charikov, Y.E., Kudryavtsev, I.V.: Spatial brightness distribution of hard X-Ray emission along flare loops. Geomagn. Aeron. **53**, 863–866 (2013)
21. Melnikov, V.F.: Electron acceleration and transport in microwave flaring loops. In: Shibasaki K. Proceedings of Nobeyama Symposium (Kiosato, 26–29 October 2004), NSRO Report, vol. 1, pp. 11–22 (2006)
22. Reznikova, V.E., Melnikov, V.F., Shibasaki, K., Gorbikov, S.P., Pyatakov, N.P., Myagkova, I.N., Ji, H.: 2002 august 24 limb flare loop: dynamics of microwave brightness distribution. Astrophys. J. **697**, 735–746 (2009)
23. Melnikov, V.F., Pyatakov, N.P., Shibasaki, K.: Constraints for electron acceleration models in solar flares from microwave observations with high spatial resolution. Hinode-3: the 3rd Hinode science meeting. In: Sekii T., Watanabe T., Sakurai T. Proceedings of the conference held 1–4 December 2009 at Hitotsubashi Memorial Hall, Tokyo, Japan. ASP Conference Series, vol. 454, p. 321. Astronomical Society of the Pacific, San Francisco (2012)
24. Altyntsev, A.T., Fleishman, G.D., Huang, G.L., Melnikov, V.F.: A broadband microwave burst produced by electron beams. Astrophys. J. **677**, 1367–1377 (2008)
25. Veronig, A.M., Brown, J.C.: A coronal thick-target interpretation of two hard x-ray loop events. Astrophys. J. **603**, L117–L120 (2004)
26. Krucker, S., Battaglia, M., Cargill, P.J., Fletcher, L., Hudson, H.S., et al.: Hard X-ray emission from the solar corona. Astron. Astrophys. Rev. **16**, 155–208 (2008)
27. Tzatzakis, V., Nindos, A., Alissandrakis, C.E., Shibasaki, K.: A statistical study of microwave flare morphologies. Sol. Phys. **253**, 79–94 (2008)
28. Petrosian, V., Donaghy, T.Q.: On the spatial distribution of hard x-rays from solar flare loops. Astrophys. J. **527**, 945–957 (1999)
29. Stepanov, A.V., Tsap, Y.T.: Electron-Whistler interaction in coronal loops and radiation signatures. Sol. Phys. **211**, 135–154 (2002)
30. Petrosian, V., Liu, S.: Stochastic acceleration of electrons and protons. I. Acceleration by parallel-propagating waves. Astrophys. J. **610**, 550–571 (2004)
31. Fletcher, L., Martens, P.C.H.: A model for hard x-ray emission from the top of flaring loops. Astrophys. J. **505**, 418–431 (1998)
32. Chen, B., Bastian, T.S.: The role of inverse compton scattering in solar coronal hard x-ray and gamma-ray sources. Astrophys. J. **750**, 35–50 (2012)
33. Melnikov, V.F., Gorbikov, S.P., Pyatakov, N.P.: Formation of anisotropic distributions of mildly relativistic electrons in flaring loops. Universal heliophysical processes. In: Proceedings of the International Astronomical Union, IAU Symposium, vol. 257, pp. 323–328 (2009)

34. Fleishman, G.D., Melnikov, V.F.: Gyrosynchrotron emission from anisotropic electron distributions. Astrophys. J. **587**, 823–835 (2003)
35. Huang, G.L., Nakajima, H.: Statistical analysis of flaring loops observed by nobeyama radioheliograph. I. Comparison of looptop and footpoints. Astrophys. J. **696**, 136–142 (2009)
36. Huang, G.L., Nakajima, H.: Statistics of flaring loops observed by nobeyama radioheliograph II. Spectral evolution. Astrophys. J. **702**, 19–26 (2009)
37. Huang, G.L., Song, Q.W., Huang, Y.: Statistics of flaring loops observed by the nobeyama radioheliograph. III. Asymmetry of two footpoint emissions. Astrophys. J. **723**, 1806–1816 (2010)
38. Shao, C.W., Huang, G.L.: Comparative study of solar hxr flare spectra in looptop and footpoint sources. Astrophys. J. **691**, 299–305 (2009)
39. Shao, C.W., Huang, G.L.: Hard-soft-hard flare spectra and their energy dependence in spectral evolution of a solar hard x-ray flare. Astrophys. J. **694**, L162–L165 (2009)
40. Song, Q.W., Huang, G.L., Nakajima, H.: Co-analysis of solar microwave and hard x-ray spectral evolutions. I. In two frequency or energy ranges. Astrophys. J. **734**, 113–124 (2011)
41. Huang, G.L., Li, J.P.: Co-analysis of solar microwave and hard x-ray spectral evolutions. II. In three sources of a flaring loop. Astrophys. J. **740**, 46–56 (2011)
42. Metcalf, T.R., Alexander, D.: Coronal trapping of energetic flare particles: Yohkoh/HXT observations. Astrophys. J. **522**, 1108–1116 (1999)
43. Minoshima, T., Yokoyama, T., Mitani, N.: Comparative analysis of nonthermal emissions and electron transport in a solar flare. Astrophys. J. **673**, 598–610 (2008)
44. Priest, E.R., Forbes, T.G.: The magnetic nature of solar flares. Astron. Astrophys. Rev. **10**, 313–377 (2002)
45. Fang, C., Ding, M.D., Chen, P.F.: Physics of Solar Active Regions. Nanjing University Press, Nanjing (2008)
46. Carmichael, H.A.: Process for flares. The physics of solar flares. In: Wilmot N.H. Proceedings of the AAS-NASA Symposium held 28-30 October, 1963 at the Goddard Space Flight Center, Greenbelt MD. National Aeronautics and Space Administration, Science and Technical Information Division, p. 451. Washington, DC (1964)
47. Sturrock, P.A.: Model of the high-energy phase of solar flares. Nature **211**, 695–697 (1996)
48. Hirayama, T.: Theoretical model of flares and prominences. I: Evaporating flare model. Sol. Phys. **34**, 323–338 (1974)
49. Kopp, R.A., Pneuman, G.W.: Magnetic reconnection in the corona and the loop prominence phenomenon. Sol. Phys. **50**, 85–98 (1976)
50. Priest, E.R.: Book-review - solar flare magnetohydrodynamics. Science **214**, 356 (1981)
51. Moore, R.L.: Evidence that magnetic energy shedding in solar filament eruptions is the drive in accompanying flares and coronal mass ejections. Astrophys. J. **324**, 1132–1137 (1988)
52. Moore, R.L., Roumeliotis, G.: Triggering of Eruptive Flares - Destabilization of the Preflare Magnetic Field Configuration. Eruptive Solar Flares. In: Svestka Z., Jackson B.V., Proceedings of Colloquium 133 of the International Astronomical Union, held at Iguazu, Argentina, 2–6 August 1991. M. E. M. Publisher, p. 69. Springer, New York (1992)
53. Shibata, K.: New observational facts about solar flares from YOHKOH studies - evidence of magnetic reconnection and a unified model of flares. Adv. Space Res. **17**, 9–18 (1996)
54. Shibata, K., Watanabe, T., Kosugi, T., Sterling, A.C.: A unified model of solar flares. Observational Plasma Astrophysics: Five Years of Yohkoh and Beyond, vol. 229, p. 187. Kluwer Academic Publishers, Boston (1998)
55. Shibata, K.: Evidence of magnetic reconnection in solar flares and a unified model of flares. Structure Formation and Function of Gaseous, Biological and Strongly Coupled Plasmas, p. 74 (1999)
56. Ji, H., Wang, H., Goode, P.R., Jiang, Y.C., Yurchyshyn, V.: Traces of the dynamic current sheet during a solar flare. Astrophys. J. **607**, L55–L58 (2004)
57. Ji, H., Huang, G., Wang, H., Zhou, T., Li, Y., Zhang, Y., Song, M.: Converging motion of H_α conjugate kernels: the signature of fast relaxation of a sheared magnetic field. Astrophys. J. **636**, L173–L174 (2006)

58. Ji, H., Huang, G., Wang, H.: The relaxation of sheared magnetic fields: a contracting process. Astrophys. J. **660**, 893–900 (2007)
59. Liu, R., Wang, H., Alexander, D.: Implosion in a coronal eruption. Astrophys. J. **696**, 121–135 (2009)
60. Yang, Y.H., Cheng, C.Z., Krucker, S., Lin, R.P., Ip, W.H.: A statistical study of hard x-ray footpoint motions in large solar flares. Astrophys. J. **693**, 132–139 (2009)
61. Sui, L., Holman, G.D.: Evidence for the formation of a large-scale current sheet in a solar flare. Astrophys. J. **596**, L251–L254 (2003)
62. Sui, L., Holman, G.D., Dennis, B.R.: Evidence for magnetic reconnection in three homologous solar flares observed by RHESSI. Astrophys. J. **612**, 546–556 (2004)
63. Li, Y.P., Gan, W.Q.: On the peak times of thermal and nontheral emissions in solar flares. Astrophys. J. **652**, L61–L63 (2006)
64. Shen, J., Zhou, T., Ji, H., Wang, N., Cao, W., Wang, H.: Early abnormal temperature structure of x-ray loop-top source of solar flares. Astrophys. J. **686**, L37–L40 (2008)
65. Li, Y.P., Gan, W.Q.: The shrinkage of flare radio loops. Astrophys. J. **629**, L137–L139 (2005)
66. Joshi, B., Veronig, A., Cho, K.-S., Bong, S.-C., Somov, B.V., et al.: Magnetic reconnection during the two-phase evolution of a solar eruptive flare. Astrophys. J. **706**, 1438–1450 (2009)
67. Nakariakov, V.M., Verwichte, E.: Coronal waves and oscillations. Living Rev. Sol. Phys. **2**, 1–65 (2005)
68. Nakariakov, V.M., Melnikov, V.F.: Quasi-periodic pulsations in solar flares. Space Sci. Rev. **149**, 119–151 (2009)
69. Erdélyi, R., Ballai, I.: Heating of the solar and stellar coronae: a review. Astronomische Nachrichten **328**, 726–733 (2007)
70. Banerjee, D., Erdélyi, R., Oliver, R., O'Shea, E.: Present and future observing trends in atmospheric magnetoseismology. Sol. Phys. **246**, 3–29 (2007)
71. Aschwanden, M.J.: Theory of radio pulsations in coronal loops. Sol. Phys. **111**, 113–136 (1987)
72. Fleishman, G.D., Fu, Q.J., Huang, G.L., Melnikov, V.F., Wang, M.: Discovery of unusual large group delay in microwave millisecond oscillating events. Astron. Astrophys. **385**, 671–685 (2002)
73. Tan, B.: Observable parameters of solar microwave pulsating structure and their implications for solar flare. Sol. Phys. **253**, 117–131 (2008)
74. Foullon, C., Verwichte, E., Nakariakov, V.M., Fletcher, L.: X-ray quasi-periodic pulsations in solar flares as magnetohydrodynamic oscillations. Astron. Astrophys. **440**, L59–L62 (2005)
75. Kislyakov, A.G., Zaitsev, V.V., Stepanov, A.V., Urpo, S.: On the possible connection between photospheric 5-min oscillation and solar flare microwave emission. Sol. Phys. **233**, 89–106 (2006)
76. Kupriyanova, E.G., Melnikov, V.F., Nakariakov, V.M., Shibasaki, K.: Types of microwave quasi-periodic pulsations in single flaring loops. Sol. Phys. **267**, 329–342 (2010)
77. Asai, A., Shimojo, M., Isobe, H., Morimoto, T., Yokoyama, T., Shibasaki, K., Nakajima, H.: Periodic acceleration of electrons in the 1998 november 10 solar flare. Astrophys. J. **562**, L103–L106 (2001)
78. Melnikov, V.F., Reznikova, V.E., Shibasaki, K., Nakariakov, V.M.: Spatially resolved microwave pulsations of a flare loop. Astron. Astrophys. **439**, 727–736 (2005)
79. Kupriyanova, E.G., Melnikov, V.F., Shibasaki, K.: Spatially resolved microwave observations of multiple periodicities in a flaring loop. Sol. Phys. **284**, 559–578 (2013)
80. Nakariakov, V.M.: MHD oscillations in solar and stellar coronae: current results and perspectives. Adv. Space Res. **39**, 1804–1813 (2007)
81. Kundu, M.R.: Measurement of solar magnetic fields from radio observations. Societá Astronomica Italiana, Memorie **61**, 431–455 (1990)
82. Preka-Papadema, P., Alissandrakis, C.E., Dennis, B.R., et al.: Modeling of a microwave burst emission. Sol. Phys. **172**, 233–238 (1997)
83. Nindos, A., White, S.M., Kundu, M.R., et al.: Observations and models of a flaring loop. Astrophys. J. **533**, 1053–1062 (2000)

84. Kundu, M.R., Nindos, A., Grechnev, V.V.: The configuration of simple short-duration solar microwave bursts. Astronomy Astrophysics **420**, 351–359 (2004)
85. Grebinskij, A., Bogod, V., Gelfreikh, G., et al.: Microwave tomography of solar magnetic fields. Astron. Astrophys. Suppl. **144**, 169–180 (2000)
86. Ryabov, B.I., Maksimov, V.P., Lesovoi, S.V., et al.: Coronal magnetography of solar active region 8365 with the ssrt and norh radio heliographs. Sol. Phys. **226**, 223–237 (2005)
87. Gary, D.E., Keller, C.U. (eds.): Solar and Space Weather Radiophysics-Current Status and Future Developments. Astrophysics and Space Science Library, vol. 314. Kluwer Academic Publishers, Dordrecht (2004)
88. Zhou, A.H., Karlický, M.: Magnetic field estimation in microwave radio sources. Sol. Phys. **153**, 441–444 (1994)
89. Dulk, G.A., Marsh, K.A.: Simplified expressions for the gyrosynchrotron radiation from mildly relativistic, nonthermal and thermal electrons. Astrophys. J. **259**, 350–358 (1982)
90. Huang, G.L.: Calculations of coronal magnetic field parallel and perpendicular to line-of-sight in microwave bursts. Sol. Phys. **237**, 173–183 (2006)
91. Huang, G.L., Ji, H.S., Wu, G.P.: The radio signature of magnetic reconnection for the M-Class flare of 2004 november 1. Astrophys. J. **672**, L131–L134 (2008)
92. Huang, G., Li, J., Song, Q., Tan, B., Huang, Y., Wu, Z.: Attenuation of coronal magnetic field in solar microwave bursts. Astrophys. J. **806**, 12–18 (2015)
93. Song, Q., Nakajima, H., Huang, G., Tan, B., Huang, Y., Wu, Z.: Turnover frequency in solar microwave bursts with an extremely flat optically-thin spectrum. Sol. Phys. **291**, 3619–3635 (2016)
94. Fleishman, G.D., Kuznetsov, A.A.: Fast gyrosynchrotron codes. Astrophys. J. **721**, 1127–1141 (2010)
95. Fleishman, G.D., Nita, G.M., Gary, D.E.: Dynamic magnetography of solar flaring loops. Astrophys. J. Lett. **698**, 183–187 (2009)
96. Morgachev, A.S., Kuznetsov, S.A., Melnikov, V.F.: Radio diagnostics of the solar flaring loop parameters by the forward fitting method. Geomagn. Aeron. **54**, 933–942 (2014)
97. Nita, G.M., Fleishman, G.D., Kuznetsov, A.A., Kontar, E.P., Gary, D.E.: Three-dimensional radio and x-ray modeling and data analysis software: revealing flare complexity. Astrophys. J. **799**, id236(15pp) (2015)
98. Gan, W.Q., Li, Y.P., Chang, J.: Energy shortage of nonthermal electrons in powering a solar flare. Astrophys. J. **552**, 858–862 (2001)
99. Kontar, E.P., Brown, J.C., McArthur, G.: Nonuniform target ionization and fitting thick target electron injection spectra to RHESSI data. Sol. Phys. **210**, 419–429 (2002)
100. Kontar, E.P., Brown, J.C., Emslie, A.G., Schwartz, R.A., Smith, D.M., Alexander, R.C.: An explanation for non-power-law behavior in the hard x-ray spectrum of the 2002 july 23 solar flare. Astrophys. J. **598**, L123–L126 (2003)
101. Holman, G.D.: The effects of low- and high-energy cutoffs on solar flare microwave and hard x-ray spectra. Astrophys. J. **586**, 606–616 (2003)
102. Zhang, J., Huang, G.L.: The effect of the compton backscattering component on the photon spectra of three yohkoh/hard x-ray telescope flare. Astrophys. J. **592**, L49–L52 (2003)
103. Zhang, J., Huang, G.L.: Joint effects of compton backscattering and low-energy cutoff on the flattening of solar hard x-ray spectra at lower energies. Sol. Phys. **219**, 135–148 (2004)
104. Kašparová, J., Karlický, M., Kontar, E.P., Schwartz, R.A., Dennis, B.R.: Multi-wavelength analysis of high-energy electrons in solar flares: a case study of the august 20, 2002 flare. Sol. Phys. **232**, 63–86 (2005)
105. Kontar, E.P., MacKinnon, A.L., Schwartz, R.A., Brown, J.C.: Compton backscattered and primary X-rays from solar flares: angle dependent Green's function correction for photospheric albedo. Astron. Astrophys. **446**, 1157–1163 (2006)
106. Kašparová, J., Kontar, E.P., Brown, J.C.: Hard X-ray spectra and positions of solar flares observed by RHESSI: photospheric albedo, directivity and electron spectra. Astron. Astrophys. **466**, 705–712 (2007)

107. Han, G., Li, Y.P., Gan, W.Q.: A study of the low energy cutoff of nonthermal electrons in RHESSI flares. 2008. Chin. Astron. Astrophys. **33**, 168–178 (2009)
108. Miyamoto, K.: Plasma Physics for Nuclear Fusion, p. 101. Science Press, Beijing (1981). (Chapter 5)
109. Huang, G.L.: Diagnostics of the low-cutoff energy of nonthermal electrons in solar microwave and hard x-ray bursts. Sol. Phys. **257**, 323–334 (2009)
110. Huang, G.L.: Initial pitch-angle of narrowly beamed electrons injected into a magnetic mirror, formation of trapped and precipitating electron distribution, and asymmetry of hard X-ray and microwave footpoint emissions. New Astron. **12**, 483–489 (2007)
111. Ning, Z., Cao, W.: Investigation of chromospheric evaporation in a neupert-type solar flare. Astrophys. J. **717**, 1232–1242 (2010)
112. Zhang, Q.M., Ji, H.S.: Chromospheric evaporation in sympathetic coronal bright points. Astron. Astrophys. **557**, L5–8 (2013)
113. Zhang, Q.M., Li, D., Ning, Z.J., et al.: Explosive chromospheric evaporation in a circular-ribbon flare. Astrophys. J. **827**, 27–37 (2016a)
114. Zhang, Q.M., Li, D., Ning, Z.J.: Chromospheric condensation and quasi-periodic pulsations in a circular-ribbon flare. Astrophys. J. **832**, 65–80 (2016b)

Chapter 2
Theory of MW Emissions of Solar Flaring Loops

It is well known that there are various acceleration mechanisms in solar flares (see review papers [1, 2]), including DC electric field (in current sheets or twisted magnetic loops), stochastic acceleration (in plasma wave turbulence and microflares), shock acceleration (in MHD shocks and standing shocks), and electron induced acceleration (in collapsed magnetic trapping). Different mechanisms make accelerated electrons inject into different parts of flaring loops, such as nearby one loop top (LT) by the acceleration in a perpendicular current sheet (called as standard model), and also possibly in a region with strong turbulence, or nearby one foot-point (FP) of a big magnetic loop in a double loop system, or in total twisted magnetic loop with a great amount of microcurrent sheets. Moreover, different mechanisms produce different pitch-angle distributions (isotropic and parallel or perpendicular anisotropic ones).

The above acceleration processes may happen simultaneously in solar flares and observations can tell us which acceleration mechanism is dominated in a specific flare. The data analysis of Nobeyama Radioheliograph (NoRH) makes us possibly find some interesting phenomena, such as the microwave (MW) optically thin source in the LT of one individual flaring loop [3, 4], subsequent studies showed that such kind of single loops may occupy 30–50% of total flares, and most other flares may have one or two FP sources [5, 6].

The strong LT emission can be explained by an enhanced concentration of moderately relativistic electrons in the LT of MW flaring loops [4]. This happens when the nonthermal (NT) electrons possess are accelerated close to the LT and they possess a perpendicular anisotropic pitch-angle distribution [7]. Another phenomenon is the MW spectrum softening from the LT toward FPs in the flare loops on solar disk [8]. This effect is confirmed by other observations [9, 10]. Also, a sufficient evidence for anisotropic pitch-angle distribution parallel to magnetic field was found in a specific flaring loop [11]. The most interesting evidence was the ordinary-mode polarization of emission from an optically thin GS source as predicted for the beam-like electron distribution [12].

G. Huang et al., *Solar Flare Loops: Observations and Interpretations*,
https://doi.org/10.1007/978-981-10-2869-4_2

The spatially resolvable telescopes in MW band may provide more evidence about the acceleration sites and pitch-angle distributions of NT electrons in future, as a valuable constraint for the study of acceleration mechanisms. The following study will be focused on the dynamic evolution of electron distributions and spectral feature of GS emission in different parts of flaring loops.

2.1 Observational Characteristics of Solar Microwave Emissions

The radio emission in solar flares was reviewed in general [13], which was extended to the radio emission in active regions [14], and to the correlation between radio and X-ray bursts [15], while reviews of radio emission mechanisms were considered [16–18]. Generally, solar radio emission can be divided into two kinds, one is the coherent emission at meter and longer waveband that dominated by plasma emission, and another one is the incoherent emission at centimeter even millimeter band that dominated by GS emission. The former mainly occurs in high corona with a relatively weaker magnetic field of several Gauss, which is almost impossible to produce the GS emission with lower harmonics in corresponding frequencies. The latter happens in low corona with an ambient magnetic field of several tens or hundreds Gauss, while the ambient plasma density is commonly smaller than $10^{10}\,\mathrm{cm}^{-3}$, which is not enough to produce the plasma emission with lower harmonics in corresponding frequencies. Nevertheless, there are many flares where coherent decimeter and even centimeter emissions with fine structures have been observed [19].

This book pays particular attention to the spatially resolvable MW and hard X-ray emission in flaring loops, while the dynamic spectrum in decimeter and meter bands and relevant theories such as plasma emission and electron cyclotron maser (ECM) are not included.

2.1.1 Intensity, Polarization, and Spectrum of MW Emission

The intensity (I_ν) of radio emission is defined as the received energy (erg) at a given frequency ν in a unit time (s^{-1}), unit frequency interval (Hz^{-1}), unit solid angle (sr^{-1}), and a unit area (cm^{-2}). If a celestial radio source is replaced by an ideal black body with the same intensity, thus the temperature of black body is called as the brightness temperature T_b of radio source, and described by the Rayleigh–Jeans law:

$$I_\nu = k_B T_b \nu^2 / c^2 \,, \tag{2.1.1}$$

here, k_B is the Boltzmann constant, and c is the light speed in vacuum. Hence, I_ν can be replaced equivalently by T_b, and a 2D distribution of T_b can be obtained by radio

telescopes with spatial resolution. It is noticed that T_b is not the real temperature of radio source. The observed T_b in solar flares is commonly 10^6–10^9 K, and even higher (such as some coherent emission like ECM), which is obviously higher than the plasma temperature in solar atmosphere.

Furthermore, for a spatially unresolvable radio telescope, the integration of T_b in the full solid angle open for the radio source can be done to obtain the radio flux density (S_ν) of the total radio source:

$$S_\nu = k_B \nu^2 / c^2 \int T_b d\Omega \ . \tag{2.1.2}$$

The unit of radio flux density is SFU ($10^{-19}\,\mathrm{erg \cdot s^{-1} \cdot Hz^{-1} \cdot cm^{-2}}$), and another one that commonly used in astrophysics is Jansky: 1 SFU = 10^4 Jansky. There is a large variation of S_ν in solar flares, from several SFU to several ten thousands SFU, which may be over two orders of magnitudes larger than that in the quiet Sun, which makes us easily recognize such a strong source from the quiet Sun.

Solar MW emission is contributed by GS emission of moderately relativistic electrons from both superthermal and nonthermal (NT) electrons with an energy distribution often similar to the power-law one. Their generated spectrum covers the full centimeter band. Its lower and higher ends are respectively connected decimeter and millimeter bands, thus it is a typical continuum. However, the spectrum often is not monotonous but has a spectral peak at so-called peak or turnover frequency. Two opposite (positive and negative) slopes of the MW spectrum are characterized by spectral indices respectively below and above the peak frequency. Characteristics of the theoretically calculated thermal and NT GS spectra differ from the corresponding characteristics of the bremsstrahlung and synchrotron spectra [16]. Figure 2.1 shows the differences of T_b and S spectral indices appeared obviously in both optically thick

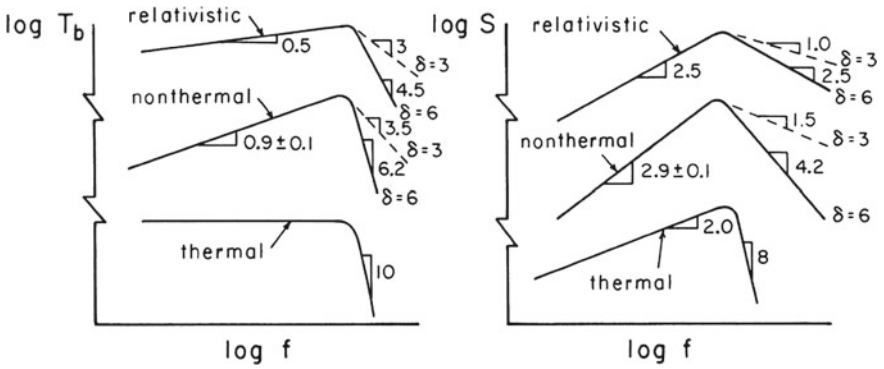

Fig. 2.1 T_b (left) and S (right) spectra of synchrotron from relativistic electrons, GS emission from NT electrons with a power-law, and bremsstrahlung from thermal electrons, when the electron spectral index $\delta = 3,\ 6$ in a logarithmic coordinate versus radio frequency f. Both electron and photon indices are marked in optically thick and optically thin parts, respectively [16]

and optically thin parts of the MW spectrum under different radiation mechanisms. Note that the absolute value of the T_b spectral index is always larger (softer) than that of S, with an identical difference of 2.

In general, the GS spectral index in the region $\nu > \nu_{peak}$, where a radio source is optically thin, is more closely related to flare energy release and NT electron energy spectral index in comparison with the spectral index in the region where $\nu < \nu_{peak}$, where the radio source is strongly affected by absorption and suppression mechanisms.

The polarization of the observed solar radio emission is dominated by the circular polarization. The elliptical and linear polarization possibly generated in a radio source is negligible due to the depolarization caused by the Faraday rotation during the emission propagation through the solar corona. So, only two Stokes parameters I and V are enough to describe the polarization of solar radio emission. From the observational point of view, the polarization can be determined by the polarization degree P_{obs}, which equals to the difference (Stokes $V = R - L$) between right circular polarization (R) and left circular polarization (L) intensities divided by the sum of the intensities (Stokes $I = R + L$):

$$P_{obs} = V/I \ . \tag{2.1.3}$$

The theoretical definition of polarization is given by the relation between intensities of the extraordinary I_x and ordinary modes I_o:

$$P_{th} = (I_x - I_o)/(I_x + I_o) \ . \tag{2.1.4}$$

The correspondence between the signs of P_{obs} and P_{th} is definite only if the direction of magnetic field in a radio source is known. For example, if the magnetic field in the source is directed from an observer, then the left polarization corresponds to the extraordinary wave, and the right polarization to the ordinary wave.

2.1.2 Radiation Transfer

Variation of the intensity $I_\nu(l)$ of radio emission along a ray path **l** through an emitting and absorbing medium is described by the radiation transfer equation:

$$\frac{dI_\nu}{dl} = \eta_\nu - \kappa_\nu I_\nu \ , \tag{2.1.5}$$

where η_ν and κ_ν are respectively emissivity and absorption coefficient in the medium. In a homogeneous medium, the solution of this differential equation is

$$I_\nu = I_o e^{-\tau} + \eta_\nu/\kappa_\nu(1 - e^{-\tau}) \ , \tag{2.1.6}$$

where $\tau_\nu = \int \kappa_\nu dl$ is optical thickness of the medium on the length of the ray path L, I_o is the emission intensity of an outer source (background). In the limiting cases of optically thick source ($\tau_\nu \gg 1$) and optically thin source ($\tau_\nu \ll 1$), the solutions can be written as

$$I_\nu = \eta_\nu/\kappa_\nu = k_B T_{eff} \nu^2/c^2 \ , \tag{2.1.7}$$

$$I_\nu = I_o(1-\tau) + \eta_\nu L \ , \tag{2.1.8}$$

respectively. The Eq. (2.1.7) is often called Kirchhoff law. It allows to obtain the relationship between the emissivity η_ν and absorption coefficient κ_ν. For thermal emission, T_{eff} is just the kinetic temperature of the medium in the radio source. For nonthermal emission, the radio source's effective temperature T_{eff} represents the average energy of emitting particles.

2.1.3 Thermal and Nonthermal (NT) Emission

Particle acceleration and plasma heating are two indivisible processes in solar flares, and the proportion of them in flare energy release is always debatable. Solar radio emission includes thermal and nonthermal (NT) GS emission, thermal bremsstrahlung (or free-free emission) and gyro-resonant emission, relativistic synchrotron emission, and coherent plasma emission and ECM etc. For MW continuum emission, it is not necessary to consider the latter three mechanisms, the thermal gyro-resonant emission mainly contributes to the emission from active regions, while the MW emission in solar flares are contributed from the NT GS emission and thermal bremsstrahlung, which mainly happens in the LT of flaring loops, especially in the decay phase of flares.

2.2 Gyrosynchrotron (GS) Emission

Now it became clear that the well-known approximated formulae [16] for the calculation of GS emission characteristics are not good for the detailed diagnostics of parameters of accelerated electrons.

Before discussing our numerical results, let us remind briefly the current idea about GS emission produced by isotropic electron distributions with a power-law energy E (or momentum p) spectrum. A typical frequency spectrum J of GS emission consists of optically thick (rising with frequency f) and optically thin (falling with frequency f) parts, the spectral maximum corresponds to the frequency defined by the condition:

$$\tau(f) \sim 1 \ , \tag{2.2.1}$$

where τ is the optical depth of the source. Alternatively, the spectral peak can be defined by Razin effect [20], the peak frequency is close to the Razin frequency $\nu_R = 2\nu_{pe}^2/3\nu_{Be}$, where ν_{pe} is the electron plasma frequency and ν_{Be} is the electron gyrofrequency. The optically thin region at the frequencies above the Razin frequency is assumed to obey a power-law:

$$J \propto \nu^{-\alpha} , \tag{2.2.2}$$

where α is the spectral index of the emission, which is specified by the spectral index δ in the electron energy distribution. In the ultrarelativistic approximation we have [21, 22]

$$\alpha = \frac{\delta - 1}{2} , \tag{2.2.3}$$

in some frequency range that depends on low-energy and high-energy cutoffs in the energy distribution of fast electrons [23, 24], while for mildly relativistic case in the limits $10 < \nu/\nu_{Be} < 100$ it was proposed by the Ref. [25] that

$$\alpha = 0.90\delta - 1.22 . \tag{2.2.4}$$

The above relation between α and δ is only usable in a limited range, and generally δ should be taken as an unknown parameter [26]. We should note, however, that the exact formalism [27] does not give a single spectral index. On the contrary, α changes continuously with frequency as shown in Sect. 2.3. At low frequencies ($\nu/\nu_{Be} < 20$), the index α increases remarkably compared with Eqs. (2.2.3) and (2.2.4) for tenuous plasma. On the other hand, if the plasma density in a source is high enough, the spectral index decreases in a rather wide optically thin region [28]. These two reasons are shown to lead to considerable corrections when estimating δ from solar MW observations [9].

The emission of ultrarelativistic electrons is linearly polarized, so the degree of circular polarization is zero [29]. However, in the mildly relativistic approach, the emission is mostly circularly polarized [27, 30]. The sense of polarization corresponds to X-mode in the optically thin region, while to O-mode in the optically thick region. The degree of polarization is large for small view angles (quasi-parallel to the magnetic field direction) and small for large view angles (quasi-transverse radiation), respectively.

Most of these commonly accepted properties are subject to change for anisotropic pitch-angle distributions [12], as shown in Sect. 2.3.

2.2.1 Emissivity and Self-absorption Coefficient

General expressions for the emissivity (j_σ) and self-absorption coefficient (κ_σ) are written to [12, 27, 31, 32]:

$$j_\sigma(\omega,\vartheta)=\frac{4\pi^2e^2}{c}\frac{\omega^2[\partial(\omega n_\sigma)/\partial\omega]}{(1+K_\sigma^2+\Gamma_\sigma^2)}\sum_{n=1}^{\infty}\int\gamma_e\beta^2d^3p(1-\mu^2)f(\mathbf{p})$$
$$\times\left[\frac{\Gamma_\sigma\sqrt{1-\eta^2}+K_\sigma(\eta-\beta\mu n_\sigma)}{n_\sigma\beta\sqrt{(1-\mu^2)(1-\eta^2)}}J_n(z)+J_n'(z)\right]^2 \tag{2.2.5}$$
$$\times\,\delta(\gamma_e\omega-n\omega_{Be}-\gamma_e\beta n_\sigma\eta\mu\omega)\ ,$$

$$\kappa_\sigma(\omega,\vartheta)=-\frac{\pi\omega_{pe}^2}{(1+K_\sigma^2+\Gamma_\sigma^2)\,(2n_\sigma[\partial(\omega n_\sigma)/\partial\omega])\,v_\sigma N}\sum_{n=1}^{\infty}\int d^3p(1-\mu^2)$$
$$\times\left[\frac{\Gamma_\sigma\sqrt{1-\eta^2}+K_\sigma(\eta-\beta\mu n_\sigma)}{n_\sigma\beta\sqrt{(1-\mu^2)(1-\eta^2)}}J_n(z)+J_n'(z)\right]^2 \tag{2.2.6}$$
$$\times\left[p\frac{\partial}{\partial p}-(\mu-n_\sigma\beta\eta)\frac{\partial}{\partial\mu}\right]f(\mathbf{p})\,\delta(\gamma_e\omega-n\omega_{Be}-\gamma_e\beta n_\sigma\eta\mu\omega)\ ,$$

where $f(\mathbf{p})$ is the distribution function of fast electrons defined as

$$f(\mathbf{p})=\frac{N_e}{2\pi}f_1(p)f_2(\mu),\qquad\int f(\mathbf{p})p^2dpd\mu d\varphi=N_e\ , \tag{2.2.7}$$

here, $\mu=\cos\theta$, and θ is the pitch-angle of electrons, both f_1 and f_2 are satisfied with their normalized conditions:

$$\int f_1(p)p^2dp=1,\qquad\int_{-1}^{1}f_2(\mu)d\mu=1\ . \tag{2.2.8}$$

The optical thickness $\tau_\sigma=\kappa_\sigma L$, and L is the scale of radio source along the LOS; $\omega_{pe}=2\pi\nu_{pe}$, and $\omega_{Be}=2\pi\nu_{Be}$; N and N_e are respectively the number density of the background plasma and fast electrons; $\eta=cos\vartheta$, and ϑ is the view angle; $J_n(z)$ and $J_n'(z)$ are the Bessel function and its derivative over argument z, respectively, $z=(\omega/\omega_{Be})\gamma_e n_\sigma\beta\sqrt{(1-\mu^2)(1-\eta^2)}$, and $\beta=v/c$ is the dimensionless particle velocity; n is the harmonic number of ω_{Be}; and n_σ is the refractive index of the σ-mode wave.

The polarization vector $\mathbf{e}_{\sigma,\mathbf{k}}$ of σ-mode wave ($\sigma=1$ for O-mode and $\sigma=-1$ for X-mode) in the reference frame with z-axes along the magnetic field B and k-vector in the (y,z) plane is

$$\mathbf{e}_{\sigma,\mathbf{k}}=\frac{(1,\ i\alpha_\sigma,\ i\beta_\sigma)}{(1+\alpha_\sigma^2+\beta_\sigma^2)^{1/2}}\ , \tag{2.2.9}$$

where,

$$\alpha_\sigma=K_\sigma\cos\vartheta-\Gamma_\sigma\sin\vartheta,\quad\beta_\sigma=K_\sigma\sin\vartheta+\Gamma_\sigma\cos\vartheta\ , \tag{2.2.10}$$

$$K_\sigma=\frac{2\sqrt{u}(1-v)\cos\vartheta}{u\sin^2\vartheta-\sigma(u^2\sin^4\vartheta+4u(1-v)^2\cos^2\vartheta)^{1/2}},\qquad K_XK_O=-1\ , \tag{2.2.11}$$

$$\Gamma_\sigma = \frac{v\sqrt{u}\sin\vartheta + uvK_\sigma\cos\vartheta\sin\vartheta}{1-u-v(1-u\cos^2\vartheta)}\ , \tag{2.2.12}$$

$$v = \omega_{pe}^2/\omega^2, \qquad u = \omega_{Be}^2/\omega^2\ . \tag{2.2.13}$$

The plasma refractive indices have the form:

$$n_\sigma^2 = 1 - \frac{2v(1-v)}{2(1-v) - u\sin^2\vartheta + \sigma(u^2\sin^4\vartheta + 4u(1-v)^2\cos^2\vartheta)^{1/2}}\ . \tag{2.2.14}$$

Before doing the numerical calculations the integrals over the azimuth angle ϕ and over μ were taken analytically (with the use of δ-function). After the integration we have:

$$j_\sigma(\omega,\vartheta) = \frac{8\pi^3e^2}{cn_\sigma|\eta|}[\partial(\omega n_\sigma)/\partial\omega]\frac{\omega\frac{\partial(\omega n_\sigma)}{\partial\omega}}{(1+K_\sigma^2+\Gamma_\sigma^2)}\sum_{n=1}^{\infty}\int\beta p^2dp(1-\mu^2)f(\mathbf{p})$$
$$\times\left[\frac{\Gamma_\sigma\sqrt{1-\eta^2}+K_\sigma(\eta-\beta\mu n_\sigma)}{n_\sigma\beta\sqrt{(1-\mu^2)(1-\eta^2)}}J_n(z)+J_n'(z)\right]^2|_{\mu=\mu_*}\ , \tag{2.2.15}$$

$$\kappa_\sigma(\omega,\vartheta) = -\frac{\pi^2\omega_{pe}^2}{\omega|\eta|v_\sigma N(1+K_\sigma^2+\Gamma_\sigma^2)\left(n_\sigma^2\frac{\partial(\omega n_\sigma)}{\partial\omega}\right)}\sum_{n=1}^{\infty}\int\frac{p^2}{\gamma_e\beta}dp(1-\mu^2)$$
$$\times\left[\frac{\Gamma_\sigma\sqrt{1-\eta^2}+K_\sigma(\eta-\beta\mu n_\sigma)}{n_\sigma\beta\sqrt{(1-\mu^2)(1-\eta^2)}}J_n(z)+J_n'(z)\right]^2$$
$$\times\left[p\frac{\partial}{\partial p}-(\mu-n_\sigma\beta\eta)\frac{\partial}{\partial\mu}\right]f(\mathbf{p})|_{\mu=\mu_*}\ , \tag{2.2.16}$$

where,

$$\mu_* = \frac{\gamma_e\omega - n\omega_{Be}}{\gamma_e\beta n_\sigma\eta\omega}, \qquad |\mu_*| \le 1\ . \tag{2.2.17}$$

2.2.2 *Formation of GS Spectrum*

The idealized GS spectrum has a single peak at $\nu = \nu_{pk}$, whose low-frequency turnover is either due to GS self-absorption [33] or due to Razin suppression [20, 28]. Also, the low-frequency turnover can be formed due to the thermal free-free absorption in the outer dense layers of the atmosphere [34]. This can happen, for instance, in the chromosphere. However, a strong free-free absorption is almost improbable in the hot coronal flaring loops. So we do not consider it in the following sections.

In the GS self-absorption case, the peak frequency occurs near optical depth unity:

$$\tau(\nu_{pk}) = \kappa_\nu L \sim 1 \ , \tag{2.2.18}$$

where κ_ν is the absorption coefficient, and L is the source thickness. In the case of Razin suppression (for classical synchrotron emission), the low-frequency turnover is associated with the Razin frequency:

$$\nu_R = \frac{2\nu_{pe}^2}{3\nu_{Be}} \approx 20 \ \frac{n_0}{B_{e\perp}} \ . \tag{2.2.19}$$

So it is proportional to the ratio of plasma number density n_0 to the perpendicular component of magnetic field strength $B_{e\perp}$. High ambient density and/or low magnetic field strength act to raise ν_R.

In the following sections, we consider how different conditions in flaring loops can influence the higher and lower frequency parts of the GS spectrum. As well, we consider how differences in the observed GS spectrum dynamics can be used for distinguishing between different mechanisms of the MW spectrum formation.

2.2.3 Influence of Magnetic Field Strength

In the calculation of electron spectral index δ from the slope of MW spectrum in an optically thin radio source, it is often neglected the fact that the slope of MW spectrum is affected by the local magnetic field strength. This neglect originates from the simplified relations between δ and synchrotron [22] and GS [25] spectral index: $\alpha = (\delta - 1)/2$ and $\alpha = 0.90\delta - 1.22$, respectively.

However, the GS spectral index with lower harmonic numbers in a low-density plasma ($\omega_{pe} < \omega_B$) is enlarged with increasing of magnetic field, as a general feature of GS emission produced by a power-law distribution of electrons, which can be obtained directly from the strict expressions for the emissivity and self-absorption coefficient [10, 27].

For illustration of this feature, we consider a homogeneous radio source with a density of $10^9\,\mathrm{cm}^{-3}$, and the angle between the magnetic field and LOS is 80°. It is assumed that the radio source is filled in with an isotropic power-law distribution of NT electrons ($N(E) = kE^{-\delta}$, $\delta = 5$). Figure 2.2a shows the GS spectrum produced by NT electrons when $B = 120\,\mathrm{G}$, and Fig. 2.2b shows the variation of high-frequency ($f > f_{max}$) spectral index with frequency under different magnetic fields ($B = 60$, 120, 360, and 720 G).

It is obvious from Fig. 2.2b that the GS spectral index α is enlarged with increasing of magnetic field strength. For different magnetic field values, the variation of α at a given frequency may reach 0.5 and even 1.5. Comparison of the calculated α

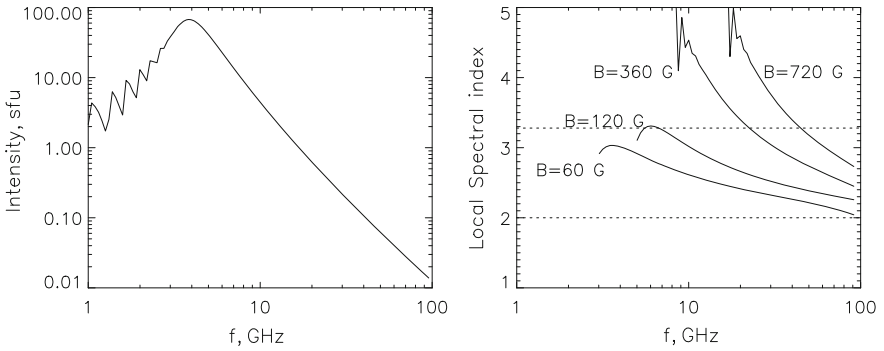

Fig. 2.2 The effect of magnetic field strength on the high-frequency slope of GS spectrum

with the approximated ultra and moderately relativistic values, $\alpha = (\delta - 1)/2$ (the lower horizontal line), and $\alpha = 0.90\delta - 1.22$ (the upper horizontal line), shows large differences between them.

2.2.4 Influence of Self-Absorption

In this section, as well as in Sects. 2.2.5–2.2.7 we follow paper [35] and carry out numerical simulations of the peak frequency dynamics for homogeneous sources using the exact formalism for the GS emissivity and absorption coefficient.

Electrons in the source are assumed to have a power-law distribution and to be distributed isotropically. The time profile of NT electrons is chosen to have a Gaussian shape with effective duration and maximum time defined by the values t_0 and t_m, respectively:

$$n(E,t) = k \exp\left[-\frac{(t-t_m)^2}{t_0^2}\right] E^{-\delta} , \tag{2.2.20}$$

where E is the electron energy in MeV in the range 0.01–500 MeV, δ is electron spectral index, and k is a constant factor. We consider the cases with low- and high plasma density, with constant and varying electron energy power-law index, and a case in which the plasma density increases with time. Figure 2.3 shows the spectral evolution of GS emission in a low-density plasma, for parameters such that the low-frequency turnover is entirely determined by GS self-absorption and Razin suppression is almost negligible at $\nu \geq 2$ GHz. The increase of GS intensity on the rise phase occurs due to the increase in number of energetic electrons and leads to the corresponding increase of $\nu_{\rm pk}$ (see panels *a* and *d*). On the decay phase, the behavior is symmetrical. Note the low initial value ($\nu_{\rm pk}$ can be as low as 1.2 GHz) and large range of peak frequency variations: $\nu_{\rm pk}$ changes by a factor of two when $S_{\rm pk}$ changes by an order of magnitude. Note also a strong change (two orders of magnitude) in

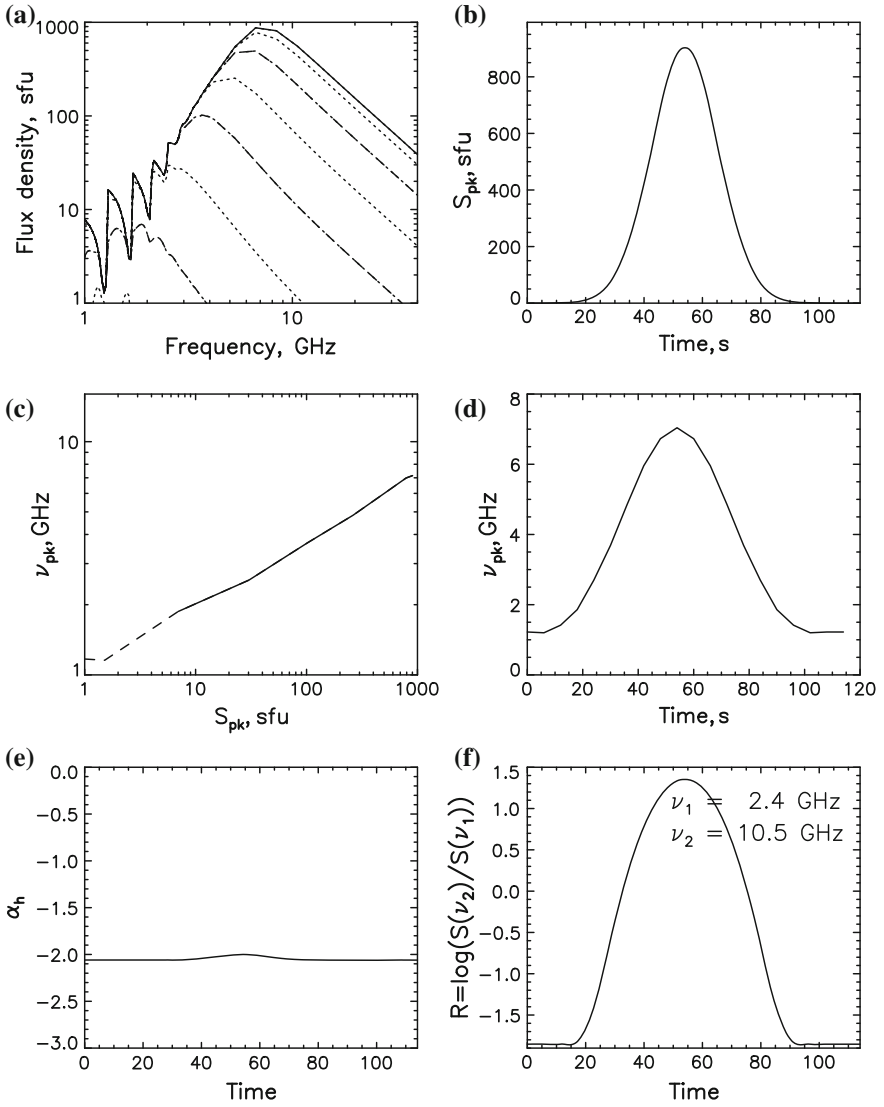

Fig. 2.3 Spectral evolution of GS emission in a low-density plasma ($n_0 = 5 \times 10^9\,\mathrm{cm}^{-3}$, $B = 150\,\mathrm{G}$, $t_\mathrm{m} = 54\,\mathrm{s}$, $t_0 = 12\,\mathrm{s}$, $\delta = 4.0$, $L = 10^9\,\mathrm{cm}$, $\phi = 17''$, $k = 10^4$). For these parameters, the low-frequency turnover is determined by GS self-absorption. Panel **a** Flux density spectrum at different times on the rising (dotted lines) and decay (dashed lines) phases. Panel **b** Peak flux time profile $S_\mathrm{pk} = S(\nu_\mathrm{pk})$. Panel **c** Dependence of the peak frequency on the peak flux on a log scale (solid and dashed lines for the rise and decay, respectively). Panel **d** Peak frequency evolution. Panel **e** High-frequency spectral index evolution. Spectral index is defined by fitting of a calculated spectrum (panel **a**) at frequencies $\nu > \nu_2$, $\nu_2 = 1.5\nu_\mathrm{pabs}$. Panel **f** Evolution of logarithm of the flux ratio R at $\nu_2 > \nu_\mathrm{pk}$ and $\nu_1 < \nu_\mathrm{pk}$

the ratio of fluxes, R, at high $\nu_2 > \nu_{\rm pk}$ and low $\nu_1 < \nu_{\rm pk}$ frequencies, which occurs due to very small variation of the flux at ν_1 where the source is optically thick. For definiteness, we define $\nu_1 = (\nu_{pabs} + \nu_{min})/2$, $\nu_2 = (\nu_{pabs} + \nu_{max})/2$, where ν_{pabs} is the absolute maximum of $\nu_{pk}(t)$ during a burst, and ν_{min}, ν_{max} indicate the frequency range in which the burst was detected. Panel *c* shows the dependence of the peak frequency on the peak flux. The dependence is roughly a power-law, $\nu_{\rm pk} \propto S_{\rm pk}^{\beta}$ with $\beta = 0.27$, in agreement with the observations (see Fig. 3.4 in Sect. 3.1.2.5) and lower than the prediction obtained from the simplified formulas for GS emission by Dulk and Marsh [25] (see Sect. 3.1.2.6).

2.2.5 *Influence of High Plasma Density: Razin Effect*

The effect of density (namely, the role of wave dispersion in a medium) on the emission of electromagnetic (EM) waves by fast electrons was discovered during early fifties of 20th century. In particular, Tsytovich (1951) [36] studied the effect of density on emission in medium with the refraction index $n > 1$. Ginzburg (1953) [37] showed that the decrease of emissivity of the synchrotron radiation becomes important in dense plasmas ($n < 1$), while Ter-Mikaelyan (1954) [38] examined the effect of density on the Bremsstrahlung. If the plasma parameter $Y = \nu_{pe}/\nu_{Be}$ is large ($Y \gg 1$), the density effect is known to provide the strong deformation of the synchrotron emission frequency spectrum (Razin effect or Razin suppression): (*a*) exponential decrease of the emissivity and absorption coefficient at low frequencies [20], $\nu < \nu_R$, and (*b*) considerable flattening of the original synchrotron power-law spectrum, $F_\nu \sim \nu^{-\alpha}$, at higher frequencies [28].

The physical meaning of the influence of the medium can be understood from the simple consideration of Lienard–Wiechert potentials [36] $\mathbf{A}$ and ϕ in a medium with index of refraction $n < 1$:

$$\mathbf{A}(t) = \left[\frac{ev}{c(r - n\mathbf{r}\cdot\mathbf{v}/c)}\right]_{t-n\frac{r}{c}}, \tag{2.2.21}$$

$$\phi(t) = \left[\frac{e}{n^2(r - n\mathbf{r}\cdot\mathbf{v}/c)}\right]_{t-n\frac{r}{c}}, \tag{2.2.22}$$

where e is the electron charge and $\mathbf{r}$ is the radius-vector of the electron moving with velocity $\mathbf{v}$ taken at the retarded time $t' = t - nr/c$. It follows from Eqs. (2.2.21) and (2.2.22) that the emissivity of a single electron depends strongly on the ratio of the electron velocity v to the wave phase velocity $v_{ph} = c/n$. In vacuo, $n = 1$ and therefore the effectiveness of emission is very high when the electron velocity is close to the speed of light c, since the denominator in Eqs. (2.2.21) and (2.2.22) tends to 0. In a plasma, $n < 1$ and the denominator can never be very close to 0, even if $v \simeq c$. So a relativistic electron has an emission efficiency comparable with a nonrelativistic one, i.e., much lower than in vacuo. This causes a strong suppression of radiation

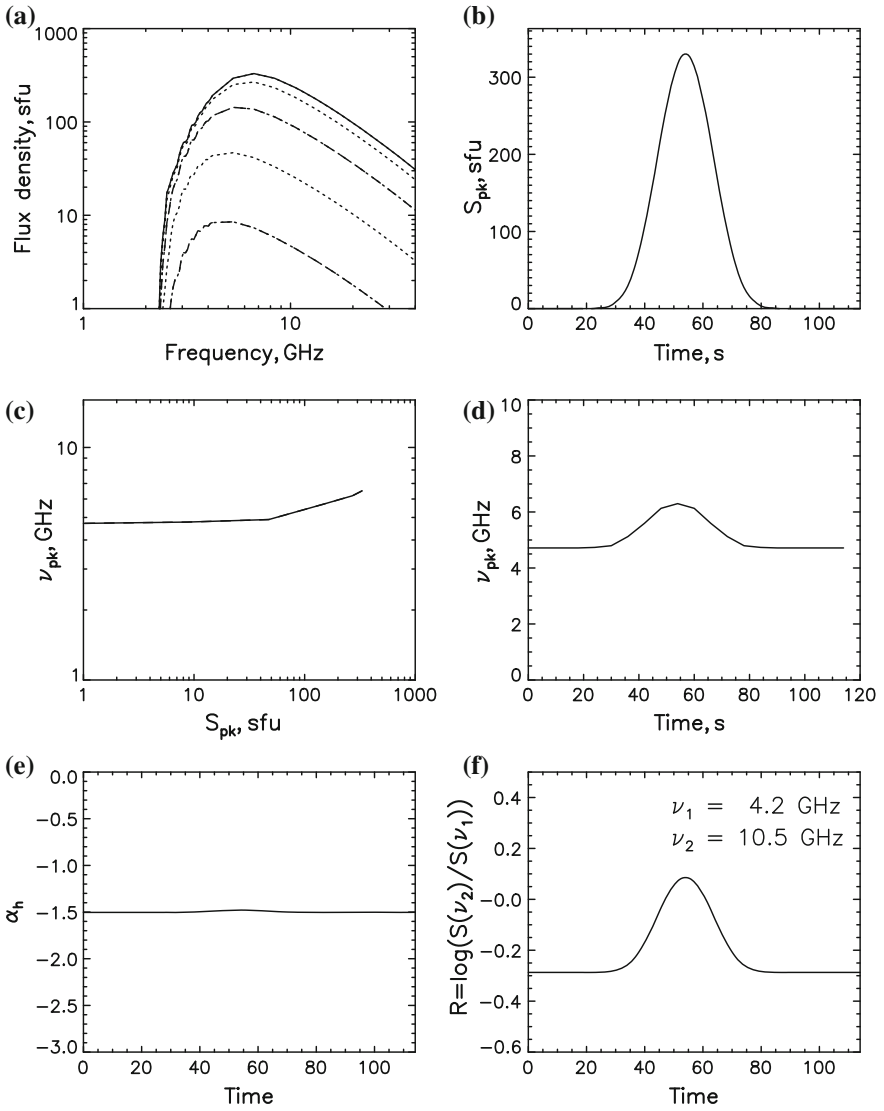

Fig. 2.4 Spectral evolution of GS emission in the presence of high density plasma: $n_0 = 5 \times 10^{10}\,\mathrm{cm}^{-3}$. The other parameters are same as in Fig. 2.3

in the plasma, especially at lower frequencies since in plasma $n^2 \simeq 1 - \nu_{pe}^2/\nu^2$. The Razin effect is predominantly a relativistic effect. As follows from Eqs. (2.2.21) and (2.2.22), the strong influence of the refraction coefficient n is only possible if the electron velocity v is close to the speed of light c.

Figure 2.4 shows the spectral evolution of GS emission for relatively high plasma density $n_0 = 5 \times 10^{10}\,\mathrm{cm}^{-3}$. In the beginning of the rise phase and during the late

decay phase the radio source is optically thin at low frequencies due to the Razin effect. Due to the high ratio of n_0/B, the values of ν_{pk} are quite high, ~5 GHz. Although the flux density is changing, the peak frequency remains nearly constant during these periods. The low- and high-frequency fluxes change nearly at the same rate leading to $R = const$. However, near the maximum of S_{pk}, when the column density of NT particles becomes high enough, the source becomes optically thick at $\nu \leq \nu_{pk}$, despite the Razin suppression, and the spectral evolution of ν_{pk} follows the familiar behavior where the self-absorption plays the main role. Note, however, the reduced range of this peak frequency variation, only about ~30% for an order of magnitude change in S_{pk}. The variation of R (<0.5 order of magnitude) is also considerably smaller than in the case of pure self-absorption (Fig. 2.3). The slope of ν_{pk} vs. S_{pk} is much flatter than in the absence of the Razin suppression, with $\beta < 0.17$. This is comparable to the values of β found for the events with moderate $\Delta\nu_{pk}/\nu_{pk}$ (see Sect. 3.1.2). It is clear that for smaller k (defining the number density of energetic electrons) the amplitude of the ν_{pk} variation and the value of β will decrease. With sufficiently small k, we get no visible change at all in ν_{pk}. Another remarkable feature of the case with high plasma density (high level of Razin suppression) is a flatter high-frequency spectral slope at $\nu > \nu_{pk}$. It follows from Figs. 2.3e and 2.4e that the difference in the spectral indices is 0.5.

The low-frequency turnover is determined by two effects: (1) by the Razin suppression on the initial rising phase and late decay phase, and (2) by the self-absorption near the maximum of the simulated burst. Note the high initial value and small range of the peak frequency and R variations. The spectral evolution shown in Fig. 2.4 is similar to the ν_{pk} evolution in Fig. 3.10 (see Sect. 3.1.2.5), while bursts with this spectral evolution indicate the presence of considerable Razin suppression, and serve as a diagnostic of high plasma density to magnetic field ratio in flaring loops.

2.2.6 *Razin Effect and Electron Power-Law Index*

We show in Fig. 2.5 the spectral evolution when both spectral hardening and Razin suppression are present. We expect a higher ν_{pk} for flatter electron spectra (lower δ). We assume a linear change of δ from 5 to 3 during the burst. To show the pure effect, here we have set the number density of energetic electrons sufficiently low that GS self-absorption is never important, even near the burst maximum. As expected, the peak frequency increases throughout the rising and decay phases while the electron energy spectrum continuously hardens (panel d). While δ changes from 5 to 3, the peak frequency increases from 3.5 up to 8 GHz. The steepest increase of ν_{pk} occurs in the late decay phase, where the electron spectrum is hardest. Note also the considerable increase of the flux ratio during the burst: almost an order of magnitude (panel f). This happens since at both frequencies, ν_1 and ν_2, the source is optically thin. Therefore, due to the electron spectral hardening, the flux at low frequency increases slower on the rise phase of the burst and decreases faster on the decay phase.

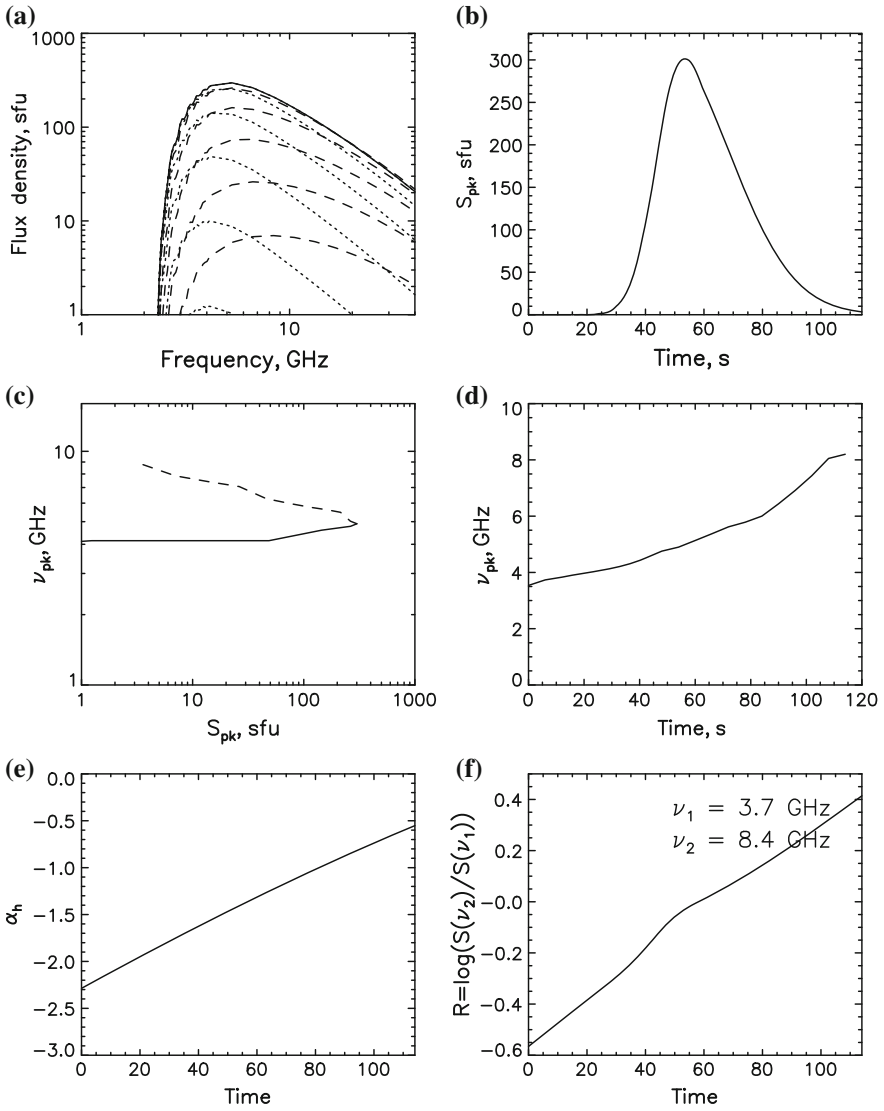

Fig. 2.5 Spectral evolution of GS emission in the presence of high-density plasma and continuous electron spectrum hardening, $\delta = 4.0 - (t - t_{max})/t_{max}$. The other parameters are same as in Fig. 2.4, except $k = 10^3$ and $\phi = 45''$. Note the continuous increase of ν_{pk} and R on the rise and decay phases. On panels **a** and **c** solid line is for the rising phase and dashed line for the decay phase

Finally, in Fig. 2.6 we add the effect of GS self-absorption by increasing the number density of energetic electrons by a factor of 10 relative to the case shown in Fig. 2.5. As we saw earlier, the behavior is modified near the peak of the burst due to a temporary increase of the optical thickness of the GS source. At other times, Razin

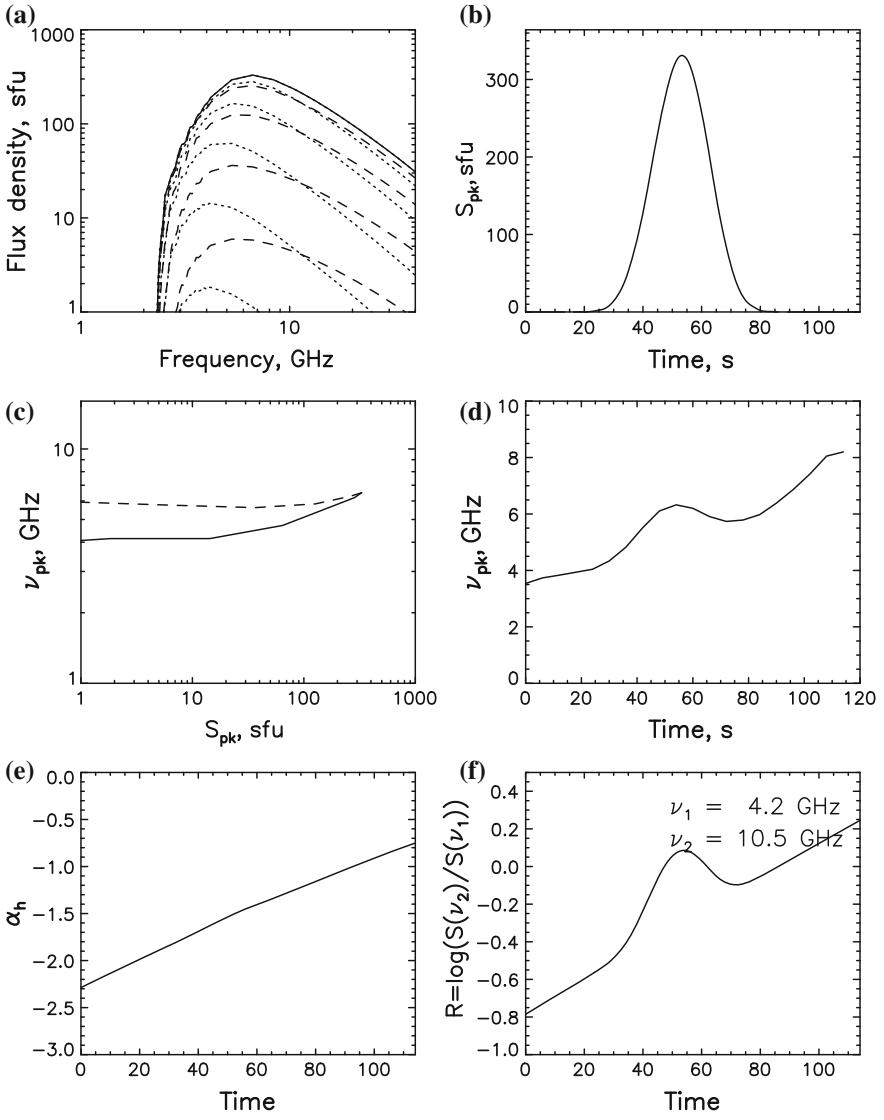

Fig. 2.6 Spectral evolution of GS emission in the presence of high-density plasma and electron spectral hardening, $\delta = 4.0 - (t - t_{max})/t_{max}$. The other parameters are same as in Fig. 2.4. The increase and decrease of ν_{pk} and R in the main part of the emission peak is due to GS self-absorption. A new increase of the peak frequency and the flux ratio with time is clearly seen on the decay phase when the source becomes optically thin at low frequencies and the Razin suppression becomes dominant in defining the spectral peak

suppression is dominant in defining the spectral peak. Note that the ν_{pk} and R on the decay phase (panels c–f) are always higher than on the rising phase similar to the observed behavior described in Sect. 3.1.2.

2.2.7 Plasma Density Increase on the Late Decay Phase

An energy release of sufficient magnitude in a flaring loop will be accompanied by chromospheric evaporation, which will increase the plasma density inside the loop over time. As we have shown, such an increase, if it is great enough, may produce a gradual increase of ν_{pk} in the middle or late decay phase as the Razin effect becomes dominant.

A simulation of this process is shown in Fig. 2.7. We suppose that the plasma density in the loop starts to increase at the burst maximum and increases throughout the decay phase. Near the burst maximum, the dominant low-frequency turnover mechanism is GS self-absorption, but in the late decay phase the Razin effect dominates. This is shown by the fact that the flux at low and high frequencies changes almost at the comparable rate (see panel a, dashed lines). On panels c and d, one can see that just after the flux maximum the peak frequency decreases more slowly than on the rising phase ($\beta = 0.02$) and then starts to increase. To get a 2 GHz increase of ν_{pk} as shown in the panel d, we need only a 50% plasma density enhancement. It is interesting to note that the high-frequency spectral index also increases (spectrum flattens) along with the plasma density on the decay phase (panel e). This occurs due to the already mentioned effect of the medium at high frequencies [20] when $\nu > \nu_{pk}$. Note that this is only true in the restricted frequency range considered here. Asymptotically at large frequencies, the spectral index does not change.

We should say that a similar ν_{pk} increase occurs if the magnetic field in the radio source gradually decreases on the late decay phase. To get the same enhancement of ν_{pk}, we need only 25% decrease of the magnetic field strength. In principle, this can happen as newly reconnected loops appear at higher levels in the corona during continuous energy release and particle acceleration in the helmet coronal structures.

2.2.8 Influence of Plasma Inhomogeneity on GS Spectrum

The influence of inhomogeneity on a total power spectrum is generally to flatten the low-frequency slope [35]. This effect can easily destroy the steep low-frequency slope expected for Razin suppression. To show this, we present a simple model of a flaring loop that is inhomogeneous perpendicular to its axis and consider the radio emission along a line of sight looking down through the top of the loop, as indicated in Fig. 2.8a. The loop axis height is taken to be $h = 6 \times 10^8$ cm, and we choose parameters for which the Razin frequency on the loop axis is $\nu_R = 20 n_e / B = 10$ GHz. Thus, we take the electron density at the apex to be $n_0 = 5 \times 10^{10}$ cm^{-3} and the magnetic field

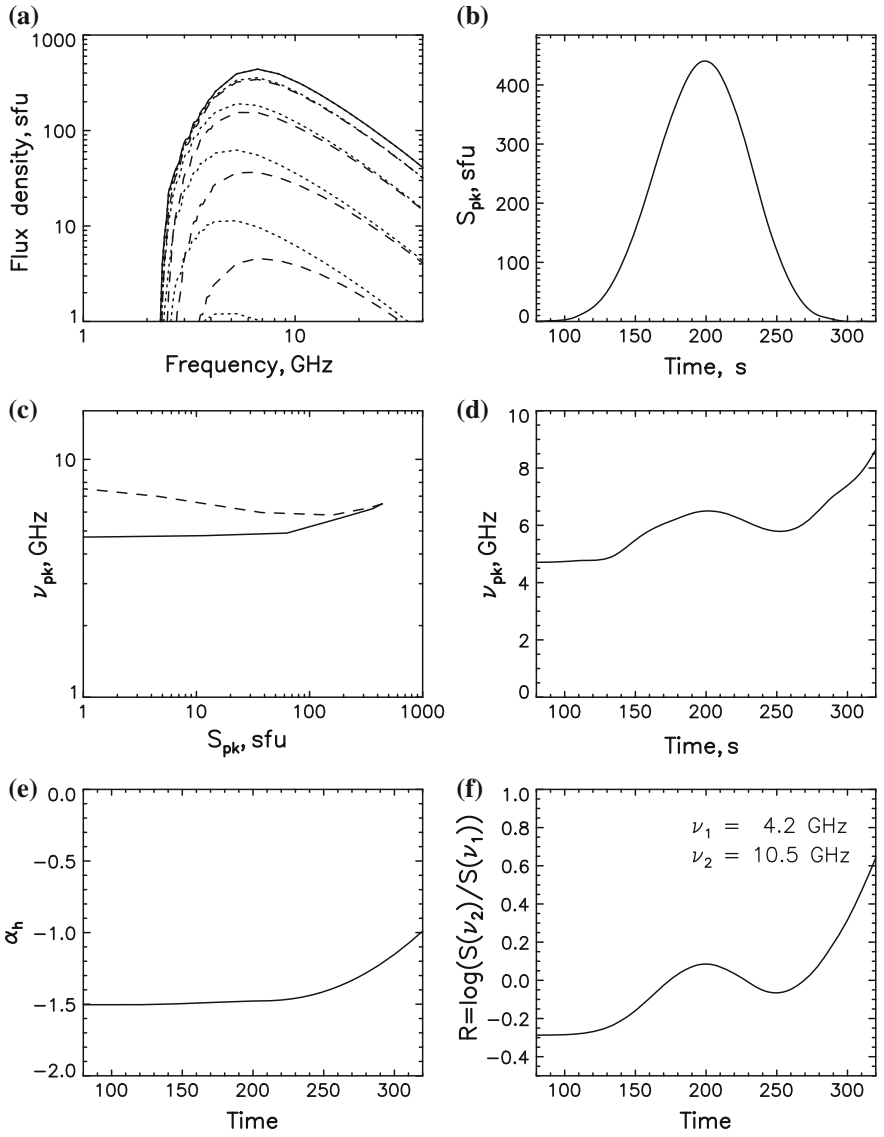

Fig. 2.7 Spectral evolution of GS emission in the case of plasma density increase on the decay phase: $n(t) = n_0[1 + 2(t - t_m)^2/t_m^2]$, where $n_0 = 5 \times 10^{10}\,\mathrm{cm}^{-3}$, $t_m = 200\,\mathrm{s}$. The other parameters are the same as in Fig. 2.4, except $\phi = 20''$. The increase of ν_{pk}, R and α_h on the late decay phase is completely due to the influence of high plasma density (Razin effect)

to be 100 G. To allow for inhomogeneity, we let the magnetic field vary slightly along the line of sight s, according to $B = 120(s_1/(s + s_1))^3$, with $s_1 = 9.6 \times 10^9$ cm. The electron density is taken to have a Gaussian profile along the line of sight, with its

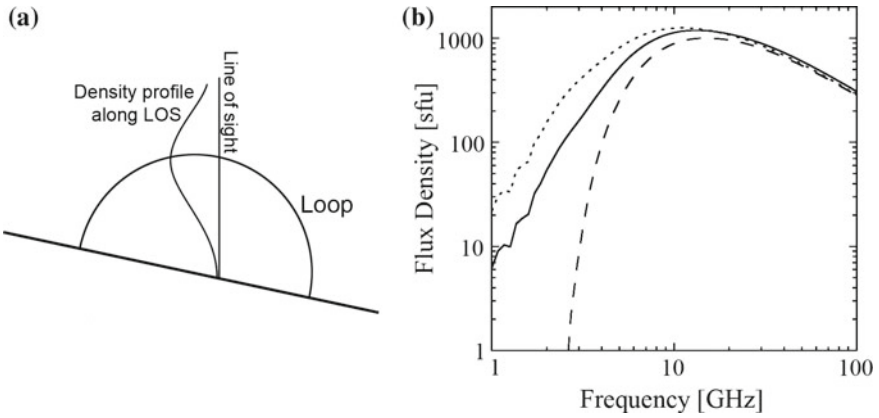

Fig. 2.8 Influence of a plasma density inhomogeneity on the low-frequency slope of the GS spectrum. **a** Sketch of the model geometry used. The Gaussian curve shows the profile of both ambient and energetic electron density along the line of sight (see text for details). **b** Dashed line: The classical Razin suppressed spectrum as it would appear for a homogeneous source with the parameters on the loop axis. Solid line: The spectrum obtained along the line of sight in **a**, due to the inhomogeneity in the model. Dotted line: The spectrum obtained with the same conditions as for the solid line spectrum, but with weighting to account for the radial dependence of area in a cylindrical geometry

maximum at the loop axis, $n_e = n_0 \ \exp\left[-(s-h)^2/s_0^2\right]$, where the $1/e$ width is $s_0 = 3.3 \times 10^8$ cm. Likewise, the high-energy electron distribution across the loop is $N(E > 1\,\mathrm{MeV}) = N_0 \ \exp\left[-1.7\,(s-h)^2/s_0^2\right]$, where $N_0 = 1.1 \times 10^5\,\mathrm{cm}^{-3}$. The angle between the magnetic field and the line of sight is approximately 78°. The electron energy spectrum is given by a single power-law in the range E = 100–31,600 keV with the electron spectral index $\delta = 3.0$.

From this model, employing quite reasonable parameters, we obtain the spectrum in Fig. 2.8b. The emission at the peak frequency and higher frequencies come mainly from the central (most dense) part of the loop, where the Razin effect suppresses the low-frequency emission and forms the spectral peak. On the other hand, the emission at lower frequencies comes mainly from the periphery of the loop, where the plasma density is much lower than at the axes and Razin suppression is almost negligible. As we can see from Fig. 2.8, the overall spectrum has a much flatter low-frequency slope (solid line) than the corresponding spectrum from a homogeneous source (dashed line). Taking into account the fact that in cylindrical geometry the source at lower frequencies becomes larger we get an even flatter spectrum (dotted line). From the spectral shape alone, one cannot distinguish these inhomogeneous spectra from an ordinary GS spectrum (one without Razin suppression).

2.3 Effects of Electron Pitch-Angle Anisotropy

In this section, we consider various effects of NT electron pitch-angle anisotropy on intensity, frequency spectrum, and polarization of GS emission of a homogeneous microwave source [12]. Recently, these effects have been widely used for understanding new properties of the microwave flare emission observed with high spatial resolution, as well as for finding constraints on electron acceleration mechanisms in specific flares [4, 6, 7, 11, 39, 40].

Soon after synchrotron radiation had been proposed as a mechanism for cosmic NT radio emission [41, 42], it was found that a power-law distribution of ultrarelativistic charged particles produced the emission with a power-law spectrum in the optically thin range [21, 22, 24]. After that, the detailed theory of cosmic synchrotron spectrum [20, 33, 43] and polarization [44–46] was developed. While the ultrarelativistic approximation is sufficient for most of the cosmic objects [47], it is not properly correct for the solar case [27, 31, 33].

Thus, a lot of efforts have been done to find simple approximations valid for GS emission produced by nonrelativistic and moderately relativistic electrons [25, 48–53] or to perform exact numerical calculations [54, 55]. While the general formalism [27] allows for arbitrary pitch-angle anisotropy, most of the papers focused on isotropic distributions of fast electrons. A few exceptions only consider weakly anisotropic pitch-angle distributions [49–51], but the authors of these papers did not find any significant effect of the pitch-angle anisotropy on the spectrum and polarization of optically thin part of the GS emission.

Synchrotron radiation by a single ultrarelativistic electron is characterized by prominent directivity along the particle velocity. Indeed, most of the energy is emitted within a narrow cone along the velocity,

$$\vartheta \sim \gamma_e^{-1} = mc^2/E \ , \tag{2.3.1}$$

where γ_e is the Lorentz factor of the electron, m, E are the mass and energy of the electron, c is the speed of light, so $\vartheta \ll 1$ if $\gamma_e \gg 1$. Only extremely strong anisotropy (when the electron distribution function changes noticeably within the small angle) can affect synchrotron emission produced by an ensemble of ultrarelativistic electrons. Hence, any expected anisotropy is entirely unimportant to calculate synchrotron emission from distant objects like supernova remnants or radio galaxies. However, this does not hold for the solar case where semi-relativistic and mildly relativistic electrons contribute the bulk to the GS emission. Thus, the anisotropy (if present) is potentially important for the modeling of solar MW continuum bursts (which are commonly believed to be produced by GS mechanism [13]).

Actually, there is presently ample evidence of the anisotropic pitch-angle distributions of energetic electrons in solar flares. Analysis of particle kinetics effect on the temporal and spectral behavior of optically thin MW and hard X-ray emissions [56–59] indicates a considerable fraction of accelerated particles to be accumulated in the loop. Under flaring loop conditions, the trapping itself suggests that electrons

are lacking within a loss-cone and, therefore, they are distributed anisotropically (perpendicularly to magnetic field lines). Further, and possibly the strongest evidence of the transverse anisotropy, is the existence of the MW LT brightness peak of optically thin GS emission [3, 60], which has been interpreted as tracer of a strong concentration of mildly relativistic electrons trapped and accumulated in the top of a flaring loop [4]. On the other hand, there are many observations of electron beams in the solar corona and flaring loops [61]. We should also mention the strong directivity of gamma ray solar flares discovered from center-to-limb variations of their intensity [62]. Center-to-limb variations of MW bursts are found as well [63]. On top of this, some acceleration processes result in anisotropic particle distributions [1, 64, 65]. Thus, non-isotropic pitch-angle distributions of fast electrons should be rather common. Nevertheless, most of the studies of GS emission neglected the effect of anisotropy except for a few papers [4, 66, 67].

2.3.1 Parameters of Numerical Simulation

To study the effect of pitch-angle anisotropy on GS emission, we varied the type of pitch-angle distributions (loss-cone-like and beam-like) and their parameters such as the widths of the $\sin^N$ and Gaussian functions, θ_c, and μ_0. The effects of these variations were considered for different involved parameters like electron spectral index γ, the parameter $\tau_0 = (\pi L \omega_{Be}/2c)(N_e/N)$ that specifies the optical depth of the source, as well as the plasma frequency to gyrofrequency ratio $Y = \omega_{pe}/\omega_{Be}$. The frequency dependence of intensity, degree of polarization, and spectral index of GS emission were calculated for quasi-parallel and quasi-transverse wave propagation (angles between magnetic field vector and the line of sight $\vartheta = 37^\circ$ and $\vartheta = 78^\circ$ respectively). To be complete, we discuss below both new properties of GS radiation directly related to the effect of pitch-angle anisotropy and some of well-known properties valid for both isotropic and anisotropic distributions.

2.3.2 Pitch-Angle Distributions of Sin^N Type

We start with the anisotropy of the loss-cone type described by $\sin^N$ function [68] with $N = 6$. The size of the loss-cone (parameter θ_c) varies from 0 (isotropic case) to $\pi/2$ (very wide loss-cone, energetic electrons are distributed perpendicular to magnetic field).

$$f_2(\mu) \propto \begin{cases} \sin^N\left(\frac{\pi}{2}\frac{\theta}{\theta_c}\right), & 0 < \theta < \theta_c, \\ 1, & \theta_c < \theta < \pi - \theta_c, \\ \sin^N\left(\frac{\pi(\theta-\pi)}{2\theta_c}\right), & \pi - \theta_c < \theta < \pi. \end{cases} \tag{2.3.2}$$

All calculations were performed for a power-law distribution over momentum

$$f_1(p) = \frac{(\gamma - 3)\, p_0^{\gamma-3}}{p^{\gamma}} \qquad p_{min} < p < p_{max}\ , \tag{2.3.3}$$

with $p_{min} \approx 0.2\ mc$ ($E_{kin} \approx 10\,\mathrm{keV}$) and $p_{max} \approx 20\ mc$ ($E_{kin} \approx 10\,\mathrm{MeV}$). The normalization coefficient in Eq. (2.3.3) is calculated for a broad spectrum with $p_{max} \gg p_{min}$, which falls with increasing momentum. The spectral index γ is related to the energy spectral index δ as follows: $\gamma = 2\delta + 1$ for $E_{kin} \ll mc^2$ and $\gamma = \delta + 2$ for $E_{kin} \gg mc^2$.

2.3.2.1 General Properties

Let us consider a relatively soft electron spectrum ($\gamma = 9$) and tenuous plasma ($Y = 0.3$) with $\tau_0 = 5 \cdot 10^4$, as shown in Fig. 2.9.

The soft electron spectrum is more favorable to observe the spectral structure of the GS radiation. The accepted parameter $Y = 0.3$ is chosen because larger values of Y produce stronger effect of density, while smaller values are favorable to produce coherent electron cyclotron maser emission that is beyond the scope of this paper. For the adopted set of parameters, the optical depth τ exceeds unity only at the lowest integer harmonics of the gyrofrequency: $s = 2$, left panels; $s = 2,\ 3$, right panels.

It is well seen that in the quasi-parallel direction ($\eta = cos\vartheta = 0.8$) the increase of anisotropy is followed by a strong decrease of intensity (up to a factor of 5–10) and an increase of polarization (up to 10–20%) at high frequencies where the radio source is optically thin. The increase of the spectral index α is especially remarkable, $\Delta\alpha \sim 1$ (see left column, bottom). The curves for relatively large anisotropy ($\theta_c = \pi/3, \theta_c = \pi/2$) deviate clearly from the curves for the isotropic distribution and the weak anisotropy $\theta_c = \pi/6$ and show a considerable enhancement over the relativistic value $\alpha = (\delta - 1)/2 = (\gamma - 3)/2 = 3$ that is the asymptotic value for each curve for sufficiently high frequencies.

The physical reasons for such a behavior are as follows. The intensity of emission in the quasi-parallel direction at low frequencies is weakly sensitive to the pitch-angle anisotropy because the low-energy electrons contribute the bulk to the emitted energy at these frequencies. The emission by a single low-energy electron does not display prominent directivity, hence, the actual angular distribution is not so important for the low-frequency emission. However, the directivity increases with the emitting electron energy, which results in lack of higher frequency emission at small view angles ϑ from the loss-cone distribution. The degree of polarization increases with the anisotropy, because O-mode emission at any given frequency is produced by electrons with higher energy than the respective X-mode emission. Accordingly, the directivity of O-mode emission is stronger than for X-mode, providing less favorable conditions for O-mode emission at quasi-parallel directions.

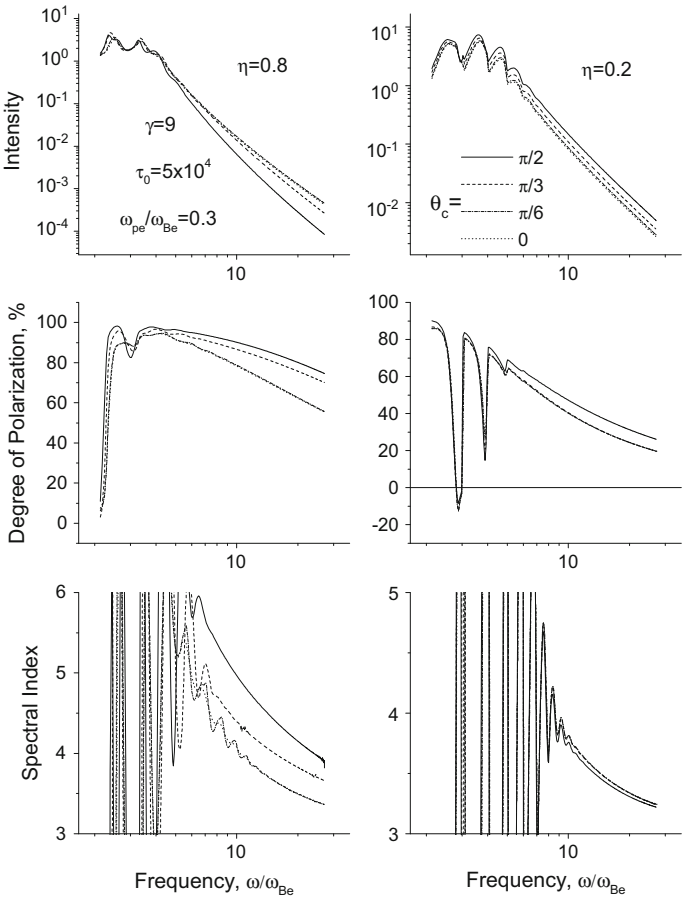

Fig. 2.9 The GS radiation intensity, degree of polarization, and spectral index vs. frequency for various loss-cone angles θ_c in $\sin^N$ pitch-angle distribution. The decrease of intensity and increase of the degree of polarization and spectral index with θ_c are clearly seen for the quasi-parallel propagation ($\eta = 0.8$). The parameters are shown in the figure

The emission properties in the quasi-transverse direction, $\eta = 0.2$ (Fig. 2.9, right panels), are not so sensitive to the loss-cone type anisotropy, which agrees with the above one electron consideration. The level of radiation intensity increases for the anisotropic distributions due to the excess of fast electrons moving at quasi-transverse to the magnetic field directions compared with the isotropic case. The degree of polarization increases noticeably for a wide loss-cone ($\theta_c = \pi/2$) only. The reason for this increase is that electrons from wider range of pitch-angles contribute to the X-mode intensity, than to O-mode intensity (again, because the X-mode radiation is produced by lower energy electrons than the O-mode radiation). The decrease of the spectral index for the anisotropic case ($\theta_c = \pi/2$) is rather weak, while present. The

degree of polarization and the spectral index do not change unless the anisotropy is moderate ($\theta_c = \pi/6, \pi/3$), since the electrons described by the flat (independent on θ) region of the distribution contribute the bulk to the quasi-transverse wave emission.

One can note the wiggles in the spectra (Fig. 2.9, top, both left and right) related to the harmonic structure of the GS radiation that are clearly visible as oscillations of spectral index (Fig. 2.9, bottom). The oscillations are visible up to $\omega/\omega_{Be} \sim 10$, which might be used for the diagnostics of the magnetic field at the source. The number of the oscillations depends on the anisotropy: the most oscillating curve (for $\eta = 0.8$, Fig. 2.9, bottom left) is for $\theta_c = \pi/6$ when the direction of emission is close to the direction of the fastest change of the distribution function with pitch-angle ($\cos\theta_c \approx 0.87$ for $\theta_c = \pi/6$).

2.3.2.2 Influence of Optical Thickness

In general, the influence of the anisotropy on the emission properties in the optically thin region holds qualitatively the same for various parameters in the radio source, while variations of the electron spectral index, the optical thickness or plasma density (the parameter $Y = \omega_p/\omega_B$) can, nevertheless, have an important effect on properties of the radiation.

Generally, an increase of the optical depth produces a shift of the spectral peak toward higher frequencies for both isotropic and anisotropic cases. Figure 2.10 displays the GS radiation for the same parameters as Fig. 2.9 except τ_0 that is increased by four orders of magnitude. The main effect of the large optical depth (for both isotropic and anisotropic cases) is well-developed spectral peak at $\omega/\omega_{Be} \approx 10$. The harmonic structure is no longer dominating the transition from the optically thick to thin region, respectively, the spectral index displays smooth curves with a well-developed maximum; the curves approach the relativistic value ($\alpha = (\gamma - 3)/2 = 3$) at higher frequencies.

The degree of polarization behaves similarly to that in Fig. 2.9 in the optically thin region, while it corresponds mainly to O-mode in the thick region. This property relates primarily to the already mentioned difference in characteristic electron energy producing O- and X-mode emission at a given frequency. Since the level of radiation in the optically thick region can be qualitatively described in terms of "effective temperature" of radiating electrons, the brightness temperature of O-waves is larger than of X-waves, providing the predominant O-polarization, which is well known for the isotropic case. The degree of O-polarization becomes weaker for the anisotropic case, because (as it has been explained above) the loss-cone distribution is more favorable to produce X-waves than the isotropic distribution.

2.3.2.3 Influence of Density

It is noteworthy that the influence of plasma density, as shown in Fig. 2.11, even for a moderate value of Y, there is no an evident suppression at low frequencies.

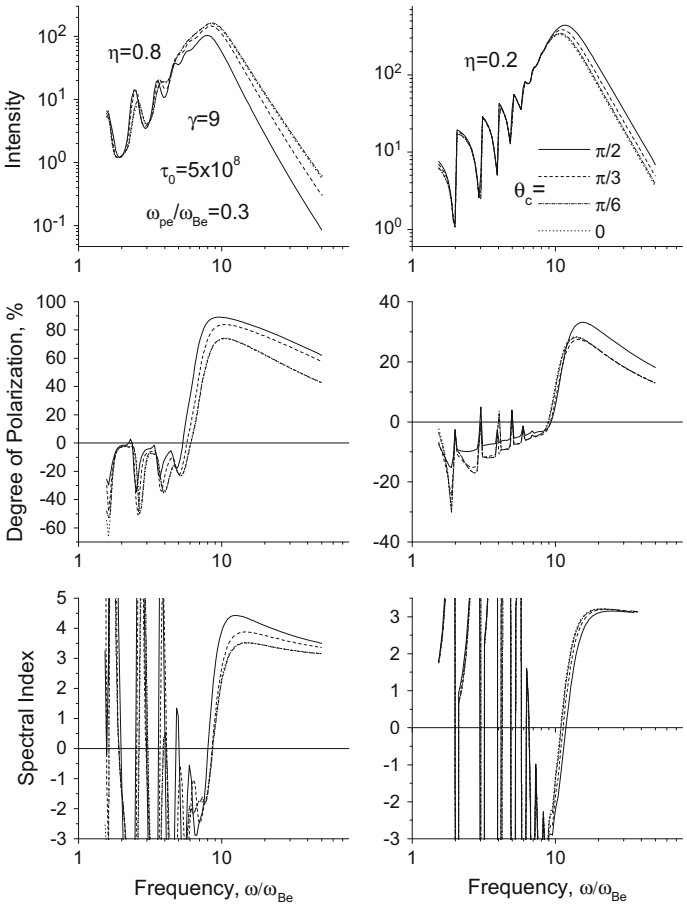

Fig. 2.10 The parameters are basically the same as those in Fig. 2.9, except τ_0 that is increased by four orders of magnitude

For the only small difference of value of Y in the two columns of Fig. 2.11, the following changes are caused by the influence of density: *a*. the optically thick part becomes more smooth in Fig. 2.11b than that in Fig. 2.11a. the X-mode polarization in optically thick part becomes more stronger, in the anisotropic case the polarization sense possibly corresponds to X-mode, but to O-mode in the isotropic case (see Fig. 2.11d), and *c*. the spectral peak becomes more broader, i.e., the spectral index more slowly approaches zero (see Fig. 2.11e).

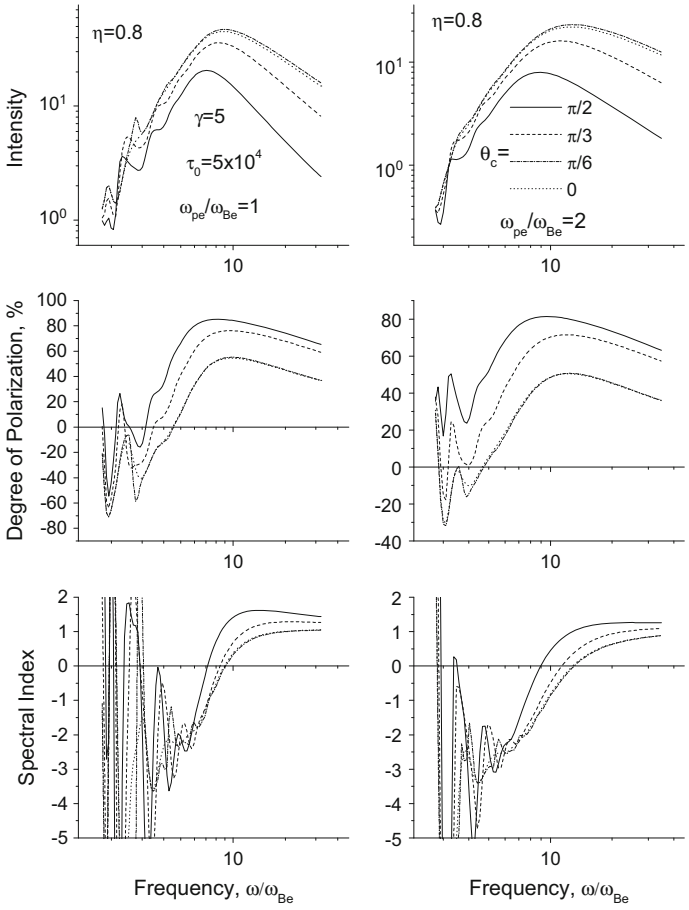

Fig. 2.11 Influence of plasma density (see relevant discussions in Sect. 2.3.2.3)

2.3.2.4 Influence of Optical Thickness and Razin Effect

It is clearly seen in Fig. 2.12 (left column) for the simultaneous influence of optical thickness and Razin effect. The spectral peaks ($\omega/\omega_{Be} = 20 \sim 30$) are mainly determined by the optical thickness, while the Razin effect is also important (Razin frequency is $\omega_R \approx 17\omega_{Be}$). The influence of density is to keep the polarization degree to be positive in the optically thick part, because it more strongly suppresses O-mode than X-mode. The polarization degree may be very large (>60%) in the anisotropic case, while it is smaller than 40% in the isotropic case. When the frequency is smaller than Razin frequency ($\omega < 17\omega_{Be}$), both emissivity and absorption coefficients decrease with an exponential factor. In any case, the emissivity slowly declines to low frequencies until $\tau > 1$, because the emission intensity is determined by the ratio of emissivity and absorption coefficient. However, when τ decreases to a value

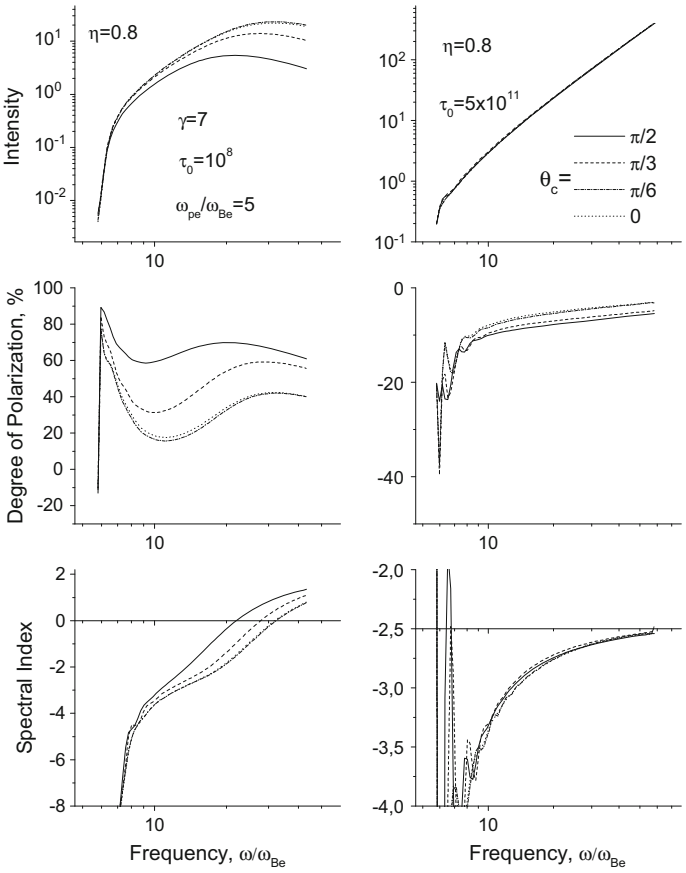

Fig. 2.12 Influence of optical thickness and Razin effect (see relevant discussions in Sect. 2.3.2.4)

smaller than unit, the intensity starts to decline exponentially due to the Razin effect ($\omega < 8\omega_{Be}$), and polarization degree starts to increase (due to a stronger suppression of O-mode than that of X-mode), while the spectral indices at these frequencies decrease rapidly.

The right column of Fig. 2.12 shows an extremely large optical thickness ($\tau_0 = 5 \times 10^{11}$), in which anisotropy has no effect on the emission intensity, while has a weak effect on the polarization degree. It is emphasized that the dependence of spectral index on frequencies: the optically thick GS emission does not display an evident power-law distribution, while it approaches the relativistic value (about $\omega^{2.5}$) at higher frequencies ($\omega > 50\omega_{Be}$), which is available for both isotropic and anisotropic cases.

2.3.3 *Effect of Pitch-Angle Distribution Shape: Gaussian Loss-Cone*

Properties of GS radiation have an exceedingly strong dependence on the functional shape of the pitch-angle distribution of the loss-cone type. To illustrate this, we assume now the distribution to obey Eq. (2.2.7) with $\mu_1 = 0$ and vary the parameter μ_0 from 0.2 to 10 (from narrow pancake-like to almost isotropic distribution).

$$f_2(\mu) \propto exp(-(\mu - \mu_1)^2/\mu_0^2). \tag{2.3.4}$$

2.3.3.1 For Tenuous Plasma

Figure 2.13 displays the plots for relatively tenuous plasma, $Y = 0.5$. The radiation intensity changes by orders of magnitude compared with the isotropic case. Respectively, the difference in the spectral index in the optically thin frequency range is up to a factor of four (left panel, bottom). Remarkable change of polarization occurs as well. The degree of polarization increases in the optically thin region for all view angles: it can exceed 50% for quasi-transverse directions and reach 100% for quasi-parallel directions. Furthermore, the sense of polarization can correspond to X-mode in the optically thick region.

2.3.3.2 For Dense Plasma

The effects hold also for denser plasma. Figure 2.14 displays the plots for $Y = 2$. Generally, the spectral peak moves toward higher frequencies as Y increases, therefore, we reduced the value of τ_0 a little to keep the spectral peak at approximately the same position as in Fig. 2.13. The optically thin region does not change much compared with that in Fig. 2.13, while the spectrum in the optically thick region becomes smoother for denser plasma, since the contribution of low-energy electrons is suppressed by the effect of density. One can also note, that the region of the spectral peak becomes a bit broader for denser plasma for both isotropic and anisotropic cases, which is similar to what we have for $\sin^N$ pitch-angle distribution. Note also that the degree of polarization of the X-mode in optically thick region increases remarkably compared with the case of tenuous plasma, Fig. 2.13.

2.3.3.3 Dependence on Electron Spectral Index

The exact results depend on the electron spectral index γ. For the similar parameters as in Figs. 2.13 and 2.14, but $\gamma = 9$, we found that the spectral index starts to oscillate around the position of the spectral peak. The oscillations become more prominent for smaller τ_0 values than in Figs. 2.13 and 2.14, which are evident from Fig. 2.15 (the Y

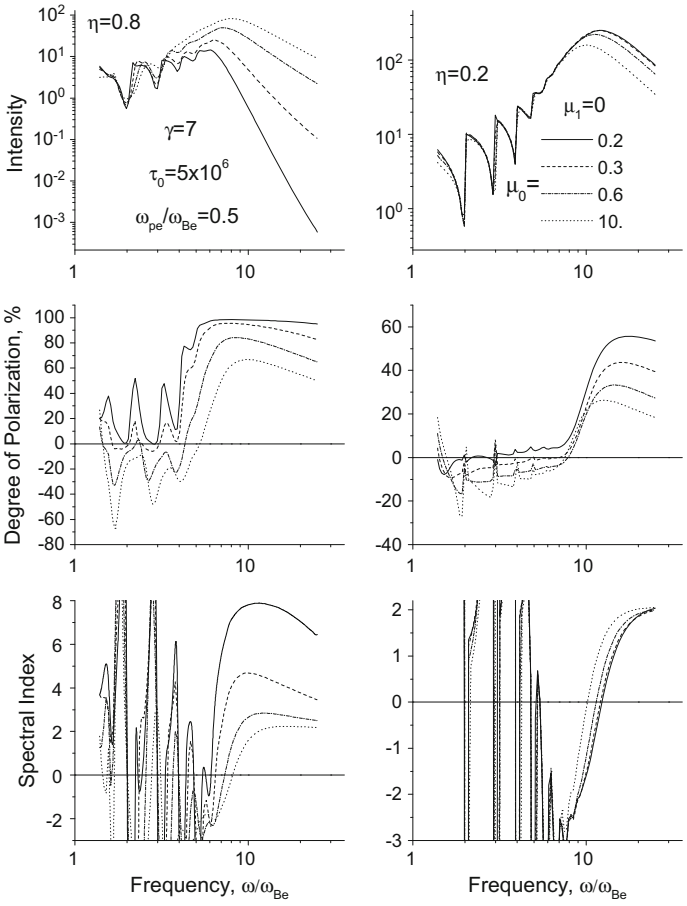

Fig. 2.13 The GS radiation intensity, degree of polarization, and spectral index vs frequency for various μ_0 in the Gaussian pitch-angle distribution $f_2(\mu) \propto exp(-(\mu - \mu_1)^2/\mu_0^2)$ of the loss-cone type ($\mu_1 = 0$). Much stronger dependence on the anisotropy compared with the $\sin^N$ pitch-angle distribution is clearly seen

value is set as 1 to be between 0.5 and 2 adopted for Figs. 2.13 and 2.14 respectively; the variations of Y value within these limits makes no important difference). For this case, the X-mode polarization varies with a frequency between 0 and 100% in the optically thick region. The oscillating behavior of the spectral index in the optically thin region is clearly evident for both quasi-parallel and quasi-transverse directions. The stronger the anisotropy, the more pronounced the oscillations of the spectral index for the quasi-parallel wave emission (Fig. 2.15, bottom left), which is different from the behavior for $\sin^N$ distribution (Fig. 2.9, bottom left, and Fig. 2.11, bottom left), where a moderate anisotropy (with $\theta_c = \pi/6$) produces the most oscillating spectral index.

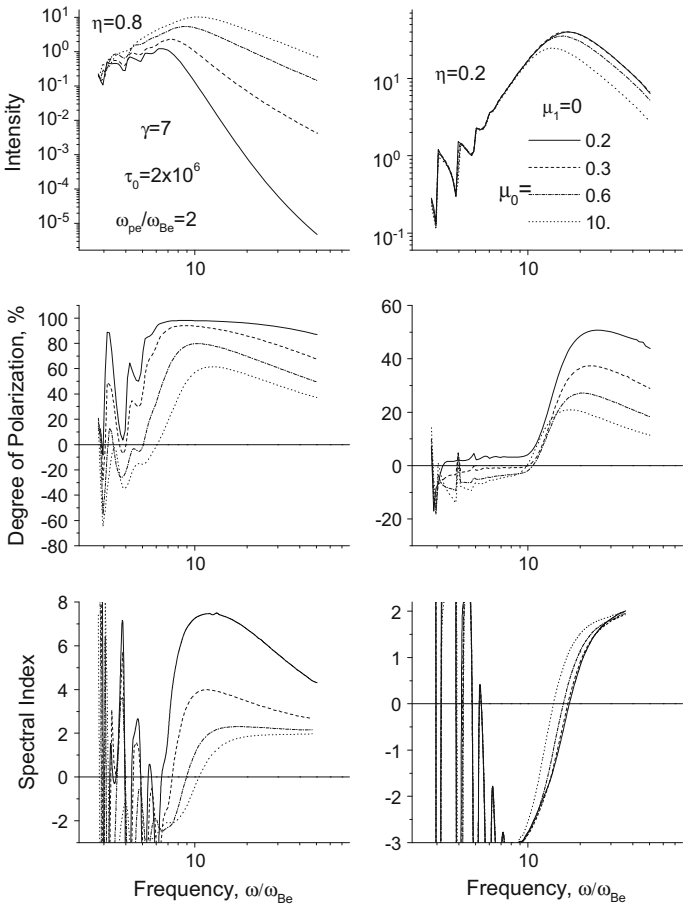

Fig. 2.14 The parameters are the same as those in Fig. 2.13, except for more dense plasma of $Y = 2$

Thus, the properties of GS emission depend substantially on the shape of angular function describing the loss-cone. We can see from Figs. 2.13, 2.14, and 2.15 that the Gaussian anisotropy affects the emission much stronger than the anisotropy of $\sin^N$ type. This is provided by faster decrease of the number of electrons in the loss-cone for the Gaussian case than for the $\sin^N$ case. Generally, for other equal conditions, the loss-cone distributions are more favorable to produce X-mode radiation compared with the isotropic distribution.

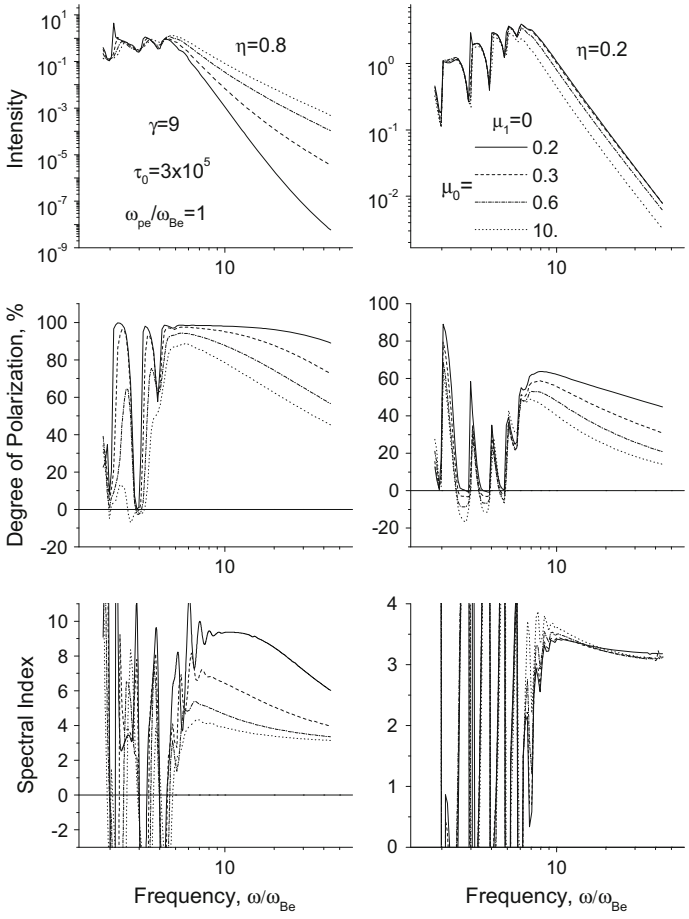

Fig. 2.15 The parameters are almost the same as those in Figs. 2.13 and 2.14, except for a soft electron spectral index of $\gamma = 9$

2.3.4 Effect of Pitch-Angle Distribution Shape: Beam-like Distribution

Let us turn to the analysis of GS emission produced by a beam-like electron distribution. For this purpose, we use the Gaussian distribution [12] with $\mu_1 = 1$.

2.3.4.1 In General

Figure 2.16 displays the plots for the view angles in the half-sphere of the beam propagation. Obviously, the beaming enhances the emission intensity along the beam

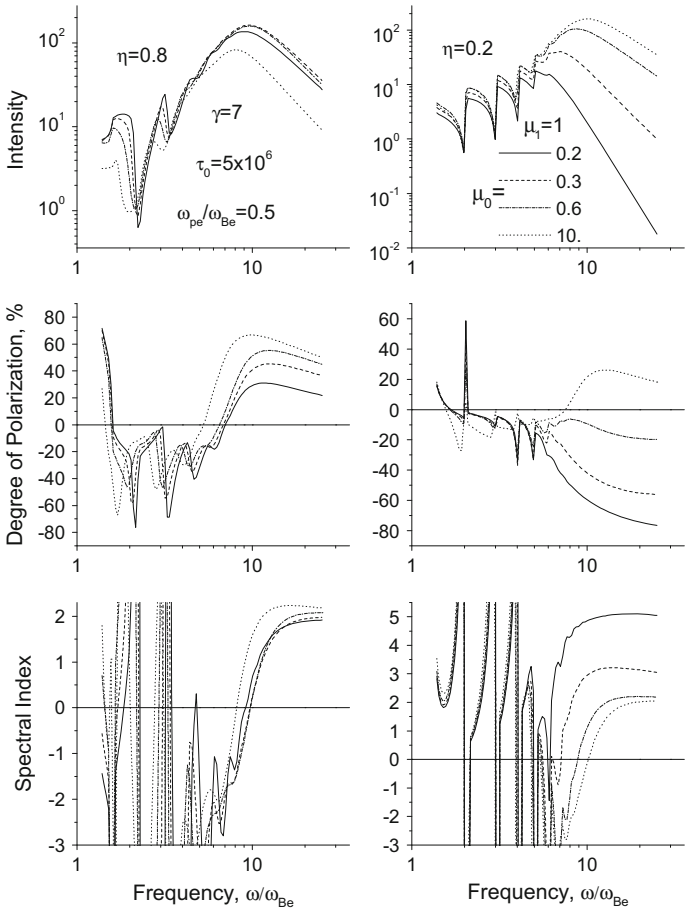

Fig. 2.16 The GS radiation intensity, degree of polarization, and spectral index vs. frequency for various μ_0 in the Gaussian $f_2(\mu) \propto exp(-(\mu-\mu_1)^2/\mu_0^2)$ pitch-angle distribution of the beam-like type ($\mu_1 = 1$). The influence of the anisotropy is especially well seen for the quasi-transverse propagation (right column). Beam-like distributions are more favorable to produce ordinary-mode GS emission even in the optically thin region

($\eta = 0.8$). The scatter of the spectral indices for various beam sizes (μ_0) is not too large, while present. However, we should mention a significant decrease of the degree of polarization in the quasi-parallel direction. While for the isotropic case it exceeds 50%, it can be less than 30% for the anisotropic case–an unusual value for quasi-parallel directions.

The effect of the beam-like anisotropy on polarization appears to be much more prominent for quasi-transverse directions: the dominant sense of polarization is O-mode here for both optically thick and thin regimes. The sense of polarization changes its sign in the optically thin region from the X-mode to the O-mode with increasing

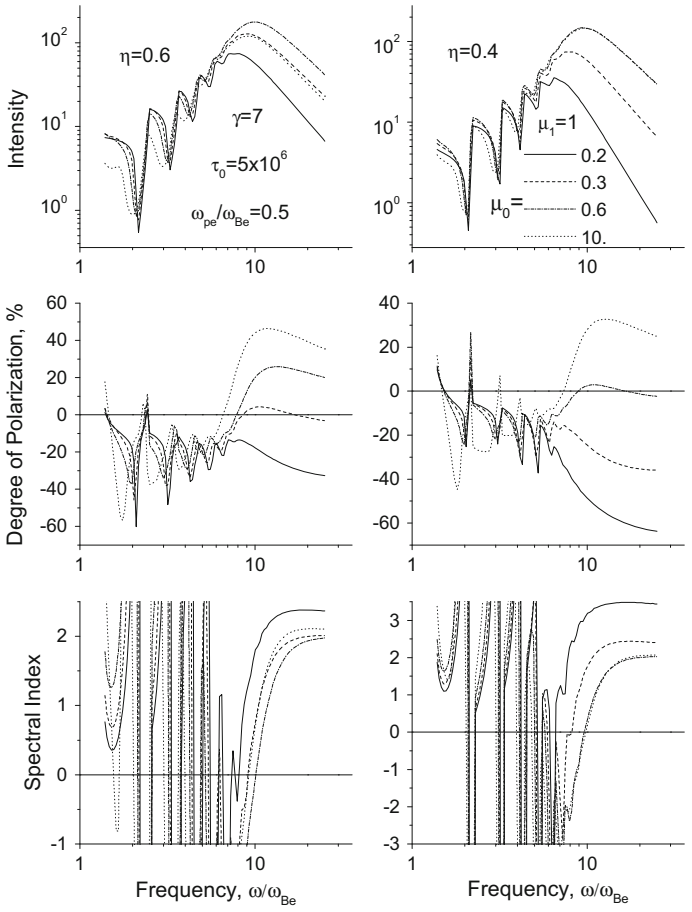

Fig. 2.17 The parameters are almost the same as those in Fig. 2.16, except for different propagation angles of $\eta = 0.6$ and 0.4

the anisotropy. Thus, beam-like distributions are more favorable to produce ordinary-mode GS emission even in the optically thin region. This happens for all view angles in this half-sphere (Fig. 2.17). We should note that the sense of polarization can change with frequency in the optically thin region.

2.3.4.2 In Other Half-Sphere

In the other half-sphere, opposite to the direction of the beam propagation, the situation is opposite: strong X-mode polarization is observed here for all view angles (Fig. 2.18). Extremely large scatter of spectral indices takes place for this case. It is commonly accepted that large spectral indices ($\alpha > 8$) are a signature of GS radiation

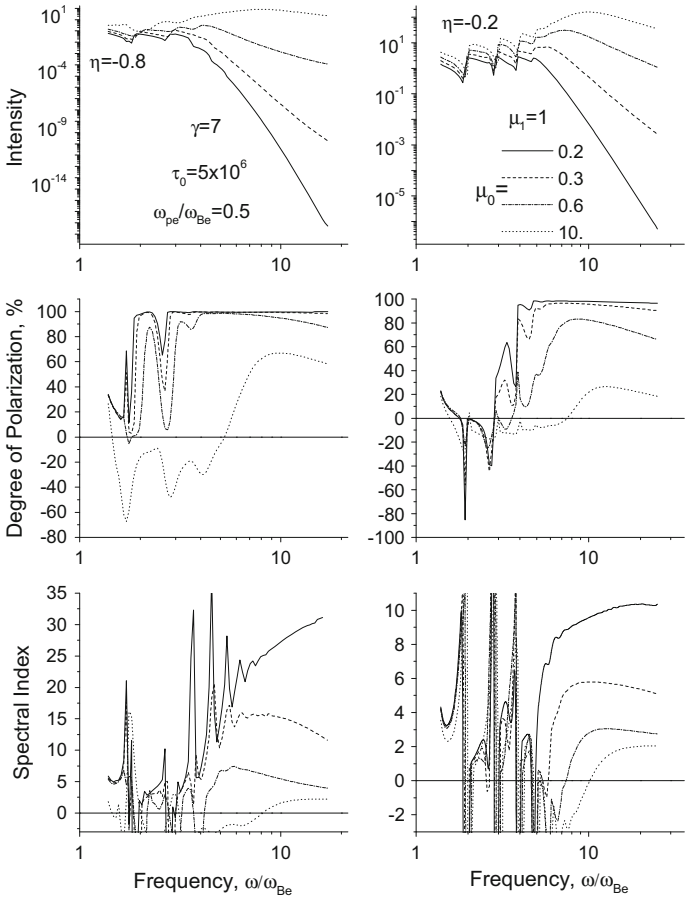

Fig. 2.18 The parameters are almost the same as those in Fig. 2.17, except for opposite propagation of beam

produced by thermal electrons [25]. However, Fig. 2.18 demonstrates that anisotropic NT distributions can produce much softer GS spectra, even for increasing a factor of 10.

2.3.4.3 For Dense Plasma

Figure 2.19 displays the GS emission by the beam in a dense plasma ($Y = 2.5$) when the optical depth is relatively large. The behavior of the polarization and the spectral index is generally the same as in Fig. 2.17. However, we should note that even a rather broad optically thick region of the spectrum does not obey any single power-law:

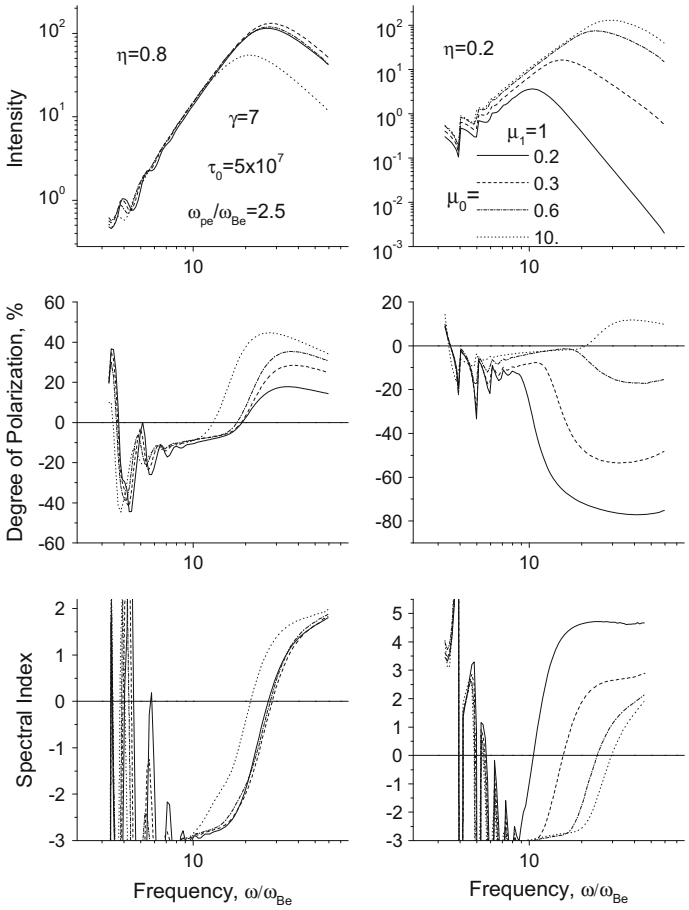

Fig. 2.19 The parameters are almost the same as those in Fig. 2.17, except for dense plasma of $Y = 2.5$

the plots of the spectral index do not contain any flat negative part; this property has already been mentioned above for the loss-cone and isotropic distributions.

2.3.4.4 Different Types of Gaussian Anisotropy

Figure 2.20 plots the curves for different types of the Gaussian anisotropy: loss-cone ($\mu_1 = 0$), beam ($\mu_1 = 1$), and the oblique beams ($\mu_1 = 0.3,\ 0.6$). From the figure, we conclude a gradual transition to occur from the loss-cone to the beam-like regime.

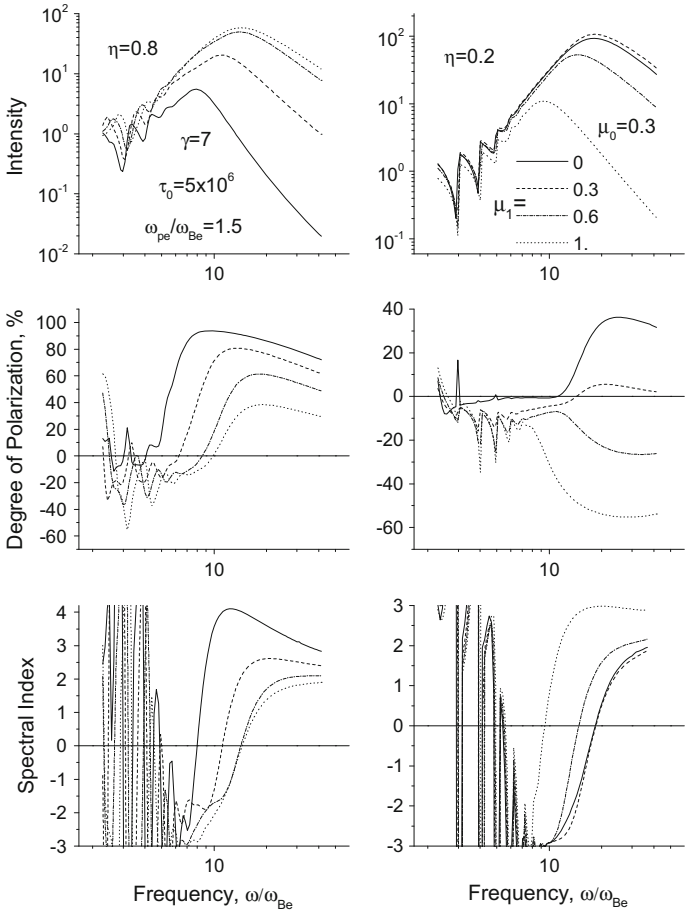

Fig. 2.20 GS emission intensity, polarization, and spectral index for different types of the Gaussian anisotropy: loss-cone ($\mu_1 = 0$), beam ($\mu_1 = 1$), and the oblique beams ($\mu_1 = 0.3,\ 0.6$)

2.3.5 Discussion

Our study proves the pitch-angle anisotropy to affect significantly the GS radiation. First of all, we should mention the strong effect of the anisotropy on the intensity and spectral index of the emission in the optically thin region, which relates primarily to the energy-dependent directivity of the synchrotron radiation by a single electron (Eq. 2.2.21).

So far, the spectral index has been commonly believed to be directly linked to the energy spectral index of radiating electrons providing the method to derive the electron distribution from the MW spectra [13]. However, this method cannot be directly applied if the radiating electrons have an anisotropic pitch-angle distribution, since

the value of the spectral index can deviate significantly from the respective value for the isotropic case. Nevertheless, the results are potentially even more powerful for the fast particles diagnostics if applied for the analysis of spectral index distribution along the magnetic loop obtained with high spectral and spatial resolution, which should become possible for the planned FASR observations [69]. Furthermore, the oscillating behavior of the spectral index can be used for the magnetic field diagnostics.

Currently, it is discovered with the NoRH data that MW emission from the FP parts of extended flaring loops displays systematically softer spectra ($\Delta\alpha \sim 1$–1.5 in the domain 17–34 GHz) than from the LT part [8, 9]. It has been shown that one of the reasons for the spectral softening is the systematic increase of the magnetic field strength from the LT toward the FPs [9]. Accordingly, the emission at a given frequency is generated at lower gyro-harmonics for the FPs than for the LT, which can result in softer FP spectra (see, e.g., Fig. 2.2 of this chapter) with $\Delta\alpha \sim 0.5-1$.

The results presented in this section show clearly that a pitch-angle anisotropy can make an important contribution to the observed spectral index variations. Indeed, if we take into account the mentioned convergence of the magnetic field lines toward the FPs, we should expect a more anisotropic electron distribution (due to a larger loss-cone) in the FP source than in the LT source. Furthermore, for the disk flares, the FP source is observed at a quasi-parallel direction, while the LT source is observed at a quasi-transverse direction. Figures 2.10, 2.11, 2.12, 2.13, and 2.14 show that anisotropic distributions provide systematically softer spectra of GS radiation (at quasi-parallel directions, the case of the FP source) than the isotropic or weakly anisotropic distribution (at quasi-transverse directions, the case of the LT source), which agrees with the NoRH data. Thus, the pitch-angle anisotropy plays probably a key role in the observed variations of the spectral index of the MW radiation along the loop.

We should note as well, that the decrease of the radiation intensity in the quasi-parallel direction due to the pitch-angle anisotropy is rather significant to explain the observed decrease of the radio brightness from the LT to the FPs of the flaring loops near the center of the solar disk [4].

Actually, the study of GS intensity and spectral index distribution together with hard X-ray and gamma ray data from the RHESSI mission can provide us with an entirely new powerful tool to study pitch-angle distributions of fast electrons along the loop. Such information is of primary importance for the models of fast electron propagation in the magnetic loops, since it can put essential constraints on the mirror ratio, background number density, level and spectra of wave turbulence in the loop, which (all together) control the particle kinetics in the magnetic loop.

Furthermore, the properties of polarization can be used for diagnostic purposes as well. The anisotropic distributions can ensure X-mode polarization in the optically thick region, or (in some cases for beam-like distributions) O-mode radiation in the optically thin region. Multiple change of the sense of polarization with frequency can occur. The degree of polarization can strongly deviate from the respective isotropic case.

We conclude that most of the effects found here can be observed (and some of them have already been observed), thus, detailed and careful interpretation of the MW data with the use of the presented results should substantially improve the particle diagnostics and provide us with essentially new observational constraints on fast particle pitch-angle anisotropy in solar flares.

2.4 Trapping and Transport Effects

To learn more about properties of MW emission and its dynamics in different parts of flaring loops and to study the properties in a more quantitative way than before, we do modeling of the time evolution of electron spectral, pitch-angle and spatial distributions along a magnetic loop by solving the nonstationary Fokker–Planck equation [70] under different assumptions on the physical conditions in the loop and for different positions of the injection site (loop top, loop legs and feet) [71, 72].

$$\frac{\partial f}{\partial t} = -c\beta\mu\frac{\partial f}{\partial s} + c\beta\frac{d\,ln B}{ds}\frac{\partial}{\partial\mu}\left[\frac{1-\mu^2}{2}f\right]$$

$$+\frac{c}{\lambda_0}\frac{\partial}{\partial E}\left(\frac{f}{\beta}\right) + \frac{c}{\lambda_0\beta^3\gamma^2}\frac{\partial}{\partial\mu}\left[\left(1-\mu^2\right)\frac{\partial f}{\partial\mu}\right] + S\,, \qquad (2.4.1)$$

where $f = f(E, \mu, s, t)$ is electron distribution function of kinetic energy $E = \gamma - 1$ (in units of mc^2), pitch-angle cosine $\mu = cos\,\alpha$, distance from the flaring loop center s, and time t, $S = S(E, \mu, s, t)$ is injection rate, $\beta = v/c$, v and c are electron velocity and speed of light, $\gamma = 1/\sqrt{1-\beta^2}$ is Lorentz factor, $B = B(s)$ is magnetic field distribution along the loop, $\lambda_0 = 10^{24}/n(s)ln\Lambda$, $n(s)$ is plasma density distribution, $ln\Lambda$ is Coulomb logarithm.

2.4.1 Dependence on the Position of Acceleration/Injection Site

In this section, we present the results of our numerical experiments only for two cases using the developed method of numerical calculations [7, 71]. In the first case (Model 1), the source of high-energy electrons is located in the magnetic trap center $s = 0$, and in the second one (Model 2) near a trap foot $s = 2.4 \times 10^9$ cm. In both models, the trap (loop) is symmetrical and its half-length is 3×10^9 cm and magnetic mirror ratio $B_{max}/B_{min} = 2$, $B_{min} = 200$ G. Plasma density is homogeneous along the loop with $n(s) = 5 \times 10^{10}\,\mathrm{cm}^{-3}$. The injection function $S(E, \mu, s, t)$ is supposed to be a product of functions dependent only on one variable (energy E, cosine of pitch-angle μ, position s, and time t):

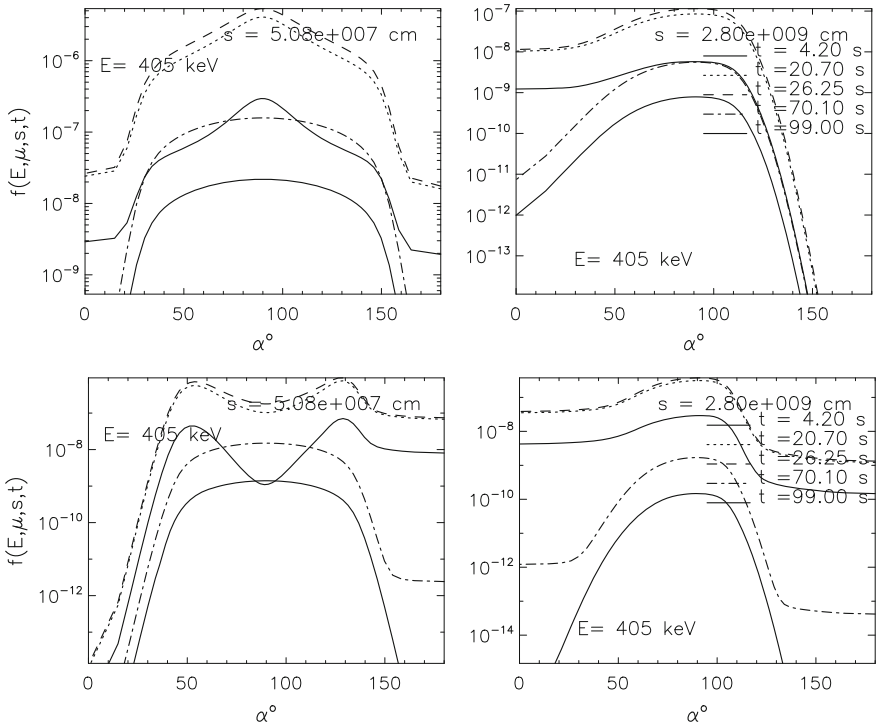

Fig. 2.21 Results of simulations for Model 1 (top panels) and for Model 2 (bottom panels) for electron energy 405 keV and for two positions in the loop: loop top (left panels) and near an FP (right panels). The distribution functions over pitch-angle α for the rising phase of injection are shown by solid ($t = 4.2$ s), dotted ($t = 20.7$ s) and dashed ($t = 26.25$ s) lines, and for the decay phase by dot-dashed ($t = 70.1$ s) and dot-dot-dot-dashed ($t = 99$ s) lines

$$S(E, \mu, s, t) = k\ S_1(E)\ S_2(\mu)\ S_3(s)\ S_4(t)\ , \tag{2.4.2}$$

where k is a normalization factor, the energy dependence is a power-law $S_1(E) = k(E/E_{min})^{-\delta}$, $E_{min} = 30$ keV, with spectral index $\delta = 5$; pitch-angle distribution is isotropic $S_2(\mu) = 1$; time dependence is Gaussian $S_4(t) = exp[-(t - t_m)^2/t_0^2]$, $t_m = 25$ s, $t_0 = 14$ s; spatial distribution is also Gaussian. For Model 1: $S_3(s) = exp(-s^2/s_0^2)$, and for Model 2: $S_3(s) = exp[-(s - s_1)^2/s_0^2]$, where $s_0 = 3 \times 10^8$ cm, $s_1 = 2.4 \times 10^9$ cm.

It is known that spectral and polarization properties of GS emission are very sensitive to peculiarities of the electron pitch-angle distribution in a radio source [10]. So, here, in Fig. 2.21 we present some results of modeling the pitch-angle distributions of mildly relativistic electrons ($E = 405$ keV) in the center and end of the magnetic trap (loop) for Model 1 and Model 2.

Model 1 (injection at the LT). In the loop center, the distribution remains anisotropic perpendicular to magnetic field lines during the injection rise, maximum (t_m = 25 s) and decay phases. However, the degree of anisotropy decreases with time, especially in the decay phase. Near a loop FP, the electron pitch-angle distribution is clearly asymmetric, showing a considerable amount of electrons with small pitch-angles. On the decay phase, the distribution becomes more and more symmetric with the peak close to $\alpha = 90°$ (transverse anisotropy increases).

In the case of Model 2 (injection near an FP), the pitch-angle distribution and its dynamics near the FP are very similar to ones in Model 1. At the loop center, however, the shape of the distribution and its dynamics are completely different. First of all, we can see two peaks near pitch-angles 50 and 130° that indicates the presence of oblique fluxes (beams) of electrons. Second, the distribution changes dramatically during the decay time getting more isotropic. Obviously, the pitch-angle scattering due to Coulomb collisions and precipitation into the loss-cone play important role in the mentioned dynamics.

2.4.2 Spectral an Polarization Responses to Specific Electron Distributions

In this section, we show the influence of electron distribution dynamics on polarization and spectral properties of MW GS emission from different parts of a magnetic loop [72]. We do simulations in the frames of assumptions accepted for Model 1 and Model 2 and use the exact formalism described in papers [12, 27]. The magnetic loop is thin (so that the MW source is optically thin in the considered frequency range) and located in the plane almost perpendicular to the LOS ($\theta = 78.5°$). Results of our simulations are presented in Figs. 2.22 and 2.23.

Figure 2.22 displays frequency spectra of polarization degree and its dynamics for Model 1 (top panels) and Model 2 (bottom panels) for two positions in the loop: in the loop top (left plots) and near an FP (right plots). For both models, the polarization spectra of emission from the region near an FP are very similar. The polarization is positive (X-mode) at all frequencies and its degree is quite high (25–30%) even at the highest frequencies. The time evolution is very weak if present at all.

The polarization spectra from the loop top region are strongly different. They show well visible dynamics. They differ from each other. The most striking differences between Model 1 and Model 2 are the following. First, the polarization degree in Model 2 (isotropic injection near an FP) is negative (O-mode) at high frequencies, whereas in Model 1 it is positive both at low and high frequencies. Such unusual phenomenon is explained by the fact that in Model 2 we have an oblique flux (beam) of electrons in the central part of the magnetic trap (Fig. 2.21). The oblique beam of energetic electrons is known to produce O-mode polarized emission in the quasi-transverse direction even in optically thin regime [12]. The second strong difference is the difference in the dynamics of the polarization spectra. In Fig. 2.22, we can see

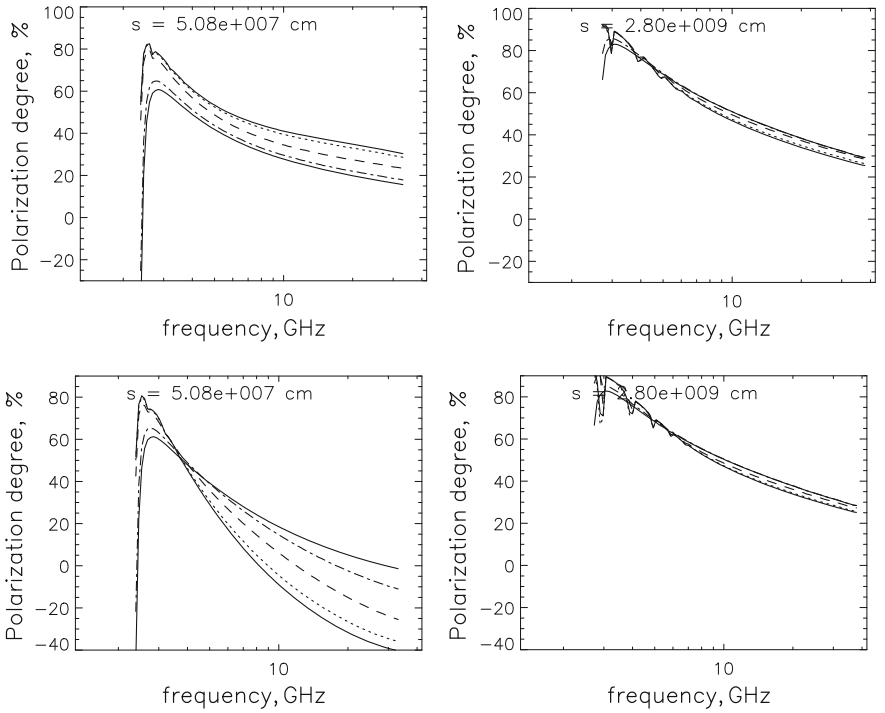

Fig. 2.22 Spectra of polarization and dynamics. Top and bottom panels are respectively for Model 1 and Model 2. Left and right columns are respectively for LT and near an FP. The line styles are similar to those in Fig. 2.21

that in Model 1 the polarization degree decreases with time, by ≈ 10–20%, whereas in Model 2 it increases considerably, by ≈20–40%, and even may change its sign on the late decay phase of the injection.

Somewhat similar picture of differences between Model 1 and Model 2 is observed for frequency spectra of the local spectral index $\alpha(f)$ and its dynamics (Fig. 2.23). In Fig. 2.23, we can see very similar values and dynamics of $\alpha(f)$ near an FP (right plots) for both models. At the same time, the values and dynamics of $\alpha(f)$ in the loop top region are noticeably different. For Model 2 the value of $\alpha(f)$ is larger than for Model 1. Moreover, at high frequencies, it is even larger than $\alpha(f)$ in the FP emission source. The higher values of $\alpha(f)$ in the loop top for Model 2 is definitely associated with the beam-like anisotropy of energetic electrons in the central part of the magnetic loop (Fig. 2.21). Such anisotropy is known to produce steeper frequency spectra of GS emission in the quasi-transverse direction [12].

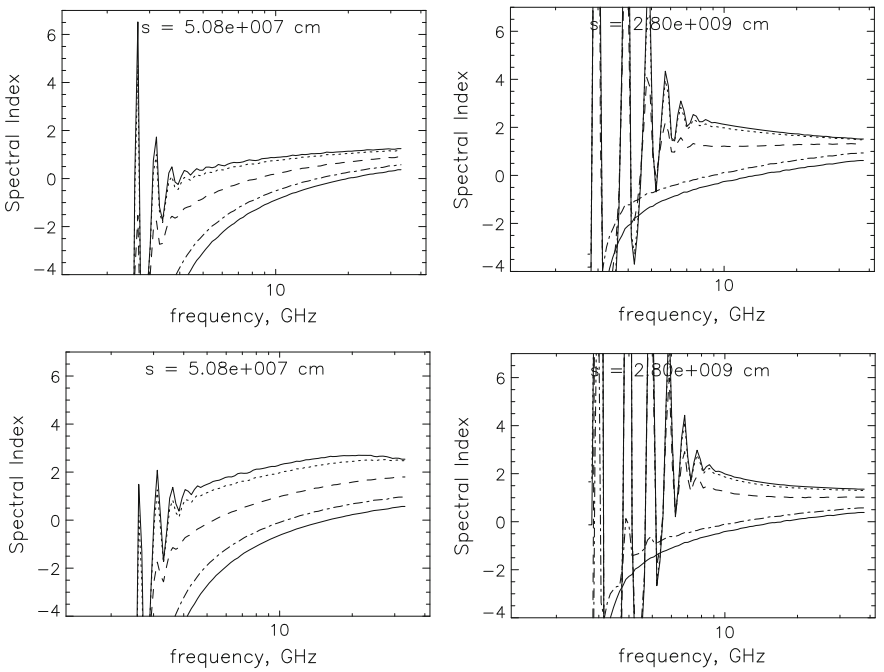

Fig. 2.23 Spectra of spectral index and dynamics. Top and bottom panels are respectively for Model 1 and Model 2. Left and right columns are respectively for LT and near an FP. The line styles are similar to those in Fig. 2.21

2.4.3 Diagnostic Potential

The differences in behavior of polarization and spectra found for two injection models can serve as a diagnostic tool for distinguishing between different types of anisotropic distributions in flaring loops. These findings, together with a set of other recent achievements in theoretical and observational studies, may be developed in a new method of direct diagnostics of acceleration mechanisms and properties of kinetics of high-energy electrons in flaring magnetic loops by means of spatially and spectrally resolved MW observations. It is clear now that building new radio instruments such as FASR, MUSER, and Siberian Radioheliograph, which are able to observe intensity and polarization of MW emission in a wide frequency range and with high spatial, spectral, and temporal resolution, is crucially important for solving the key problems in the physics of solar flare particle acceleration.

2.5 Effects of Other Parameters on GS Emission

The effects of various plasma and energetic parameters on GS emission have been studied intensively [73], there are 6 parameters mentioned in the classical theory of GS emission [27]: the local magnetic field B_0 in the source of GS emission, the NT electron spectral index δ, the low-energy and high-energy cutoffs of NT electrons (E_{min} and E_{max}), the ambient plasma density n_0, and the view angle θ in respect to B_0. The effects of these parameters on GS emission has been compared [74] with the well-known code (vmramaty_gysy_core.pro) [35] given in Solar-Software (SSW).

2.5.1 Spectral Shape

The effects of these parameters on the spectral shape of GS emission are shown in Fig. 2.24, and the selected parameters are given in Table 2.1.

It can be clearly seen from Fig. 2.24 that the sensitivity of GS spectrum to the 6 parameters is quite different. The parameters more sensitive to the GS spectrum (e.g., spectral shape, peak frequency, and spectral slopes) are B_0, δ, and θ.

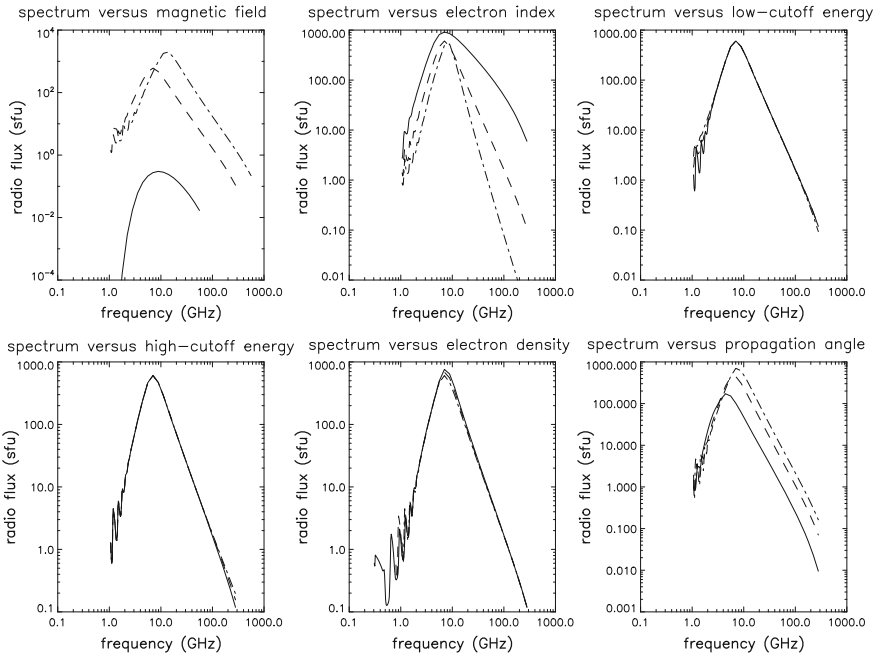

Fig. 2.24 The GS spectrum varied with the 6 ambient and energetic parameters

2.5.2 *Radio Flux Density*

Furthermore, we have calculated the theoretical radio flux density at the working frequencies 17 and 34 GHz of NoRH varied with the 6 parameters as shown by Fig. 2.25, and the calculated parameters are given in Table 2.2.

Table 2.1 Parameters selected in Fig. 2.24

Para.	B_0 (G)	δ	E_{min}(keV)	E_{max}(MeV)	n_0(cm^{-3})	ϑ(°)
B_0	20.0, 100.0, 200.0	5.0	30.0	10.0	1.0×10^{10}	60.0
δ	100.0	3.0, 5.0, 7.0	30.0	10.0	1.0×10^{10}	60.0
E_{min}	100.0	5.0	10.0, 50.0, 90.0	10.0	1.0×10^{10}	60.0
E_{max}	100.0	5.0	30.0	10.0, 20.0, 35.0	1.0×10^{10}	60.0
n_0	100.0	5.0	30.0	10.0	1.0×10^{8}, 1.0×10^{9}, 1.0×10^{10}	60.0
ϑ	100.0	5.0	30.0	10.0	1.0×10^{10}	30, 50, 70

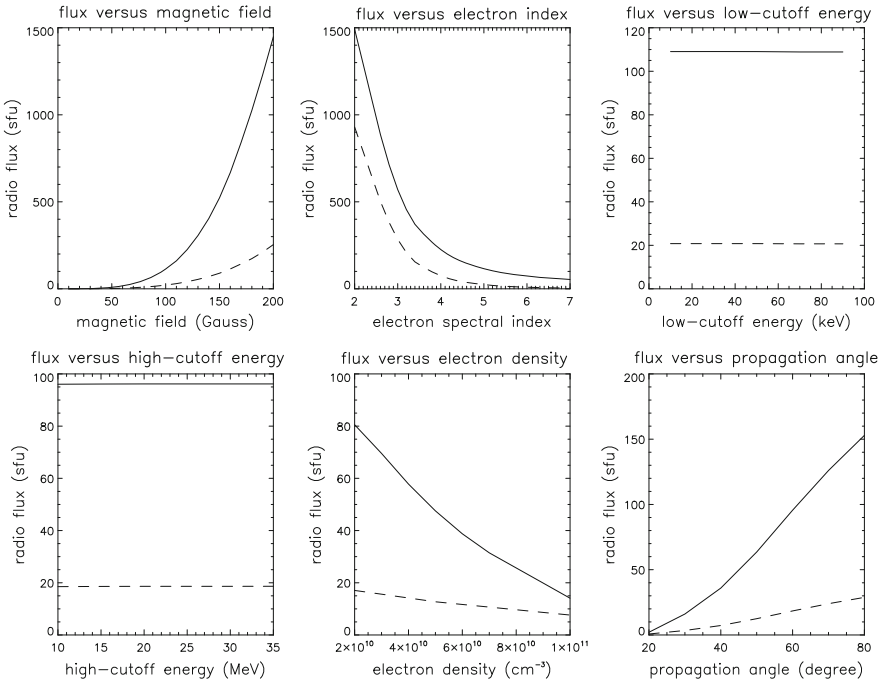

Fig. 2.25 The radio flux at 17 (solid line) and 34 (dashed line) GHz varied with the 6 ambient and energetic parameters

Table 2.2 Parameters selected in Fig. 2.25

Para.	B_0 (G)	δ	E_{min}(keV)	E_{max}(MeV)	n_0(cm^{-3})	ϑ(°)
B_0	10.0−200.0	5.0	30.0	10.0	1.0×10^{10}	60.0
δ	100.0	2.0−7.0	30.0	10.0	1.0×10^{10}	60.0
E_{min}	100.0	5.0	10.0−90.0	10.0	1.0×10^{10}	60.0
E_{max}	100.0	5.0	30.0	10.0−35.0	1.0×10^{10}	60.0
n_0	100.0	5.0	30.0	10.0	1.0×10^{10} − 1.0×10^{10}	60.0
ϑ	100.0	5.0	30.0	10.0	1.0×10^{10}	20−80

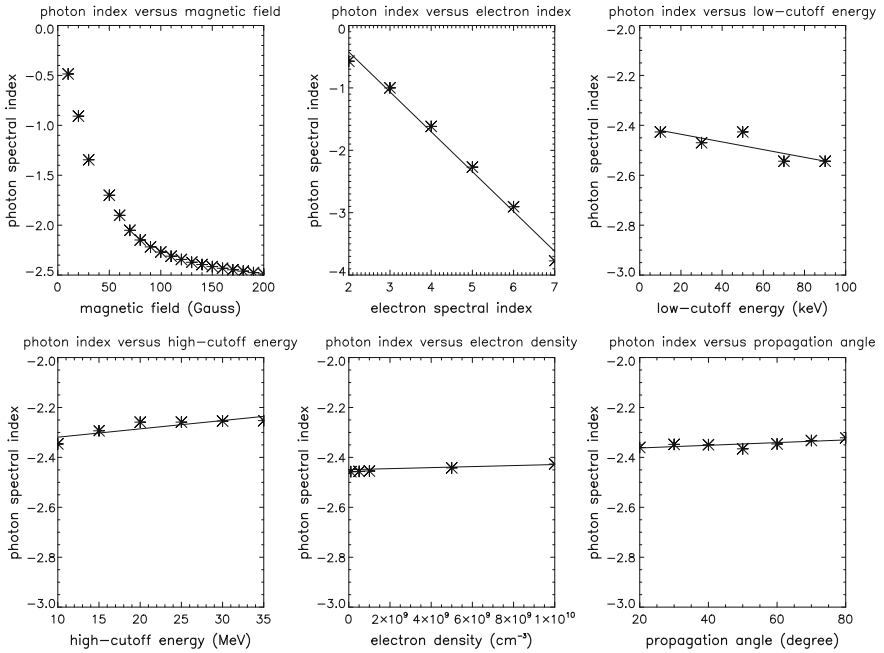

Fig. 2.26 The GS optically thin spectral index varied with the 6 ambient and energetic parameters

The results in Fig. 2.25 are basically consistent with those in Fig. 2.24. It is definitely confirmed that the effect of E_{min} and E_{max} is negligible in both the calculations of GS spectrum and flux, but the effect of n_0 on GS flux is evident, especially it is more sensitive to the lower frequency, such as 17 GHz. The GS flux increases with increasing of B_0 and θ, but decreases with increasing (softening) of δ, which is well consistent with the theoretical prediction of GS emission. In addition, the GS flux decreases with increasing of n_0 may be caused by the effect of self-absorption.

Table 2.3 Parameters selected in Fig. 2.26

Para.	B_0 (G)	δ	E_{min}(keV)	E_{max}(MeV)	n_0(cm^{-3})	ϑ(°)
B_0	10.0−200.0	5.0	30.0	10.0	1.0×10^{10}	60.0
δ	100.0	2.0−7.0	30.0	10.0	1.0×10^{10}	60.0
E_{min}	100.0	5.0	10.0−90.0	10.0	1.0×10^{10}	60.0
E_{max}	100.0	5.0	30.0	10.0−35.0	1.0×10^{10}	60.0
n_0	100.0	5.0	30.0	10.0	1.0×10^{8} − 1.0×10^{10}	60.0
ϑ	100.0	5.0	30.0	10.0	1.0×10^{10}	20−80

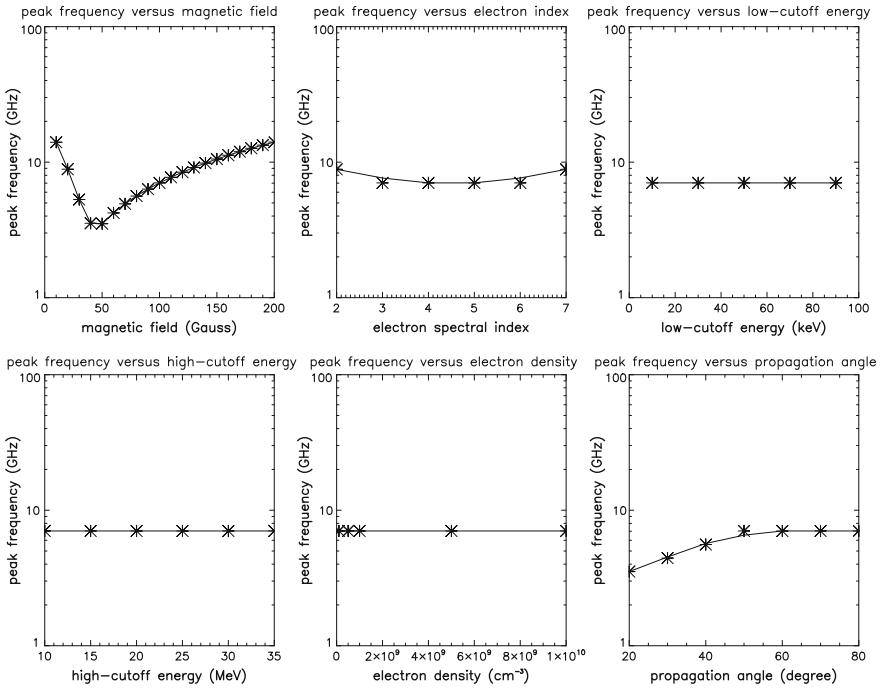

Fig. 2.27 The turnover frequency calculated by Ramaty's theory

2.5.3 Spectral Index

Moreover, we have compared the sensitivity of GS optically thin spectral index to the 6 parameters in Fig. 2.26, and the selected parameters are shown in Table 2.3.

The most important result in Fig. 2.26 is that the GS optically thin spectral index is sensitive only to B_0 and δ, which will be used for the diagnostics of B_0 and δ in Chap. 6.

Table 2.4 Parameters selected in Fig. 2.27

Para.	B_0 (G)	δ	E_{min}(keV)	E_{max}(MeV)	n_0(cm^{-3})	θ(°)
B_0	10.0−200.0	5.0	30.0	10.0	1.0×10^{10}	60.0
δ	100.0	2.0−7.0	30.0	10.0	1.0×10^{10}	60.0
E_{min}	100.0	5.0	10.0−90.0	10.0	1.0×10^{10}	60.0
E_{max}	100.0	5.0	30.0	10.0−35.0	1.0×10^{10}	60.0
n_0	100.0	5.0	30.0	10.0	1.0×10^{8} − 1.0×10^{10}	60.0
θ	100.0	5.0	30.0	10.0	1.0×10^{10}	20−80

2.5.4 Turnover Frequency

Finally, Fig. 2.27 gives the turnover frequency calculated by Ramaty's theory in a typical group of 6 coronal parameters listed in Table 2.4.

We can see from Fig. 2.27 that the turnover frequency is only sensitive to the local magnetic field, which is negatively correlated in lower magnetic field (<40–50 G), but becomes positively correlated in higher magnetic field (>40–50 G), which is also useful for the diagnostics of B_0 and δ in Chap. 6.

2.6 Numerical Codes for Fast GS Emission Calculations

As it was already mentioned in Sect. 2.3, the exact formulae for the GS emissivities and absorption coefficients [27, 31, 32] are valid for rather arbitrary conditions in solar flaring loops, including plasma density and magnetic field as well as pitch-angle and energy distributions [12]. However, their computations are very slow, especially at high harmonic numbers.

Recently, Fleishman and Kuznetsov [75] developed algorithms and computer codes that allow to calculate GS emission characteristics much faster than the existing codes. Computation time for the exact formulae grows exponentially with the harmonic number, while for the developed algorithm this time is nearly constant. As a result, at high frequencies (i.e., where the continuous algorithm is very accurate), the computation time for anisotropic electron distributions can be reduced by two to three orders of magnitude in comparison with the exact formulae. The so-called fast GS codes have the sufficient accuracy, and they are applicable to both isotropic and anisotropic electron distributions. The codes are freely available for use (http://iopscience.iop.org/0004-637X/721/2/1127/suppdata/apj351391_sourcecode.tar.gz).

The authors developed several fast GS codes: continuous, hybrid, and their optimized versions (for details, see Fleishman and Kuznetsov [75]). The continuous code gives very high overall accuracy of radiation intensity, degree of polarization, and

spectral index, especially at high frequencies. At low frequencies, the continuous approximation is unable to reproduce the harmonic structure of the GS emission, although the mean level of the spectra is reproduced remarkably well. The hybrid code is developed to overcome this problem. It involves both the exact code and continuous code contributions. As authors say, their numeric experiments show that for full recovery of noticeable low-frequency harmonics it is typically sufficient to use the exact code at frequencies below $12 f_b$ and the continuous code above $12 f_b$, where f_b is electron gyrofrequency in the radio source.

Note that the development of the fast GS codes allows one to apply the automated forward fitting method for diagnostics of solar flare MW sources [76]. Provided that the good spatially resolved MW emission characteristics at several frequencies are available, this method can give us various information not only on the magnetic field strength and electron spectrum, but also on such intrinsic properties of flaring loops as its magnetic field orientation, plasma density, the type of electron pitch-angle anisotropy etc. [77].

Another very important application of these codes is simulations of the 3D spatial structure of microwave sources. The corresponding tool is called GX Simulator [78]. Due to the microwave source nonuniformity along the line of sight, a computation time for previous codes was unreasonably long. The new tool allows one to get the line of sight integrated intensity and frequency spectrum at each pixel of 3D images of MW emission of model flare loops for 2–3 orders of magnitude faster. Moreover, it allows one to model loops on the basis of a linear force-free magnetic field (LFFMF) extrapolation of the photosphere magnetic field obtained from SOHO/MDI or SDO/HMI magnetograms. The GX Simulator package is incorporated to be the very popular among solar researchers Solar Soft Ware package (http://www.lmsal.com/solarsoft/ssw_packages_info.html, for detailed instructions see: https://web.njit.edu/~gnita/gx_simulator_help/).

References

1. Aschwanden, M.J.: Particle acceleration and kinematics in solar flares - a synthesis of recent observations and theoretical concepts (invited review). Space Sci. Rev. **101**, 1–227 (2002)
2. Vlahos, L.: Magnetic complexity, fragmentation, particle acceleration and radio emission from the sun. The High Energy Solar Corona: Waves, Eruptions, Particles. Lecture Notes in Physics, vol. 725, p. 15. Springer, Berlin (2007)
3. Kundu, M.R., Nindos, A., White, S.M., Grechnev, V.V.: A multiwavelength study of three solar flares. Astrophys. J. **557**, 880–890 (2001)
4. Melnikov, V.F., Shibasaki, K., Reznikova, V.E.: Loop-top nonthermal microwave source in extended solar flaring loops. Astrophys. J. **580**, L185–L188 (2002)
5. Martynova, O.V., Melnikov, V.F., Reznikova, V.E.: Proceedings of 11th Pulkovo International Conference on Solar Physics, pp. 241. Saint-Peterburg (2007)
6. Tzatzakis, V., Nindos, A., Alissandrakis, C.E., Shibasaki, K.: A statistical study of microwave flare morphologies. Solar Phys. **253**, 79–94 (2008)
7. Melnikov, V.F.: Electron acceleration and transport in microwave flaring loops. In: Shibasaki, K. (ed.) Proceedings of the Nobeyama Symposium, Kiosato, 26–29 Oct 2004. NSRO Report, vol. 1, pp. 11–22 (2006)

8. Yokoyama, T., Nakajima, H., Shibasaki, K., Melnikov, V.F., Stepanov, A.V.: Microwave observations of the rapid propagation of nonthermal sources in a solar flare by the Nobeyama radioheliograph. Astrophys. J. **576**, L87–L90 (2002)
9. Melnikov, V.F., Yokoyama, T., Shibasaki, K., Reznikova, V.E.: Spectral dynamics of mildly relativistic electrons in extended flaring loops. In: Wilson, A. (ed.) The 10th European Solar Physics Meeting, 9-14 Sept 2002, Prague, Czech Republic. ESA SP-506, vol. 1, pp. 339–342 (2002)
10. Fleishman, G.D., Gary, D.E., Nita, G.M.: Decimetric spike bursts versus microwave continuum. Astrophys. J. **593**, 571–580 (2003)
11. Altyntsev, A.T., Fleishman, G.D., Huang, G.L., Melnikov, V.F.: A broadband microwave burst produced by electron beams. Astrophys. J. **677**, 1367–1377 (2008)
12. Fleishman, G.D., Melnikov, V.F.: Gyrosynchrotron emission from anisotropic electron distributions. Astrophys. J. **587**, 823–835 (2003)
13. Bastian, T.S., Benz, A.O., Gary, D.E.: Radio emission from solar flares. Annu. Rev. Astron. Astrophys. **36**, 131–188 (1998)
14. Lee, J.: Radio emissions from solar active regions. Space Sci. Rev. **133**, 73–102 (2007)
15. White, S.M., Benz, A.O., Christe, S., Farnik, F., Kundu, M.R., et al.: The relationship between solar radio and hard X-ray emission. Space Sci. Rev. **159**, 225–261 (2011)
16. Dulk, G.A.: Radio emission from the sun and stars. Annu. Rev. Astron. Astrophys. **23**, 169–224 (1985)
17. Melrose, D.B.: Collective plasma radiation process. Annu. Rev. Astron. Astrophys. **29**, 31–57 (1991)
18. Zheleznyakov, V.V.: Radiation in Astrophysical Plasmas. Astrophysics and Space Science Library, vol. 204. Kluwer, Dordrecht (1996). ISBN 0-7923-3907-X
19. Chernov, G., Fomichev, V., Tan, B., Yan, Y., Tan, C., Fu, Q.: Dynamics of flare processes and variety of the fine structure of solar radio emission over a wide frequency range of 30–7000 MHz. Solar Phys. **290**, 95–114 (2015)
20. Razin, V.A.: Izv. Vyssh. Uchebn. Zaved. Radiofiz. **3**, 584 (1960)
21. Korchak, A.A., Terletsky, Y.P.: Zh. Eks. Teor. Fiz. **22**, 507 (1952)
22. Getmantsev, G.G.: Dokl. Akad. Nauk. SSSR **83**, 557 (1952)
23. Korchak, A.A.: Electromagnetic radiation by cosmic-ray particles in the galaxy. Sov. Astron. **1**, 360–365 (1957)
24. Syrovatskii, S.I.: The distribution of relativistic electrons in the galaxy and the spectrum of synchrotron radio emission. Astronomicheskii Zhurnal **36**, 17 (1959)
25. Dulk, G.A., Marsh, K.A.: Simplified expressions for the gyrosynchrotron radiation from mildly relativistic, nonthermal and thermal electrons. Astrophys. J. **259**, 350–358 (1982)
26. Huang, G.L.: Diagnostics of the low-cutoff energy of nonthermal electrons in solar microwave and hard X-ray bursts. Solar Phys. **257**, 323–334 (2009)
27. Ramaty, R.: Gyrosynchrotron emission and absorption in a magnetoactive plasma. Astrophys. J. **158**, 753–770 (1969)
28. Razin, V.A.: Izv. Vyssh. Uchebn. Zaved. Radiofiz. **3**, 921 (1960)
29. Korchak, A.A., Syrovatsky, S.I.: Astron. Zh. **38**, 885 (1961)
30. Takakura, T.: The self absorption of gyro-synchrotron emission in a magnetic dipole field: microwave impulsive burst and hard X-ray burst. Solar Phys. **26**, 151–175 (1972)
31. Eidman, V.Y.: Sov. Phys. -JETP **7**, 91 (1958)
32. Eidman, V.Y.: Sov. Phys. -JETP **9**, 947 (1959)
33. Twiss, R.Q.: Philos. Mag. **45**, 249 (1954)
34. Ramaty, R., Petrosian, V.: Free-free absorption of gyrosynchrotron radiation in solar microwave bursts. Astrophys. J. **178**, 241–250 (1972)
35. Ramaty, R., Schwartz, R.A., Enome, S., Nakajima, H.: Gamma-ray and millimeter-wave emissions from the 1991 June X-class solar flares. Astrophys. J. **436**, 941–949 (1994)
36. Tsytovich, V.N.: VestnikMosk. Gos. Univ. **4**, 27 (1951)
37. Ginzburg, V.L.: Uspekhi Fiz. Nauk. **51**, 343 (1953)
38. Ter-Mikaelyan, M.L.: Dokl. Akad. Nauk. SSSR **94**, 1033 (1954)

39. Reznikova, V.E., Melnikov, V.F., Shibasaki, K., Gorbikov, S.P., Pyatakov, N.P., Myagkova, I.N., Ji, H.: 2002 august 24 limb flare loop: dynamics of microwave brightness distribution. Astrophys. J. **697**, 735–746 (2009)
40. Morgachev, A.S., Kuznetsov, S.A., Melnikov, V.F.: Modeling the distribution of the circular polarization degree of microwave emission along flare loops in event on july 19, 2012. Geomagn. Aeron. **55**, 1118–1123 (2015)
41. Alfven, N., Herlofson, N.: Phys. Rev. **78**, 616 (1950)
42. Kiepenheuer, K.O.: Phys. Rev. **79**, 738 (1950)
43. Trubnikov, B.A.: Dokl. Akad. Nauk. SSSR **118**, 913 (1958)
44. Garibyan, G.M., Goldman, I.I.: Izv. Krymskoi Astrofiz. Obs. **7**, 31 (1954)
45. Sokolov, A.A., Ternov, IMZh: Eksp. Teor. Fiz **31**, 473 (1956)
46. Westfold, K.C.: The polarization of synchrotron radiation. Astrophys. J. **130**, 241–258 (1959)
47. Ginzburg, V.L., Syrovatsky, S.I.: The Origin of Cosmic Rays. Macmillan, New York (1964)
48. Petrosian, V.: Synchrotron emissivity from mildly relativistic particles. Astrophys. J. **251**, 727–738 (1981)
49. Grebinskii, A.S., Sedov, A.P.: Microwave emission of solar flares. Sov. Astron. **26**, 220–224 (1982)
50. Robinson, P.A.: Gyrosynchrotron emission - generalizations of Petrosian's method. Astrophys. J. **298**, 161–169 (1985)
51. Klein, K.-L.: Microwave radiation from a dense magneto-active plasma. Astron. Astrophys. **183**, 341–350 (1987)
52. Zhou, A.H., Ma, C.Y., Zhang, J., Wang, X.D., Zhang, H.Q.: Two sets of improved approximate expressions of the gyrosynchrotron radiation. Solar Phys. **177**, 427–437 (1998)
53. Zhou, A.H., Huang, G.L., Wang, X.D.: Approximate expressions for gyrosynchrotron radiation in transverse propagation. Solar Phys. **189**, 345–356 (1999)
54. Hildebrandt, J., Kruger, A.: Kleinheubacher Berichte **39**, 717 (1996)
55. Belkora, L.: Time evolution of solar microwave bursts. Astrophys. J. **481**, 532–544 (1997)
56. Melnikov, V.F.: Electron acceleration and capture in impulsive and gradual bursts: results of analysis of microwave and hard X-ray emissions. Radiophys. Quantum Electron. **37**, 557–568 (1994)
57. Melnikov, V.F., Magun, A.: Spectral flattening during solar radio bursts at cm-mm-wavelengths and the dynamics of energetic electrons in a flare loop. Solar Phys. **178**, 591–609 (1998)
58. Melnikov, V.F., Silva, A.V.R.: Temporal evolution of solar flare microwave and hard X-ray spectra: evidence for electron spectral dynamics-II. In: Ramaty, R, Mandzhavidze, N (eds.) High Energy Solar Physics Workshop — Anticipating Hessi, ASP Conference Series, vol. 206, pp. 475–477 (2000)
59. Lee, J., Gary, D.E.: Solar microwave bursts and injection pitch-angle distribution of flare electrons. Astrophys. J. **543**, 457–471 (2000)
60. Melnikov, V.F., Shibasaki, K., Nakajima, H., Yokoyama, T., Reznikova, V.E.: Loop-top nonthermal microwave source in extended flaring loops: evidence from 17 GHz and 34 GHz NoRH observations. Abstracts of the CESRA workshop on Energy Conversion and Particle Acceleration in the Solar Corona. In: CESRA Workshop, Zurich: ETH, 17 (2001)
61. Aschwanden, M.J., Benz, A.O., Schwartz, R.A., Lin, R., Pelling, R.M., Stehling, W.: Flare fragmentation and type III productivity in the 1980 June 27 flare. Sol. Phys. **130**, 39–55 (1990)
62. McTiernan, J.M., Petrosian, V.: Center-to-limb variations of characteristics of solar flare hard X-ray and gamma-ray emission. Astrophys. J. **379**, 381–391 (1991)
63. Silva, A.V.R., Valente, M.M.: Center-to-limb variation of solar microwave bursts. Sol. Phys. **206**, 177–188 (2002)
64. Miller, J.A., Cargill, P.J., Emsly, A.G., et al.: Critical issues for understanding particle acceleration in impulsive solar flares. J. Geophys. Res. **102**, 14631–14660 (1997)
65. Pryadko, J.M., Petrosian, V.: Stochastic acceleration of electrons by plasma waves. III. Waves propagating perpendicular to the magnetic field. Astrophys. J. **515**, 873–881 (1999)
66. Lee, J., Gary, D.E., Shibasaki, K.: Magnetic trapping and electron injection in two contrasting solar microwave bursts. Astrophys. J. **531**, 1109–1120 (2000)

67. Fleishman, G.D., Melnikov, V.F.: Optically thick gyrosynchrotron emission from anisotropic electron distributions. Astrophys. J. **584**, 1071–1083 (2003)
68. Hewitt, R.G., Melrose, D.B., Rönnmark, K.G.: The loss-cone driven electron-cyclotron maser. Aust. J. Phys. **35**, 447–471 (1982)
69. Gary, D.E., Bastian, T.S., White, S.M., Hurford, G.J.: The Frequency-Agile Solar Radiotelescope (FASR) (invited). Asia-Pacific Radio Science Conference AP-RASC '01, Proceedings of a conference held 1–4 Aug, 2001 at Chuo University, Tokyo, Japan. Sponsored by Japan National Committee of URSI and the Institute of Electronics, Information and Communication Engineers. Co-sponsored by International Union of Radio Science, 236 (2001)
70. Hamilton, R.J., Lu, E.T., Petrosian, V.: Numerical solution of the time-dependent kinetic equation for electrons in magnetized plasma. Astrophys. J. **354**, 726–734 (1990)
71. Gorbikov, G.D., Melnikov, V.F.: The numerical solution of the Fokker–Plank equation for modeling of particle distribution in solar magnetic traps. Math. Model. **19**, 112–122 (2007)
72. Melnikov, V.F., Gorbikov, S.P., Pyatakov, N.P.: Formation of anisotropic distributions of mildly relativistic electrons in flaring loops. In: Universal Heliophysical Processes, Proceedings of the International Astronomical Union, IAU Symposium vol. 257, pp. 323–328 (2009)
73. Benka, S.G., Holman, G.D.: A thermal/nonthermal model for solar microwave bursts. Astrophys. J. **391**, 854–864 (1992)
74. Song, Q., Nakajima, H., Huang, G., Tan, B., Huang, Y., Wu, Z.: Turnover frequency in solar microwave bursts with an extremely flat optically-thin spectrum. Solar Phys. **291**, 3619–3635 (2016)
75. Fleishman, G.D., Kuznetsov, A.A.: Fast gyrosynchrotron codes. Astrophys. J. Lett. **721**, 1127–1141 (2010)
76. Fleishman, G.D., Nita, G.M., Gary, D.E.: Dynamic magnetography of solar flaring loops. Astrophys. J. Lett. **698**, L183–L187 (2009)
77. Morgachev, A.S., Kuznetsov, S.A., Melnikov, V.F.: Radio diagnostics of the solar flaring loop parameters by the forward fitting method. Geomagn. Aeron. **54**, 933–942 (2014)
78. Nita, G.M., Fleishman, G.D., Kuznetsov, A.A., Kontar, E.P., Gary, D.E.: Three-dimensional radio and X-ray modeling and data analysis software: revealing flare complexity. Astrophys. J. **799**, id236 (15pp) (2015)

Chapter 3
Observations and Explanations of MW Emissions in Solar Flaring Loops

3.1 Studies on Spatially Unresolvable Observations

3.1.1 Flattened Spectra in Solar Radio Bursts at Cm and Mm Bands and Dynamics of Energetic Electrons in Flaring Loops

The MW burst emission holds valuable information about the processes of electron acceleration and their storage in solar flare loops. During the last years, new results regarding particle acceleration have been obtained from HXR and MW observations as: (*a*) the considerable increase of the MW to HXR flux ratios (I_μ / I_x) from impulsive to gradual flares [1, 2]; and (*b*) the flattening of hard X-ray spectra during the decay phase of gradual bursts together with large temporal delays between MWs and HXRs. On the other hand softening during the decay phase and no temporal delays have been found for impulsive flares [2, 3].

Two fundamentally different approaches have been used for the explanation of these peculiarities. The first proposes that basically different particle acceleration processes occur in gradual (long) and impulsive (short) flares. The acceleration process during gradual flares occurs in two phases or steps, the second being more effective at high energies [4]. The second approach assumes that the process of acceleration is the same for both types of flares, but that physical conditions in the sources of emissions are different.

The first hypothesis meets several difficulties. Often, the second acceleration is assumed to be associated with a shock propagating into high levels of the corona after being generated during the first step. However, associated metric type II bursts have in some gradual flares not been observed or finished before the end of the HXR and MW emission [5]. Moreover, direct observations with spatial resolution show that locations of MW and type II sources have a large distance between them [6, 7]. Another problem arises from the absence of clustering in the statistical relation between I_μ / I_x and the HXR burst duration (between 10 and 1000 s) and the observation that the

G. Huang et al., *Solar Flare Loops: Observations and Interpretations*,
https://doi.org/10.1007/978-981-10-2869-4_3

delay between MW and HXR peaks increases linearly and monotonically with duration [8]. If the acceleration processes would basically differ for the two classes of flares the transition from short to long duration bursts would be not monotonic over such a large observed range of durations.

In the framework of the second approach, however, these and further problems can be solved quantitatively if we take into account the dynamics of energetic electrons injected into closed magnetic field structures during a flare and also the effect of increasing size and height of flare loops with increasing duration of flares (normally impulsive flares occur in compact flare loops and gradual ones in large high magnetic arcs [6, 9]). Under these conditions, the hardening of the HXR spectrum in gradual bursts can be naturally explained by the hardening of the electron energy spectrum in a trap due to the energy-dependent Coulomb collisions [10]. The statistical increase of I_μ/I_x with the duration of bursts occurs due to the increasingly effective accumulation of mildly relativistic electrons responsible for the MW emission in the less dense plasma of the larger magnetic loops. Only due to this effect the increase of I_μ/I_x by 2–3 orders of magnitude can be explained [8]. Also, the observed delays between the MW and HXR maxima and their increase with burst duration can be easily understood. In the context of the temporal evolution of the electron spectrum, it is also possible to eliminate the well-known discrepancies found between the numbers and spectra of energetic electrons calculated from MWs and HXRs [11–13].

3.1.1.1 Overview

The dynamic effects in flare loops need further studies by comparing their consequences with different kinds of observations, since only with adequate models a correct diagnosis of particle spectra and physical conditions (magnetic field, plasma density, etc.) in the emission region can be carried out. One of the possibilities of improving the dynamic model is to study the impact of the temporal deformation of the electron spectrum in a flare loop on the emitted GS spectrum, particularly at mm waves where only little research has been carried out.

In recent times, millimetric observations of flares became available from Itapetinga, Bern, BIMA, Itapetinga, Metsöhovi and Nobeyama, some of them with high temporal and spatial resolution (see for instance Refs. [14–17]). The results of these observations (time delays, spectral changes, etc.) give new information on the temporal development of the energy release and acceleration site and on the physical conditions in flare loops [18–21]. The millimeter wave spectrum carries important information about very energetic flare electrons (from hundreds keV to several MeV). Its observation gives unique possibilities to check some consequences of the dynamic model on the temporal evolution of the optically thin radio emission for a large number of continuum MW bursts including impulsive and gradual events. This kind of study was earlier possible for only a few bursts of the gradual type for which the peak frequency was less than 5 GHz [12, 13].

What features in the temporal evolution of the mm burst spectrum can be expected? It is well known that intense broadband solar MW bursts originate from mildly

relativistic electrons in flare loops. Therefore, the temporal evolution of the electron spectrum must be known before the dynamics of the MW spectrum can be calculated. The evolution of the electron energy spectrum in the framework of the trap-plus-precipitation model has been analyzed in a number of papers [22–25]. Usually this model exploits the simple assumption, that the electrons are captured inside a trap with homogeneous plasma density and magnetic field. It is also assumed, that the source function of the electron injection has a simple time profile and a constant power-law spectral index γ, and that the electrons are isotropically distributed. The calculated electron spectra are continuously hardening because the lifetime of electrons increases with energy. Moreover, the number of electrons accumulated in the trap reaches its maximum later for electrons at higher energies.

It is not difficult to show that this will strongly influence the radio spectrum of GS emission and that the most important features of it become visible in the optically thin part of the spectrum, which can be compared to the results of cm-mm burst observations:

1. the slope of the spectrum at high frequencies continuously flattens during the whole injection and after it; and
2. significant delays occur between the peaks of the injection and MW time profiles that increase with frequency.

The aim of this section is to study these peculiarities at frequencies above the spectral maximum where the source becomes optically thin.

3.1.1.2 Observations and Data Analysis

In the study by Melnikov and Magun (1998) [26], a total of 23 events was selected for which simultaneous observations from Bumishus (IAP, University of Bern, Switzerland) and Zimenki (NIRFI, Nizhnii Novgorod, Russia) are available. For most of these events, the MW spectrum between 0.95 and 50 GHz was recorded. The most important selection criteria were the presence of spectral maxima in the observed frequency range and flux values well above the noise level. For these events, having typical fluxes between 100 and 10000 sfu, spectral peak frequencies between 5 and 20 GHz were found. No selection was made regarding the duration and complexity of time profiles. For the present investigation, that concentrates on optically thin spectra, only the observations from Bumishus were used. They were carried out at 3.1, 5.2, 8.4, 11.8, 19.6, 35, and 50 GHz with a sampling time of 0.1 s during bursts.

Strong and characteristic spectral changes with time were noticeable throughout all the studied events. A burst of a typical duration of one minute on March 13, 1991 is given in Fig. 3.1. The top left frame shows the time profiles of the flux near spectral maximum. The top right frame presents the MW spectra at times marked in the flux time profiles by vertical lines. Due to the lack of spectral resolution and significant systematic flux errors the spectra are rather coarse. However, spectral changes above the spectral maximum are obvious and indicate a general flattening of the spectrum during the decay phase of the emission.

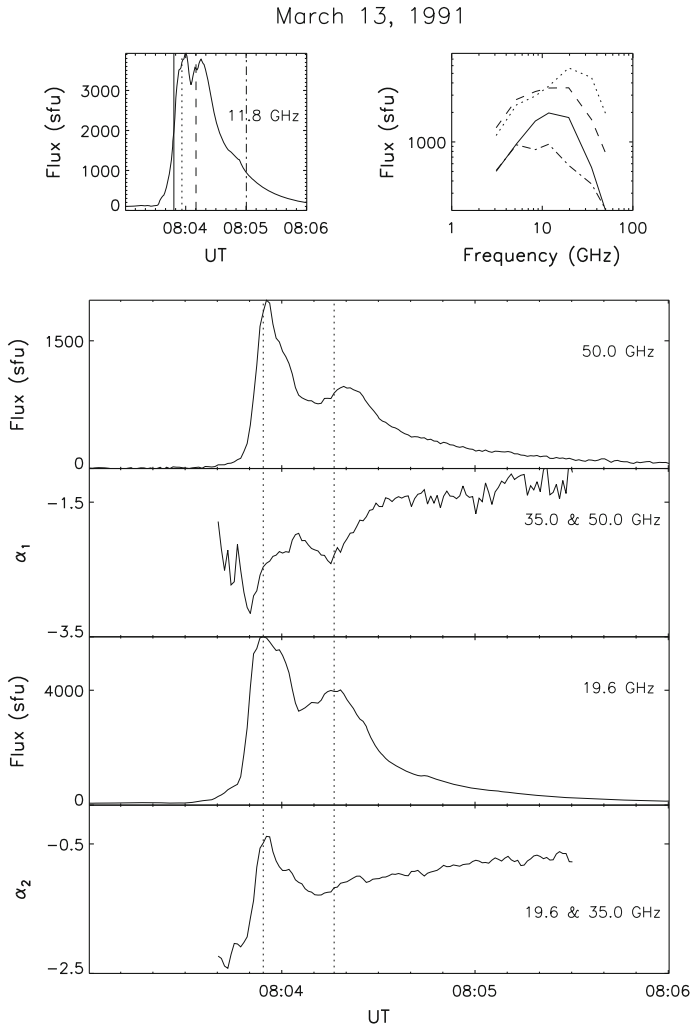

Fig. 3.1 Spectral evolution of 1-minute duration MW burst on March 13, 1991. Upper row of panels: Flux time profile near spectral maximum and spectra at four selected times marked by the vertical lines in the time profiles. Lower panels: Temporal evolution of fluxes and spectral indices α_1 and α_2 well above and near the spectral maximum

Important details relevant to the temporal evolution of MW spectra become more clearly apparent in the dynamics of the spectral index α of the MW emission:

$$\alpha(t) = \frac{ln\{S_h(t)/S_l(t)\}}{ln(f_h/f_l)}\ , \tag{3.1.1}$$

Here f_l and f_h are neighbor frequencies, at which the time-dependent fluxes $S_l(t)$ and $S_h(t)$ were recorded. Due to the limited spectral resolution α represents an approximation to the actual spectral index.

The lower four panels of Fig. 3.1 show the temporal evolution of fluxes and approximated spectral indices in two spectral ranges well above (α_1) and close (α_2) to the spectral maximum. At these frequencies, the effects of changes in the slope of the electron spectrum and in the optical thickness can be seen most clearly. Vertical dotted lines mark the temporal flux maximum at the frequency close to the spectral maximum.

The most conspicuous and typical features of the temporal evolution of the spectral indices and their relation to the flux profiles are the following: (*a*) The spectral index α_1, at frequencies well above the spectral maximum, shows in all cases a strong and gradual increase and, therefore, a flattening of the spectrum, starting from the onset of the emission and continuing until the end of the event; (*b*) As shown by the temporal evolution of the spectral index α_2, at a frequency close to the spectral maximum, this effect is still visible during the late decay phase. On the other hand, a significant and short decreasing of α_2 occurs during the decay phase of each pronounced peak; (*c*) Another typical feature is the temporal delay of the flux density profiles at frequencies well above the spectral maximum.

These typical characteristics of spectral evolution have been observed in nearly all 23 events under investigation. The analysis was carried out for the rise and decay phases of distinctive flux peaks. By including several flux density peaks occurring during the same event a total of approximately 35 peaks were investigated. Only those peaks were selected whose rise or decay phases were well visible. The duration of flux density peaks was obtained by measuring the difference between the start and end times at the 20% levels of the peak flux near spectral maximum. It covers a wide range between 4 and 280 s.

All the statistical results are shown in the form of a histogram in Fig. 3.2. The characteristic changes of the approximated spectral index α in four different frequency ranges (8–12, 12–20, 20–35, and 35–50 GHz) during the rise phase of the peaks were measured. Symbols are used to indicate an increase (+), no change (0), a decrease (–) of the spectral index and for completeness a sequential combination of them. The frequency ranges are defined by pairs of rounded observing frequencies. They all lie typically above or close to the spectral maximum.

The statistical results in Fig. 3.2 can be characterized as follows:

1. In the two upper frequency ranges (20–35 and 35–50 GHz) positive time delays dominate (14 positive and 4 negative delays). This is different for delays in the two lower frequency ranges (8–12, 12–20 GHz), close to the spectral maximum, where nearly equal numbers of positive and negative delays (7 and 9, respectively) have been found. For most of the observed peaks the delay is less than 1 s and could not be resolved due to the chosen integration time.
2. During the decay phase an increase of the spectral index and, therefore, spectral flattening is very common at frequencies well above the spectral maximum (see the second panel of Fig. 3.1). On the other hand, at frequencies close to the spectral

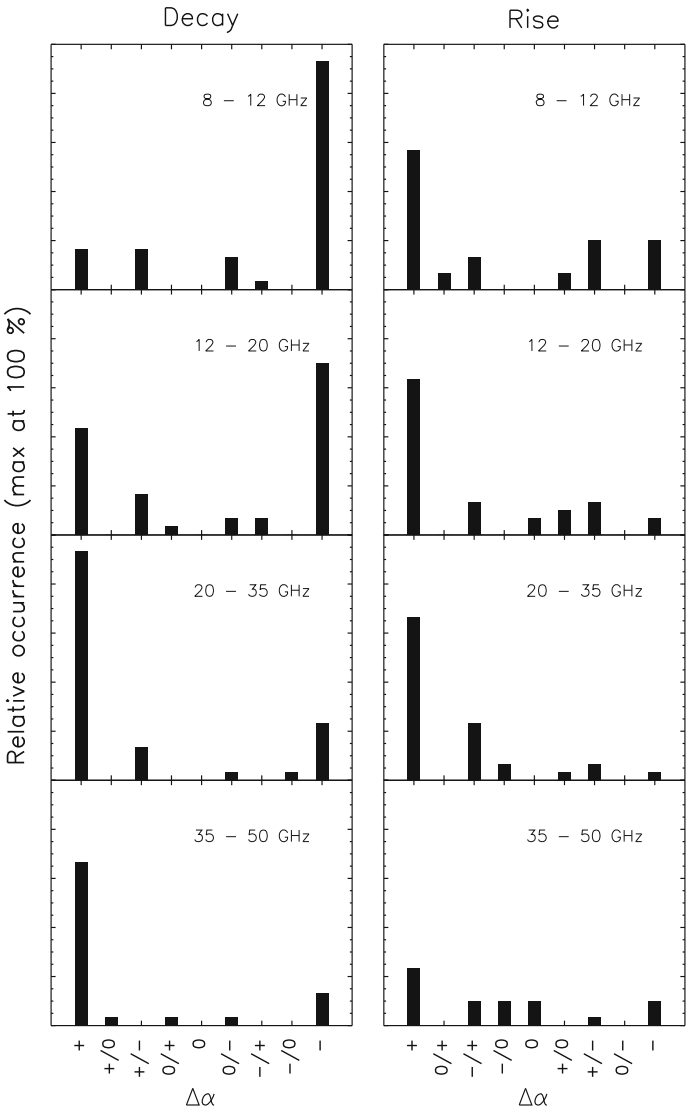

Fig. 3.2 Distribution of temporal changes $\Delta\alpha$ of the spectral index during the rise and decay phase of isolated peaks in the flux time profiles. The characteristics are denoted with "+" for an increasing, with "–" for a decreasing, and "0" for a constant spectral index. A temporal sequence of these changes are indicated by the combinations of these symbols

maximum, a decrease of α becomes obvious. In the intermediate frequency ranges (12–20 and 20–35 GHz) a transition between the "+" and "–" behavior of α can be noticed in the statistics.

3. During the rise phase the development of the spectral index is less clear. However, it seems that spectral flattening occurs in all frequency ranges and that it is predominant during simple events and during the first peak of multiple peak events. Secondary peaks in the latter, however, show a different type of behavior (+/–, –/+, etc.).
4. The delays and other spectral features that have been found are common: They occur not only in gradual long duration bursts (several 10 minutes) but also in intermediate (minute) and short (second) impulsive bursts.

3.1.1.3 Discussions

Dynamic Trap Model

These facts are in a good agreement with the predictions of the dynamic trap models mentioned in the overview. Indeed, the continuous flattening of optically thin mm-spectra is consistent with the expected hardening of the energy spectrum of electrons, accumulated in a flare loop during the injection. The delays of flux maxima at higher frequencies are expected from the fact that electron life times increase with energy and that in a trap their instantaneous number reaches its maximum later.

In order to obtain a more quantitative picture, the temporal evolution of the MW spectrum emitted by trapped electrons was simulated. Fluxes and spectral indices α_i (see Eq. (3.1.1)), together with reasonable source and electron injection parameters, are given in Fig. 3.3 The selected frequencies have similar ratios f/f_{peak} as defined by the observations and are given in units of the ambient gyrofrequency f_{g0}. The two upper panels represent the relative flux and the spectral index α_1 for a frequency well above spectral maximum, whereas the results near spectral maximum are shown in the two lower panels. It can be clearly seen in Fig. 3.3 that significant spectral flattening and time delays between flux peaks at different frequencies are to be expected, in agreement with the results of our analysis of observed MW spectra.

The dynamic model is able to explain also other, more detailed, features in the spectral variation of the observed spectra: One of them is the "+/–" behavior of α_1 at high frequencies during the decay phase of peaks in multicomponent mm-bursts (see temporal evolution of α_1 in Fig. 3.1). This occurs because a new injection shortly steepens the energy spectrum of previously injected electrons, whose spectrum has already flattened due to the dynamic hardening mentioned above. The same consideration explains also the "–/+" behavior of the spectral index during the rising phase of a following peak.

Another interesting result is the fast "+/–" behavior of α_2 near the spectral maximum and during the flux peaks (Fig. 3.1). From Fig. 3.3 it becomes obvious that the calculated behavior of α_2, for frequencies below and above spectral maximum, is very similar to observational results in Fig. 3.1 with a similar frequency ratio f/f_{peak}. This can be easily understood in the framework of the dynamic model if we take into account the effect of time-dependent self-absorption which becomes most pronounced at frequencies close to the spectral maximum. In the case of an optically thin source, the flux is strongly related to the number of radiating electrons whereas for

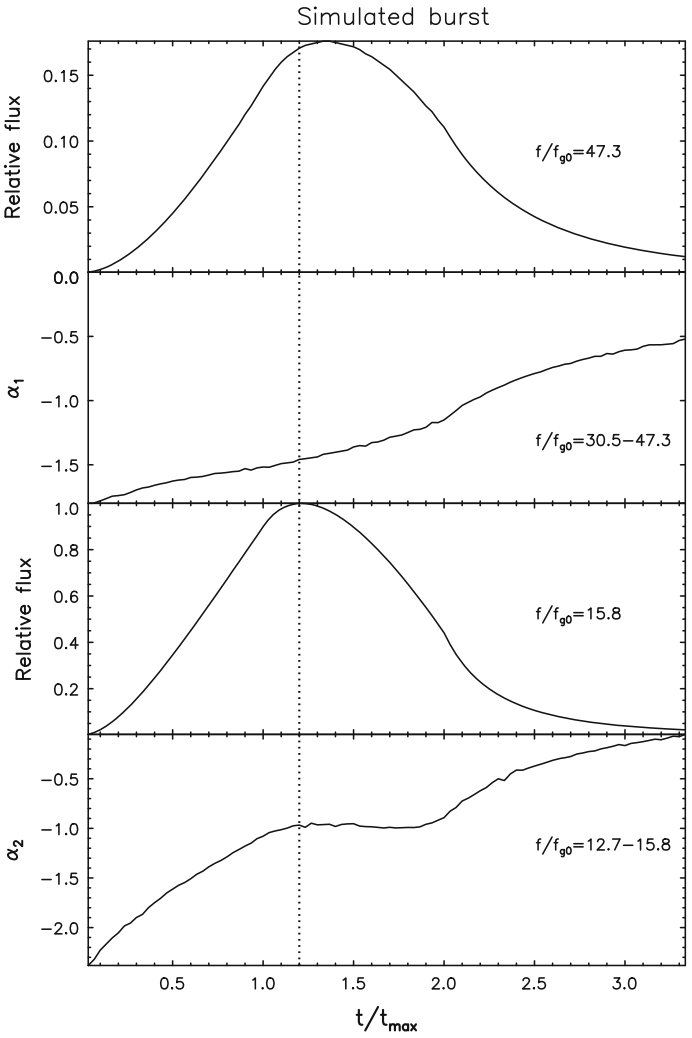

Fig. 3.3 Calculated flux time profiles and temporal evolution of approximated spectral indices near (α_2) and well above the spectral maximum (α_1). The source parameters are: plasma density $5 \cdot 10^{10}$ cm^{-3}, magnetic field 300 G, viewing angle 60° and source thickness $3 \cdot 10^8$ cm. The electron injection function $J(E,t) = K(t)E^{\gamma}$ has a power law spectral index $\gamma = -4$ and a triangular time profile $K(t) = a(2t_m - t)$ with $t_m = 30$ s, $a = 6 \cdot 10^{10}$ cm^{-3} keV^{-1}s^{-2}. The emissivity and the absorption coefficients have been computed with a precision of 5% for a range of electron energies between 10 and 6000 keV

the optically thick part of the spectrum this dependence becomes weak. During the rising phase the flux increases faster at higher frequencies not only because energetic electrons are accumulated more efficiently but also because the source is optically thinner ($t < t_{max}$). Just after the flux maximum the value of α_2 decreases and then

increases again. This is due to the fact that the emission above the spectral maximum is optically thinner and, therefore, the decay in emission from the decreasing number of electrons becomes more noticeable. The decrease of α_2 lasts until the optical thickness becomes much less than 1 at both frequencies and the dynamic effects of the electron spectrum dominate. Note that this "+/–" spectral behavior of α_2 has been earlier found for the majority of continuum MW bursts in the frequency range between 1 and 9 GHz [27]. Since these frequencies lie usually below or near the spectral maximum this result can be explained by the same effect.

Our observational results seem to contradict the softening of HXR spectra during the decay phase [2] which occurs in the majority of impulsive bursts. However, this can still be understood in the framework of the dynamic model, as under some conditions spectral hardening of trapped electrons at high energies can dominate over the softening of the injected electron spectrum. Besides the explanation which exploits the simple dynamic approach there are other possibilities to explain the time delays and spectral flattening during the decay phase of a burst. However, all of them are not as self-consistent and natural as the dynamic approach and need more comprehensive data and analysis.

Multiple Injections

Fine structures near the top of the main peaks have been noticeable for almost half of the analyzed MW bursts. This indicates that acceleration was not completely continuous and that several distinct and superimposed injections of fast electrons followed each other. The spectral dynamics of the observed MW emission then depends also on the location and the energy spectrum of these injections. We have carried out simulations in which similar electron spectra are repeatedly injected and trapped in the same loop and found nearly the same evolution of the cm-mm spectrum as for continuous injection. However, if the subsequent injections of electrons occur into compact regions with stronger and stronger magnetic fields [13, 18] the observed spectral flattening and delays of peaks could also be due to the resulting increase of MW emission at higher frequencies. It is difficult to reject this possibility by using MW observations without good spatial and temporal resolution. If this phenomenon exists it must be very common because spectral flattening is present almost in every simple burst and well-pronounced peaks of multiple peak bursts.

Thermal Bremsstrahlung

The gradual increase of thermal bremsstrahlung from an optically thin plasma that has been generated as a result of thermalization by fast electrons or been created by chromospheric evaporation could also result in spectral flattening. However, this becomes effective only during the late phase of bursts (some minutes after the impulsive peak). Usually, a short and intensive peak of mm-emission coincides in time with a hard X-/gamma-ray peak, while a less intensive gradual component is synchronized with a delayed SXR enhancement [16, 28]. The typical time scales of the observed soft X-ray enhancement are much larger than the half intensity duration of the impulsive bursts analyzed in this paper. We, therefore, believe that thermal bremsstrahlung can be neglected in the interpretation of our results for times less than a minute after

the MW peak. It is worthwhile to note that the increase of the ambient electron density connected with chromospheric evaporation leads, in the context of trapping, to an amplified flattening. This might have been the reason for the gradual flattening throughout the whole event.

Second Step Acceleration

Second step acceleration is believed to result in a continuous spectral hardening of accelerated electrons throughout long duration (gradual) HXR bursts and short impulsive bursts with gamma-ray line emission [2]. The majority of short impulsive HXR bursts, however, show spectral softening during the decay phase as mentioned above. This is in contrast to the observed typical dynamic evolution of cm-mm spectra which is very similar for both long duration (gradual) and short duration (impulsive) bursts. At present we do not know whether the analyzed cm-mm impulsive bursts were accompanied by a hardening of the HXR spectra during the burst decay phase. In this case, the flattening of the cm-mm spectra could then be due to the hardening of electron spectra during acceleration.

In order to reconcile the "SHS" behavior of the HXR spectrum with the mm-spectrum flattening during the decay phase it must be assumed that the HXR and MW emissions originate from electrons in different energy ranges, and that electrons from a higher energy range are accelerated more efficiently by a different (second step) acceleration process. On the other hand, this spectral evolution can also be understood in the framework of the dynamic model, as mentioned before. However, we need to check these assumptions using HXR and gamma-ray data for each event.

In conclusion, we would like to emphasize that our observational results indicate the hardening of electron spectra at energies above several hundred keV during the decay phase of simple bursts that qualitatively does not depend on burst duration (gradual or impulsive). Our results are consistent with the dynamic trap-plus-precipitation model but could also be explained by the hardening of the electron spectrum during acceleration or multiple injection of electrons into compact loops with increasing magnetic fields. Before final conclusions can be made further studies are needed in which HXR and gamma-ray spectra are compared with those of the MW emission from the same events.

Our analysis so far dealt only with some aspects of the spectral evolution. For instance, we can not check quantitatively the dynamic model concerning the peak frequency of radio emission, the precise values of the spectral slope, absolute fluxes and time delays between mm-emission and electron injection time profiles because many assumptions have to be made on the parameters of the electron spectrum, on the magnetic field and the plasma density in the flare loop. It is possible, however, to draw this information from a joint mm/cm- and hard X/γ -ray analysis.

3.1.2 Dynamics of Peak Frequency in Solar MW Bursts: Self-absorption and Razin Effect

3.1.2.1 Introduction

MW broadband emission during solar flares can give us valuable information about processes of particle acceleration and transport, as well as about magnetic field and plasma density in solar flaring loops (see for review) [29–32]. Studies of the shape of observed solar MW spectra started in the early 1960s [33, 34]. A detailed analysis of the shape of MW flux density spectra was done by the Ref. [35]. Their analysis was based on data obtained at fixed, well-separated frequencies. Theoretical studies, motivated by the observational findings, showed that the solar broadband MW bursts are generated by NT electrons via the GS emission mechanism [35–38] and provided some simplified schemes for MW diagnostics of solar flares [39–41].

The spectrum of such emission usually has a characteristic shape, with a single peak at the peak frequency ν_{pk}. Emission above ν_{pk} falls because the emission is optically thin, with the spectral slope being determined chiefly by the electron energy distribution, while ν_{pk} and the low-frequency slope may be determined either by self-absorption [42] or by Razin suppression [43]. Different parts of the MW burst spectrum give different tools for flaring loop diagnostics. For example, the high-frequency slope, flux density, and polarization of emission at $\nu > \nu_{pk}$ can provide information about the spectral index of NT electrons [44], total number of high-energy electrons [45], and also about pitch-angle anisotropy [30]. The low-frequency slope and flux density strongly depend on magnetic field strength and inhomogeneity and on effective energy of emitting electrons. They also may depend on the ratio of plasma density and magnetic field if Razin suppression is important [46].

Striking results were obtained in a comprehensive and multi-frequency study of 49 bursts [47], and it was found that during the rise and decay phases of majority of the bursts the deviation of ν_{pk} was much less than that predicted by the simplified theory of the GS radiation from a homogeneous radio source [39]. It was analyzed how the peak frequency was affected by such parameters as (1) magnetic field strength B, (2) column number density of NT electrons NL along LOS, (3) the viewing angle θ with respect to magnetic field direction, and (4) the size of a radio source Ω. It was pointed out that a change in the burst source size has no effect on the peak frequency, but that an increase in any other source parameter results in an increase in the peak frequency. As an explanation of the constancy of ν_{pk} during a burst, it was suggested that for most of the events the source parameters (number of energetic electrons and/or magnetic field strength) may vary over the course of a burst in such a way that the peak frequency does not change.

A comprehensive analysis of the peak frequency evolution for one particular flare was done [48] by using the OVSA data with a spatial resolution, so it was possible to derive the brightness temperature spectrum rather than the total flux density spectrum. A striking peculiarity of the burst was that the peak frequency remained nearly constant while the peak brightness temperature varied over two

orders of magnitude. As an explanation, the Razin effect was suggested. If Razin suppression is present, only a change in the number of NT electrons is required to cause the observed change in brightness temperature. The steep low-frequency slope of the observed burst spectrum gave additional support for Razin suppression. The parameters required to explain the event in terms of the Razin effect are electron density $n_e = 2 \times 10^{11}$ cm^{-3} and magnetic field $B = 300$ G, respectively.

The main purposes of present study are to: (*a*) show that the wide range of behavior in peak frequency evolution seen in our large sample of bursts can be explained in terms of two competing effects, self-absorption and Razin suppression, (*b*) develop an analysis procedure to distinguish between the two effects using the temporal behavior of the MW spectrum, (*c*) investigate statistically which effect is dominant at which times during a typical burst evolution, and (*d*) determine in what percentage of bursts each effect is important.

3.1.2.2 Observational Data

The data for this study come from the set of 412 bursts observed in MWs with the solar-dedicated OVSA [49] during the period of 2001–2002. After some upgrades the array operated during this study with six antennas (two 27 m dishes and four 2 m dishes). OVSA data comprise both total power from each antenna and correlated amplitudes and phases from each baseline (pair of antennas), but this study is limited to total power (integrated flux density, without spatial resolution). Because of difficulties with absolute flux calibration of the 27-m dishes due to their restricted field of view, we further limit our analysis to data from the 2-m antennas, and hence discuss only total intensity (Stokes I). The 2-m dishes have a total power sensitivity of a few solar flux units (sfu; 1 sfu = 10^{-22} W m^{-2} Hz^{-1}). The data are taken at typically 40 frequencies, distributed approximately logarithmically from 1 to 18 GHz, with 4 s time resolution. The 2-m flux calibration is based on the quiet Sun total flux density as reported by the National Oceanic and Atmospheric Administration (NOAA). OVSA data are highly suitable for studies of the peak frequency evolution of GS spectra due to OVSA's relatively large number of closely spaced frequencies covering the relevant range of 1–18 GHz over which most bursts have their spectral maximum.

The 412 bursts included decimetric bursts with no clear GS component [49]. We restrict our initial selection to bursts with well defined spectral peaks in the range $\nu_{pk} = 3 - 16$ GHz, which are identified with GS emission. This results in a total of 338 events used in this study. After calibration, we performed a 4-parameter fit to the burst spectrum at each time using the generic function [47]

$$S(\nu) = a_1 \, \nu^{\,a_2} \, [1 - \exp(-a_3 \, \nu^{-a_4})] \, , \tag{3.1.2}$$

which yields four physically relevant parameters, the low-frequency spectral index (a_2), the high-frequency spectral index ($\alpha_h = a_4 - a_2$), the peak, or turnover frequency (ν_{pk}), and the peak flux $S(\nu_{pk})$. This generic function has a shape similar to

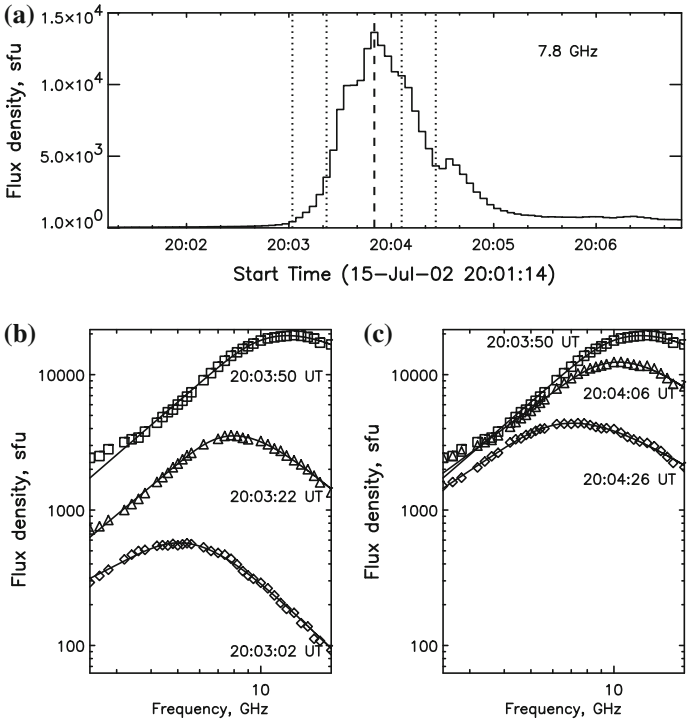

Fig. 3.4 Spectral evolution of the first peak in the MW multicomponent burst of July 15, 2002. Solid lines show the best fit with the generic function Eq. (3.1.2). An increase of the turnover frequency on the rising phase (left panel) and a corresponding decrease on the decay phase (right panel) is clearly seen

the GS emission spectrum obtained using the simplified formulas [39]. An example of such fitting is shown in Fig. 3.4. In some events, the low-frequency part of the spectrum contains an additional low-frequency spectral peak, $\nu_{\rm pk} \approx 1$–$2\,$GHz [49, 50]. In these cases, we limit the range of frequencies by a reasonable value $\nu_{\rm min}$ that varies from burst to burst, but was generally around 2–3 GHz.

In addition to our statistical study of the 338 bursts, we also performed a more detailed analysis of a much smaller subset of bursts. To avoid complexities due to overlapping spectral or temporal components, for the detailed study we selected only bursts having a single, well-defined spectral peak at the burst maximum and a simple time profile with peak flux density $S_{\rm pk} > 100$ sfu. This selection reduced the 338 bursts to a total of 40 events. We checked the flare locations for these 40 events from the NOAA Geophysical Data Center and found that two events in December 2001 were located at the limb and may have been partially occulted. We have dropped these from further consideration, leaving 38 bursts for more in-depth study.

3.1.2.3 Peak Frequency Dynamics

Comparison of spectra at different times during a burst clearly shows a change of peak frequency with time for most of the bursts in our dataset. In Fig. 3.4 we show an example of the typical spectral evolution. In this figure, spectra at different times are plotted in two panels, separately for the rise phase and decay phase. We can see a considerable increase of $\nu_{\rm pk}$ on the rise phase and then a decrease after the burst maximum. A remarkable feature of the spectral evolution in this example is the much faster increase of the flux at frequencies $\nu > \nu_{\rm pk}$ than at $\nu < \nu_{\rm pk}$, which is an indication that the source is optically thick at $\nu < \nu_{\rm pk}$. In what follows, we use a parameter, R, that serves as a measure of the difference in rate of change of flux density on either side of the spectral peak. We define it as:

$$R = \log \frac{S(\nu_2)}{S(\nu_1)} \,, \tag{3.1.3}$$

where $\nu_1 < \nu_{\rm pk}$ and $\nu_2 > \nu_{\rm pk}$ are frequencies (constant for a given burst) that are well away from $\nu_{\rm pk}$. For definiteness, we define $\nu_1 = (\nu_{\rm pabs} + \nu_{\rm min})/2$, $\nu_2 = (\nu_{\rm pabs} + \nu_{\rm max})/2$, where $\nu_{\rm pabs}$ is the absolute maximum of $\nu_{\rm pk}(t)$ during a burst, and $\nu_{\rm min}$, $\nu_{\rm max}$ indicate the frequency range in which the burst was detected. As we show quantitatively, a ratio R that increases during the rise phase and decreases during the decay indicates that the spectral turnover is due to self-absorption, while a relatively constant R indicates that frequencies on both sides of the turnover frequency are optically thin—a signature of Razin suppression. In contrast to the burst in Fig. 3.4, the burst in Fig. 3.5 displays constant R throughout the rise and most of the decay. This is an excellent example of a burst for which Razin suppression would be suspected, as further indicated by the constancy of the peak frequency over most of the burst.

A traditional spectral signature of Razin suppression, a steep low-frequency slope [41], is not seen in this burst, and in fact, is rare in spatially integrated total power spectra. In Sect. 2.2.8 we show that plasma density inhomogeneity, expected for flaring loops, can flatten the low-frequency GS spectrum, even in the presence of significant Razin suppression in the main part of a radio source, additionally flattening can occur due to magnetic field inhomogeneity [51].

Time profiles for several key spectral parameters of the event shown in Fig. 3.4 are represented in Fig. 3.6. The three parameters $S_{\rm pk}$ (panel *a*), $\nu_{\rm pk}$ (panel *b*), and R (panel *c*) all show a clear, positive correlation. The high-frequency spectral index $\alpha_{\rm h}$ in panel *d* shows a low positive correlation in this burst. It is an important parameter, however, as it gives a measure of the evolution of the NT electron energy distribution.

To determine how common is the correlation shown in Fig. 3.6a, b, we plot in Fig. 3.7 the distribution of correlation coefficients between $\nu_{\rm pk}$ and $S_{\rm pk}$ separately for the rise and decay phases for those bursts from our dataset that had sufficiently clean rise and decay phases (at least in the time interval where the flux is over 70% of maximum). The number of bursts used in Fig. 3.7a is 202, and the number used in Fig. 3.7b is 216.

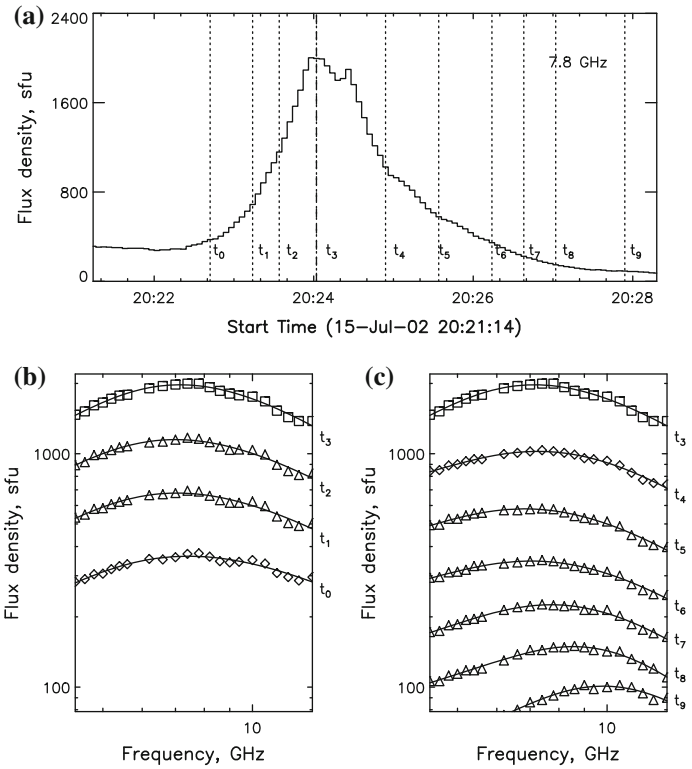

Fig. 3.5 Spectral evolution as in Fig. 3.4 for a secondary peak in the MW burst of July 15, 2002. Note the remarkable stability of the peak frequency during the most of the burst, the equal rise and fall on both sides of the peak frequency (which yields a constant R, and as well as its increase and steepening of the spectra at low frequencies on the late decay phase

It is clearly seen from the distributions that there is a large subset of bursts with strong positive correlation (correlation coefficient $r > 0.5$) between peak frequency and peak flux of a burst, both on the rise phase (50%) and on the decay phase (52%). However, a similar number of bursts show a random scatter of correlations, and a minor peak in the distribution occurs near $r = -1.0$, showing a distinct anticorrelation. Qualitatively, a positive correlation between the peak frequency and the burst flux is expected in the simple GS model, in which the low-frequency turnover occurs due to self-absorption. We can show this semi-quantitatively using the simplified formulas [39]. For the simple case of a homogeneous radio source, the emitted spectral flux density $S(\nu)$ is given by the radiation transfer equation in the form:

$$S(\nu) = \frac{2k_{\rm B}T_{\rm eff}(\nu)}{c^2}\nu^2[1 - e^{-\tau(\nu)}] \times \frac{A}{R_{\rm s}^2}\ , \tag{3.1.4}$$

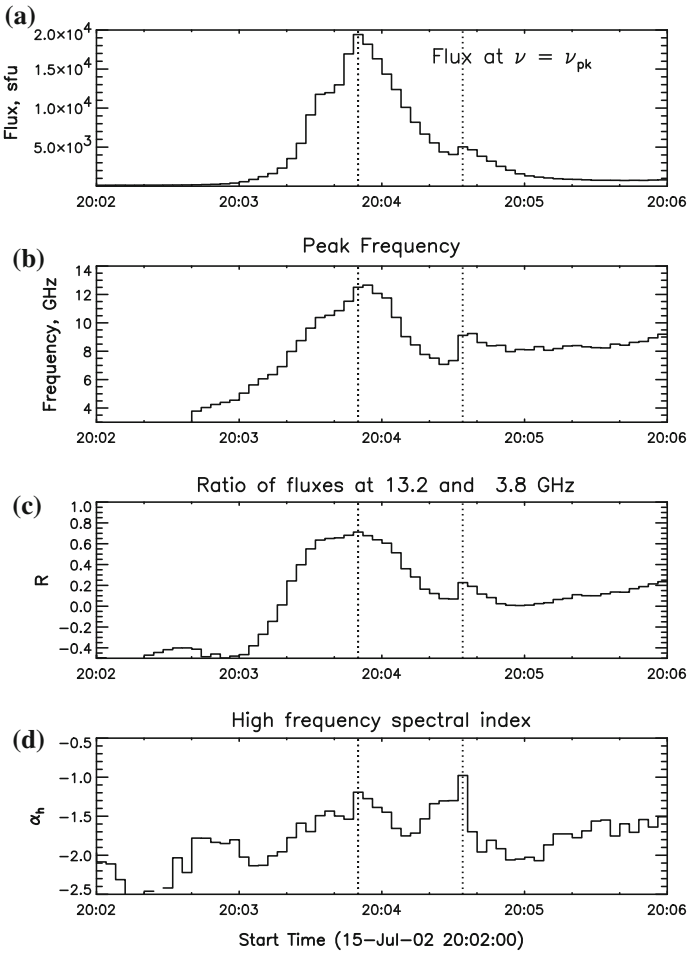

Fig. 3.6 Time profiles of several key parameters of the spectral evolution of the burst shown in Fig. 3.4: **a** Flux density, **b** peak frequency, **c** ratio R of fluxes at two frequencies, one (13.2 GHz) on the high-frequency side and one (3.8 GHz) on the low-frequency side of ν_{pk}, and **d** the high-frequency spectral index, α_h. A strong correlation is seen among the top three panels, both on the rise phase and initial part of the decay phase. The dotted vertical lines in each panel mark the peak times in panel *a*

where k_B and c are the Boltzmann constant and velocity of light, R_s is the distance from the Sun to the Earth, and A is the area of the source. In general [30, 36], the effective brightness temperature, $T_{eff}(\nu)$, and optical thickness, $\tau(\nu)$, are complicated functions of the electron energy and pitch-angle distributions, magnetic field strength, B, viewing angle between the directions of magnetic field and the line of sight, θ, plasma density, n_0, and the source depth, L. The flux density $S(\nu)$ reaches its maximum value, S_{pk}, at the frequency $\nu = \nu_{pk}$ where $\tau(\nu_{pk}) \simeq 1$, so the expres-

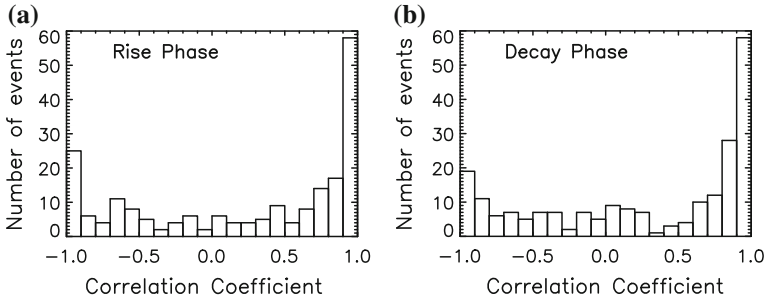

Fig. 3.7 Distribution of correlation coefficients between the peak frequency $\nu_{\rm pk}$ and peak flux $S_{\rm pk}$ on the rise (upper panel) and decay (lower panel) phases of the bursts from our set of events

sion $1 - e^{-\tau(\nu_{\rm pk})} \simeq 0.6$. In the case where the formulas [39] are valid, i.e., for low plasma density and energetic electrons with an isotropic, single power-law energy distribution of spectral index δ, we obtain

$$S_{\rm pk} \simeq 1.9 \times 10^{-54.0-0.31\delta} (\sin\vartheta)^{-0.36-0.06\delta} \nu_B^{-0.50-0.085\delta} \nu_{\rm pk}^{2.50+0.085\delta} A \ , \qquad (3.1.5)$$

where ν_B is the gyrofrequency. A positive correlation between the peak flux and peak frequency is clearly seen from Eq. (3.1.5). The Ref. [39] also gives an expression for the peak frequency in this homogeneous model,

$$\nu_{\rm pk} \simeq 2.72 \times 10^{3+0.27\delta} (\sin\vartheta)^{0.41+0.03\delta} B^{0.68+0.03\delta} (NL)^{0.32-0.03\delta} \ , \qquad (3.1.6)$$

which depends on the number density, N, of NT electrons with energies $E > 10\,{\rm keV}$, their spectral index, magnetic field strength, viewing angle and the source depth, L. Note that $\nu_{\rm pk}$ does not depend on the source area A. As is seen from Eqs. (3.1.5) and (3.1.6), any increase or decrease of the electron column number density, NL, leads to a simultaneous increase or decrease of both the MW flux density and the peak frequency (see Fig. 8 of the Ref. [46]).

The optically thin flux density is $S_{\rm thin} \propto$ emissivity $\times$ volume, and the optically thick flux density is $S_{\rm thick} \propto T_{\rm eff} \nu^2 A$. Using the GS formulas for emissivity and $T_{\rm eff}$ given by the Ref. [39], we obtain the ratio:

$$\frac{S_{\rm thin}}{S_{\rm thick}} \simeq 10^{4-0.21\delta} (\sin\vartheta)^{0.71\delta-0.07} \nu_1^{-2} \left(\frac{\nu_2}{\nu_B}\right)^{1.22-0.90\delta} B \left(\frac{\nu_1}{\nu_B}\right)^{-0.985\delta-0.72} (NL) \ . \qquad (3.1.7)$$

Thus, for GS emission, the ratio of these fluxes (and hence, $R = \log \frac{S_{\rm thin}}{S_{\rm thick}}$) should change in proportion to NL, B, and δ in a similar way as $\nu_{\rm pk}$ (Eq. (3.1.6)) and $S_{\rm pk}$ (Eq. (3.1.5)) do. Note that Eq. (3.1.7) is valid only for a homogeneous source. In the real flaring loop the source is inhomogeneous and emission at different frequencies comes from different parts of the loop. So we should use different values of B, A

and, possibly, δ for $S_{\rm thin}$ and $S_{\rm thick}$, but the general correlation of R with $S_{\rm pk}$ should remain.

We have checked the relationship between R and $\nu_{\rm pk}$ for all 38 events from our sample and found a strong correlation ($r > 0.5$), for 76% of events in the rise phase and for 70% of events in the decay phase. Only for 13% of events on the rising phase and 17% on the decay phase does the correlation between R and $\nu_{\rm pk}$ become negative.

However, in general, bursts show many different time behaviors and extent of $\nu_{\rm pk}$ variation during a burst. We can see in Fig. 3.7 that there is a small but non-negligible percentage of bursts showing strong ($r < -0.5$) negative correlation (27 and 22% of all bursts for the rising and decay phases, respectively), as well as very poor or no correlation, $|r| < 0.5$ (23 and 26% of bursts). The same is true for the correlation between R and $S_{\rm pk}$. These spectral behaviors cannot be explained on the basis of GS self-absorption alone.

3.1.2.4 Magnitude of Peak Frequency Variations

For more careful analysis of the spectral evolution during the rise and decay phases, we selected only bursts with relatively simple time profiles and well-defined peaks. The total number of such bursts is 38, including 24 with the smooth rise phase and 34 with the smooth decay phase. To understand what follows, it is important to realize that solar flares are not symmetric about their peak time. During their rise phase, the changes are typically rapid and monotonic, resulting in relatively simple behavior in the key parameters. Their decay, in contrast, is often slower and may show confounding behaviors as the complex, energized system of magnetic fields and plasma adjust to its new configuration. This general trend is readily seen in the MW peak frequency evolution we now discuss. The rise phase in our sample shows just a few, rather easily understood behaviors, while the decay phase is far more complex.

A simple measure of peak frequency variations is the overall shift in peak frequency during the burst. We show this shift in Fig. 3.8, normalized by $\nu_{\rm pk}$, since we might expect larger shifts for larger $\nu_{\rm pk}$. Figure 3.8a shows the distribution of $\Delta\nu_{\rm pk}/\nu_{\rm pk}$ during the time over which the flux density increases from 25 to 100% of its maximum value, while Fig. 3.8b shows the same during the decay to 25% of maximum. Almost all of the events (83%) on the rise phase have positive values of $\Delta\nu_{\rm pk}$, and most events (62%) on the decay phase have negative $\Delta\nu_{\rm pk}$ as expected for GS self-absorption. An interesting feature of the distributions is the relatively high percentage of events with small frequency shifts ($-0.1 < \Delta\nu_{\rm pk}/\nu_{\rm pk} < 0.1$): 33 and 30% for the rising and decay phases respectively. Note, however, that this is still a much smaller percentage than found by the Ref. [47]. Another interesting feature is the high percentage of events (38%) with positive shifts on the decay phase, which is not explained within the framework of the GS self-absorption model.

For the following analysis we will divide the events into three groups: those with high ($|\Delta\nu_{\rm pk}/\nu_{\rm pk}| \geq 0.3$)), moderate ($0.1 \leq |\Delta\nu_{\rm pk}/\nu_{\rm pk}| < 0.3$), and low ($|\Delta\nu_{\rm pk}/\nu_{\rm pk}| < 0.1$) relative peak frequency shifts and discuss them in detail below. Our aim

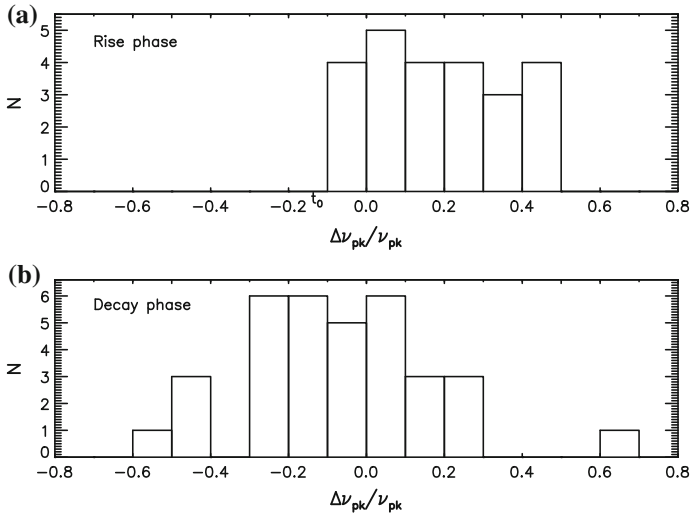

Fig. 3.8 The distributions of shift in peak frequency, $\Delta\nu_{\rm pk}/\nu_{\rm pk}$, **a** on the rise and **b** decay phases. The corresponding flux density increase (decrease) is from (to) 25% of its maximum value. The total number of bursts used in the distributions is 24 in **a** and 34 in **b**. Here $\nu_{\rm pk}$ is taken at the peak time of $S_{\rm pk}(t)$

is to show that, despite the wide variety of behavior, the different classes of events can be interpreted in terms of two competing effects, GS self-absorption and Razin suppression.

3.1.2.5 Peak Frequency Evolution on the Rising Phase of Bursts

Large Peak Frequency Shifts

In Fig. 3.9 we show the correlation between $\nu_{\rm pk}$ and $S_{\rm pk}$ on the rising phase of the seven events with the highest relative peak frequency shifts, $\Delta\nu_{\rm pk}/\nu_{\rm pk} > 0.3$. The straight lines are the best linear fits (in logarithmic scale) near the peak of the bursts. Generally, we can see that the dependence is a power-law

$$\nu_{\rm pk} \propto S_{\rm pk}^{\beta} \,, \tag{3.1.8}$$

with the index β varying from event to event. The values of β for each event are listed in Table 3.1. As we can see the mean value of β is 0.27.

For comparison, in Table 3.1 we show also the power-law indices β_1 and β_2 obtained for the fluxes at the previously defined frequencies ν_1 and ν_2 (see Eq. (3.1.3)), below and above the peak. The mean values are $\beta_1 = 0.41$ and $\beta_2 = 0.19$. We can understand the differences between β, β_1, and β_2 in the context of self-absorption. Indeed, the value of β_2 is minimal, and β_1 is maximal, since in the optically thin

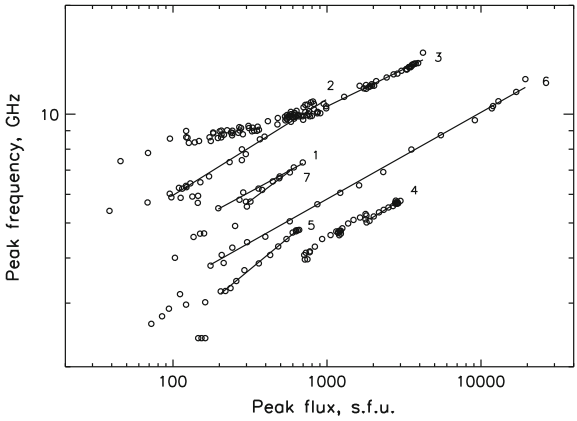

Fig. 3.9 Peak frequency versus peak flux density on the rise phase of seven events. The straight lines are the best linear fits (in logarithmic scale) near the peak of the bursts. The numbers indicate the events: 1–22 April 2001, 2–19 October 2001, 3–22 October 2001, 4–04 November 2001, 5–22 November 2001, 6–15 July 2002, and 7–04 December 2002

Table 3.1 Regression coefficients for events with $\Delta\nu_{pk}/\nu_{pk} > 0.3$ in Fig. 3.9

No	Event	$\beta(\nu_{pk}, S_{pk})$	$\beta(\nu_{pk}, S_2)$	$\beta(\nu_{pk}, S_1)$
1	22 Apr 2001	0.23	0.14	0.30
2	19 Oct 2001	0.27	0.17	0.31
3	22 Oct 2001	0.21	0.18	0.27
4	04 Nov 2001	0.26	0.20	0.34
5	22 Nov 2001	0.34	0.27	0.66
6	15 Jul 2002	0.26	0.17	0.43
7	04 Dec 2002	0.32	0.22	0.54
	Mean	0.27	0.19	0.41

regime the GS flux variations are expected to be much greater than in the optically thick regime under variations of the parameters like N, L, δ or B. The value of β falls between these limits, because flux density S_{pk} is from a partly optically thick, partly thin source with optical depth $\tau \simeq 1$.

Quantitatively the value of β also corresponds well with Eq. (3.1.5) under the assumption that the area A, spectral index δ and magnetic field B do not change during the rising phase of these bursts. For electron spectral index $\delta = 2.0$–6.0, the theoretical value $\tilde{\beta} = 1/(2.50 + 0.085\delta) = 0.37$–$0.33$ is slightly greater than β, giving a mean difference $\tilde{\beta} - \beta = 0.08$. This slight but systematic reduction in β seems to arise from the approximate nature of Eq. (3.1.5), since S_{pk} is actually formed at higher opacity than $\tau \approx 1$. Indeed, our simulations confirm that the GS shift in ν_{pk} is slightly less than given by Eq. (3.1.5).

Moderate Peak Frequency Shifts: Time Delays

Our comparative analysis of the flux and peak frequency time profiles for the eight bursts that show moderate $0.1 < \Delta\nu_{pk}/\nu_{pk} < 0.3$ show that the bursts can be divided into two subsets according to the temporal behavior of ν_{pk}.

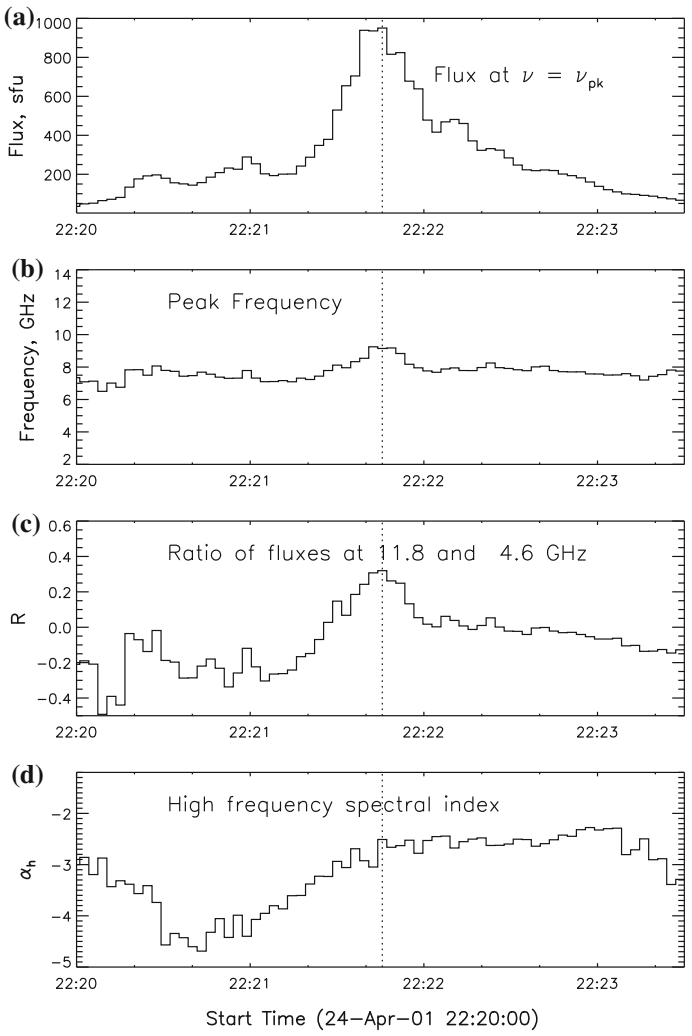

Fig. 3.10 Time profiles for the burst of April 24, 2001. The peak frequency in **b** remains high and nearly constant except near the main peak in **a**. The ratio R in **c** also becomes high and constant during the decay. Note that the spectral index α_{h} in **d** increases all during the rise phase and is constant in most of the decay phase

The first subset is characterized by relatively high and stable values of the peak frequency in the very beginning of the rising phase. The peak frequency starts to increase only after some delay relative to the flux increase, and peaks simultaneously (within the 4 s time resolution of OVSA) with the flux maximum. An example of such behavior is shown in Fig. 3.10a, b. Here ν_{pk} maintains a relatively high and constant value during the entire burst. Only near the very peak does it slightly increase, with

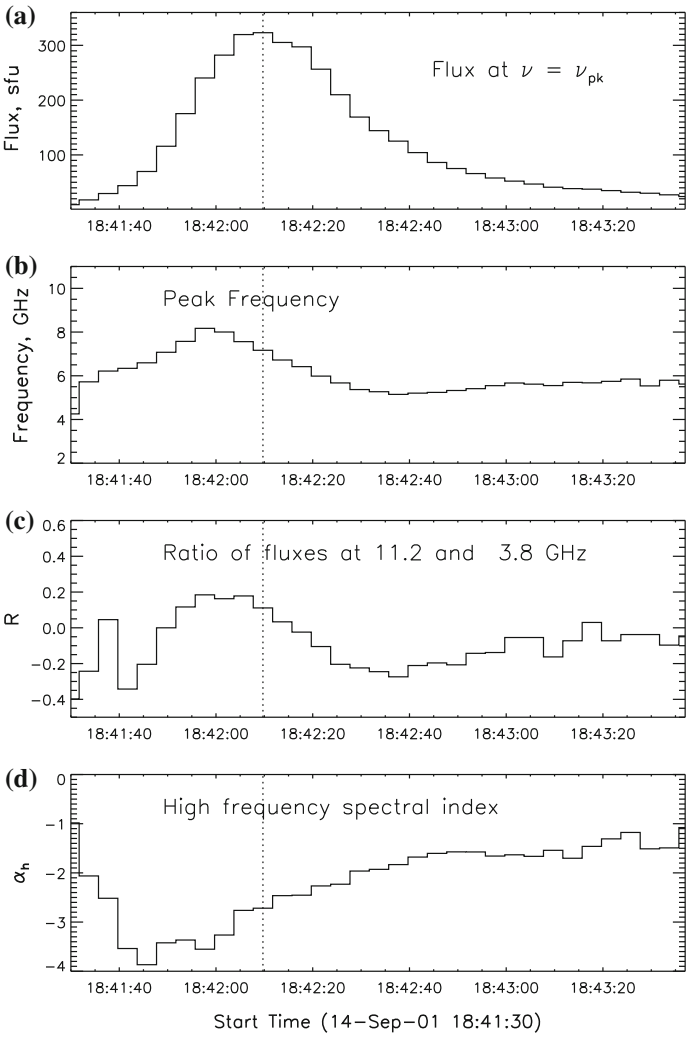

Fig. 3.11 Time profiles for the burst of September 14, 2001. This example shows a time delay between ν_{pk} in **b** and S_{pk} in **a**. Note also that on the decay ν_{pk} first decreases and then slightly increases. The α_h in **d** increases throughout the burst

$\Delta\nu_{pk}/\nu_{pk} = 0.21$. We suggest that such behavior is indicative of Razin suppression, and will consider the effect in detail as follows.

The second subset of events in this category is characterized by ν_{pk} reaching its maximum value prior to the peak time of S_{pk}, as shown in Fig. 3.11. For these events, the peak frequency increases at a regular rate in the beginning of a burst, but then decreases prior to and throughout the peak of the burst. Note that the behavior of R in Fig. 3.11 shows a similar time behavior. Such time delays also occur for events with

small $\Delta\nu_{pk}/\nu_{pk}$ discussed in the next section. As a whole, we found 10 events out of 24 where such time delays occur. The key to understanding this behavior, we believe, is that all of them show a significant increase (flattening) in α_h, which corresponds to a systematic flattening in the electron energy index δ. Flattening (steepening) of the electron spectrum over time can also cause the maximum value for ν_{pk} to occur after (before) the flux density maximum.

Note that it is quite common for radio spectra to flatten during the decay phase of bursts, in apparent contradiction to the SHS behavior most often seen in HXRs. The SHH radio behavior and its relationship to HXRs has been examined in detail by the Refs. [52, 53], where the differences are ascribed to the fact that HXRs reflect the precipitating component, while the radio spectrum reflects the trapped component. When the trapped (LT, or coronal, source) component can be isolated in HXRs [54], it is found to have a significantly harder spectrum than the FP source. Although both may derive from the same injected population (e.g., see the Ref. [44]), they evolve differently. Differences in electron spectral behavior derived from the radio spectrum relative to that derived from HXRs from FP sources should not be seen as a conflict. For our purposes, it is the trapped component, reflected in the high-frequency radio spectral slope, that is of interest.

To show that the flattening or steepening of the electron energy spectrum can affect the evolution of ν_{pk} to such an extent as to cause these differences in timing, in Fig. 3.12 we show the results of a simulation. We used the relation $\alpha_h = 0.90\delta - 1.22$ from the Ref. [39], for three different linear variations in electron spectral index, $\Delta\delta = -1, \ -0.5, \ +0.5$ and a Gaussian time profile of nL. These variations of δ correspond to MW slope variations of $\Delta\alpha_h = +0.9, +0.45, -0.45$. It is clearly seen that hardening or softening of the electron spectrum affects the time of maximum of ν_{pk} in the way indicated by the observations.

Small Peak Frequency Shifts

A total of nine bursts show small ($-0.1 < \Delta\nu_{pk}/\nu_{pk} < 0.1$) relative peak frequency shifts on their rise phase. Of these, five show complex behavior despite our attempt to choose only simple bursts. An example is the event of August 31, 2001 (not shown), where a burst with a simple flux density profile nevertheless displays a complicated shift of ν_{pk}, decreasing rapidly in the beginning before showing a more normal behavior through the peak. Such behavior may be a result of some previous burst activity or a radical source shift from a region of strong magnetic field to the one with the weak magnetic field. We do not consider these events further.

The remaining four bursts with small $\Delta\nu_{pk}/\nu_{pk}$ are characterized by a nearly constant ν_{pk} right through the flux density peak, while S_{pk} first increases and then decreases by a factor of several. Examples of two such events are shown in Fig. 3.13. The constancy of the high-frequency spectral index in both bursts indicates a constant electron spectral index δ, so it cannot influence the ν_{pk} behavior. These bursts are relatively long and have smooth, gradual profiles. In fact, both bursts are secondary components of earlier, strong multicomponent bursts. We can see in both events that R is nearly constant as well, indicating that the flux density increases and decreases almost with equal rate both at low ($\nu < \nu_{pk}$) and high ($\nu > \nu_{pk}$) frequencies. As we

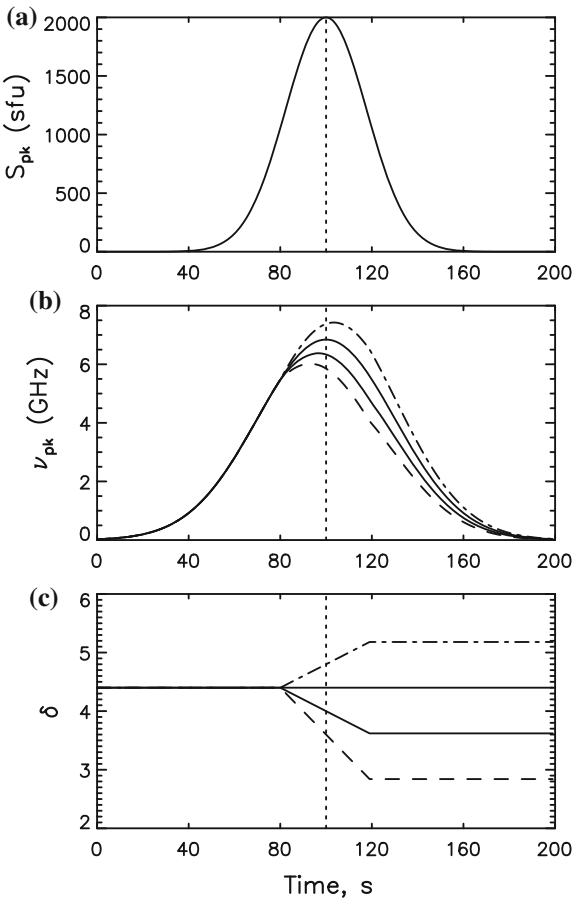

Fig. 3.12 Simulation of the spectral evolution for **a** a Gaussian flux density profile under the influence of hardening or softening of the electron spectrum, **b** the leading or lagging of the time of maximum of $\nu_{\rm pk}$. The assumed electron spectral index evolution is shown in **c** solid line, $\delta = \text{const}$; dashed line, $\Delta\delta = -0.5$; dotted line, $\Delta\delta = -1.0$; dot-dashed line, $\Delta\delta = +0.5$. The peak frequency time profile leads the flux maximum if the electron spectrum flattens, and it lags if the electron spectrum steepens

mentioned earlier, this is an indication of optically thin emission on both sides of the spectral peak, which is a clear signature of Razin suppression. This is investigated in more detail as follows.

3.1.2.6 Peak Frequency Evolution on the Decay Phase of Bursts

In general, peak frequency evolution on the decay phase considerably differs from the evolution on the rising phase. The power-law dependence of $\nu_{\rm pk}$ on $S_{\rm pk}$ seen in the rise phase is observed typically only in the beginning of the decay phase. In the late decay phase, the opposite dependence (i.e., $\nu_{\rm pk}$ begins to increase again) is seen for a significant fraction of events.

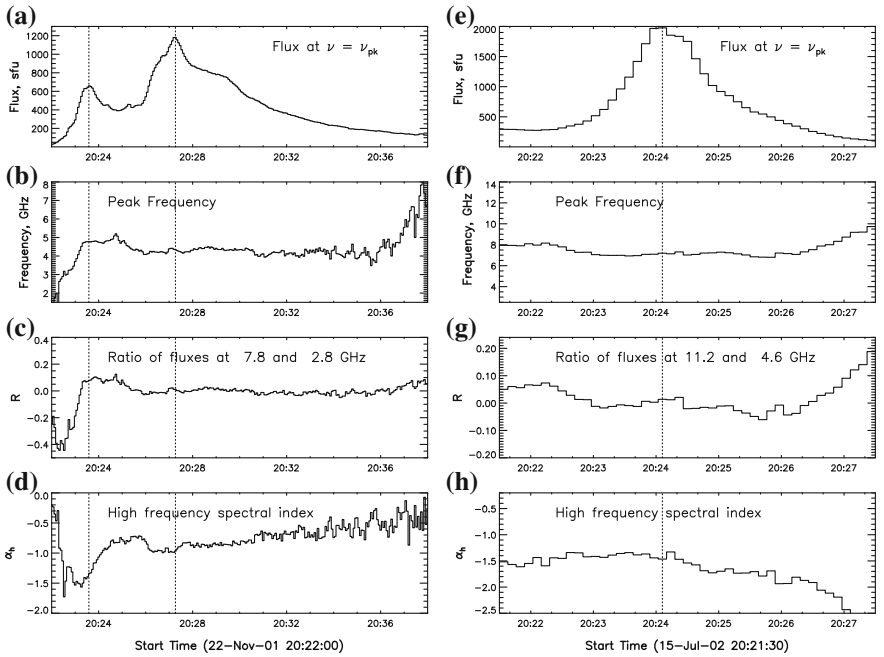

Fig. 3.13 Time profiles for the second major peak of the bursts of November 22, 2001 (panels **a**–**d**) and July 15, 2002 (panels **e**–**h**). The peak frequency in both bursts (panels **b** and **f**) is remarkably constant during the main part of the rise and decay. The same is true for the ratio R (panels **c** and **g**). On the late decay phase, the peak frequency starts to increase

Large Negative Frequency Shifts

Of the 34 bursts that we could study in the decay phase, there are 4 events with large negative relative frequency shifts, $\Delta\nu_{\rm pk}/\nu_{\rm pk} = -0.4$ to -0.6. In Fig. 3.14 we show the relationship between $\nu_{\rm pk}$ and $S_{\rm pk}$ for these events. The straight lines are the best linear fits (in logarithmic scale) near the peak of the bursts. This dependence can be described by the same power-law expression as Eq. (3.1.8). The values of β for each of the four events are listed in Table 3.2. From the table we can see remarkably high values of slope β (average $\beta = 0.57$) relative to the value of $\beta = \tilde{\beta} \simeq 0.35$ expected from Eq. (3.1.5), much higher than the highest values of β found during the rising phase of bursts (see Table 3.1).

Such a strong decrease of $\nu_{\rm pk}$ on the decay phase can be explained by one or more of the effects that we discussed earlier: increase of the source area A, flattening of the electron energy spectrum (decrease of δ), or decrease in magnetic field B. Again, we cannot investigate the change of the magnetic field and area without spatially resolved observations, but we can use the observed MW spectral index $\alpha_{\rm h}$ to investigate δ. First of all, we have found that $\alpha_{\rm h}$ does flatten on the decay phase of the bursts, giving $\Delta\alpha_{\rm h} = 1.8,\ 1.3,\ 1.3$, and 0.6 for the events August 30, 2001, August 31, 2001, October 22, 2001, and August 28, 2002, respectively. These correspond

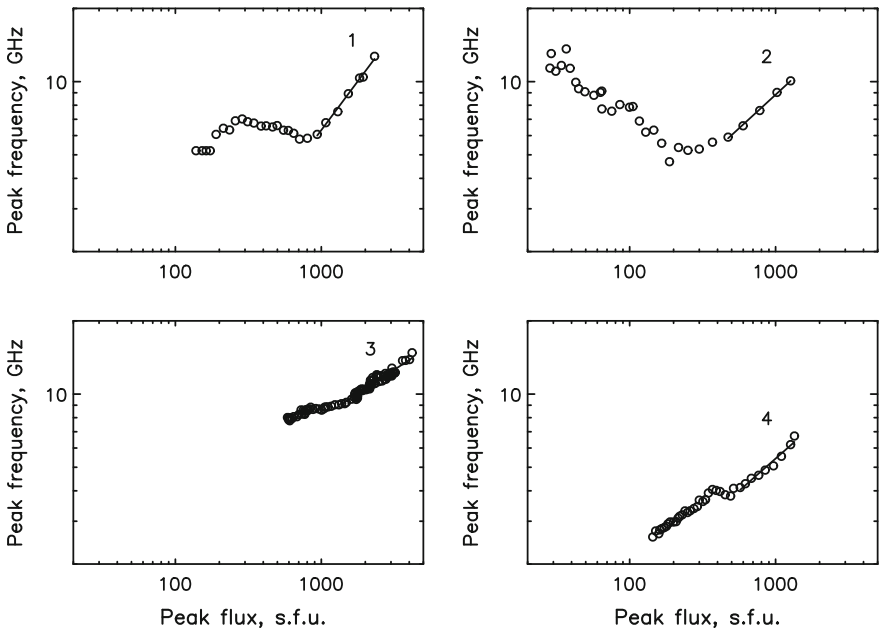

Fig. 3.14 The relationship between the peak frequency, ν_{pk}, and peak flux density, $S_{pk} = S(\nu_{pk})$ on the decay phase of four events with the highest values of $\Delta\nu_{pk}/\nu_{pk}$. The straight lines are the best linear fits (in logarithmic scale) near the peak of the bursts. The numbers indicate the events: 1–30 August 2001, 2–31 August 2001, 3–22 October 2001, 4–28 August 2002

Table 3.2 Regression coefficients for events with $\Delta\nu_{pk}/\nu_{pk} < -0.4$ in Fig. 3.14

No	Event	$\beta(\nu_{pk}, S_{pk})$	$\beta(\nu_{pk}, S_{thin})$	$\beta(\nu_{pk}, S_{thick})$
1	30 Aug 2001	0.80	0.45	>0.78
2	31 Aug 2001	0.55	0.39	>0.55
3	22 Oct 2001	0.39	0.32	>0.52
4	28 Aug 2002	0.53	0.27	>0.42
	Mean	0.57	0.36	>0.57

to $\Delta\delta = 2.0,\ 1.4,\ 1.4$, and 0.7, respectively. These spectral index variations can explain a considerable part of the difference $\tilde{\beta} - \beta$, but not all of it. In our opinion, some of the enhanced decrease of ν_{pk} must be ascribed to some other effect, such as the radio source shift into the LT region with a weaker magnetic field [55]. We conclude that GS self-absorption can explain the four bursts with large negative peak frequency shifts, but only when other effects are included.

It is interesting that the opposite case, strong Razin suppression, can in some special circumstances also result in large negative shifts in ν_{pk} on the decay. As shown in Fig. 8c, d of Ref. [46], a plausible combination of plasma heating (which

Table 3.3 Regression coefficients for events with $-0.3 < \Delta\nu_{\rm pk}/\nu_{\rm pk} < -0.1$

No	Event	$\beta(\nu_{\rm pk}, S_{\rm pk})$	$\beta(\nu_{\rm pk}, S_{\rm thin})$	$\beta(\nu_{\rm pk}, S_{\rm thick})$
1	25 Aug 2001	0.95	0.52	1.97
2	28 Dec 2001	0.35	0.19	0.65
3	20 Jul 2001	0.21	0.16	0.38
4	26 Jul 2001	0.27	0.20	0.56
5	28 Aug 2002	0.27	0.20	0.43
6	31 Oct 2002	0.38	0.20	>0.7
	Mean	0.40	0.24	>0.8

lowers free-free opacity) and a drop in density of high-energy particles may result in an arbitrarily high $\beta(\nu_{\rm pk})$, i.e., a decrease in $\nu_{\rm pk}$ at nearly constant $S_{\rm pk}$.

Moderate Negative Frequency Shifts

A total of 12 events show relative shifts ($-0.3 < \Delta\nu_{\rm pk}/\nu_{\rm pk} < -0.1$). Six of these are chosen for illustration and listed in Table 3.3. These bursts have mean value $\beta \simeq 0.4$ that is closer to the theoretical expectations. The detailed analysis shows that in some cases the moderate values of $\Delta\nu_{\rm pk}/\nu_{\rm pk}$ are actually large-shift events whose overall slope is moderated due to a change of the evolution from an initial steep decrease to a constant or increasing value of $\nu_{\rm pk}$ on the time interval over which the slope is measured. Such a change in slope during the decay is quite typical. In fact, in only four of the 12 events did the peak frequency decrease monotonically. In the other eight events, the peak frequency initially dropped quickly, but became constant or started to increase before $S_{\rm pk}$ had dropped by an order of magnitude. We will discuss these flat or increasing frequency shifts on the decay shortly.

Small Frequency Shifts

Eleven events show small relative frequency shifts on the decay, in the range $-0.1 < \Delta\nu_{\rm pk}/\nu_{\rm pk} < 0.1$. About half of these bursts (6 of 11) are explained by a similar change of slope of $\nu_{\rm pk}$ vs $S_{\rm pk}$ that we saw in the previous section, from an initial decrease to a later increase. In the other five events we observe small, gradual monotonic shifts or even remarkably flat values of $\nu_{\rm pk}$ on the decay phase similar to what we have already discussed for the rising phase. The examples of such a behavior can be seen in Fig. 3.13. For seven of these 11 events, the peak frequency became constant or started to increase before $S_{\rm pk}$ dropped by an order of magnitude (see Fig. 3.14).

Positive Frequency Shifts

Despite the fact that GS self-absorption requires a decrease in $\nu_{\rm pk}$ during the decay phase, a large percentage (23 of 34 events, i.e., ≈68%) in our sample display a considerable *increase* of $\nu_{\rm pk}$ starting at some point during the decay phase. As we have already mentioned above, in most cases the increase begins after some decrease of the burst flux, often by a factor of 2–3 and sometimes by a larger factor.

The characteristic time delay of the beginning of the peak frequency increase relative to burst maximum is 2 min. However, the delay varies considerably from event to event. In several events it begins just after the intensity peak, while in more than 1/3 of events it is quite long, varying from 2 to 8 min. These events are usually long lasting gradual bursts with relatively low peak frequency, $\nu_{pk} \leq 7$ GHz, prior to the increase (see the examples in Fig. 3.13). In Fig. 3.13f, g one can clearly see the considerable increase of ν_{pk} and ratio R on the late decay phase, starting from 20:26 UT. The increase of R means that the flux decrease at low frequency $\nu_1 = 4.6\,\text{GHz} < \nu_{pk}$ goes faster than at high frequency $\nu_2 = 11.2\,\text{GHz} > \nu_{pk}$. The faster flux decrease at lower frequencies (steepening of the spectrum at $\nu < \nu_{pk}$) after moment t_6 is easily seen in Fig. 3.5c, which is the same burst as in Fig. 3.13e–h. Note that the shape of the MW spectrum during this increase remains the typical GS spectrum with a well pronounced spectral peak.

We have examined possible reasons for an increase in ν_{pk} in the late decay phase, such as thermal GS emission, or variations in parameters (decrease in source area A, or increase in magnetic field strength B), and again find that the most plausible explanation is an increase in density in the decay phase, which increases the effect of Razin suppression with time.

3.1.2.7 Model Simulations

We showed earlier that in a majority of bursts the peak frequency shifts are well correlated with flux density (at least near the maximum of the burst), as expected if the spectral turnover is due to GS self-absorption (see Sect. 2.2.4). We also showed that other effects such as evolution of the electron energy distribution can act in concert with GS self-absorption to account for some other peculiarities of spectral dynamics (e.g., time delays between ν_{pk} and S_{pk}).

However, GS self-absorption cannot explain behavior found in a significant number of events including: (1) slight variations or even constancy of the peak frequency even when the burst intensity changes by an order of magnitude or more, or (2) a shift of the peak frequency to higher frequencies starting in the middle or late decay phase. A common feature that seems associated with the above behavior is a relatively low maximum value for ν_{pk}. In some events ν_{pk} can be as small as 3 GHz, which indicates a relatively weak magnetic field in the radio source. In Sects. 2.2.5–2.2.7 we have examined Razin suppression as a mechanism to explain each of these properties.

One of the main observational clues of the existence of Razin suppression that has been cited in the literature is the steep low-frequency total power spectra expected from a homogeneous source. With rare exceptions, our events do *not* show such steep spectra. But it is well known that steep low-frequency spectra are expected in total power only for the case of a homogeneous source, whereas typical flares display considerable inhomogeneity that we argue will destroy this signature of Razin suppression. In Sect. 2.2.8 we present a simple model to demonstrate the effect.

3.1.2.8 Discussion and Conclusion

Dynamical changes in the peak frequency of the GS spectrum of MW bursts have been analyzed using data on 338 bursts obtained in 2001–2002 with OVSA. We find that the dynamical changes show a few distinct behaviors, which we have interpreted in terms of two competing effects: (a) GS self-absorption and (b) Razin suppression.

Observationally we find that, for a majority of a subset of 38 simple bursts, the peak frequency is very well correlated with the intensity of MW bursts, at least near the burst maximum. The peak frequency increases on the rise phase in ≈83% of 24 bursts where it could be clearly measured, and decreases on the decay phase in ≈62% of 34 bursts, in qualitative agreement with GS self-absorption as the origin of the low-frequency turnover. For some bursts of this type, however, we find a faster than expected decrease of $\nu_{\rm pk}$ on the decay phase. This behavior is correlated with flattening of the high-frequency slope (increasing $\alpha_{\rm h}$) of the MW spectrum, which is indicative of hardening of the electron energy distribution. The presence in many bursts of a positive or negative time difference between the maxima of $\nu_{\rm pk}$ and $S_{\rm pk}$ time profiles is also shown to be due to GS self-absorption under evolution (usually hardening but sometimes softening) of the electron spectral index.

However, we also find that for ≈30–36% of bursts the peak frequency increase near the burst maximum is much smaller than expected or even may be entirely absent. Typically in these bursts $\nu_{\rm pk}$ starts at a rather high frequency in the very beginning of the burst and remains almost constant during a considerable (factor of ≈10) increase and decrease of the burst intensity. We explain this temporal behavior as follows: In the beginning of the rise phase and during the late decay phase the radio source is optically thin at low frequencies due to the Razin effect. But briefly near the maximum, when the column density of NT particles becomes high enough, the source becomes nearly optically thick at $\nu \leq \nu_{\rm pk}$, despite the Razin suppression, and the spectral evolution of $\nu_{\rm pk}$ takes on the characteristics for GS self-absorption.

About 70% of bursts show a gradual increase in $\nu_{\rm pk}$ starting at some point in the decay phase. We show that this behavior can easily be explained by Razin suppression together with either hardening of the high-energy electron spectrum or an increase in Razin parameter (due to an increase in plasma density or a decrease in magnetic field strength in the MW source). Again, the evidence for electron spectral hardening, when present, can be obtained directly from the observed flattening of the MW high-frequency spectral slope. An increase in $\nu_{\rm pk}$ in the late phase that is unaccompanied by MW spectral flattening may thus be a direct signature of chromospheric evaporation and/or evolution of the source to greater heights where the magnetic field strength is lower.

Using numerical calculations from GS theory, including the effect of the medium, we have confirmed that the wide range of evolutionary behavior can be interpreted as an interplay between GS self-absorption and Razin suppression . In Fig. 3.15 we show a schematic representation summarizing our theoretical predictions. The time profiles of $\nu_{\rm pk}$ are shown in each panel for three cases: (1) GS self-absorption is dominant throughout the burst (solid lines), (2) Razin suppression is dominant in the beginning and end of the burst, while GS self-absorption is important near

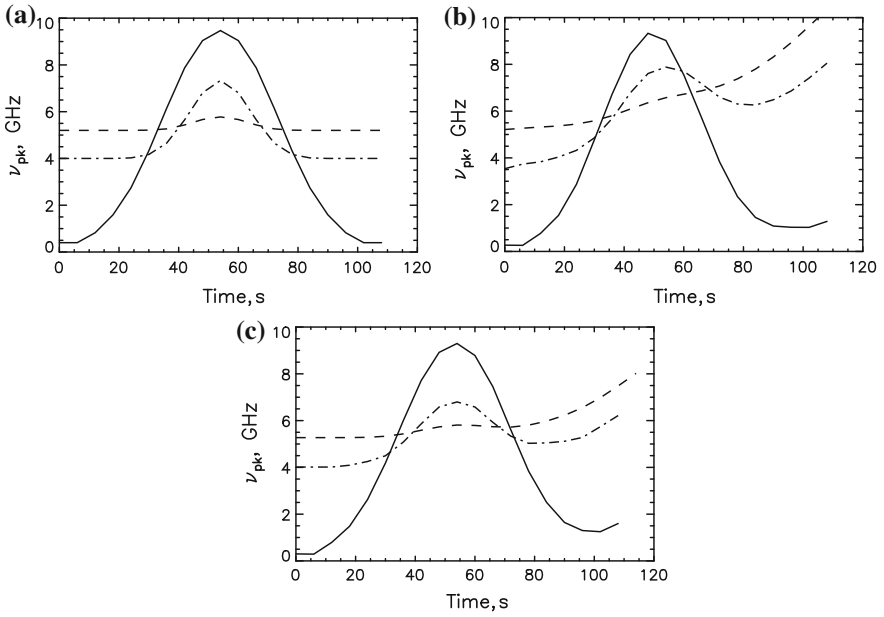

Fig. 3.15 Schematic representation of characteristic time profiles of the peak frequency expected from GS theory. The three curves in each panel are (solid line) self-absorption dominant throughout a burst, (dot-dashed line) Razin suppression dominant in the beginning and end of a burst, but self-absorption important near the burst maximum, and (dashed line) Razin suppression dominant throughout a burst. The panels show three cases: **a** electron spectral index is constant, **b** continuous hardening of the electron spectrum, and **c** stable electron index but Razin suppression (as expressed by $Y = \nu_p/\nu_B$) increases on the decay phase

the burst maximum (dot-dashed lines), and (3) the Razin suppression is dominant throughout the burst (dashed lines). These three cases correspond to increasing values of parameter $Y = \nu_p/\nu_B$ from low to moderate to high.

Applying these theoretical predictions to our observational findings, we can say that Razin suppression plays an important role in the spectral dynamics of more than 70% of bursts, at least in their decay phase. For the Razin effect to be important for a relatively large number of bursts (with average $\nu_{pk} \approx 6\,\mathrm{GHz}$), we require that the magnetic field in the source be relatively weak (100–300 G for a corresponding plasma density $1\text{–}10 \times 10^{10}$ cm^{-3}). Now that we have shown how to recognize the presence of Razin suppression from the dynamical changes in ν_{pk} and R during a burst, the changes in ν_{pk} can be used quantitatively as a further constraint on the evolution of plasma parameters, especially ambient density and magnetic field strength. Together, the combination of spectral measures (1) temporal evolution of ν_{pk}, (2) R, the logarithm of the ratio of flux densities above and below ν_{pk}, and (3) the high-frequency slope α_h, relative to the flux density at spectral maximum, S_{pk}, provide a new, valuable diagnostic for MW bursts of GS origin.

It is well known [29] that MW burst sources typically have an inhomogeneous spatial structure. Inhomogeneous magnetic field, plasma density and high-energy electron distributions in these sources (see e.g., the Refs. [51, 56, 57]) can considerably disturb the total MW spectrum and its evolution. So, to be of greatest diagnostic power, the spectral dynamics should be measured in brightness temperature, i.e., using spatially resolved spectra. In this case, the above theoretical predictions are more directly applicable since the inhomogeneity is only that along the line of sight. Such measurements require simultaneous spatial and spectral resolution over a wide band of frequencies. The Refs. [48, 58] are the only published examples that showed Razin suppression in a brightness temperature spectrum. Such observations will be possible routinely with a new generation radio facility, the Frequency Agile Solar Radiotelescope (FASR) and MUSER in China, now under development. For more comprehensive application of these new diagnostics to flaring loops, such MW data should be analyzed in combination with diagnostics from EUV, X-ray, and gamma-ray data [59].

3.1.3 Optically Thin Emission, Power-Law Distribution of Flares, and Occurrence Rate of Flares

The occurrence rate of radio bursts at different frequencies can be taken as an indicator for the flare occurrence rate at different coronal altitudes, due to a definite relationship between radio frequencies and the altitudes of radio sources in solar corona. In general, the position of radio sources at lower frequencies is above that at higher frequencies in respect to solar photosphere, but it is difficult to obtain an exact expression for this relationship, because the radio frequency may correspond to different source parameters (density or magnetic field) in respect to different radiation mechanisms, and a great uncertainty exists for the models of density or magnetic field in solar atmosphere, especially, there is no reliable method to measure coronal magnetic field so far (see Chap. 6).

On the other hand, a statistics of X-ray flares showed that the flare occurrence rate with different intensities satisfying a power-law distribution [60], and the power-law index approximately equals to 1.8. Based on this statistics, a general avalanche model has been proposed for the magnetic energy release processes in solar flares, and the observed power-law index can be well explained by this model. Similar statistics have been made in optical, radio, and UV bands, all of which strongly support the avalanche model, and it becomes a well-known theory for magnetic energy release, particle acceleration, and coronal heating (see a recent review about that [61]).

Table 3.4 The lower cutoff (weak event number) N_1, the event number satisfying power-law N_2, the power-law indices $\hat{\alpha}$ and its error, and the peak flux f_p corresponding to lower cutoffs at 6 frequencies ν of NoRP

ν(GHz)	1	2	3.75	9.4	17	35
N_1	433	347	342	251	190	141
N_2	53	139	144	235	296	345
$\hat{\alpha}$	1.87 ± 0.12	1.83 ± 0.07	1.82 ± 0.07	1.78 ± 0.05	1.74 ± 0.04	1.77 ± 0.04
f_p(sfu)	392	84	100	118	81	41

3.1.3.1 Data Selection

In practice, different wavebands, instruments, and data processes will definitely affect the calculation of power-law index, to cause its straggling from the theoretically prediction [61]. One study tried to compare the power-law indices of radio bursts at 2–11.8 GHz, and found that the a maximum may be reached at a middle frequency in this range, and it actually varied in different solar circles [62]. However, some uncertainty was caused by the observations of different instruments at different frequencies in this study, so that, we select 486 bursts observed by NoRP at 1, 2, 3.75, 9.375, 17, and 35 GHz in 1994–2005 [63], here we exclude the data at 80 GHz with a worse SNR, and earlier (1992–1994) observations of NoRP in different locations.

3.1.3.2 Data Process

There is a shortage in the method of maximum likelihood that widely used in previous statistics to fit the power-law distribution, i.e., there is no a definite criterion (so-called lower cutoff) to remove the weak bursts, which are evidently deviated from a power-law, and the criterion is arbitrarily selected at different frequencies, which can seriously affect the comparison of power-law indices at different frequencies. An improved method of maximum likelihood has been accepted, in which a strict criterion is proposed to select the lower cutoff, and to verify the power-law distribution [64, 65].

The obtained power-law indices varied with lower cutoffs at different frequencies of NoRP are shown in Fig. A.1 in Appendix A, in which the lower cutoffs selected by the improved method of maximum likelihood at different frequencies are marked by vertical dashed lines with different colors. The statistical parameters in Fig. A.1 are summarized in Table 3.4, which includes the lower cutoff N_1 (the weak event number), the event number satisfying power-law N_2, the power-law index $\hat{\alpha}$, and the peak flux f_p corresponding to the lower cutoff in 486 bursts.

It is clearly seen from Table 3.4 that the obtained power-law indices ($1.74 \sim 1.87$) are much close to the theoretically predicted value (1.8) in comparison with previous studies. It is interesting that the lower cutoff (weak event number) N_1 is larger, and thus the event number satisfying power-law N_2 is smaller at lower frequencies, which will be discussed later [66].

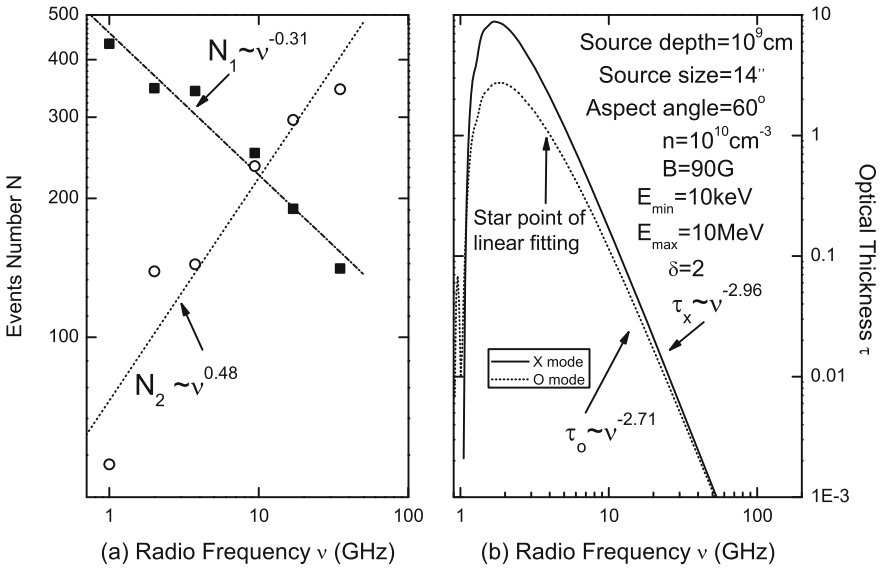

Fig. 3.16 **a** The variation and linear fitting of N_1 and N_2 versus frequencies in Table 2.4, and **b** theoretical calculations of optical thickness of X-mode and O-mode versus frequencies

3.1.3.3 Physical Nature of Event Number Satisfying Power-Law Varied with Frequencies

We can make a linear fitting for both the variations of N_1 and N_2 versus frequencies in a logarithm coordinate in Fig. 3.16a, with a power-law index of -0.31 and 0.48, respectively. The optical thickness of X-mode and O-mode calculated by a standard code [39] in SSW is given in Fig. 3.16b for understanding Fig. 3.16a. It is well known that the optical thickness decreases rapidly with increasing of frequencies, i.e., the probability of optically thin emission at higher frequencies will exceed that at lower frequencies, which predicts an intrinsic relation between the power-law event and optically thin emission. On the other and, the optically thin emission is much closely related to flare energy release than optically thick emission as mentioned in Sect. 3.1.1, and it could be considered as an indicator of flare occurrence rate.

3.1.3.4 Optically Thin Event Number Varied with Peak Frequency

It is well known that there is a peak (turnover) frequency in a typical MW spectrum, and the regions below and above the peak frequency are respectively defined as optically thick and optically thin parts, because the optical thickness is much larger and smaller than 1 respectively in these two parts. Figure 3.17a gives the statistics of event number versus peak frequency for the 486 bursts of NoRP. Due to the low-frequency resolution of NoRP, we simply assume that in the events with a given

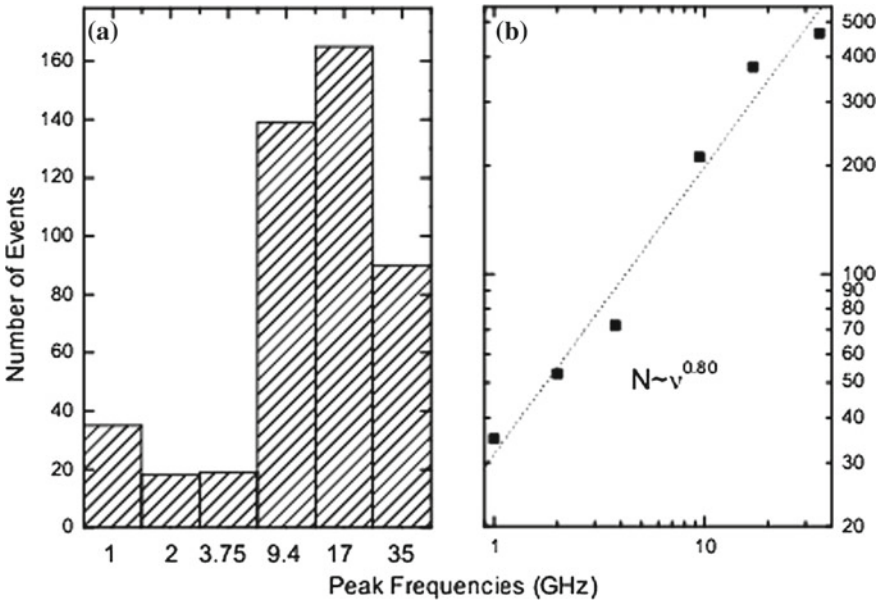

Fig. 3.17 **a** Statistics of event number versus peak frequency for the 486 bursts of NoRP, and **b** the optically thin event number versus frequency with a linear fitting

peak frequency, there are a half events belong to optically thick part, while the rest half events belong to optically thin part. Hence, the total optically thin events at this frequency just equals a half of optically thin events plus all the events with a peak frequency smaller than this frequency. In this way, we obtain the optically thin event number versus frequency in Fig. 3.17b, which is well fitted by a power-law.

It is evident that the power-law index of optically thin events in Fig. 3.17b (0.8) is comparable with that of power-law events in Fig. 3.17a (0.48), which confirms the intrinsic relation between power-law event and optically thin emission proposed from Fig. 3.16a.

3.1.3.5 Flare Occurrence Rate Versus Frequency

Now, we can use the statistical result of power-law events in Fig. 3.16 and Table 3.4 to discuss the flare occurrence rates at different frequencies, and we define the difference of power-law events at two adjacent frequencies divided by the corresponding frequency interval as the flare occurrence rate, to remove the effect of different frequency intervals if we simply use the power-law events at a given frequency. Figure 3.18 gives the flare (burst) occurrence rate at a unit frequency interval (GHz^{-1}) versus frequency.

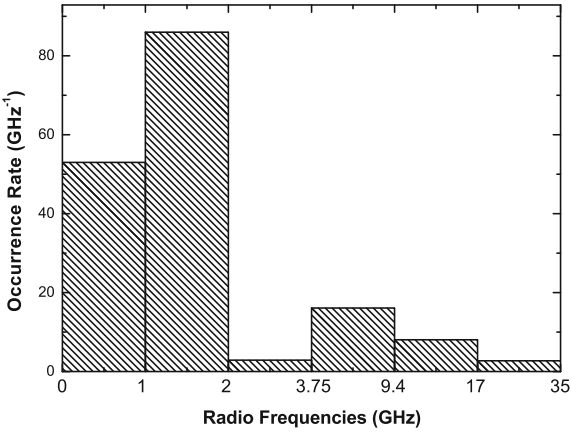

Fig. 3.18 The histogram of power-law event number per unit frequency interval versus frequency

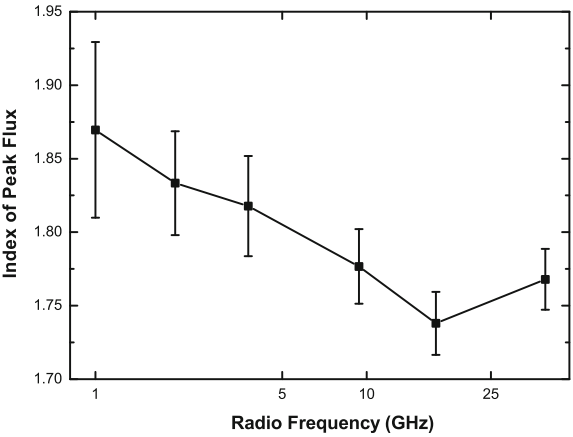

Fig. 3.19 The power-law index varied with frequency

It is clearly seen from Fig. 3.18 that the flare occurrence rate at lower frequencies (1–2 GHz) is obviously larger than that at high frequencies, which means that most flares occur in higher corona, and this result can be confirmed by the relationship of power-law index versus frequency as shown in Fig. 3.19.

It is evident from Fig. 3.19 that the power index decreases monotonously with frequency (a small enhancement at 35 GHz does not exceed the error bar). A larger power-law index refers to that there are more relatively smaller events, for instance, when the power-law index is larger 2.0, the energy of total small events can satisfy the requirement of coronal heating by micro flares [67]. Hence, the results of Figs. 3.18 and 3.19 support each other.

3.1.3.6 Conclusion

Finally, we summarized three reasons to support the intrinsic relation between the MW optically thin emission and power-law distribution of flares:

(1) There are no more effects of propagation or absorption in the MW optically thin emission, which should be closely related to flare energy release process (for instance, we can estimate electron energetic spectral index directly from the MW optically thin spectral index).

(2) The MW optical thickness decreases rapidly with increasing of frequency, which is similar to the tendency that the power-law event number increases with increasing of frequency.

(3) The optically thin event number estimated by peak frequency increases with increasing of frequency, which is quite similar to the variation of power-law event number with frequency, and their linear fitting indices are also close to each other.

3.2 Spatial Distribution of Microwave Brightness

Spatial distribution of NT emission along a single flare loop can bring us important information on the particle acceleration and transport. Studies of the MW spatial distribution began in the 80s using the WSRT and VLA facilities. The discovery of two kinds of MW sources, single compact LT sources and double sources with their peaks located close to the conjugate magnetic FPs [68–71], stimulated the development of theoretical simulations of GS brightness distribution along model magnetic loops (see the Refs. [29, 56, 72]). Later the similar studies were carried out using the Nobeyama Radioheliograph (NoRH) observations at single frequency 17 GHz [73–75]. They showed the existence of the double and triple radio sources associated with the FPs of large and smaller flaring loops.

In recent years, the new NoRH facilities have allowed to obtain images of solar flares at two high frequencies, 17 and 34 GHz, simultaneously with high angular (5–10 arcsec) and temporal (0.1 s) resolution. These frequencies are remarkably higher than the usually observed spectral peak frequency, $f_{peak} = 5$–10 GHz [49], at which the optical thickness of GS emission $\tau \approx 1$. This gives a chance to study the brightness distribution having the information on MW spectrum slope, and, therefore, on the optical thickness in different parts of a flaring loop. Such high capabilities provide us with unique opportunity to get constraints on properties of mildly relativistic electrons accelerated and propagating in flaring magnetic loops.

Already the first reports on these two frequency observations [76, 77] gave quite unexpected results showing that at least in some events the bright LT source is optically thin. This fact is in evident disagreement with the simulated brightness distribution of optically thin MW emission along inhomogeneous magnetic loop. Several new studies were published during the last years developing further understanding of the problem [55, 58, 78–84]. Of special interest are new results concerning the spatial distribution and dynamics of the MW spectral slope along flaring loops [30, 79, 85, 86].

This section is restricted to properties of single well-resolved loop-like MW sources. We review mainly our recent studies of Nobeyama observations concerning (1) spatial distribution of MW brightness and spectral slope along flaring loops; (2) peculiarities of their temporal dynamics in different parts of a loop; and (3) consequences of the obtained findings on spatial, spectral, and pitch-angle distributions of high-energy electrons, to give us some new important constraints on the acceleration/injection mechanisms and kinetics of mildly relativistic electrons in solar flares.

3.2.1 Nonthermal MW Source at the Top of Extended Flaring Loops

The existence of the double and triple radio sources associated with the FPs of flaring loops, as well as asymmetric sources [73–75], agrees well with the existing theoretical models of radio emission [29, 56, 72]. The obvious reason for such a location is the strong dependence of GS intensity on magnetic field strength. On the other hand, the location of the brightness peak of optically thin MW emission in the LT is a challenge to our understanding of processes in flaring loops [55, 78, 87].

For the detailed study of the spatial properties of MW emission from a flare loop we selected only flares, which are characterized by the presence of well-resolved extended single MW sources and relatively simple time profiles both at 17 and 34 GHz. We have chosen five flares occurred on 1999 August 28, 2000 January 12 and March 13, 2001 October 23, and 2002 August 24. Their sizes (25–90 arcsec) exceed considerably the beam size of NoRH ($\Delta\varphi \sim 5$ arcsec and ~ 10 arcsec at 34 and 17 GHz, respectively). The 1st, 3rd, and 4th flares occurred on the solar disk, the 2nd and 5th near the East and West limbs, respectively. The projections of the radio sources on the disk display a well developed loop-like structure at both frequencies. The limb source has an elliptic shape. Their peak brightness temperature varies from source to source from $7.0 \cdot 10^6$ K up to $1.2 \cdot 10^8$ K at 17 GHz and from $8.0 \cdot 10^5$ K up to $2.5 \cdot 10^7$ K at 34 GHz. The bursts show quite simple time profiles at 17 and 34 GHz with the half-power duration of main peaks in a range of $\Delta T_{0.5} = 20 - 110$ s.

All the radio sources are optically thin at least at 34 GHz. Indeed, as analysis shows, the flux density spectral slope in the range 17–34 GHz is negative during the impulsive phase of the MW bursts. For the analysis of the MW source structure we also used NoRH polarization maps as well as magnetographic data from SOHO/MDI. An example of overplotted NoRH and MDI maps is displayed in Fig. 3.20. A loop-like MW source with the brightness maximum in its center is seen at 34 GHz map (white contours). Our analysis of MDI data has shown that the central part of the source is not associated with photospheric sunspots under the loop top. At the same time, the MDI maps display the magnetic field enhancements of opposite polarities near two ends of the loop-like structures (supposed to be the indications of the loop FPs).

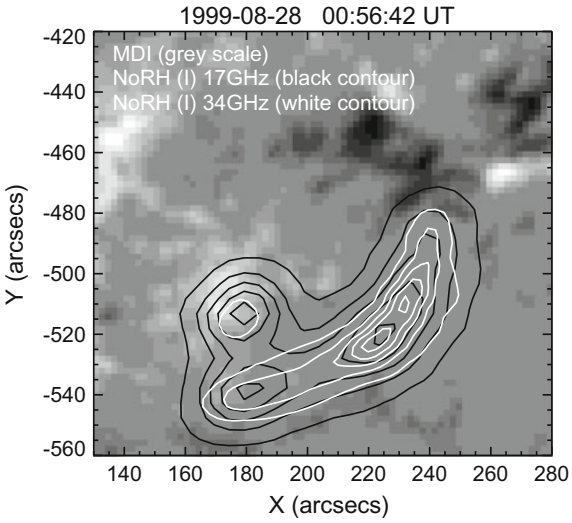

Fig. 3.20 SOHO/MDI photospheric magnetograms (gray scale) overlaid by contours of radio images at 0.1, 0.3, 0.5, 0.7, and 0.9 levels of the maximum brightness temperature (black for 17 GHz and white for 34 GHz). Magnetograms were obtained near the time of radio burst and were rotated to the moment of radio images

The spatial profiles of the brightness along the loop-like radio sources at the peak time for each event are shown in Fig. 3.21. We can clearly see the brightness maxima to be located close to the central part of the sources. This is especially well pronounced for the highest frequency, 34 GHz, where the sources must be optically thin.

Note that the similar brightness distributions at the peak time of three limb flares observed with NoRH were obtained by Kundu et al. (2001) [78]. This proves that such kind of the brightness distribution for extended flaring loops is quite common and, therefore, should be studied in detail.

3.2.2 Time Delays Between MW Emissions from Different Parts of Flaring Loop

It was shown that the time delays of the emission from different parts of a loop-like MW source can bring us important information on trapping and accumulation of high-energy electrons in flaring magnetic loops [87]. At the top of Fig. 3.22 we show the flux time profiles from the regions corresponding to different parts of the loop source for the event on March 13, 2000: the LT (black contour at the bottom of Fig. 3.22), and the north-east FP (white dashed-dotted contour at the same plots). Time profiles of the emission from the second FP are not shown here since their behavior is very similar. The size of the regions used for the flux calculations is 10" × 10".

It is well seen that the burst of emission from the loop top is delayed against the burst from the FP source by several seconds. This delay is more pronounced

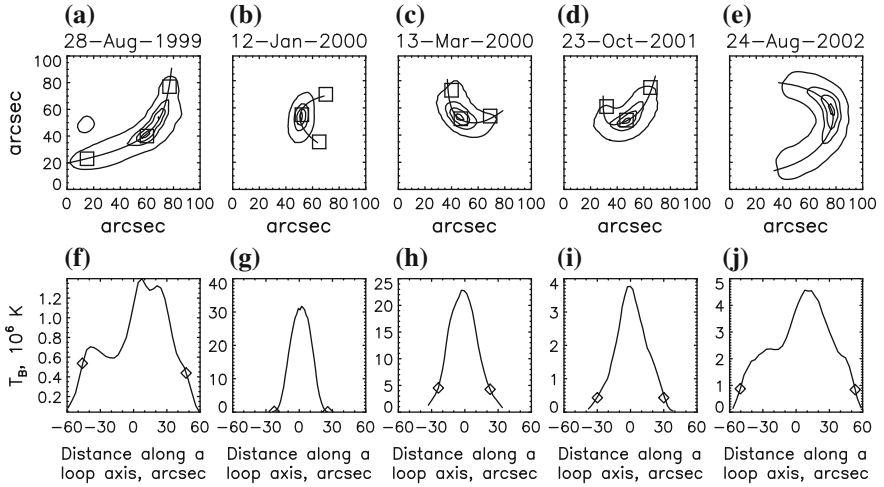

Fig. 3.21 **a**–**e** 34 GHz contour images of the sources at the moment of the bursts peaks (except **e**, this image is for the rise phase) for five events under study. Contours show 0.1, 0.5, 0.75, and 0.95 levels of the maximum brightness temperature. Thin curve shows the visible flaring loop axis. Three boxes of the size 10×10 arcsec, two near FPs and one near the LT show the areas which the flux time profiles were calculated from. **f**–**j** Spatial distributions of radio brightness temperature at 34 GHz along a visible flaring loop axes shown on top panel for each event by thin curve. Zero position on the x-axes of bottom panel corresponds to the middle of the loop axis, calculated as a half of the axis length. Negative values correspond to left FP on **a**, **c**, and **d** and lower FP on **b** and **e**

at 34 GHz than at 17 GHz. Furthermore, it is clearly seen that the time profiles of emission from the loop top are wider, and their decay is slower than those from the region near the FP. We did not find any noticeable delay between time profiles at both frequencies from the conjugate FPs.

The similar delays and differences in the characteristic decay time are observed for all the events from our sample (see, for instance, Fig. 10 in the Ref. [87] for the event of 28 Aug 1999). Note that the flux peaks from the FP sources are coincident in time with the flux peaks of HXR emission (compare Figs. 10 and 11 in the Ref. [87] where the vertical line indicates the moment of the HXR emission peak, 00:56:42 UT).

3.2.3 Time Delays of MW Emissions at Different Frequencies

A comparison of the MW time profiles of emission at the frequencies 17 and 34 GHz from the same parts of a loop-like radio source is shown on Figs. 29c, d and 10 in the Ref. [87]. One can clearly see that, for the main peak of the bursts, the emission at higher frequency, 34 GHz, is delayed against that at 17 GHz. This is well pronounced for the LT part of the sources. However, there are no such delays for the FP parts.

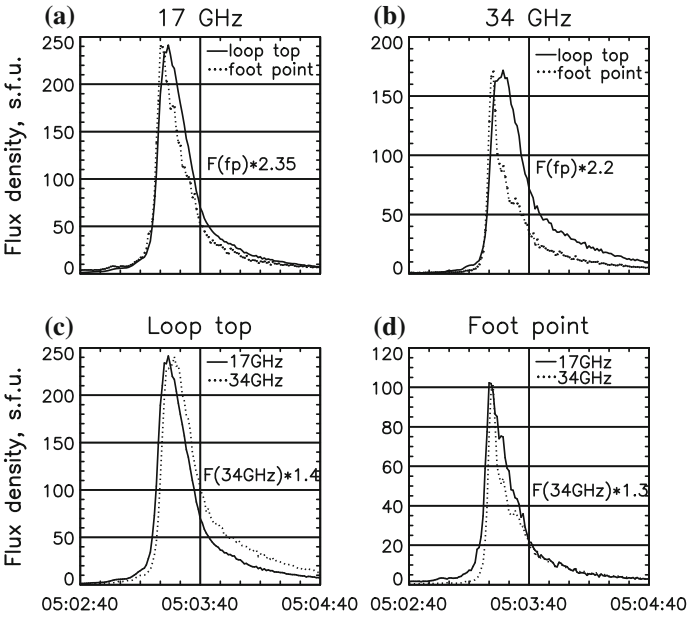

Fig. 3.22 NoRH time profiles of the flux densities from the 10"x10" boxes located at the LT and the left FP (see Fig. 3.23) of the flare on 2000 March 13

The FP emission at both frequencies reaches its maximum almost simultaneously with the peak of the corresponding HXR burst (see Figs. 10–11 in the Ref. [87]).

3.2.4 Redistribution of MW Brightness in Flaring Loops

Further analysis of the MW brightness distribution along the five well-resolved flaring loops shows that it does not remain constant during a single peak of a burst [79]. In almost all the analyzed events there is the same tendency (see, for example, Fig. 3.23). In the beginning of a burst there is always a time interval when brightness peaks (or one peak) are situated near the FPs of a loop (both or only one). And close to the burst maximum or on the decay phase, an area near the LT becomes most bright. A similar dynamics of brightness distribution was observed and studied in detail in the event 1999 May 29 [80].

To show this tendency more quantitatively, in Fig. 3.24 we compare the time profiles of fluxes and their ratios from the 10"x10" boxes, located near the left FP (*a*), right FP (*c*), and in the LT (*b*) of the flaring loop in the event 2000 March 13. The location of the boxes is shown in Fig. 3.21c. The *dotted* and *solid* lines correspond to the 17 and 34 GHz emission, respectively. The flux densities ratio F_{LT}/F_{FP} from the LT and the FP regions is calculated for the left FP (*d*) and for the right one (*e*).

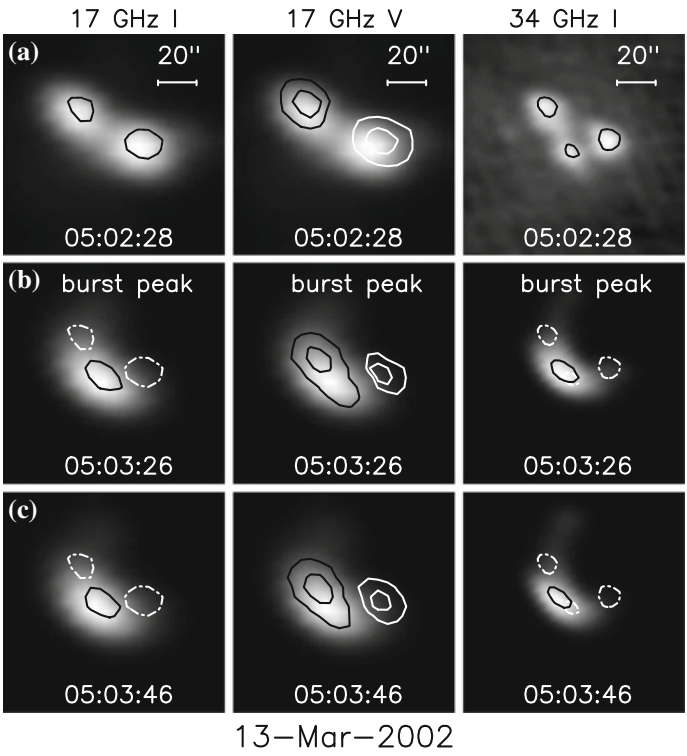

Fig. 3.23 NoRH images at the rise and peak phases of the flare 2000 March 13. Left and right panels: intensity at 17 and 34 GHz with the contours at the level 95% of the maximum at the current time (black solid line) and at the moment 05:02:28 UT (white dashed-dotted line). Middle panel: polarization V with the contours at the levels 40 and 80% of the maximum, black for positive V, and white for negative V

It is well seen that the ratios increase during the burst, especially fast on the early decay phase where maximum values of ratios reach 4–5.

Quite different evolution of the brightness distribution is realized during the limb event 2002 August 24. During the main peak of the burst, on its rising phase from 00:59:00, the southern FP of the loop becomes most bright at 34 GHz and remains the brightest part of the loop till the maximum at 01:00:30. At the peak time, the brightness temperature reaches extremely high value at 34 GHz: $T_{Bmax} \approx 250$ MK. In Fig. 3.25a, b we can also see two other brightness peaks: one near the opposite (northern) FP and one near the LT. But they are much weaker. Only on the decay phase the LT becomes relatively brighter than the FP sources which almost disappear to the moment of the valley before the second peak on the time profile (Fig. 3.25c, d). During the decay the brightness temperature in the southern FP source decreases by five times, and in the LT only by 20%.

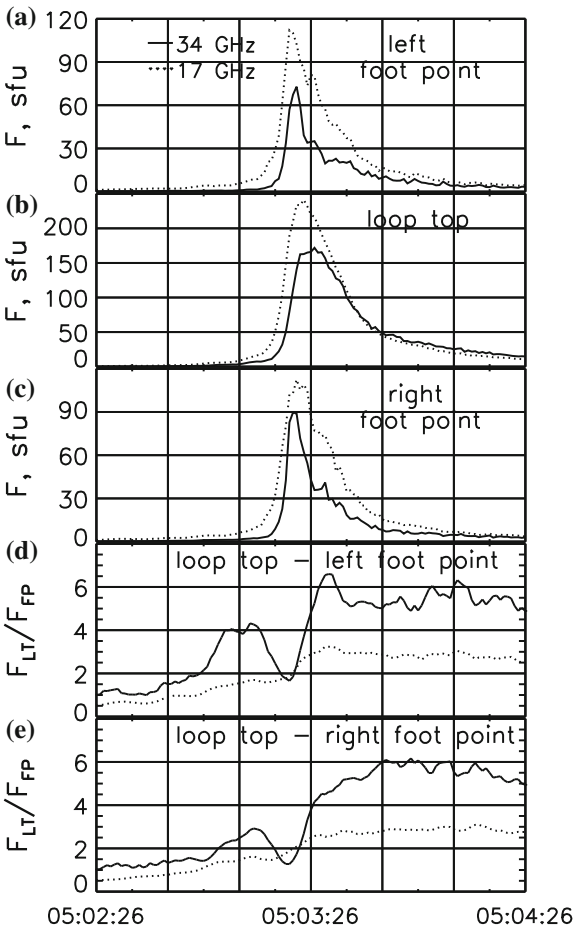

Fig. 3.24 NoRH time profiles of the flux densities from the 10"x10" boxes, located at the left FP (**a**), right FP (**c**) and in the LT (**b**) of the flare 2000 March 13. The flux densities ratio F_{LT}/F_{FP} from the LT and the FP regions is calculated for the left FP (**d**) and for the right one (**e**)

It is worth to note that during the main peak, when the total flux changes by 20–30 times, the visible size of the MW flaring loop has almost not changed. It means that the emission flux changes entirely due to changes in number of mildly relativistic electrons in the loop but not in the area or volume of the source. More or less similar situation was observed for other flares from our set.

3.2.5 Comparison of Observations and Model Predictions

The most interesting feature of all the flares is that the peak of a MW brightness distribution is located near the LT at the burst maxima (except 2002 August 24). This fact disagrees with the well known model simulations [56, 72] that predict the

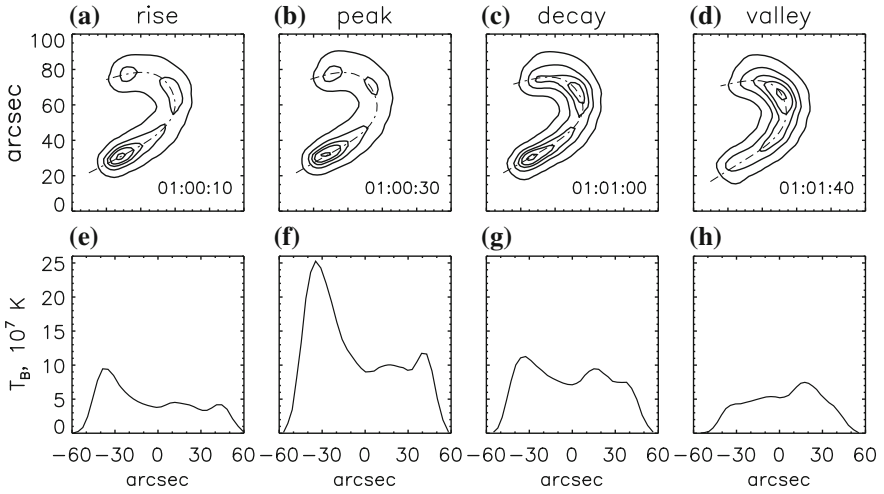

Fig. 3.25 Evolution of the brightness distribution during the limb event 2002 August 24

brightness peaks of optically thin emission to be near the FPs of extended loops with a nonuniform magnetic field. The increase of the brightness temperature occurs because of the strong dependence of GS intensity, I_f, on the magnetic field strength, B, that is expected to be larger near the feet of an extended loop. For example, if the electron power-law spectral index $\delta = 4$, then according to the Ref. [39]

$$I_f \propto NB^{3.4}(\sin\vartheta)^{2.2}\ , \tag{3.2.1}$$

where N is the number of NT electrons, θ is the viewing angle (angle between the magnetic vector and line of sight). It follows from the model [72] that even if an observer looks at a loop from above, the ratio of brightness temperatures in the LT, I_{fLT}, and at the peak near FPs, I_{fFP}, is equal to $I_{fLT}/I_{fFP} \simeq 0.5$ for the magnetic field difference $B_{LT}/B_{FP} = 1/2$. Note that the brightness peak near an FP is localized above the layers of strong chromospheric absorption, in the region where the view angle $\theta \ll 90$ arcdeg, but is still not too small.

The striking fact is that the brightness peak at the LT may be also observed for limb flares. For a limb loop which plane is almost perpendicular to the line of sight, θ = 80–90 arcdeg, like for the events 2000 January 12 and 2002 August 24 from our set, the ratio is expected to be much lower for the same difference in magnetic strength: $I_{fLT}/I_{fFP} \sim 0.1{-}0.2$. As can be seen in Fig. 3.25 (and also from the analysis of the limb events by the Refs. [78, 80]) the observable ratios at the highest frequency 34 GHz are just opposite: $I_{fLT}/I_{fFP} \sim 3{-}20$.

In the frame of the existing models, such a strong increase of the brightness near the loop top is not possible to explain with usual assumptions on physical conditions in a flaring loop. The possibility to have a hump in brightness near the LT due to the effect of optically thick emission [29, 88] is ruled out in our case since for all the

events under study the frequency spectral index between 17 and 34 GHz is negative and, therefore, the MW emission from the loops is optically thin at least at 34 GHz.

For loops near the solar disk center where the viewing angle θ is small near the FPs the following two assumptions can make the LT brighter than the FPs. The first is constant magnetic field along the flaring loops (see the Refs. [89] and Eq. (3.2.1)). The second is considerable transverse pitch-angle anisotropy of emitting electrons [30, 90]. The first assumption is problematic since the constancy of magnetic field strength along a loop suggests no trapping effect in contrast with our observations of well-pronounced time delays in the analyzed events. The second assumption looks very probable. It is supported by observations of the spectral steepening toward FPs that is also may be a consequence of the anisotropy, as well as by the model simulations of electron distributions in flaring loops.

For loops close to the limb with their plane almost perpendicular to the line of sight, the effects of both mentioned assumptions are too small to explain the observable ratios I_{fLT}/I_{fFP} and the shape of spatial profile along a loop [30, 78, 80].

3.2.6 *Spatial Distribution of Energetic Electrons in Flaring Loops*

We have to notice that the existing model simulations were made for the homogeneous distribution of energetic electrons along a loop. This assumption may strongly deviate from the reality. Indeed, the existence of delays between the higher and lower frequency and HXR intensity time profiles is an evident indication of electron trapping in MW sources [26, 91]. The delays between MW emissions from the LT and FPs as well as longer decay of the emission from the LT are a strong evidence of the trapping and accumulation of high-energy electrons in the upper part of flaring loops.

A strong relative enhancement of energetic electron density near the LT can eliminate the contradiction between the observations and the model predictions [58]. Under this assumption, we can easily derive the magnitude of the electron number density enhancement from Eq. (3.2.1) and the observed ratios I_{fLT}/I_{fFP} mentioned above. The corresponding difference in the number densities in the LT and FPs falls in the range $N_{LT}/N_{FP} \sim 10-100$.

To illustrate this idea, Fig. 3.26 displays three types of normalized spatial distributions along a loop. On the left hand, the number density (dashed line) and column number density (solid line) electron distributions, and magnetic field distribution (dotted line) are shown. These types of electron spatial distributions are obtained in the collisionless case when the first adiabatic invariant constancy along a magnetic field line with nonuniform strength $B(s)$ is fulfilled: $[1-\mu^2(s)]/B(s) = const$, and the corresponding electron pitch-angle distributions in the loop center are taken to be (a) beam-like $\phi(\mu) = exp[-(1-\mu^2)/\mu_{\parallel}^2]$, with the beam width along magnetic field $\mu_{\parallel} = 0.3$, (b) isotropic (with taking into account the loss-cone), and (c) pancake-like

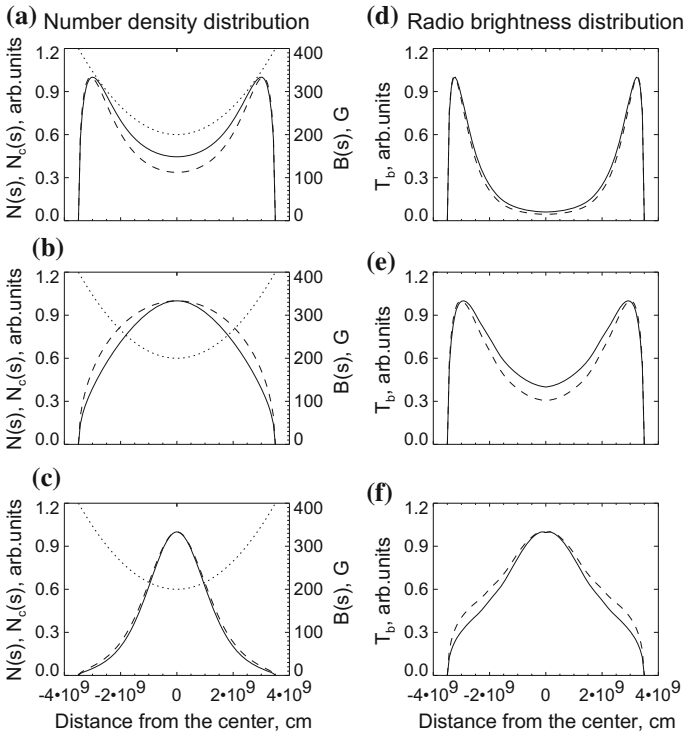

Fig. 3.26 Normalized spatial distributions along a loop [30]. Left column: number density (dashed line) and column number density (solid line) for the beam-like **a**, loss-cone **b**, and pancake **c** electron pitch-angle distributions; magnetic field distribution is shown by dotted line. Right column: corresponding GS intensity in optically thin regime (at 34 GHz)

$\phi(\mu) = exp[-\mu^2/\mu_\perp^2]$, with the beam width transverse to magnetic field $\mu_\perp = 0.4$, where $\mu = cos\alpha_0$, and α_0 is the pitch-angle in the loop center.

The corresponding GS intensity distributions along the model loop in optically thin regime (at 34 GHz) are shown on the right-hand panels of Fig. 3.26. The emission is calculated using the exact formalism [30, 36]. It is supposed that electrons have a power-law energy dependence: $g(E) = g_0 E^{-\delta}$; the model loop is located close to the limb and the viewing angle $\theta = 80°$. Two strong peaks of radio emission are observed for the beam-like and even for the loss-cone distribution, while the well defined peak of the number density exists in the loop center (see Fig. 3.26a–d, b–e). Only in the case of the pancake distribution, we can get a pronounced radio brightness peak at the center of a limb loop (Fig. 3.26c–f). A degree of brightness concentration to the loop center (the ratio I_{fLT}/I_{fFP}) can vary in wide range depending on the parameter $\mu_\perp$ of the Gaussian distribution function.

3.2.7 Dynamics of Electron Spatial Distribution

To understand the origin of peculiarities of MW brightness distribution and its dynamics along different flaring loops we do modeling of the time evolution of electron spatial distribution along a magnetic loop by solving the nonstationary Fokker-Planck equation under different assumptions on the physical conditions in the loop and for different positions of the injection site (loop top, loop foot) [87]. We consider the nonstationary Fokker–Planck equation in the form [92], which takes into account Coulomb collisions and magnetic mirroring:

$$\frac{\partial f}{\partial t} = -c\beta\mu\frac{\partial f}{\partial s} + c\beta\frac{d\,lnB}{ds}\frac{\partial}{\partial\mu}\left[\frac{1-\mu^2}{2}f\right]$$

$$+\frac{c}{\lambda_0}\frac{\partial}{\partial E}\left(\frac{f}{\beta}\right) + \frac{c}{\lambda_0\beta^3\gamma^2}\frac{\partial}{\partial\mu}\left[\left(1-\mu^2\right)\frac{\partial f}{\partial\mu}\right] + S\,, \qquad (3.2.2)$$

where $f = f(E, \mu, s, t)$ is electron distribution function of kinetic energy $E = \gamma - 1$ (in units of mc^2), pitch-angle cosine $\mu = cos\,\alpha$, distance from the flaring loop center s, and time t, $S = S(E, \mu, s, t)$ is injection rate, $\beta = v/c$, v and c are electron velocity and speed of light, $\gamma = 1/\sqrt{1-\beta^2}$ is Lorentz factor, $B = B(s)$ is magnetic field distribution along the loop, $\lambda_0 = 10^{24}/n(s)ln\Lambda$, $n(s)$ is plasma density distribution, $ln\Lambda$ is Coulomb logarithm.

We conducted our numerical calculations for two cases using the method developed by Gorbikov and Melnikov (2007) [93]. In the first case (Model 1) the source of high-energy electrons is located in the magnetic trap center $s = 0$, and in the second one (Model 2) near a trap foot $s = 2.4 \times 10^9$ cm. In both models, the trap (loop) is symmetrical and its half-length is 3×10^9 cm and magnetic mirror ratio $B_{max}/B_{min} = 5$. Plasma density is homogeneous along the loop with $n(s) = 2.5 \times 10^{10}\,\mathrm{cm}^{-3}$. The injection function $S(E, \mu, s, t)$ is supposed to be a product of functions dependent only on one variable (energy E, cosine of pitch-angle μ, position s, and time t):

$$S(E, \mu, s, t) = S_1(E)S_2(\mu)S_3(s)S_4(t)\,, \qquad (3.2.3)$$

where the energy dependence is a power-law $S_1(E) = (E/E_{min})^{-\delta}$, $E_{min} = 30$ keV, with spectral index $\delta = 5$; pitch-angle distribution is isotropic $S_2(\mu) = 1$; time dependence is Gaussian $S_4(t) = exp[-(t - t_m)^2/t_0^2]$, $t_m = 2.5$ s, $t_0 = 1.4$ s; spatial distribution is also Gaussian. For Model 1: $S_3(s) = exp(-s^2/s_0^2)$, and for Model 2: $S_3(s) = exp[-(s - s_1)^2/s_0^2]$, where $s_0 = 3 \times 10^8$ cm, $s_1 = 2.4 \times 10^9$ cm.

The results of the model simulations are presented in Fig. 3.27 where one can see the time evolution of electron number density along the loop for electrons with energy $E = 454$ kev.

It follows from Fig. 3.27 that for the case of Model 1 the shape of the spatial distribution does not change much with time. During all the injection phases the

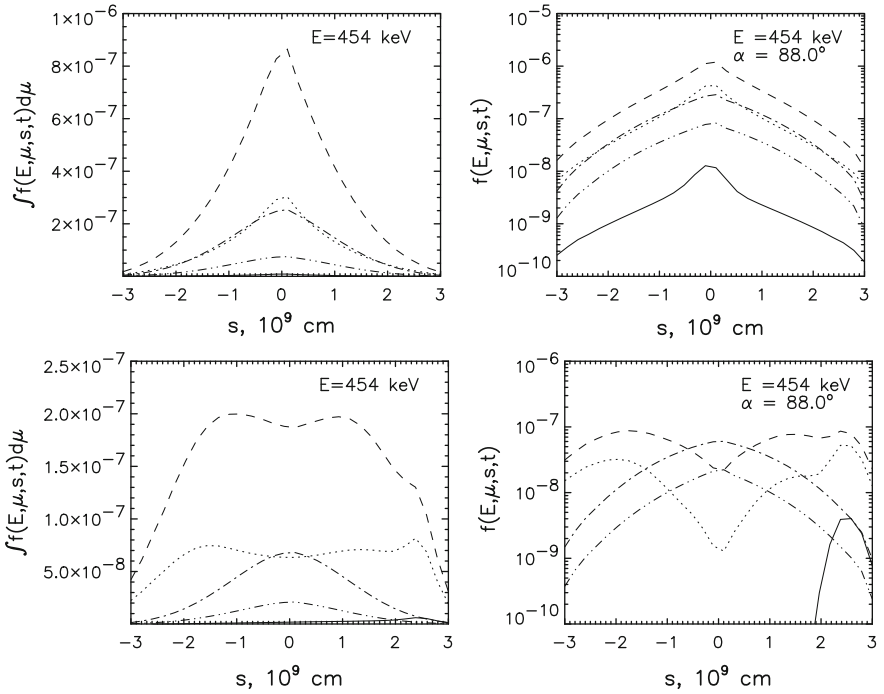

Fig. 3.27 Results of the model simulations using the Fokker–Planck equation [92]. The distribution functions for the rising phase of injection are shown by solid ($t = 0.2$ s), dotted ($t = 1.7$ s) and dashed ($t = 3.25$ s) lines, and for the decay phase by dot-dashed ($t = 7.1$ s) and dot-dot-dot-dashed ($t = 10$ s) lines. Top panels represent the time evolution for Model 1 (the maximum of injection function is located in the center of the trap, $s = 0$), and bottom panels for Model 2 (the maximum of injection function is located near the foot, $s = 2.4 \times 10^9$ cm). On the left panels: the electron distribution function is integrated over all μ and displayed in linear scale. On the right panels: the distribution function is shown only for electrons with pitch-angle $\alpha = 88°$

distribution remains similar, with the peak located at the LT. The simulation also reveals strong perpendicular anisotropy of the electron pitch-angle distribution in the loop. The degree of electron concentration near the LT is strong enough to produce a peak of the MW brightness distribution (compare with Fig. 3.26). In the case of Model 2, the shape of the spatial distribution changes with time dramatically forming a sequence of distributions from double peak in the beginning to single peak on the decay phase. The comparison with Fig. 3.26 shows that such distributions should produce two well-pronounced radio brightness peaks near the FPs in the beginning and maximum phases of a burst, and the brightness peak at the loop top in the decay phase of the burst.

3.2.8 *Constraints on Particle Acceleration, Projection, and Motion*

The findings above put some constraints on the particle acceleration/injection and kinetics of high-energy electrons in flaring magnetic loops. It follows from our analysis that the LT peak of the electron distribution on the maximum phase of a burst may be produced if the injection region is located near the loop top. The injected pitch-angle distribution should be isotropic or anisotropic of the pancake type. Such kind of injection is considered in some acceleration/injection models [94–96]. Recently developed models [83, 97, 98] consider a magnetic trap collapsing after reconnection and provide the conditions for the betatron acceleration of electrons transverse to magnetic field lines. On the other hand, there are models suggesting the DC-electric field acceleration along the axes of a twisted loop or the stochastic MHD-turbulent cascade acceleration, in which the acceleration occurs along the magnetic field lines (see for the reviews [99] and [100]). Our simulations show that this type of injection can not produce MW brightness peak in the LT during the main phase of injection. However, we can not exclude the chance of the LT source formation due to pitch-angle scattering and accumulation of trapped electrons in the top part of a loop on the decay phase.

The results of this sections show that MW brightness peaks near the FPs of a loop is easy to get if the injection region is located near one of the FPs. This conclusion is quite general, simulations reveal that it works for any pitch-angle distribution of injected electrons. It means that the acceleration mechanism itself is not very important, the main thing here is the position of the acceleration/injection region. We can conclude that in cases when MW flaring loops show brightness maxima near FPs (like for the event 24 August 2002 or the events observed by the Refs. [73–75]), the acceleration may take place in the loop leg close to one FP. We have to note, however, that this explanation is not unique. The FP brightening could be observed even if the acceleration takes place in the LT. But in this case, the injection should occur preferably along the loop axes ("beam-like" injection). To distinguish between the two possibilities we have to involve some other observational properties of the MW flaring loop. For this some further detailed investigations are needed. A more rigid set of constraints can be obtained from a study of spatial/spectral dynamics of MW/HXR emissions.

3.3 Statistical Studies on MW Brightness Distributions

3.3.1 *Data Selection*

Twenty four burst events have been selected from NoRH database with an obvious loop-like structure or three separated sources (one LT and two FPs), to analyze the

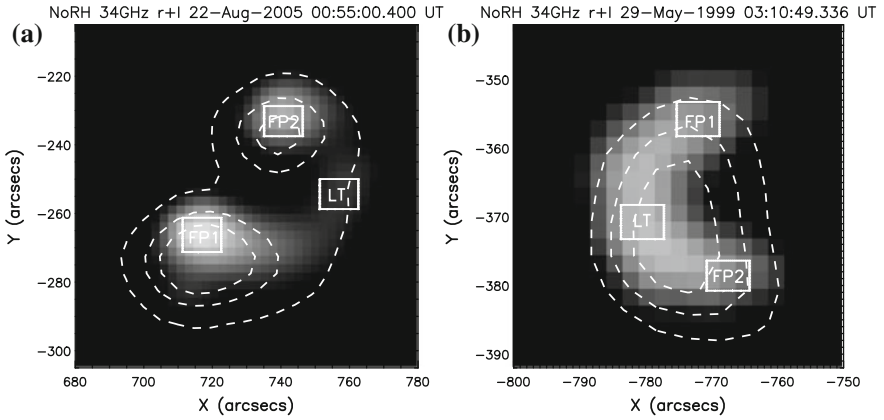

Fig. 3.28 The typical events respectively with **a** three separated sources and **b** a uniform loop-like structure observed by NoRH

distribution of T_b at the peak time in different sources, with several criterions for data selection and process [101]:

(1) The MW spectrum obtained by NoRP at six frequencies of $1 \sim 35$ GHz is used to exclude the events with an obviously thermal component, or with a peak frequency much larger than 17 GHz, which makes the working frequencies of NoRH (17 and 34 GHz) be located in the optically thin region of NT MW spectrum.

(2) Using some specific programs to remove those events with a larger jitter of antenna due to the effects of weather, etc., and to select the events with a ratio between the half-power area of burst and beam size larger than 4, which assures the error of spectral index caused by the jitter of antenna to be smaller than ± 0.3.

(3) The 17 and 34 GHz T_b at peak time of selected events is always larger than 5×10^4 K, which is much larger than the 17 and 34 GHz T_b in the quiet Sun (about 10^4 K).

(4) A specific program of NoRH softwares is used to calculate the optically thin spectral index, it is noticed that the spatial resolutions at 17 and 34 GHz are different, and it is necessary to calculate the convolution of T_b at these two frequencies.

(5) For the sources with a uniformly distributed T_b, the contour of 0.1 maximum of T_b is used to determine the positions of FPs at the two ends of flaring loops, and the position of LT at the middle of contour.

(6) The calculated area of all selected events should be larger than 3×3 pixel square.

Figure 3.28 gives the 34 GHz images at the peak time of two typical events of 1999 May 9 and 2005 August 22 respectively with a uniform loop-like structure and three separated sources, which are overlaid by the simultaneously observed 17 GHz contours. The positions of one LT and two FPs are respectively marked by three rectangles.

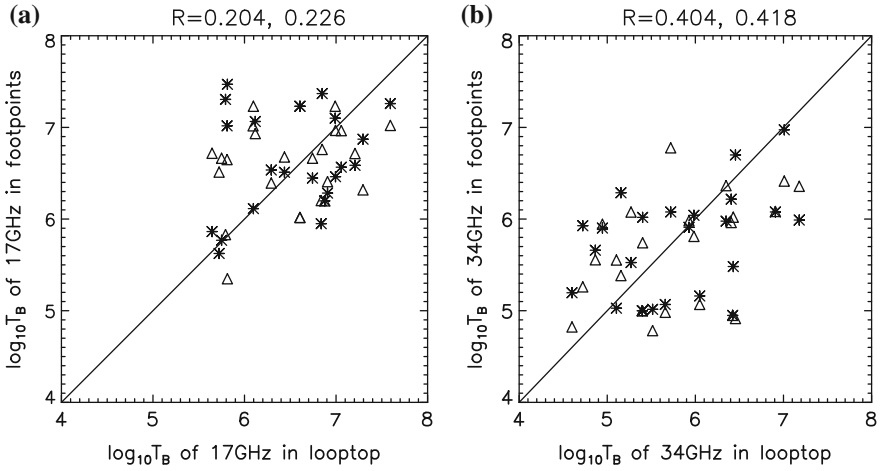

Fig. 3.29 Comparison of T_b in the LT and two FP sources, respectively for **a** the 17 and **b** 34 GHz images in the 24 selected events

3.3.2 Comparison of MW Brightness in LT and FPs

Figure 3.29 shows the relationship of T_b in the LT and two FP sources, in which the symbols of asterisk and triangle represent the FP1 and FP2 sources, respectively, while the spectrum of FP1 is always selected to be harder than that of FP2.

It is clearly seen from Fig. 3.29 that there are always a definite proportion of events with a brighter LT in comparison with two FPs in both 17 and 34 GHz images, which are located above the diagonal lines. The event number with the LT brighter than both two FPs is 10 and 9, and the proportion is 42 and 38% of total events for 17 and 34 GHz, respectively. A weakly positive correlation coefficient between the T_b in LT and each FP is respectively marked at the top of Fig. 3.29.

3.3.3 Relation of MW Brightness and Other Parameters

Figure 3.30 gives the comparison of B_0 and column density NL of NT electrons in LT and two FP sources, respectively for the 17 and 34 GHz images in the 24 selected events, in which B_0 is calculated by using Dulk's approximations (see Sect. 6.2), and the symbols are defined as the same as in Fig. 3.29.

It can be seen from Fig. 3.30 that the event number with NT in LT is higher than that in two FPs is 13 (about 54% of total events), which can be used to explain the reason why the T_b in LT is higher than that in two FPs for considerable events in Fig. 3.29. Moreover, B_0 in LT is always weaker than that in two FPs, which is well consistent with the prediction of magnetic mirror in flaring loops. In addition, the

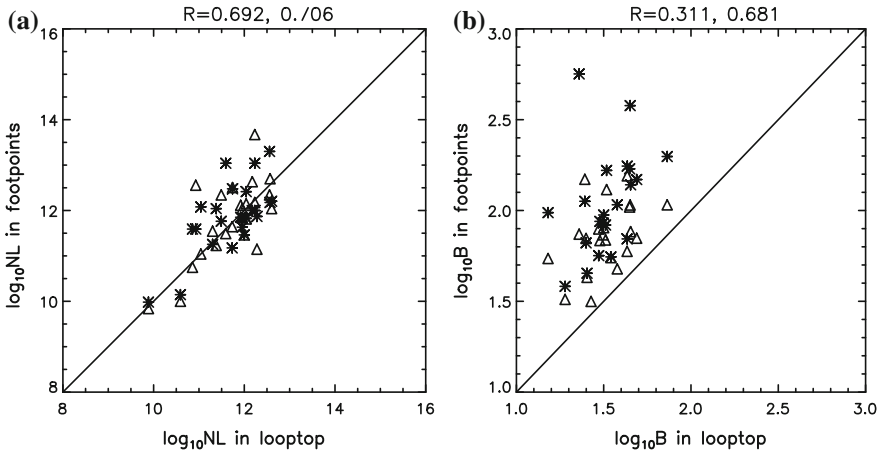

Fig. 3.30 Comparison of **a** log *NL* and **b** B_0 in the LT and two FP sources in the 24 selected events, respectively

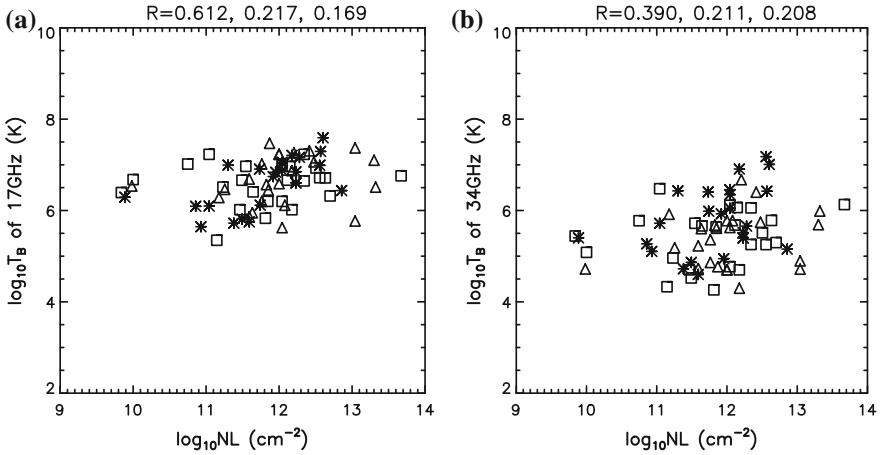

Fig. 3.31 Comparison of **a** 17 and **b** 34 GHz emissions in the LT and two FP with *NL* in the 24 selected events, respectively

correlation coefficient between the *NL* in LT and FPs is evidently larger than that of B_0. Furthermore, Figs. 3.31, 3.32 and 3.33 show the relationships of 17 and 34 GHz T_b with *NL*, B_0, and optically thin spectral index α in LT (asterisk) and two FPs (triangle and box), respectively.

The correlations of 17 and 34 GHz emissions in the LT and two FP with *NL*, B_0, and α are always weak (for the sample number of 24, the correlation coefficient with the 95% confidence level is 0.21). Here, it is easy to understand the weak positive correlation between T_b and *NL* in Fig. 3.31, and the negative correlation between T_b and B_0 (Fig. 3.32) is predicted by the diagnostics of B_0 (see Sect. 6.2), and the

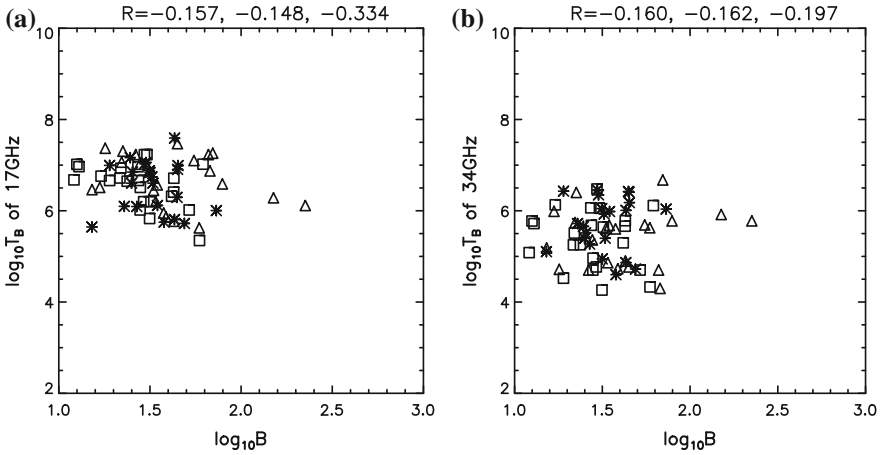

Fig. 3.32 Comparison of **a** 17 and **b** 34 GHz emissions in the LT and two FP with B_0 in the 24 selected events, respectively

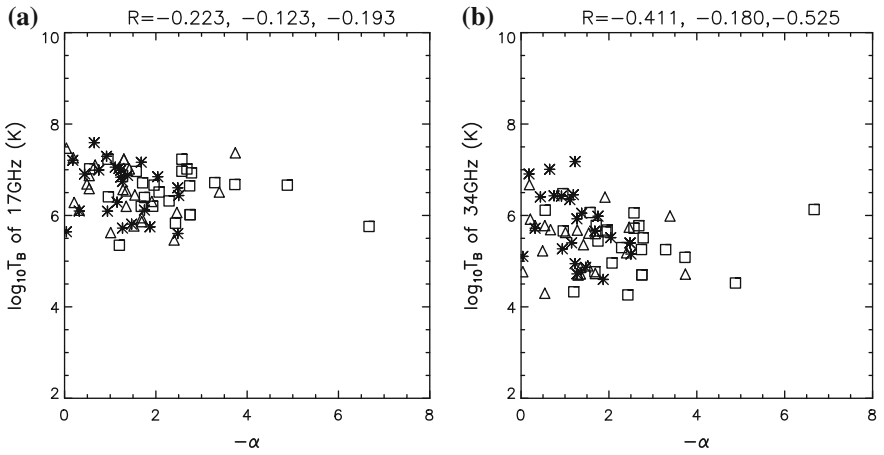

Fig. 3.33 Comparison of **a** 17 and **b** 34 GHz emissions in the LT and two FP with α in the 24 selected events, respectively

negative correlation between T_b and α (Fig. 3.33) is also consistent with the earlier calculation [102]. Actually, T_b depends simultaneously on all the three (even more) parameters, so that all the weak correlations are reasonable, and the tendencies of T_b vs three parameters Figs. 3.31, 3.32 and 3.33 are reliable.

3.3.4 Asymmetry of MW Brightness in Flaring Loop FPs

3.3.4.1 In General

It is well known that the X-ray and MW emissions in the FP source of flaring loops are contributed by NT bremsstrahlung and GS emissions respectively from precipitating and trapping electrons, and it is evident that the brightness of FP source directly depends on *NL* of NT electrons in the FP source.

The earlier studies on the asymmetry of two FP emissions were concentrated in X-ray band, the magnetic mirroring effect is generally considered as the explanation for the asymmetry by different magnetic fields of two FPs, which means that the FP with a strong magnetic field reflects (traps) more electrons before they reach the FP, thus decreases the X-ray intensity in the FP. For example, most X-ray observations of Yohkoh satellite supported the mirroring explanation [103–105], but there were still fewer events with the observed asymmetry just opposite to the mirroring prediction [103, 106], and more detailed studies found the asymmetry varied with time and energy, such as the decreasing of asymmetry with increasing of energy, even to the reversal of asymmetric emissions in two FPs [107, 108].

There were relatively less studies on the asymmetry of two FPs in MW band, it should be mentioned that the statistical studies of NoRH indicate that double or multiple loop-like structures appear in most events with coincident X-ray observations, and commonly a compact flaring loop is located nearby one FP with a stronger magnetic field in a huge flaring loop, there are strong X-ray emissions in the two FPs of compact loop, while MW emission appears only nearby another FP with a weaker magnetic field in the huge loop [74, 109]. It is difficult to explain the above results simply by the mirroring effect.

On the other hand, a series studies on the data of OVSA indicate that the MW emission in FPs is closely associated with the initial pitch-angle of NT electrons [110, 111], which supports a relatively narrow distribution rather than isotropic one. The initial pitch-angle distributions of trapping and precipitating electrons have been derived in Sect. 4.2:

$$f_1 = C \sin\theta_0 \cos\theta_c \left(\frac{E}{E_0}\right)^{-\delta} \ln\left[\frac{\tan(\theta/2)}{\tan(\theta_c/2)}\right], \tag{3.3.1}$$

$$f_2 = C \cos\theta_0 \sin\theta_c \left(\frac{E}{E_0}\right)^{-\delta} \ln\left[\frac{\tan(\theta_c/2)}{\tan(\theta/2)}\right], \tag{3.3.2}$$

$$C = \frac{n}{\left(2\pi \frac{T}{m}\right)^{3/2} \ln\left(\frac{1}{\sin\theta_c}\right)}, \tag{3.3.3}$$

$$\sin\theta_c = \left(\frac{B_{min}}{B_{max}}\right)^{1/2}, \tag{3.3.4}$$

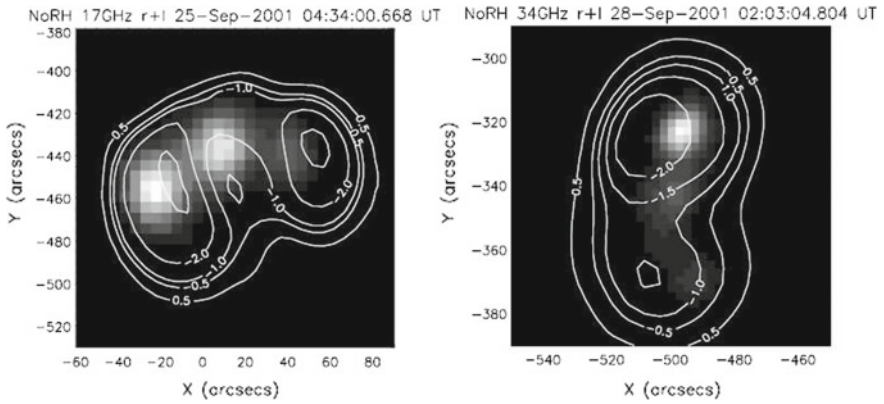

Fig. 3.34 The typical examples of T_b images overlaid by contours of α for two groups: left panel: the LT spectral index is harder than both two FP indices, and right panel: the LT index is at least softer than one of two FP indices

here, E_0 is the normalized value of kinetic energy for the NT electrons with a power-law distribution, and it is commonly taken as the thermal energy of electrons. T and m in the expression of normalized constant C are electron temperature and mass, respectively. It can be seen from Eqs. (3.3.1)–(3.3.2) that the trapping particle number increases with decreasing of the critical mirroring angle θ_c and increasing of the initial pitch-angle θ_0, while the precipitating particle number increases with increasing of θ_c and decreasing of θ_0. All of these results can be understood directly by the magnetic mirroring effect.

3.3.4.2 Selection of Two Groups of Samples

The 24 events are divided into two groups: one is that the LT spectral index is harder than both two FP indices, and another one is that the LT index is at least softer than one of two FP indices. Figure 3.34 gives two typical examples of T_b images overlaid by contours of α for these two groups, and there are 12 events in both the two groups [112].

According to the standard flare model for a single flaring loop, the acceleration site is commonly located above the LT, and the accelerated electron beam injects into the loop from LT to two FPs, while the energetic spectral index becomes softer hereby, which just belongs to the case of the first group (see the left panel of Fig. 3.34. The other case is the collision of one compact loop and another huge loop nearby one FP of the huge loop, thus the acceleration site is located in the joint part of double loop system, the LT spectral index should be between the two FP indices, which just belongs to the case of the second group (see the right panel of Fig. 3.34). Figure 3.35 shows a carton respectively for these two cases, from which it is predicted directly that the asymmetry of the second group should be more evident than that of the first group.

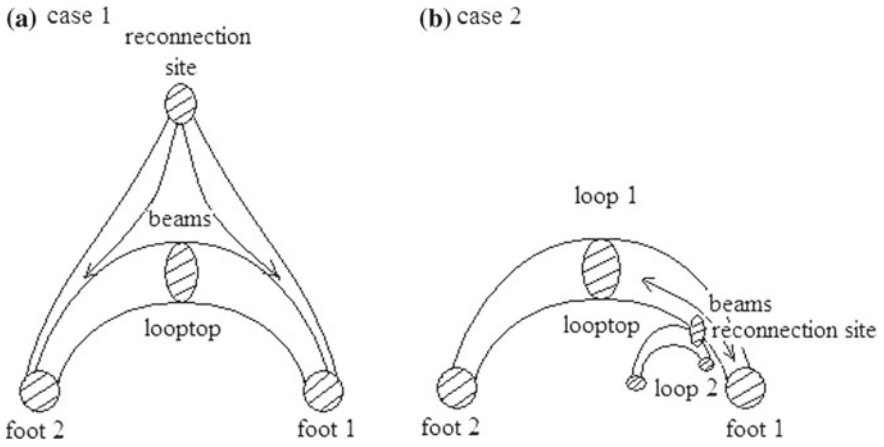

Fig. 3.35 Cartons of two groups of events: **a** standard flare model of single flaring loop, and **b** interaction of a compact loop and a huge loop

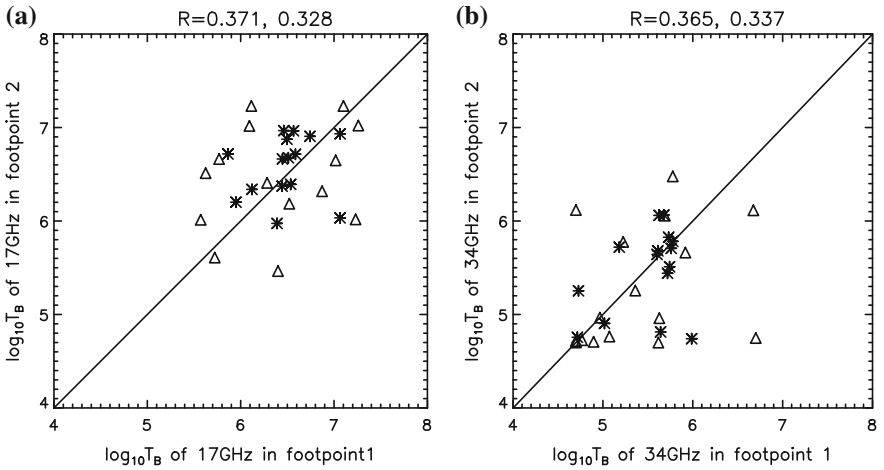

Fig. 3.36 Comparison of **a** 17 and **b** 34 GHz log T_b at two FPs of two groups

3.3.4.3 Common Features of Two Groups of Samples

The asymmetry of two FPs are statistically analyzed by 17 and 34 GHz T_b, the polarization degree at 17 GHz, the MW spectral index α, and the calculated B_0 and NL, as shown respectively in Figs. 3.36, 3.37 and 3.38. Two groups of events are marked respectively by asterisk and triangle in all figures.

The statistical results show that all the six parameters in two FPs are well correlated in the two groups of events, and most correlation coefficients are larger than the critical value 0.576 for the 95% confidence of 12 samples.

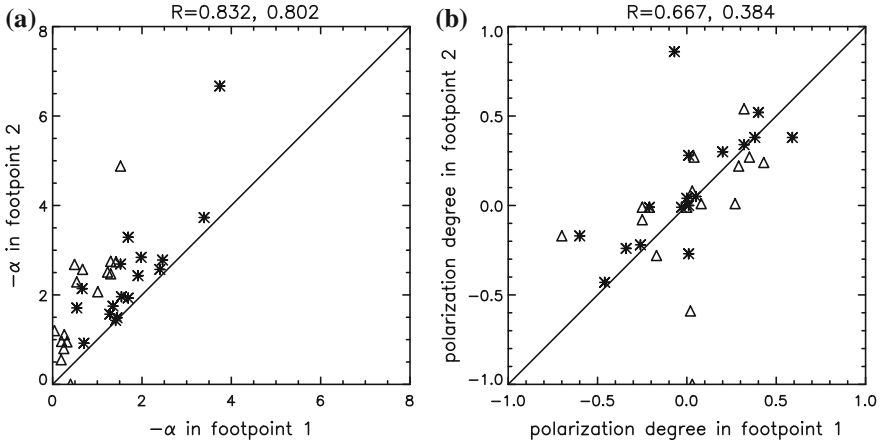

Fig. 3.37 Comparison of **a** α and **b** polarization degree at two FPs of two groups

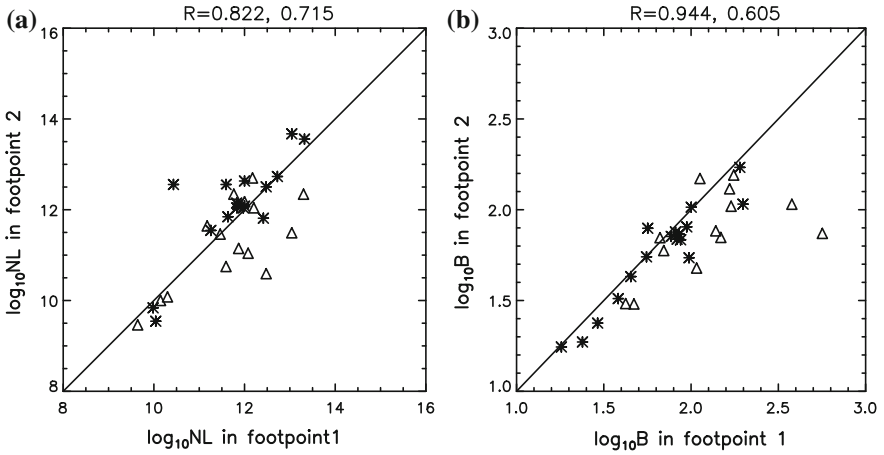

Fig. 3.38 Comparison of **a** $\log B_0$ and **b** $\log NL$ at two FPs of two groups

The asymmetry of all parameters in two FPs generally exist as shown by the extension of deviation from the diagonal lines of these figures, and the maximum difference of T_b, B_0, and NL in two FPs may exceed one or two orders of magnitudes. In addition, the spectral index at FP1 is always harder than that in FP2 (Fig. 3.37a), which is caused by the data selection as mentioned before, while Fig. 3.37b shows that there are same polarization senses in most events, because most data are concentrated in the first or fourth quadrant, which will further studied in detail. Figure 3.38b also shows that B_0 in FP1 is mostly stronger than that in FP2, which just means that B_0 is inversely proportional to the absolute value of α.

For further analyzing the asymmetry of two FPs, some new parameters are defined as the logarithm of the ratios of 17 and 34 GHz T_b, B_0, and NL at two FPs, and the

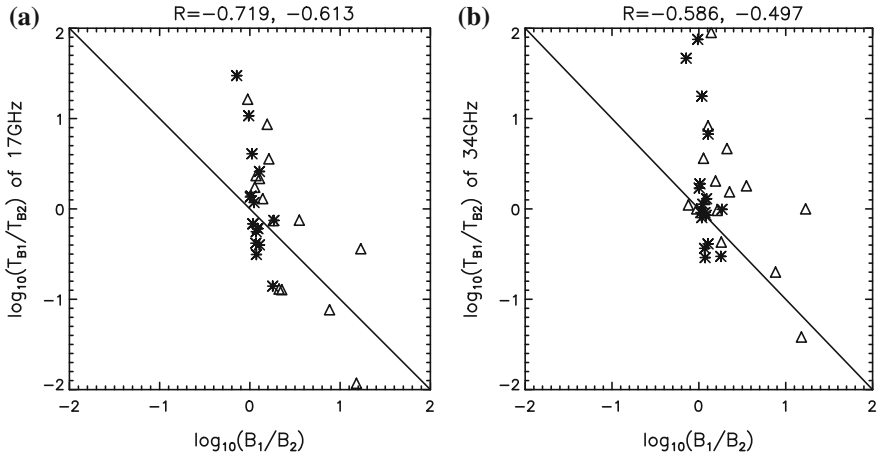

Fig. 3.39 Correlation between the logarithm of the ratios of **a** 17 GHz T_b and B_0 and **b** 34 GHz T_b and B_0 at two FPs of two groups

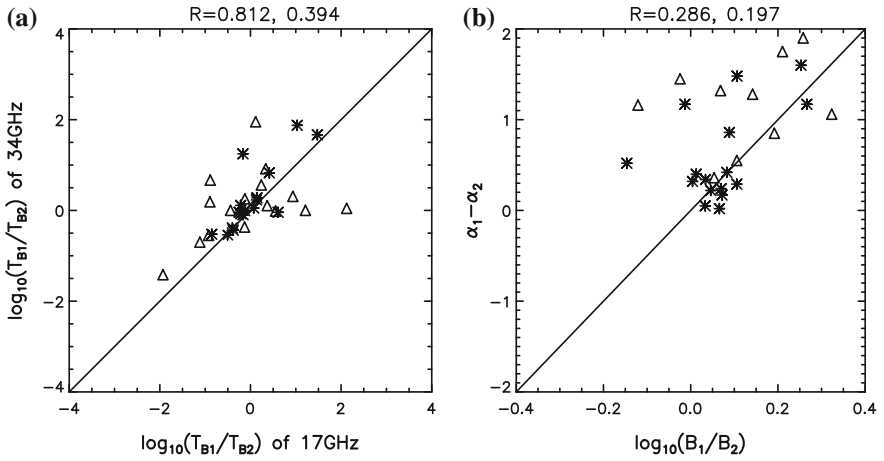

Fig. 3.40 Correlation between **a** the logarithm of the ratios of 17 GHz T_b and 34 GHz T_b, and **b** the logarithm of the ratio of B_0 and difference between the absolute values of α at two FPs of two groups

differences between the absolute values of α and polarization degree at two FPs. The statistical analysis shows that there is always a negative correlation between the logarithm of the ratios of 17 and 34 GHz T_b and B_0 in two FPs for both two groups of events (Fig. 3.39), while there is always a positive correlation between the logarithm of the ratios of 17 and 34 GHz T_b in two FPs (Fig. 3.40a), and the logarithm of the ratio of B_0 at two FPs and the difference between the absolute values of α at two FPs (Fig. 3.40b).

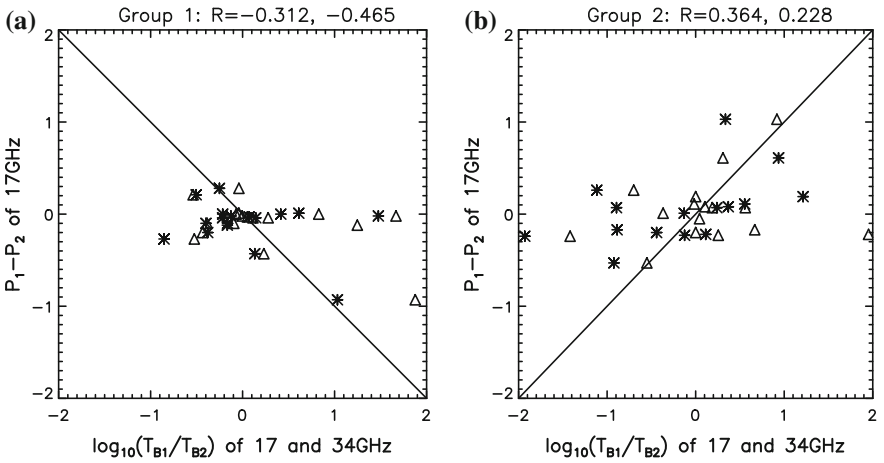

Fig. 3.41 Correlation between the logarithm of the ratios of 17 GHz (asterisk) and 34 GHz (triangle) T_b, and the difference between the absolute values of polarization degree at two FPs of **a** group 1 and **b** group 2 of events

Here, the negative correlation between the ratio of 17 and 34 GHz T_b and the ratio of B_0 in two FPs is consistent with Fig. 3.36, an important information is also provided that the asymmetry of 17 and 34 GHz T_b in two FPs (one or two orders of magnitude) is evidently stronger than that of B_0 in two FPs (most data are concentrated around zero of ordinate), which just means that the asymmetry can not be explained simply by magnetic mirroring effect. In addition, Fig. 3.40b shows that B_0 in FP1 is mostly strong than that in FP2 (the data are mostly concentrated in the first quadrant), which is also consistent with that in Fig. 3.38b.

3.3.4.4 Different Features of Two Groups of Samples

It is interesting that there are also some opposite correlations appeared in two groups of events: between the logarithm of the ratios of 17 (asterisk) and 34 (triangle) GHz T_b and the difference of absolute value of polarization degree in two FPs as shown in Fig. 3.41, between the difference of absolute value of polarization degree and relative variation of B_0 in two FPs (the latter is defined by the difference of B_0 in two FPs divided by B_0 in FP1) as shown in Fig. 3.42, between the logarithm of the ratios of 17 (asterisk) and 34 (triangle) GHz T_b and the logarithm of the ratio of NL in two FPs as shown in Fig. 3.43, and between the logarithm of the ratio of NL and the difference of absolute value of α in two FPs as shown in Fig. 3.44.

Combined Figs. 3.41 and 3.42, it is ready to deduce the negative correlation between the 17/34 GHz T_b and B_0 for both two groups of events, which is well consistent with Figs. 3.32 and 3.39, while combined Figs. 3.43 and 3.44, the 17/34 GHz T_b is negatively correlated with the absolute value of α for both two groups of events,

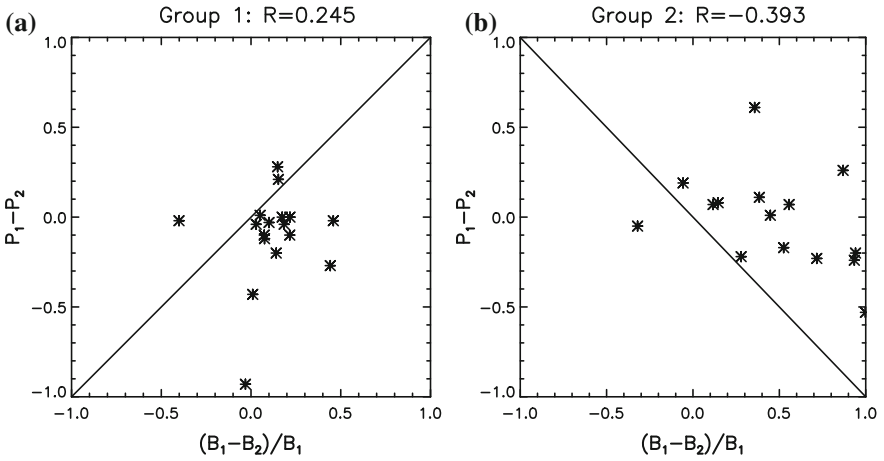

Fig. 3.42 Correlation between the difference of absolute value of polarization degree and relative variation of B_0 in two FPs of **a** group 1 and **b** group 2 of events

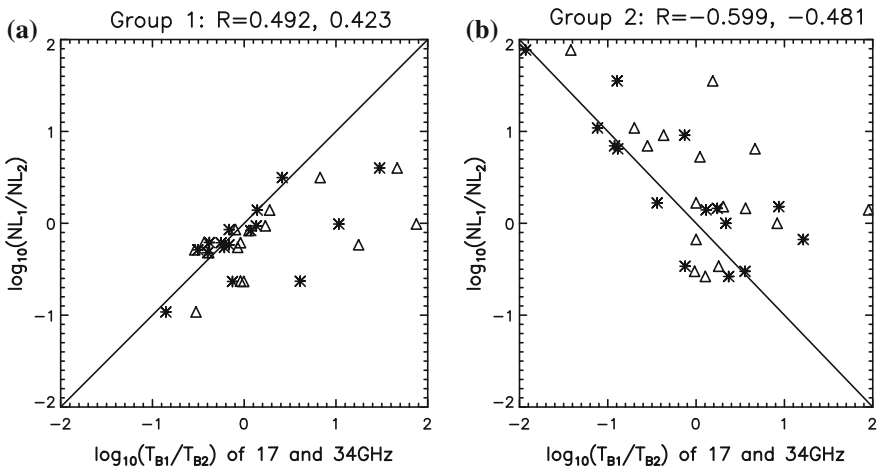

Fig. 3.43 Correlation between the logarithm of the ratios of 17 GHz (asterisk) and 34 GHz (triangle) T_b, and the logarithm of the ratio of NL at two FPs of **a** group 1 and **b** group 2 of events

which is also consistent with Fig. 3.33 and theoretical prediction of GS emission. Furthermore, the asymmetry of two FPs is clearly demonstrated by these figures for different observed and calculated parameters.

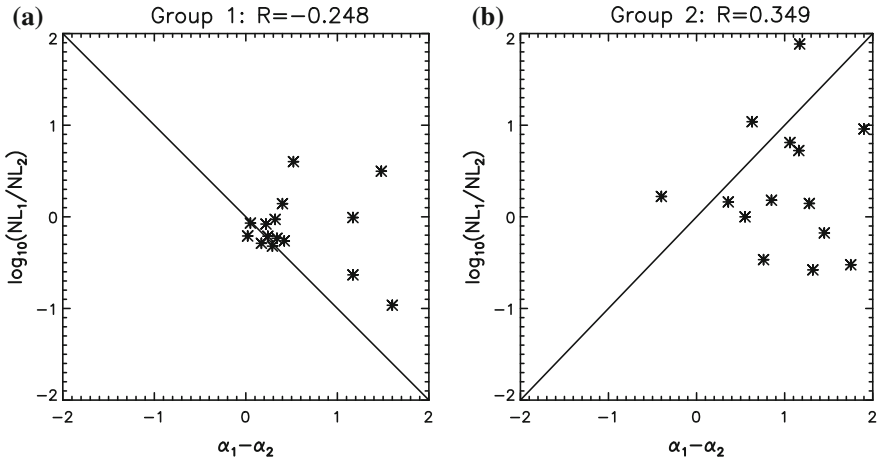

Fig. 3.44 Correlation between the logarithm of the ratio of *NL* and the difference of absolute value of α at two FPs of **a** group 1 and **b** group 2 of events

3.3.4.5 Quantitative Analysis of Asymmetry in Two FPs

Finally, the probability distribution of asymmetry in two FPs is displayed in Fig. 3.45 by 4 parameters (the logarithm of the ratios of 17 and 34 GHz T_b, the difference between the absolute values of polarization degree, the logarithm of the ratio of *NL*, and relative variation of B_0 in two FPs), respectively in two groups and total events.

Some critical values of the 4 parameters can be selected to valuate the asymmetry of two FPs reasonably, such as 2.0 and 0.5 for the ratios of 17 GHz T_b and *NL* in two FPs (or the logarithmic value of 0.3 and −0.3), 0.2 and −0.2 for the difference of absolute values of polarization degree and relative variation of B_0 in two FPs. Hence, the number and proportion of asymmetric events can be determined in Fig. 3.45 respectively for the 4 parameters: 4 (33%), 3 (25%), 4 (33%), and 3 (25%) in group 1; 8 (67%), 6 (50%), 5 (42%), and 7 (58%) in group 2; and 12 (50%), 9 (38%), 9 (38%), and 10 (42%) in total events. We can obtain two conclusions about the asymmetry in two FPs:

(1) In spite of different parameters selected to valuate the asymmetry, there are always a considerable number or proportion of events satisfying the critical values, which means the asymmetry in two FPs exists generally. (2) In spite of different parameters selected to valuate the asymmetry, the asymmetry in group 2 is always stronger than that in group 1, which is consistent with the prediction of two flare models in Fig. 3.35, i.e., the asymmetry is much easily caused by loop interaction than that by a single flaring loop.

However, one question still remains for the asymmetric mechanism, i.e., why the asymmetry of T_b in two FPs is much stronger than that of B_0 in two FPs (Fig. 3.39)? Such a difference is actually not so evident in Fig. 3.45, which may be caused by the

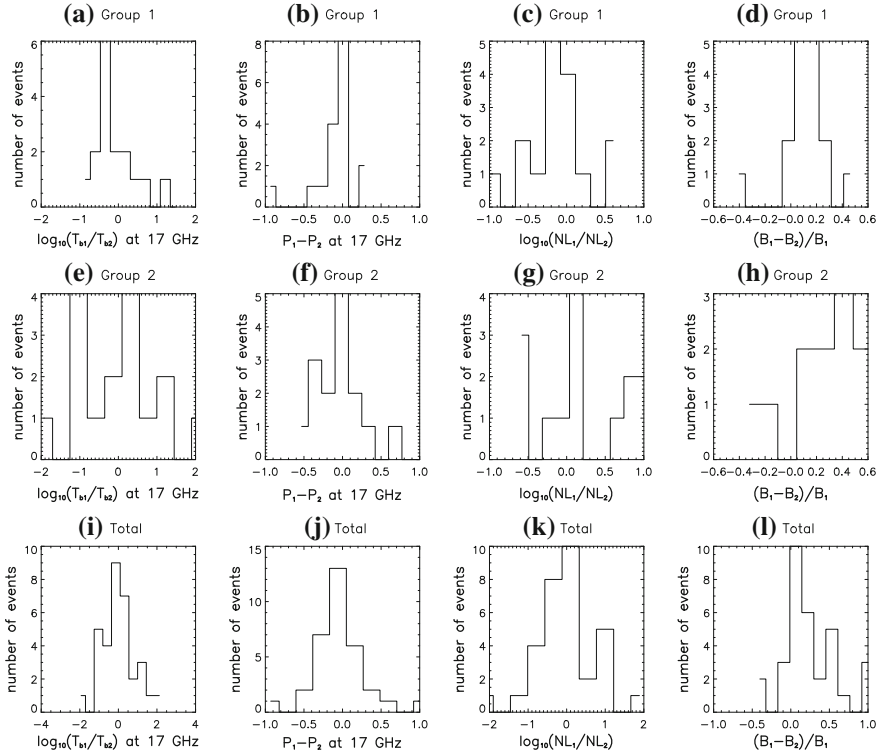

Fig. 3.45 The probability distribution of 4 parameters in two groups and total events

arbitrary selection of critical values. According to Sect. 4.2, the ratio of T_b in two FPs depends on the ratio of trapping particle number in two FPs:

$$\frac{T_{b1}}{T_{b2}} = \frac{\sin\theta_{01}\cos\theta_{c1}}{\sin\theta_{02}\cos\theta_{c2}}, \tag{3.3.5}$$

here, θ_0 and θ_c are respectively the initial pitch-angle and critical mirroring angle ($\sin\theta_c = (B_{top}/B_{foot})^{1/2}$). It is assumed that the other plasma parameters (density and temperature) have the same values in two FPs, the ratio of θ_0 can be calculated from the ratios of T_b and B_0 obtained in Figs. 3.39, and 3.46 shows the correlation between the logarithm of the ratios of 17 (asterisk) and 34 (triangle) GHz T_b and the ratio of $\sin\theta_0$, respectively in the two FPs for each group of events.

It is evident that the 17 and 34 GHz T_b is always enlarged with increasing of θ_0 (trapping electrons), and it is important that the varied range of θ_0 in group 2 is two times larger than that in group 1, which is well consistent with the varied range of 17 and 34 GHz T_b in these two groups, to confirm that the asymmetry is mainly determined by the ratio of θ_0 in two FPs, rather than by the ratio of θ_c in two FPs.

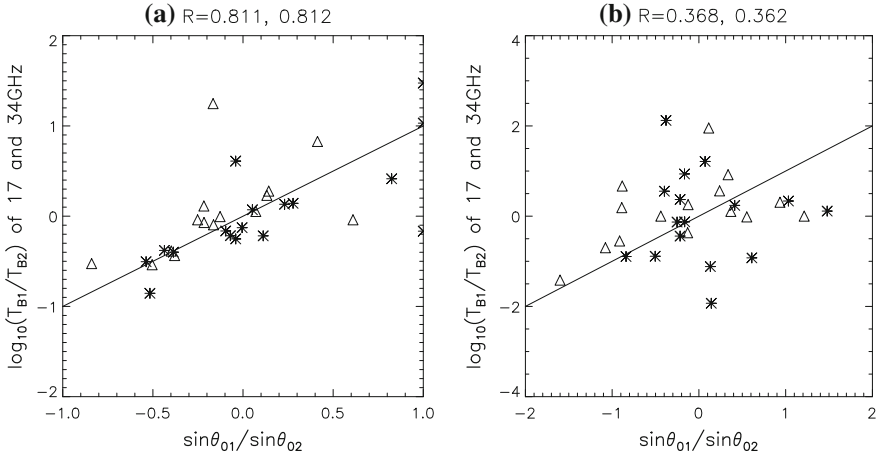

Fig. 3.46 Correlation between the logarithm of the ratios of 17 GHz (asterisk) and 34 GHz (triangle) T_b, and the ratio of θ_0 at two FPs of **a** group 1 and **b** group 2 of events

3.4 Spectral Properties of MW Emissions

Spectral features of mildly relativistic electrons accelerated in solar flaring loops can be studied using observations of their optically thin GS emission which spectrum can usually be described by the power-law:

$$F_\nu \propto \nu^\alpha \ , \tag{3.4.1}$$

where F_ν and ν are the flux density and frequency, respectively.

One of the important findings related to this topic is the dynamic flattening of the frequency spectrum during the rise and decay phases of impulsive bursts in the cm-mm wavelengths [26]. In the majority of events such the spectral flattening on the decay phase of bursts is accompanied by the simultaneous spectral softening of the corresponding HXR emission [52]. This striking difference in the spectral behavior was interpreted as the natural consequence of the nonstationary "trap + precipitation" model, which takes into account the energy spectrum hardening of trapped electrons due to Coulomb collisions as well as the difference between the spectral evolutions of injected/directly precipitated and trapped electrons [113]. On the other hand, Lee and Gary (2000) [111] have shown that the evolution of the pitch-angle distribution of NT electrons in a flaring loop can play an important role in the interpretation of the MW spectral flattening.

Till recently, studies of the spectral evolution of optically thin MW emission of solar flares were carried out for the full Sun observations without any spatial resolution. One has got only the spectral relationships averaged over a whole source. Consequently, the physical models of a radio source were quite simplified. They

considered the electron energy spectral evolution in a flare loop as a whole not taking into account possible inhomogeneity of both magnetic field and plasma density along the loop. Evidently, a study of MW spectral evolution in different parts of a flare loop on the base of observations with a good spatial resolution may provide us with new and additional information. This information may help us to develop a more appropriate physical model of a radio source and get a better understanding of particle acceleration and transport in flare loops.

3.4.1 Distribution of Spectral Slopes Along Flaring Loops

NoRH provides us with observations at two high frequencies 17 and 34 GHz. So it gives a unique possibility to study spectral slope's dynamics and its spatial distribution along flaring loops.

The parameter α described as

$$\alpha = \frac{ln(F_{34}/F_{17})}{ln(34/17)} \ . \tag{3.4.2}$$

characterizes the spectral slope between 17 and 34 GHz. For some extent this parameter can serve as an approximation to the frequency spectral index. This approximation is quite reasonable when the spectral peak of the emission is located at frequencies $f < 17$ GHz, which is the case for the events we discuss here. Note that due to the difference of the beam sizes at 17 and 34 GHz, the corresponding intensities F_{34} and F_{17} must be calculated after the adjustment of images at 17 and 34 GHz to the same antenna beam size. This is achieved by the convolution of the 17 GHz image with the 34 GHz beam and vice versa.

The very first study of the MW spectral distribution along the extended flaring loop in the event 28 August 1999 has revealed very interesting regularity [85]. The value of the radio spectral index is considerably higher (by approximately 1) in the FPs than in the LT. It is valid all the time during the main emission peak. This can be clearly seen in Fig. A.2 in Appendix A, where distributions of intensity (left and middle panels) and spectral slope α (right panel) along the loop are shown. The color map of α and the color bar clearly indicate the increase of α near the FPs of the loop. This regularity has been confirmed further in detailed studies of other extended flaring loops characterized by negative spectral slope between 17 and 34 GHz [79, 86].

3.4.1.1 MW Spectral Evolution

A study of the MW spectral evolution in different parts of five well-resolved loop-like radio sources (flares on 28 Aug 1999, 12 January 2000, 11 and 13 Mar 2000, 23 Oct 2001) were undertaken in the Ref. [79]. For the analysis of these flares, HXR data

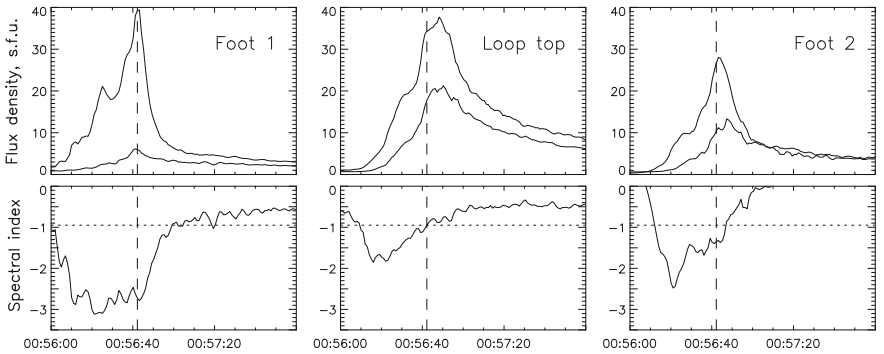

Fig. 3.47 Top panel: NoRH time profiles of the flux densities from the 20 × 20 arcsec boxes located at the loop top (middle panel) and the FPs (left and right panels) of the flare 1999 August 28. Bottom panel: the corresponding time profiles of the spectral index calculated with Eq. (3.4.2). Vertical line indicates the moment of the HXR emission peak, 00:56:42 UT

detected with the Yohkoh/HXT and the BATSE/CGRO HXR spectrometers as well as magnetographic data from SOHO/MDI were also used. The frequency spectrum slope in the range 17–34 GHz during the impulsive phase of the bursts was negative throughout the sources extension. The common features found for all the events are as follows. The temporal evolution of α for different parts of a loop-like source, where it is optically thin (negative α), shows the very common behavior: a gradual increase of its value in the rise and decay phases of the bursts, as shown in Fig. 3.47. This "SHH" behavior of the MW emission is associated with the "SHS" behavior of the corresponding HXR emission (Fig. 3.48). Such opposite evolution of the spectral slopes of the MW and HXR emissions on the decay phase is similar to the spectral evolutions of these emissions integrated over a whole source [52].

Along with this it was found that the temporal increase of α (flattening of the MW spectrum) during the decay phase goes remarkably faster in the regions close to the FPs than near the loop top. In the event 28 August 1999 (see Fig. 3.47), the index α changes from -2.7 to -1.0 and from -1.3 to -0.2 for the left and right loop FPs, respectively, whereas from -1.0 to -0.6 for the LT during the interval of 20 s after HXR-peak.

3.4.1.2 Possible Physical Reasons of the Spectral Properties

We see four possible reasons for the observed difference in spectral slopes between the LT and FPs regions.

The first one is associated with a perpendicular anisotropy of the electron pitch-angle distribution. Due to stronger directivity of GS emission at higher frequencies the anisotropic distribution provides systematically steeper frequency spectra at quasi-parallel directions than at quasi-transverse directions [30]. This reason may well work for disk flares since for them the FP source is observed at a quasi-parallel direction,

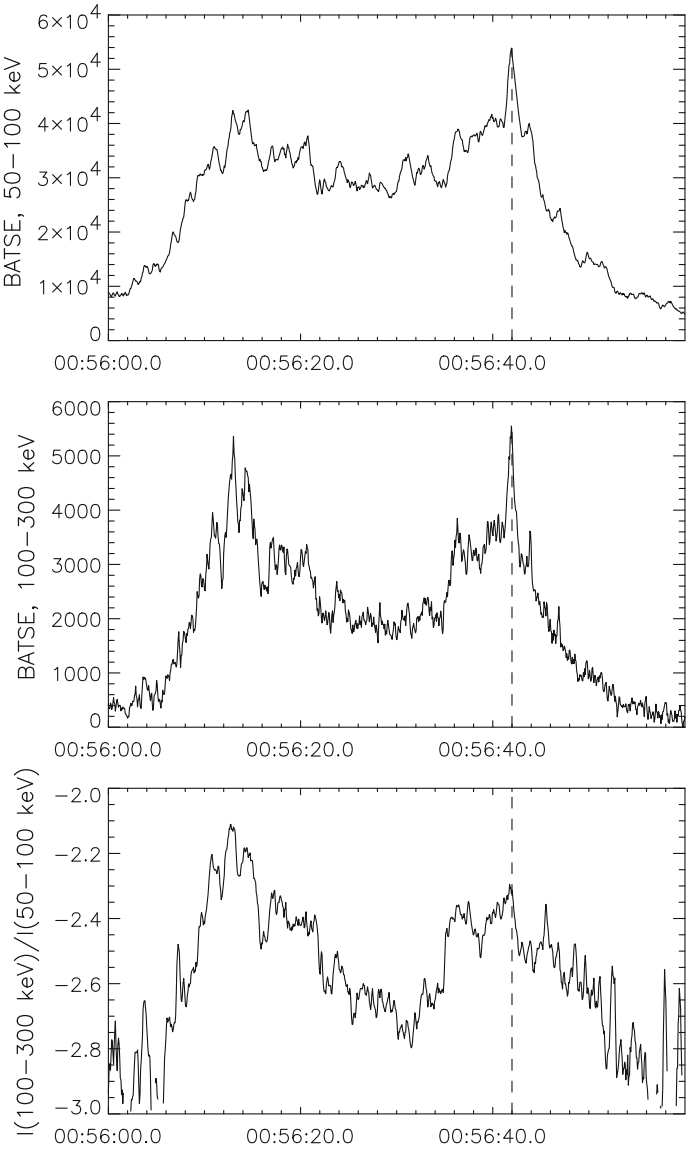

Fig. 3.48 Temporal profiles of HXR emission during the event of 1999 August 28. Top and middle panels: Total fluxes at energy intervals $E_1 = 50-100$ keV and $E_2 = 100-300$ keV. Bottom panel: Flux ratio $I(E_2)/I(E_1)$ time profile corresponding the spectral index γ_x time profile of the HXR spectrum $I(E) \propto E^{-\gamma_x}$. Vertical line indicates the moment of the emission peak at 00:56:42 UT

while the LT source in quasi-transverse. In the left bottom panel of Fig. 2.9 one can see that in the optically thin regime, at $f > f_{peak}$, the spectral index considerably (by 0.5–1) increases with the degree of anisotropy (change of the loss-cone angle θ_c from 0 to $\pi/2$), while it is almost constant in the case of quasi-transverse propagation (the right bottom panel). Note that the effect of the anisotropy is expected to be less pronounced for limb flaring loops (though this depends on a specific difference between the electron pitch-angle distributions in the LT and FPs). Meanwhile, sometimes one observes the same spectral slope distribution also for limb flares [58]. The following effects are free of this limitation.

The second reason is the influence of magnetic field strength on the frequency spectral slope around a fixed frequency. An increase of spectral index at lower harmonics is a general feature of GS emission from a power-law electron energy distribution in the case of low-density plasma $\omega_{pe} < \omega_{Be}$. The increase from the relativistic limit ($\alpha_{rel} = (\delta - 1)/2$) that is realized at harmonic number $\omega/\omega_{Be} \geq 100$ may reach 0.5–1 as can be seen on the bottom left and right panels in Fig. 2.9. In an FP the magnetic field strength is expected to be higher than in the loop top. Therefore, the corresponding emission at a given frequency is generated at a lower harmonics and with a steeper spectrum.

Another effect that may greatly influence the spectral slope at frequencies $f > f_{peak}$ is Razin suppression [56]. Due to this effect, the spectral index α may be considerably (by 0.5–2) smaller than even α_{rel} if the parameter ω_{pe}/ω_{Be} in the source is sufficiently high [30]. Since this parameter has to be larger in the LT than near FPs due to weaker magnetic field strength, we expect a spectral flattening in the LT. A detailed diagnostics of flare plasma shows that this effect may be the main one at least for some flares [56]. In Fig. 3.49 one can clearly see that due to enhanced Razin suppression in the top part of the flaring loop the spectral peak shifts to higher frequencies and the spectral slope at $f > f_{peak}$ becomes flatter than in the source near an FP.

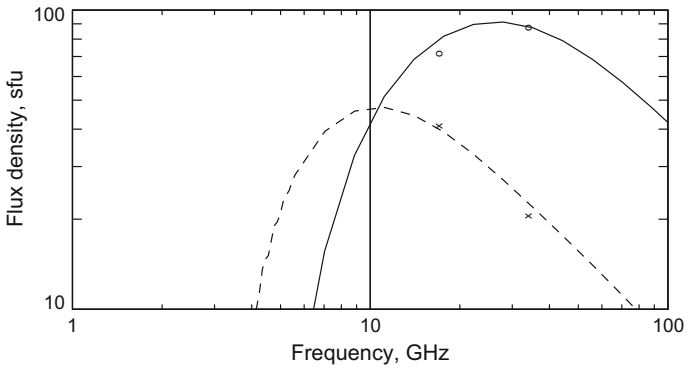

Fig. 3.49 Comparison of observed fluxes at 17 and 34 GHz from the loop top (circles) and FP (crosses) sources with 10" × 10" area and the corresponding MW spectra calculated for these sources [58]. The plasma density is assumed constant along the loop, $n_0 = 8 \times 10^{10}\,\mathrm{cm}^{-3}$, the magnetic field is 100 and 200 G in the loop top and FP sources, respectively

The fourth possible reason is a difference in energy spectrum slopes of electrons propagating in the LT and FPs regions. It is expected that the population of emitting electrons consists of two parts: trapped and directly precipitating into FPs. The first part gives its contribution into MW emission mainly in the LT region while the second part in the FP regions. The energy spectrum of trapped electrons is supposed to be harder than of precipitating ones due to long-lasting Coulomb interactions with the background plasma. Therefore, the frequency spectral slope of emission from the FPs should be steeper. This idea may be exploited as an explanation of a better fit between electron spectra derived from MWs and HXR spectra coming from FPs than from the LT. However, it has to be checked by careful modeling with an use of the Fokker–Planck equation.

The observed temporal flattening of the MW spectrum in its optically thin part is another interesting property. The flattening occurs throughout the loop-like source (from the loop top to the FPs) in parallel with simultaneous softening of HXR spectrum during the decay phase of bursts. Together with observed time delays at higher frequencies, these properties indicate on a different spectral behavior of low-energy electrons generating HXR emission and mildly relativistic electrons trapped in flaring loops and generating the MW emission. The most probable explanation of this is that the HXR emission is generated by directly precipitating electrons, and the MWs mostly by trapped ones whose energy spectral evolution is defined by transport effects like Coulomb collisions (or wave-particle interactions) [52]. New properties of temporal behavior which may correct the explanation are the differences in the dynamics of flux and spectral slope of emissions coming from the top and FP parts of a flaring loop. They include: (1) slower intensity decay and time delays of MW emission from the loop top part compared to the FP part; and (2) faster spectral flattening of emission from the FP part.

These spatial-temporal peculiarities, together with spatial dependence of the spectral slope, may be adjusted to each other if one takes into account the magnetic field inhomogeneity in a flaring loop. The physical reason for that is the following. The GS emission at a given frequency from the loop top is generated at higher harmonics of gyrofrequency due to the lower magnetic field compared to the FP region. In its turn the emission at higher harmonics is generated by more energetic electrons that have a remarkably longer life time in the trap. The longer lifetime of these electrons explains naturally (*a*) the slower intensity decay, and (*b*) the delays of emission and more gradual spectral flattening of emission from the loop top compared to the FPs. Moreover, as it was mentioned earlier, the emission at higher harmonics also is expected to have flatter frequency spectrum that fits well with the observed flattening in the LT.

Right now we can not exclude that some of the spatial-temporal properties of the frequency spectrum are caused by an acceleration mechanism itself. Before making firm conclusions all of them need to be carefully checked using self-consistent theoretical modeling and additional independent information on magnetic field strength, plasma density and electron energy spectrum in specific flaring loop.

3.4.1.3 Conclusion

Recent NoRH observations reveal a set of new important spatial-spectral-temporal properties of MW flaring loops. Among them are (1) the fact that the brightness distribution along flaring loops may have the maximum in the LT even in the case of optically thin emission; (2) change of the initial distribution with brightness maxima near FPs to the distribution with the LT brightness maximum on the decay phase of a burst; (3) the existence of delays between the time profiles of emission from the loop top and FPs; time delays at higher frequency; (4) the steepening of the MW frequency spectrum along a loop from the top to its FPs; (5) temporal flattening of the spectrum on the rise and decay phases of bursts; the faster flattening near FPs than in the LT on the decay phase.

Consideration of possible reasons explaining these properties reveal an importance of such effects as: (1) trapping and accumulation of accelerated electrons in the upper part of flaring loops, (2) transverse anisotropy of the electron pitch-angle distribution and its influence on the MW intensity and spectral slope, (3) scattering of energetic electrons leading to a redistribution of electrons in a flaring loop and hardening of their energy spectrum, (4) Razin suppression and its influence on the MW frequency spectrum, (5) dependence of the frequency spectrum slope on the magnetic field strength in a source. We should also emphasize an importance of the position of an acceleration/injection site inside a flaring loop. It greatly influences upon many observable spatial characteristics of MW flaring loops.

So far we have not got sufficient information about the main effects which are mostly responsible for the observed properties. We believe that relative significance of the listed effects may be determined only under complex, multiwavelength and detailed case studies of some specific flares. Altogether the discussed findings put important new constraints on the particle acceleration/injection mechanisms and the kinetics of high-energy electrons in flaring magnetic loops. We hope that future NoRH observations will give us new excellent keys for solving problems of solar flare physics.

3.4.2 Statistics of Optically Thin Spectral Indices of MW Emissions in LT and FPs

For statistically studying the MW optically thin spectral indices in LT and FPs of flaring loops [101, 103], we have selected 24 bursts of NoRH with a loop-like structure or three separated sources as mentioned in Sect. 3.2.2, which are further divided into two groups: one is that the LT spectral index is harder than both two FP indices, and another one is that the LT index is at least softer than one of two FP indices as mentioned in Sect. 3.2.4, and each group has 12 events with one example, respectively given in left and right panels of Fig. 3.34, in respect to two flare models as shown in Fig. 3.35a, b. Figure 3.50a, b respectively compare the two FP spectral indices and

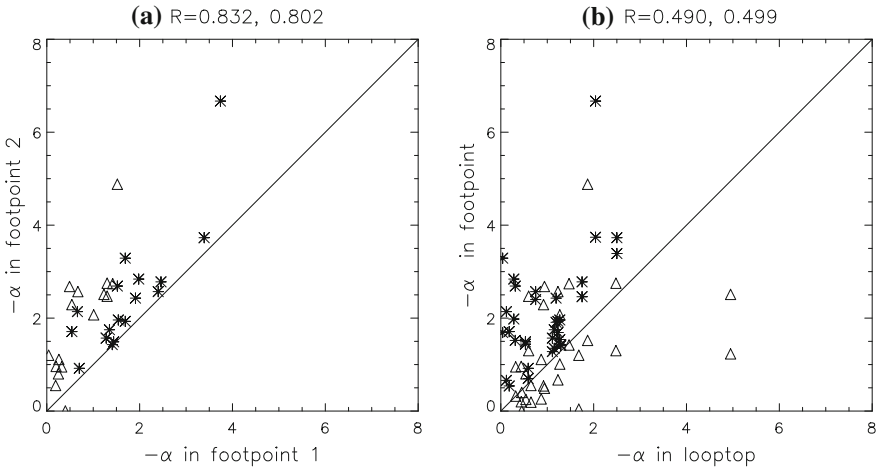

Fig. 3.50 Comparisons between the optically thin spectral indices in **a** two FPs and **b** LT and FPs of two groups of events

the spectral indices in LT and FPs in the two groups (asterisk for group 1 and triangle for group 2).

All data points are located above the diagonal line in Fig. 3.50a, because the spectrum in FP1 is always selected to be harder than that in FP2, and it is clearly seen that the spectral indices in two FPs are well correlated. Moreover, the all data points of group 1 (asterisk) are located above the diagonal line in Fig. 3.50b, because in group 1 the spectrum in LT is selected to be harder than that in two FPs, and a positive correlation between the spectral indices in LT and FPs for both the two groups. The statistical results in Fig. 3.50 are physically reasonable.

3.4.3 Hard-Soft-Hard (HSH)—a New Pattern of MW Spectral Evolution

Ten events in two cases are further selected from the 24 bursts of NoRH [114], case 1 includes 5 simply impulsive bursts, and case 2 includes 5 complicated bursts with multiple peaks in their light curves. Figure 3.51 shows a typical example of case 1, in which panels *a* and *c* give the light curves at 17 GHz and spectral evolutions calculated by 17 and 34 GHz images in LT and two FPs, respectively, while panels *b* and *d* give the light curves at 17 GHz (solid) and 35 GHz (dashed) and spectral evolution observed and fitted by NoRP, respectively. Three vertical lines in Fig. 3.51 respectively mark the peak time, rising, and decay phases.

It is obvious in Fig. 3.51 that a typical SHH (SHH) pattern appears in the spectral evolutions of LT and two FPs (NoRH), as well as in the full-disk observations (NoRP),

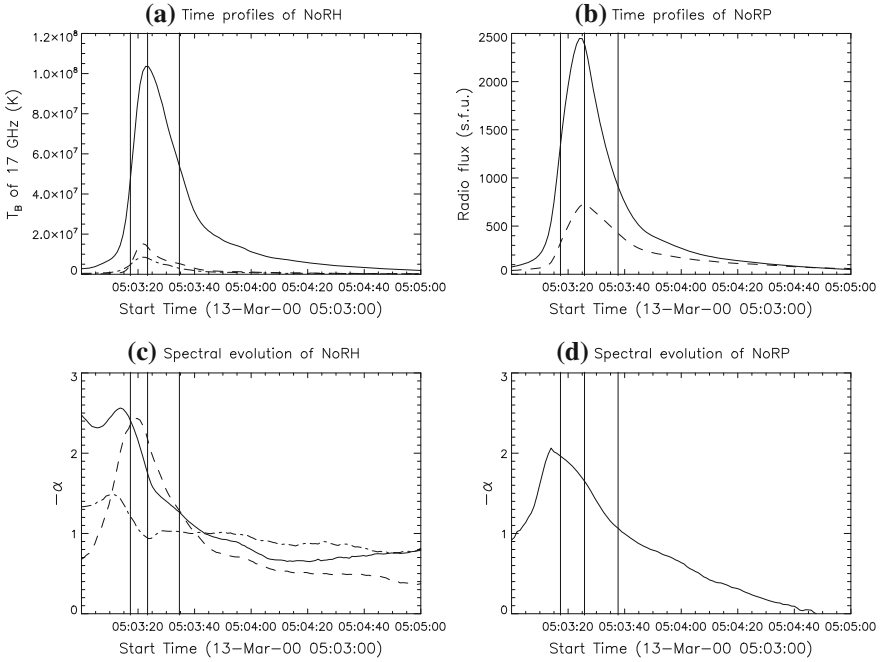

Fig. 3.51 Light curves and spectral evolutions in LT and two FPs of an impulsive event observed by NoRH in panels **a** and **c**, and full-disk observations of NoRP in panel **b** and **d**

the monotonous decline of absolute spectral indices can be explained readily by the spectral evolution of accelerated electrons and the long lifetime of trapping electrons, which is well consistent with previous studies.

However, a quite new pattern appears in a typical example of case 2 with multiple peaks (marked by a vertical line for each peak) as shown in Fig. 3.52, in which all the panels are absolutely the same as those in Fig. 3.51.

The absolute value of spectral indices in LT and two FPs always vary from small to large first and then from large to small around each peak (including the main peak), thus, the spectral evolutions are always negatively correlated with the light curves in case 2, which can be defined as the HSH (hard-soft-hard) pattern.

It is noticed that the overall evolution in case 2 still keeps the normal SHH pattern in Fig. 3.52 if the light curve with multiple peaks has been smoothed, which is actually consistent with that of simply impulsive case in Fig. 3.51. Moreover, the results of spatially resolvable data of NoRH are supported by the full-disk observations of NoRP in both two cases of Figs. 3.51 and 3.52.

Regarding the explanation for HSH pattern, the 10 s sample rate of NoRH is commonly longer than the lifetime of a single peak in Fig. 3.52, while a complicated event with multiple peaks means that the accelerated NT electrons inject into the flaring loop discontinuously, and the sampling time (10 s) is longer than each injecting

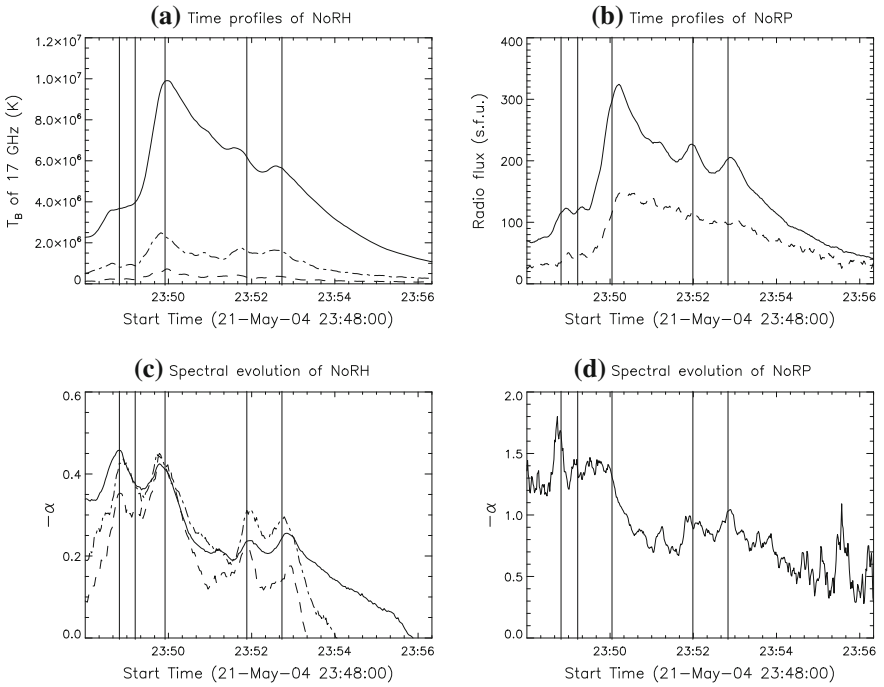

Fig. 3.52 Light curves and spectral evolutions in LT and two FPs of a complicated event observed by NoRH in panels **a** and **c**, and full-disk observations of NoRP in panel **b** and **d**

time of NT electrons. According to an in-depth theoretical study on trapping effect [115], when the trapping time is larger than sampling time (for accumulated data), which is also longer than the injecting time of electrons, the energetic spectrum of trapping electrons will be hardened gradually from an initial index of δ to $\delta - 1.5$, while the power-law index of precipitating electrons will be $\delta + 0.5$ (softer than that of trapping electrons). In addition, the energy of electrons responsible for the 17–34 GHz emission is as high as several hundreds keV (in the moderately relativistic level), when the local magnetic field is smaller than 500 Gauss [29], the trapping time may be estimated by the energy relaxation time of NT electrons [116, 117]:

$$\tau_t = 2.6 \times 10^9 \times \frac{E}{n}\,, \tag{3.4.1}$$

here, the energy E of NT electrons is taken as 500 keV, the ambient electron density is taken as $3 \times 10^{10}\mathrm{cm}^{-3}$, the calculated trapping time is about 44 s, after this time the power-law index of injected electrons will be about $\delta - 1.0$, and when a new injection starts, the index will be softened as δ, then the hardening process occurs again due to the trapping effect, which may qualitatively even semi-quantitatively explain the HSH pattern in a single peak. In practice, the power-law index of total

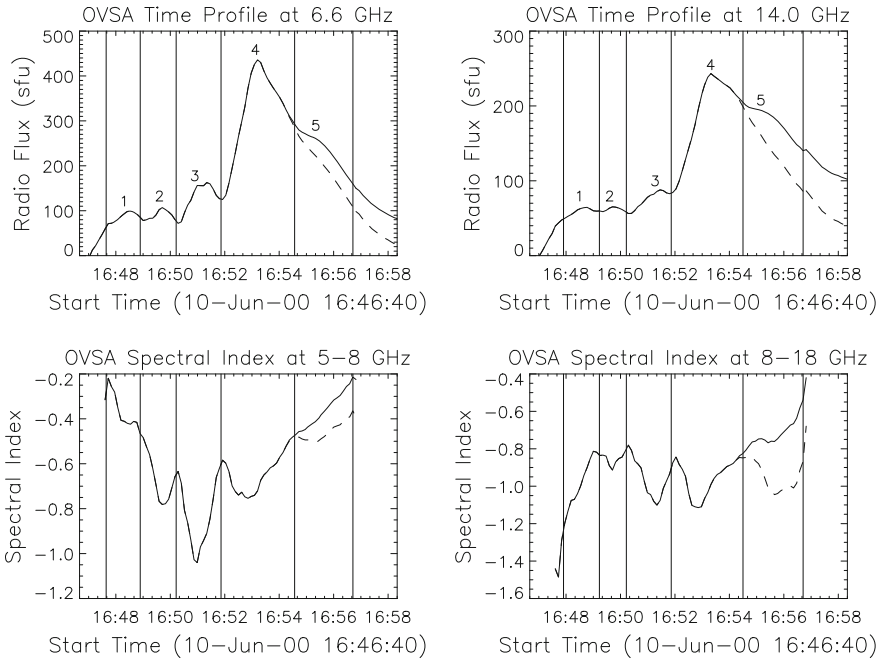

Fig. 3.53 Light curves and spectral evolutions in the 2000 June 10 event observed by OVSA at different frequencies

NT electrons may be in a range of $\delta - 1.0 \sim \delta + 0.5$, which depends on the number ratio of trapping and precipitating electrons. Hence, the multiple peak event or the short-time injection for each peak is the necessary condition of HSH pattern, and for a simple impulsive event with a longer lifetime, the trapping effect can only make the spectrum be hardened continuously.

3.4.4 Dependence of Spectral Evolution on Frequencies

Figure 3.53 left column shows the light curve at 6.6 GHz and spectral evolution at 5–8 GHz observed by OVSA in 2000 June 10, respectively, while Fig. 3.53 right column gives the light curve at 14.0 GHz and spectral evolution at 8–18 GHz, respectively, for the same event but at higher frequencies [118]. The peak frequency in this event always varied in a range of 4–5 GHz, so that the above spectral evolutions are always located in the optically thin region. Each peak in the event is marked by a vertical line in Fig. 3.53.

It is interesting that at lower frequencies (left column of Fig. 3.53), the spectral evolution always shows the new HSH pattern for each individual peak and overall event, while at higher frequencies (right column of Fig. 3.53), the HSH pattern still

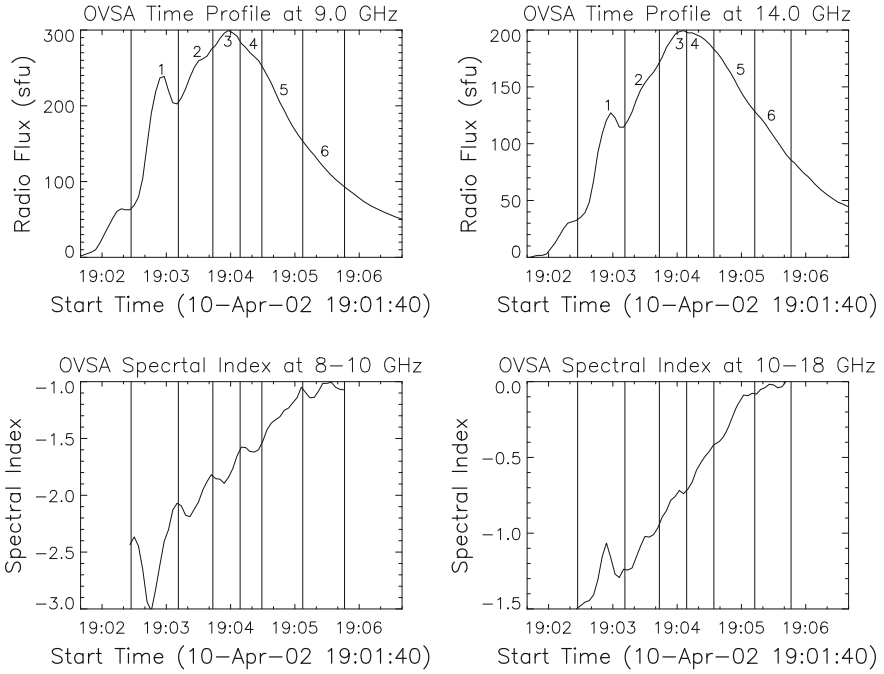

Fig. 3.54 Light curves and spectral evolutions in the 2002 April 20 event observed by OVSA at different frequencies

keeps for each peak, but the fluctuations becomes weaker, and a common SHH pattern appears in overall event, which is quite similar to the above five complicated events as shown by Fig. 3.52. The opposite overall spectral evolutions in lower and higher frequencies are quantitatively proven by a negative and positive correlation coefficient, i.e., −0.28 and 0.25, respectively in lower and higher frequencies. For 80 time points in this event, a critical value of correlation coefficient is 0.05 for the confidence level of 0.95, which is well satisfied in Fig. 3.53. The dashed lines overlaid in Fig. 3.53 give the results after the thermal bremsstrahlung (calculated by the temperature measured by Yohkoh/SXT) has been removed.

Moreover, Fig. 3.54 gives another example in 2002 April 20 observed by OVSA that similar to Fig. 3.54, in which the left column shows the light curves at 9 GHz and spectral evolutions at 8–10 GHz, respectively, while, the right column shows the light curves at 14 GHz and spectral evolutions at 10–18 GHz, respectively, and each peak in the event is marked by a vertical line.

There is a little difference between Figs. 3.53 and 3.54, the HSH pattern appears for each peak, and a common SHH pattern (instead of SHS pattern in Fig. 3.53) appears for overall event at lower frequencies, while the HSH pattern almost disappears together with the overall SSH evolution at higher frequencies. Moreover, the correlation coefficients −0.23 and 0.30 at lower and higher frequencies well satisfy

the confidence level of 0.95, and here, the critical value of correlation coefficient is 0.05 for the sample number of 50 in this event.

Finally, the two events with multiple peaks analyzed in this section show the frequency dependence of spectral evolving pattern. In general, the fluctuations of light curves are more obvious at lower frequencies than that at higher frequencies, because the fluctuations caused by the periodically injection of electrons accelerated above flaring loops are gradually smoothed when the accelerated electrons reach the low corona, thus the HSH pattern can not produced at higher frequencies. More detailed explanation for the frequency dependence of MW spectral evolution will be discussed in Sect. 5.5.

3.4.5 Evolution of MW Spectra in Different Parts of Flaring Loops

Regarding the explanation of HSH pattern by trapping effect, it is predicted that the trapping effect in LT should be stronger than that in FPs, so that we can check the difference of spectral evolution in different parts of flaring loops [119]. One flare in 2003 October 24 with a loop-like structure simultaneously observed by NoRH and RHESSI on solar limb, Fig. A.3 in Appendix A shows a bright EUV loop overlaid by contours of SOHO/MDI magnetogram (solid lines of 100, 500, and 1000 Gauss, dot-dashed lines of −100, −500, and −1000 Gauss), 34 GHz brightness temperature of NoRH (dashed lines of 0.2, 0.4, 0.6, and 0.8 of its maximum in left panel of Fig. A.3), and photon counts at 15–20 keV (LT) and 35–40 keV (FPs) of RHESSI (dashed lines of 0.5, 0.7, and 0.9 of its maximum in right panel of Fig. A.3). The positions of LT and two FPs are respectively marked by 1, 2, and 3 in the MW and X-ray contours, and both the positions of LT at MW and X-ray bands are located nearby the maximum EUV brightness, but the positions of two FPs at MW and X-ray bands have a small deviation. The HXR data process will be done in Sect. 5.6. Figure 3.55 show the 17 GHz light curves of NoRH, optically thin spectral indices, and correlations between light curves and spectral evolutions at LT and FPs, respectively.

It is interesting that the light curve is negatively correlated with spectral evolution in LT and FP1 (i.e., with the HSH pattern), while there is positive correlation between the light curve and spectral evolution in FP2 (i.e., with the SHS pattern). For understanding the different spectral evolving patterns in two FPs, we use the Trace image with a higher spatial resolution in this event (left panel of Fig. A.4 in Appendix A), from which we find that this event is not a simple flaring loop, but caused by multiple-loop interaction, as shown by a carton in right panel of Fig. A.4.

It can be clearly seen from Fig. A.4 that the bright EUV loop in Fig. A.4 is actually collided with another huge loop in LT, and with a small loop in FP1, to cause the EUV brightening in both LT and FP1, so that FP1 is just located at the top of the small loop, which may be used to explain the reason why the HSH pattern appeared in FP1 due to the trapping effect.

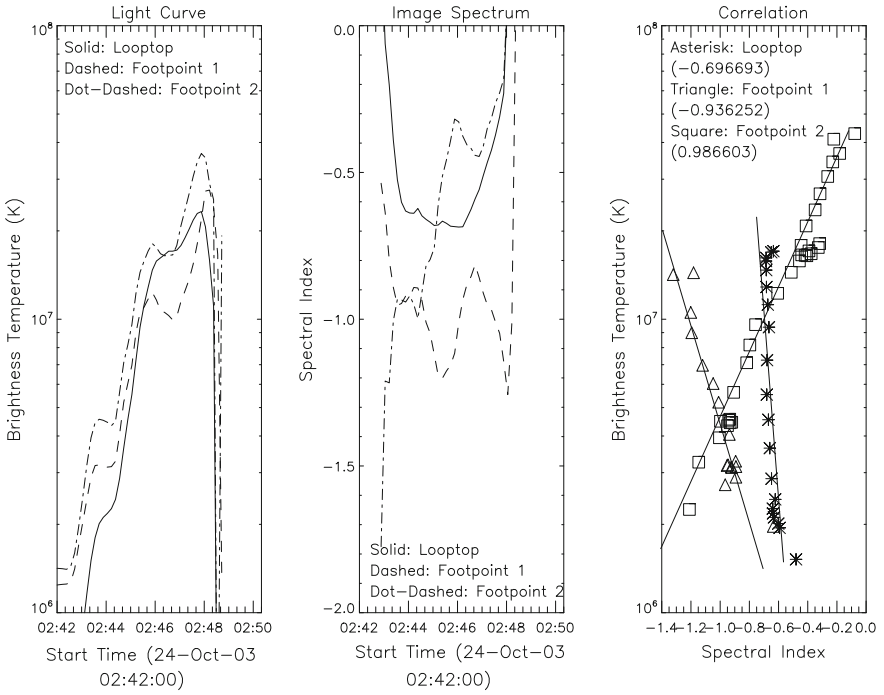

Fig. 3.55 Light curves, spectral evolutions, and correlations of them in LT and FPs of 2003 October 24 event observed by NoRH

3.5 Distribution and Evolution of Radio Polarization

Polarization is an important parameter in solar radio observations. In general, the full information of polarization sense and degree can be determined by four Stokes parameters (I, Q, U, and V), however, the elliptical component of solar radio emission will be depolarized by Faraday rotation of polarization plane in propagation along magnetic field lines in solar atmosphere, so that, only the RCP and LCP components can be observed in the Earth, by two Stokes parameter I and V, which represents the sum and difference of RCP and LCP components, respectively. In practice, the error of polarization in solar radio emission may be caused by different interferences, including nonsolar emission, unpolarized emission, and distributed polarization of instruments, etc., such as the accuracy of 1% for NoRH and 10% for the solar radio spectrometer in China.

From a theoretical point of view, the LCP and RCP components observed along the positive direction of solar magnetic field correspond respectively to the O-mode and X-mode in plasma dispersion relation, which is just reversed along the negative direction of solar magnetic field, thus the polarization degree (p_{th}) is theoretically defined as [39] the difference between X-mode and O-mode emission divided by

the sum of them, while the observed polarization degree (p_{ob}) is commonly defined by the difference between RCP and LCP emission divided by the sum of them. It is obvious that $p_{ob} = p_{th}$ when the magnetic field in radio source is positive (or the angle between the magnetic field and line of sight (LOS) is an acute angle), but $p_{ob} = -p_{th}$ when the magnetic field in radio source is negative (or the angle between the magnetic field and LOS is an obtuse angle). On the other hand, when the magnetic field in radio source is unknown, and if we use the observed polarization to calculate the angle between the magnetic field and LOS, an uncertainty of 180 degrees will be caused by the different definitions of p_{ob} and p_{th}, which is discussed for detail in Sect. 3.5.5. Moreover, the polarization sense and degree may be changed during the propagation of radio emission in solar corona, which is associated with so called linear mode coupling (also see Sect. 3.5.5).

Furthermore, the study on polarization of solar radio emission is relatively weaker up to now, including the NoRH images of polarization at 17 GHz, which should be strengthened urgently in future studies. For statistically studying the polarization of solar radio emission in LT and FPs of flaring loops, we have selected 24 bursts of NoRH with a loop-like structure or three separated sources as mentioned in Sect. 3.2.2, which are further divided into two groups: one is that the LT spectral index is harder than both two FP indices, and another one is that the LT index is at least softer than one of two FP indices as mentioned in Sect. 3.2.4, and one example is respectively given in left and right panels of Fig. 3.34 for each group with 12 events, with respect to two flare models as shown by Fig. 3.35a, b.

3.5.1 Comparison of Polarization of MW Emissions in LT and FPs

Figure 3.56a, b and respectively compare the two FP polarization degrees and the polarization degrees in LT and FPs in the two groups (asterisk for group 1 and triangle for group 2) [101, 103].

The polarization degrees are well correlated between two FPs and between LT and FPs of two groups of events, and the correlation coefficients as marked at the top of Fig. 3.56 are always larger than the critical value 0.05 with the confidence level of 0.95. Another interesting result in Fig. 3.56 is that most data points are concentrated in the first or third quadrant, which means that the polarization senses in LT and two FPs are mostly the same one of LCP or RCP, and the proportion of such kind of events reaches 82% in Fig. 3.56a and 83% in Fig. 3.56b, respectively. This is consistent with one earlier study on 4 NoRH events [87], but it looks to be conflicted with the prediction that two FPs with opposite magnetic polarities will have opposite polarization senses, which may be explained further by the linear mode coupling theory in Sect. 3.5.5.

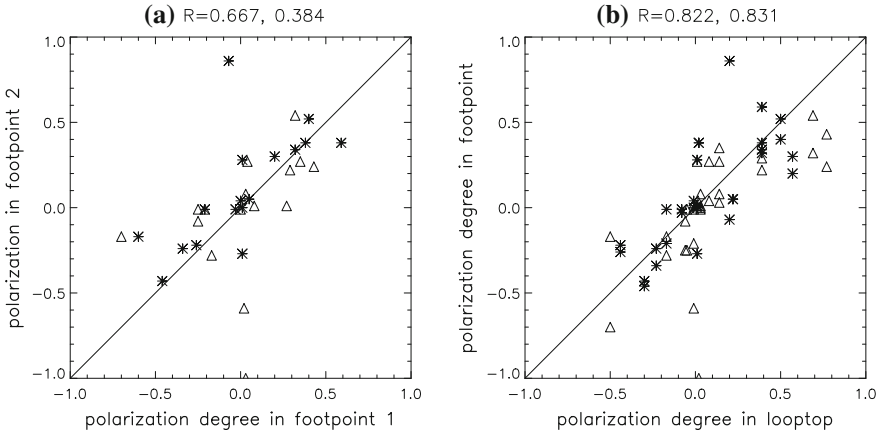

Fig. 3.56 Comparisons between the polarization degrees in **a** two FPs and **b** LT and FPs of two groups of events

3.5.2 *Relation of Polarization and Other Parameters in LT and FPs*

It is traditionally suggested that polarization degree is directly proportional to the local magnetic field strength, but in the correlation between the absolute difference of polarization degrees in two FPs and relative variation of magnetic field strengths in two FPs (see Fig. 3.42 in Sect. 3.2.4), only the events of group 1 shows a positive correlation, while a negative one appears in the events of group 2. Moreover, opposite correlations also appear in the two groups between the logarithm of the ratios of 17–34 GHz T_b in two FPs and the absolute difference of polarization degrees in two FPs (see Fig. 3.41 in Sect. 3.2.4), which is negative and positive respectively in group 1 and 2. Combined of Figs. 3.41 and 3.42, we can deduce that in the events of the two groups 17–34 GHz T_b in two FPs is always negatively proportional to magnetic field strength in two FPs, which is well consistent with the statistics in Figs. 3.32 and 3.39 as well, and will be discussed further in Sect. 6.2.

3.5.3 *Relation of Polarization and Magnetic Field in LT and FPs*

It is found by Kundu et al. [120] in the MW observations that a stronger emission frequently corresponds to a stronger local magnetic field strength, hereby a stronger polarization as well, which is defined as a normal case, and consistent with the prediction of mirroring effect. However, the above statistics in Figs. 3.41 and 3.42 show opposite correlations among the polarization degree, brightness temperature,

Table 3.5 Comparison of log T_b and P in two FPs of group 1

Date	Peak time (UT)	log T_{b117}(K)	log T_{b217}(K)	P_1	P_2	Mirroring effect
19981128	05:39:52	0.73	5.22	0.01	0.28	Normal
19990216	02:57:50	0.89	1.59	−0.01	−0.27	Normal
19990828	00:56:42	2.80	4.61	0.08	0.05	Abnormal
20010925	04:34:01	2.90	9.27	0.59	0.38	Abnormal
20011023	00:16:14	3.68	9.21	0.20	0.30	Normal
20011122	23:01:46	3.43	2.47	−0.01	0.04	Abnormal
20020818	22:47:22	3.13	7.50	−0.21	−0.01	Abnormal
20031027	06:14:20	20.2	0.676	0.32	0.34	Abnormal
20031028	01:32:33	3.24	4.75	0.40	0.52	Normal
20031104	05:49:23	23.4	5.74	0.02	0.01	Normal
20050822	00:55:00	11.6	8.56	−0.60	−0.17	Normal
20070603	01:57:32	3.86	5.18	−0.03	−0.01	Abnormal

Table 3.6 Comparison of log T_b and P in two FPs of group 2

Date	Peak time (UT)	log T_{b117}(K)	log T_{b217}(K)	P_1	P_2	Mirroring effect
19990529	03:10:49	1.92	2.56	0.04	0.27	Normal
20000312	23:05:48	0.587	4.60	0.01	0.08	Normal
20000313	05:03:22	12.6	17.0	0.03	0.01	Abnormal
20010325	04:17:26	2.25	4.45	0.35	0.27	Abnormal
20010928	02:03:05	0.421	3.25	−0.08	−0.25	Normal
20020812	02:17:24	7.44	2.08	−0.17	−0.28	Abnormal
20031024	05:07:47	29.5	0.223	0.03	0.08	Abnormal
20031027	01:35:32	18.2	10.5	0.29	0.22	Normal
20040105	03:20:34	1.03	10.4	−0.17	−0.7	Normal
20040521	23:50:15	3.32	1.53	−1.0	0.03	Normal
20040722	00:21:21	1.30	17.0	0.01	0.27	Normal
20050115	06:07:44	17.0	1.04	0.24	0.43	Abnormal

and magnetic field strength in the events of two groups, which means an abnormal case possibly exists, as shown in Tables 3.5 and 3.6, respectively for the two groups.

Actually, normal and abnormal events appear in both the groups with an equal probability (50%) as shown by Tables 3.5 and 3.6, which means the relationships among polarization degree, brightness temperature, and magnetic field strength is determined not only by mirroring effect, but also by the initial pitch-angle of NT electrons as mentioned in Sect. 3.2.4.

3.5.4 *Time Variation of Polarization in LT and FPs*

For studying in-depth the relationship between the MW intensity and polarization in different parts of flaring loops, we select two events with a loop-like structure observed by NoRH, and analyze the evolution of intensity and polarization, as well as their correlation [121, 122]. Figure 3.57 shows an C6.2 flare accompanied by CME in 2003 October 27 (AR10486, S20E29), the left top panel: SOHO/MDI magnetogram overlaid by the contours of 17 GHz (solid) and 34 GHz (dashed) T_b of NoRH, as well as the 17 GHz polarization degree (dot-dashed), and the positions of LT and two FPs (FP1 and FP2) are marked; the right-top panel: 17 GHz T_b image of NoRH overlaid by the contours of 34 GHz T_b (solid), and calculated magnetic field (dot-dashed); the left bottom panel: 17 GHz T_b image of NoRH overlaid by the contours of 34 GHz T_b

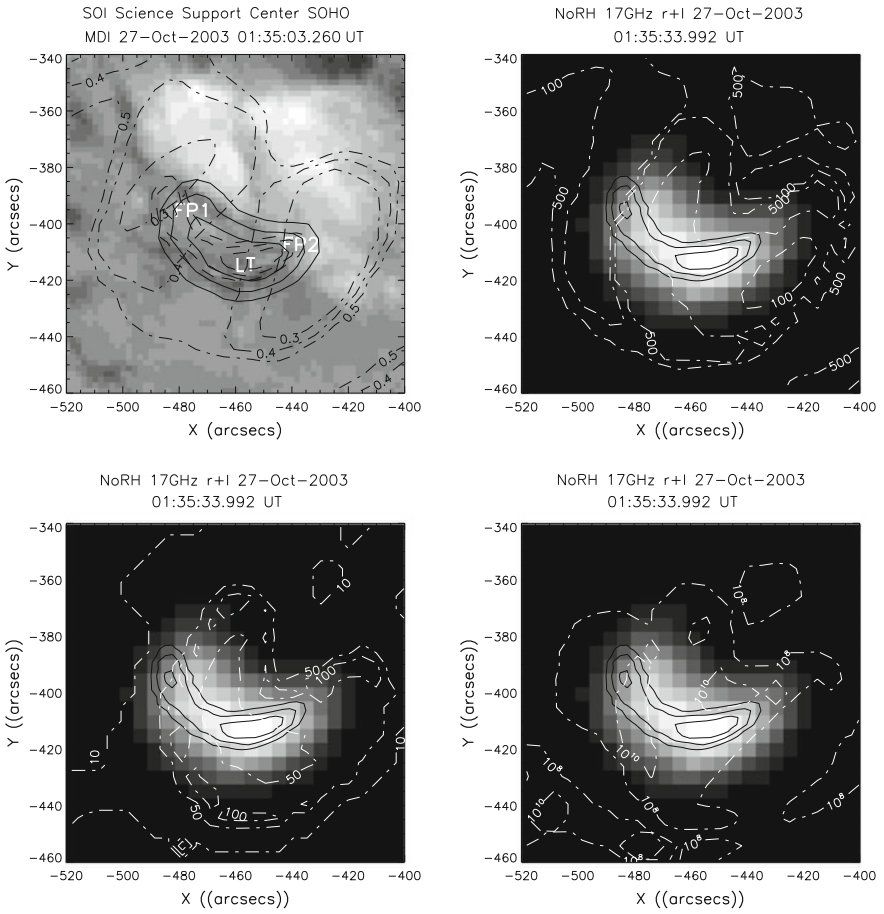

Fig. 3.57 Images of SOHO/MDI and NoRH at the peak time of 2003 October 27 event

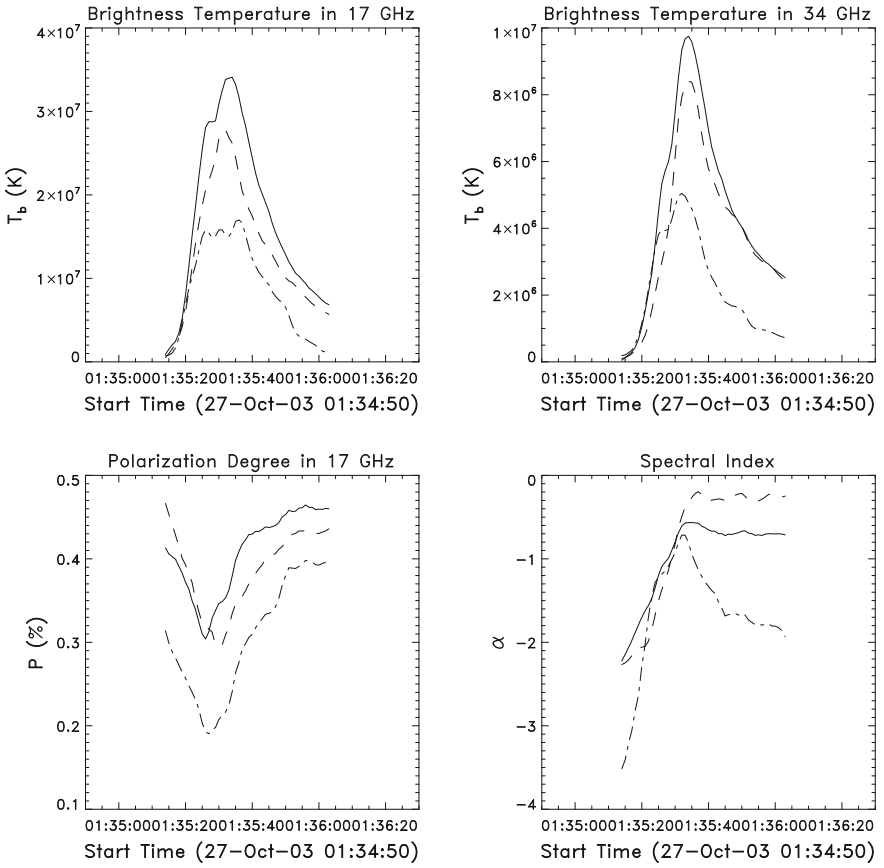

Fig. 3.58 Evolutions of 17 and 34 GHz T_b, polarization degree, and spectral index in the LT and two FPs of 2003 October 27 event

(solid) and calculated view angle (dot-dashed); and the right bottom panel: 17 GHz T_b image of NoRH overlaid by the contours of 34 GHz T_b (solid) and calculated column density of NT electrons (dot-dashed).

It can be seen from Fig. 3.57 that the distribution of 17 and 34 GHz T_b is basically a uniform and symmetric loop-like structure, as well as the distribution of polarization degree at 17 GHz. The view angle always exceeds 50°, and the column density of NT electrons is around 10^{10} cm^{-2}. Furthermore, Fig. 3.58 shows the light curves of 17 GHz (left top) and 34 GHz (right top), the evolutions of polarization degree (left bottom) and spectral index (right bottom) in LT (solid), FP1 (dashed), and FP2 (dot-dashed), respectively.

It is obvious from Fig. 3.58 that there is always a negative correlation between the light curves and evolution of polarization degree in LT and FPs, with correlation coefficients of −0.376, −0.903, and −0.582, respectively. Meanwhile, the spectral

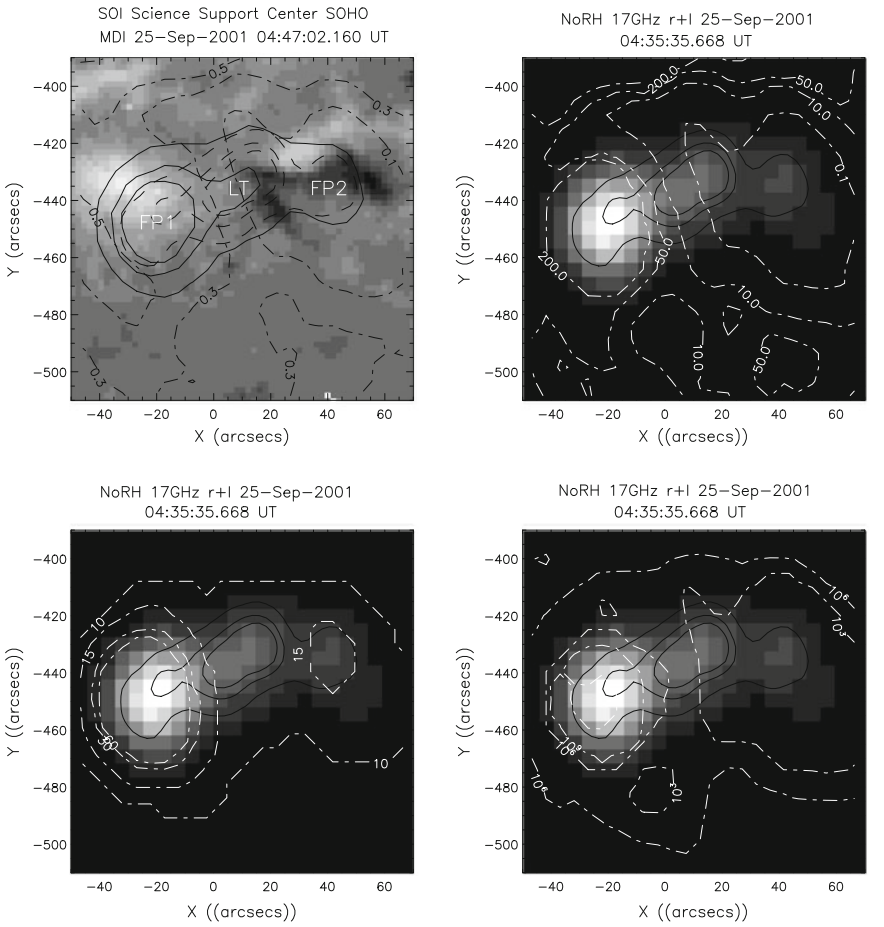

Fig. 3.59 Images of SOHO/MDI and NoRH at the peak time of 2001 September 25 event

evolution always belongs to a common SHS or SHH pattern for the simple impulsive event as mentioned in Sect. 3.3. In comparison with the 2003 October 27 flare, an M7.6 flare with different features in 2001 September 25 (NOAA9628, S21E01) is shown in Fig. 3.59, in which the content in each panel is absolutely the same as that in Fig. 3.57.

The main difference of Fig. 3.59 in comparison with Fig. 3.57 is that all the observed and calculated values in two FPs of flaring loop are obviously asymmetric, and all the observed and calculated values in FP1 are always larger than those in FP2, which has been confirmed by the observed time profiles in different parts of flaring loop (Fig. 3.60, with the same content in each panel as that in Fig. 3.58).

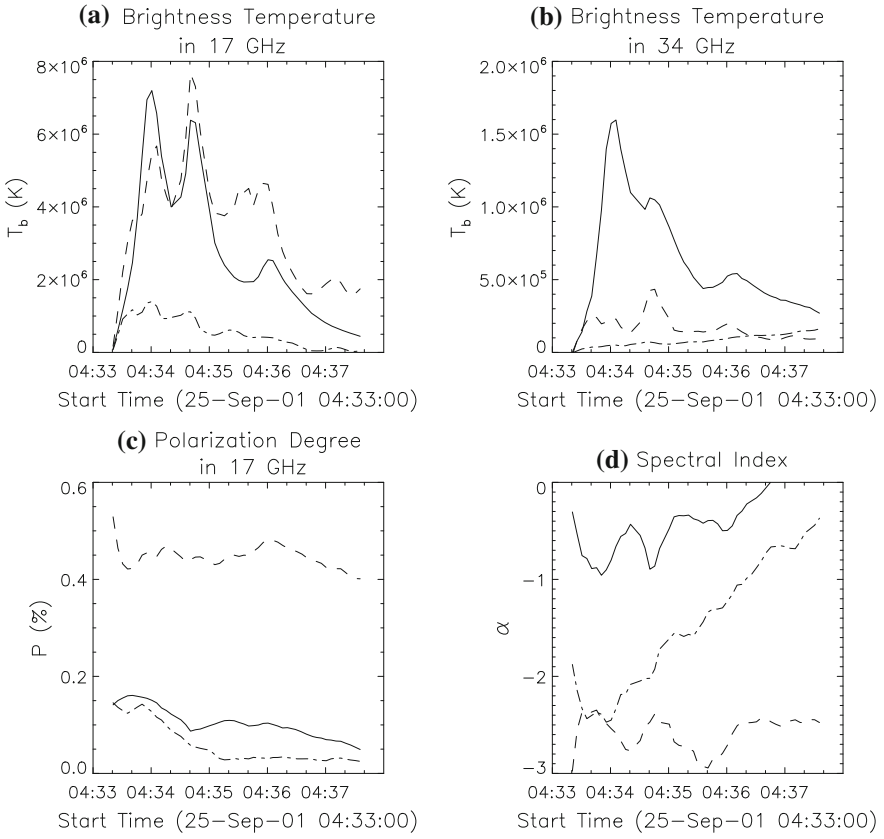

Fig. 3.60 Evolutions of 17 and 34 GHz T_b, polarization degree, and spectral index in the LT and two FPs of 2001 September 25 event

Besides the asymmetry of two FPs, the 2001 September 25 flare is a complicated event with multiple peaks, and the correlations between brightness temperature and polarization degree are always positive with correlation coefficients of 0.546, 0.382, and 0.782, respectively in LT and two FPs, which just corresponds to the normal case in Sect. 3.5.3, and the HSH pattern always exists in LT and two FPs.

There is also more complicated evolutions of polarization, such as the X-class flare with CME and loop expansion in 2002 April 21 [123], in which the RCP in LT varied with a period of $10 \sim 20$ s that started from 5 min before the loop expansion, and gradually turned to LCP, while, the emission in FPs kept RCP sense during the event. This event may be explained by a quasiperiodic injection of NT electrons in the flaring loop, and detailed information will be introduced in Sect. 7.6.1.1.

3.5.5 Linear Mode Coupling and Reversal of Polarization

The polarization sense and degree of solar radio emission are determined mainly by radiation mechanism, magnetic field in radio source, and properties of emitted electrons. On the other hand, the observed polarization can be varied due to the variation of ambient plasma parameters (density and magnetic field) in propagation of solar radio emission, such as the depolarization of Faraday rotation. In addition, because the variation of magnetic field in corona is commonly faster than that of plasma density, the ratio between electron plasma and cyclotron frequencies increases gradually, and intrinsic mode of ECM gradually changes from X-mode to O-mode with a critical ratio of 1.4 in the reversal of polarization sense [124].

Here, we pay attention to another mechanism of linear mode conversion, which happens when the radio emission travels the so-called quasi-transverse (QT) region, where the angle between emission and magnetic field equals to about 90°, which may cause a conversion of X-mode and O-mode. Because the dispersive curves of X-mode and O-mode are close to each other in very high frequencies (so-called strong coupling), thus a critical frequency is theoretically defined to distinguish the strong coupling region from weak one, where the dispersive curves of X-mode and O-mode can be separated evidently, and the conversion of X-mode and O-mode is practically meaningful. Hence, there are two necessary conditions: (*a*) radio emission travels the QT region, and (*b*) radio emission in the frequencies below the critical value of weak coupling [125]. For a common flaring loop rooted in a dipolar magnetic field, such a linear mode conversion is predicted to occur nearby solar limb, and if we select the observed direction of LOS to be a connection of solar center and the Earth, it is obvious that only the emission from a source nearby solar limb can travel the QT region. Moreover, if there is the same polarization sense observed in two FPs with opposite magnetic polarities, the mode conversion of weak coupling should happen, otherwise, when the polarization senses are opposite in two FPs, even radio emission travels the QT region, it should belong to the strong coupling case [126].

On the other hand, based on the approximated GS formula [39], two equations of magnetic field and view angle of emission in radio source are obtained [122]:

$$\log\left(\frac{\nu}{\nu_B}\right) = \frac{A_1 + 0.5A_2\log(1-x^2)}{A_3}\,, \tag{3.5.1}$$

$$\log\left(\frac{\nu}{\nu_B}\right) = \frac{A_4 - 0.071x}{0.782 - 0.545x}\,, \tag{3.5.2}$$

$$A_1 = -9.30 + 0.30\delta + (1.30 + 0.98\delta)\log\left(\frac{\nu}{\nu_p}\right) + \log T_{b\nu}\,, \tag{3.5.3}$$

$$A_2 = 0.34 + 0.07\delta\,, \tag{3.5.4}$$

$$A_3 = 0.52 + 0.08\delta\,, \tag{3.5.5}$$

$$A_4 = 0.10 + 0.035\delta - \log r_c \ . \tag{3.5.6}$$

Here, the magnetic field is included by the electron cyclotron frequency $\nu_B \approx 2.8 \times 10^6 B$, and the view angle is included by $x = \cos\vartheta$. The other parameters in Eqs. (3.5.1) and (3.5.2) all observable, including the radio frequency ν, the peak frequency ν_p, the brightness temperature $T_{b\nu}$ at a given frequency ν, the polarization degree r_c, and electron spectral index $\delta \approx (1.22 - \alpha)/0.9$, where α is the observed spectral index in optically thin region [39]. Furthermore, the terms with B can be removed in Eqs. (3.5.1) and (3.5.2), to obtain a nonlinear equation of $\cos\theta$:

$$0.782A_1 - A_3A_4 + (0.071A_3 - 0.545A_1)x + \\ + 0.5A_2(0.782 - 0.545x)\log(1 - x^2) = 0 \ . \tag{3.5.7}$$

Figure 3.61 gives a group of calculations with typical observable parameters in solar GS busts, the abscissa is $x = \cos\vartheta$ (the approximate formula [39] only refer to the case of an acute angle), and the ordinate is the calculated result in the left-side of Eq. (3.5.7). The results given in Fig. 3.61 are respectively with $r_c = 0.4$, 0.5, and 0.6 (left top); $T_{b\nu} = 0.8 \times 10^6$ K, 1.0×10^6 K, and 1.2×10^6 K (right top); $\nu_p = 4$, 5 and 6 GHz (left bottom); and $\alpha = -2.5$, -3.0, and -3.5 (right bottom), the other parameters are fixed to be their middle value in all the panels, and the radio frequency is selected as 17 GHz for NoRH.

It is evident that the calculated values of y monotonously decreases with increasing of x, and travels through the horizontal line of $y = 0$, which gives a unique solution of the view angle in Eq. (3.5.7). It is noticed that θ just implies the angle between the local magnetic field in radio source and LOS, and when $\theta = 90°$, it just means the radio emission travels the QT region, thus the linear mode conversion of X-mode and O-mode possibly takes place.

However, there is an implicit condition in the calculation of Eq. (3.5.7), i.e., the approximated formula [39] are used only for the emission dominated by X-mode, and due to the uncertainty of 180° caused by the different definitions of polarization degree in the theories and observations as mentioned above, when the magnetic polarity in radio source is unknown, we are actually not sure whether θ equals to the calculated value or 180° minus the calculated value. On the other hand, in spite of θ varies from an acute angle to an obtuse angle or vice-versus, it always travels the QT region to produce the mode conversion, so that the uncertainty of 180 degree does not affect the prediction of linear mode conversion around $\theta = 90°$.

One event in 2001 September 25 can be taken as an example of liner mode conversion (see Figs. 3.59 and 3.60 in Sect. 3.5.4), which further described in Fig. 3.62 with the Stokes I and V at 6 frequencies of NoRP, fitted spectra, and evolution of peak frequency in this event. The light curves at 1, 2, 3.75, 9.375, 17, and 35 GHz are respectively marked by solid, dashed, dot-dashed, long-dashed, dot-dot-dashed, and dotted lines, and the fitted spectra at three peaks as shown by a, b, and c in the light curves.

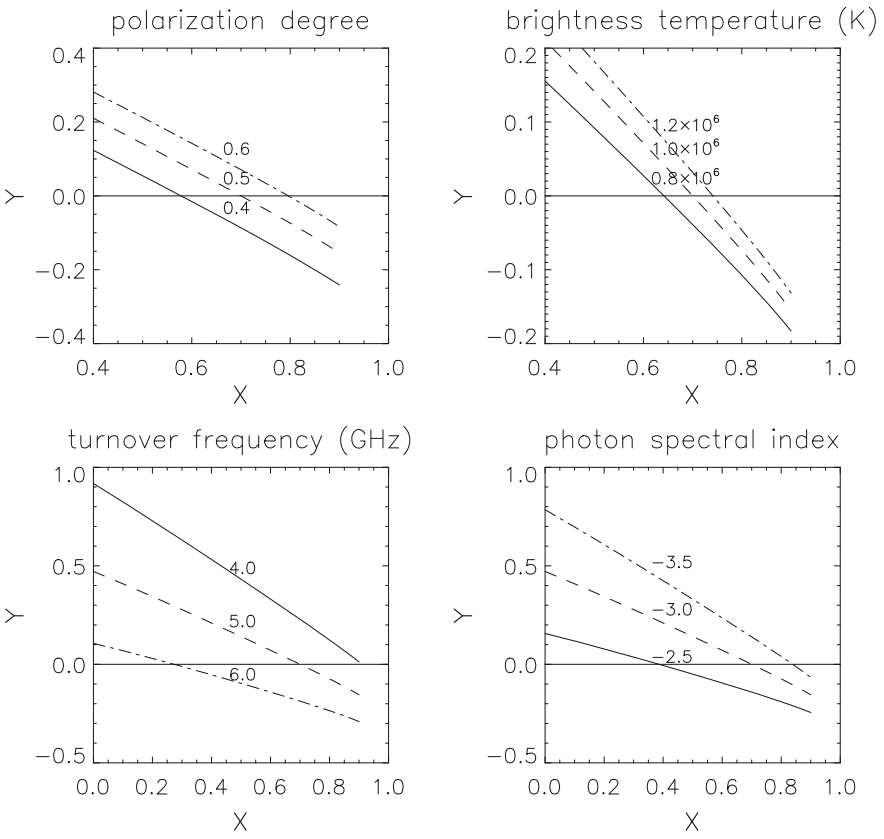

Fig. 3.61 The solution of $\cos\theta$ under typical parameters of solar GS bursts

It is found in Fig. 3.62 that there are different polarization senses in different frequencies, for instance, RCP appears in higher frequencies such as 17 GHz, which is consistent with that observed by NoRH in Fig. 3.60, and RCP declines with increasing of frequency, it finally turns to a strong LCP at the lowest frequency 1 GHz, which is consistent with the prediction of GS theory [39] about O-mode dominated in optically thick part, and X-mode dominated in optically thin part. Meanwhile, the peak frequency increased fast in rising phase, afterward it varied in $10 \sim 15$ GHz, which means that 35 GHz definitely belongs to optically thin part, but 17 GHz is close to the peak frequency, to cause a big error for calculating the optically thin spectral index.

Moreover, the left top panel of Fig. 3.63 shows the Yohkoh/SXT image at the peak time, overlaid by 17 GHz T_b and polarization observed by NoRH; the right-top panel gives SOHO/MDI magnetogram overlaid by the contours of 1500 and 2000 Gauss (dashed), −200 and −800 Gauss (dot-dashed), and view angle 20°, 60°, and 100° (solid) calculated from Eq. (3.5.7); the left bottom panel gives the light curves

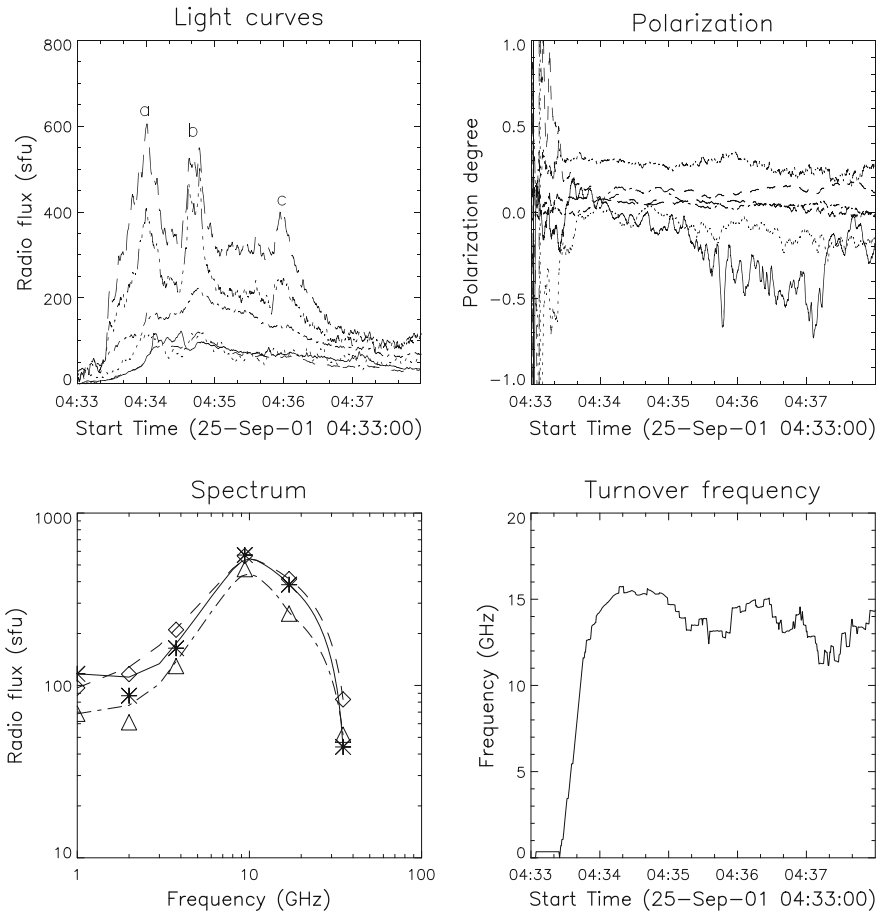

Fig. 3.62 Radio flux (left top), polarization (right top), fitted spectra (left bottom), and evolution of peak frequency (right bottom) observed by NoRP in the 2001 September 25 event

of 17 GHz T_b and polarization degree in two FPs as marked in the left to panel; and the right bottom panel shows the theoretical evolutions of view angle in two FPs respectively by solid and dashed lines (the effective range of calculation is $0 \sim 90°$ as mentioned before, and the extended range of obtuse angle is marked by dotted line).

It is predicted from Fig. 3.63 that the linear mode conversion should happen in this event due to the opposite magnetic polarities and same polarization sense in two FPs [126], but it is difficult to determine which FP is more close to solar limb, because the flaring loop is almost located in the central meridian passage. The calculated view angles in the right bottom panel of Fig. 3.63 shows that the FP1 emission traveled the QT region ($\theta = 90°$) four times, while the view angle of FP2 kept an acute angle, which means that only the first condition of mode conversion is only satisfied in FP1.

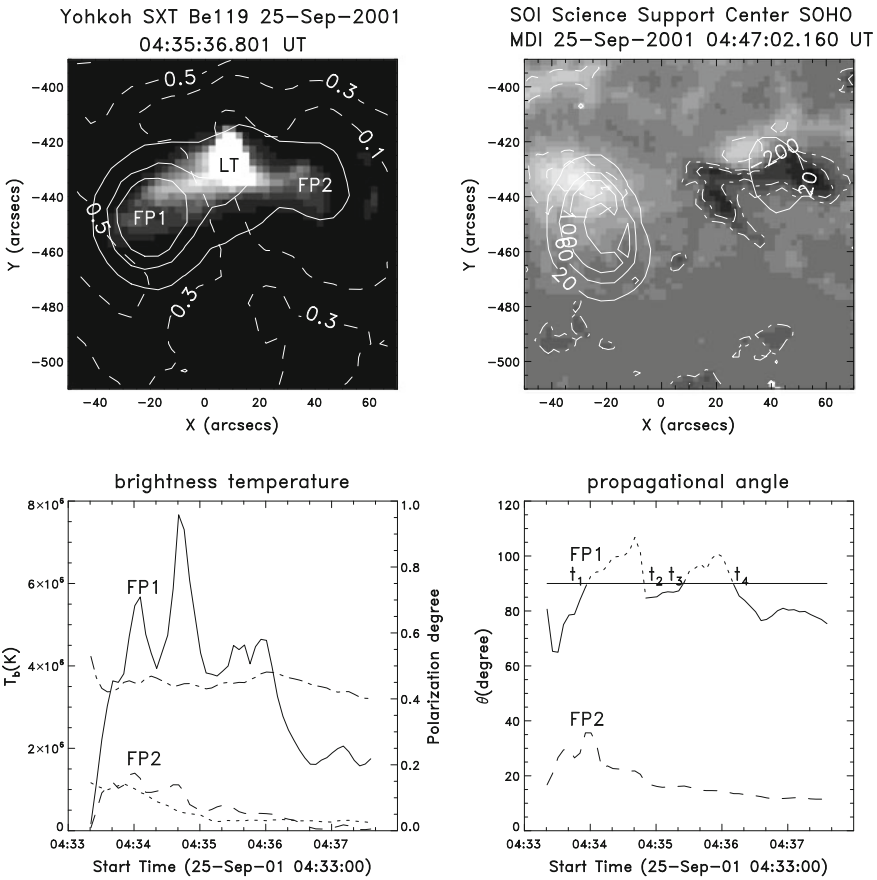

Fig. 3.63 Observations of Yohkoh, SOHO, and NoRH and calculations of view angle of the 2001 September 25 event

Moreover, the magnetic field in FP1 is one order of magnitude larger than that in FP2, the critical frequency is defined by $f_t^4 = 10^{17} NSB^3$, here N is ambient plasma density, S is the scale of magnetic field, and B is the local magnetic field strength [125], we can estimate that f_t in FP1 is higher than 17 GHz, while it is lower than 17 GHz in FP2 when $N = 10^9 \text{cm}^{-3}$, and $S = 10^9$cm, thus the second condition of mode conversion is also satisfied only in FP1.

3.5.6 Determination of Intrinsic Mode

The GS mechanism emitted by moderately relativistic electrons is dominated in solar MW bursts, X-mode and O-mode are respectively dominated in optically thin and

optically thick parts of a typical MW spectrum [36]. Some examples of optically thin O-mode emission are also reported, one possibility is that thermal cyclotron resonant absorption of third harmonic may suppress the X-mode emission in the FP close to solar limb [127], to cause the O-mode emission to be dominated in the FP close to solar center, which requires an enough strong magnetic field to produce the absorption of third harmonic [128]. Another possibility is originated from the scattering by a strong Langmuir turbulent plasma, which is more effective for X-mode than O-mode [129]. The third possibility is hereby the linear mode conversion as mentioned in Sect. 3.5.5.

It is obvious that the intrinsic mode is determined by the magnetic polarity in radio source, which is selected by the magnetic polarity in photosphere in many studies, but it is not always coincident with that in radio source. For instance, in the FP1 of Fig. 3.63 the magnetic field in photosphere is positive, but the calculation of view angle shows the FP1 emission travels the QT region four times, which just means that the magnetic polarity in radio source transverses four times. Regarding the uncertainty of 180° as mentioned before, there are two possibilities of the intrinsic mode in this event [122]:

(a) The FP1 emission changes from initial X-mode to O-mode at two time intervals $t_1 \sim t_2$ and $t_3 \sim t_4$, while the FP2 emission always keeps X-mode.

(b) The FP1 emission changes from initial O-mode to X-mode at two time intervals $t_1 \sim t_2$ and $t_3 \sim t_4$, while the FP2 emission always keeps O-mode.

3.5.7 Modeling the MW Polarization Distribution Along Flaring Loops

3.5.7.1 Observation

A limb event on July 19, 2012, from the NoRH is selected on MW intensity at frequencies of 17 and 34 GHz and the polarization degree at a frequency of 17 GHz with a spatial resolution of 5" (34 GHz) and 10" (17 GHz) and with a time resolution of 1 sec. The main observational fact consists in the specific type of inversion of the circular polarization sign along the flare loop [130, 131]. The map of the circular polarization degree distribution (Fig. A.5 in Appendix A, upper panel, left plot) shows that there is a change of its sign along the observed loop, from positive at the LT to negative at the FPs. Analysis of the polarization degree time profiles in different parts of the source shows that the polarization takes negative values during the burst near the flare loop FPs (Fig. A.5, upper and lower panels right side). In turn, the polarization degree remains positive at all times at the top of the loop (Fig. A.5, middle panel, right plot).

It is interesting that the polarization degree dynamics differs in different legs of the loop. From the rise phase to the decay phase of the radio burst, the polarization degree changes from negative to positive in the northern leg of the loop (Fig. A.5,

middle panel, left plot) and, conversely, from positive to negative in the southern (Fig. A.5, lower panel, left plot).

The circular polarization sign inversion along the flare loop was previously predicted in a theoretical study [132], in which spatial distributions of brightness, polarization, and slope of the frequency spectrum along the model magnetic loop were analyzed for different assumptions about the location and type of the pitch-angle distribution of energetic electrons injected into the loop. It was found that in case of isotropic injection of electrons near one of the FPs, the microwave source polarized in the ordinary mode appears in the LT region, while the emission sources polarized in the X-mode appear close to both FPs. The polarization inversion at the LT is caused by the formation of the pitch-angle distribution of electrons with longitudinal anisotropy in this region.

In order to explain the polarization features in a particular event, a more detailed study is required; it must take into account the observed characteristics of the flare loop obtained from radio diagnostics and physical parameters of plasma and magnetic field inside the loop.

3.5.7.2 Modeling

The modeling of the kinetics of electrons in a magnetic trap is based on the solution of the nonstationary kinetic Fokker-Planck equation (see Eq. (3.2.2) in Sect. 3.2.7), which includes the function of electron injection and describes effects of the magnetic trapping and precipitation of particles, as well as Coulomb scattering on the background plasma [92, 93].

The source function in Eq. (3.2.2) is $S(E,\ \mu,\ s,\ t) = S_1(E)S_2(\mu)S_3(s)S_4(t)$, where $S_1(E) = (E/E_{min})^{-\delta}$, $S_2(\mu) = \exp((\mu - \mu_0)^2/\mu_1^2)$, $S_3(s) = \exp((s - s_0)^2/s_1^2)$, and $S_4(t) = \exp((t - t_0)^2/t_1^2)$, for energy E, the distance s, pitch-angle cosine μ, and time t. Next, we calculated the characteristics of their GS emission using a method and set of programs described in the Ref. [133]. Calculations were carried out for the model loop of finite thickness based on the radiation transfer equation, which takes into account the inhomogeneity of the electron distributions and thermal bremsstrahlung absorption. The orientation of the model flare loop is defined by three angles, i.e., the azimuth, which determines the loop turn around its vertical axis, solar latitude, and longitude.

3.5.7.3 Simulation Results

We considered six basic models of electron injection into the magnetic loop (quasi-longitudinal, quasi-transverse, and isotropic injection at the LT or in one of the FPs of the loop). Distribution maps of the circular polarization degree at different times were built for each of the models, and, in line with the purpose of the work, we selected those for which the polarization sign changed along the loop and in time in some of its parts. Based on the results of Refs. [130, 134], in which microwave (with

NoRH data) and X-ray (with RHESSI data) diagnostics of flare loop parameters in the event on July 19, 2012, was carried out, we set the following parameters of the model.

The longitudinal size of the model loop was $S = 6 \times 10^9$ cm. The loop thickness was set to $h = 10^9$ cm. The injection source was specified by the electron power-law distribution with energies in the range from $E_{min} = 30$ keV to 10 MeV with an exponent of $\delta = 3$. The total amount of injected electrons was $N = 10^{32}$. The magnetic field in the loop varies from 400 G at the FPs to 100 G at the LT [130]. The background plasma density was inhomogeneous along the loop with a sharp rise near FPs $n(s) = n_0(s) \exp(4.6(s/s_{max})^6)$, where $n_0 = 10^{10}$ cm^{-3} is the electron density of the plasma at the LT. This relationship reflects the jump in plasma density in the transition region between the chromosphere and the corona. In accordance with the observations and the results of the diagnostics [130], the model loop was located on the western limb of the Sun (latitude 0°, longitude 90°). The angle between its plane and the line of sight was 80°. In addition, the electron source power was characterized by the Gaussian distribution profile along the loop with a maximum at the point called the injection site ($s_0 = 0$). The duration of the electrons injection was about 60 s with a maximum at $t_0 = 11$ s. The study found that models (*a*) with the quasi-longitudinal electron injection at the loop top and (*b*) with the isotropic electron injection near one of the FPs provide suitable spatial and temporal distributions of GS emission characteristics.

In Fig. A.6 in Appendix A (left column), 2-D maps of the distribution of the polarization degree, $P = (R - L)/(R + L)$, are shown for the model with the anisotropic electron injection at the top of the loop ($s_0 = 0$) for the time $t = 9$ s at three frequencies (17, 7, and 5 GHz). From left column of Fig. A.6 it can be seen that the polarization degree in the LT has a positive value at a frequency of 17 GHz and a negative value in the FPs (similar to observations). Figure A.6 (right column) shows the graph of the polarization degree distribution along the loop for the described model of injection at various times ($t = 3$, 12, 21, 30, 39, 48, and 57 s). It is clearly seen that the polarization remains negative ($P = -0.5, \ldots, -1$) at the FPs and remains positive ($P = 0.2 \ldots 0.5$) at the LT during the model burst. In the transition region (highlighted by circles) during the burst, the circular polarization sign changes with time (from the right polarization to the left one). A similar change in the polarization sign was observed in our study of the flare loop (Fig. A.5, upper panel left plot, box 4). However, let us point out that a more complex dynamics is implemented in observations. Changes in the polarization sign with time occur in different directions for the northern (box 2) and southern (box 4) legs of the loop. Apparently, this difference is caused by a more complicated distribution of the physical parameters within the loop than in the model.

Figure A.6 (right column) show that the polarization degree along the loop varies slightly (from $-0.7, \ldots, -1$ at the FPs to 0.1, …, 0.3 at the top) at a frequency of 7 GHz; at 5 GHz there are no temporal and spatial changes in the polarization sign at all.

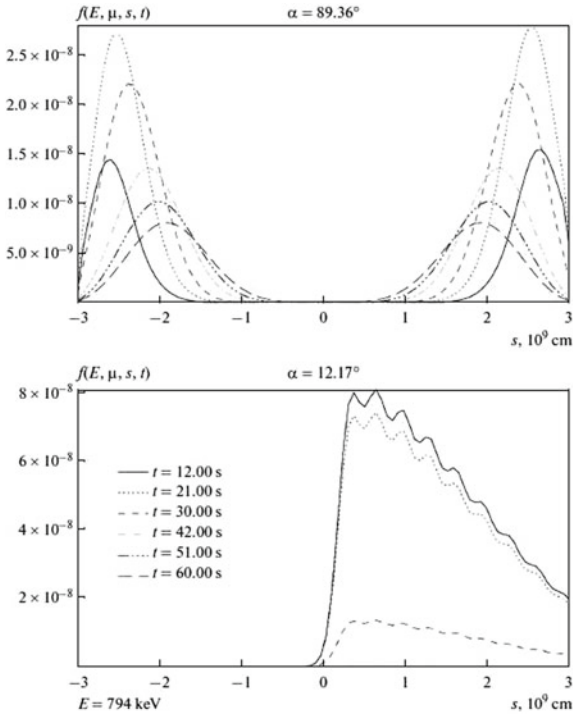

Fig. 3.64 Distribution function of the electrons along the loop for values of pitch angles 12° and 89° at times $t = 12$, 21, 30, 42, 51, and 60 s (solid, dotted, dashed, dash-dotted, three-dots-dashed, and long dashed lines, respectively)

3.5.7.4 Discussions

In order to understand the causes of the change of the polarization sign along the loop and overtime in the model, let us use the electron distribution function along the loop (Fig. 3.64) that we obtained as a result of the simulation. The bottom panel of Fig. 3.3 shows the function distribution for electrons with small pitch angles close to 0°. It is evident that they are mostly located at the top of the loop, while electrons with large pitch angles close to 90°, on the contrary, are primarily concentrated in the area of FPs (Fig. 3.64, top panel). According to the Ref. [30], in the GS emission generated in a quasi-transverse direction to magnetic field, the X-mode dominates if emitting electrons are isotropic or have the perpendicular pitch-angle anisotropy. On the contrary, if emitting electrons have the longitudinal anisotropy, then the O-mode dominates in their GS emission. Such an effect is more pronounced at higher frequencies, at which the emission has a greater directivity, since it is generated by more energetic electrons [135]. For this reason, we do not obtain the effect of the polarization sign change at a relatively low frequency of 5 GHz in model calculations.

Thus, the observed polarization sign change in the event on July 19, 2012, may be caused by the presence of the longitudinal anisotropy of energetic electrons at the upper part of the flare loop.

References

1. Kai, K., Kosugi, T., Nitta, N.: Flux relations between hard X-rays and microwaves for both impulsive and extended solar flares. Publ. Astron. Soc. Jpn. **37**, 155–162 (1985)
2. Bai, T., Dennis, B.: Characteristics of gamma-ray line flares. Astrophys. J. **1985**(292), 699–715 (1985)
3. Cliver, E.W., Dennis, B.R., Kiplimger, A.L., Kane, S.R., Neidig, D.F., Sheeley, N.R., Koomen, M.J.: Solar gradual hard X-ray bursts and associated phenomena. Astrophys. J. **305**, 920–935 (1986)
4. Bai, T.: Two classes of gamma-ray/proton flares - Impulsive and gradual. Astrophys. J. **308**, 912–928 (1986)
5. Akimov, V.V., Leikov, N.G., Belov, A.V., Chertok, I.M., Kurt, V.G., Magun, A., Melnikov, V.F.: High energy gamma-rays at the late state of the large solar flare of June 15, 1991 and accompanying phenomena. 23rd ICRC **3**, 111–114 (1993)
6. Tsuneta, S., Takakura, T., Nitta, N., Ohki, K., Makishima, K., Marakami, T., Oda, M., Ogawara, Y.: Hard X-ray imaging of the solar flare on 1981 May 13 with the HINOTORI spacecraft. Astrophys. J. **280**, 887–891 (1984)
7. Klein, K.-L., Trottet, G.: Energetic electron injection into the high corona during the gradual phase of flares: Evidence against acceleration by a large scale shock. AIP Conf. Proc. **294**, 187–192 (1994)
8. Melnikov, V.F.: Electron acceleration and capture in impulsive and gradual bursts: Results of analysis of microwave and hard x-ray emissions. Radiophys. Quant. Electron. **37**, 557–568 (1994)
9. Bakunin, L.M., Ledenev, V.G., Nefedyev, V.P., et al.: Spatial, spectral, and polarization properties of radio emission of the 3 February, 1983 proton flare. Solar Phys. **135**, 107–129 (1991)
10. Trottet, G., Vilmer, N.: Electron spectra deduced from solar hard X-ray bursts. Adv. Space Res. **4**, 153–156 (1984)
11. Klein, K.-L., Trottet, G., Magun, A.: Microwave diagnostics of energetic electrons in flares. Solar Phys. **104**, 243–254 (1986)
12. Melnikov, V.F.: Ph.D. thesis, NIRFI, N. Novgorod (1990)
13. Bruggmann, G., Vilmer, N., Klein, K.-L., Kane, S.R.: Electron trapping in evolving coronal structures during a large gradual hard X-ray/radio burst. Solar Phys. **149**, 171–193 (1994)
14. Kaufmann, P., Costa, J.E.R., Vaz, A.M.Z., Dennis, B.R.: Solar burst with millimetre-wave emission at high frequency only. Nature **313**, 380–382 (1985)
15. Herrmann, R., Magun, A., Costa, J.E.R., Correira, E., Kaufmann, P.: A multibeam antenna for solar mm-wave burst observations with high spatial and temporal resolution. Solar Phys. **142**, 157–170 (1992)
16. Kundu, M.R., White, S.M., Gopalswamy, N., Lim, J.: Millimeter, microwave, hard X-ray, and soft X-ray observations of energetic electron populations in solar flares. Astrophys. J. Suppl. Ser. **90**, 599–610 (1994)
17. Nakajima, H., Sekiguchi, H., Sawa, M., Kai, K., Kawashima, S., et al.: The radiometer and polarimeters at 80, 35, and 17 GHz for solar observations at Nobeyama. Publ. Astron. Soc. Jpn. **37**, 163–170 (1985)
18. Kaufmann, P., Costa, J.E.R., Strauss, F.M.: Time delays in solar bursts measured in the mm-cm range of wavelengths. Solar Phys. **81**, 159–172 (1982)
19. Correia, E., Costa, J.E.R., Kaufmann, P., Magun, A., Herrmann, R.: Spatial positions of fast-time structures of a solar burst observed at 48 GHz. Solar Phys. **159**, 143–155 (1995)
20. Chertok, I.M., Fomichev, V.V., Gorgutsa, R.V., Hildebrandt, J., Krueger, A., Magun, A., Zaitsev, V.V.: Solar radio bursts with a spectral flattening at millimeter wavelengths. Solar Phys. **160**, 181–198 (1995)
21. Urpo, S., Bakhareva, N.M., Zaitsev, V.V., Stepanov, A.V.: Comparison of mm-wave and X-ray diagnostics of flare plasma. Solar Phys. **154**, 317–334 (1994)
22. Melrose, D.B., Brown, J.C.: Precipitation in trap models for solar hard X-ray bursts. Mon. Not. R. Astron. Soc. **176**, 15–30 (1976)

23. MacKinnon, A.L., Brown, J.C., Trottet, G., Vilmer, N.: The effect of precipitation on diagnostics for electron trap models of solar hard X-ray bursts. Astron. Astrophys. **119**, 297–300 (1983)
24. Vilmer, N., Kane, R., Trottet, G.: Impulsive and gradual hard X-ray sources in a solar flare. Astron. Astrophys. **108**, 306–313 (1982)
25. Hulot, E., Vilmer, N., Chupp, E.I., Dennis, B.R., Kane, S.R.: Gamma-ray and X-ray time profiles expected from a trap-plus-precipitation model for the 7 June 1980 and 27 April 1981 solar flares. Astron. Astrophys. **256**, 273–285 (1992)
26. Melnikov, V.F., Magun, A.: Spectral flattening during solar radio bursts at cm-mm-wavelengths and the dynamics of energetic electrons in a flare loop. Solar Phys. **178**, 591–609 (1998)
27. Melnikov, V.F.: Evolution of the spectral index of solar microwave bursts. In: Sol. Aktiv., Nauka, Alma-Ata, pp. 106–113 (1983)
28. Kundu, M.R.: Radio and X-ray imaging observations of solar flares and coronal transients. Solar Phys. **169**, 389–402 (1996)
29. Bastian, T.S., Benz, A.O., Gary, D.E.: Radio emission from solar flares. Ann. Rev. Astron. Astrophys. **36**, 131–188 (1998)
30. Fleishman, G.D., Melnikov, V.F.: Gyrosynchrotron emission from anisotropic electron distributions. Astrophys. J. **587**, 823–835 (2003)
31. Lee, J.W.: Solar and space weather radiophysics. In: Gary, D.E., Keller, C.U. (eds.), vol. 177, Springer (2004)
32. Bastian, T.S.: Solar physics with the nobeyama radioheliograph. Nobeyama Solar Radio Obs. Rep. **1**, 3 (2006)
33. Takakura, T., Kai, K.: Spectra of solar radio type IV bursts. Publ. Astron. Soc. Jpn. **13**, 94–107 (1961)
34. Takakura, T., Kai, K.: Energy distribution of electrons producing microwave impulsive bursts and X-Ray bursts from the sun. Publ. Astron. Soc. Jpn. **18**, 57–76 (1966)
35. Guidice, D.A., Castelli, J.P.: Spectral distributions of microwave bursts. Solar Phys. **44**, 155–172 (1975)
36. Ramaty, R.: Gyrosynchrotron emission and absorption in a magnetoactive plasma. Astrophys. J. **1969**(158), 753–770 (1969)
37. Takakura, T.: The self absorption of gyro-synchrotron emission in a magnetic dipole field: microwave impulsive burst and hard X-Ray burst. Solar Phys. **26**, 151–175 (1972)
38. Petrosian, V.: Synchrotron emissivity from mildly relativistic particles. Astrophys. J. **251**, 727–738 (1981)
39. Dulk, G.A., Marsh, K.A.: Simplified expressions for the gyrosynchrotron radiation from mildly relativistic, nonthermal and thermal electrons. Astrophys. J. **259**, 350–358 (1982)
40. Gary, D.E.: The numbers of fast electrons in solar flares as deduced from hard X-ray and microwave spectral data. Astrophys. J. **297**, 799–804 (1985)
41. Klein, K.-L.: Microwave radiation from a dense magneto-active plasma. Astron. Astrophys. **183**, 341–350 (1987)
42. Twiss, R.Q.: Philos. Mag. **45**, 249 (1954)
43. Razin, V.A.: Izv. Vyssh. Uchebn. Zaved. Radiofiz. **3**, 584 (1960)
44. Klein, K.-L., Trottet, G., Magun, A.: Microwave diagnostics of energetic electrons in flares. Solar Phys. **104**, 243–252 (1986)
45. Gary, D.E., Hurford, G.J.: Solar and space weather radiophysics. In: Gary, D.E., Keller, C.U. (eds.), vol. 69. Springer (2004)
46. Bastian, T.S., Fleishman, G.D., Gary, D.E.: Radio spectral evolution of an x-ray-poor impulsive solar flare: implications for plasma heating and electron acceleration. Astrophys. J. **666**, 1256–1267 (2007)
47. Stähli, M., Gary, D.E., Hurford, G.J.: High-resolution microwave spectra of solar bursts. Solar Phys. **120**, 351–368 (1989)
48. Belkora, L.: Time evolution of solar microwave bursts. Astrophys. J. **481**, 532–544 (1997)

49. Nita, G.M., Gary, D.E., Lee, J.W.: Statistical study of two years of solar flare radio spectra obtained with the owens valley solar array. Astrophys. J. **605**, 528–545 (2004)
50. Fleishman, G.D., Nita, G.M., Gary, D.E.: Evidence for resonant transition radiation in decimetric continuum solar bursts. Astrophys. J. **620**, 506–516 (2005)
51. Preka-Papadema, P., Alissandrakis, C.E.: Spatial and spectral structure of a solar flaring loop at centimeter wavelengths. Astron. Astrophys. **191**, 365–373 (1988)
52. Melnikov, V.F., Silva, A.V.R.: Temporal evolution of solar flare microwave and hard x-ray spectra: evidence for electron spectral dynamics-II. In: Ramaty, R., Mandzhavidze, N. (eds.), ASP Conference Series High Energy Solar Physics Workshop — Anticipating Hessi, vol. 206, pp. 475–477 (2000)
53. Silva, A.V.R., Wang, H., Gary, D.E.: Correlation of microwave and hard x-ray spectral parameters. Astrophys. J. **545**, 1116–1123 (2000)
54. Krucker, S., Hurford, G.J., MacKinnon, A.L., Shih, A.Y., Lin, R.P.: Coronal γ-ray bremsstrahlung from solar flare-accelerated electrons. Astrophys. J. **678**, L63–L66 (2008)
55. Melnikov, V.F., Shibasaki, K., Reznikova, V.E.: Loop-top nonthermal microwave source in extended solar flaring loops. Astrophys. J. **580**, L185–L188 (2002)
56. Klein, K.-L., Trottet, G.: Gyrosynchrotron radiation from a source with spatially varying field and density. Astron. Astrophys. **141**, 67–76 (1984)
57. Simões, P.J.A., Costa, J.E.R.: Solar bursts gyrosynchrotron emission from three-dimensional sources. Astron. Astrophys. **453**, 729–736 (2006)
58. Melnikov, V.F., Reznikova, V.E., Shibasaki, K., Nakariakov, V.M.: Spatially resolved microwave pulsations of a flare loop. Astron. Astrophys. **439**, 727–736 (2005)
59. Melnikov, V.F., Gary, D.E., Nita, G.M.: Peak frequency dynamics in solar microwave bursts. Solar Phys. **253**, 43–73 (2008)
60. Lu, E.T., Hamilton, R.J.: Avalanches and the distribution of solar flares. Astrophys. J. **380**, L89–L92 (1991)
61. Charbonneau, P., McIntosh, S.W., Liu, H.-L., Bogdan, T.J.: Avalanche models for solar flares (Invited Review). Solar Phys. **203**, 321–353 (2001)
62. Nita, G.M., Gary, D.E., Lanzerotti, L.J., Thomson, D.J.: The peak flux distribution of solar radio bursts. Astrophys. J. **570**, 423–438 (2002)
63. Song, Q., Huang, G., Tan, B.: Frequency dependence of the power-law index of solar radio bursts. Astrophys. J. **750**, 160–163 (2012)
64. Clauset, A., Young, M., Gleditsch, K.S.J.: Confl. Resolut **51**, 58 (2007)
65. Clauset, A., Shalizi, C.R., Newman, M.E.J.: Power-law distributions in empirical data. SIAM Rev. **51**, 661–703 (2009)
66. Song, Q., Huang, G., Huang, Y.: Frequency dependence of solar flare occurrence rates ł inferred from power-law distribution. Astrophys. Space Sci. **347**, 15–19 (2013)
67. Parker, E.N.: Magnetic neutral sheets in evolving fields - part two - formation of the solar corona. Astrophys. J. **264**, 642–647 (1983)
68. Marsh, K.A., Hurford, G.J.: Two-dimensional VLA maps of solar bursts at 15 and 23 GHz with arcsec resolution. Astrophys. J. **240**, L111–L114 (1980)
69. Kundu, M., Schmall, E.J., Velusamy, T.: Magnetic structure of a flaring region producing impulsive microwave and hard X-ray bursts. Astrophys. J. **253**, 963–974 (1982)
70. Kawabata, K., Ogawa, H., Takakura, T., Tsuneta, S., Ohki, K., et al.: Fan-beam observations of millimeter wave burst associated with x-ray and gamma-ray events detected from HINOTORI. In: Proceedings of Hinotori Symposium on Solar Flares, vol. 168, Tokyo, ISAS (1982)
71. Nakajima, H.: Particle acceleration in the 1981 April 1 flare. Solar Phys. **86**, 427–432 (1983)
72. Alissandrakis, C.E., Preka-Papadema, P.: Microwave emission and polarization of a flaring loop. Astron. Astrophys. **139**, 507–511 (1984)
73. Hanaoka, Y.: Flares and plasma flow caused by interacting coronal loops. Solar Phys. **165**, 275–301 (1996)
74. Nishio, M., Yaji, K., Kosugi, T., Nakajima, H., Sakurai, T.: Magnetic field configuration in impulsive solar flares inferred from coaligned microwave/x-ray images. Astrophys. J. **489**, 976–991 (1997)

75. Hanaoka, Y.: High-energy electrons in double-loop flares. Publ. Astron. Soc. Jpn. **51**, 483–496 (1999)
76. Melnikov, V.F., Shibasaki, K., Yokoyama, T., Nakajima, H., Reznikova, V.E.: In: Abstracts of the CESRA Workshop. Munich, Germany, 2–6 July 2001
77. Nindos, A., Kundu, M., White, S.: In: Abstracts of the CESRA Workshop. Munich, Germany, 2–6 July 2001
78. Kundu, M.R., Nindos, A., White, S.M., Grechnev, V.V.: A multiwavelength study of three solar flares. Astrophys. J. **557**, 880–890 (2001)
79. Melnikov, V.F., Yokoyama, T., Shibasaki, K., Reznikova, V.E.: Spectral dynamics of mildly relativistic electrons in extended flaring loops. In: Wilson, A. (ed.) The 10th European Solar Physics Meeting, ESA SP-506, 9–14 Sept 2002, vol. 1, pp. 339–342. Prague, Czech Republic (2002)
80. White, S., Kundu, M., Garaimov, V., Yokoyama, T., Sato, J.: The physical properties of a flaring loop. Astrophys. J. **576**, 505–518 (2002)
81. Lee, J.W., Gary, D.E., Qiu, J., Gallacher, P.T.: Electron transport during the 1999 August 20 flare inferred from microwave and hard x-ray observations. Astrophys. J. **572**, 609–625 (2002)
82. Lee, J.W., Bong, S.C., Yun, H.S.: Solar microwave bursts and electron kinetics. J. Korean Astron. Soc. **36**, S63–S73 (2003)
83. Karlický, M., Kosugi, T.: Acceleration and heating processes in a collapsing magnetic trap. Astron. Astrophys. **419**, 1159–1168 (2004)
84. Su, Y.N., Huang, G.L.: Polarization of loop-top and footpoint sources in microwave bursts. Solar Phys. **219**, 159–168 (2004)
85. Yokoyama, T., Nakajima, H., Shibasaki, K., Melnikov, V.F., Stepanov, A.V.: Microwave observations of the rapid propagation of nonthermal sources in a solar flare by the nobeyama radioheliograph. Astrophys. J. **576**, L87–L90 (2002)
86. Zhou, A.H., Su, Y.N., Huang, G.L.: Energetic electrons in loop top and footpoint microwave sources. Solar Phys. **226**, 327–336 (2005)
87. Melnikov, V.F.: Electron acceleration and transport in microwave flaring loops. In: Shibasaki, K. (ed.) Proceedings of Nobeyama Symposium (Kiosato, 26–29 Oct 2004), NSRO Report, vol. 1, pp. 11–22 (2006)
88. Preka-Papadema, P., Alissandrakis, C.E.: Two-dimensional model maps of flaring loops at cm-wavelengths. Astron. Astrophys. **257**, 307–314 (1992)
89. Petrosian, V.: Structure of the impulsive phase of solar flares from microwave observations. Astrophys. J. **255**, L85–L89 (1982)
90. Fleishman, G.D.: Radio emission from anisotropic electron distributions. In: Shibasaki, K. (ed.) Proceedings of Nobeyama Symposium (Kiosato, 26–29 October 2004), NSRO Report, vol. 1, pp. 51–62 (2006)
91. Melnikov, V.F.: Electron acceleration and capture in impulsive and gradual bursts: results of analysis of microwave and hard x-ray emissions. Radiophys. Quant. Electr. **37**, 557–568 (1994)
92. Hamilton, R.J., Lu, E.T., Petrosian, V.: Numerical solution of the time-dependent kinetic equation for electrons in magnetized plasma. Astrophys. J. **354**, 726–734 (1990)
93. Gorbikov, G.D., Melnikov, V.F.: The numerical solution of the Fokker–Plank equation for modeling of particle distribution in solar magnetic traps. Math. Model. **19**, 112–122 (2007)
94. Somov, B.V., Kosugi, T.: Collisionless reconnection and high-energy particle acceleration in solar flares. Astrophys. J. **485**, 859–868 (1997)
95. Fletcher, L.: Looptop hard x-ray sources. In: Wilson, A. (ed.) The 9th European Meeting on Solar Physics, held 12–18 Sept. 1999, vol. 2, pp. 693 European Space Agency, ESA, SP-448, Florence, Italy (1999)
96. Petrosian, V., Donaghy, T.Q., McTierman, J.M.: Loop top hard x-ray emission in solar flares: images and statistics. Astrophys. J. **569**, 459–473 (2002)
97. Jakimiec, J.: A new model of electron acceleration in solar flares. In: Proceedings of 10th European Solar Physics Meeting, Solar Variability: From Core to Outer Frontiers, ESA SP-506, vol. 2, pp. 645–647. Prague, Czech Republic (2002)

98. Somov, B.V., Bogachev, S.A.: The betatron effect in collapsing magnetic traps. Astron. Lett. **29**, 621–628 (2003)
99. Miller, J.A., Cargill, P.J., Emsly, A.G., et al.: Critical issues for understanding particle acceleration in impulsive solar flares. J. Geophys. Res. **102**, 14631–14660 (1997)
100. Aschwanden, M.J.: Particle acceleration and kinematics in solar flares - a synthesis of recent observations and theoretical concepts (invited review). Space Sci. Rev. **101**, 1–227 (2002)
101. Huang, G.L., Nakajima, H.: Statistical analysis of flaring loops observed by nobeyama radioheliograph. I. Comparison of looptop and footpoints. Astrophy. J. **696**, 136–142 (2009)
102. Benka, S.G., Holman, G.D.: A thermal/nonthermal model for solar microwave bursts. Astrophys. J. **391**, 854–864 (1992)
103. Sakao, T.: Characteristics of solar flare hard X-ray sources as revealed with the Hard X-ray Telescope aboard the Yohkoh satellite. Ph.D. thesis, University of Tokyo (1994)
104. Sakao, T., Kosugi, T., Masuda, S., Yaji, K., Inda-Koide, M., Makishima, K.: Characteristics of hard X-ray double sources in impulsive solar flares. Adv. Space Res. **17**, 67–70 (1996)
105. Aschwanden, M.J., Fletcher, L., Sakao, T., Kosugi, T., Hudson, H.: Deconvolution of directly precipitating and trap-precipitating electrons in solar flare hard x-rays. III. Yohkoh hard x-ray telescope data analysis. Astrophys. J. **517**, 977–989 (1999)
106. Asai, A., Shimojo, M., Isobe, H., Morimoto, T., Yokoyama, T., Shibasaki, K., Nakajima, H.: Periodic acceleration of electrons in the 1998 November 10 solar flare. Astrophys. J. **562**, L103–L106 (2001)
107. Siarkowski, M., Falewicz, R.: Variations of the hard X-ray footpoint asymmetry in a solar flare. Astron. Astrophys. **428**, 219–226 (2004)
108. Alexander, D., Metcalf, T.R.: Energy dependence of electron trapping in a solar flare. Solar Phys. **210**, 323–340 (2002)
109. Hanaoka, Y.: Double-loop configuration of solar flares. Solar Phys. **173**, 319–346 (1997)
110. Lee, J., Gary, D.E.: Solar microwave bursts and injection pitch-angle distribution of flare electrons. Astrophys. J. **543**, 457–471 (2000)
111. Gary, D.E., Hurford, G.J.: Coronal temperature, density, and magnetic field maps of a solar active region using the owens valley solar array. Astrophys. J. **420**, 903–912 (1994)
112. Huang, G.L., Song, Q.W., Huang, Y.: Statistics of flaring loops observed by the nobeyama radioheliograph. III. Asymmetry of two footpoint emissions. Astrophys. J. **723**, 1806–1816 (2010)
113. Takasaki, H., Kiyohara, J., Asai, A., Nakajima, H., Yokoyama, T., Masuda, S., Sato, J., Kosugi, T.: Imaging spectroscopy of a gradual hardening flare on 2000 November 25. Astrophys. J. **661**, 1234–1241 (2007)
114. Huang, G.L., Nakajima, H.: Statistics of flaring loops observed by nobeyama radioheliograph II. Spect. Evol. Astrophys. J. **702**, 19–26 (2009)
115. Metcalf, T.R., Alexander, D.: Coronal trapping of energetic flare particles: Yohkoh/HXT observations. Astrophys. J. **522**, 1108–1116 (1999)
116. Ginzburg, V.L., Syrovatskii, S.I.: The Origin of Cosmic Rays. Macmillan, New York (1964)
117. Bai, T., Ramaty, R.: Hard X-ray time profiles and acceleration processes in large solar flares. Astrophys. J. **227**, 1072–1081 (1979)
118. Song, Q.W., Huang, G.L., Nakajima, H.: Co-analysis of solar microwave and hard x-ray spectral evolutions. I. In two frequency or energy ranges. Astrophys. J. **734**, 113–124 (2011)
119. Huang, G.L., Li, J.P.: Co-analysis of solar microwave and hard x-ray spectral evolutions. II. In three sources of a flaring loop. Astrophys. J. **740**, 46–56 (2011)
120. Kundu, M.R., Nitta, N., White, S.M., Shibasaki, K., Enome, S., et al.: Microwave and hard x-ray observations of footpoint emission from solar flares. Astrophys. J. **454**, 522–530 (1995)
121. Huang, G.L., Li, J.P., Song, Q.W.: Calculation of coronal magnetic field and density of nonthermal electrons in 2003 October 27 microwave burst. Res. Astron. Astrophys. **13**, 215–225 (2013)
122. Huang, G.L., Song, Q.W., Li, J.P.: Determination of intrinsic mode and linear mode coupling in solar microwave bursts. Astrophys. Space Sci. **345**, 41–47 (2013)

123. Huang, G.L., Lin, J.: Quasi-periodic reversals of radio polarization at 17 GHz observed in the 2002 April 21 solar event. Astrophys. J. **639**, L99–L102 (2006)
124. Huang, G.L.: Plasma Kinetic Theory and Application in Solar Physics. Science Press, Beijing (2009)
125. Cohen, M.H.: Magnetoionic mode coupling at high frequencies. Astrophys. J. **131**, 664–680 (1960)
126. Melrose, D.B., Robinson, P.A.: Reversal of the sense of polarization in solar and steller flares. Proc. Astron. Soc. Aust. **11**, 16–20 (1994)
127. Preka-Papadema, P., Alissandrakis, C.E.: Spatial and spectral structure of a solar flaring loop at centimeter wavelengths. Astron. Astrophys. **191**, 365–373 (1988)
128. Alissandrakis, C.E., Nindos, A., Kundu, M.R.: Evidence for ordinary mode emission from microwave bursts. Solar Phys. **147**, 343–358 (1993)
129. Ledenev, V.G., Tirsky, V.V., Tomozov, V.M., Zlobec, P.: Polarization changes in solar radio emission caused by scattering from high-frequency plasma turbulence. Astron. Astrophys. **392**, 1089–1094 (2002)
130. Morgachev, A.S., Kuznetsov, S.A., Melnikov, V.F.: Radio diagnostics of the solar flaring loop parameters by the forward fitting method. Geomagn. Aeron. **54**, 933–942 (2014)
131. Morgachev, A.S., Kuznetsov, S.A., Melnikov, V.F., Simões, J.A.: Modeling the distribution of circular polarization degree of microwave emission along the flare loops in event 19 July 2012. Geomagn. Aeron. **55**, 1118–1123 (2015)
132. Melnikov, V.F., Pyatakov, N.P., Shibasaki, K.: constraints for electron acceleration models in solar flares from microwave observations with high spatial resolution. In: Sekii, T., Watanabe, T., Sakurai, T. (eds.) Hinode-3: The 3rd Hinode Science Meeting, Proceedings of the conference held 1–4 December 2009 at Hitotsubashi Memorial Hall, Tokyo, Japan. ASP Conference Series, vol. 454, pp. 321. Astronomical Society of the Pacific, San Franciso (2012)
133. Simões, P.J.A., Costa, J.E.R.: Gyrosynchrotron emission from anisotropic pitch-angle distribution of electrons in 3-D solar flare sources. Solar Phys. **266**, 109–121 (2010)
134. Battaglia, M., Kontar, E.P.: Electron distribution functions in solar flares from combined x-ray and extreme-ultraviolet observations. Astrophys. J. **779**, 107–116 (2013)
135. Melnikov, V.F., Gorbikov, S.P., Pyatakov, N.P.: Formation of anisotropic distributions of mildly relativistic electrons in flaring loops. In: IAU Symposium Proceedings of the International Astronomical Union Universal Heliophysical Processes, vol. 257, pp. 323–328 (2009)

Chapter 4
Theory of X-Ray Emissions in Solar Flaring Loops

X-rays are one of the important way to observe and study the solar flares which are able to radiate the emissions with a wide spectrum. Observationally, the soft and hard X-rays are dependent on the energy, the low and high bands respectively. Physically, the former is related with the thermal plasma, while the latter is produced by the NT electrons. Therefore, the solar flares show smoothed light curves of SXRs, but many spikes or sub-peaks with a short timescale (down to 10 milliseconds dependence on the time resolution of the instruments) are superposed on the HXR light curves. From the spatial topology, the solar flares usually display a loop system, and the SXRs are bright of the whole loop, while the HXRs exhibit an LT and double FP sources associated with it. The observations with a broad dynamic energy range and a high sensitivity provide the second coronal source, named the above-the-LT source during the solar flare. They are generally thought to be produced by the bidirectional NT electrons beams accelerated by the magnetic reconnection. The gradient distributions dependence on the energy band between the LT and above-the-LT sources indicated the existence of the current sheet there.

The question is how and where these thermal plasma which radiate the SXRs come from during solar flares? Much more observations suggest that these thermal plasmas are related with the NT electrons which produce the HXRs. For example, the time derivatives of the SXR light curves are positively correlated with the HXRs in the same event. Such relationship is called the Neupert effect. In this model, the bidirectional NT electron beams are accelerated by the magnetic reconnection above the LT. The upward beams propagate outer and produce the normal type *III* bursts on their way through the corona. Meanwhile, the downward beams move to the chromospheric layer where the plasma have a high density and a low temperature. These NT electrons would collide with the chromospheric plasma. The HXRs are radiated by the thick-target bremsstrahlung model around the two FPs of the loops. However, the bulk of the NT energies are lost to quickly thermalize and heat the local plasma. This results into the temperature and pressure of the chromospheric plasma increased rapidly, and further drives them to move along the flare loop upward into

G. Huang et al., *Solar Flare Loops: Observations and Interpretations*,
https://doi.org/10.1007/978-981-10-2869-4_4

the corona. This process is called as chromospheric evaporation. There are much more observational facts to support the evaporation process in the solar flares. The hot plasma would fill the whole loop and to radiate the SXRs. Therefore, the SXRs reach their peaks around the time of the HXRs tail. On the other hand, there is also other mechanism attribution to heat the thermal plasma, especially on the flare precursor. Observations with high spatial resolution show many bright and thermal structures appeared before the HXRs. It is possible that there are also NT electrons already accelerated, but hardly to be observed by the present instruments. Therefore, no evidences are found to prove whether the heating mechanisms are similar to the precursor and flare thermal plasma. But the NT electron heating is dominated during solar flares.

It is a general way to investigate the electron distribution and acceleration information from the study of the X-ray emissions. Based on the thermal bremsstrahlung mechanism, we get the Maxwellian distribution of the thermal plasma from the inversion of the SXR spectra, and the power-law distribution of the NT electrons from the inversion of the hard X-ray spectra through the thick-target bremsstrahlung mechanism. This power-low electrons are just a high-energy tail of Maxwellian distribution, like the Kappa distribution mentioned in the documents. These NT electrons would produce the double FPs and coronal source. One event can produce numerous NT beams with different electron numbers or spatial scales, which is thought to be the physical reasons that the HXR light curves display many spikes or sub-peaks with various time scales.

One interesting thing to be noted here is the microwave emissions with many properties similar as the HXRs during solar flares. For example, There are usually many spikes and sub-peaks on the MW light curves, and a good correlation is found between the MW and HXR emissions. The solar flares also display an LT and double FP sources, and a power-law spectra at the MW emissions. This is because the NT electrons to produce the MW emissions have the same origination as that of HXRs, but they are at different energy bands, from serval to tens keV for the HXR electrons and from hundreds keV to several MeV for the MW electrons based on the GS mechanism. In some case, their power-law indexes are different, which indicates some different physics in their acceleration mechanisms. Therefore, the correlation between the MW and HXR emissions is an interesting topic for the solar physics, and is also emphasized in this book.

4.1 Thick-Target and Thin-Target Models

4.1.1 Overview

Except for the microwave emissions through the GS mechanism in Sect. 2.2, the NT electrons accelerated during solar flares also can radiate the HXRs at the energy band from 10–100 keV through the bremsstrahlung collision with the chromospheric

plasma. From observations, there is no way to detect the NT electron distributions and other physical properties directly, but can indirectly get some from their HXR emissions. Solar flares generally show a single or double power-law spectra (the index from 3–8) [1–4] at the high-energy bands (above 20 keV) and connect with a Maxwellian distribution at the low-energy band. These NT electrons radiate the HXR emissions after they are completely thermalized though the collisions with the local plasma, which is called as thick-target model [5]. While they also produce the HXRs they propagate through the plasma layer, which is called thin-target model. Put simply, the latter indicates the NT electrons do not change their power-law distribution after the HXR emissions, while the former model suggests that the NT electron distributions are changed, for example, from the power-law to the Maxwellian distribution.

The HXRs of solar flares can be absorbed by the earth atmosphere. Therefore, the solar X-ray instruments are space-boarded, for example, SMM, CGRO, Hinotori, and Yohkoh. With its full disk solar imaging capability, wide energy coverage (3–17,000 keV), and high sensitivity, RHESSI [6] provides unprecedented capabilities for investigating X-ray emissions from solar flares at a wide energy band and with a high time resolution after the onset. Thus, RHESSI is an important telescope to study the X-rays at the present time.

4.1.2 Thin-Target Model

Both the thin-target and thick-target models are the bremsstrahlung mechanism, which provides a basic process of physics. In brief, bremsstrahlung process is an electron to radiate emissions through the collision between it and the Coulomb electric fields when it moves into them around a proton. We can get the radiation power and spectra from the electron-proton (e−p) plasma. Figure 4.1 shows the elastic scattering of a single electron (−e) off an ion with charge of +Ze. The electron moves with velocity v on a path with the impact parameter b, then it is deflected by an angle of 2θ. The electron and proton densities are n_e and n_p, respectively. The electron velocity is written into $v \propto \sqrt{kT/m}$ from the plasma temperature ($kT \sim mv^2$, k is

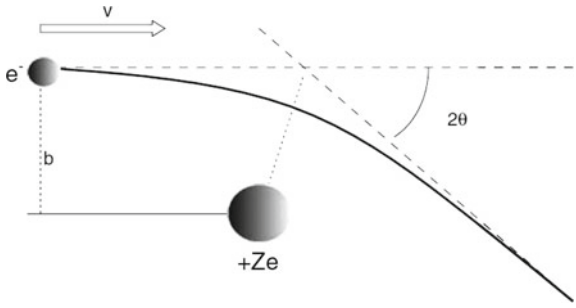

Fig. 4.1 The electron (−e) moves with velocity v on a path with impact parameter b to an ion (+Ze) and is deflected by an angle of 2θ. Electromagnetic radiation named the bremsstrahlung is emitted as a consequence of the acceleration of the particle during the swing-by around the ion

the Boltzmann constant). Thus, the collision time is same as the period (τ) that the electron passes through the ion field, i.e. $\tau \simeq \frac{b}{v}$. Based on the Larmor formula, when the acceleration (a) is assumed to be independent of the time, such as $a \simeq \frac{e^2}{mb^2}$, the radiation power ($P$) of this electron is

$$P = \frac{2e^2a^2}{3c^3} \simeq \frac{e^6}{m_e^2c^3b^4}. \tag{4.1.1}$$

The emissions of this electron have a typical frequency range (ω) with a relationship as $\omega \simeq \tau^{-1} = \frac{v}{b}$. In this case, the radiation power at the frequency ω is

$$P(\omega) \simeq \frac{P}{\omega} = \frac{e^6}{m_e^2c^3vb^3} = \frac{e^6n_p}{m_e^2c^3v}. \tag{4.1.2}$$

The impact parameter (b) is calculated from the proton density (n_p) in the e−p plasma, i.e. $b \simeq n_p^{-3}$. The electron radiance $j(\omega)$ at the frequency of ω is the total radiance from the all electrons, namely, the product of the electron density and the single electron radiance. When the electron is assumed to produce radiation isotropically (divided 4π in this formula), the radiance per unit solid angle is

$$j(\omega) = n_e \times P(\omega)/4\pi \simeq \frac{n_en_p}{4\pi}\frac{e^6}{m_e^2c^3}\left(\frac{m_e}{kT}\right)^{1/2}, \tag{4.1.3}$$

where the radiance $j(\omega)$ depends on the radiation frequency. The total radiance from this electrons is the integration ($j(\omega)$) on all the frequency range, i.e. from 0 to ω_{max}. An interesting question is how to detect the typical frequency with the maximum radiance? According to the fact, the electron can not radiate an energy above its thermal energy, such as $h\omega_{max} = kT$ to calculate the maximum frequency (ω_{max}). In this case, the total radiance from this electron is

$$\begin{aligned} j &= \int_0^{\omega_{max}} j(\omega)d\omega \sim \frac{n_en_p}{4\pi}\frac{e^6}{m_e^2c^3}\left(\frac{m_e}{kT}\right)^{1/2}\frac{kT}{h} \\ &= \frac{n_en_pe^6}{4\pi m_e^2c^3}\frac{(m_ekT)^{1/2}}{h}. \end{aligned} \tag{4.1.4}$$

From the accurate calculation, the electrons with the energy above KT also attribute the emissions below ω_{max}. These electrons are nonthermal, and have a power-law spectra on the tail of the thermal Maxwellian distribution. From the observations, these electrons can radiate the X-ray emissions, especially for the hard X-rays at the energy from 10–300 keV.

Elastic scattering of a single electron (−e) off a proton (+e) or an ion (+Ze) is quantified by the differential scattering cross section ($\frac{d\sigma}{d\Omega}$) using the Rutherford formula (1911), such as

$$\frac{d\sigma}{d\Omega} = \frac{Z^2}{4}\left(\frac{e^2}{mv^2}\right)^2 \frac{1}{sin^4(\theta/2)}. \tag{4.1.5}$$

It is the probability of scattering of a single electron off a proton or an ion with the impact parameter from b to $b + db$ into the solid angle $d\Omega = 2\pi sin\theta d\theta$. The total cross section is the integration of the solid angle, i.e. $\sigma = \int(\frac{d\sigma}{d\Omega})d\Omega$ with a units of cm^2keV^{-1}. The cross section is the Bethe-Heitle formula for solar flares, especially that to radiate the X-rays at the energy of E_0, such as

$$\sigma(E_0, E) = \frac{16\pi e^6}{3hm_e c^3}\frac{1}{E_0 E} ln \frac{1 + (1 - E_0/E)^{1/2}}{1 - (1 - E_0/E)^{1/2}}$$

$$= \frac{7.9 \times 10^{-25}}{E_0 E} \ln \frac{1 + (1 - E_0/E)^{1/2}}{1 - (1 - E_0/E)^{1/2}} \ (cm^2 \cdot keV^{-1}), \tag{4.1.6}$$

where h, c, m_e, and e are Planck constant, light speed, single electron mass and charge, respectively. The HXR emissions in solar flares are directly proportional to the densities of the injected electrons (n_e(E)) and the protons (n_p) in the whole source region, for example, $\int n_e(E) n_p dV$, where V is the volume of the source region. The volume has a value of $\sigma(E, E_0)v(E)$ (the product between the cross section $\sigma(E, E_0)$ and the electron speed $v(E)$). The hard X-ray emissions at the energy of E_0 are radiated from the all electrons with the energy above E_0. Therefore, the hard X-ray photons per unit time and unit energy are computed with this formula

$$\frac{dN_{phot}}{dtdE} = \int_{E_0}^{\infty} \sigma(E, E_0)v(E)\left(\int n_p n_e(E)dV\right)dE \ (s^{-1}keV^{-1}). \tag{4.1.7}$$

Then, the source region is assumed with an uniform density, such as $n_p =$ constant, thus $\int n_p dV = n_0$, where n_0 is all the protons in the source region. When the HXR emissions are isotropic on the Sun, the measurements on the Earth are only $\frac{1}{4\pi r^2}$ of the total emissions. The HXR intensity detected on the Earth is

$$I(E) = \frac{1}{4\pi r^2}\frac{dN_{phot}}{dtdE} = \frac{n_0}{4\pi r^2}\int_{E_0}^{\infty} \sigma(E, E_0)v(E)n_e(E)dE. \tag{4.1.8}$$

$I(E)$ has a unit of the photon number per unit time, unit energy, and unit detector area. The density (n_e) and the speed ($v(E)$) are the parameters of NT electrons which radiate the HXR intensity ($I(E)$). Therefore, the product of $n_e v(E) = N_e$ is the total electron number to radiate the HXRs in the unit time. The total electrons number is calculated using the formula

$$N_e = \int_{E_{min}}^{E_\infty} f_{source}(E)dE, \tag{4.1.9}$$

when the NT electrons have a distribution as f_{source}(E), where E_{min} and E_{∞} are respectively the minimum and maximum energy values of the electrons. Generally, there are two possibilities of the electron distribution functions, such as Maxwellian or power-law distributions. They correspond to the thermal bremsstrahlung and thin- or thick-target models in the documents. For both distributions, there is a low-energy limit or cutoff, $E_{min} = E_{cutoff}$. But we can not detect the high-energy limit from the observations, and it is up to infinity in Eq. (4.1.8), $E_{max} = \infty$. The reason is the electron number decreasing with the energy, and the electrons with very high energy have small numbers and few contributions to the HXR radiations, whatever Maxwellian or power-law or Kappa distributions. Combined Eq. (4.1.8) with Eq. (4.1.9), the HXR intensity is shown with the electron distributions as follows

$$I(E) = \frac{n_0}{4\pi r^2} \int_{E_0}^{\infty} \sigma(E, E_0) f_{source}(E) dE. \tag{4.1.10}$$

This is general formula of the hard X-ray intensity at the energy of E_0 radiated by the electrons with a distribution of $f_{source}(E)$. Both the thin- and thick-target model are uniform with Eq. (4.1.10). According to the thin-target model, the electrons to radiate the HXRs have the same distribution function as the injection electrons, i.e. $f_{source}(E) = f_{injection}(E)$. Therefore, based on the thin-target model, the HXR intensity is

$$I(E_0) = \frac{n_0}{4\pi r^2} \int_{E_0}^{\infty} \sigma(E, E_0) f_{injection}(E) dE, \tag{4.1.11}$$

which describes the relationship between the observational HXR intensity I(E) and the injection electron spectral distribution $f_{injection}(E)$.

4.1.3 Thick-Target Model

As mentioned before, the electron spectra of the radiation source ($f_{source}(E)$) are changed and different from that $f_{injection}(E)$ injected initially in the solar flares. The injected electrons downward are strongly collided by the dense and cool plasma in chromosphere, and they are thermalized and lose the energy to heat the local plasma. In this case, Eq. (4.1.11) does not works, and the thick-target model is needed. From the observation, there is no way to detect the spectral distributions ($f_{source}(E)$) of these electrons which radiate the HXRs. Therefore, the injected electron spectrum is still used, but the cross section is revised in the thick-target model. As noted earlier, the injected electrons would lose their energies though the collisions with the chromospheric plasma during the solar flares. According to the conservation of momentum, the energy loss rate of the electrons is

$$\frac{dE}{dt} = -\frac{2\pi e^4 ln\Lambda}{E} n_p v = -\frac{C}{E} n_p v, \tag{4.1.12}$$

during the e−p collisions, where $C = 2\pi e^4 \ln \Lambda$, ln Λ and n_p are respectively Coulomb logarithm and proton density in the source region. Considering a single electron injection the source region, from the time t_1 (corresponding to the energy of E_0) to t_2 (corresponding to the energy of E), the HXR photons ($m(E_0,\ E)$) are related to the proton numbers which are collided by this electron, i.e. the production between the proton density and the volume on the electron path, $\sigma(E_0, E(t))v(t_2 - t_1)$. Thus the hard X-ray photons are calculated by

$$m(E_0, E) = \int_{t_1}^{t_2} n_p \sigma(E_0, E) v dt. \tag{4.1.13}$$

To do the integral transformation as $\int_{E_0}^{E} E_x dE_x = -C \int_{t_1}^{t_2} n_p v dt$ in Eq. (4.1.13), one can get

$$m(E_0, E) = \int_{E_0}^{E} \frac{E_x \sigma(E_0, E)}{C} dE_x. \tag{4.1.14}$$

Equation (4.1.14) gives the hard X-ray intensity radiated by a single electron collided by the chromospheric plasma. If there are many electrons with a distribution of $f_{injection}(E)$ injected into the flare region, the HXR photons above the energy of E_0 ($I(E_0)$) are radiated by the electrons with the energy above E_0. Namely, based on the thick-target model, the hard X-ray intensity is

$$\begin{aligned} I(E_0) &= \frac{1}{4\pi r^2} \int_{E_0}^{\infty} f(E) m(E_0, E) dE \\ &= \int_{E_0}^{\infty} f(E) \left[\int_{E_0}^{E} \sigma(E_0, E_x) \frac{E_x}{C} dE_x \right] dE. \end{aligned} \tag{4.1.15}$$

Combination the cross section in Eq. (4.1.6) and the HXR intensity Eq. (4.1.15), the hard X-ray photon spectra are able to be computed from the injection electrons with a distribution of $f_{injection}(E)$. According to Eq. (4.1.15), we can get the photon spectra from the injected electrons. Meanwhile, we can invert the electron distribution from the observations of the HXR spectra. There are many observations of HXR spectra in the solar flares detected by RHESSI. However, it is hard to use Eqs. (4.1.7) and (4.1.15) to invert the electron spectral distributions. The reason is both formulas are complicated. In solar physics, the general way is to try to fit the photon spectra using the various distributions of the injected electrons. The parameters of the injected electrons are detected from the best fitting. This method is widely used for the observations, such as RHESSI. Figure 4.2 shows a spectral fitting example of the X-ray photons at the energy band between 3 and 300 keV, where includes the Maxwellian distribution at the low-energy band and the power-law distribution at the high-energy band. Thus, the thermal parameter of temperature and emission measure are also detected as well as the NT parameters of power-law index, break energy, and lower energy cutoff.

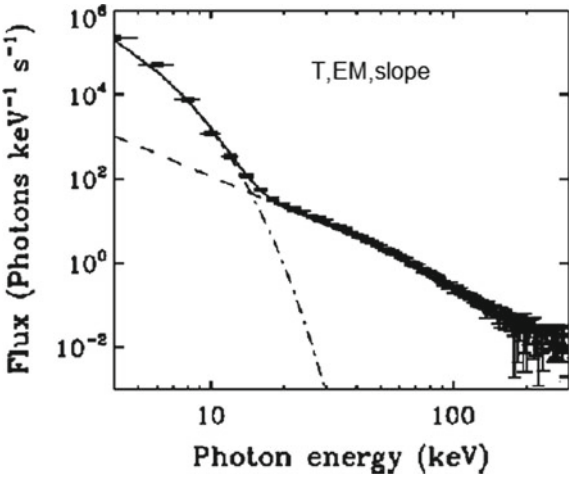

Fig. 4.2 RHESSI spectra fitting. Dots with error bars represent the observational spectral data. Different lines show model spectral fits for thermal component (dot-dashed lines), NT power-law component (dashed lines), and a summation of the two (thick-solid lines) [7]

Much more observations have been found that the HXR photons show the power-law spectra, sometimes, the broken power-law in solar flares. These observational facts suggest that the electrons have a power-law distribution as well, for example, $f_{injection}(E_0) = AE_0^{-\delta}$. Considering this power-law distribution and combination Eqs. (4.1.6), (4.1.7), and (4.1.15), the HXR intensities are

$$I_{thin}(E_0) = \frac{7.9^2 \cdot 5n_0 A}{4\pi r^2 E_0} \int_{E_0}^{\infty} E^{-(\delta+1)} \ln \frac{1+(1-E_0/E)^{1/2}}{1-(1-E_0/E)^{1/2}} dE \ , \qquad (4.1.16)$$

$$I_{thick}(E_0) = \frac{7.9^2 \cdot 5A}{4\pi r^2 E_0} \int_{E_0}^{\infty} E^{-\delta} \int_{E_0}^{E} \ln \frac{1+(1-E_0/E)^{1/2}}{1-(1-E_0/E)^{1/2}} dE_x dE \ , \qquad (4.1.17)$$

for the thin- and thick-target model, respectively. After the computation, we can get the HXR spectra of $I(E_0) = AE_0^{-\gamma}$, where the constant A and the spectral index γ are different for the thin- and thick-target models, such simple forms as $\gamma_{thin} = \delta + 1$, $\gamma_{thick} = \delta - 1$, here δ is the power-law index of injection electrons. Thus, the HXRs have the spectral indexes of $\delta + 1$ and $\delta - 1$ from the thin- and thick-target models, respectively, for the same injection electrons with the spectral index δ. Observationally, the NT electrons are accelerated by the magnetic reconnection above the LT (i.e., coronal source), and these electrons would penetrate into the flare loop from the top. There are one LT (or a coronal source) and double FP HXR sources. The former is thought to be produced by the thin-target model, while the latter is the thick-target model. According to the theoretic expert, the difference between the spectral indexes of the LT (coronal) source and that of FPs cold be around 2. Figure 4.3 gives the differences in spectra index between the coronal source and two FPs of five solar flares, and they range from −1–6 with an average value less than 2. This fact indicates that the coronal source is not able to be explained simply by a thin-target model.

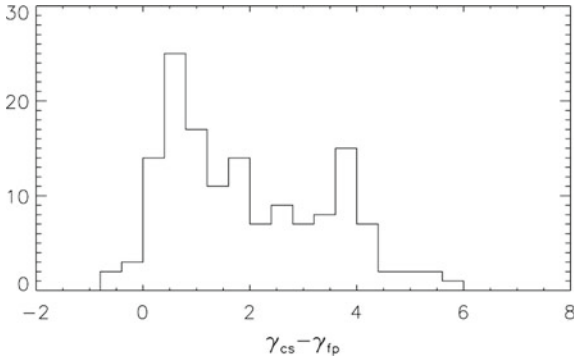

Fig. 4.3 Distributions of the differences in spectral index between the coronal source (γ_{cs}) and two foot-points (γ_{fp}) of five events at all time bins [8]

4.1.4 Relation of Two Models

In the solar physics, the thin- and thick-target models are relative concepts, especially to be comparative to the chromospheric plasma. In short, if the injected electrons (with the energy of E) are collided and completely stopped by the chromospheric plasma, whatever the plasma temperature and density, the HXR emissions are followed by the thick-target model. For example, the LT and coronal sources are usually observed at the HXRs in the energy band of 10−20 keV, which is determined by the plasma density around the LT. If the injected electrons had a spectral energy band less than 20 keV, the HXRs could be radiated by the thick-target model. In this case, the thick-target model could be more accurate than the thin-target model. However, there is no way to prove this from the observations. Theoretically, the NT electrons with an energy of E_0 could be collided and stopped by the plasma which should have a column density as

$$N_{stop} = \frac{\mu_0}{3C} E_0^2 \simeq 10^{17} E_0^2 [\text{keV}] \ (\text{cm}^{-2}), \tag{4.1.18}$$

where the constant C is same as one in Eq. (4.1.12), μ_0 is the cosine value of the initial angle, i.e. $\mu_0 = \frac{v_\perp}{v}$, and $v_\perp$ is the perpendicular (magnetic field) component of the electron velocity. According to the formula (4.1.17), when the solar plasma (column) density is stratification, the HXR sources exhibit the spatial distributions like this topology, the lower energy and the closer LT, the higher energy and the closer FPs, and the middle energy sources located in between. If the solar plasma density would be an ideal stratification, it is possible to observe the HXR sources with a distribution as shown in Fig. A.7 of Appendix A.

However, the plasma density has a large gradient closer to the solar surface. Observationally, most of the solar flares exhibit an LT at the low energy (i.e. 10–20 keV), and double FPs at the high energy (above 50 keV), but the middle energy sources (at 30 keV) are not located at the legs, but closer to the FPs. It is difficult to distinguish the source positions of the middle energy from that of the high energy

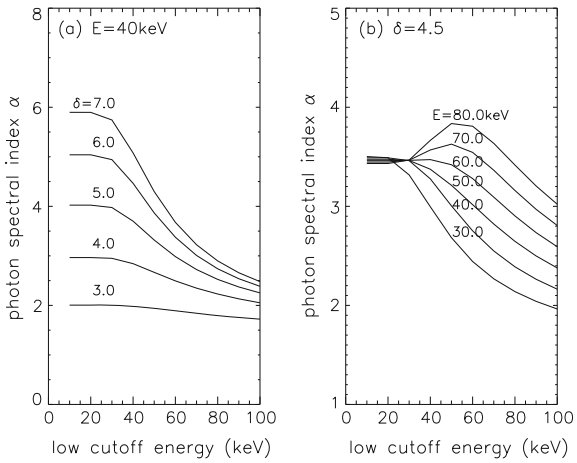

Fig. 4.4 The variations of α (photon spectral index) versus the low-energy cutoff under the standard thick-target model for *a*. different values of δ (electron spectral index) and a given photon's energy, and *b*. different photon's energies and a given δ

for the disk event. The solar plasma density would be an ideal stratification after the chromospheric evaporation. In this case, it is possible to observe a uniform distribution of HXR source along the flare loop (Fig. A.8 of Appendix A).

Figure A.8 shows the X-ray source distribution during the Oct 30, 2004 flare detected by RHESSI, which is the evidence of the chromospheric evaporation seen at the HXRs and consistent with the ultraviolet spectral observations [11].

4.1.5 Effect of Low-Energy Cutoff on Spectral Indices of Electrons and Photons

The thick-target model is commonly used for studying the low-energy cutoff, and the emitted photons at different energies have been calculated under different single power-law indices of NT electrons, and afterward the photon power-law indices have been obtained by linearly fitting. It should be noticed that in the standard thick-target model Eq. (4.1.17) or thin-target model Eq. (4.1.16) can be integrated to get an analytical result of the photons at a given energy only when the lower limit (i.e. the low-energy cutoff) is smaller than the photon's energy, and further to obtain a simple relation between the photon power-law index α and electron power-law index δ, i.e., $\alpha = \delta$-1 (thick-target) or $\alpha = \delta$+1 (thin-target).

On the other hand, when the low-energy cutoff increases to exceed the photo's energy, the integration in Eq. (4.1.16) or (4.1.17) should be separated into two energy intervals, and numerical results show that there is an obvious effect of the low-energy cutoff on the relation between α and δ. For example [12], Fig. 4.4 gives the curves of α versus the low-energy cutoff varied with *a*) different values of δ and a given photon's energy, and *b*) different photon's energies and a given δ under the standard thick-target model Eq. (4.1.17).

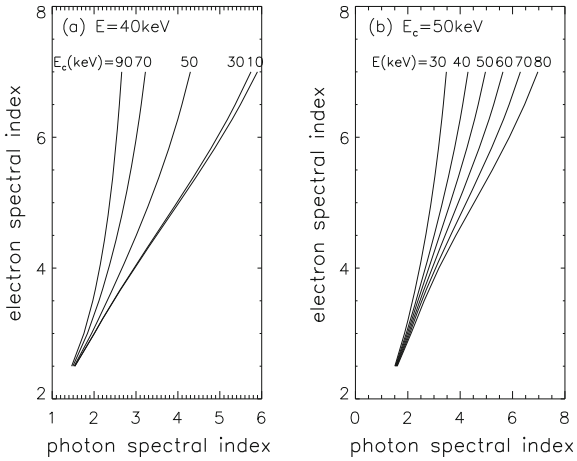

Fig. 4.5 The relations between α (photon spectral index) and δ (electron spectral index) under the standard thick-target model for **a**. different low-energy cutoffs and a given photon's energy, and **b**. different photon's energies and a given low-energy cutoff

It is found from Fig. 4.4a that when the low-energy cutoff is smaller than 20 keV the relation between α and δ is basically consistent with the prediction of the standard thick-target model ($\alpha = \delta$–1), while with increasing of low-energy cutoff, α gradually becomes smaller or harder than the prediction of the standard thick-target model, and this deviation becomes more evident gradually for a larger or softer δ. Moreover, this deviation also varies with the photon's energy as shown by Fig. 4.4b, when the photon's energy is smaller than 60 keV, α monotonously becomes smaller (harder) than the prediction of the standard thick-target model, while, when the photon's energy is larger than 60 keV, α first becomes larger (softer) then smaller (harder) than the prediction of the standard thick-target model.

Furthermore, Fig. 4.5 shows the relations between α and δ with a. different low-energy cutoffs and a given photon's energy, and b. different photon's energies and a given low-energy cutoff under the standard thick-target model Eq. (4.1.17).

It is evident in Fig. 4.5a that when the low-energy cutoff is smaller ($10 \sim 30$ keV), the relation between α and δ basically satisfies the common one ($\alpha = \delta$–1) predicted by the standard thick-target model, but it is deviated from the standard thick-target model when the low-energy cutoff is larger than 30 keV, and this deviation becomes larger for a larger (softer) α. Moreover, it can be seen from Fig. 4.5b that for a given low-energy cutoff 50 keV, the deviation from the standard thick-target model is the smallest when the photon's energy equals 70 keV, with increasing and decreasing of photon's energy, α tends to be larger (softer) and smaller (harder) respectively in comparison with the prediction of standard model.

Finally, the variation of low-energy cutoff will cause the relation between α and δ to be deviated from predicted one by the standard model, and the deviated extension strongly depends on photon's energy and α itself, so that the low-energy cutoff is a very sensitive parameter for HXR studies.

4.2 Propagation of Electrons and Its Effect on X-Ray Emission

4.2.1 Overview

It is well known that the magnetic energy release occurs in coronal loops rooted in photospheric magnetic field and 10^{3-5} km above AR, and can be observed by optical, radio, EUV, and X-ray telescopes, which is naturally explained by the full-band radiations of thermal and NT electrons confined by the extended photospheric magnetic field lines. The observed loop-like structures in different bands can be considered as the coincident magnetic configuration in corona, and thus to construct various flare models. For instance, a typical flare model is caused by the magnetic reconnection between opposite magnetic field lines above the top of single magnetic loop, and the charged particles accelerated (heated) by the electric fields and shocks in reconnection site inject into the magnetic loop, and collide with high-density photosphere, to produce chromosphere evaporation, and thus the total loop is filled by high-temperature plasma, i.e., the observed coronal loops with different temperatures at different bands.

Based on the flare model as mentioned above, the magnetic field strength in LT of a single loop should be weaker than that in FPs, to construct a typical magnetic mirror to divide the injected electrons into two parts, a part of electrons with a larger speed parallel to the magnetic field will escape from the confinement of magnetic mirror, and collide with high-density photosphere, to excite NT bremsstrahlung in X-ray band, while another part of electrons with a smaller speed parallel to the magnetic field will be trapped in the loop, and reflected back and forth to emit bremsstrahlung and GS emissions in MW band. This physical process is called mirroring effect to be described theoretically as in below.

4.2.2 Magnetic Mirror and Loss-Cone Distribution

When $\mathbf{q}$ and $\mathbf{p}$ are a pair of canonical variables in a periodic mechanical system, we can define an adiabatic invariant as an integration during a period of the system:

$$J = \oint \mathbf{p} \cdot d\mathbf{q}, \tag{4.2.1}$$

which means that the parameter J varies slowly and conservatively, and called as the magnetic moment of charged particles moving in magnetic mirror. For a single particle with the perpendicular speed of $v_\perp$, and cyclotron radius of $\rho_B = v_\perp/\Omega$, here, Ω is the gyro-frequency, we can integrate Eq. (4.2.1) and obtain

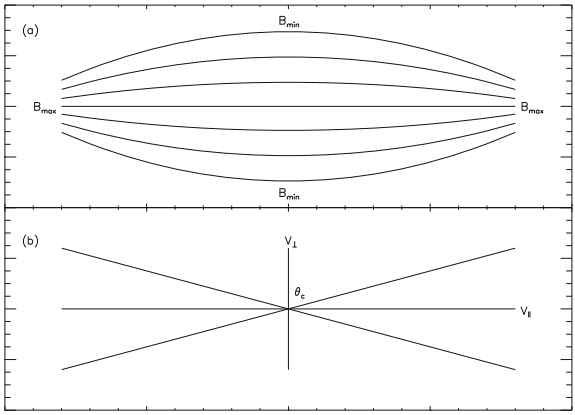

Fig. 4.6 The diagrams of **a**. magnetic mirror, and **b**. loss-cone distribution

$$J_\perp = \oint m v_\perp \rho_B d\phi$$

$$= \frac{4\pi m}{q}\mu_m, \tag{4.2.2}$$

$$\mu_m = \frac{m v_\perp^2/2}{B}, \tag{4.2.3}$$

and μ_m is defined as the magnetic moment invariant, i.e., the ratio between the perpendicular kinetic energy and magnetic field, m and q are respectively the mass and electric quantity of the particle. Figure 4.6a is a diagram of magnetic mirror, when a particle moves from the top to the two ends, the perpendicular energy will increase with increase of magnetic field due to the magnetic moment invariant, once the parallel speed decreases to zero before the particle reaches one end, it will return to another end, thus reflects back and forth, i.e., the particle is trapped by magnetic mirror, otherwise, the particle will escape from magnetic mirror.

The magnetic field strengths in the top and ends of magnetic mirror are respectively written to B_{min} and B_{max}, while the parallel and perpendicular speeds of a particle on the top of magnetic mirror are respectively written to $v_\parallel$ and $v_\perp$, and the total speed is v, if the parallel speed just equals to zero when the particle reaches the ends, according to the magnetic moment invariant and energy conservation, the perpendicular energy equals to the total energy or parallel energy equals zero at this time, thus a critical angle is defined as:

$$\sin\theta_c = \left(\frac{B_{min}}{B_{max}}\right)^{1/2}, \tag{4.2.4}$$

Regarding the symmetry of cyclotron motion around the magnetic field lines, we can reduce 3D velocity space ($v_\perp$, $v_\parallel$, ϕ) to 2D ($v_\perp$, $v_\parallel$) Fig. 4.8b shows that the trapping and escaping particles can be distinguished by the critical angle θ_c, all the

particles below θ_c have a larger parallel speed enough to escape from the magnetic mirror, while all the particles above θ_c will be trapped by the magnetic mirror. Though the distribution of escaped particles in Fig. 4.6b has a conic shape, we commonly call the trapped particle distribution as loss-cone. The initial distribution is assumed to be thermally equivalent (Maxwellian), after the escaped particles leave the magnetic mirror, the trapped particles are somehow deviated from Maxwellian, or have a free energy to excite plasma instabilities like ECM. In addition, the parallel speed $v_\parallel$ has two opposite directions, while perpendicular speed $v_\perp$ is always positive, so the distribution in Fig. 4.6b is meaningful only in the top half plane.

There are various forms of trapping particle distribution, one is [14]:

$$f = \begin{cases} A \exp\left(\frac{v^2}{2kT/m}\right) & \text{if} \alpha \geq \theta_c \\ 0 & \text{if} \alpha \leq \theta_c \end{cases} \tag{4.2.5}$$

which simply supposes that the initial distribution is Maxwellian with the normalized constant A. Another form is called the translated loss-cone[15]:

$$F_s(u_\perp, u_\parallel) = \frac{(2\pi)^{-3/2}}{\beta_{\perp 1}^2 - q\beta_{\perp 2}^2} \exp\left[-\frac{(u_\parallel - u_{0\parallel})^2}{2\beta_\parallel^2}\right] \times$$

$$\times \left[\exp\left(-\frac{u_\perp^2}{2\beta_{\perp 1}^2}\right) - \exp\left(-\frac{(u_\perp^2}{2\beta_{\perp 2}^2}\right)\right], \tag{4.2.6}$$

here, q is a parameter to determine the ratio of trapped particles, and β implies the thermally broadening in the velocity space (parallel and perpendicular).

4.2.3 Formation of Loss-Cone Distribution

4.2.3.1 Equation and Boundary Condition

The formation of loss-cone distribution has been discussed in fusion plasmas [13], with the Fokker–Planck equation as below [16]:

$$\frac{\partial f}{\partial t} + \mathbf{v} \cdot \nabla_{\mathbf{r}} f + \frac{\mathbf{F}}{m} \cdot \nabla_{\mathbf{v}} f + \nabla_{\mathbf{v}} \cdot \mathbf{J} = q(\mathbf{r}, \mathbf{v}), \tag{4.2.7}$$

$$J_i = A_i f - \sum_j D_{ij} \frac{\partial f}{\partial v_j}, \tag{4.2.8}$$

$$A_i = \langle \Delta v_i \rangle_t - \frac{1}{2} \sum_j \frac{\partial}{\partial v_j} \langle \Delta v_i \Delta v_j \rangle_t, \tag{4.2.9}$$

$$D_{ij} = \frac{1}{2}\langle \Delta v_i \Delta v_j \rangle_t. \tag{4.2.10}$$

The fourth term in left side of Eq. (4.2.7) is the divergence of stream function J, which is composed of the dynamic friction coefficient A_i in Eq. (4.2.9) and the diffusion tensor D_{ij} in Eq. (4.2.10). It is noticed that a source function q is added to the right side of Eq. (4.2.7) to compensate the particles escaped from the magnetic mirror, thus to ensure a stable solution existed in Eq. (4.2.7), and it is naturally expressed by the injection of accelerated electrons from the reconnection site into the flaring loops. Hence, the lifetime of the stable solution should be shorter than the time scale of particle acceleration, and we first take $\frac{\partial f}{\partial t} = 0$. Afterwards, a series of approximations are taken into consideration reasonably for Eq. (4.2.7): a uniform plasma ($\mathbf{v} \cdot \nabla_{\mathbf{r}} f = 0$), the electric field in Lorenz force and collision between electrons and ions are negligible, and the distribution function in the spherical coordinates is independent from the phase angle ϕ, so that $\frac{\mathbf{F}}{m} \cdot \nabla_{\mathbf{v}} f = 0$, and Eq. (4.2.7) is further simplified to:

$$v\frac{\partial}{\partial \theta}(\sin\theta J_\theta) + \sin\theta \frac{\partial}{\partial v}(v^2 J_v) = qv^2 \sin\theta, \tag{4.2.11}$$

or

$$D_\perp \frac{\partial}{\partial \theta}\left(\sin\theta \frac{\partial f}{\partial \theta}\right) + \sin\theta \frac{\partial}{\partial v}\left[v^2\left(D_\parallel \frac{\partial f}{\partial v} - Af\right)\right] = \\ = -qv^2 \sin\theta, \tag{4.2.12}$$

here, the parallel and perpendicular components of diffusion tensor have been derived under the Maxwellian distribution of ambient plasma [17], while the accelerated particles posses a power-law distribution, and we can write the solution of Eq. (4.2.12) to:

$$f = \Theta(\theta) V(v), \tag{4.2.13}$$

$$V(v) = \left(\frac{E}{E_0}\right)^{-\delta}, \tag{4.2.14}$$

here, the dimensionless kinetic energy $E = \frac{mv^2}{2}$ is divided by the thermal energy $E_0 = kT$, k is Boltzman constant, and Θ is an arbitrary function of pitch-angle θ. It is ready to prove $\left(\frac{mv}{kT} D_\parallel + A\right) f = 0$ under the Maxwellian distribution of ambient plasma [16, 17], and with the approximation of $\frac{E}{\delta kT} \approx 1$ (an underestimated E), Eq. (4.2.12) can be finally simplified to:

$$D_\perp \frac{\partial}{\partial \theta}\left(\sin\theta \frac{\partial f}{\partial \theta}\right) = -qv^2 \sin\theta. \tag{4.2.15}$$

We can write the source function to a form of $q(v, \theta) = q_0(v)\phi(\theta)$, here ϕ is an arbitrary function of pitch-angle θ, and the solution of Eq. (4.2.15) is integrated:

$$f = C\left(\frac{E}{E_0}\right)^{-\delta}\int_{\theta_c}^{\theta}\frac{d\theta'}{\sin\theta'}\int_{\theta'}^{\pi/2}\phi(\theta")\sin\theta"d\theta". \tag{4.2.16}$$

In addition, the boundary conditions for the trapping and escaping components are respectively written to:

$$\begin{cases} f = 0 & \text{when } \theta = \theta_c, \\ \frac{\partial f}{\partial \theta} = 0 & \text{when } \theta = \pi/2., \end{cases} \tag{4.2.17}$$

$$\begin{cases} f = 0 & \text{when } \theta = \theta_c, \\ \frac{\partial f}{\partial \theta} = 0 & \text{when } \theta = 0, , \end{cases} \tag{4.2.18}$$

here, the critical angle θ_c is defined by Eq. (4.2.4). Equation (4.2.17) means that the number of trapped particles starts from zero when $\theta = \theta_c$, then increases with increasing of θ, and reaches the maximum when $\theta = \pi/2$. Equation (4.2.18) implies that the number of escaped particles is maximum when $\theta = 0$, then decreases with increasing of θ, and finally equals zero when $\theta = \theta_c$.

4.2.3.2 Isotropically Injected Source

When the source function is independent from the pitch-angle, i.e., $\phi(\theta) = 1$ in Eq. (4.2.13), it is ready to integrate Eq. (4.2.16) to obtain the distributions of trapped and escaped particles under the boundary conditions Eqs. (4.2.17) and (4.2.18), respectively:

$$f_1 = C\left(\frac{E}{E_0}\right)^{-\delta}\ln\left(\frac{\sin\theta}{\sin\theta_c}\right), \tag{4.2.19}$$

$$f_2 = C\left(\frac{E}{E_0}\right)^{-\delta}\ln\left(\frac{\sin\theta_c}{\sin\theta}\right), \tag{4.2.20}$$

here, the normalized constant C can be derived from $\int f d\mathbf{v} = n$ (n the particle density):

$$C = \frac{n}{\left(2\pi\frac{T}{m}\right)^{3/2}\left(\ln^{-1}\left(\tan\frac{\theta_c}{2}\right) - \cos\theta_c\right)}. \tag{4.2.21}$$

Finally, the expression of source function is derived from Eq. (4.2.16):

$$q = \frac{CD_{\perp}}{v^2}\left(\frac{E}{E_0}\right)^{-\delta}. \tag{4.2.22}$$

Therefore, the source function is not freely chosen but actually determined by the power-law velocity distribution of trapped and escaped particles, while, the pitch-angle distribution of trapped and escaped particles is mainly determined by their boundary conditions.

4.2.3.3 Injection at an Arbitrary Angle

According to the observations of solar flares, the pitch-angle distribution of particle injected into flaring loops is very narrow [18], so we consider the particle injection at a given angle θ_0 as a δ function:

$$q(v,\theta) = q_0(v)\phi(\theta),$$

$$= \frac{CD_{\perp}}{v^2}\left(\frac{E}{E_0}\right)^{-\delta}\cos\theta_c\delta(\theta-\theta_0), \tag{4.2.23}$$

here, the pitch-angle distribution $\phi(\theta) = \cos\theta_c\delta(\theta-\theta_0)$ should satisfy the normalized condition as below:

$$\int_{\theta_c}^{\pi/2}\phi(\theta)\sin\theta d\theta = \cos\theta_c, \tag{4.2.24}$$

thus when $\phi(\theta) = 1$, it can be reduced to the case of isotropic injection. Similarly, we can integrate Eq. (4.2.16) to obtain the solutions of trapped and escaped particles, respectively from the boundary conditions in Eqs. (4.2.17) and (4.2.18):

$$f_1 = C\sin\theta_0\cos\theta_c\left(\frac{E}{E_0}\right)^{-\delta}\ln\left[\frac{\tan(\theta/2)}{\tan(\theta_c/2)}\right], \tag{4.2.25}$$

$$f_2 = C\cos\theta_0\sin\theta_c\left(\frac{E}{E_0}\right)^{-\delta}\ln\left[\frac{\tan(\theta_c/2)}{\tan(\theta/2)}\right], \tag{4.2.26}$$

$$C = \frac{n}{\left(2\pi\frac{T}{m}\right)^{3/2}\ln\left(\frac{1}{\sin\theta_c}\right)}. \tag{4.2.27}$$

When $\theta_0 = \pi/2$, the solution of trapped particles in Eq. (4.2.25) can be reduced to the result under the Maxwellian distribution [13]. It can be seen from Eqs. (4.2.25) and (4.2.26) that the numbers of trapped and escaped particles are jointly determined by two independent parameters, i.e., the initial pitch-angle θ_0 and mirroring critical angle θ_c. It is well known that trapped particles increase with decreasing of θ_c or with increasing of mirror ratio B_{max}/B_{min}, while escaped particles decrease with decreasing of θ_c or with increasing of B_{max}/B_{min}. It also should be noticed that

trapped particles increase with increasing of θ_0, while escaped particles decrease with increasing of θ_0.

It is also noticed that even $\theta_0 < \theta_c$, which does not mean that all particles will be escaped, there are still a part of trapped particles due to the scattering effect, while even $\theta_0 > \theta_c$, which does not imply that all particles will be trapped, there are still a part of escaped particles due to the same scattering effect, i.e., so called "secondary escaped particles".

4.2.3.4 Injected Depth of Trapped Particles

HXR and MW emissions in flaring loops are contributed to the escaping (precipitating) and trapping electrons in a magnetic mirror, respectively. There are different injected depths or reflected points of trapping electrons in different magnetic mirrors, which can be determined by the magnetic moment invariant and distribution of trapped particles as mentioned above, as well as a scaling law of coronal magnetic field. For a given initial energy E_i and θ_0, and the magnetic fields in the top of magnetic loop and reflected point are respectively assumed to be B_t and B_r, thus we have:

$$\frac{E_{\perp t}}{E_{\perp r}} = \frac{B_t}{B_r}, \tag{4.2.28}$$

here, $E_{\perp t} = E_i \sin\theta_0$ and $E_{\perp r}$ are the perpendicular energy of trapped particles in the LT and reflected point, respectively. From the conservation of magnetic moment:

$$\frac{E_{\perp t}}{E_{\perp r} - E_{\perp t}} = \frac{B_t}{B_r - B_t}. \tag{4.2.29}$$

From the energy conservation, $E_{\perp r} - E_{\perp t} = E_{\parallel} = E_i \cos\theta_0$, which means that the injected depth depends on the initial parallel energy of trapped particles. Furthermore, we can write the radial distribution of coronal magnetic field in a dipolar configuration [19]:

$$B(h) = B_p \times \frac{d^3}{(d+h)^3}, \tag{4.2.30}$$

here, B_p is the strength of dipolar magnetic loop rooted in photosphere, d represents the distance of dipolar magnetic field from photosphere to the LT, and h implies a given height inside the loop, from Eqs. (4.2.29) and (4.2.30) we have:

$$1 + \frac{\cos\theta_0}{\sin\theta_0} = \left(\frac{d+h_t}{d+h_r}\right)^3, \tag{4.2.31}$$

here, h_t and h_r are respectively the distance of LT and reflected point from photosphere. From Eq. (4.2.31), we can obtain the injected depth of trapped particles and its approximation at a larger pitch-angle:

$$h_r = \frac{h_t + d}{\left(1 + \frac{\cos\theta_0}{\sin\theta_0}\right)^{1/3}} - d$$

$$\approx h_t - \frac{\cos\theta_0 (h_t + d)}{3\sin\theta_0}. \tag{4.2.32}$$

Therefore, the injected depth decreases with increasing of θ_0, while the reflected point rises with increasing of θ_0, which can be directly understood from the conservation of magnetic moment in Eq. (4.2.29). It is interesting that the injected depth and reflected point are independent from θ_c or mirror ratio [20].

4.3 Spatial Distribution of X-Ray and γ–Ray Brightness

Detection of HXR emission of solar flares with a spatial resolution indicates an inhomogeneous brightness distribution along a flare loop. In recent years, using the Yohkoh and RHESSI space vehicles, HXR sources with brightness maxima not only at the FPs but also at the top of the loop were detected [21]. Coronal γ radiation sources with a very hard photon spectrum are of special interest [22]. Owing to the low dynamic range of RHESSI (about an order of magnitude in intensity), coronal sources are mainly detected in behind-the-limb flares, in which powerful sources in the loop FPs are screened by the limb [23].

The existing HXR and gamma radiation models meet difficulties in interpreting coronal sources [23] that are first of all associated with an insufficiently high plasma density at the LT. To overcome this problem, the following suppositions were proposed: *a*. an extremely high plasma density at the LT [21]; *b*. acceleration and trapping of electrons in a region with a high level of plasma turbulence [24–26]; *c*. trapping of electrons injected into the loop perpendicularly to the magnetic field lines [27]; and *d*. inverse Compton scattering of mildly relativistic electrons on photons of soft X-ray and extreme ultraviolet radiation [28].

We develop the ideas connected to the trapping and accumulation of energetic electrons at the top of an inhomogeneous magnetic loop, based on a more general and rigorous approach to solving the nonstationary relativistic kinetic equation as compared to the aforementioned works [29]. These methods were developed and successfully applied to the analysis of the dynamics of spatial distributions of mildly relativistic electrons and brightness of microwave GS radiation of flare loops [30, 31], as well as to calculations of the polarization degree [32] and the HXR directivity[33]. When solving the kinetic equation, we restrict ourselves to the consideration of the Coulomb scattering and change the pitch-angle of electrons in a nonuniform magnetic field. We do not consider the scattering of energetic electrons on plasma turbulence (Langmuir waves and whistlers), the existence of which in a flaring loop is postulated in some works, e.g., see the Ref. [34]. This can be justified by observations of the presence of a fine time HXR structure with a duration of a single pulse on the order of

a hundred milliseconds in many bursts. As was shown in the Ref. [32], time profiles with a fine structure are completely determined by Coulomb collisions in a dense plasma. The effect of electron scattering on plasma waves is insignificant. From a theoretical point of view, low efficiency of electron scattering on wave turbulence also has certain grounds. For example, whistlers are subjected to the Landau damping which sharply increases with wave deviations from the direction of the magnetic field line. For this reason, whistlers efficiently attenuate at any reasonable curvature of magnetic field lines in flare loops (see, e.g., the paper [32]).

4.3.1 Numerical Simulations of Spatial Distribution of Energetic Electrons in Flaring Loops

To find the spatial, temporal, energetic, and pitch-angle distributions of injected energetic electrons propagating in a magnetic loop, we solve a relativistic kinetic equation in the Fokker–Planck form (see details in Sect. 2.4). This equationwas solved numerically by the finite difference method using the operator splitting technique and with the boundary conditions described in the Refs. [30, 31, 35]. The magnetic field convergence, providing the effect of magnetic trapping, is given by the choice of a distributionin the form $B(s) = B_0 \exp[(s - s_1)^2/s_2^2]$ where $s_2^2 = s_{max}^2/ln(B_c/B_0)$, B_0 and B_c are respectively the magnetic field inductions at the LT and at the FPs of the loop; $s_1 = 0$ and $s_{max} = 3 \times 10^9$ cm are respectively the coordinates of the center and FPs of the loop; and s_2 characterizes the height scale of the magnetic field along the loop. The following values of the parameters were taken for the calculations: $B_0 = 200$ G and the mirror ratio $B_c/B_0 = 2$ and 5. The sharp increase in the plasma density toward the FPs of the loop was specified by the expression $n(s) = n_0 \exp[4.6(s/s_{max})^6]$, where $n_0 = 5 \times 10^{10}$ cm^{-3} is the plasma number density at the top of the loop. It was taken into consideration that the NT electron injection function has the form $S(E, \mu, s, t) = S_1(E)S_2(\mu)S_3(s)S_4(t)$, where $S_1(E) = K(E/E_0)^{-\delta}$ with $\delta = 3$ and $\delta = 7$, $E_0 = 511$ keV, and K is the common normalizing factor.

In this work, two cases of electron injection were considered: isotropic injection (model 1) and anisotropic injection along the field lines (model 2). In the case of isotropic injection, $S_2(\mu) = 1$. In the case of anisotropic injection, $S_2(\mu) = \exp[-(\mu - \mu_1)^2/\mu_0^2]$, where $\mu_1 = 1$ and $\mu_0 = 0.2$. The value $\mu_0 = 0.2$ corresponds to a cone with the tapering angle $\Delta\theta = 36°$. The spatial distribution was specified by the function $S_3(s) = \exp[-(s - s_1)^2/s_0^2]$. Electrons were injected at the top of the magnetic loop $s = s_1 = 0$ in a region with a characteristic width of the source $s_0 = 2 \times 10^8$ cm. Electron injection in time was supposed to be pulse-wise: $S_4(t) = \exp[-(t - t_1)^2/t_0^2]$ with $t_1 = 2.5$ s and $t_0 = 1.4$ s.

Figure 4.7 shows the number density distributions of NT electrons along the loop for energies of 49 and 388 keV and times t = 1, 2.5, 3, 4, 6, and 10 s. The calculations were performed for a magnetic loop with the mirror ratio $B_c/B_0 = 2$ and the spectral index of injected electrons $\delta = 3$. For model 1 (left two columns of Fig. 4.7), the

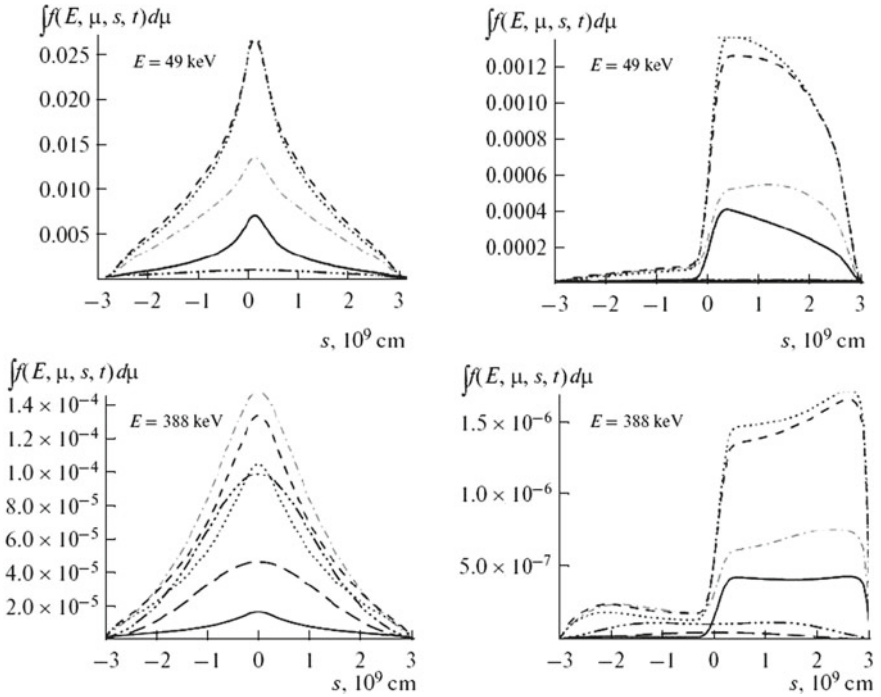

Fig. 4.7 Distributions of nonthermal electrons along the loop for energy values of 49 and 388 keV and for time instants t = 1, 2.5, 3, 4, 6, and 10 s (the solid, dotted, dot-and-dash, short-dashed, dots-dashed and long-dashed lines, respectively): on the left two columns, for the case of isotropic injection at the loop top (model 1); on the right two columns, for the case of longitudinal injection from the loop top to the right FP (model 2). The mirror ratio $B_c/B_0 = 2$ and the spectrum index of injected electrons $\delta = 3$

distribution of energetic electrons has a sharp maximum in the center of the loop. Its shape is preserved at all energies during the whole time of injection (10 s). For model 2 (right two columns of Fig. 4.7), the electron distributions over the loop for energies of 49 and 388 keV strongly differ in the positions of the maxima: at a low level of energy, the maximum is close to the LT; at a high level of energy, to the FP.

4.3.2 Simulated Results of Spatial Distribution of X-Rays and γ-Rays

When calculating the spatial distribution of HXR and GAMMA radiation based on the obtained electron distributions, we use the formalism described in our earlier work [32]. The differential HXR intensity (per unit length) is defined by the relationship

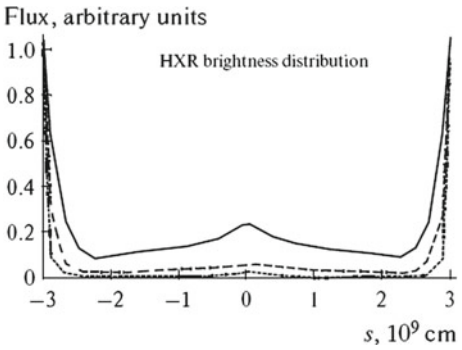

Fig. 4.8 HXR brightness distributions along the loop for t = 3 s, for photon fluxes with energies $h\nu = 30$, 98, and 1039 keV (the solid, dashed, and dotted lines, respectively) under isotropic injection. The mirror ratio $B_c/B_0 = 2$ and $\delta = 3$; the angle of vision $\alpha = 90°$

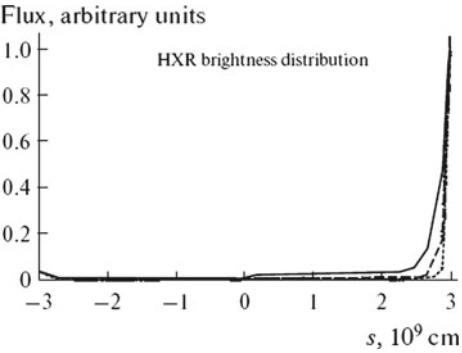

Fig. 4.9 Same as in Fig. 4.8 but for the anisotropic injection model

$$\frac{dI(\epsilon,\alpha,s,t)}{ds} = \frac{S(s)\times n(s)}{R^2}\int_{\epsilon}^{\infty} v(E)dE\int_{-1}^{1} f(E,s,\mu,t)d\mu\int_{0}^{2\pi}\sigma(\epsilon,E,\alpha,\mu,\varphi)d\varphi, \tag{4.3.1}$$

where $S(s)$ is the area of the transverse cross-section of the source (loop) in the general case and depends on the coordinate along the axis of the magnetic loop (decreases with an increase in s); $n(s)$ is the concentration of plasma ions (depends on coordinate s and is determined using a model); and $R = 1.5\times10^{13}$ cm is the astronomical unit. The dependence of the area of the transverse cross-section on coordinate s is determined from the condition of the invariance of the magnetic flux $B(s)S(s) = const$ and model dependence of the magnetic field on coordinate s.

The total (summated over the polarization) relativistic cross-section σ for the bremsstrahlung radiation was obtained in the paper [36]. Note that the cross section depends on the parameters of accelerated electrons, on the energy of X-ray quanta, and on observation angle α. At the same time, as was shown by calculations [37], the dependence on the observation angle, together with the energy distribution, is most significant in calculations of HXR characteristics.

Below, we present the results of calculations performed for the viewing angle $\alpha = 90°$. Figures 4.8 and 4.9 show the difference in HXR brightness distributions along the loop at t = 3 s for models 1 and 2, respectively. As should be expected, the HXR sources are localized at the FPs in the case of longitudinal injection along

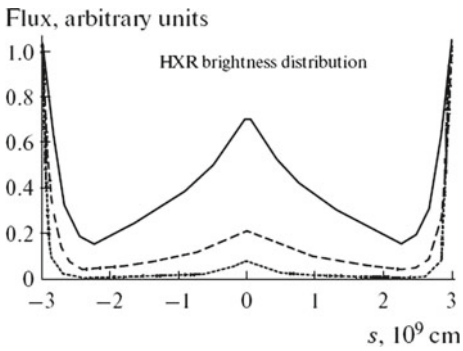

Fig. 4.10 Same as in Fig. 4.8 but for the mirror ratio $B_c/B_0 = 5$

the loop. Moreover, the FP HXR source, in the direction of which the injection occurs, is significantly brighter (Fig. 4.9). This is caused by the fact that the overwhelming majority of injected electrons precipitate into the loss cone (to the dense chromospheric layers), where the thick-target approximation is implemented. In the case of isotropic injection, three sources manifest themselves in the magnetic loop: two sources with maxima in the FPs and one source with a maximum at the LT (Fig. 4.8).

The appearance of a source at the LT is associated with the trapping and accumulation of a considerable number of energetic electrons with large pitch-angles (Fig. 4.7). However, due to a relatively low plasma density, the HXR source at the LT is not as bright as at the FPs. This effect especially manifests itself at higher energies of photons, which can be a cause of the fact that the source at the LT is not often detected in high-energy RHESSI channels; to detect it, one should observe behind-the-limb flares at which the FP sources are screened.

4.3.2.1 Role of Mirror Ratio

To illustrate the role of the mirror ratio in the formation of a source at the loop top, Fig. 4.10 demonstrates the HXR distribution for $B_c/B_0 = 5$ and $\delta = 3$. It is seen from a comparison with Fig. 4.9 that an increase in the mirror ratio from $B_c/B_0 = 2$ to $B_c/B_0 = 5$ sharply increases the relative brightness of the source at the LT as compared to the FP one: from 0.25–0.7 at $h\nu = 30\,\text{keV}$ and from 0.05–0.2 at $h\nu = 100\,\text{keV}$.

4.3.2.2 For Steep Electron Spectra

An increase in the HXR source brightness is especially distinct (Fig. 4.11) at the loop top for steep spectra of injected electrons ($\delta = 7$, $B_c/B_0 = 2$). For low energies of HXR photons ($h\nu = 30\,\text{keV}$) and the spectrum index $\delta = 7$, an HXR source appears at the LT even in the case of longitudinal injection of electrons. It is evident that

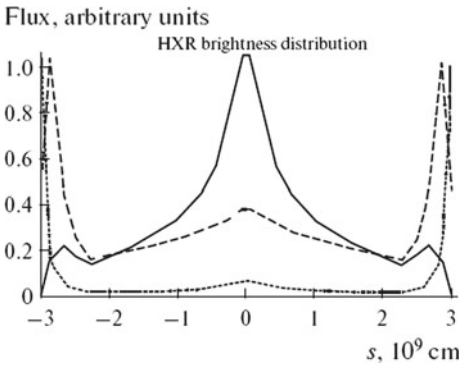

Fig. 4.11 Same as in Fig. 4.10 but for a steeper electron spectrum $\delta = 7$

the amplification of the source brightness at the LT at low photon energies for steep electron spectra is caused by the small length of the free path of the accelerated electrons ($\lambda \ll s_{max}$).

4.3.3 Conclusions

The intensity distribution of HXR along a magnetic loop was simulated numerically based on the solution of a nonstationary relativistic kinetic equation in the Fokker–Planck form. It is shown that a sharp increase in the brightness of the radiation from the upper part of the loop can appear due to the effect of accumulation of energetic electrons with large pitch-angles under isotropic injection of energetic electrons at the top of the magnetic loop. The effect is amplified with an increase in the mirror ratio in the magnetic loop. It was established that a similar increase in the HXR brightness at the loop top can also occur with electron injection that is anisotropic along the magnetic field. However, this is only possible in the case of steep energetic spectra of accelerated electrons.

4.4 Spatial Distribution of X-Ray Directivity and Polarization

The directivity and polarization of hard X-ray (HXR) and gamma-ray emission of solar flares contain data on the angular distribution of accelerated electrons that produce these types of radiation. Specifically, the type of this distribution (isotropic, anisotropic longitudinal, or anisotropic transverse to the magnetic field) may be determined by analyzing these parameters. Therefore, detailed experimental and theoretical studies are of great interest for researchers trying to understand the specifics of electron acceleration in solar flares.

The theoretical aspects of directivity and polarization of HXR for longitudinal (along the magnetic field) and isotropic pitch-angle distributions of energetic electrons were discussed in a number of papers. However, the HXR source was assumed to be homogeneous at the early stage of these studies, and the geometry of the flare magnetic loop, and, consequently, the spatial dynamics of electron distributions within the loop, were not taken into account (see, for example, paper [37]). These simplifications were caused by the lack of suitable instruments for measurements with a high spatial resolution. Modern techniques of observing hard X-ray and gamma-ray emission of flares require novel, spatially resolved and nonstationary models of the sources of such radiation. The characteristics of HXR from different regions of a flare loop were analyzed in detail in the study [38] with the use of the nonrelativistic kinetic equation for radiating electrons. The obtained results were thus valid only at low energies. The spatial distributions of the HXR intensity and spectrum were calculated in papers [29, 32] by solving the nonstationary kinetic Fokker–Planck equation in the relativistic form (including electrons with $E_e > 100\,\mathrm{keV}$) with arbitrary directions of electron injection into an inhomogeneous magnetic loop.

Our goal in this section of the book is to investigate the peculiarities of the directivity and polarization dynamics of hard X-ray and gamma radiation from different regions of a flare loop via numerical modeling of the dynamics of pitch-angle, energy, and spatial distributions of energetic electrons in the loop upon their nonstationary but fairly long-lasting injection at the top of the magnetic loop. We will follow our recent study [39].

4.4.1 Modeling

For the modeling, the equations and techniques were described in our earlier papers [32, 33]. It was assumed that the function of NT electron injection is a product of the independent functions of energy, pitch-angle, distance to the loop center, and time: $S(E,\ \mu,\ s,\ t) = S_1(E)S_2(\mu)S_3(s)S_4(t)$. The energy distribution was assumed to be a power-law ($S_1(E) = K(E/E_{min})^{-\delta}$, where K is the general normalizing factor and $E_0 = 511$ keV), and calculations were carried out for the electron energy spectrum index $\delta = 5$. The electrons were injected at the LT isotropically or anisotropically along the field. In the case of isotropic injection, the angular distribution part $S_2(\mu) = 1$. In the case of anisotropic injection, this part was set in the Gaussian form: $S_2(\mu) = \exp((\mu - \mu_1)^2/\mu_0^2)$, where $\mu_1 = 1$ and $\mu_0 = 0.2$, which corresponds to a cone with angular width $\Delta\theta = 36°$. The spatial distribution of the injection function was also set by the Gaussian function: $S_3(s) = \exp((s - s_1)^2/s_0^2)$. Electrons were injected at the top of a magnetic loop ($s = s_1 = 0$) into the region with a source width of $s_0 = 2 \times 10^8$ cm. The electron injection was assumed to be nonstationary but long-lasting: $S_4(t) = \exp((t - t_1)^2/t_0^2)$, where $t_1 = 25\,\mathrm{s}$ and $t_0 = 14\,\mathrm{s}$.

The variation of the electron density in corona with height h was set as follows: $n(h) = n_0 \exp((R - h)/h_c)$, where $h_c = 1.3 \times 10^9$ cm and $n_0 = 5 \times 10^{10}\,\mathrm{cm}^{-3}$. The increase in electron density with height in the chromospheric plasma was

described based on the analysis of RHESSI data [40]: $n(h) = 10^{12}(h/h_{ch})^{-2.5}$, where $h_{ch} = 3 \times 10^8$ cm is the height scale. The electron density was set to $10^{15}\,\mathrm{cm}^{-3}$ at heights where $n(h) > 10^{15}\,\mathrm{cm}^{-3}$. The strengthening of the magnetic field with distance from the LT (s) was set as $B(s) = B_0 \exp[(s - s_1)^2/s_2^2]$, where $s_2^2 = s_{max}^2/\ln(B_c/B_0)$; B_0 and B_c are the magnetic induction values at the center and at the FPs of the loop, respectively; $s_1 = 0$ and $s_{max} = 3 \times 10^9$ cm are respectively the coordinates of the center and the FP of the loop; $B_0 = 200$ G; and mirror ratio $k = B_c/B_0 = 2$.

4.4.2 *Directivity at Different Positions in Flaring Loops*

The formalism described in the papers [32, 40] was used to calculate the parameters of hard X-ray and γ-ray emission based on the obtained distributions of electrons. The results of calculations of directivity dynamics $D(\alpha) = J_\varepsilon(\alpha)/J_\varepsilon(\alpha = 0°)$ of radiation produced in various regions of a flare loop in the process of longitudinal and isotropic injection of electrons are detailed below.

4.4.2.1 Longitudinal Injection

Figure 4.12 shows the angular distributions of HXR intensity with a photon energy of 98 keV produced at various distances from the top in the right part of the loop in the case of longitudinal injection of electrons. Electrons were injected towards the right FP of the loop. It can be seen that the directivity of radiation varied only slightly with time at that energy at different distances regardless of the position within the loop. The radiation directivity had its maximum at observation angle $\alpha = 0°$ at different distances from the LT. While the ratio of the radiation intensity at an angle of 0° to the HXR intensity at an angle of 180° was 5.5-7.6 at distance $s = 3.37 \times 10^7$ cm from the LT, the same ratio at $s = 2.5 \times 10^9$ (loop leg) and 3×10^9 cm (loop footpoint) was 3.3 and 1.6, respectively (see Fig. 4.12b, c).

Electrons reflected from the magnetic mirrors manifested themselves in the angular dependence of directivity when the energy was increased. Figure 4.13 shows the directivity of HXR with an energy of 318 keV. This effect was clearly seen at the LT (Fig. 4.13a) at observation angle $\alpha \approx 120°$ in 30 s after the start of the injection, and a counterstream of particles emerged within 50 s. However, the maximum radiation intensity was produced at angle $\alpha \approx 0°$. Counterstreams of particles ceased to appear when the distance from the LT was increased (Fig. 4.13b, c), while the HXR directivity was still fairly high: $J(318\,\mathrm{keV}, \alpha = 0°)/\mathrm{J}(318\,\mathrm{keV}, \alpha = 180°) = 4.2$ at the loop FP.

Only reflected electrons with large pitch-angles were present in the left half of the loop away from the LT. The radiation produced by high-energy electrons had a fairly high directivity. Therefore, at the loop FP ($s = 3.0 \times 10^9$ cm), the maximum intensity of radiation with a photon energy of 318 keV was produced at angles $\alpha \approx 110°$, and the HXR intensity varied by a factor of up to 3 when the observation angle was

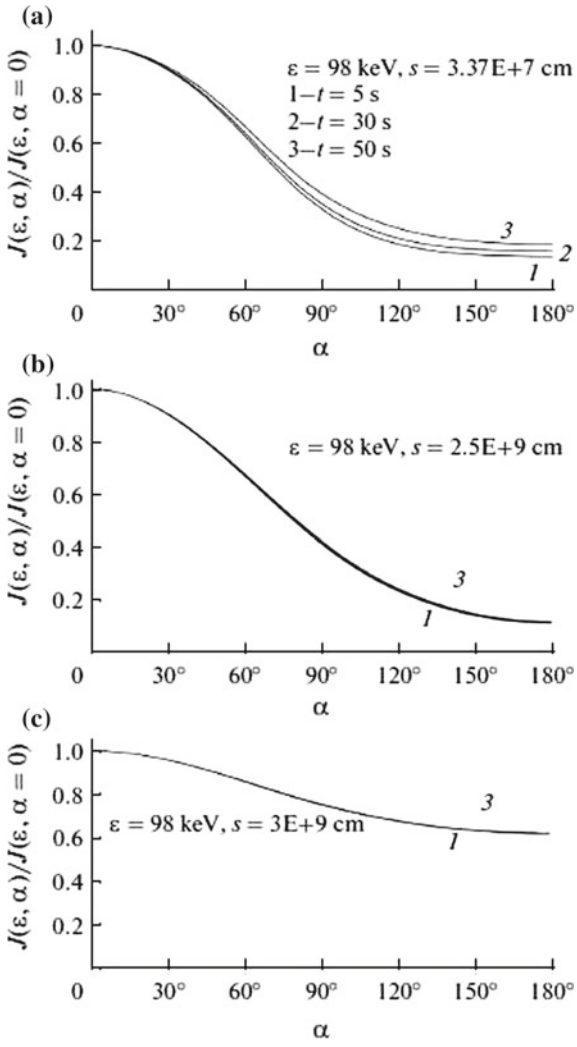

Fig. 4.12 Directivity of HXR with an energy of 98 keV in the case of longitudinal injection. Right half of the loop (loop's top, leg, footpoint)

altered (Fig. 4.14a). At a distance of $s = 2.5 \times 10^9$ cm, the radiation intensity was maximized at angle $\alpha \approx 95°$ (Fig. 4.14b). Particle counterstreams again emerged near the top (Fig. 4.14c). The transverse radiation intensity was continuously increasing with time in all loop regions.

4.4.2.2 Isotropic Injection

It was already mentioned that a long-lasting pitch-angle distribution of electrons with a maximum transverse to the loop is formed in the case of isotropic injection

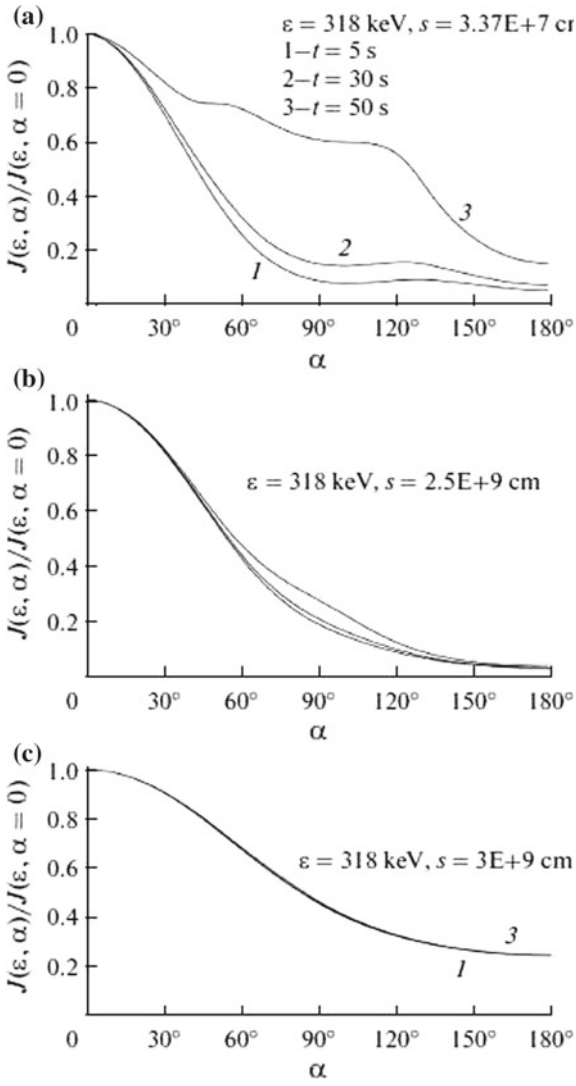

Fig. 4.13 Directivity of HXR with an energy of 318 keV in the case of longitudinal injection. Right half of the loop (loop's top, leg, footpoint)

at the top. Consequently, the HXR directivity pattern changed greatly in the case of isotropic injection. Figure 4.15 shows the HXR and gamma-ray directivity with a photon energy of 98 and 318 keV. The directivity maximum of emission at the LT is shifted to angle $\alpha \approx 90°$, while the directivity magnitude increases with time. For example, the ratio J (98 keV, $\alpha = 90°$)/J(98 keV, $\alpha = 0°$) is roughly equal to 1.7 at moment 30 s after the start of the injection, and the same ratio in 50 s after the start of the injection is roughly equal to 2.1 (Fig. 4.15a). Especially strong perpendicular

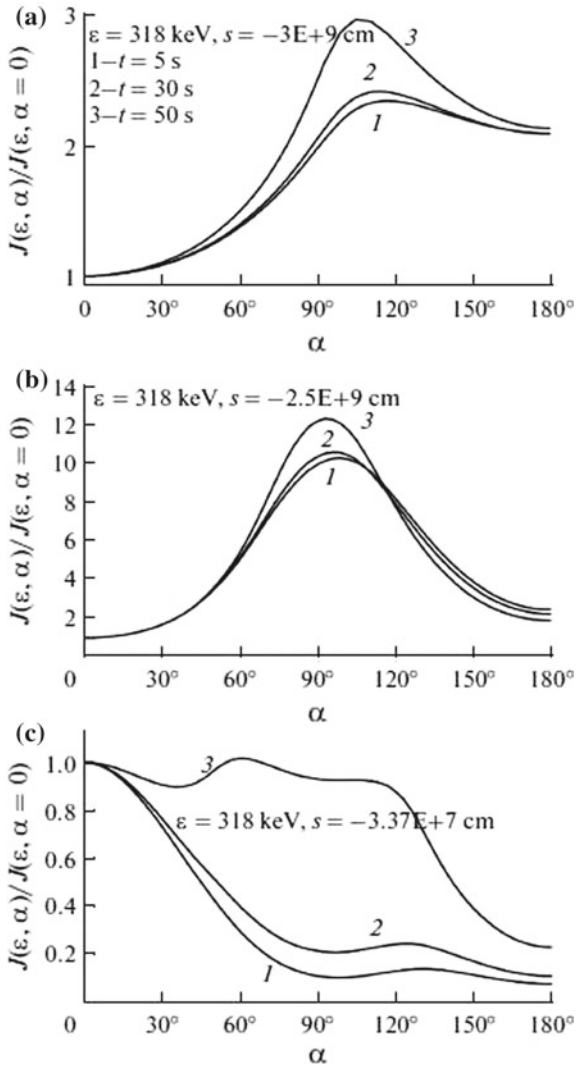

Fig. 4.14 Directivity of HXR with an energy of 318 keV in the case of longitudinal injection. Left half of the loop (loop's top, leg, footpoint)

directivity is formed for gamma-rays. For photon energy 318 keV, the corresponding numbers are 7.6 and 9.4. As the distance from the LT was increased, the observation angle corresponding to the HXR intensity maximum is shifted towards lower values (Fig. 4.15b, c). The degree of directivity was also reduced considerably due to strong scattering and the isotropization of electrons.

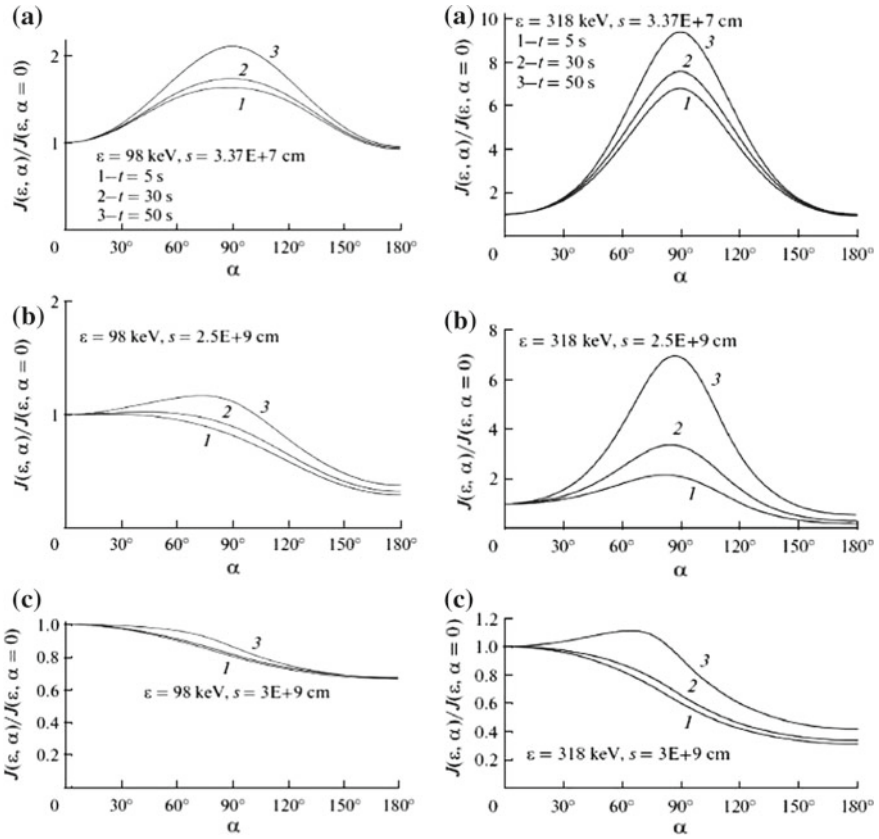

Fig. 4.15 Directivity of hard X-rays and gamma-rays with energies of 98 and 318 keV at the loop's top, leg, and footpoint in the case of isotropic injection

4.4.3 Polarization at Different Positions in Flaring Loops

The HXR polarization degree is defined by the difference between intensities I_1 and I_2 of the emission of quanta with polarization vectors lying in plane (kB) and perpendicular to it: $P = (I_2 - I_1)/(I_2 + I_1)$, where I_1 and I_2 are determined through the bremsstrahlung mechanism cross sections [36].

Figure 4.16a, c show the results of calculations of the linear polarization of HXR emission produced at different distances s from the LT and for various observation angles α in the case of isotropic injection of fast electrons at the loop top with energy spectrum index $\delta = 5$ at the 30th second after the start of the injection.

It can be seen from Fig. 4.16a that the degree of HXR polarization at photon energy $\varepsilon = 30$ keV from the LT reaches $\approx$25% at $\alpha = 90°$. As the distance from the top increased, the polarization value was reduced and changed its sign. HXR radiation from the loop FP was almost nonpolarized. It should also be noted that the degree

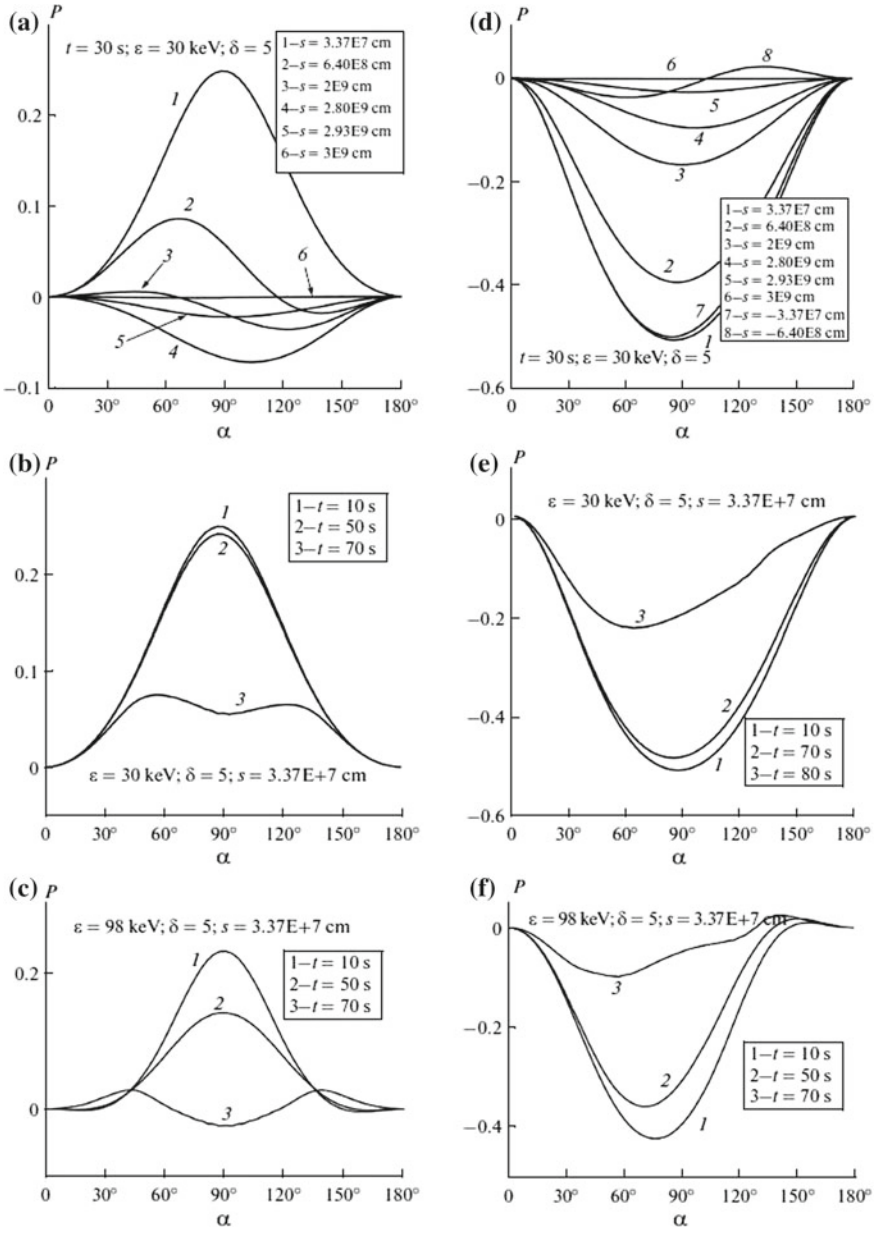

Fig. 4.16 Degree of linear polarization of HXR in the case of (*a*–*c*) isotropic and (*d*–*f*) anisotropic injection

of HXR polarization decreased as the energy of quanta increased: the polarization degree was no higher than 14 and 10% at $\varepsilon = 176$ and 318 keV, respectively. When the energy spectrum index of injected electrons was reduced to $\delta = 3$, the degree of emission polarization at a photon energy of 30 keV at the LT at the 30th second after the start of the injection was no higher than 11%.

The HXR polarization upon isotropic injection is caused by the fact noted above that electrons with small pitch-angles leave the loop, while a fraction of electrons with large pitch-angles become trapped in a magnetic trap. As a result, an anisotropic electron distribution of the loss-cone type is formed, and polarized radiation is produced. As the electrons are scattered due to Coulomb collisions, their number (and, consequently, the HXR intensity) in the loop is reduced. However, the radiation remained polarized for several tens of seconds (Fig. 4.16b, c) due to the fact that the anisotropy of the distribution of fast electrons was retained.

Figure 4.16d shows the results of calculations for anisotropic (longitudinal) injection of electrons with energy spectrum index $\delta = 5$. One can see a dramatic difference with the case of the isotropic injection, namely the change of the polarization sign. The degree of HXR polarization from the loop top at the 30th second after the start of the injection was ≈–50% at photon energy $\varepsilon = 30$ keV. The negative polarization was reduced smoothly as one moved away from the top toward the right FP of the loop (curves 1–6). The HXR polarization decrease was steeper in the left half of the loop (curves 7 and 8). The polarization degree was reduced as the energy of quanta was increased. The degree of HXR polarization at photon energy $\varepsilon = 176$ keV from the loop top was ≈–28%, and it dropped to about –13% at $\varepsilon = 318$ keV.

Just as in the case of isotropic injection, the HXR remained polarized for several tens of seconds upon anisotropic injection. The polarization degree was reduced considerably in the injection decay phase. These changes were particularly well-seen at higher energies (compare Fig. 4.16e, f). When δ was reduced from 5 to 3, the HXR polarization was reduced: for example, the degree of HXR polarization from the top was as high as ≈–50% at $\varepsilon = 30$ keV and $\delta = 5$ but was reduced to ≈–38% at $\delta = 3$. It was demonstrated above that the two analyzed means of injecting fast electrons into a flare loop lead to the opposite signs of produced HXR polarization. The difference was especially large for radiation from the LT. In the case of isotropic injection, the polarization from the left and right parts of the loop exhibited symmetry. This was true both for the spatial dependence of the polarization degree at different energies of quanta and for the character of its variation with time. No symmetry was observed in the anisotropic case. Such differences in the values and angular dependences of polarization may be used to characterize the nature of electron injection into a flare loop.

4.4.4 Conclusions

The peculiarities of the directivity and polarization dynamics of hard X-ray and gamma-ray emission from different regions of a flaring loop were studied based

on the numerical modeling of the dynamics of energetic electrons distributions in the loop upon their nonstationary but fairly long-lasting injection at the top of the magnetic loop. The modeling results suggested that the degree of directivity and polarization and the variation of these parameters in time depend on the position within the loop and vary fundamentally between cases of isotropic and anisotropic (longitudinal) injection of electrons. The revealed properties of the directivity and polarization dynamics may be used in X-ray and gamma-ray diagnostics of the type of pitch-angle distribution of electrons accelerated in a certain specific observed flare.

References

1. Ramaty, R.: Gyrosynchrotron emission and absorption in a magnetoactive plasma. Astrophys. J. **158**, 753–770 (1969)
2. Lin, R., Schwartz, R., Kane, S., Pelling, R., Hurley, K.: Solar hard X-ray microflares. Astrophys. J. **283**, 421–425 (1984)
3. Lin, R., Barnes, W., Hurley, K., Smith, D., Pelling, R.: A search for solar hard X-ray microflares near solar minimum. Bull. Am. Astron. Soc. **21**, 847–847 (1989)
4. Fleishman, G., Yastrebov, S.: On the harmonic structure of solar radio spikes. Sol. Phys. **154**, 361–369 (1994)
5. Brown, J.: The directivity and polarisation of thick target X-Ray bremsstrahlung from solar flares. Sol.Phys. **26**, 441–459 (1972)
6. Lin, R., 65 colleagues: The Reuven Ramaty High-Energy Solar Spectroscopic Imager (RHESSI). Solar Physics **210**, 3–32 (2002)
7. Ning, Z.: Microwave and hard X-Ray spectral evolution in two solar flares. Astrophys. J. **659**, L69–L72 (2007)
8. Battaglia, M., Benz, A.: Relations between concurrent hard X-ray sources in solar flares. Astron. Astrophys. **456**, 751–760 (2006)
9. Ning, Z.: Speed distributions of merging X-Ray sources during chromospheric evaporation in solar flares. Sol. Phys. **273**, 81–92 (2012)
10. Ning, Z.: Chromospheric evaporation in solar flares. EAS Publ. Ser. **55**, 245–249 (2012)
11. Ning, Z., Cao, W.: Investigation of Chromospheric evaporation in a neupert-type solar flare. Astrophys. J. **717**, 1232–1242 (2010)
12. Huang, G.L.: Diagnostics of the Low-Cutoff energy of nonthermal electrons in solar microwave and hard X-Ray bursts. Sol. Phys. **257**, 323–334 (2009)
13. Miyamoto, K.: Plasma Physics for Nuclear Fusion, pp. 101. Science Press (Chapter 5). Science (1981)
14. Melrose, D.B.: Plasma Astrophysics. Cambridge University Press, London (1980)
15. Sharma, R.R., Vlahos, L.: Comparative study of the loss cone-driven instabilities in the low solar corona. Astrophys. J. **280**, 405–415 (1984)
16. Landau, L.D.: J. Phys. **10**, 45–49 (1946)
17. Landau, L.D.: Zh. E. T. F. **7**, 203–209 (1937)
18. Lee, J., Gary, D.E.: Solar microwave bursts and injection pitch-angle distribution of flare electrons. Astrophys. J. **543**, 457–471 (2000)
19. Sakao, T., Kosugi, T., Masuda, S., Yaji, K., Inda-Koide, M., Makishima, K.: Characteristics of hard X-ray double sources in impulsive solar flares. Adv. Space Research **17**, 67–70 (1996)
20. Huang, G.L.: Initial pitch-angle of narrowly beamed electrons injected into a magnetic mirror, formation of trapped and precipitating electron distribution, and asymmetry of hard X-ray and microwave footpoint emissions. New Astron. **12**, 483–489 (2007)
21. Veronig, A.M., Brown, J.C.: A coronal thick-target interpretation of two hard X-ray loop events. Astrophys. J. Lett. **603**, L117–120 (2004)

22. Krucker, S., Hurford, G.J., Mackinnon, A.L., Shih, A.Y., Lin, R.P.: Coronal X-ray bremsstrahlung from solar flare accelerated electrons. Astrophys. J. Lett. **678**, L63–66 (2008)
23. Krucker, S., Battaglia, M., Cargill, P.J., et al.: Hard X-ray emission from the solar corona. Astron. Astrophys. Rev. **16**, 155–208 (2008)
24. Petrosian, V., Donaghy, T.Q.: On the spatial distribution of hard X-rays from solar flare loops. Astrophys. J. **527**, 945–957 (1999)
25. Stepanov, A.V., Tsap, Y.T.: Electron whistler interaction in coronal loops and radiation signatures. Sol. Phys. **211**, 135–154 (2002)
26. Petrosian, V., Liu, S.: Stochastic acceleration of electrons and protons. I. Acceleration by parallel-propagating waves. Astrophys. J. **610**, 550–571 (2004)
27. Fletcher, L., Martens, P.C.H.: A model for hard X-ray emission from the top of flaring loops. Astrophys. J. **505**, 418–431 (1998)
28. Chen, B., Bastian, T.S.: The role of inverse Compton scattering in solar coronal hard X-ray and γ-ray sources. Astrophys. J. **750**, 35–51 (2012)
29. Melnikov, V.F., Charikov, Y.E., Kudryavtsev, I.V.: Spatial brightness distribution of hard X-rays along flare loops. Geomagn. Aeron. **53**, 863–866 (2013)
30. Melnikov, V.F., Gorbikov, S.P., Reznikova, V.E., Shibasaki, K.: Spatial distribution of relativistic electrons in microwave flare loops. Izv. Akad. Nauk, Ser. Fiz. **70**, 1472–1474 (2006)
31. Reznikova, V.E., Melnikov, V.F., Shibasaki, K., Gorbikov, S.P., Pyatakov, N.P., Myagkova, I.N., Ji, H.: 2002 August 24 limb flare loop: Dynamics of microwave brightness distribution. Astrophys. J. **697**, 735–746 (2009)
32. Charikov, Y.E., Melnikov, V.F., Kudryavtsev, I.V.: Intensity and polarization of the hard X-ray radiation of solar flares at the top and footpoints of a magnetic loop. Geomagn. Aeron. **52**, 1021–1031 (2012)
33. Melnikov, V.F., Kudryavtsev, I.V., Charikov, Y.E.: Directivity of hard X-ray and gamma emissions from a flare loop. In: Stepanov, A.V., Nagovitsyn, Y.A. (eds.). Proceedings Pulkovo All-Russian Annual International Conference on Solar Physics, pp. 275–278. St. Petersburg (2012)
34. Kontar, E.P., Ratcliffe, H., Bian, N.H.: Wave-particle interactions in non-uniform plasma and the interpretation of hard X-ray spectra in solar flares. Astron. Astrophys. **539**, 43–51 (2012)
35. Gorbikov, S.P., Melnikov, V.F.: Numerical solution of the Fokker–Planck equation for modeling the particle distribution in solar magnetic traps. Mat. Model. **19**, 112–122 (2007)
36. Gluckstern, R.L., Hull, M.H.: Polarization dependence of the integrated bremsstrahlung cross section. Phys. Rev. **90**, 1030–1035 (1953)
37. Bai, T., Ramaty, R.: Backscatter, anisotropy, and polarization of solar hard X-Rays. Astrophys. J. **219**, 705–726 (1978)
38. Zharkova, V.V., Kuznetsov, A.A., Siversky, T.V.: Diagnostics of energetic electrons with anisotropic distributions in solar flares. I. Hard X-rays bremsstrahlung emission. Astron. Astrophys. **512**, A8–26 (2010)
39. Melnikov, V.F., Charikov, Yu, E., Kudryavtsev, I.V.: Directivity and polarization dynamics of hard X-ray and gamma-ray emission of a flare loop. Geomagn. Aeron. **55**, 983–990 (2015)
40. Aschwanden, M.J., Brown, J.C., Kontar, E.P.: Chromospheric height and density measurements in a solar flare observed with RHESSI II. Data Anal., Sol. Phys. **210**, 383–405 (2002)

Chapter 5
Observations and Explanations of X-Ray Emissions in Flaring Loops

5.1 Overview

The studies on solar X-ray emission can provide a direct imaging about flaring loops, which is commonly composed of thermal and NT components, and the HXR emission is closely associated with the acceleration of energetic electrons [1, 2]. The soft-hard-soft (SHS) pattern appears in spectral evolution of a considerable part of X-ray flares, which can be directly understood by the evolution of energetic electrons in the acceleration process [3–11], while the soft-hard-harder (SHH) pattern also appears in a part of X-ray flares, which is commonly explained by the mirroring effect on energetic electrons in flaring loops [12–14]. Most studies as mentioned above were limited in spatially unresolvable data observed in the full-disk, and a part of studies were comparatively made on HXR and MW data [15, 16].

Regarding the spatially resolvable data from earlier Yohkoh to recent RHESSI satellites, the X-ray brightness and spectral distributions in flaring loops have been performed [17–23]. According to the classical flare models, after the energetic electrons are accelerated in the reconnection site above the loop top (LT) and injected into flaring loops, they are separated into trapped and escaped parts due to the mirroring effect in flaring loops, the former one collides with high-density plasma in photosphere to emit bremsstrahlung, while it is thermalized fast, and the latter one moves forth and back between two reflected points inside the loop to emit MW, and it is finally thermalized. It is first noticed that two temporally and spatially coincident sources of HXR and MW frequently observed nearby the footpoints (FPs), which supports that both of them are contributed by the particle acceleration in the same flare, and consistent with the joint analysis of HXR and MW time profiles.

With continuous enhancement of spatial resolution of relevant telescopes, it was first found by Yohkoh that there is possibly a stronger X-ray source nearby or above LT (called as Masuda flare) [17], which is considered to the evidence of particle acceleration due to magnetic reconnection above the LT, furthermore, RHESSI detected the coronal source that more close to the reconnection or acceleration site [24]. Meanwhile, a stronger MW emission also detected by NoRH nearby the LT, which may

G. Huang et al., *Solar Flare Loops: Observations and Interpretations*,
https://doi.org/10.1007/978-981-10-2869-4_5

be explained by the anisotropy of pitch-angle distribution of NT electrons [25]. It is noticed that the X-ray LT source is often observed at lower energies in comparison with that nearby the FPs, which means that the X-ray sources in LT and FPs are detected from different energies, while MW emission at a given frequency can be measured simultaneously in LT and FPs.

In a study of five HXR flares observed by RHESSI [21], the SHS pattern was found in the spectral evolution of both LT and FPs, and the spectrum of LT was always softer than that in FPs, which is similar to the result in another paper [26]. Moreover, in a statistical study of 27 HXR limb flares observed by RHESSI, the averaged spectral indices in LT and FPs were respectively 6.84 and 3.35, with an inversely correlated evolution but without a physical explanation [27, 28].

5.2 Distribution of Hard X-Ray (HXR) Brightness: Loop Top and Feet

We selected 13 RHESSI flares with a single-loop structure composed of one LT and two FPs, to study statistically the relationship of spectral indices at peak time in different sources [22]. Due to multiple peaks existed in a part of events, there are altogether 28 main peaks and sub-peaks as the statistical samples. The criterions of data selection are: (1) there were enough photons observed in both main peaks and sub-peaks; (2) the state of attenuator kept invariant in the observed time intervals of both main peaks and sub-peaks; (3) the effects of pickup and strong particles were negligible in the observed time intervals of both main peaks and sub-peaks; and (4) the events with photons at 25–50 keV more than 1000 s^{-1}detector^{-1} were excluded, also to decrease the pickup effect. A part of these events were studied by the RHESSI core team, as a reference to test the data processing [8]. Meanwhile, most of these events occurred in solar limb, so that the albedo effect may be neglected. The exact dates and time intervals may refer to the Table 2 of the paper [22].

As one example of single-loop structure, Fig. 5.1 gives the image at the peak time of 2005 December 4 flare, with one LT (10–12 keV) and two FPs (33–37 keV). The circles in this figure mark the range of calculation in order to ensure that there is no overlap among these sources, while the contours are overlaid on the LT source (80% and 90%).

Figure 5.2 shows the positive flux correlation of LT (12 keV) and FPs (35 keV) of the selected 28 samples, with correlation coefficient of 0.826 that satisfying the confidence of 0.99, which supports the LT and FPs are contributed by the X-ray emissions of NT electrons at different energies and accelerated in the same flare.

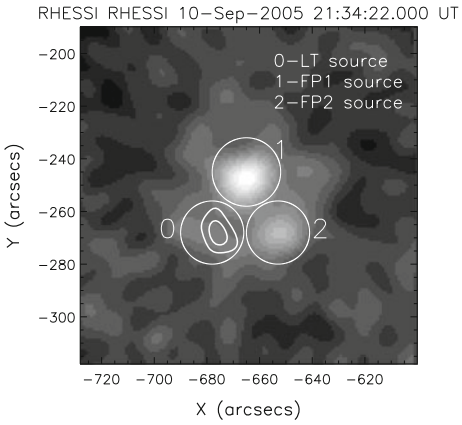

Fig. 5.1 The single-loop structure observed by RHESSI at the peak time of 2005 December 4 flare

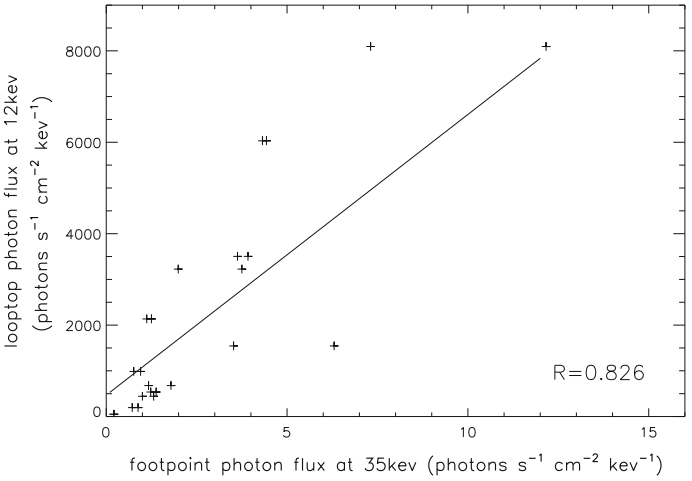

Fig. 5.2 Correlation of LT (12 keV) and FPs (35 keV) of the selected samples

5.3 Spectral Index of HXR Emissions: Loop Top and Feet

Using the standard software OSPEX of RHESSI to fit the photon spectra of different sources, in which it is fitted by thermal distribution and a single power-law in the LT sources (6–30 keV), while the FP sources (30–60 keV) are well fitted by a single power-law [22]. Figure 5.3 shows the correlation of photon spectral indices between LT and FP sources of all 28 samples. In general, the indices in LT are always larger than those in FPs (all samples are above the diagonal line), i.e., the spectra in LT are always softer than those in FPs, which is consistent with the previous results

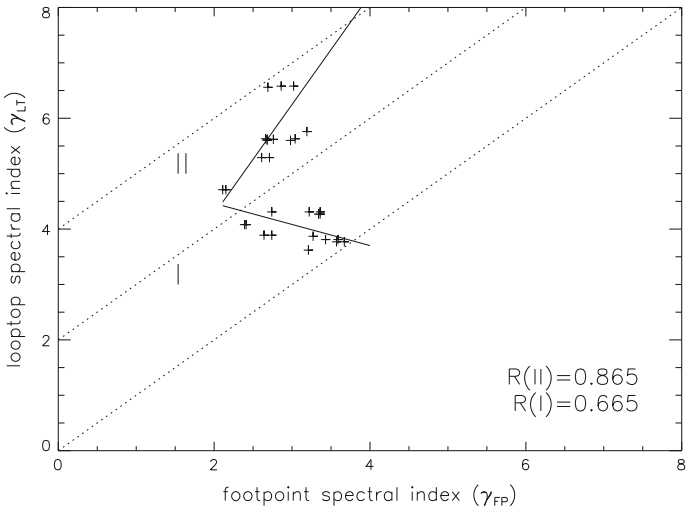

Fig. 5.3 Correlation of spectral indices in LT and FPs of the selected samples

[21, 26–28]. In addition, two straight lines parallel to the diagonal line just mark the difference of spectral indices in LT and FPs to be 2 and 4, respectively. It is assumed that the standard thick-target model is accepted in the FPs, under the same spectra of NT electrons, the difference of 2 just means the standard thin-target model in the LT source; if the difference is larger than 2, it can only be explained by the existence of thermal emission in the LT source. Hence, all of the samples are divided into two groups as marked by I and II in Fig. 5.3, group I means the radiation mechanisms in LT and FPs are respectively thin-target and thick-target models, including the mixed mechanisms of two models in the LT sources, while group II means that the LT sources are contributed by thin-target and thermal emission.

It is most interesting that there are two opposite correlations appeared in two groups, negative in group I but positive in group II, with correlation coefficients of 0.865 and 0.665, respectively, and both of them satisfy the confidence of 0.99. In order to further analyze this result, Figs. 5.4 and 5.5 give the correlations between photon flux and spectral index in LT and FPs of these two groups, respectively.

Figure 5.4 shows that a negative correlation between photon flux and spectral index always existed in FPs of the selected samples, which is consistent with the common prediction of thick-target, thin-target, and thermal bremsstrahlung. However, there are opposite correlations between photon flux and spectral index appeared in LT of two groups as shown in Fig. 5.5, which is just coincident with the result in Fig. 5.3, with the same division of spectral index around 4.7, and group I is located in the side with smaller indices. The question to be answered is which effect can produce the positive correlation between photon flux and spectral index? We take the code of thin-target model in RHESSI software to calculate the theoretical curves of photon flux at 18 and 20 keV and spectral index, and the spectral index of NT electrons is

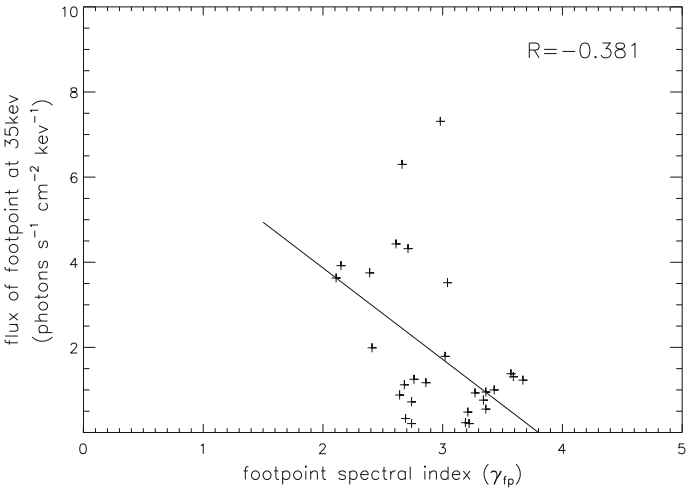

Fig. 5.4 Correlation of photon flux and spectral index in FPs of the selected samples

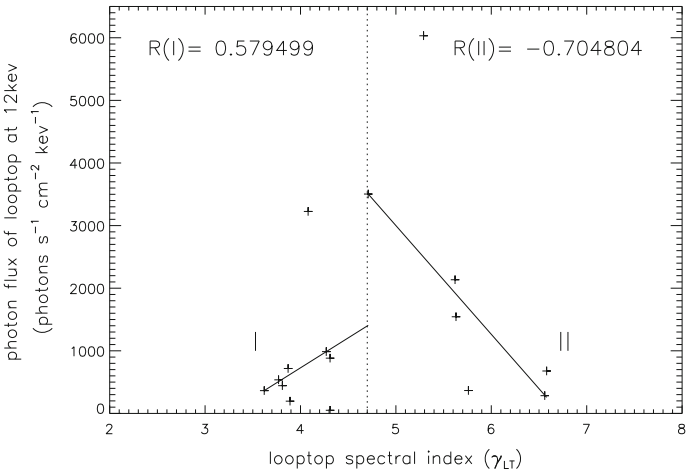

Fig. 5.5 Correlation of photon flux and spectral index in LT of the selected samples

taken as 2–7. It is found that when the lower energy cutoff is smaller, the photon flux always decreases with increasing of the spectral index (i.e., a negative correlation), while with increasing of the lower energy cutoff, a positive correlation gradually appears in the photon flux corresponding to smaller spectral indices as shown in Fig. 5.6, which is consistent with the opposite correlations in LT sources in Figs. 5.3 and 5.5. For a larger photon energy (e.g., 20 keV), a relatively larger value of lower energy cutoff is needed to produce a positive correlation. Therefore, a larger lower energy cutoff in LT (trapping electrons) can be used to explain the abnormal positive correlation of group I under the thin-target model.

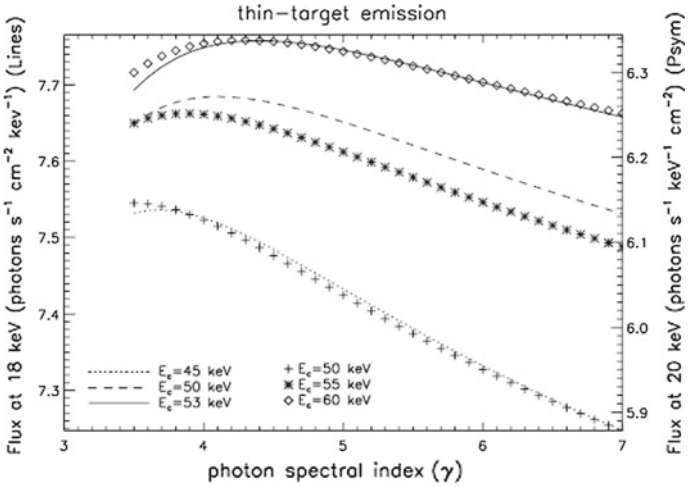

Fig. 5.6 Theoretical curves of photon flux at 18 keV (solid, dashed, and dotted) and 20 keV (plus, asterisk, and diamond) versus photon spectral index with different lower energy cutoffs

5.4 A New Pattern of HXR Spectral Evolution

Because hard-soft-hard (HSH) pattern has been found in the MW spectral evolution, it is predicted that the similar pattern may appear in HXR bursts. Hence, an event with multiple peaks on 2004 November 3 was selected from RHESSI data, and the

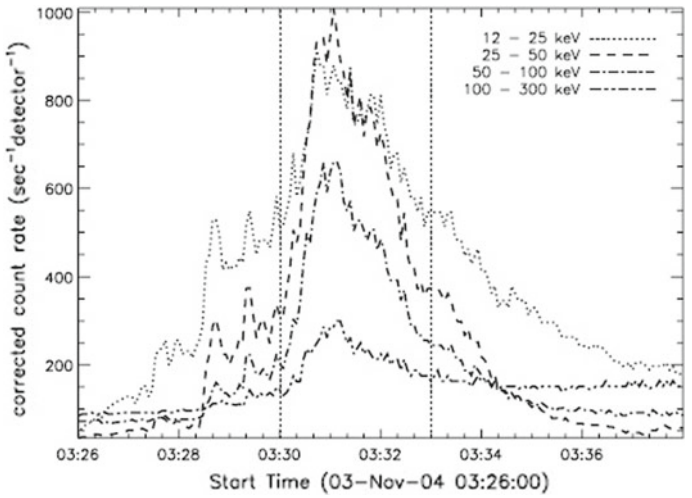

Fig. 5.7 The light curves on 2004 November 3 at different energies observed by RHESSI

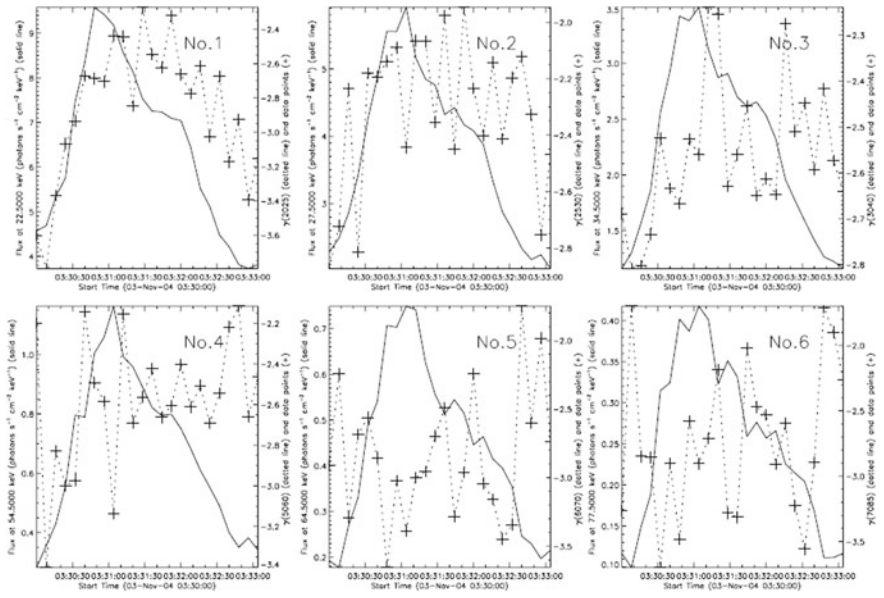

Fig. 5.8 The light curves and spectral evolution on 2004 November 3 at different energies

light curves at 12–25, 25–50, 50–100, and 100–300 keV are displayed in Fig. 5.7, two vertical lines mark the time interval for spectral analysis [23]. Due to enough photons in a larger range of energies and high-energy resolution of RHESSI, we can analyze the spectral evolution in different energies (with an energy interval of 5 keV in 20–85 keV). The standard code OSPEX has been used as mentioned before, to fit each energy interval with a single power-law, as shown in Fig. 5.8, in which the light curves at the central energy of each intervals are shown by solid lines, while the spectral indices are marked by plus and connected by dashed lines, and Fig. 5.9 gives the analysis of the correlation between the light curve and spectral evolution.

In lower energies (the first and second panels of 20–25 keV and 25–30 keV in Figs. 5.8, 5.9), the absolute value of spectral index is inversely correlated with photon flux with correlation coefficients of –0.659 and –0.472, respectively, which just means a common soft-hard-soft pattern in these lower energies. With increasing of photon energies, the correlation is gradually weakened to 0.250 and 0.080 in 30–40 keV and 50–60 keV (the moderate energies), respectively, and finally, the correlation is reversed to a positive one in higher energies of 60–70 keV and 70–85 keV, with correlation coefficients of 0.497 and 0.416, respectively, which means a new pattern of HSH appeared only in higher energies. It is noticed that such a new pattern not only exists in the overall burst, but also in each sub-peak as shown in Fig. 5.8, which is consistent with the spectral evolution of one MW burst in Fig. 3.53. The difference of MW and HXR is that the overall evolution of MW burst keeps the common SHH

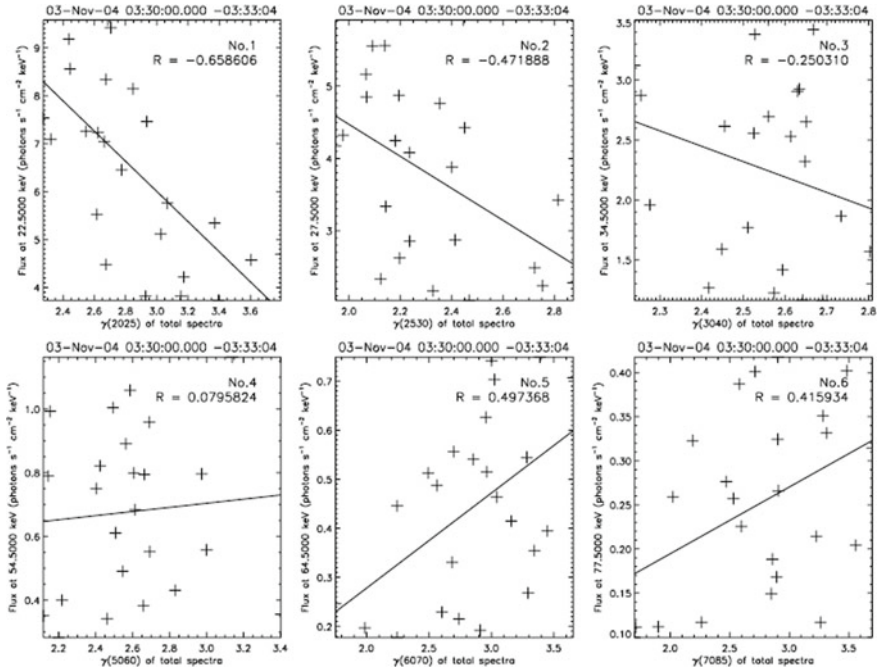

Fig. 5.9 The correlation of photon flux and spectral index on 2004 November 3 at different energies

pattern, but the overall evolution of HXR burst is also reversed to the new pattern of HSH.

One explanation for the HSH pattern in HXR bursts was suggested by the return current [23], which means that due to the collision of precipitating electrons and dense plasma in photosphere, a part of them are thermalized, and another part returns back to corona to form the return current [29]. The theoretical calculations show that the spectrum in lower energies is softened, while the spectrum in higher energies is hardened, and because the return current is positively proportional to the injected electrons, the SHS and HSH patterns are respectively appear in lower and higher energies, which is just consistent with the observed energy dependence of spectral evolution given in Figs. 5.8 and 5.9. Actually, some other mechanisms can also explain these results, such as the trapping effect as mentioned in Sect. 3.4.

5.5 Evolution of HXR Spectra in Dependence of Energies

The energy dependence of spectral evolution exists in HXR bursts, while the frequency dependence of spectral evolution in MW bursts is introduced in Sect. 3.3, we select two events with both HXR and MW data to prove the university of energy

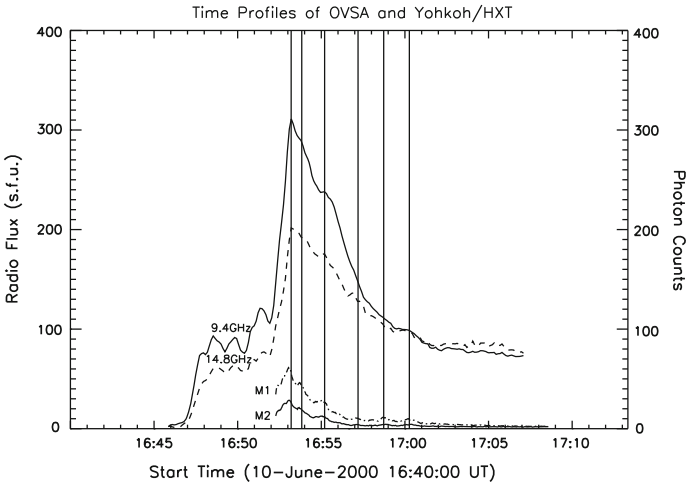

Fig. 5.10 Light curves of simultaneous observations of Yohkoh and OVSA in 2000 June 10

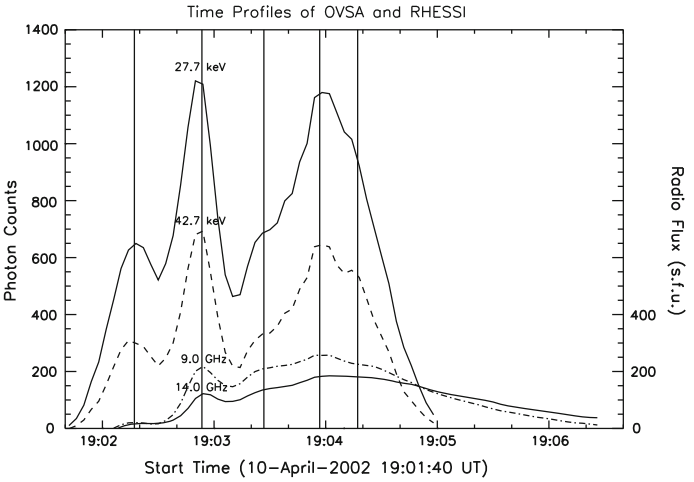

Fig. 5.11 Light curves of simultaneous observations of Yohkoh and OVSA in 2002 April 10

and frequency dependence [30]. The MW bursts in 2000 June 10 and 2002 April 10 have been discussed in Sect. 3.4 (see Figs. 3.54 and 3.55), Fig. 5.10 gives the light curves of Yohkoh/HXT M1-M2 and OVSA 9.4–14.8 GHz, and Fig. 5.11 gives the light curves of RHESSI 27.7–42.7 keV and OVSA 9–14 GHz, the vertical lines in Figs. 5.10 and 5.11 mark the peak times in both HXR and MW bursts.

The upper and bottom panels on the left side of Fig. 5.12 give the light curve in Yohkoh/M1 channel and the spectral index calculated by the data of Yohkoh/M1-M2

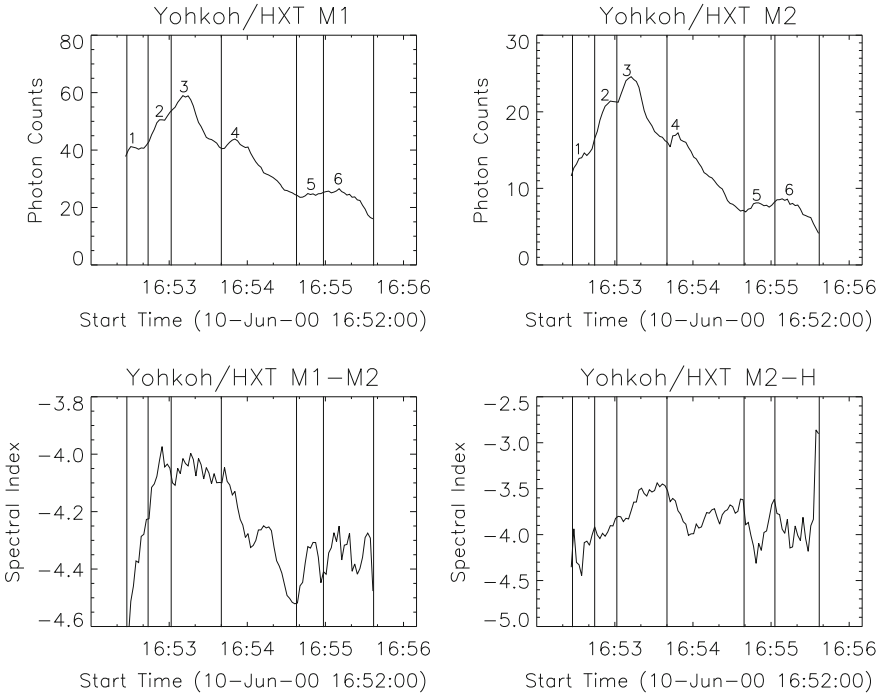

Fig. 5.12 Light curves and spectral evolution of Yohkoh/HXT at different energies in 2000 June 10

(lower energies) channels, while the right side of Fig. 5.12 corresponds to the light curve at M2 and index of M2-H at higher energies.

It is found from Fig. 5.12 that there is evidently a positive correlation between the light curve of Yohkoh/M1 and spectral index of Yohkoh/M1-M2 (lower energies), with a correlation coefficient of 0.41 and the confidence of 0.99, which means that the common SHS pattern exists in lower energies. Meanwhile, a negative correlation appears between the light curve of Yohkoh/M2 and spectral index of M2-H (higher energies), with a correlation coefficient of –0.19 and confidence of 0.95, which supports the HSH pattern in higher energies, and there are totally 96 temporal points in this event.

Second event was observed by RHESSI satellite on 2002 April 10. The upper and bottom panels on the left side of Fig. 5.13 give the light curve in 22.7–32.7 keV (with a central energy of 27.7 keV), and the spectral index calculated by the data of 27.7–42.7 keV (lower energies), while the right side of Fig. 5.13 corresponds to the light curve at 32.7–52.7 keV (with a central energy of 42.7 keV), and index of 42.7–72.8 keV (higher energies). All the selection of energies is consistent with four Yohkoh/HXT channels for the compatibility of two events.

The result in Fig. 5.13 is well consistent with that in Fig. 5.12, a positive correlation between the light curve and spectral evolution is satisfied in lower energies, while it

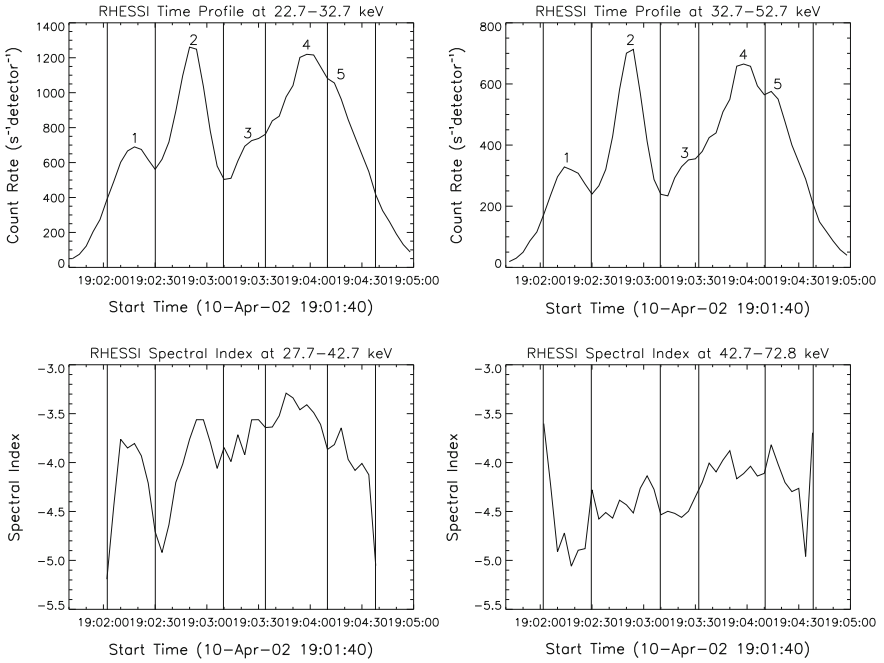

Fig. 5.13 Light curves and spectral evolution of Yohkoh/HXT at different energies in 2002 April 10

becomes a negative one in higher energies, with the correlation coefficient of 0.59 and –0.19, and the confidence of 0.99 and 0.95 under 45 samples, respectively.

One possible mechanism to explain the HSH pattern of HXR and MW spectral evolution is mentioned in Sect. 3.3, which requires a quasiperiodic projection of NT electrons into flaring loops appeared as multiple peaks in light curves. For MW spectral evolution, a hardened spectrum of trapping electrons becomes softer during a new ejection, and it is hardened again when the injection is finished, such a process forms the HSH pattern and repeats in each ejection, while the overall spectral evolution still keeps original SHS or SHH pattern, which is determined by the particle acceleration plus trapping effect. For HXR spectral evolution, the return current may form the SHS pattern in lower energies and HSH pattern in high energies of NT electron as well as the photon spectra, actually, similar effect includes albedo (see the diagnosis of lower energy cutoff in Sect. 6), because the strongest albedo occurs in 30–40 keV [31], which causes the photons with a single power-law to increase in these energies, which becomes a double power-law, i.e., the SHS pattern in lower energies and HSH pattern in higher energies, similar to the return current.

It is better to select the same mechanism to explain both of HXR and MW spectral evolutions, which are contributed by the NT electrons accelerated in the same flare, and the trapping effect can play an important role in both of HXR and MW bands. In

reference 32, the trapping plus precipitating model has been calculated based on the Fokker–Planck equation especially for the perpendicular injection of NT electrons with a stronger trapping effect, which causes an evident time delay between the HXR spectral evolution in lower and higher energies, and the spectral evolution in higher energies becomes synchronous with the MW one, and HSH pattern appeared in both of them, while the common SHS pattern exists in HXR spectral evolution of lower energies.

5.6 Evolution of HXR Spectra in Dependence of Locations

One limb event [33] on 2003 October 24 was used to analyze the MW spectral evolution in different parts of flaring loop (see Fig.A.3. in Appendix A), which also includes the HXR data observed by RHESSI, Fig. 5.14 shows the light curves at 12–25, 25–50, and 50–100 keV, in which each vertical line marks the peak time in each sub-peak, and followed by Figs. 5.15, 5.16, and 5.17 with the light curves, spectral evolutions, and correlations in different energies of photons (12.5–32.5, 32.5–52.5, 52.5–72.5, and 72.5–97.5 keV) of one LT and two FPs as marked in Fig.A.3.

At first, in spite of LT and FPs, the HXR spectral evolution always from a positive correlation (SHS) in lower energies gradually turns to a negative correlation (HSH) in higher energies, and all the correlations satisfy a confidence above 0.95 under the given samples, which strongly supports that the energy dependence of HXR spectral evolution is definitely a universal rule.

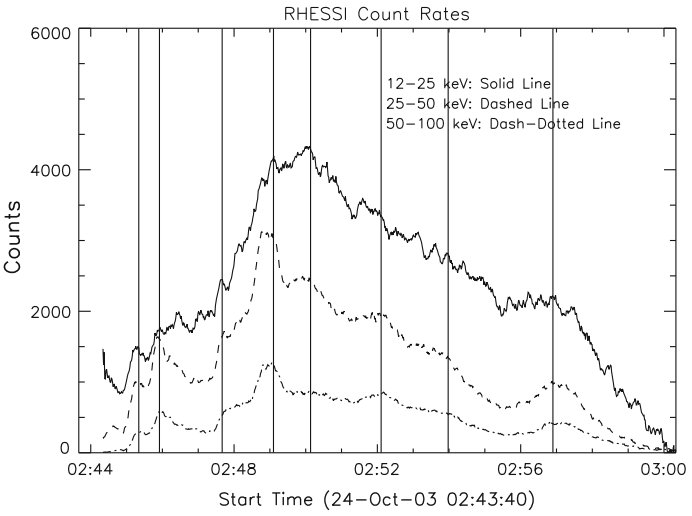

Fig. 5.14 Light curves at different energies in 2003 October 24 observed by RHESSI

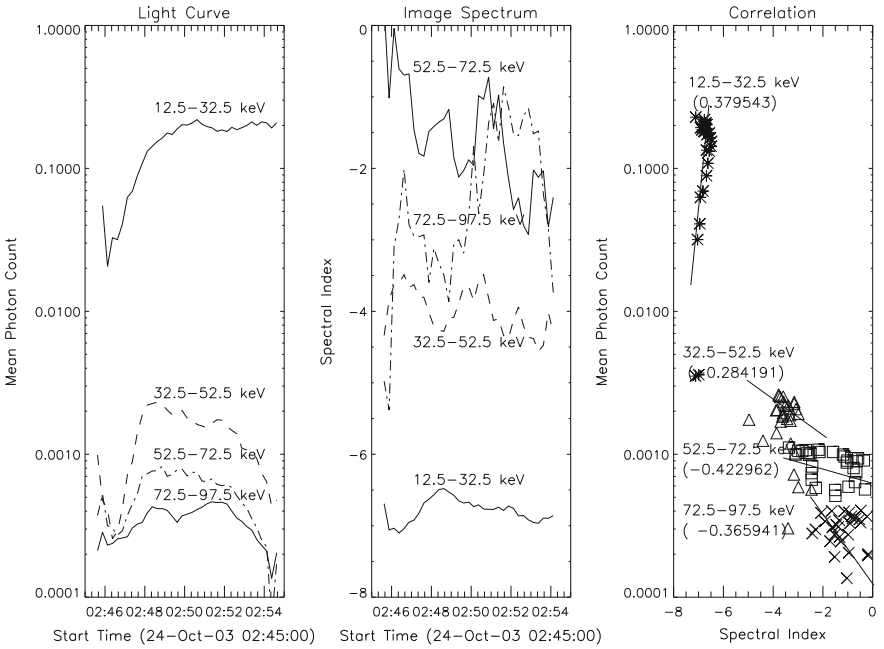

Fig. 5.15 Light curves, spectral evolution, and correlation at different energies in the LT on 2003 October 24 observed by RHESSI

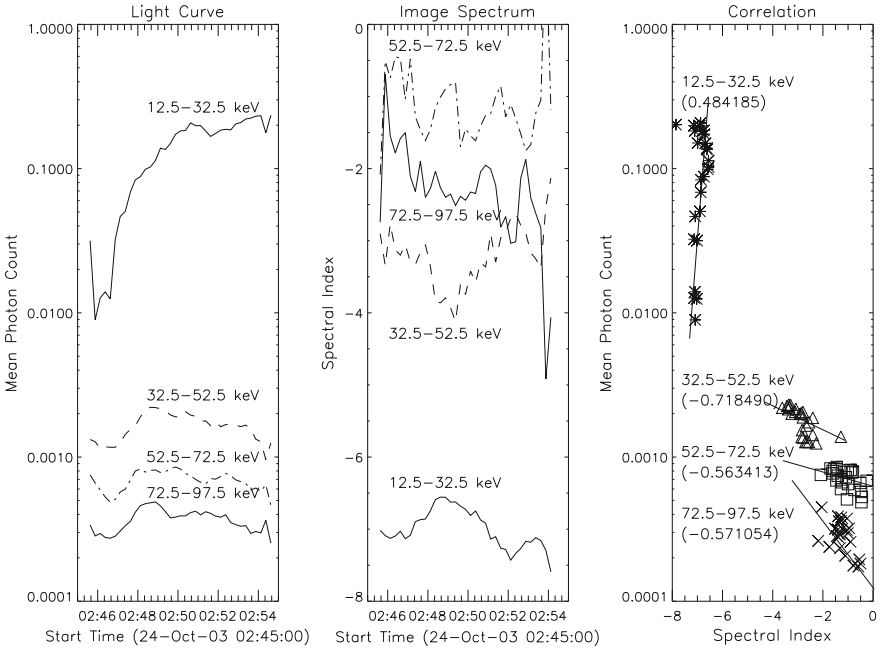

Fig. 5.16 Light curves, spectral evolution, and correlation at different energies in the FP1 on 2003 October 24 observed by RHESSI

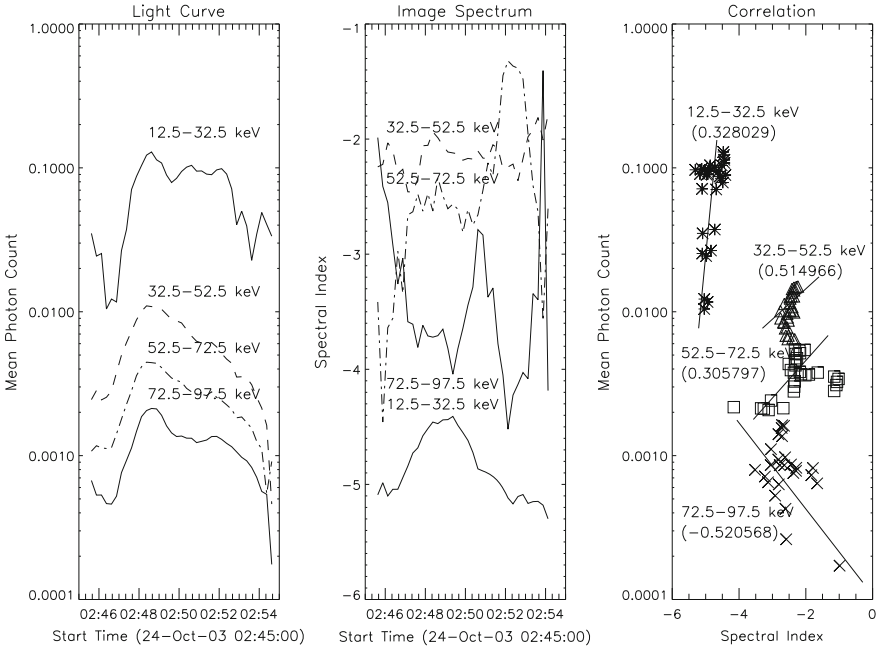

Fig. 5.17 Light curves, spectral evolution, and correlation at different energies in the FP2 on 2003 October 24 observed by RHESSI

Further analysis shows that the reversal from SHS to HSH at the LT and FP1 always happens above 32.5 keV, while for FP2, it happens only at the highest energy interval (72.5–97.5 keV), which just means that the trapping effect is evidently stronger in LT and FP1 in comparison with FP2. Here, we may see Fig. A.4 in Appendix A, the Trace image with higher spatial resolution, which shows a multiple-loop system, FP1 is brightened by the collision of a huge loop and a compact loop, and actually located on the top of compact loop, which well explains the reason why the trapping effect is stronger in FP1.

5.7 Asymmetry of HXR Brightness in Flaring Loop Feet

It is well known that the MW and HXR emissions in the FPs of flaring loops are respectively contributed to the GS and bremsstrahlung mechanisms from the trapping and precipitating electrons, and the brightness of FPs is determined by the density of NT electrons in FPs. Earlier studies on the asymmetry of radiation in two FPs were concentrated in HXR band, and generally considered the asymmetry of magnetic field in two FPs as the explanation for the asymmetry of radiation in two FPs, i.e., the FP with a stronger magnetic field will reflect more electrons before they reach the

FP, and thus to decrease the intensity of brightness of radiation. For example, most observations of Yohkoh/HXT support this opinion [34–36], but the observations opposite to the prediction of magnetic mirroring effect still existed [34–37], and more detailed studies found some complicated asymmetry in two FPs varied with time and energy, such as the decreasing of asymmetry with increasing of energy even reversed [38, 39]. Meanwhile, there were less studies on the asymmetry of two FPs in MW band, here it should be mentioned that a series of statistics of NoRH [40, 41], most of which were temporally and spatially coincident with the observations of Yohkoh/HXT. It is interesting that most of the events have a double-loop or multiple-loop structure, and it is commonly composed of a compact loop located nearby one FP of a huge loop with stronger magnetic field, stronger HXR emission was detected in FPs of the compact loop, while the MW emission appeared in the FP of huge loop with weaker magnetic field. All the results cannot be explained simply by the magnetic mirroring effect.

On the other hand, the observations of OVSA showed that the MW emission in FPs is closely associated with the pitch-angle distribution of NT electrons [42, 43], which supports a narrow distribution of the initial distribution of pitch-angle, rather than an isotropic one. In the theory of electron propagation of Sect. 4.2, the distributions of trapping and precipitating electrons are derived for a given initial pitch-angle [44]:

$$f_1 = C \sin\theta_0 \cos\theta_c \left(\frac{E}{E_0}\right)^{-\delta} \ln\left[\frac{\tan(\theta/2)}{\tan(\theta_c/2)}\right], \tag{5.1}$$

$$f_2 = C \cos\theta_0 \sin\theta_c \left(\frac{E}{E_0}\right)^{-\delta} \ln\left[\frac{\tan(\theta_c/2)}{\tan(\theta/2)}\right], \tag{5.2}$$

$$C = \frac{n}{\left(2\pi \frac{T}{m}\right)^{3/2} \ln\left(\frac{1}{\sin\theta_c}\right)}, \tag{5.3}$$

$$\sin\theta_c = \left(\frac{B_{min}}{B_{max}}\right)^{1/2}, \tag{5.4}$$

here, E_0 represents the normalized value of kinetic energy in the power-law distribution, and it is commonly taken as the thermal energy, T and m in the normalized constant Eq. (5.3) are respectively electron temperature and mass. It is found from Eqs. (5.1) and (5.2) that the trapping electrons increase with decreasing of θ_c (critical angle of magnetic mirror) and increasing of θ_0 (initial pitch-angle of NT electrons), while the precipitating electrons decrease with decreasing of θ_c and increasing of θ_0, which are all directly predictable in a magnetic mirror.

Figure 5.18 gives a carton of the asymmetric magnetic loop, in which the strong magnetic field line B_2 is naturally below the weaker magnetic field line B_1, and a

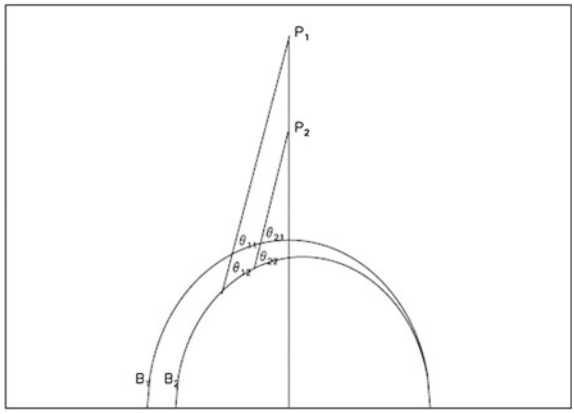

Fig. 5.18 A carton of asymmetric magnetic loop

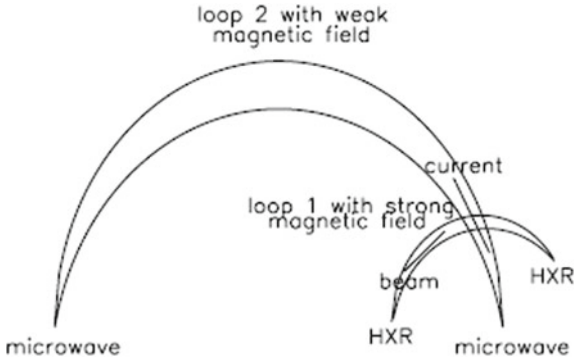

Fig. 5.19 A carton of collided loops

beam of NT electrons is ejected from the acceleration site P_1 or P_2 above the top of magnetic loop with two different initial pitch-angles.

It is obvious in Fig. 5.18 that for a given height of injection and initial pitch-angle, the incident angle in respect to the weaker magnetic field line B_1 is always larger than that to the stronger magnetic field line B_2, i.e., $\theta_{11} > \theta_{12}$, and $\theta_{21} > \theta_{22}$ as shown in Fig. 5.18, which causes more precipitating electrons in the stronger magnetic field line B_2, and just opposite to the result caused by the magnetic mirroring effect. It is noticed that it is more evident with increasing of the height of injection, and in most cases the acceleration site is a little above the LT of flaring loops, which is not enough to cancel the magnetic mirroring effect, but in less events, if the height of injection is much higher than the top of flaring loops, the effect of initial pitch-angle may produce an opposite result to the magnetic mirroring effect [44].

Figure 5.19 gives a carton of two collided loops with different scales, the huge loop has a weaker dipolar magnetic field, while the compact loop has a stronger dipolar magnetic field, the diamagnetic current (current sheet) produced by the collision will be perpendicular to the compact loop with stronger magnetic field, while the induced

electric field and accelerated electrons should be parallel to the compact loop with stronger magnetic field as shown by two line segments in Fig. 5.19, which means that the initial pitch-angle of NT electrons along the compact loop is much larger than that along the huge loop. Hence, the ratio of precipitating electrons along the two loops is:

$$r = \frac{\cos\theta_{01}\sin\theta_{c1}}{\cos\theta_{02}\sin\theta_{c2}} \tag{5.5}$$

It is assumed that the mirror ratios of two loops are different for 5-times, i.e., $\sin\theta_{c1}/\sin\theta_{c2} = 0.2$, which requires the opposite effect of initial pitch-angle is enough large, for instance, we select respectively 10° and 88° for the huge and compact loops, thus $\cos\theta_{01}/\cos\theta_{02} \ll 5.0$, it can be calculated from Eq. 5.5 that the density ratio of precipitating electrons in compact and huge loops is about 5.5, i.e., the intensity of X-ray emission in compact loop will be at least 5 times stronger than that in huge loop [44], which may explain the observations of NoRH [40, 41].

References

1. Aschwanden, M.J.: Physics of the Solar Corona. An Introduction. Chichester, UK, and Springer, Berlin: Published by Praxis Publishing Ltd (2004)
2. Dennis, B.R.: Solar hard X-ray bursts. Sol. Phys. **100**, 465–490 (1985)
3. Parks, G.K., Winckler, J.R.: Sixteen-second periodic pulsations observed in the correlated microwave and energetic X-Ray emission from a solar flare. Astrophys. J. **155**, L117–L120 (1969)
4. Kane, S.R., Anderson, K.A.: Spectral characteristics of impulsive solar-flare X-Rays ≤10 KeV. Astrophys. J. **162**, 1003–1018 (1970)
5. Benz, A.O.: Spectral features in solar hard X-ray and radio events and particle acceleration. Astrophys. J. **211**, 270–280 (1977)
6. Brown, J.C., Loran, J.M.: Possible evidence for stochastic acceleration of electrons in solar hard X-ray bursts observed by SMM. Mon. Not. R. Astron. Soc. **212**, 245–255 (1985)
7. Lin, R.P., Johns, C.M.: Two accelerated electron populations in the 1980 June 27 solar flare. Astrophys. J. Lett. **417**, L53–L56 (1993)
8. Fletcher, L., Hudson, H.S.: Spectral and spatial variations of flare hard X-ray footpoints. Sol. Phys. **210**, 307–321 (2002)
9. Hudson, H. S., Fárník, F.: Spectral variations of flare hard X-rays. In: A Wilson (ed.) Solar variability: from core to outer frontiers. The 10th European Solar Physics Meeting, 9-14 September 2002, Prague, Czech Republic. ESA SP-506, Noordwijk: ESA Publications Division, vol. 1, pp. 261–264 (2002)
10. Grigis, P.C., Benz, A.O.: The spectral evolution of impulsive solar X-ray flares. Astron. Astrophys. **426**, 1093–1101 (2004)
11. Grigis, P.C., Benz, A.O.: Spectral hardening in large solar flares. Astrophys. J. **683**, 1180–1191 (2008)
12. Frost, K.J., Dennis, B.R.: Evidence from hard X-Rays for two-stage particle acceleration in a solar flare. Astrophys. J. **165**, 655–659 (1971)
13. Cliver, E.W., Dennis, B.R., Kiplinger, A.L., Kane, S.R., Neidig, D.F., et al.: Solar gradual hard X-ray bursts and associated phenomena. Astrophys. J. **305**, 920–935 (1986)
14. Kiplinger, A.L.: Comparative studies of Hard X-Ray spectral evolution in solar flares with high-energy proton events observed at earth. Astrophys. J. **453**, 973–986 (1995)

15. Melnikov, V. F., Silva, A. V. R.: Temporal Evolution of Solar Flare Microwave and Hard X-Ray Spectra: Evidence for Electron Spectral Dynamics-II. In: Ramaty R, Mandzhavidze N (eds.), High Energy Solar Physics Workshop — Anticipating HESSI, ASP Conference Series, vol. 206, pp. 475–477 (2000)
16. Ning, Z.: Different behaviors between microwave and hard X-Ray spectral hardness in two solar flares. Astrophys. J. **671**, L197–L200 (2007)
17. Masuda, S., Kosugi, T., Hara, H., Tsuneta, S., Ogawara, Y.: A loop-top hard X-ray source in a compact solar flare as evidence for magnetic reconnection. Nature **371**, 495–497 (1994)
18. Petrosian, V., Donaghy, T.Q.: On the spatial distribution of hard X-Rays from solar flare loops. Astrophys. J. **527**, 945–957 (1999)
19. Petrosian, V., Donaghy, T.Q., McTiernan, J.M.: Loop top hard X-Ray emission in solar flares: images and statistics. Astrophys. J. **569**, 459–473 (2002)
20. Jiang, Y.W., Liu, S., Liu, W., Petrosian, V.: Evolution of the loop-top source of solar flares: heating and cooling processes. Astrophys. J. **638**, 1140–1153 (2006)
21. Battaglia, M., Benz, A.O.: Relations between concurrent hard X-ray sources in solar flares. Astron. Astrophys. **456**, 751–760 (2006)
22. Shao, C., Huang, G.: Comparative study of solar HXR flare spectra in looptop and footpoint sources. Astrophys. J. **691**, 299–305 (2009a)
23. Shao, C., Huang, G.: Hard-soft-hard flare spectra and their energy dependence in spectral evolution of a solar hard X-Ray flare. Astrophys. J. Lett. **694**, L162–L165 (2009)
24. Sui, L., Holman, G.D.: Evidence for the formation of a large-scale current sheet in a solar flare. Astrophys. J. **596**, L251–L254 (2003)
25. Melnikov, V.F., Shibasaki, K., Reznikova, V.E.: Loop-top nonthermal microwave source in extended solar flaring loops. Astrophys. J. **580**, L185–L188 (2002)
26. Petrosian, V., Liu, S.: Stochastic acceleration of electrons and protons. I. Acceleration by parallel-propagating waves. Astrophys. J. **610**, 550–571 (2004)
27. Liu, W., Jiang, Y.W., Petrosian, V., Metcalf, T.R.: A Statistical Study of Limb Flares Observed by RHESSI: Imaging. American Astronomical Society, SPD meeting, Bulletin of the American Astronomical Society **35**, 839 (2004)
28. Liu, W., Liu, S., Jiang, Y.W., Petrosian, V.: RHESSI observation of chromospheric evaporation. Astrophys. J. **649**, 1124–1139 (2006)
29. Zharkova, V.V., Gordovskyy, M.: The effect of the electric field induced by precipitating electron beams on hard X-Ray photon and mean electron spectra. Astrophys. J. **651**, 553–565 (2006)
30. Song, Q.W., Huang, G.L., Nakajima, H.: Co-analysis of solar microwave and hard X-Ray spectral evolutions. I. In two frequency or energy ranges. Astrophys. J. **734**, 113–124 (2011)
31. Bai, T., Ramaty, R.: Backscatter, anisotropy, and polarization of solar hard X-rays. Astrophys. J. **219**, 705–726 (1978)
32. Minoshima, T., Yokoyama, T., Mitani, N.: Comparative analysis of nonthermal emissions and electron transport in a solar flare. Astrophys. J. **673**, 598–610 (2008)
33. Huang, G.L., Li, J.P.: Co-analysis of solar microwave and hard X-Ray spectral evolutions. II. In three sources of a flaring loop. Astrophys. J. **740**, 46–56 (2011)
34. Sakao, T.: Characteristics of solar flare hard X-ray sources as revealed with the Hard X-ray Telescope aboard the Yohkoh satellite. Ph.D. thesis, University of Tokyo (1994)
35. Sakao, T., Kosugi, T., Masuda, S., Yaji, K., Inda-Koide, M., Makishima, K.: Characteristics of hard X-ray double sources in impulsive solar flares. Adv. Space Res. **17**, 67–70 (1996)
36. Aschwanden, M.J., Fletcher, L., Sakao, T., Kosugi, T., Hudson, H.: Deconvolution of directly precipitating and trap-precipitating electrons in solar flare hard X-Rays. III. Yohkoh hard X-Ray telescope data analysis. Astrophys. J. **517**, 977–989 (1999)
37. Asai, A., Shimojo, M., Isobe, H., Morimoto, T., Yokoyama, T., Shibasaki, K., Nakajima, H.: Periodic acceleration of electrons in the 1998 November 10 solar flare. Astrophys. J. **562**, L103–L106 (2001)
38. Siarkowski, M., Falewicz, R.: Variations of the hard X-ray footpoint asymmetry in a solar flare. Astron. Astrophys. **428**, 219–226 (2004)

39. Alexander, D., Metcalf, T.R.: Energy dependence of electron trapping in a solar flare. Sol. Phys. **210**, 323–340 (2002)
40. Hanaoka, Y.: Double-loop configuration of solar flares. Sol. Phys. **173**, 319–346 (1997)
41. Nishio, M., Yaji, K., Kosugi, T., Nakajima, H., Sakurai, T.: Magnetic field configuration in impulsive solar flares inferred from coaligned microwave/X-Ray images. Astrophys. J. **489**, 976–991 (1997)
42. Lee, J., Gary, D.E.: Solar microwave bursts and injection pitch-angle distribution of flare electrons. Astrophys. J. **543**, 457–471 (2000)
43. Gary, D.E., Hurford, G.J.: Coronal temperature, density, and magnetic field maps of a solar active region using the owens valley solar array. Astrophys. J. **420**, 903–912 (1994)
44. Huang, G.L.: Initial pitch-angle of narrowly beamed electrons injected into a magnetic mirror, formation of trapped and precipitating electron distribution, and asymmetry of hard X-ray and microwave footpoint emissions. N. Astron. **12**, 483–489 (2007)

Chapter 6
Diagnostics of Flaring Loop Parameters

6.1 Overview

With continuously deepened studies on flaring loops, the diagnostics of plasma parameters in flaring loops becomes an important topic based on matured theories and observations. In present condition of solar observations, we can not directly measure the plasma parameters in solar atmosphere, but can only use the observed EM waves and relevant theories to inverse these parameters. In general, these parameters can be divided into three groups, (1) ambient plasma parameters (magnetic field, density, and temperature), (2) the density, spectral index, and energy (lower and higher limits) of charged particles (especially the NT electrons to produce radio and X-ray bursts), and (3) the properties of EM (frequency, wavelength, and phase speed). Actually, the observing frequency is known, and thus the wavelength or phase speed can be obtained from the plasma dispersion relation.

The energy of solar activities is originated from the magnetic field in solar atmosphere, so far we can only measure the photospheric magnetic field by the Zeeman splitting of the optical line emissions in solar photosphere. However, in solar corona, i.e., the main source to produce flares, CMEs, and other solar activities, the plasma density rarefies to weaken the optical line emissions, which make us almost impossible to acquire the message of coronal magnetic field from the line emissions in corona. Meanwhile, radio emissions becomes the only window for observing the different heights of corona, in which GS, cyclotron resonance, and cyclotron maser and absorption are closely related to the magnetic field in radio sources, and thus we possibly obtain the knowledge about coronal magnetic field.

The famous solar radio physicist Kundu reviewed the diagnostics of the magnetic field in active regions above chromosphere with the polarization at centimeter band, the coronal magnetic field above active regions by the cyclotron resonance in MW band, and the coronal magnetic field by cyclotron line emission etc. [1]. There were also some studies on the diagnosis of magnetic field by the nonuniform GS emissions distributed in flaring loops [2–4], the measurements of magnetic field in corona and

G. Huang et al., *Solar Flare Loops: Observations and Interpretations*,
https://doi.org/10.1007/978-981-10-2869-4_6

chromosphere by the intensity and polarization of GS emissions produced by free-free mechanism [5], and the coronal magnetogram deduced from the GS emissions transversely passing the coronal magnetic field [6]. In addition, there were a lot of studies on radio fine structures and their theories to inverse the local magnetic field that not mentioned here. The late review papers about radio diagnosis of coronal magnetic field were written by Gary and Keller [7]. Based on the approximately fitted emissivity and absorption coefficient of GS emission by Dulk and Marsh [8], Zhou and Karlický [9] proposed an analytical expression to calculate the magnetic field and NT electron density in the GS burst sources with the observable radio flux density, spectral index, and turnover frequency. More recently, Huang [10, 11] suggested to include the polarization measurement of GS emissions for uniquely calculating the view angle between magnetic field and GS emissions, thus to obtain the transverse and perpendicular components of local magnetic field in the GS burst sources.

The radio diagnosis of coronal magnetic field depends on the instruments, which are roughly divided into two kinds: dynamic spectrograph and heliograph for radio images. The spectrograph has no spatial resolution, but has high time and frequency resolutions, it is possible to obtain the time variation of local magnetic field and to estimate the height of radio source by the corresponding relationship between radio frequency and magnetic field, while the heliograph can obtain 2D magnetogram. Therefore, it is predicted 3D diagnosis of coronal magnetic field with the newly developed radio heliograph in multiple frequencies.

Energetic particles accelerated in flares or CMEs take a definite proportion of the magnetic energy release in solar atmosphere. Hence, the diagnosis of energetic particles is necessary for the studies on particle acceleration and magnetic reconnection. The HXR and MW emissions are originated from the same NT electrons, but respectively belong to precipitating and trapping components [12]. As the dominated mechanism of MW emission, GS theory is related to a lot of parameters of ambient plasma and NT electrons, Huang et al. (2005) found that the spectral index of MW emission is determined by the ratio of MW intensities at two adjacent frequencies, but independent from the electron density, the ambient plasma density and temperature, and propagational angle, thus the local magnetic field, electron spectral index, and lower-energy cutoff are key parameters [13]. If the approximation of dipolar magnetic field is accepted, under the condition of that the magnetic field in photosphere is known [14], we only need to calculate the spectral index and lower-energy cutoff of NT electrons. When the double power-law of MW emission is obtained by OVSA with high frequency resolution, the spectral index and lower-energy cutoff of NT electrons can be calculated self-consistently, and compared with the HXR diagnosis [15].

6.2 Diagnosis of Coronal Magnetic Field and Non-thermal Electron Density

6.2.1 Diagnosis Method

6.2.1.1 Method 1

Considering the approximations of Dulk and Marsh [9] for the GS emission in a uniform magnetic field (with electron spectral index of 2–7, harmonic number of 10–100, propagational angle of 20–80 degrees, and a fixed lower-energy cutoff of 10 keV, the fitting error is about 26% for the emissivity and absorption coefficient), Zhou and Karlický [8] deduced two expressions for the magnetic field and NT electron density at a given view angle from the observable MW spectral index (to deduce the electron spectral index), brightness temperature or radio flux density, and turnover frequency, in which two equations of the brightness temperature in optical-thin part, and the optical thickness at turnover frequency are used in the derivation [8]:

$$T_{b\nu} \approx \frac{c^2}{k_B \nu^2} \eta_\nu L \qquad (\tau \ll 1), \tag{6.2.1}$$

$$\tau_{\nu_p} = \kappa_{\nu_p} L \approx 1, \tag{6.2.2}$$

here, $T_{b\nu}$ is the brightness temperature at a given frequency ν, L is the scale of radio source along the view (propagational) angle, τ_{ν_p} is the optical thickness at turnover frequency ν_p, the emissivity η_ν and absorption coefficient κ_ν at a given frequency ν are respectively [9]

$$\frac{\eta_\nu}{BN} \approx 3.3 \times 10^{-24-0.52\delta} (\sin\vartheta)^{-0.43+0.65\delta} \left(\frac{\nu}{\nu_B}\right)^{1.22-0.90\delta}, \tag{6.2.3}$$

$$\frac{\kappa_\nu}{BN} \approx 1.4 \times 10^{-9-0.22\delta} (\sin\vartheta)^{-0.09+0.72\delta} \left(\frac{\nu}{\nu_B}\right)^{-1.30-0.98\delta}, \tag{6.2.4}$$

in which B is the local magnetic field in radio source, c is the speed of light in vacuum, k_B is Boltzman constant, NT electron density N is obtained by the integration of a single power-law distribution above the lower-energy cutoff E_0, δ is the spectral index of NT electrons, ϑ is the angle between magnetic field and LOS, the electron gyrofrequency is defined as $\nu_B = 2.8 \times 10^6 B$ (Hz). Substitute Eqs. (6.2.3) and (6.2.4) into Eqs. (6.2.1) and (6.2.2), and take the logarithm in the two sides [10]

$$-(0.30+0.98\delta)\log\left(\frac{\nu}{\nu_B}\right)+\log(NL)=2.41+0.22\delta+$$

$$+(0.09-0.72\delta)\log(\sin\vartheta)+(1.30+0.98\delta)\log\nu_p-(0.30+0.98\delta)\log\nu, \tag{6.2.5}$$

$$(0.22+0.90\delta)\log\left(\frac{\nu}{\nu_B}\right)+\log(NL)=-6.89+0.52\delta+$$

$$+(0.43-0.65\delta)\log(\sin\vartheta)+\log T_{b\nu}+\log\nu. \tag{6.2.6}$$

Furthermore, Eqs. (6.2.5) and (6.2.6) are solved together with the polarization degree r_c of GS emission [9]:

$$r_c=1.26\times10^{0.035\delta-0.071\cos\vartheta}\left(\frac{\nu}{\nu_B}\right)^{0.782-0.545\cos\vartheta}. \tag{6.2.7}$$

Three equations are deduced to calculate B, NL (column density of NT electrons), and ϑ with the observable $T_{b\nu}$, r_c, ν_p, and spectral index α of MW emission (the electron spectral index $\delta\approx(1.22-\alpha)/0.9$) [10]. After $\log(NL)$ is removed from Eqs. (6.2.5) and (6.2.6), it is ready to derive an equation of B (ν_B) and ϑ ($\cos\vartheta$):

$$\log\left(\frac{\nu}{\nu_B}\right)=\frac{A_1+0.5A_2\log(1-x^2)}{A_3}, \tag{6.2.8}$$

while another equation of B and ϑ is rewritten by Eq. (6.2.7):

$$\log\left(\frac{\nu}{\nu_B}\right)=\frac{A_4-0.071x}{0.782-0.545x}. \tag{6.2.9}$$

Finally, $\log\left(\frac{\nu}{\nu_B}\right)$ (the only term including B) in Eqs. (6.2.8) and (6.2.9) can be removed, and to deduce a nonlinear equation [16] of ϑ:

$$0.782A_1-A_3A_4+(0.071A_3-0.545A_1)x+0.5A_2(0.782-0.545x)\log(1-x^2)=0, \tag{6.2.10}$$

$$A_1=-9.30+0.30\delta+(1.30+0.98\delta)\log\left(\frac{\nu}{\nu_p}\right)+\log T_{b\nu}, \tag{6.2.11}$$

$$A_2=0.34+0.07\delta, \tag{6.2.12}$$

$$A_3=0.52+0.08\delta, \tag{6.2.13}$$

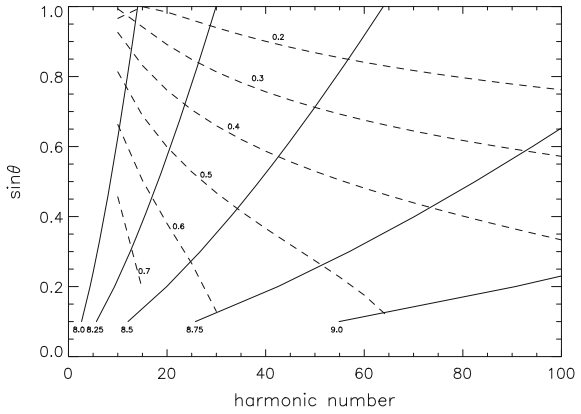

Fig. 6.1 One example to calculate B and ϑ based on Dulk and Marsh's approximations

$$A_4 = 0.10 + 0.035\delta - \log r_c. \tag{6.2.14}$$

It is obvious that the coefficients in Eqs. (6.2.11)–(6.2.14) are determined by the observable values, Fig. 6.1 gives one example to calculate B and ϑ from Eqs. (6.2.5) and (6.2.7) [10], in which $\delta = 3.0$, $\frac{\nu}{\nu_p} = 2.0$, and $\log T_{b\nu} = 8.0, 8.25, 8.5, 8.75, 9.0$. From abscissa and ordinate corresponding to the cross point of different contours of $T_{b\nu}$ and r_c in Fig. 6.1, the harmonic number (i.e., the ratio between ν and ν_B, for calculating B) and ϑ can be obtained uniquely.

It is also obtained uniquely that the solution of ϑ in Eq. (6.2.10) under a group of typical parameters $r_c = 0.4, 0.5, 0.6$, $T_{b\nu} = 0.8\times\ 10^6\,\mathrm{K}$, $1.0\times\ 10^6\,\mathrm{K}$, $1.2\times\ 10^6\,\mathrm{K}$, $\nu_p = 4.0, 5.0, 6.0\,\mathrm{GHz}$, and $\delta = -2.5, -3.0, -3.5$ as shown in Sect. 3.5.5 (see Fig. 3.62) [16]. Substitute the solution of ϑ into Eq. (6.2.8) or (6.2.9), it is ready to calculate the transverse and perpendicular components of B, and finally we can obtain NL from Eq. (6.2.5) or (6.2.6). The advantage of this method is the analytical solutions of B, ϑ, and NL can be calculated uniquely from the observable values. However, under the Dulk and Marsh's approximations, the solutions of B, ϑ, and NL can be only obtained in a limited range of observed parameters.

6.2.1.2 Method 2

The theory of Ramaty [17] is widely used to calculate the GS emission in a uniform magnetic field. As shown by Fig. 2.26 in Sect. 2.5 that the calculated spectral index in optically thin part is not sensitive to the ambient plasma density and temperature, propagation angle, lower-energy and higher-energy cutoffs of NT electrons. The only sensitive parameters are the local magnetic field and electron spectral index, which has been confirmed by another calculation [13], because the spectral index depends on the ratio of GS emission at two adjacent frequencies, depending on the same parameters of ambient plasma and NT electrons. In principle, we can fix all the insensitive parameters, to inverse the local magnetic field and electron spectral

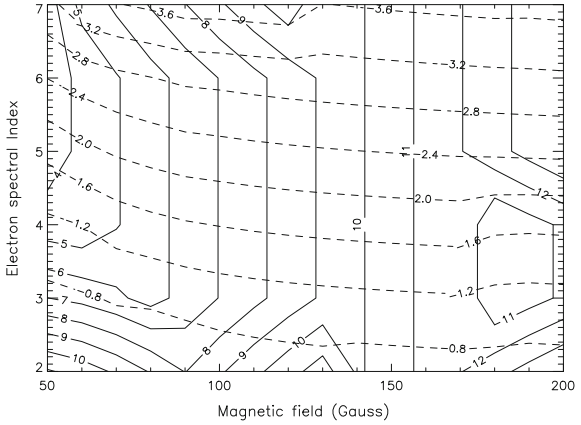

Fig. 6.2 One example to calculate magnetic field and electron spectral index uniquely by turnover frequency and single power-law index in MW bursts

index uniquely from the observed double power-law in MW bursts, the problem is the uncertainty in the division of double power-law, so that we can use the turnover frequency and single power-law instead of double power-law. It is shown in Fig. 2.27 that the turnover is not sensitive to most relevant parameters except the local magnetic field strength. Hence, we can use the observable turnover frequency and single power-law index to calculate the local magnetic field and electron spectral index uniquely as shown by one example in Fig. 6.2.

It is shown in Fig. 2.25 in Sect. 2.5 that the MW flux is sensitive to the local magnetic field, propagation angle, NT electron density and spectral index, so that after we obtain the local magnetic field and electron spectral index from the turnover frequency and single power-law index, we can do further diagnosis of the propagational angle and density of NT electrons from the observable MW fluxes at two frequencies.

6.2.2 Sudden Change of Transverse Coronal Magnetic Component Around Magnetic Neutral Line

Using the method under the Dulk's approximations as mentioned in Sect. 6.2.1, we calculated the transverse and longitudinal magnetic components in an event observed simultaneously by NoRH, RHESSI, and SOHO on November 1, 2004 [11], and we set all transverse magnetic fields to point to the right direction (to the west), the positive longitudinal magnetic field is set to point upward (to the north), and the negative longitudinal magnetic field is set to point downward (to the south), thus to form a "quasi 2D vector magnetogram" overlaid on the SOHO/MDI magnetogram together with the 25–50 keV contours of RHESSI in Fig. 6.3, in which the locations of LT and FPs, as well as the region along magnetic neutral line are marked.

Meanwhile we can obtain 2D distribution of NT electron density in Fig. 6.4, in which the solid contours refer to the NT electron density, the dashed contours are the

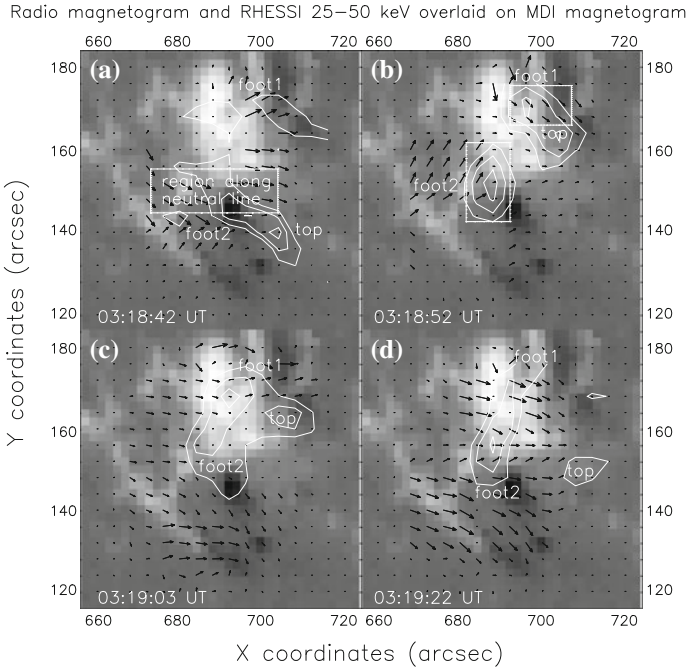

Fig. 6.3 Calculated "quasi 2D vector magnetogram" on 2004 November 1

spectral index calculated by the 17 and 34 GHz brightness temperatures of NoRH, and the background is the 25–50 keV image of RHESSI. It is obvious that the NT electron density concentrated to the LT during the maximum phase (panel c), while the spectral index in LT is harder than that in FPs.

Now we can obtain the time variations of two magnetic components in different locations of flaring loop in this event, as shown in Fig. 6.5, in which the left panel gives the averaged longitudinal magnetic field in two FPs (solid in FP2 and dashed in FP1) and view angle (dot-dashed in FP2 and dot-dot-dashed in FP1), and in the right panel the solid line is the brightness temperature at 17 GHz, dashed and dot-dashed are respectively the averaged transverse magnetic field in the region along the magnetic neutral line and all burst source.

It can be seen from the left panel of Fig. 6.5 that the opposite polarities of longitudinal magnetic field in FP1 and FP2 are respectively negative and positive, in consistency with the polarities of photosphere measurement by SOHO/MDI. The longitudinal magnetic field in FP2 increases from small to large then return to small during the flare, while the absolute value of negative one continuously increases from small to large then saturates in FP1. It is most interesting that the transverse magnetic component the region along the magnetic neutral line has a sudden change in seconds of rising phase with respect to the first peak of RHESSI at 25–50 keV, and the fastest decreased time of magnetic shear angle in this event [18], the variation

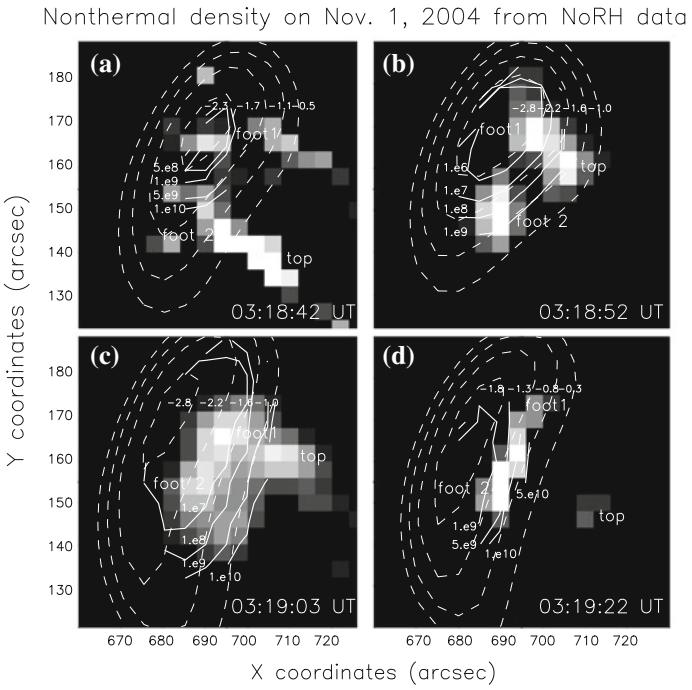

Fig. 6.4 Calculated 2D distribution of NT electron density on November 1, 2004

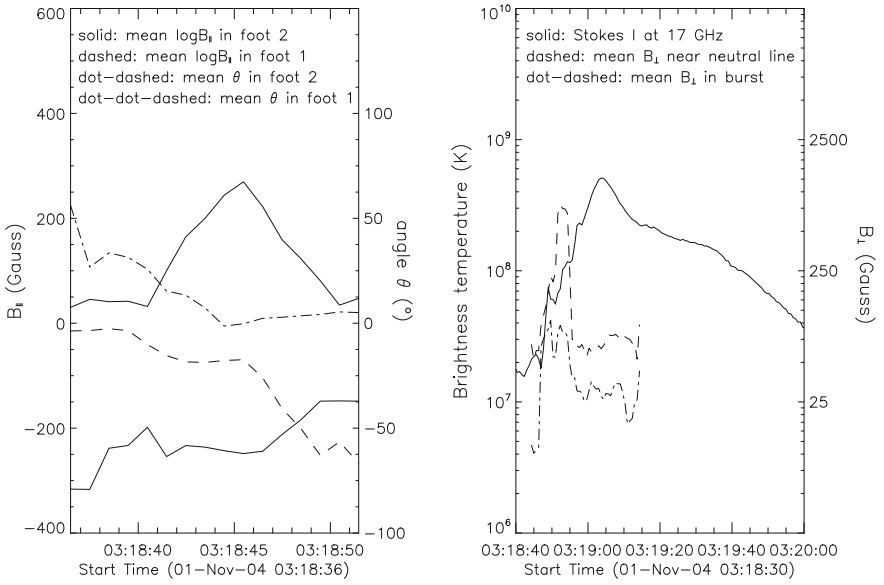

Fig. 6.5 Time profiles of transverse and longitudinal magnetic components in different locations of flaring loop on 2004 November 1

in the region along the magnetic neutral line is over one order of magnitude (from several tens to thousand Gauss), while the variation in total source is only around ten Gauss, which supports the prediction that the flare energy release mainly depends on the transverse component, and the variation of shear angle is also an important signature for the magnetic reconnection.

6.2.3 Attenuation of Coronal Magnetic Field in Solar MW Bursts

6.2.3.1 Background and Data Selection

The variation of transverse magnetic energy becomes a hot topic in recent studies of photospheric magnetograms. For instance, Wang et al. (2012) provided a remarkably clear example of rapid flux emergence to show an increase in the transverse fields in the middle of the loop [19]. The back reaction of Lorentz forces on the photosphere and solar interior may be caused by the coronal field evolution required to release flare energy resulting in the magnetic field of the photosphere becoming more horizontal [20–22].

One event in October 23, 2001 is selected in Fig. A.9 (Appendix A) to compare the radio diagnosis of coronal magnetic field with photospheric results as mentioned above [23]. Two flare ribbons observed by Trace 171 Å in October 23, 2001 are overlaid by the SOHO/MDI contours with opposite magnetic polarities (solid for positive and dashed for negative), and the 17 GHz dot-dashed contours of brightness temperatures observed by NoRH around the peak time of the burst. Hence, we can locate the FPs in two compact areas with strong EUV emissions, in which the Trace image is about 40 s after the peak time of burst, while the MDI magnetogram is about 17 min before the peak time of the burst.

The time profiles of brightness temperatures at 17 and 34 GHz, the polarization degree at 17 GHz, and the spectral index calculated from the 17 and 34 GHz emissions are given in Fig. 6.6a–d, respectively in the LT (solid) and the two FPs (dashed and dot-dashed) of the October 23, 2001 flaring loop, in respect to the positions located in LT, FP1, and FP2 in Fig. A.9 (Appendix A). It is a complicated burst with multiple subpeaks of different timescales, so that a digital filter from the IDL routines was used to rule out some fast fluctuations, and to recognize clearly the overall evolutions of observed and calculated parameters in Fig. 6.6 and following figures.

The asymmetry is apparent in the two FP emissions; both the brightness temperature and polarization degree at 17 GHz in FP2 (dot-dashed line) are larger than those in FP1 (dashed line). The data of NoRH at 17 and 34 GHz are not enough to determine the exact turnover frequency for the radio diagnosis in this paper; and Fig. 6.7 gives the time evolutions of the radio flux of NoRP at six frequencies, the typical MW spectra at different phases of the burst, the spectral index of the optically

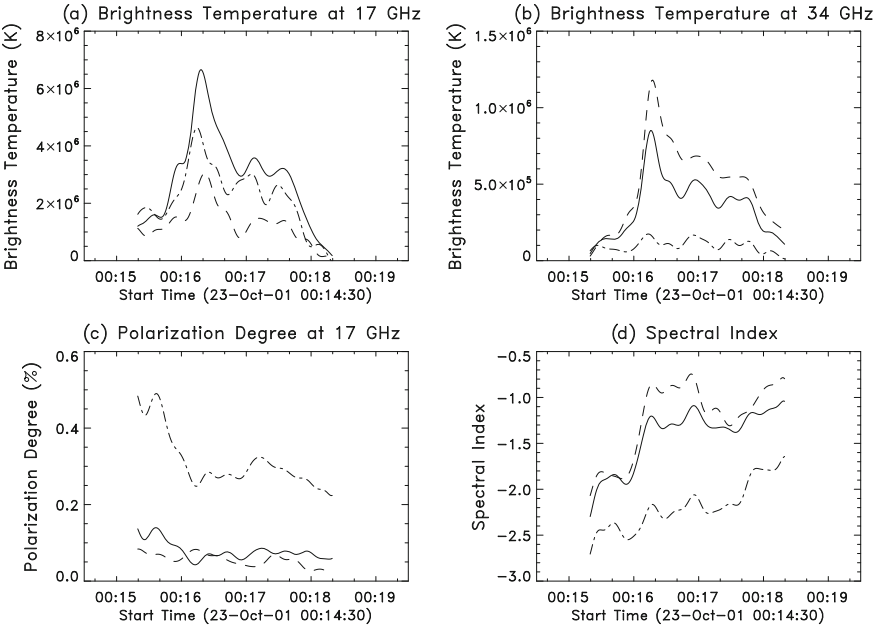

Fig. 6.6 Time profiles of **a** brightness temperature of NoRH 17 GHz, **b** brightness temperature of NoRH 34 GHz, and **c** polarization degree of 17 GHz, and **d** spectral index in 2001 October 23

thin part, and the turnover frequency, respectively, in which the turnover frequency is mostly below 10 GHz except in the maximum phase.

6.2.3.2 Radio Diagnosis

Using the method under the Dulk's approximations as mentioned in Sect. 6.2.1, we calculated first the minimum of Eq. (6.2.10), thus to obtain the propagational angle θ, the total magnetic field B_{total}, and the harmonic number (i.e., the ratio between the working frequency 17 GHz and calculated electron gyrofrequency), respectively in the LT (solid) and the two FPs (dashed and dot-dashed) of the October 23, 2001 flaring loop (Fig. 6.8), and further to obtain the transverse and longitudinal magnetic components, and the ratio between these two components, as well as the column density of NT electrons (Fig. 6.9).

The most important evolutionary behavior of B_{total} is that it decreases rapidly from the start time to the maximum time of burst and keeps low strength until the decay phase, and the total variation is up to one order of magnitude (from hundreds to tens Gauss), but this attenuation evidently does not appear in the FP1 source (dashed line in Fig. 6.8c) with very weak magnetic fields (less than 1 Gauss). Meanwhile, a similar attenuation of θ appears in the three sources from tens to about ten degrees, and due to the similar behavior of θ and B, the attenuation of the transverse magnetic component

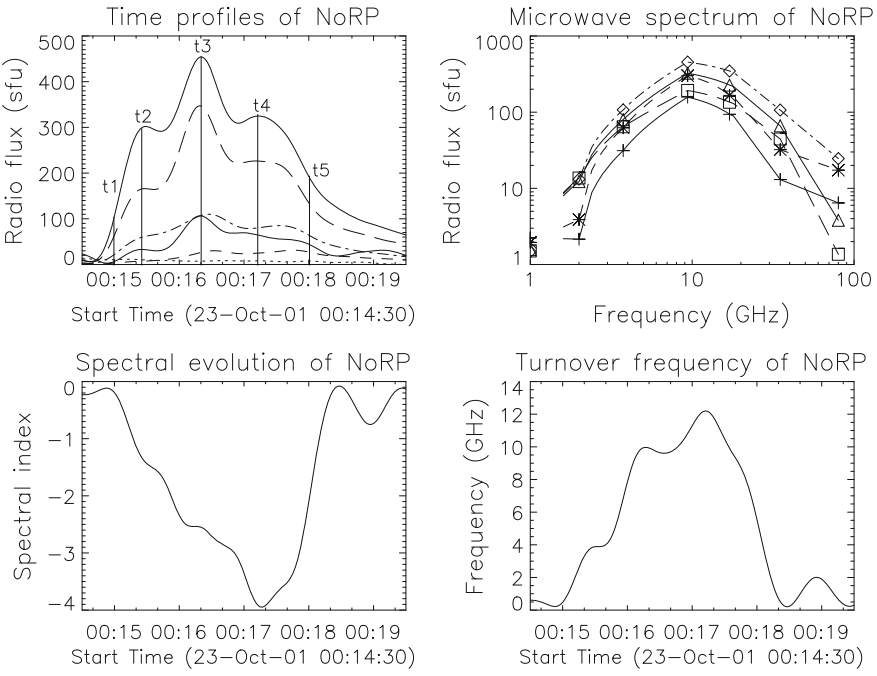

Fig. 6.7 Observations of NoRP in October 23, 2001

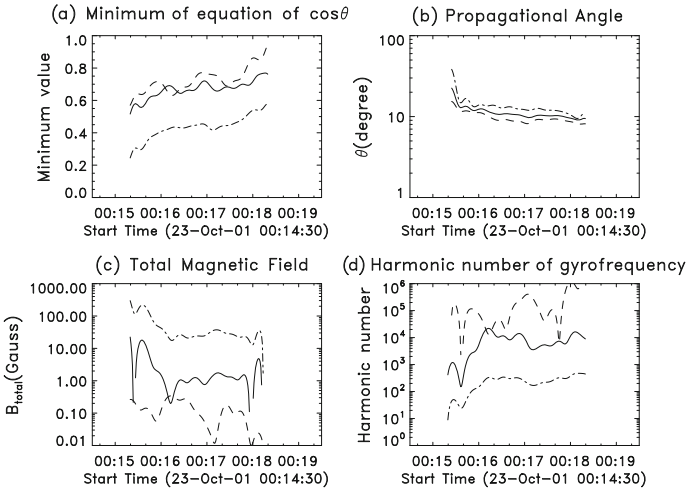

Fig. 6.8 Radio diagnosis of propagational angle and coronal magnetic field in 2001 October 23

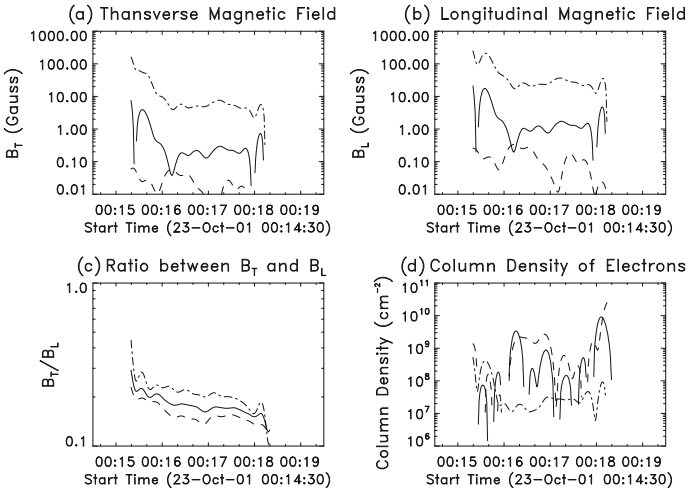

Fig. 6.9 The calculated **a** transverse and **b** longitudinal magnetic components, **c** the ratio between them, and **d** the column density of NT electrons in 2001 October 23

is more apparent than that of the longitudinal one, which is clearly shown by the ratio between the transverse and longitudinal magnetic components in Fig. 6.9c.

6.2.3.3 Discussions

Based on the magnetic energy release process in solar flares, it is not difficult to understand such an attenuation of the calculated magnetic field in a flaring loop. We can directly predict that the coronal magnetic field is inversely proportional to the brightness temperature or radio flux of solar MW bursts from an analytical expression when the other parameters do not change much as well as from some earlier calculations [24]. Therefore, this is probably a common behavior of coronal magnetic fields in solar flares. Even the time evolution of the total magnetic field and view angle is somehow similar to that in this paper, but their enhancement during the decay phase does not appear in the event of this paper, hence the coronal magnetic attenuation is an irreversible or permanent change for this event under investigation.

Moreover, the transverse magnetic attenuation in a flaring loop is more evident than that of longitudinal component due to the similar behavior of the total magnetic field and view angle, which is also consistent with our knowledge about the dependence of flare energy mainly on the transverse magnetic energy, as well as the recent studies about the magnetic field of the photosphere becoming more horizontal during flares [21]. The variation of the propagation angle from tens to about ten degrees during the rising phase indicates the change of the overall magnetic configuration during flares. Thus, we can use it to probe the magnetic shear changes of the coronal magnetic field, while a fast relaxation process of a sheared coronal magnetic field

was reported by Ji et al. [25], the relaxation is believed to be a shrinking process, and the decrease of the angle by radio diagnosis may provide additional evidence for the relaxation process.

Regarding the strong asymmetry of the calculated magnetic field and column density up to one or two orders of magnitude in the flaring loop, the mirroring effect can be used to explain why a stronger magnetic field and smaller column density appear in FP2, while a weaker magnetic field and larger column density exist in FP1 and LT (Fig. 6.9c). It also helps us to understand why the polarization degree in FP2 is evidently larger than that in FP1 and LT (Fig. 6.7c) due to the dependence of the polarization degree on the local magnetic field strength.

The minimum of equation of $\cos\theta$ is used to evaluate the calculated error in this paper, which depends on the deviation of the NT GS model from the observed events. We may check with Fig. 6.8a that the minimum of the equation of $\cos\theta$ in FP2 (dot-dashed line) with a stronger magnetic field is evidently smaller than that in LT (solid line) and FP1 (dashed line) with weaker magnetic fields, because the NT GS theory is not enough to cover all radiation processes, such as the thermal bremsstrahlung mechanism in the radio source with very weak magnetic fields. A theoretical error (26%) was given by Dulk and Marsh [9] under the approximated conditions, but this error will increase rapidly beyond those conditions. In this paper, we can roughly estimate the error by the minimum of the equation of $\cos\theta$ with respect to the analytical approximations, for instance, the error is $20\% \sim 40\%$ in the FP2, and $60\% \sim 80\%$ in the LT and FP1.

We can also check the harmonic numbers in the three sources (Fig. 6.8d), and find that the harmonic number is smaller than 100 only in FP2 (dot-dashed line), which is suitable for the GS theory of Dulk and Marsh [9]. In fact, a full GS spectrum is predicted by the GS theory in a uniform magnetic field (Ramaty) [17], which means that the GS emission at a given frequency is actually determined by an integration of different harmonics of gyrofrequency in a nonuniform magnetic field, such as a dipole (Takakura and Scalise) [14]. Hence, the harmonic number obtained in this paper can be approximately considered to be its mean value in a nonuniform magnetic field, which is useful for estimating the mean height of radio source at a given frequency above the photosphere.

6.2.4 Evolution of Turnover Frequency and Magnetic field with Flattened Optically Thin Spectra

6.2.4.1 Overview

Solar radio bursts with a flat spectrum were first reported at centimeter band [26, 27], which may be reproduced by the GS emission under a dipole magnetic field with a large contrast (1:300) of the field strengths from LT to FPs [14, 28], or by the free-free absorption of GS emission [29] of NT electrons with a very large

density (10^{10} cm^{-3}). Afterward, the observed flat spectrum may extend to millimeter even sub-mm band [30], which may be consistent with the optically thin thermal bremsstrahlung emission, but the lack of observed soft X-ray emission and other properties of the flare cannot easily be accommodated by this mechanism. The other possibilities, such as the optically thick emission due to thermal absorption of NT GS emission or the optically thin GS emission absorbed by high-density material intervening along the LOS also face difficulties. More observations of flat spectra at centimeter and millimeter bands were detected by different instruments [31–34].

With a newly developed Solar Sub-mm Telescope (SST) at 200–400 GHz [35, 36], together with other instruments at centimeter band, a very flat spectrum was reported in the maximum phase of three bursts [37–39], which were actually composed of two components, one is the typical GS emission (e.g., observed by OVSA at 1–18 GHz), and another one is a new component at sub-mm band observed by SST [40], with a big frequency gap between these two components, and the observed flat spectra were just located in this gap, which seems to belong to the GS emission rather than the new sub-mm component.

Moreover, the flat spectrum just means that a very high turnover frequency appeared in above MW bursts' spectra [30]. The self-absorption and Razin effects play an important role to determine the magnitude and time evolution of turnover frequency in solar MW bursts [41]. However, the turnover frequency was rarely discussed in above studies on the flat spectrum, thus we plan to select more MW bursts with a flat spectrum in the data of NoRP at 1–80 GHz covering the centimeter and millimeter bands [42, 43], and pay attention to the analysis of turnover frequency in these events.

6.2.4.2 Observations

Four events have been selected from NoRP's database with an extremely flat spectrum in optically thin part and a very hard spectral index between 0 and −1 in the maximum phase of all bursts [44]. The peak flux is up to hundreds even thousands SFU (solar flux unit) to ensure that the NT GS emission is dominated in these events. All of these events were simultaneously observed by NoRP and NoRH, with a single and compact source.

One typical example in 2004 January 7 as an M4.5 flare in NOAA537 (N02E73) is given in Fig. 6.10, which shows *a*. time profiles of NoRP at 9.4 GHz (solid), 17 GHz (dashed), 35 GHz (dot-dashed), and 80 GHz (dot-dot-dashed), *b*. the spectra at five selected times as marked in panel '*a*' by solid and plus, dashed and asterisk, dot-dashed and diamond, dot-dot-dashed and triangle, long dashed and square, as well as a fitted spectrum at the peak time by thick solid line, *c*. the time evolution of spectral indices of NoRP (solid) and NoRH (dashed), *d*. the time evolution of turnover frequency (solid) and Razin frequency with electron density of 1.0×10^{10} cm^{-3} (dashed) and 10^{11} cm^{-3} (dot-dashed), *e*. the calculated electron spectral index, and *f*. the calculated magnetic field.

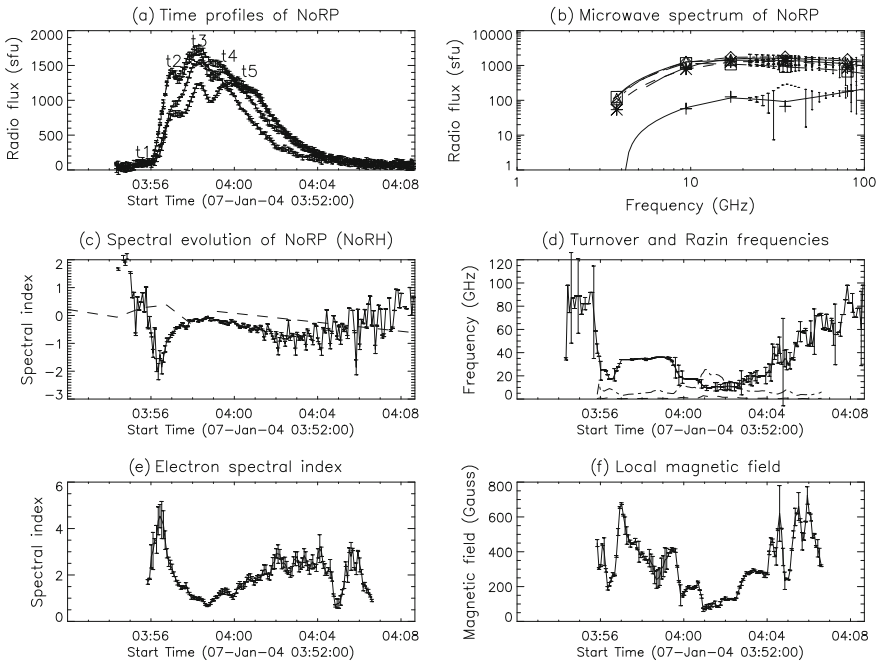

Fig. 6.10 Observations and calculations of the 2004 January 7 event with an extremely flat spectrum

It is clearly seen in Fig. 6.10b that the flat MW spectrum at the peak time has been well fitted by the theoretical calculation [35], even we cannot observe the radio flux at frequencies above 80 GHz by NoRP. In the case of limited frequency resolution of NoRP, especially, there are only 2 or 3 frequencies in optically thin part, which strongly affects the fitting accuracy of turnover frequency and spectral index in optically thin part from the observed data of NoRP. So that 10 frequencies are randomly selected (22, 26, 30, 36, 42, 50, 60, 72, 84, and 98 GHz) to solve this problem, while the two-frequency spectral index of NoRH is only given for verifying the spectral evolution of NoRP in Fig. 6.10c. Moreover, the spectral evolution of NoRP and NoRH in Fig. 6.10c shows a typical SHS or SHH pattern.

The most important feature is that the turnover frequency is inversely proportional to the time profiles of radio flux as shown in Fig. 6.10d, which is quite different from the earlier statistics of 38 bursts with a single spectral maximum observed by OVSA [42]. The turnover frequency increases in the rise phase by about 83% of 24 bursts where it could be clearly measured, and decreases immediately after the peak time in about 62% of 34 bursts, which is in qualitative agreement with the theoretical expectations based on the GS self-absorption. However, for a significant number of events (30–36%) the peak frequency variation is much smaller than expected from the self-absorption, or may be entirely absent [108], and the anomalous behavior is well explained by the effects of Razin suppression.

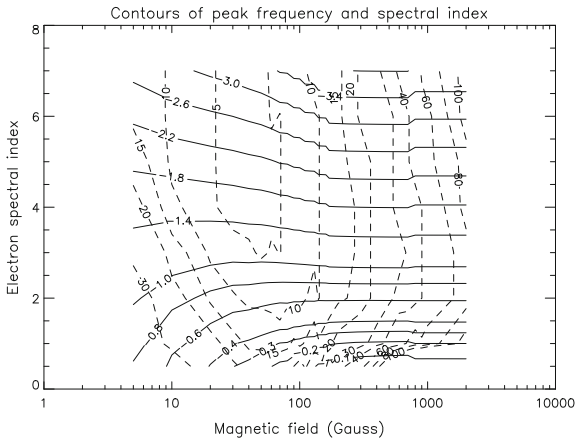

Fig. 6.11 Overlaid contours of turnover frequency and optically thin spectral index

6.2.4.3 Calculations of Magnetic Field

Using the second method introduced in Sect. 6.2.1, and well accepted Ramaty's code in solar softwares [45], the calculated arrays of spectral index (solid contours) and turnover frequency (dashed contours) in MW spectra actually provide two numerical equations of B_0 and δ as shown in Fig. 6.11 (with respect to the observations of very flattened optically thin spectrum in Fig. 6.10).

It is noticed that the high turnover frequencies in the selected event with flattened optically thin spectrum can exclude the cross points of two kinds of contours in lower magnetic field ($< 40 \sim 50$ Gauss), we can obtain unique solutions of B_0 and δ in higher magnetic fields ($> 40 \sim 50$ Gauss), and the calculated B_0 and δ in the 2004 January 7 event are added to Fig. 6.10e–f.

6.2.4.4 Discussions and Conclusions

The inverse correlations of the radio flux at a selected frequency 9.4 GHz $f_{9.4}$ with the observed turnover frequency f_p and the calculated magnetic field strength B_0 in Fig. 6.11 have been verified by the correlation coefficients $r_1 = -0.5$ (between $f_{9.4}$ and f_p) and $r_2 = -0.353$ (between $f_{9.4}$ and B_0), which are well satisfied with the critical value -0.159 of 95% confidence level for the sample number of 125 in this event.

A negative correlation of radio flux and local magnetic field was deduced [8] (see Eq. (9) in that paper), while, a positive correlation of turnover frequency and local magnetic field (> 40 Gauss) has been shown in Fig. 2.27. Hence, the observed inverse correlation of radio flux and turnover frequency in this event is an expectable result, at least in the case of stronger magnetic field.

On the other hand, the strong attenuation of local magnetic field strength in this event (Fig. 6.11f) implies that the observed extremely flat spectra is possibly con-

tributed to the Razin effect during the maximum phase, and the Razin frequency ν_R is defined as a frequency criterion [46]

$$\nu_R = \frac{2\nu_p^2}{3\nu_B}, \tag{6.2.15}$$

here, ν_p and ν_B are respectively the electron plasma and cyclotron frequencies. It is supposed a typical value of electron density is $10^{10}\,\mathrm{cm}^{-3}$, the calculated ν_R (dashed line) is added to Fig. 6.10d, which is evidently below the turnover frequency, and the Razin effect is not important, while, if the electron density increases to $10^{11}\,\mathrm{cm}^{-3}$, the calculated ν_R (dot-dashed line) will be larger than the turnover frequency in the impulsive or maximum phase of the selected events. Therefore, the Razin effect may be used to explain the extremely flat spectra together with a very hard electron spectral index when the electron density is high enough.

Finally, the calculated electron spectral index is between 0 and 2, which can be considered as a natural explanation for the observed extremely flat spectra, together with the observed high turnover frequencies, as well as the Razin effect in the case of very high density.

6.2.5 Theoretical Scaling Laws of Coronal Magnetic Field and Electron Power-Law Index in Corona

6.2.5.1 Overview

In an earlier review of Newkirk [47], the coronal magnetic fields in solar active regions estimated from various observations (especially at radio band) were somehow comparable with an inverse square law ($0.01 \sim 1.0 R_\odot$) or dipolar potential model ($0.1 \sim 100.0 R_\odot$), and here $R_\odot$ is solar radius. Later for a given model of plasma density, Dulk and Mclean [48] compared radio diagnosis of coronal magnetic field from various observations around three criterions (the ratio $\sim$1 between electron plasma and cyclotron frequencies, the Alfvén velocity $\sim 10^3$ km, and plasma $\beta \sim 1$) to evaluate the coronal magnetic field in active regions, and obtained an empirical formula

$$B = 0.5 \times \left(\frac{R}{R_\odot} - 1\right)^{-1/5} G, \tag{6.2.16}$$

which can fit different observations to about a factor of three in the range of $1.02 \sim 10.0\ R_\odot$. The radio diagnosis of coronal magnetic field was also reviewed by Krüger and Hildebrandt [49] under a dipole approximation:

$$B_z = B_m z_d^3 (z + z_d)^{-3}, \tag{6.2.17}$$

where z_d is the assumed dipole depth below the photosphere, B_m is the dipole field strength, and when $B_m = 2500$ G, $z_d = 2 \times 10^4$ km, it was consistent with the force-free extrapolated field from a measured magnetogram and the results from other observations.

Moreover, a statistical scaling law of coronal magnetic field versus length of magnetic tubes was based on the linear force-free potential extrapolation (see Mandrini et al. [50]) in 14 active regions to restrain the models for coronal heating:

$$\log\langle B\rangle = C_1 + C_2 \log L + C_3/2 \log(L^2 + S^2), \tag{6.2.18}$$

here, $\langle B\rangle$ means the averaged coronal field strength, $C_2 \approx 0$, $-3 \leq C_3 \leq -1$, and $40 \leq S \leq 240$ mm is related to the characteristic size of the active region. Thus, for flux tubes with an intermediate length, $\langle B\rangle \propto L^{\delta}$, where $\delta = 0.88 \pm 0.3$.

All of above results are only available in solar active regions, and recently we pay particular attention to the coronal magnetic field in the MW burst sources, which are dominated by non-thermal gyro-synchrotron radiation (Ramaty 1969) [17], and closely related to solar flares and energetic electrons. It is possible to solve the local magnetic field strength, view angle, and column density of non-thermal electrons from the observable brightness temperature (or flux density), optically thin spectral index, and polarization degree (Huang 2006, Huang et al. 2008, 2015) [10, 11, 19], which depends on the approximations of Dulk and Marsh, and limited by electron power-law index $\delta = 2 \sim 7$, view angle $\theta = 20^\circ \sim 80^\circ$, and harmonic number (10 $\sim$ 100), as well as a 180-degree ambiguity of θ due to the uncertainty of intrinsic mode (Huang et al. 2013) [16].

6.2.5.2 Calculations

Using the well-known Ramaty's code in solar softwares (SSW), two groups of typical MW spectra are calculated respectively with electron power-law index $\delta = 2$–6 in Fig. 6.12a, and local magnetic field $B = 40$–200 G in Fig. 6.12b, while the other parameters are insensitive to the optically thin spectral index (Huang et al.) [13], and taken as fixed values: $B = 120$ G, electron density $n_e = 5 \times 10^9\,\mathrm{cm}^{-3}$, view angle $\theta = 60^\circ$, the low and high-energy cutoff respectively of 10 keV and 100 Mev in Fig. 6.12 (left), while $\delta = 4.0$ in Fig. 6.12 (right), and the rest parameters in the left panel of Fig. 6.12 (except B) are the same as those in the right panel of Fig. 6.12.

It is clear from Fig. 6.12 that the optically thin spectral index γ is more sensitive to δ than that to B. An important effect to be considered in this paper is that γ actually varies with frequency as shown by Fleishman and Melnikov [51], thus the optically thin part in Fig. 6.12 is divided into four intervals with central frequency respectively of 14, 25, 62, and 156 GHz, and Fig. 6.13 (left) shows the averaged γ in all initial values of B (5 $\sim$ 1000 G) versus frequency under a given initial value of δ (1 $\sim$ 4), which means that γ is always softened with increasing of ν, while Fig. 6.13 (right) shows the averaged ν_{peak} in all initial values of B (5 $\sim$ 1000 G) versus δ, and the averaged ν_{peak} decreases gradually with increasing of δ.

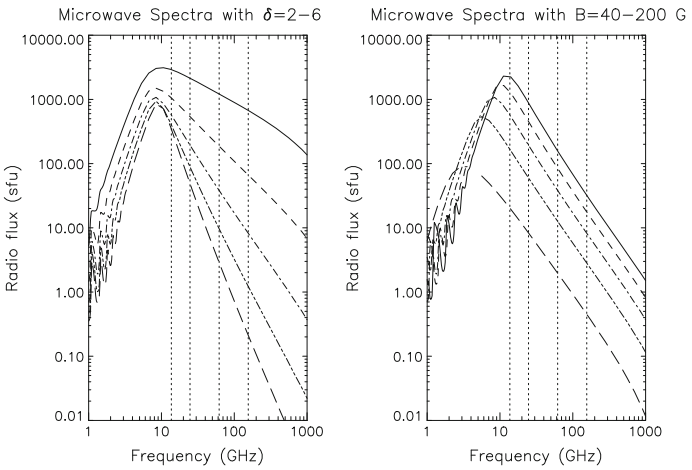

Fig. 6.12 The MW spectra with different electron power-law indices (left panel) of 2 (solid), 3 (dashed), 4 (dot-dashed), 5 (dot-dot-dashed), and 6 (long dashed), and **b** different magnetic field strengths (right panel) of 200 G (solid), 160 G (dashed), 120 G (dot-dashed), 80 G (dot-dot-dashed), and 40 G (long dashed)

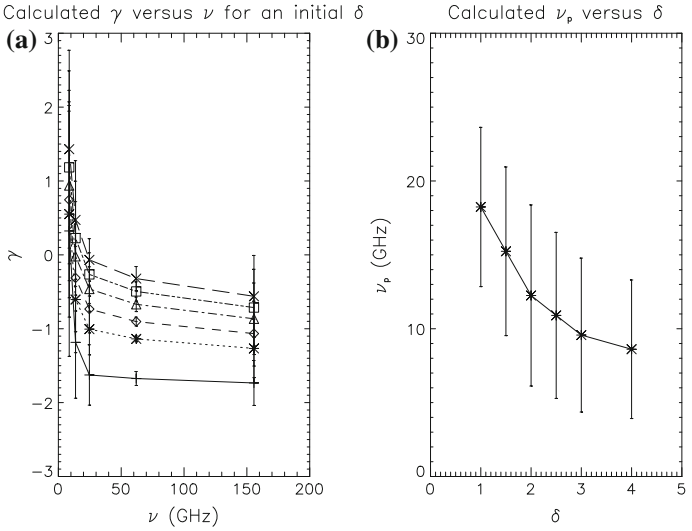

Fig. 6.13 Left: The averaged spectral index versus frequency with different electron power-law indices of 4 (plus and solid), 3 (asterisk and dotted), 2.5 (diamond and dashed), 2 (triangle and dot-dashed), 1.5 (square and dot-dot-dashed), and 1 (cross and long dashed). Right: The averaged peak frequency versus electron power-law index

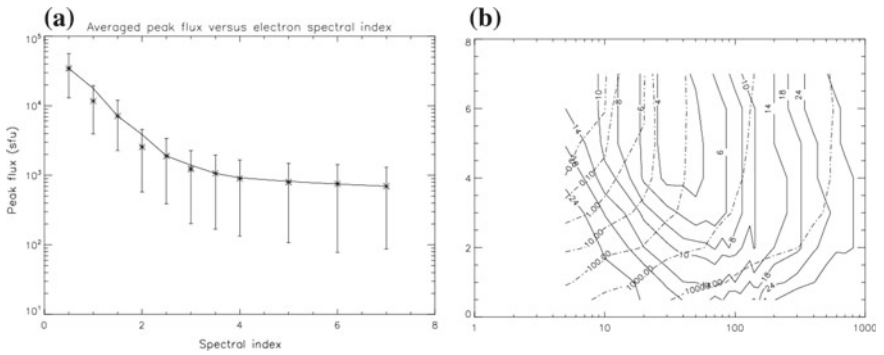

Fig. 6.14 **a** The peak flux versus δ averaged for all initial values of B. **b** The range of solutions of B and δ restricted by the contours of peak flux (dashed)

The key procedure in this paper is to use two numerical functions of ν_{peak} and γ calculated by the Ramaty's code to solve B and δ, and the solutions are determined by a series of intersections in Fig. 6.11. There are often two intersections for a group of given values of γ and ν_{peak}, but the intersections in weaker magnetic fields (several tens Gauss) can be excluded by the peak flux contours over 10^3 sfu as shown in Fig. 6.14a–b.

6.2.5.3 Scaling Laws of B and δ Versus ν

It is ready to obtain B from the abscissa of intersections in Fig. 6.11 with the averaged γ in Fig. 6.13a and ν_{peak} in Fig. 6.13b, and the error bars are determined by both of γ and ν_{peak}. Figure 6.15 (left) gives the solution of B versus frequency for a given δ but averaged for all values of B, while Fig. 6.15 (right) gives δ from the ordinate of intersections for a given initial value of δ but averaged for all initial values of B.

The left and right panels of Fig. 6.16 respectively give the averaged B and δ in all initial values of δ versus frequency, with error bars for the selected frequencies, and fitted with a logarithmic cubic model as in below:

$$\langle B\rangle = 128.63 + 7.34\log\nu - 12.83(\log\nu)^2 + 10.44(\log\nu)^3, \tag{6.2.19}$$

$$\langle \delta\rangle = 0.86 + 0.75\log\nu - 0.21(\log\nu)^2 + 0.14(\log\nu)^3, \tag{6.2.20}$$

here, $\langle B\rangle$ and $\langle\delta\rangle$ are respectively the value of B and δ averaged in all initial values of δ, and ν means the radio frequency with a unit of GHz.

The tendency is reasonable that B increases with ν, while the tendency is evident that δ increases (softened) with increasing of ν in both of Figs. 6.15 and 6.16.

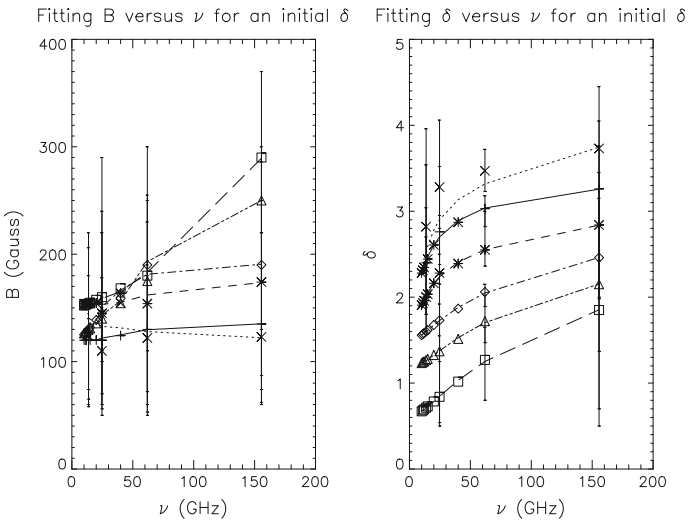

Fig. 6.15 Left: The solution of B versus frequency for a given initial value of δ of 4 (plus and solid), 3 (asterisk and dotted), 2.5 (diamond and dashed), 2 (triangle and dot-dashed), 1.5 (square and dot-dot-dashed), and 1 (cross and long dashed) but averaged for all initial values of B. Right: The optically thin spectral index γ versus frequency for a given initial value of δ of 4 (plus and solid), 3 (asterisk and dotted), 2.5 (diamond and dashed), 2 (triangle and dot-dashed), 1.5 (square and dot-dot-dashed), and 1 (cross and long dashed) but averaged for all initial values of B

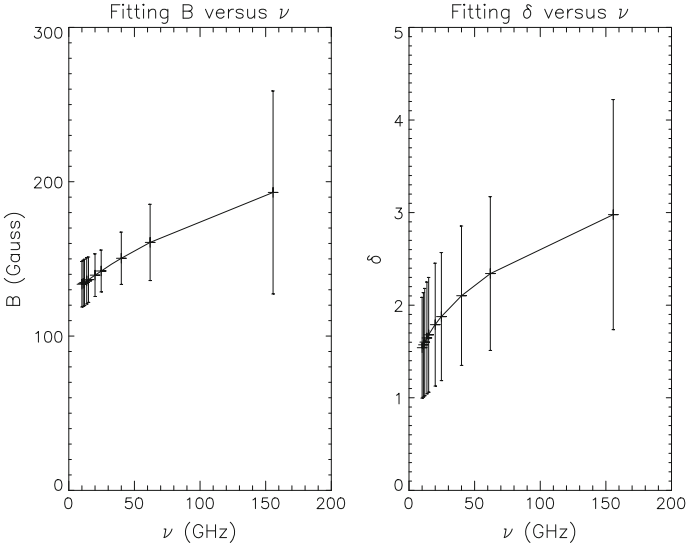

Fig. 6.16 The averaged B (left) and δ (right) for all initial values of δ versus frequency, with error bars for the selected frequencies, and fitted with a logarithmic cubic model

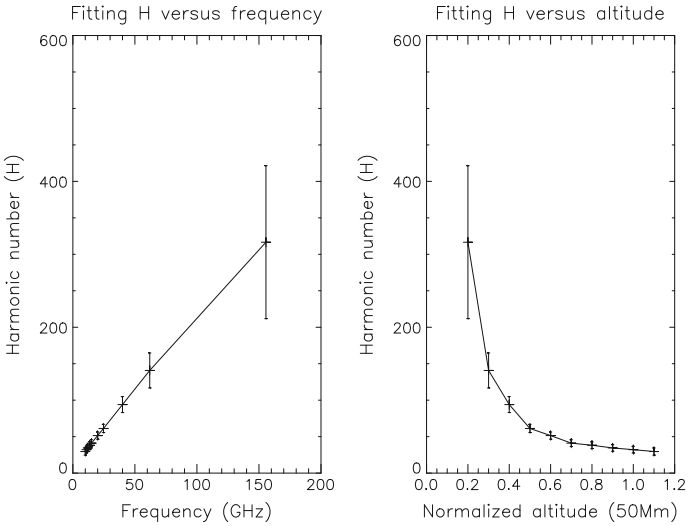

Fig. 6.17 The averaged harmonic number for all initial values of δ versus frequency (left) and the coronal height of burst source (right)

6.2.5.4 Scaling Laws of B and δ Versus Coronal Height

A full GS spectrum is predicted by the GS theory in a uniform magnetic field (Ramaty) [17], which means that the GS emission at a given frequency is actually determined by an integration of different harmonics of gyrofrequency in a nonuniform magnetic field, such as a dipole one (Takakura and Scalise) [14]. Using the calculated B at different frequencies in Fig. 6.16 (left), we can directly obtain the harmonic number at different frequencies as shown in Fig. 6.17 (left), which can be considered to be its mean value in a nonuniform magnetic field, and useful for estimating the mean height of radio source at a given frequency above the photosphere.

For calibrating the relationship between radio frequency and burst source, a formula was used by Fu et al. [52] based on the model of dipole magnetic field [14]:

$$h = d\left(\frac{H \cdot 2.8B_0}{\nu_{MHz}}\right) = d\left(\frac{B_0}{B}\right), \tag{6.2.21}$$

here, h is the mean altitude of burst source, d is the depth of dipole magnetic field, H represents the mean harmonic number, B and B_0 are respectively the magnetic fields of the burst source and photosphere. It is assumed that $d \approx 0.07R_\odot = 50\,\text{mm}$, and B_{10MHz} represents the magnetic field at 10 GHz, and just corresponds to $h = d$, thus, we can simply estimate $B_0 = 8B_{10MHz}$ from the above formula, and further obtain

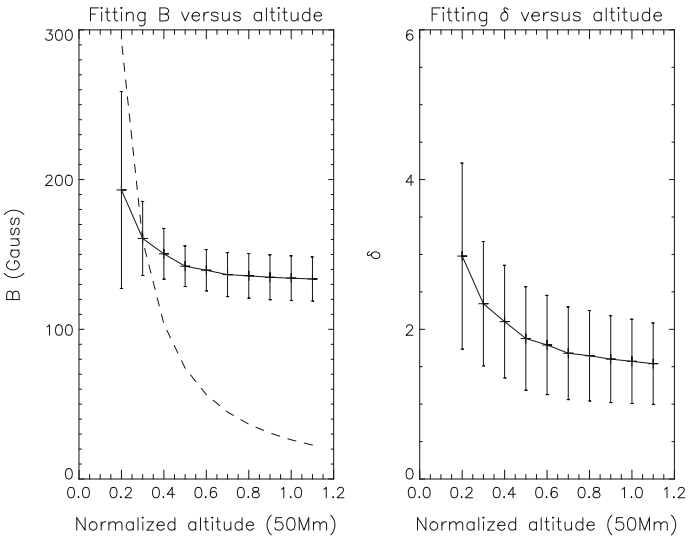

Fig. 6.18 The averaged B (left) and δ (right) for all initial values of δ versus the coronal height of burst source

B and δ versus the coronal height of burst source above photosphere from Fig. 6.18 and the above equation, as shown in Fig. 6.18, while the averaged harmonic number versus the coronal height of burst source is shown in Fig. 6.17 (right).

Moreover, the results of B and δ in Fig. 6.18 can be fitted by a logarithmic square model respectively:

$$\langle B\rangle = 136.94 - 107.14\log h + 7192.29(\log h)^2, \tag{6.2.22}$$

$$\langle \delta\rangle = 1.75 - 2.81\log h + 81.94(\log h)^2, \tag{6.2.23}$$

here, the coronal height h has a unit of 50 mm, and the error bars are the same as those in Fig. 6.17. The dashed line in Fig. 6.18 (left) is calculated by the formula of Dulk and Mclean [48], which has a comparable range of magnetic field but a larger radial gradient.

6.2.5.5 The Observed Magnetic Field and Spectral Index Versus Frequency

It is possible to observe directly the microwave spectral index versus frequency when we have an enough high frequency resolution in a broad range of microwave band. Here, we use the flare data of NoRP in 1–80 GHz observed on 2012 August 18, and interpolate a series of frequencies in optically thin part, thus to fit a typical microwave

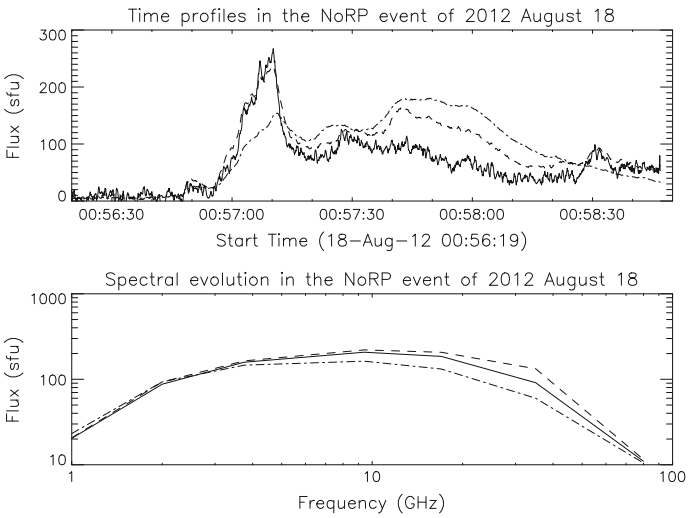

Fig. 6.19 Top: time profiles at 9.4 GHz (solid), 17 GHz (dashed), and 35 GHz (dot-dashed). Bottom: microwave spectra at 00:57:08 UT (solid), 00:57:10 UT (dashed), and 00:57:12 UT (dot-dashed) in the 2012 August 18 flare

Table 6.1 The fitted spectral index (γ), central frequency (ν), and peak frequency (ν_p), as well as the calculated magnetic field (B) and electron index (δ) in each frequency interval of the 2012 August 18 event

ν (GHz)	12	16	20	28	40	60	80
γ	−0.41	−0.51	−0.85	−1.16	−1.54	−3.47	−6.0
ν_p (GHz)	10	14	18	24	32	48	64
B (Gauss)	70	90	120	400	500	800	1000
δ	1.47	1.56	1.86	2.14	2.48	4.22	7.0

spectrum as shown in the bottom panel of Fig. 6.19, while the time profiles at 9.4, 17, and 35 GHz are given in the top panel of Fig. 6.19. We can divide the optically thin part into seven frequency intervals, all of which have three frequencies to fit a spectral index linearly in each frequency interval, and listed in Table 6.1 together with the central frequency and peak frequency (as the lower frequency boundary) in each frequency interval. Therefore, we can do the diagnostics of local magnetic field and electron spectral index in each frequency interval by using Fig. 6.11, which is also listed in Table 6.1.

Finally we can plot the magnetic field and electron index versus frequency in Fig. 6.20, and compare it with Fig. 6.16.

It is evident that there is a common tendency for both magnetic field and electron index versus frequency in Figs. 6.16 and 6.20, i.e., both of magnetic field and electron index increase with increasing of frequency. However, the variations of magnetic field

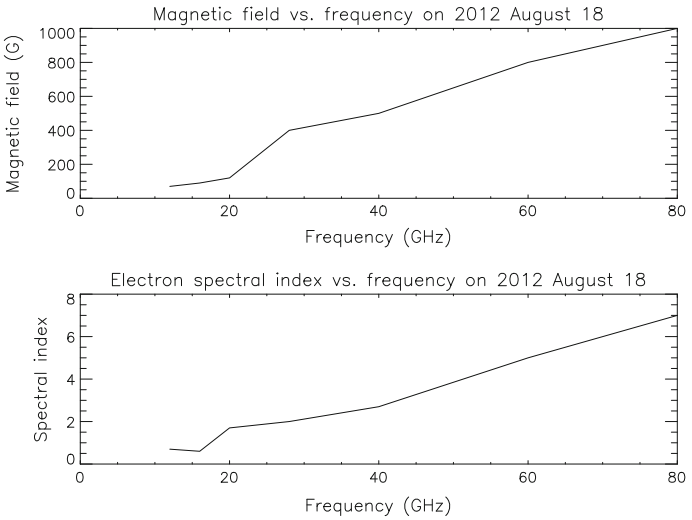

Fig. 6.20 The calculated magnetic field (top) and electron index (bottom) versus frequency in the 2012 August 18 flare

and electron index versus frequency in the observed event are much faster than that in the theoretical prediction.

6.2.6 Comparison of Radio Diagnosis with Extrapolation of Solar Photospheric Magnetogram

The extrapolation of photospheric magnetogram has been widely applied to acquire the direction, structure, and even magnitude of coronal magnetic field, and the method of extrapolation is continuously improved and developed. However, the comparison of radio diagnosis with the extrapolation of photospheric magnetogram is still empty up to now, the main scientific objective of the new generation of radio heliographs is just the radio diagnosis of coronal magnetic field, which may be supported by the the extrapolation of photospheric magnetogram.

A C6.2 flare in active region NOAA 10486 (S20E29) of 2003 October 27 is selected to compare the radio diagnosis [53] with the extrapolation of photospheric magnetogram (see Fig. 3.58 in Sect. 3.5.4). It is clearly shown that a compact loop-like structure (about 40×40 arc s^2) appears in both NoRH 17 and 34 GHz images, with symmetric emissions in the two FPs, but slightly stronger emission in the LT around the peak time. The contour shape of the polarization degree (see top-left panel of Fig. 3.58 in Sect. 3.5.4) appears similar to that of the calculated magnetic field strength (see top-right panel of Fig. 3.58). The contour levels of the calculated propagational angle (see bottom-left panel of Fig. 3.58) are mostly larger than 50°

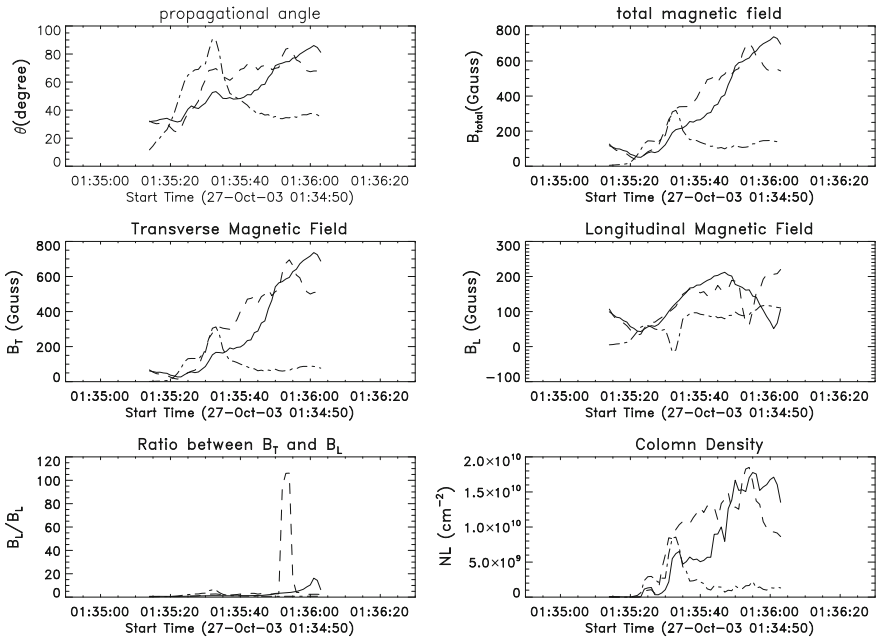

Fig. 6.21 The calculated parameters in the 2003 October 27 flare

in the burst source, which just implies that the transverse magnetic field is larger than the magnetic component longitudinal to the LOS. The contour levels of the calculated electron column density (bottom-right panel) are roughly homogeneous around $10^{10}\,\mathrm{cm}^{-2}$.

Based on the observed time profiles of 17 and 34 GHz brightness temperatures, 17 GHz polarization, and optically thin spectral index in the one LT (solid), FP1 (dashed), and FP2 (dot-dashed) as shown in Fig. 3.59 in Sect. 3.5.4, Fig. 6.21 respectively shows the time profiles of calculated propagational angle, total magnetic field, transverse and longitudinal magnetic components, the ratio between the two components, and electron column density in the one LT (solid), FP1 (dashed), and FP2 (dot-dashed), based on the Dulk and Marsh's approximations [9].

As shown in Fig. 3.59 in Sect. 3.5.4, this is a typical impulsive MW burst with a lifetime of about one minute in the impulsive phase, and with similar peak times and maximum emissions in the three sources, the time evolution of the polarization degree is always anti-correlated with that of the brightness temperature in the three sources, and the spectral evolutions in the three sources have the well-known SHS or SHH pattern. As shown in Fig. 6.21, the transverse magnetic field in both the LT and FP1 monotonically increased from the start time of the burst, through the peak time, until the decay phase, and its magnitude varied from several tens of Gauss to one thousand Gauss in this duration. The transverse magnetic field in FP2 varied impulsively, and reached its maximum just at the peak time of the burst. The variations

of the longitudinal magnetic field in the three sources were more complicated than those of the transverse magnetic field, and always less than one order of magnitude during the burst. The variations of the electron column density in the three sources were quite similar to those of the transverse magnetic field, and more than one order of magnitude during the burst. The most important feature in this event is that the magnitude and range of the transverse magnetic field were always much larger than those of the longitudinal magnetic field in the three sources.

On the other hand, the variations of photospheric magnetic field can be divided roughly into two kinds [54], one is permanent and irreversible, which may reflect the reaction of coronal flares on the photospheric magnetic field [20–22], another one is the fast variation of the line profiles induced by flares [55–57], which may correspond to the magnetic field by the radio diagnosis, and both of them are caused by the effect of flare energy release on different radiation mechanisms. In addition, the 2D contours of extrapolated magnetic field can be compared with that from the radio diagnosis. Based on the above consideration, the SOHO/MDI magnetogram was accepted for this event, under the force-free field with a constant α, the analytical expressions of three Fourier components of magnetic field were deduced from a semi-infinite columnar Green function with an arbitrary section [58]. The altitude of 17 GHz burst source can be estimated as 10^4 km by the model of dipole magnetic field [14], the 3D magnetic field lines and 2D contour at the peak time of this event are respectively given in Fig. A.10a and b in Appendix A. Comparing Figs. A.10 and 6.21, the direction, topological structure, and magnitude of extrapolated magnetic field are basically consistent with that of radio diagnosis. Furthermore, the longitudinal and transverse components of extrapolated magnetic field in the one LT and two FPs as shown in Fig. 6.22 can be deduced from Fig. A.10.

It is clear from Fig. 6.22 that there was an instantaneous change of several Gauss at the peak time in both of longitudinal and transverse extrapolated magnetic components, which is completely coincident with the radio diagnosis in Fig. 6.21. However, the time resolution of SOHO/MDI and NoRH were respectively minutes and seconds, it is impossible to make a detailed comparison between them. In addition, this event was deviated from the center of solar disk, and without a vector magnetogram, it is impossible to distinguish the longitudinal and transverse extrapolated magnetic components under the limitation of potential magnetic field. Hence, the present comparison is only a preliminary work.

6.2.7 Summary and Prospective

This section pays particular attention to the temporal and spatial variations of coronal magnetic field in MW burst sources, based on the NT GS theories. Started from the approximated fitting formulae of Dulk and Marsh [9], Zhou and Karlický [8] first proposed an analytical expression for the magnetic field in MW burst sources, which depends on observable flux or brightness temperature, spectral index, and peak frequency. Afterward, Huang [10] suggested to add the observed polarization

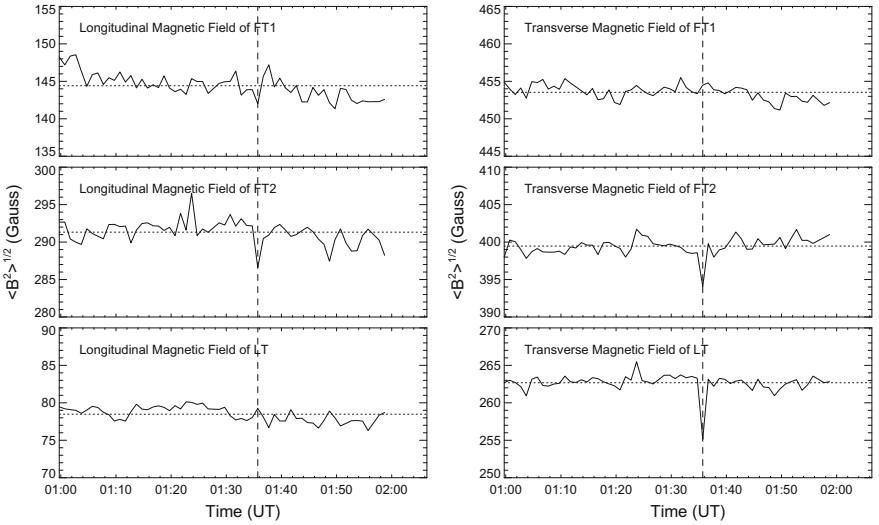

Fig. 6.22 The longitudinal (left panel) and transverse (right panel) components in the one LT and two FPs of 2003 October 27 flare, the peak time is marked by the vertical dashed lines in each panel

degree to calculate the angle between the GS emission and magnetic field, thus to obtain two magnetic components parallel and perpendicular to the LOS. However, the above diagnosis is still limited as follows.

(1) At first, a homogeneous magnetic field is assumed in MW burst sources, this diagnosis is only available in the compact sources. Secondly, it is limited by the non-thermal GS theory, it only works in the impulsive phase of MW bursts. Thirdly, the approximated fitting formulae are limited by a series of parameters, with electron spectral index of 2–7, harmonic number of 10–100, propagational angle of 20–80 degrees, and a fixed lower-energy cutoff of 10 keV, and when these parameters are beyond these ranges, very big errors are produced with respect to the strict GS theory.

(2) From the point of view of physical nature, the low-energy cutoff plays an important role in the GS emission, especially, to determine the relationship between electron and radiation spectral indices, thus the simple expression in Dulk and Marsh [9] can not be used for different low-energy cutoffs, and the strict GS theory (e.g., Ramaty [17]) should be accepted to solve this problem. However, it is not as convenient as the analytical formulae in Dulk and Marsh' approximations, so the approximated theory is still used in many cases.

(3) From the observational point of view, the brightness temperature at a given frequency is actually contributed by the overlapped MW emissions from different coronal heights with different magnetic field strengths, but a homogeneous magnetic field is accepted in both of approximated and strict GS theories as mentioned above, the obtained magnetic field only represents a mean value of the magnetic field in MW burst sources. Even a scaling law is deduced in Sect. 6.2.5.4, based on the model of dipole magnetic field [14], but it is unavoidable to deviate from the real one.

In spite of these limitations, some important results have been achieved in this section, such as the variation of transverse magnetic component much larger than that of the longitudinal component etc., and these methods should be improved and applied further with the future developed solar radio heliographs.

6.3 Diagnosis of Low-Energy Cutoff and Spectral Index of NT Electrons

6.3.1 Meaning and Debate of Low-Energy Cutoff

The energy of astrophysical energetic particles is commonly characterized by a power-law distribution, i.e., an approximate linear relation between the number density and and energy in a logarithm coordinate. In practice, the high energy-resolution of RHESSI data shows that the distribution may deviated from a single power-law, and a double power-law with a flattened lower-energy distribution often appears in RHESSI data. For a typical single power-law, the property of energetic (non-thermal) electrons is determined by four parameters: the logarithmic slope of power-law (i.e., spectral index), intercept (i.e., the coefficient of energetic spectrum), the maximum and minimum energies (so called as high-energy and low-energy cutoffs). Afterward, we can do integration of energy distribution in the energy space to obtain the total number density. However, we still can not directly observe the energetic particle distribution in solar atmosphere, but only indirectly obtain the information from the radiations at different wavebands. For instance, with the known radiation mechanisms at X-ray and MW bands, we may establish the relation between the photon and particle spectral indices to estimate the latter by the observable former. Moreover, the energetic particle number decreases with increasing of energy, which makes the contribution of high-energy cutoff is evidently smaller than that of low-energy cutoff to the integration, so it is often assumed to be infinite.

In recent years, many effects have been studied to explained the flattened photon spectrum in lower X-ray energies, such as the low-energy cutoff, Compton scattering (albedo) etc. [59–68], a part of studies suggested that it is not necessary to consider the low-energy cutoff if the albedo effect is removed the RHESSI data [65–67], but it was shown by a statistical study that even the albedo is removed from the RHESSI data, the flattened low-energy spectrum still exists in a part of the selected events [68], which means that the effect of low-energy cutoff can not neglected in these events. The existence of low-energy cutoff is reasonable, because an effective energy range should exist for any acceleration mechanism relevant to a given electric field, which can only accelerate the particles above one criterion, in other word, for a given energy, the accelerated electric field should exceed a critical value [69]. The recent studies show that the relation between the photon and electron spectral indices actually depends on the low-energy cutoff in both of X-ray and MW emissions, and some well-known formulae in thick-target, thin-target, and GS models can only be

used in the case with a very small low-cutoff [15], while the deduced low-energy cutoff may have a rather large varied range [59].

6.3.2 Cross Point of Spectral Lines at Different Times

It was first found by Gan et al. [70] in the HXR data of SMM satellite that there is possibly a common cross-point of the power-law spectra of emitted photons at different times, and if the X-ray emissions at different times are originated from the same non-thermal electrons, the energy corresponding to the common cross-point may refer to the low-energy cutoff. It is interesting that Huang [71] found a similar feature in the OVSA data analysis, i.e., a common cross-point also existed in the optically thin spectra at different times, which can be confirmed equivalently by the linear relation between the electron density and spectral index. Furthermore, Huang [72] studied the physical meaning of cross-point in HXR and MW spectra, the general expression of single power-law distribution of NT electrons is written to:

$$n(E) = KE^{-\delta}, \tag{6.3.1}$$

here, $n(E)$ is the electron number in a unit volume with the energy range of $E - \Delta E$, and E is a normalized energy. If E_{max} and E_{min} represent the maximum and minimum energy, respectively, the total number in a unit volume is integrated to be:

$$\begin{aligned} N &= \int_{E_{min}}^{E_{max}} KE^{-\delta} dE \\ &= \frac{K(E_{max}^{1-\delta} - E_{min}^{1-\delta})}{1-\delta}. \end{aligned} \tag{6.3.2}$$

It is assumed that $E_{max} = 1\,\text{MeV}$ and $E_{min} = 10\,\text{keV}$, and E_c and $n(E_c)$ represent the coordinates of the cross-point of power-law spectra at any two times, we can discuss three cases: (1) the cross-point is located in the low-energy cutoff, i.e., $E_c = E_{min}$ and $n(E_c) \approx 10^8\,\text{cm}^{-3}$; (2) the cross-point is located in the high-energy cutoff, i.e., $E_c = E_{max}$ and $n(E_c) \approx 10^2\,\text{cm}^{-3}$; and (3) the cross-point is located between the low-energy cutoff and high-energy cutoff, e.g., $E_c \approx 25\,\text{keV}$ and $n(E_c) \approx 10^6\,\text{cm}^{-3}$. After these coordinates are substituted into Eq. (6.3.1), it is ready to obtain the relation between the coefficient K and spectral index δ, which can be substitute to Eq. (6.3.2) to further deduce the relation between N and δ in the three cases, as shown by Fig. 6.23.

It is evident from Fig. 6.23 that there is an anti-correlation appeared when the cross-point is located in the low-energy cutoff, a positive correlation appeared when the cross-point is located in the high-energy cutoff, and an anti-correlation appeared in smaller values of δ, while a positive correlation appeared in larger values of δ when the cross-point is located between the low-energy cutoff and high-energy cutoff (the

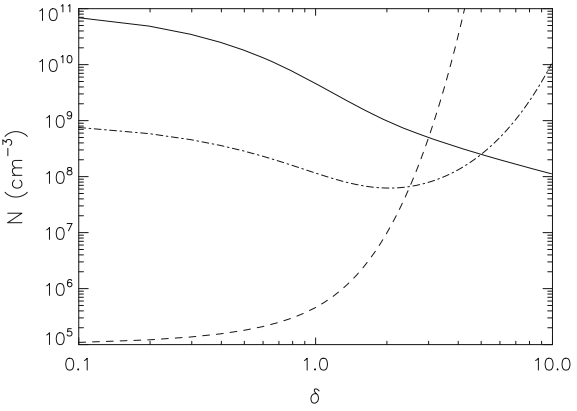

Fig. 6.23 The curves of N versus δ when the cross-point is located in the low-energy cutoff (solid), high-energy cutoff (dashed), and between low-energy cutoff and high-energy cutoff (dot-dashed)

reversed value of δ is about 1.8). So that we can check the relations between N and δ at different times to evaluate the position of cross-points. The cross-points are actually dispersive when the cross-points are located between the low-energy cutoff and high-energy cutoff, while the cross-points are more concentrated when the cross-points are close to the low-energy cutoff or high-energy cutoff. It is ready to deduce the expressions of low-energy cutoff and high-energy cutoff from Eq. (6.3.2):

$$\log E_{min} = \frac{\log K_1 - \log K_2}{\delta_1 - \delta_2}, \tag{6.3.3}$$

$$\log E_{max} = \frac{\log K_1 - \log K_2}{\delta_1 - \delta_2}, \tag{6.3.4}$$

here, K_1 and δ_1, K_2 and δ_2 respectively represent the coefficients and spectral index at any two times. When the cross-points are close to the low-energy cutoff or high-energy cutoff, under the approximations of $E_{max} = \infty$ or $E_{min} = 0$, Eq. (6.3.2) can be written to respectively:

$$N \approx \frac{E_{min}^{1-\delta}}{\delta - 1}, \tag{6.3.5}$$

$$N = \frac{K E_{max}^{1-\delta}}{1 - \delta}, \tag{6.3.6}$$

here $\delta \geq 1$ or $\delta \leq 1$ should be satisfied by the above two equations. When the cross-points are close to the low-energy cutoff, we can substitute Eq. (6.3.3) into Eq. (6.3.5) and rewrite it in a logarithm coordinate to obtain two equation at the two times:

$$\frac{1 - \delta_2}{\delta_1 - \delta_2} \log K_1 - \frac{1 - \delta_1}{\delta_1 - \delta_2} \log K_2 = \log N_1 + \log(\delta_1 - 1), \tag{6.3.7}$$

$$\frac{1-\delta_2}{\delta_1-\delta_2}\log K_1 - \frac{1-\delta_1}{\delta_1-\delta_2}\log K_2 = \log N_2 + \log(\delta_2 - 1). \tag{6.3.8}$$

It is noticed that the left sides of Eqs. (6.3.7) and (6.3.8) are identical, which means that the non-zero solutions of K_1 and K_2 exist only under a necessary condition:

$$\log N + \log(\delta - 1) = constant, \tag{6.3.9}$$

which just means that an anti-correlation should be satisfied in the case of $\delta > 1$, and consistent with the solid line in Fig. 6.23. The constant in the right side of Eq. (6.3.9) should be satisfied for the power-law spectra at different times, which just means that the common cross-point exists for the power-law spectra at different times. In the same say, when the cross-points are close to the high-energy cutoff, we can substitute Eq. (6.3.4) into Eq. (6.3.6) and rewrite it in a logarithm coordinate to obtain two equation at the two times:

$$\frac{1-\delta_2}{\delta_1-\delta_2}\log K_1 - \frac{1-\delta_1}{\delta_1-\delta_2}\log K_2 = \log N_1 + \log(1 - \delta_1), \tag{6.3.10}$$

$$\frac{1-\delta_2}{\delta_1-\delta_2}\log K_1 - \frac{1-\delta_1}{\delta_1-\delta_2}\log K_2 = \log N_2 + \log(1 - \delta_2), \tag{6.3.11}$$

thus to obtain the necessary condition of non-zero solutions of K_1 and K_2 when the cross-points are close to the high-energy cutoff:

$$\log N + \log(1 - \delta) = constant, \tag{6.3.12}$$

which just means that a positive correlation should be satisfied in the case of $\delta < 1$, and consistent with the dashed line in Fig. 6.23. In this case, a common cross-point exists close to the high-energy cutoff.

Furthermore, it is ready found from Eq. (6.3.2) that when a common cross-point (n(E_0), E_0) exists for the power-law spectra at different times, a linear relation between log K and δ should be satisfied at different times, with a slope of log E_0 and intercept of log $n(E_0)$, which is equivalent to the existence of common cross-point at different times. In other word, if we obtain such a linear relation, we can easily calculate the coordinates of common cross-point from the slope and intercept, the cross-point corresponds to the low-energy cutoff when the slope is negative or the high-energy cutoff when the slope is positive.

6.3.3 *Relation of Low-Energy Cutoff and Ratio of Radiation Intensities or Spectral Index*

In previous studies of X-ray spectrum, a forwardly fitting of observation and theory is used to acquire the low-energy cutoff and coefficient of power-law of NT electrons, while the electron spectral index can be directly deduced from the photon spectral index, and the high-energy cutoff is assumed to be infinite. It is noticed that the photon spectral index actually depends on the ratio of the intensities at two adjacent energies, which should be originated from the identical distribution of NT electrons, thus the coefficient of power-law is canceled, thus the ratio only depends on the low-energy cutoff, and the fitting process is greatly simplified.

Based on this idea, Zhang and Huang [63] studied three HXR flares with an evidently flattened low-energy spectrum recorded by Yohkoh/HXT, a simple power-law was assumed first, then the thick-target model was used to calculate the ratio of intensities at L (13.9–22.7 keV), M1 (22.7–32.7 keV), M2 (32.7–52.7 keV), and H (52.7–92.8 keV) bands for different electron spectral indices and low-energy cutoffs, i.e., to obtain three photon spectral indices at two adjacent bands of γ_1, γ_2, and γ_3, respectively from lower to higher energies. Figure 6.24a shows the intensity ratio at M1 and L bands versus the spectral index at H and M2 (γ_3), in which the low-energy cutoff is 10, 30, 40, 50, and 60 keV, respectively from bottom to top, and three black dots with an error bar are the observed values, thus the low-energy cutoff can be estimated as $40 \sim 60$ keV, but in Fig. 6.24b a completely different low-energy

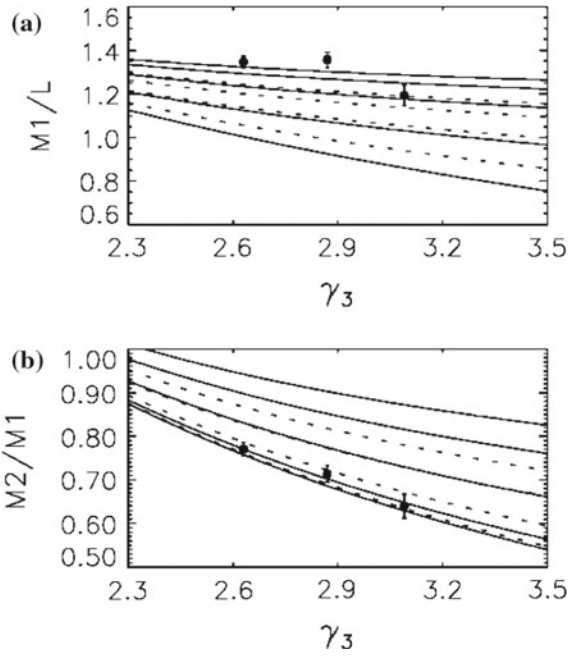

Fig. 6.24 Intensity ratio versus spectral index in three Yohkoh/HXT events, and fitted by the thick-target model

cutoff of $10 \sim 30$ keV is obtained from the ratio at M2 and M1 and spectral index γ_3, which implies that it is impossible to use a single power-law and low-energy cutoff to explain the flattened spectrum at low energies, and there should be other mechanism working in this case.

Naturally, the albedo effect is considered for the observed intensity to be the sum of original photons and the reflected photons by photosphere. The relevant theory was established by Bai and Ramaty [73], it was shown that the strongest reflected photons occur at about 30 keV, to make the intensity be enhanced around this energy, and the spectrum be flattened at lower energies, while the spectrum be steepened at higher energies. Finally, a qualitative interpretation of joint effect of low-energy cutoff and albedo is given for this result. It is also noticed that the ratio and spectral index are selected in different bands, and only in this case the theoretical curves are evidently separated for different low-energy cutoffs.

6.3.4 Joint Effect of Low-Energy Cutoff and Compton Scattering on Flattened Spectra at Lower Energies

The joint effect of low-energy cutoff and albedo is quantitatively studied by Zhang and Huang [64] by using the same Monte Carlo method as that in Bai and Ramaty [73], to which the low-energy cutoff is added to assure the result can return to that of Bai and Ramaty [73] when the effect of low-energy cutoff is removed. A double power-law distribution is accepted with a flattened spectrum (γ_l) in lower energies and a steepened spectrum (γ_h) in higher energies, and the difference between the two power-law indices just represents the flattened extent. The vertical coordinate of Fig. 6.25 is the ratio between the difference of spectral indices (γ_h-γ_l) divided by γ_h, and the horizontal coordinate is γ_h, the solid curves mean that both the low-energy cutoff and albedo are taken into consideration, while the dashed curves refer to that only the low-energy cutoff is considered, with the energy range of $15 \sim 55$ keV from bottom to top, the gap between two adjacent curves is 5 keV, and the dotted curve means that only the albedo is considered.

It is obvious from Fig. 6.25 (left) that the flattened extent is the most remarkable when both the low-energy cutoff and albedo are taken into account, and the flattened extent becomes more obvious with increasing of the low-energy cutoff, and the effect of albedo becomes less important with increasing (softening) of γ_h. To further analyze the joint effect of low-energy cutoff and albedo, two typical single power-law spectra respectively with an index of 2 and 4 are compared in Fig. 6.23 (right), the solid, dashed, and dotted curves respectively mean that only the albedo, low-energy cutoff, and the joint effect of them are taken into account. It is clear from Fig. 6.25 (right) that when the spectrum is harder (such as $\gamma = 2$), the albedo is dominated, while when the spectrum is softer (such as $\gamma = 4$), the low-energy cutoff is dominated to flatten the spectrum at lower energies, so that we can roughly take $\gamma = 3$ as a boundary to distinguish these two effects.

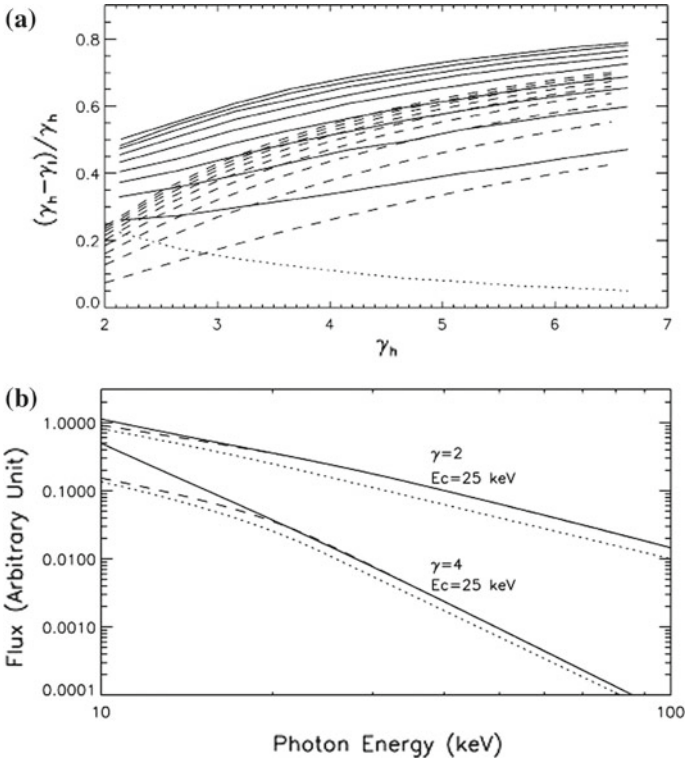

Fig. 6.25 Left: The difference between the spectral indices in higher and lower energies versus those in higher energies. Right: comparison of two typical single power-law spectra under the joint effect of low-energy cutoff and albedo, and each of them

6.3.5 Low-Energy Cutoff and Spectral Index of MW and HXR with Two Methods

In order to check the feasibility of these two methods in Sects. 6.3.2 and 6.3.3, an impulsive event simultaneously observed by Yohkoh/HXT and OVSA in 2000 June 10 is shown in Fig. 6.26.

6.3.5.1 Result of Method 1 in Sect. 6.3.3

At first, the X-ray data are processed based on the thick-target model of NT bremsstrahlung [74]:

$$I_\varepsilon = \frac{SA\kappa_{BH}Z^2}{4\pi R^2 C\varepsilon(\delta-1)}\int_\varepsilon^\infty dE E^{1-\delta}\ln\frac{1+(1-\varepsilon)^{1/2}}{1-(1-\varepsilon)^{1/2}}, \tag{6.3.13}$$

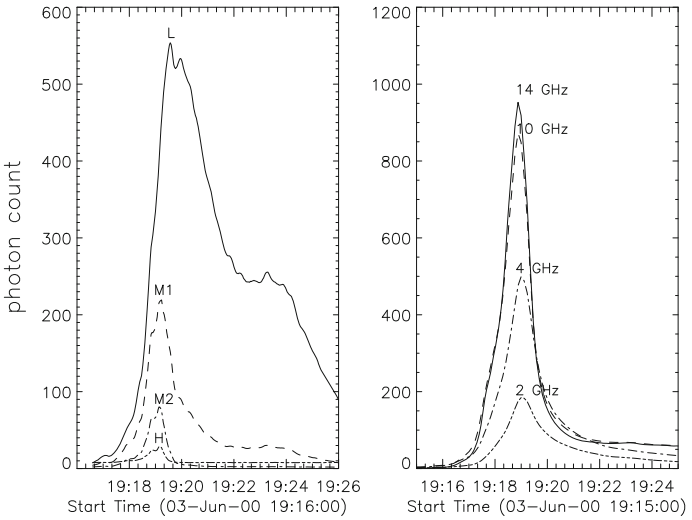

Fig. 6.26 The time profiles of an impulsive event observed by Yohkoh/HXT (left) and OVSA (right) in 2000 June 3

here, I_ε(photons cm^{-2}sec^{-1} keV^{-1}) means the HXR intensity emitted by the electron power-law $F(E) = AE^{-\delta}$ (electrons cm^{-2} sec^{-1} keV^{-1}) with energy between E_{min} and E_{max}. When $\varepsilon \leq E_{min}$, the low limit of integration should be changed to E_{min}. S is the area of flares, the constant $\kappa_{BH} = 7.9 \times 10^{-25}$ cm^2 keV represents the Bethe–Heitler section, the solar-terrestrial distance is $R = 1AU$, the constant $C = 2\pi e^4 \ln \Lambda$, e is the electric quantity of a unit charge, ln Λ means the Coulomb logarithm, and Z is the charge number of target particles.

The solid curves in Fig. 6.27 (left) are the theoretically calculated intensity ratio at M1 and L bands of Yohkoh/HXT versus the spectral index at M2 and M1 bands with the low-energy cutoff of 10, 20, and 25 keV, and different symbols refer to the observations in different time intervals in Fig. 6.27 (left): the boxes at 19:16–19:17 UT (initial phase), the crosses at 19:17–19:18 UT (earlier rising phase), and asterisk at 19:18–19:19 UT (close to maximum). Figure 6.27 (right) corresponds to the intensity ratio at M2 and M1 bands versus the spectral index at H and M2 bands, the theoretical curves and observed symbols are defined as those in Fig. 6.25 (left).

The low-energy cutoff in this event can be evaluated from Fig. 6.27, and it is found that the range of low-energy cutoff is $10 \sim 30$ keV gradually increased with time in the rising phase of flare. Secondly, we use the formulae of NT GS emission in a dipole magnetic field with the thermal gyro-resonant absorption, but the self-absorption and Razin effect in optically thin part are neglected [14], to process the OVSA data in this event:

$$T_{b\nu_\mp} = \frac{A\pi e^2 cd}{3k_B}(2.8 \times 10^6 B_0)^{1/3} F_{\nu_\mp}, \tag{6.3.14}$$

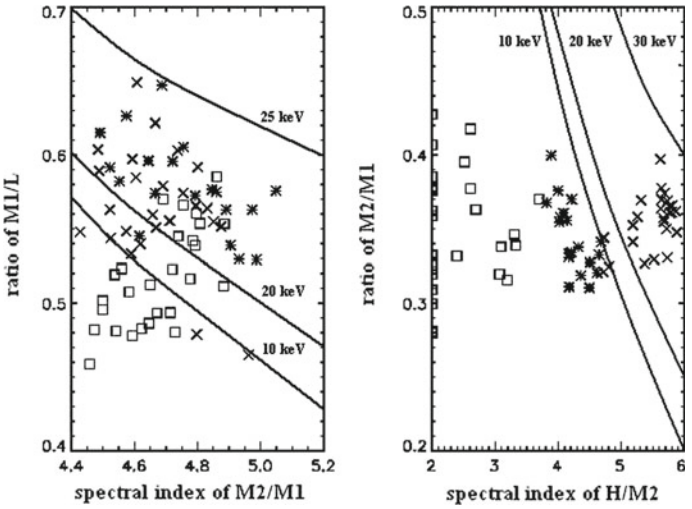

Fig. 6.27 The theoretical and observational comparison of the intensity ratio and spectral index at different energy bands of Yohkoh/HXT in the 2000 June 3 flare

$$F_{\nu_\mp} = \int \eta_{\nu_\mp} s^{-2/3} \exp^{-\sum_{s+1}^{6} \tau_{js}} ds, \tag{6.3.15}$$

$$\eta_{\nu_\mp} = \frac{1}{2|\cos\vartheta|} \sum_{n=s+1} \int_{p_{min}}^{p_{max}} (a \pm b)^2 \frac{(\sqrt{1+p^2}-1)^{-\delta}}{1+p^2} dp, \tag{6.3.16}$$

$$\tau_{js} = \frac{\pi e^2}{m_0 c} \left(\frac{k_B T}{m_0 c^2}\right)^{s-1} \frac{s^{2s}}{2^s s!} dN\nu(\sin\vartheta)^{2(s-1)} \times n_\pm, \tag{6.3.17}$$

$$n_\pm = \frac{(\sin^2\vartheta + 2s\cos^2\vartheta \pm \sqrt{\sin^4\vartheta + 4s^2\cos^2\vartheta})^2}{\sin^4\vartheta + 4s^2\cos^2\vartheta \pm \sin^2\vartheta\sqrt{\sin^4\vartheta + 4s^2\cos^2\vartheta}}. \tag{6.3.18}$$

Here, $T_{b\nu_\mp}$, $F_{\nu_\mp}$, and $\eta_{\nu_\mp}$ are respectively the brightness temperature, radio flux, and emissivity at a given frequency ν; the positive and negative signs of refractive index $n_\pm$ refer respectively to ordinary and extraordinary modes; m_0 is the mass of a single electron; s is the harmonic number, and the lower limit is determined by the ratio between ν and ν_B, and actually by the magnitude of B; B_0 is the magnetic field in photosphere, d is the scale of dipolar magnetic field; N and T are respectively the ambient density and temperature; p_{min} and p_{max} are respectively the lower and upper limits of momentum in respect to those of energy E_{min} and E_{max}.

Hence, there are totally 8 free parameters to fit the observation with the above equations: A, δ, p_{min}, p_{max}, B_0, N, T, and θ. When we calculate the intensity

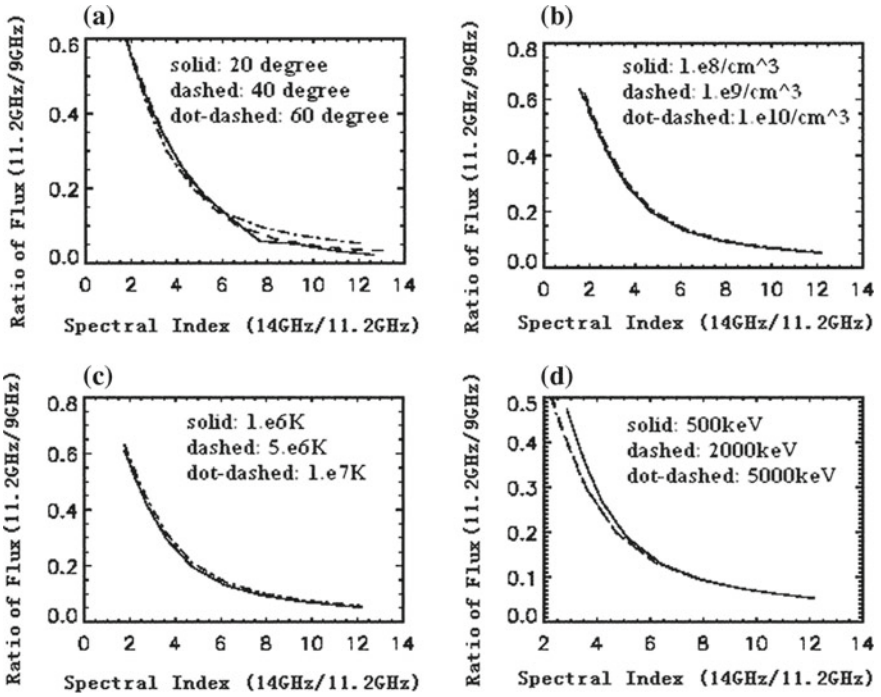

Fig. 6.28 The calculated flux ratio at 9–11.2 GHz versus the spectral index at 11.2–14 GHz for different values of **a** θ, **b** N, and **c** T, and **d** E_{max}, in which the middle value of other parameters is selected, and some parameters are fixed be $B_0 = 800$ Gauss, $\delta = 2$–7, and $E_{min} = 10$ keV

ratio at two adjacent frequencies, some parameters (like A, d, and B_0) are canceled automatically:

$$\frac{T_{b\nu_1}}{T_{b\nu_2}} = \frac{F_{\nu_1}}{F_{\nu_2}} \left(\frac{\nu_1}{\nu_2}\right)^{-4/3}. \tag{6.3.19}$$

Furthermore, we calculate the intensity ratio versus spectral index at two adjacent frequencies under different values of θ, N, T, and p_{max} (with respect to E_{max}), and find the effect of these parameters is negligible as shown in Fig. 6.28.

Thus only one free parameter E_{min} remained with respect to the low limit p_{min} of integration. The theoretically calculated curves (solid) of flux ratio at 9–11.2 GHz versus the spectral index at 11.2–14 GHz in Fig. 6.29 are compared with the observations (asterisk) given in Fig. 6.26 (right), here $E_{min} = 10$–90 keV from bottom to top with an energy interval of 10 keV.

It can be seen from Fig. 6.29 that the estimated E_{min} in the main phase of burst is in a range of 10–30 keV, which is basically consistent with the result of Yohkoh/HXT in Fig. 6.27. The only difference is that E_{min} becomes evidently larger in the decay phase, which may be caused by the trapping effect or thermal emission.

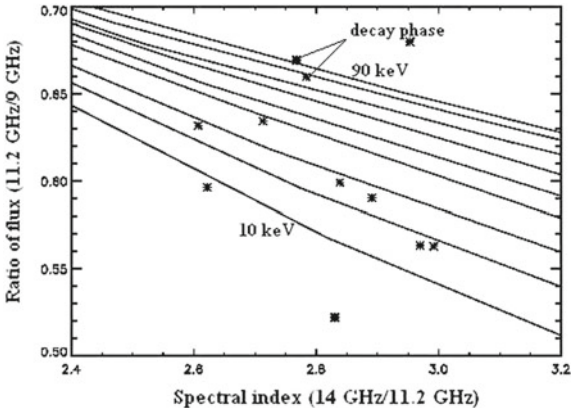

Fig. 6.29 The calculated flux ratio (solid curves) at 9–11.2 GHz versus the spectral index at 11.2–14 GHz for different values of E_{min} in comparison with the observational result (asterisk) in the 2000 June 3 event at different times in Fig. 6.24 (right)

6.3.5.2 Result of Method 2 in Sect. 6.3.2

Figure 6.30 shows the linearly fitting of the logarithm of the coefficient of power-law spectrum normalized by 20 keV versus the spectral index at M1-L, M2-M1, and H-M2 bands observed by Yohkoh/HXT, in which the confidence of 0.99 is well satisfied for the linearly fitting.

The slope of linearly fitting in Fig. 6.30 is respectively -0.12, -0.26, and -0.28, which can be used to calculate the horizontal coordinate of the common cross-point (i.e., E_{min}) to be 26, 36, and 38 keV, which is a little larger than but comparable with that in Fig. 6.27 by the method 1. Figure 6.31 shows the linear relation between the electron density and radiation spectral index as mentioned in Sect. 6.3.2, and the anti-correlation between them just supports the predicted common cross-point with respect to E_{min}, but which can not be directly deduced like that from the HXR data.

6.3.6 Low-Energy Cutoff and Spectral Index of MW and HXR with Strict Methods

6.3.6.1 Hard X-Ray

In the thick-target model Eq. (6.3.13) for the NT HXR emission, a well-know relation between the electron and photon spectral indices under a single power-law can be derived as $\gamma = \delta - 1$ when $E_{min} < \varepsilon$ (the photon energy) [74]. In practical observations, E_{min} has a large range [59], if $E_{min} > \varepsilon$, it is failed to derive the result of single power-law with $\gamma = \delta - 1$ From Eq. (6.3.13), and the calculated result in Fig. 6.32 clearly shows the effect of E_{min} on the thick-target model [15]:

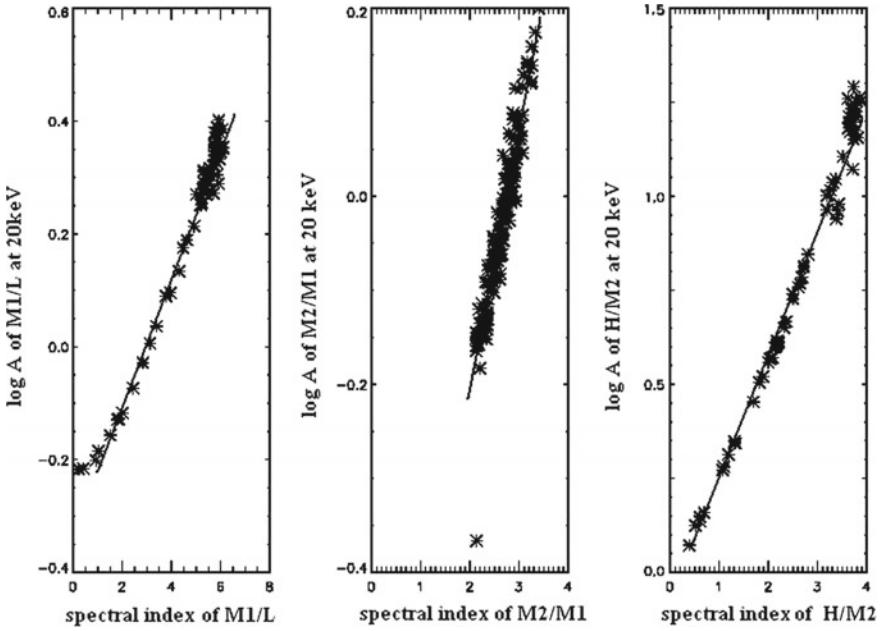

Fig. 6.30 The linearly fitting of the logarithm of the coefficient of power-law spectrum normalized by 20 keV versus the spectral index at M1-L (left), M2-M1 (middle), and H-M2 (right) bands observed by Yohkoh/HXT on 2000 June 3

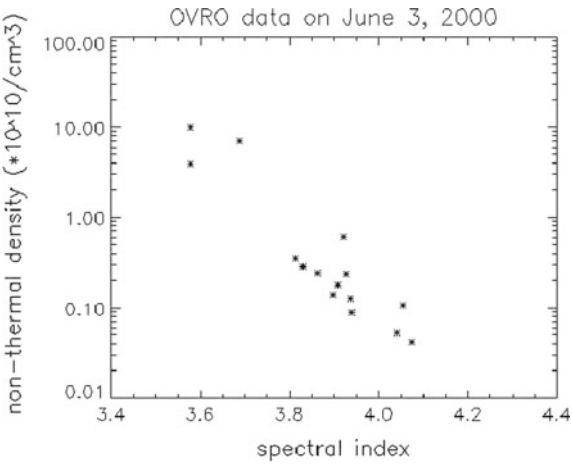

Fig. 6.31 The linear relation between the electron density and spectral index in the MW burst on 2000 June 3

It is evident from Fig. 6.32 that a flattened spectrum in lower energies becomes more obvious with increasing of E_{min}, and Table 6.2 gives the intensity ratio and spectral index at two adjacent energies of Yohkoh/HXT varied with E_{min}.

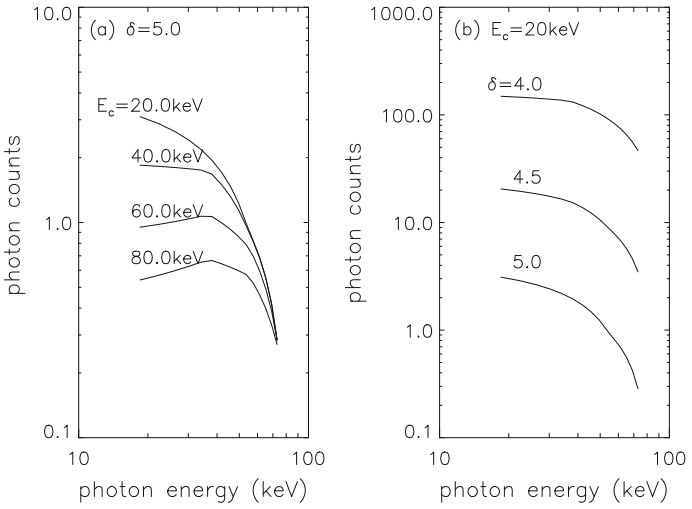

Fig. 6.32 The calculated photon spectra by the thick-target model in Eq. (6.3.13) with different values of **a** E_{min} and **b** electron spectral indices

Table 6.2 The calculated intensity ratio and spectral index at two adjacent energies of M1/L, M2/M1, and H/M2 of Yohkoh/HXT with the thick-target model in Eq. (6.21), in which $E_{min} =$ 20–80 keV, $\delta = 4.0$, 5.0, and 6.0

δ	4.0	4.0	4.0	5.0	5.0	5.0	6.0	6.0	6.0
E_c (keV)	20.0	40.0	60.0	20.0	40.0	60.0	20.0	40.0	60.0
M1/L	0.91	1.08	1.22	0.65	0.94	1.15	0.47	0.85	1.10
γ_1	3.00	2.48	2.10	3.97	2.89	2.30	4.92	3.18	2.42
M2/M1	0.67	0.71	0.83	0.45	0.52	0.70	0.31	0.40	0.63
γ_2	2.97	2.82	2.41	4.03	3.63	2.82	5.04	4.33	3.12
H/M2	0.52	0.52	0.56	0.31	0.31	0.37	0.19	0.19	0.26
γ_3	2.95	2.94	2.81	4.00	3.98	3.64	5.03	4.99	4.39

It can be seen from Table 6.2 that the well-known relation of $\gamma = \delta - 1$ is only satisfied when E_{min} is rather small, γ becomes harder obviously with increasing of E_{min} and deviates from the well-known relation, and the effect of E_{min} becomes weaker with increasing of photon energy, which is consistent with Fig. 6.32. Due to the effect of E_{min} (including albedo etc. as mentioned before), a double power-law frequently appears in the observed HXR spectra, from which we can obtain a unique solution of E_{min} and δ as shown in Fig. 6.33.

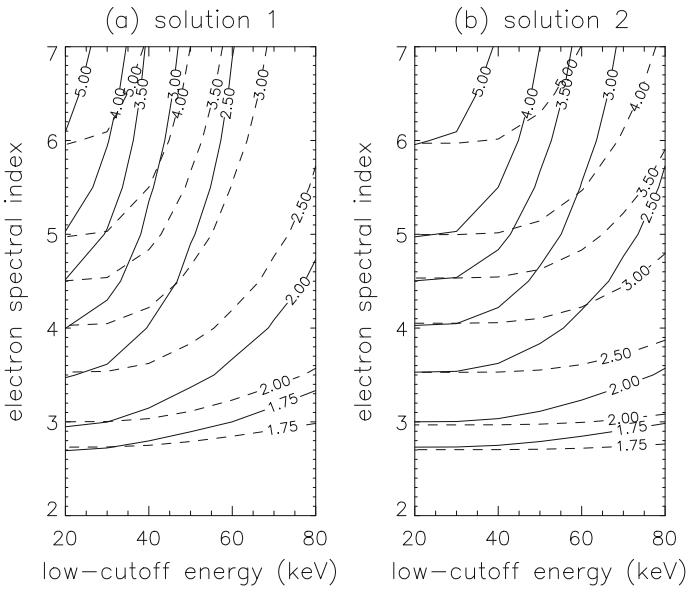

Fig. 6.33 One example to show the diagnosis of E_{min} and δ from the horizontal and perpendicular coordinates of the cross-points of **a** M1/L (solid) and M2/M1 (dashed) contours, and **b** M2/M1 and H/M2 contours of Yohkoh/HXT

6.3.6.2 Microwave

We can calculate the MW spectra with different values of B_0, E_{min}, and δ from Eqs. (6.3.14)–(6.3.18), in which some insensitive parameters are fixed to be $N = 10^9\,\mathrm{cm}^{-3}$ and $T = 5 \times 10^6\,\mathrm{K}$ for the ambient plasma, $E_{max} = 5\,\mathrm{MeV}$, and $\theta = 60°$, as shown in Fig. 6.34 [15].

We pay particular attention to the optically thin spectrum, which is also flattened with increasing of E_{min}, but the effect of E_{min} is less than that for HXR in Fig. 6.32, because the NT electrons with higher energies are needed for MW, and the effect of E_{min} is weakened reasonably. Table 6.3 gives the theoretical calculations of flux ratio and spectral index at two adjacent frequencies of OVSA from Eqs. (6.3.14)–(6.3.18) [15].

Similar to Table 6.2 for HXR, the optically thin spectrum is hardened with increasing of E_{min}, but the relation between δ and γ is much more complicated than that for HXR. Figure 6.35 gives an example of the radio diagnosis of E_{min} and δ by the cross-point of double power-law, in which $\vartheta = 60°$, the ambient temperature $T = 5 \times 10^6\,\mathrm{K}$, density $n = 10^9\,\mathrm{cm}^{-3}$, and $E_{max} = 5\,\mathrm{MeV}$, the magnetic field in photosphere B_0 is respectively 800 and 900 Gauss in Fig. 6.35a and b. The spectral indices of double power-law are respectively fitted in 11.2–14.0 and 14.0–16.4 GHz, and the coronal magnetic field can be roughly estimated by the dipolar magnetic model at a given frequency or coronal height.

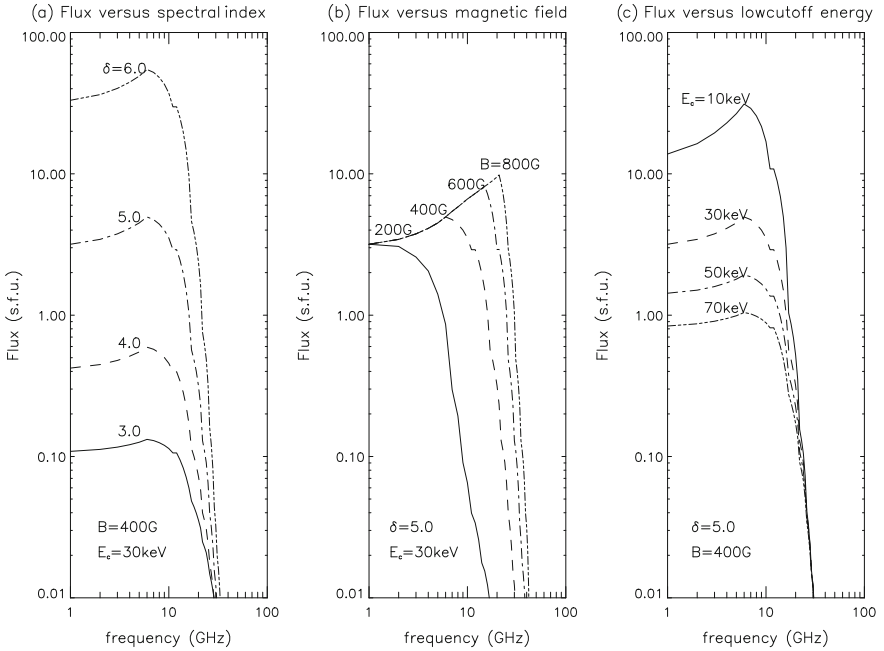

Fig. 6.34 The calculated MW spectra with **a** $\delta = 2$–6, **b** $B_0 = 200$–800 Gauss, and **c** $E_{min} =$ 10–70 keV from Eqs. (6.3.14)–(6.3.18)

Table 6.3 The theoretically calculated of flux ratio and spectral index at 9.0–11.2, 11.2–14.0, and 14.0–16.4 GHz of OVSA, in which $E_{min} = 30$–70 keV, and $\delta = 4.0$, 5.0, and 6.0

δ	4.0	4.0	4.0	5.0	5.0	5.0	6.0	6.0	6.0
E_c (keV)	30.0	50.0	70.0	30.0	50.0	70.0	30.0	50.0	70.0
11.2/9.0	0.29	0.35	0.40	0.19	0.27	0.33	0.15	0.23	0.30
γ_1	5.74	4.79	4.22	7.49	5.91	5.01	8.55	6.63	4.83
14.0/11.2	0.39	0.43	0.46	0.26	0.33	0.38	0.19	0.27	0.33
γ_2	4.21	3.82	3.51	6.00	5.00	4.39	7.37	5.86	4.99
16.4/14.0	0.48	0.50	0.52	0.35	0.39	0.42	0.25	0.31	0.36
γ_3	4.59	4.38	4.17	6.71	6.00	5.44	8.84	7.36	6.43

6.3.6.3 One Example

One event in Fig. 6.36 was simultaneously observed by Yohkoh/HXT and OVSA on 2000 June 10, with time profiles and double power-law indices at different energy channels and frequencies, in which 5 different times in the main phase are marked by a series of vertical lines.

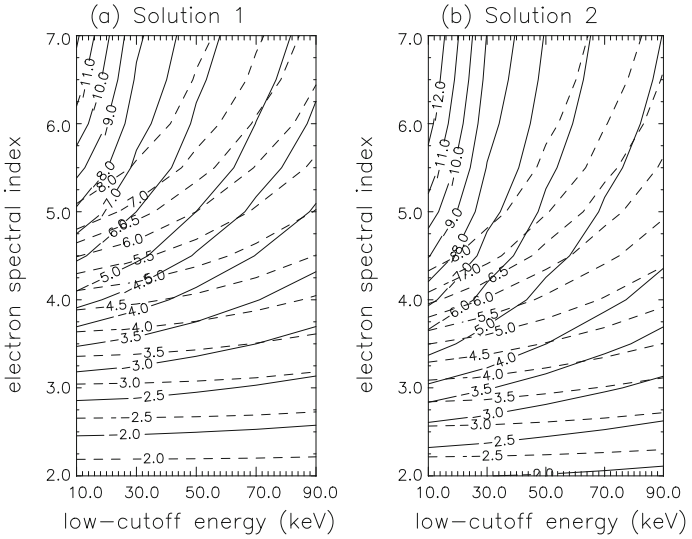

Fig. 6.35 One example to calculate δ and E_{min} from Eqs. (6.3.14)–(6.3.18)

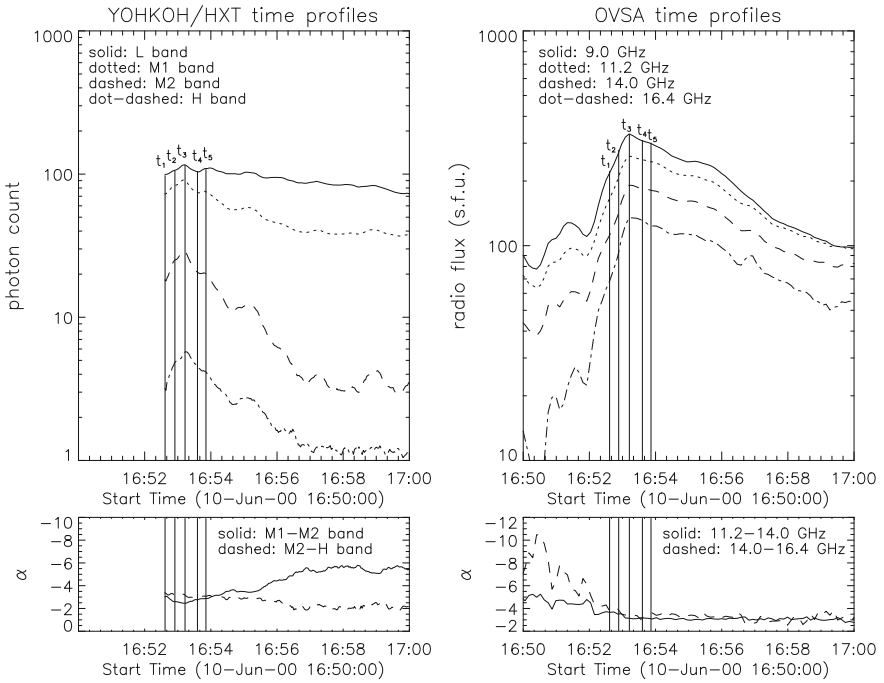

Fig. 6.36 The time profiles and spectral evolution in the 2000 June 10 flare observed by Yhkoh/HXT (left) and OVSA (right)

Table 6.4 The observed Yohkoh/HXT spectral indices of M2/M1 (α_1) and H/M2 (α_2), and OVSA spectral indices of 11.2–14 GHz (α_3) and 14.0–16.4 GHz (α_4), and the theoretically calculated E_{c1} and E_{c2}, δ_1 and δ_2, respectively for the HXR and MW cases

Time	α_1	α_2	E_{c1} (keV)	δ_1	α_3	α_4	E_{c2} (keV)	δ_2
t_1	−3.30	−3.50	38.0	4.50	−3.60	−4.00	33.0	3.80
t_2	−2.70	−3.40	58.0	4.60	−3.50	−3.80	32.0	3.70
t_3	−2.60	−3.20	60.0	4.30	−3.40	−3.70	31.0	3.50
t_4	−2.90	−3.10	50.0	4.20	−3.20	−3.40	30.0	3.30
t_5	−3.00	−3.10	35.0	4.10	−3.20	−3.60	34.0	3.40

The diagnosis of E_{min} and δ from the theoretical calculations in Figs. 6.33 and 6.35 together with the observed double power-law indices in Fig. 6.36 is given by Table 6.4:

It can be seen from Table 6.4 that the value of E_{min} deduced from the HXR data (E_{c1}) is obviously larger than that from the MW data (E_{c2}). The former increases with time in the rising phase ($t_1 \sim t_3$) but decreases with time in de decay phase ($t_3 \sim t_5$), while there is no evident variation of the latter during the event, which further supports the less effect of E_{min} on the MW data. The electron spectral evolution in both of the HXR and MW data shows a well-known SHH or SHS pattern, while the index deduced from the HXR data is always softer than that from the MW data, which just reflects the difference between the precipitating and trapping electrons accelerated from the same flare.

6.3.7 Discussions and Conclusions

Even there are different opinions for the importance of low-energy cutoff in the HXR and MW spectra, E_{min} exists undoubtedly and depends on the escape velocity (energy) of charged particles in a given electric field, which is believed to play an important role on the flattened spectrum at lower energies or frequencies to produce a double power-law even a multiple power-law (together with the other effects like the albedo in the HXR data). Though there are much more parameters in the MW radiation mechanism than that in the HXR one, we can still neglect or fix some parameters, and remain three parameters: E_{min}, δ, and B_0 for the MW data, while only two parameters of E_{min} and δ for the HXR data. There are three methods for diagnosis of E_{min} as follows:

(1) A common cross point may exist in the HXR and MW spectra at different times, when it is close to E_{min}, the electron density is inversely proportional to the spectral index, while when it is close to E_{max}, the electron density is positively proportional to the spectral index, and it is generally located between E_{min} and E_{max}, and the cross points are dispersively distributed in this case. Moreover, the value of E_{min} can

also estimated equivalently by the linear relation between the electron density (or the coefficient of power-law) and spectral index.

(2) The intensity ratio at two adjacent energies or frequencies is independent from the coefficient of power-law, thus we can evaluate the value of E_{min} by the observed intensity ratio versus spectral index, and it is noticed we can not take the intensity ratio and spectral index in the same energy or frequency bands, otherwise, the theoretical calculation is not sensitive to the value of E_{min}.

(3) The strict bremsstrahlung and GS theories can be accepted to compare the calculated and observed spectral indices at two adjacent energies or frequencies, to acquire a unique solution of E_{min} and δ (the photospheric magnetic field should be known for the GS data).

6.4 Diagnosis of Pitch-Angle of NT Electrons

6.4.1 Overview

It is believed that the magnetic field strength in the feet of a coronal magnetic loop is stronger than that in the loop top, thus to form a typical magnetic mirror. When the accelerated electrons by the magnetic reconnection above the loop top or in the connection of two loops are injected into the loop, the perpendicular kinetic energy is directly proportional to the local magnetic field, and the ratio between them is defined as the magnetic moment, which is proven to be a conserved quantity in the quasi-static process (see Sect. 4.2). Hence, the perpendicular kinetic energy increases while the parallel one decreases when the electrons move from the loop top to the feet, a part of electrons with larger parallel kinetic energy can reach the feet and escape from the magnetic mirror, to collide with the dense plasma in chromosphere and photosphere, and to emit X-ray in the two feet; while another part of electrons with larger perpendicular kinetic energy can only move forth and back in the loop, and to emit MW or bremsstrahlung. In this way, the injected electrons are divided into two kinds as precipitating and trapping electrons, respectively to contribute to X-ray and MW emissions in flaring loops. We can deduce a static solution of these two kinds of electrons from the Fokker–Planck equation and boundary conditions of them [75]. For instance, the distribution of trapping and precipitating electrons under an arbitrary initial pitch-angle is respectively written to:

$$f_1 = C \sin\theta_0 \cos\theta_c \left(\frac{E}{E_0}\right)^{-\delta} \ln\left[\frac{\tan(\theta/2)}{\tan(\theta_c/2)}\right], \tag{6.4.1}$$

$$f_2 = C \cos\theta_0 \sin\theta_c \left(\frac{E}{E_0}\right)^{-\delta} \ln\left[\frac{\tan(\theta_c/2)}{\tan(\theta/2)}\right], \tag{6.4.2}$$

$$C = \frac{n}{\left(2\pi \frac{T}{m}\right)^{3/2} \ln\left(\frac{1}{\sin\theta_c}\right)}, \tag{6.4.3}$$

in which θ_c represents a critical angle in the magnetic mirror, when the initial pitch-angle $\theta_0 > \theta_c$, the electrons will be trapped, when $\theta_0 < \theta_c$, the electrons will escape, and θ_c is actually determined by the mirror ratio in the loop top (B_{min}) and feet (B_{max}):

$$\sin\theta_c = \left(\frac{B_{min}}{B_{max}}\right)^{1/2}. \tag{6.4.4}$$

In addition, E_0 is a normalized kinetic energy in the power-law distribution, which is commonly taken as the thermal energy of electrons, T and m are respectively the electron temperature and mass. It is clear that θ_c and θ_0 are two independent parameters for the ratio of trapping and precipitating electrons, the trapping electrons increase with decreasing of θ_c and increasing of θ_0, while the precipitating electrons increase with increasing of θ_c and decreasing of θ_0.

For a given radiation mechanism, such as the thick-target model for HXR or GS model for MW emission, we can substitute the distribution of precipitating or trapping electrons into the formula of the intensity for the corresponding mechanism, and obtain a theoretical intensity at the given band. Inversely, if we can observe the intensity of HXR or GS emission, and observe or calculate the magnetic field in the loop top and feet, we can try to calculate θ_0. It is noticed that θ_0 is different from θ appeared in Eqs. (6.4.1)–(6.4.2), because θ in integrated in the formula of the intensity for the corresponding mechanism, but θ_0 in a constant that independent from the integration, and this is the reason why we only pay attention to θ_0.

6.4.2 *Diagnosis of Mirror Ratio of Coronal Loops*

It is already discussed in detail about the radio diagnosis of the magnetic field and column density of NT electrons in MW burst sources. For instance, using the observed brightness temperature or flux, spectral index, peak frequency, and polarization degree, we can calculate the magnetic field and electron density uniquely [10], based on Dulk and Marsh's approximations [9].

24 loop-like events (or with three separate sources as one LT and two FPs) were selected [76] from the database of NoRH (see Fig. 3.28), which can be divided into two groups with respect to two typical flare models: the standard model of a single flaring loop, and the interaction of a compact loop with a huge loop (see Fig. 3.35). The calculated magnetic field and electron column density in the 24 events are statistically studied in Fig. 3.30, which evidently shows that the magnetic field in the FPs is always stronger than that in the LT, thus it is ready to obtain the mirror ratio in the 24 events.

Furthermore, we have studied the asymmetry in the two FPs of 24 events [77] (see Fig. 3.39), and found that the asymmetry of brightness temperatures in the two FPs is quite obvious up to two orders of magnitude, however, the asymmetry of mirror ratio in two FPs is relatively weaker, hence, we can not explain the asymmetry of brightness temperatures simply by different mirror ratios in the two FPs.

6.4.3 Diagnosis of Initial Pitch-Angle

It is commonly believed that the MW emission in flaring loops is originated mainly from the trapping electrons, according to Eq. (6.4.1), the ratio of the brightness temperatures in the two FPs of one flaring loop equals:

$$\frac{T_{b1}}{T_{b2}} = \frac{\sin\theta_{01}\cos\theta_{c1}}{\sin\theta_{02}\cos\theta_{c2}}, \tag{6.4.5}$$

here, we assume that the other ambient parameters (such as plasma temperature and density) in the two FPs are identical for the same event, and the ratio of the mirror ratios in the two FPs is already obtained, thus it is ready to calculate the ratio of θ_0 in the two FPs (see Fig. 3.46). Finally we can find that the asymmetry of brightness temperatures in the two FPs can be well explained by the different values of θ_0 in the two FPs (see the detailed discussion in Sect. 3.2.4).

6.5 Evidence for Dynamic Evolution of Energetic Electron Spectrum

6.5.1 Overview

The well-known similarity between HXR and MW time profiles suggests that both emissions are generated by a common population of electrons. However, it has been known for a long time that in some solar impulsive bursts the electron energy spectra derived from MW spectra, δ_μ, are harder than ones derived from HXR spectra, δ_x [78–80]. An extensive statistical study of MW and HXR spectral indices was conducted by Silva et al. [81] using BATSE and OVRO data. It was observed that the effect mentioned above occurs for 75% of the events studied. Similar results were obtained for some individual events observed at mm-waves [82–85].

Usually this contradiction is explained by assuming a break-up of the electron spectrum at high energies which results in a flatter MW spectrum (see the calculations in the Ref. [86]). It is supposed that the break-up is caused by the acceleration process itself. On the other hand, the energy spectrum flattening of trapped electrons at low energies due to Coulomb collisions is the natural consequence of the non-stationary

"trap" and "trap + precipitation" models [87–89]. This effect has been confirmed by the recently found dynamic flattening of the frequency spectrum at cm-mm-wavelengths during the decay phase of intensive MW bursts [90].

In order to check some predictions of the different models, we analyze variations of the relation between HXR and MW spectral indices during the evolution of a burst, using the data obtained in 1991–1994 with BATSE and OVRO. Finally, we carry out calculations of the non-stationary trap-plus-precipitation model considering the soft-hard-soft behavior of accelerated/injected electron spectra and compare the results with the new empirical relationships obtained from observations.

6.5.2 Theoretical Prediction of MW and HXR Spectral Evolution

The thick-target model taken both for the HXR and radio sources (MW emission is generated by very anisotropic electrons propagating along the flare loop and then precipitating from it) can explain the observed discrepancy between δ_x and δ_μ only by assuming that the accelerated energetic electrons have a double power-law spectrum with a break-up, as we mentioned above. Note that some evidence for the existence of this break-up has been obtained recently from observations of a break-up in the high-energy part ($\sim$300–500 keV) of HXR/gamma-ray spectra for some intensive events [91–93]. The thick-target model predicts qualitatively the same behavior both for HXR and MW spectral indices during a burst. In particular, the softening of HXR spectrum in the decay phase has to be followed by the simultaneous steepening of the MW spectrum. Note, however, that this is true only if the same acceleration process acts both at low and high energies.

On the other hand, the existence of trapping of the MW generating electrons is confirmed by many observational studies of the relationships between HXR and MW emission. The trapping of part of the accelerated electrons plays a considerable role in the observed HXR and MW spectra. According to the models, the difference between the electron spectral index inferred from HXR spectra, δ_x (usually defined as $\delta_x = \gamma + 1.5$), and the electron spectral index in a radio source, δ_μ, can reach 2 or 1.5 in the case of the trap model and 0.5 or 1.5 in the case of the trap-plus-precipitation model, respectively for impulsive or stationary injections [94]. Both the non-stationary trap and the trap-plus-precipitation models also make certain testable predictions on the spectral evolution. Particularly, they predict considerable decrease of the radio spectral index, α, during the rise and decay of injection even with a constant spectral index of injected electrons [89]. On the contrary, the HXR spectral index, γ, in the trap-plus-precipitation model, has to be constant or decrease a little due to the contribution of trapped electrons (especially during the decay phase of bursts). Moreover, Melnikov and Magun [90] suggest that the spectrum of trapped electrons at mildly relativistic energies may not follow the softening of the injection spectrum due to the relatively high lifetime of these electrons. As a consequence,

the spectrum in the cm-mm-range may flatten gradually despite the simultaneous softening of the HXR spectrum of impulsive bursts. Therefore, according to these models, one should expect from the observational data an increase of the difference $\gamma - \alpha$ during an impulsive burst. It would be interesting to check the behavior of this difference in the decay phase of impulsive bursts, especially when the softening of HXR spectra occurs. Both predictions, from thick target and trap-plus-precipitation models, are quite testable and the next sections of the paper are dedicated to them.

6.5.3 Observational Data

We have analyzed a total of 57 bursts from multiple peaked flares that were simultaneously observed in HXRs by BATSE mainly in the energies of 30–200 keV and in MWs from 1–18 GHz by the solar dedicated Owens Valley Radio Observatory (OVRO). These data are fully described by Silva et al. [81]. The HXR spectrum was fit by a power-law of slope γ. For each time interval, the MW spectrum was fit by a generic function with the same shape as GS emission [95]: $f(\nu) = a_1\, \nu^{a_2}\, [1 - \exp(-a_3\, \nu^{-a_4})]$, which yields the low ($a_2$) and high ($\alpha = a_4 - a_2$) frequency slopes. Assuming the thick target for the production of the HXRs, the electron energy spectral index, δ_x, can be calculated from the photon spectral slope, γ, obtained from the power-law fit: $\delta_x = \gamma + 1.5$. For GS emission, the optically thin slope, α, is related to the spectral index of the accelerated electrons, δ_μ, that emitted the MWs [9] $\delta_\mu = (\alpha + 1.22)/0.9$. Although the last formula does not always correctly connect the radio spectral index α and the electron spectral index δ we use the value δ_μ just as some approximation to within 0.5.

An example of the temporal evolution of the MW and HXR spectral indices can be seen in Fig. 6.37 for the flare of 1991 August 7, which peaked at 19:04 UT. The top panel shows the time profile of the emission at 30 keV and 10 GHz, the spectral indices, δ_x and δ_μ are shown in the second panel with their difference, Δ, plotted on the panel just below. The MW and HXR spectra at the peak are shown in the bottom left and right panels, respectively. We would like to point out that the spectral indices at both wavelengths have almost the same value at the beginning of the flare, while they differ later in the flare, with their difference, Δ, increasing with time.

6.5.3.1 Rise Phase

For the analysis of the spectral index behavior during the rise phase of bursts we selected 34 simple bursts with a clear well pronounced rise phase. As is expected [96], in the majority of events (75%) the HXR spectral index, γ, decreases during the rise phase of the burst. For the rest of events γ increases or remains constant. Similarly, for most of the events (70%) the MW spectral index α continuously decreases in the rise phase of a burst. In the remaining events, it either remains with almost the same value (15%), or continuously increases (15%). As a whole this behavior is in

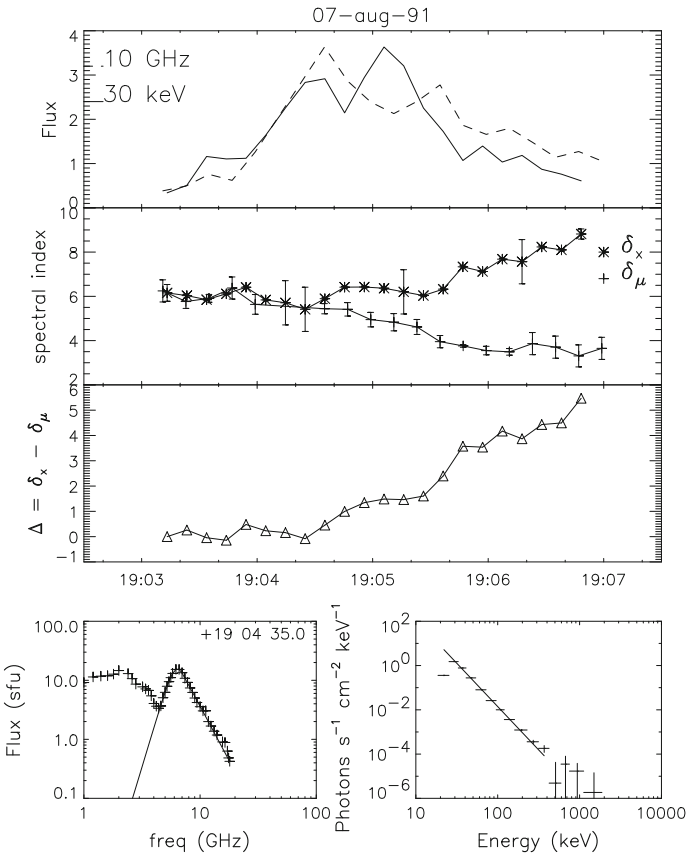

Fig. 6.37 Plot of the temporal evolution and spectra at time of peak for the 1991 August 7 flare

agreement with the results obtained for intensive bursts in the cm-mm-range [90]. In 55% of events the decrease of α is accompanied also by the decrease of γ.

During the rise phase and at maximum of bursts the typical value of the difference $\Delta = \delta_x - \delta_\mu$ lies in the range 0.5–1.5 and rarely exceeds +2, reaching sometimes the values 2–3. In some events, Δ has zero or negative values, usually in the beginning of a burst. In such events Δ ranges from 0 to −3.

6.5.3.2 Decay Phase

The picture of temporal evolution of γ and α during the decay phase of bursts is quite different from that during the rise phase. In this case, the total number of events analyzed was 39. In 74% cases (29 events) γ increases during the decay phase, that is, the HXR spectrum softens. In other events γ decreases or stays constant. On the

other hand, in 67% of cases (26 events) the MW spectral index α does not increase, but decreases (50%) or is constant (17%) during the decay phase. The value of α increases only in 33% of the events. A similar result was obtained earlier by Melnikov and Magun [90]. Also, the difference $\Delta = \delta_x - \delta_\mu$ increases during the decay phase in 74% of events, sometimes reaching 4–6. This opposes the behavior of Δ during the rise phase, when, on the contrary, in most of the events (60%) the value of Δ decreases or is constant.

6.5.4 *Theoretical Simulation of Electron Spectral Evolution in MW Sources*

We have done some model simulations in order to obtain the spectral evolution of trapped electrons that cause the MW spectral evolution. The model assumptions were as follows: homogeneous magnetic trap (radio source), Gaussian time profile for the injection function, $J(E, t)$, and a single power-law energy spectrum of accelerated electrons with the spectral index varying in time according to a parabolic law. We varied the injection duration and plasma density for a quite large interval of values.

The results of the simulations are shown in Fig. 6.38. We see that the energetic spectrum of trapped electrons flattens during the rise phase for all energies. The difference between trapped and injected spectra (responsible for MW and HXR emissions, respectively) at the time of maximum becomes large. During the decay phase, the spectrum at low energies (<100 keV) softens following the spectral evolution of injected electrons, whereas at high energies the spectrum continues to flatten forming a break-up.

The results of modeling show that the particles generating HXR and the particles generating MW emission are physically separated, their spectra have their own evolution that can be considerably different from each other, especially during the decay phase. The HXR emission can also be generated by trapped electrons like MWs, and not only by precipitated ones. However, the time evolution of their spectrum closely relates to the spectrum of injected/accelerated electrons because of their shorter lifetime due to the lower energy.

One can easily show that in the case of long injection time, when the time scale exceeds characteristic life time, the spectrum of high-energy electrons generating MW emission can soften during the decay phase following the spectral evolution of injected electrons. Actually this is consistent with the higher percentage of synchronous changes of α and γ occurring in long duration bursts (>2 min) rather than in short ones.

Note that the non-stationary trap-plus-precipitation model can explain the values of Δ close to 0 in the beginning of a burst and its increase afterward. The reason is that in the beginning of the injection, when t is less than the lifetime, the spectrum of trapped electrons is almost identical to the spectrum of accelerated/injected electrons.

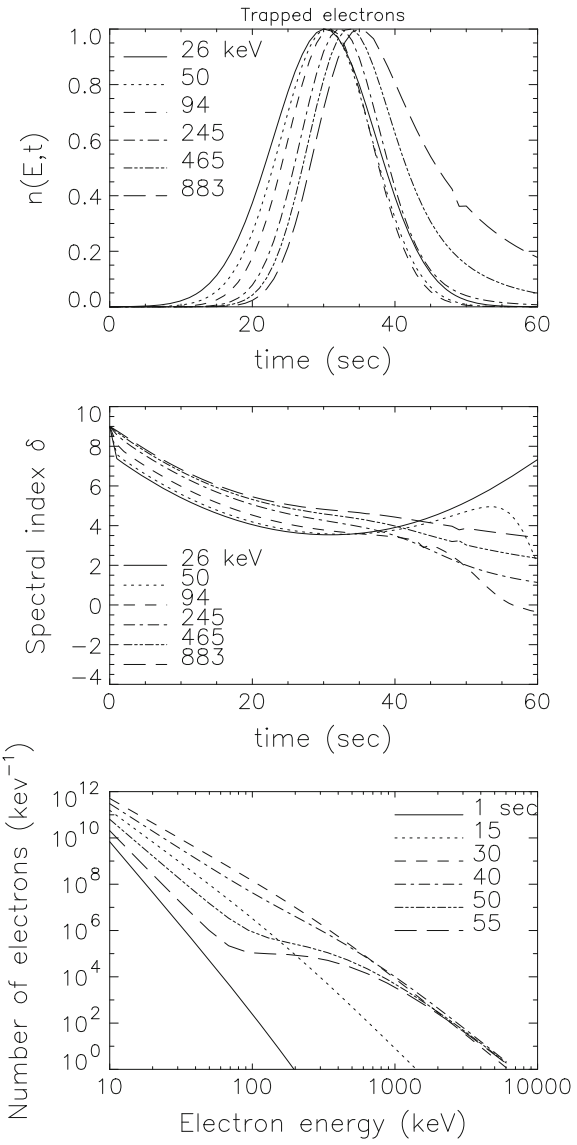

Fig. 6.38 Top: Temporal evolution of the trapped electrons of different energies. Middle: spectral index of trapped electrons for same energies. Bottom: Spectra of trapped electrons for different times during the injection

6.5.5 Conclusions

A most interesting result of our study is the simultaneous decrease of the MW spectral index and increase of the hard X-ray spectral index during the decay phase for the majority of bursts. A characteristic new feature of our statistical analysis is that it is based on the data obtained with the OVRO multi-channel spectrometer supplying

detailed and high-resolution frequency spectra of MW bursts. This, together with BATSE HXR spectral data, has allowed us to get the most extensive quantitative information about temporal evolution of MW and HXR spectral indices.

A common type of spectral evolution for HXR spectra is the 'soft-hard-soft' behavior, that is, the HXR spectral index has a minimum near the burst maximum. However, this is not the case for the MW emission. The optically thin spectral index of MW emission does not reach minimum value near or just after the peak maximum for the majority of events. On the contrary, during the decay phase it continues to decrease. In general, during the decay phase there is a tendency of opposite behavior for HXR and MW spectral indices. The difference between the values of electron spectral index derived from HXRs and MWs can increase from 0.5–1.5 in the rise phase up to 4–6 on decay phase, the spectral index derived from MWs being usually smaller than that from the HXRs throughout the flare.

This result is a strong evidence that the energy spectra of electrons generating MWs and those generating HXRs followed different histories after their common injection into the flare loop. The thick-target approach, according to which both the HXR and MW emissions are generated by precipitated electrons, cannot explain either the difference between electron spectral indices derived from the spectra of these emissions nor the strong variations of this difference in the course of a burst. The only way to explain the observed temporal behavior is to make two quite strong assumptions. First, the acceleration process has to create electron spectra with a break-up at high energies. Second, this process has to act in such a way that simultaneously the low-energy part of the spectrum has to soften, and the high-energy part of it has to flatten.

On the other hand, the model taking into account the trapping/accumulation and the dynamic energy spectrum flattening due to Coulomb collisions (or due to wave particle interactions) of trapped electrons can successfully explain the main features of the evolution and relation between MW and HXR spectral indices. In particular, the simultaneous MW spectral flattening and HXR spectral softening during the decay phase can be easily explained by the long lifetime of high-energy electrons (which generate MWs) in a trap which causes their spectrum to be disconnected from the fast changes of the injected (accelerated) electron spectrum. The high-energy part of their spectrum continues to flatten in the decay phase while the injected spectrum softens. On the other hand, those more rare events, in which both MW and HXR emissions display softening of their spectra, can be explained in the frame of the same model but with conditions inside a flare loop that favors a small lifetime of energetic electrons (e.g. high plasma density or high level of turbulence). In this case the changes of the energy spectrum of electrons generating the MW emission follow the changes of the injection spectrum, giving rise to the similarity of MW and HXR spectral evolution.

6.6 Diagnosis of Acceleration Site and Pitch-Angle Distribution of Accelerated Electrons

6.6.1 Overview

NT emission of solar flares can bring us information on the important questions which are still not fully resolved: location of acceleration and injection sites, mechanisms of acceleration and transport of NT particles inside flaring loops. The main mechanism of MW bursts is GS (GS). Therefore, spatial structure of MW emission in optically thin regime depends mainly on magnetic field strength and geometry and characteristics of NT electrons. GS intensity increases with growth of magnetic field strength B, viewing angle θ (the angle between field lines and the line of sight), and number density of accelerated electrons.

Studies of the MW emission spatial distribution using VLA facilities in 1980s [97–100] and later research using Nobeyama Radioheliograph (NoRH) observations at single frequency 17 GHz [101–103] showed the existence of single compact LT sources, double sources with their peaks located close to the conjugate magnetic FPs, and triple radio sources associated with the FPs of large and smaller flaring loops. The possibility to use two-frequency NoRH observations at 17 and 34 GHz simultaneously with high angular ($5'' - 10''$) and temporal (0.1 s) resolution gives a chance to study the brightness distribution having the information on MW spectrum slope, and, therefore, on the optical thickness in different parts of a flaring loop.

Already the first reports on these observations gave unexpected results showing the presence of the bright loop top source in optically thin regime [104, 105], which was in a disagreement with the simulated MW brightness distribution [106–108]. Preliminary statistical study of MW morphologies using NoRH database of single loop flares [8, 109, 110] have shown that approximately half of optically thin resolved loops have the emission peak between the FPs at the time of burst maximum. The most probable explanation of the observed phenomenon is the presence of inhomogeneous spatial distribution of non-thermal electrons with its maximum in the LT [105].

Another unexpected result relates to the dynamics of brightness spatial distribution. It was found [105, 111] that in some events its morphology changes with time from the distribution with two peaks near FPs in the early phase of a burst to the distribution with one peak in the top of the MW loop in the maximum and decay phases of the bursts. This tendency was explained by the change of the NT electron number density distribution leading to its relative enhancement in the loop top [112, 113]. Formation of the loop top source occurs due to the pitch-angle scattering and accumulation of trapped mildly relativistic electrons with high pitch-angles mostly in the top part of a loop.

Only a few flares showing MW source propagation inside a flaring loop were studied in detail [102, 111, 114, 115]. Nevertheless, a statistical study fulfilled on the database of all single loop-like flares recorded by NoRH in 2002–2007 revealed [110] that most of optically thin MW sources show a redistribution of radio brightness along a loop. Namely, in the rising phase the radio brightness peak is located in the

LT in half of cases, while on the peak and decay phases this occurs in most of cases (80 and 66%, respectively). Therefore, a further analysis is needed to understand better the nature of this phenomenon. Investigation of such a dynamics should shed light on the NT electrons transport and acceleration site location in particular events.

The event of 2002 August 24 is characterized by a spectacular giant MW flaring loop with its FP separation of about 5×10^4 km and maximum height of 3.3×10^4 km well seen above the west solar limb. It was very well resolved by NoRH. The loop plane was aligned almost parallel to the solar limb. It means that the effect of the viewing angle on GS emission is negligible for this event. Therefore this is a good case for a detailed analysis of MW brightness distribution and its dynamics along the loop. This flare was a subject of several studies [116–118]. But none of them considered the redistribution of MW brightness along a flaring loop. In fact, the main impulsive phase of the flare, which consisted of multiple emission peaks, has shown really interesting evolution of MW brightness distribution. The purpose of our paper is to study properties of the spatial dynamics and understand its origin.

6.6.2 Observations

The intense solar flare, which was X3.1 on the GOES scale, occurred at 01:00 UT, 2002 August 24 near to the western limb with heliographic coordinates $S01°$, $W73°$. It was the last from the serious of flares connected with AR NOAA 10069 and was followed the high speed CME. The corresponding MW burst was observed by Nobeyama Radio Polarimeter and NoRH [119]. Unfortunately, 17 and 34 GHz data processed by standard NoRH routine and presented at http://solar.nro.nao.ac.jp/ on the event were saturated during the main peak.

For the diagnostic of physical parameters in the flare we needed also some complimentary data on optical, EUV and soft X-ray and HXR emissions. So, we have used the data of SOHO/MDI [120], Trace [121] and GOES (http://www.oso.noaa.gov/goes). We could not use RHESSI imaging observations of the HXR burst since its impulsive phase corresponded to the RHESSI night. Fortunately, the full Sun HXR data for the necessary time interval were available from detector SONG [122] aboard of space solar observatory CORONAS-F [123].

6.6.2.1 Time Evolution of MW and HXR Emissions

The flare 2002 August 24 was extremely strong at MWs. Its maximum flux density reached $F_{17} = 1.6 \times 10^4$ sfu at 17 GHz and $F_{34} = 1.1 \times 10^4$ sfu at 34 GHz. NoRP frequency spectrum at the same moment showed its peak frequency about 17 GHz. The total flux time profiles of the burst at 17 GHz (thin line) and 35 GHz (thick line) obtained with NoRP are shown in Fig. 6.39a. The profiles have multiple emission peaks well separated from each other. Every peak is numbered at the top of Fig. 6.39.

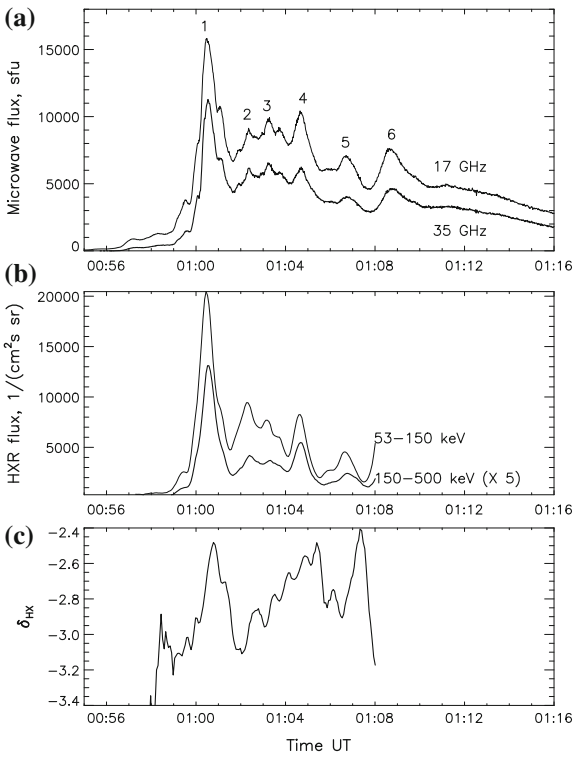

Fig. 6.39 **a** NoRP total flux time profiles at 17 GHz (thin line) and 35 GHz (thick line); **b** HXR fluxes from SONG/CORONAS-F at 53–150 keV (solid) and 150–500 keV (dotted line), the flux at channel 150–500 keV is multiplied by 5; and **c** HXR spectral index calculated for channels 53–150 and 150–500 keV. After 01:08 UT, HXR signals were contaminated by influence of fluxes of energetic particles of the Earth radiation belts, and therefore are not shown on the figure

The radio burst duration $\Delta T_{0.5} \approx 300$ s at the level of 50% of the 35 GHz maximum flux density.

Figure 6.39b demonstrates time profiles of HXR emission in two energy channels 53–150 and 150–500 keV. Note that after 01:08 UT signals are disturbed by fluxes of energetic particles of the Earth radiation belts, and are not presented on the figure. One can see that as a whole the HXR time profiles resemble very much the MW time profiles. The comparison shows one to one correspondence of their subpeaks. Figure 6.39c shows HXR spectral index calculated in the energy range defined by channels 53–150 and 150–500 keV. The flux at channel 150–500 keV is multiplied by 5 times for better comparison. In a large scale, the spectral index behavior is the so- called 'SHS' type. However, a closer look reveals hardening of the spectrum during some time right after each peak maximum ('SHH' behavior).

A comparative cross-correlation analysis reveals time delays between main peaks of MW (NoRP) and HXR (53–150 keV) emission: 6 s ($\pm$2 s) for 17 GHz and 8 s ($\pm$2 s) for 35 GHz. Such kind of temporal delays are quite usual for long duration, gradual bursts, and described in literature [94, 124].

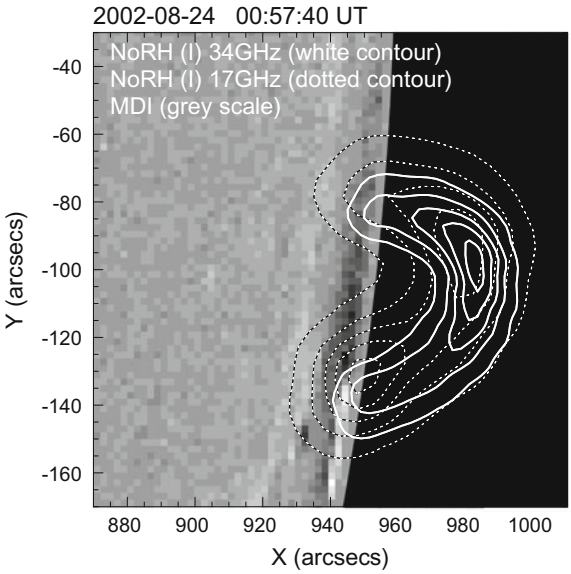

Fig. 6.40 SOHO/MDI photospheric magnetogram (gray scale) overlaid by contours of radio images at 0.1, 0.3, 0.5, 0.7 and 0.9 levels of the maximum brightness temperature (dotted for 17 GHz and white for 34 GHz). Magnetogram was obtained near the time of radio burst and was rotated to the moment of radio images. White color indicates positive, and black color - negative magnetic field polarity

6.6.2.2 Radio, Optical, and EUV Images

Figure 6.40 represents radio images taken in the early rise phase of the flare, at 00:57:40 UT, after small increase of the radio flux (see Fig. 6.39). The projections of radio sources display a well developed loop-like structure at both frequencies. MW intensity contours are overlaid on photospheric magnetograms from SOHO/MDI (gray scale). Magnetogram was obtained at 01:35:00 UT. In the figure it is adjusted to the time of the radio images. Magnetogram shows the negative (black color) and the positive (white color) magnetic structures of the flare AR that can hardly be accurately associated with two loop ends because the region is close to the limb. However, a magnetogram obtained 2 days before the event for the same AR shows $B_{min} \approx -1200$ G and $B_{max} \approx +1000$ G. Contours (dotted for 17 GHz and white for 34 GHz) show 0.1, 0.3, 0.5, 0.7 and 0.9 levels of the maximum brightness temperature. The angular sizes of a source taken along a loop axis at the level of 50% of the 34 GHz maximum brightness temperature are $80''$ at 34 GHz and $90''$ at 17 GHz.

The high spatial resolution ($\sim 1 - 2''$) of Trace images allowed us to estimate characteristic transverse scales of the flaring magnetic loops with much better resolution than corresponding MW images. Figure A.11 in Appendix A represents differential EUV (195 Å) images (color) obtained by subtracting the earlier image (01:00:24 UT) from the later one (01:00:51 UT). Differential image shows the most abrupt changes happened between two images. Therefore, on this figure we can see only those magnetic loops (or filaments, ropes), which were involved in the flare in the time interval close to the maximum time of peak 1 on Fig. 6.39. A superposed 34 GHz Nobeyama loop is shown by white contours. Contours correspond to 0.25 and 0.5 levels of max-

imum brightness temperature. Figure A.11 in Appendix A reveals that the width of the specific EUV loops involved in the flare is about $1'' - 3''$, but they are united in a common wisp, almost corresponding to the MW loop. The cross section of the MW loop is about $10''$ on the level 0.5 of T^{34}_{Bmax} near the south FP, it is only partly filled by bright EUV filaments (loops) which alternate with dark spaces between them. So, we have estimated the filling factor of the MW loop as $k = 2$. This factor will be used later for diagnostics of plasma parameters inside the radio loop.

6.6.3 Evolution of Brightness Distribution

The radio burst started with the brightening of the southern FP at 00:54:00 UT at both NoRH frequencies, 17 and 34 GHz. At the early rise phase there were several temporal subpeaks and the brightness distribution changed from almost homogeneous glowing to the configuration with 34 GHz brightness peak in the top part of the loop at the time 00:57:40 (see Fig. 6.38) with $T^{34}_B = 25$ MK. Even more dramatic changes occurred during the most intensive part of the burst.

6.6.3.1 Dynamics of Brightness Distribution at 34 GHz

Figure 6.41 represents brightness evolution of 34 GHz emission during the main temporal peak denoted as peak 1 on Fig. 6.39. Top panel displays contour images of the radio source at four different moments taken in the rise, peak and decay phases as well as at the end of the decay phase of the main peak just before the start of the second peak (denoted as valley). Contours show 0.1, 0.4, 0.6, 0.75, 0.95 levels of the maximum brightness temperature. On the rising phase of the main peak from 00:59:00, the southern FP of the loop again becomes most bright at 34 GHz and remains the brightest part of the loop until the maximum at 01:00:30. In Fig. 6.41a and b we can also see two other brightness peaks: one near the opposite (northern) FP and one near the loop top, but they are much weaker. Only in the decay phase the loop top becomes relatively brighter than the FP sources (Fig. 6.41c) which almost disappear to the time of the valley (Fig. 6.41d).

To show quantitatively how the high frequency intensity of MW emission changes along extended flaring loops we define the visible magnetic loop axis (shown by dot-dashed line) and plot the radio brightness temperature as a function of distance along this axis. Bottom panel displays spatial distributions of radio brightness temperature at 34 GHz along a visible flaring loop axes at the moments of time corresponding to the upper images. During the decay after the main peak the brightness temperature in the southern FP source decreases 5 times, but in the loop top only 2 times: from 100 MK down to 50 MK (compare Fig. 6.41f and h). Moreover, T^{34}_B in the loop top retains the same value 50 MK during the next two peaks (peaks 2, 3) and following valleys until 01:04:10 UT (see Fig. 6.42 first and second rows).

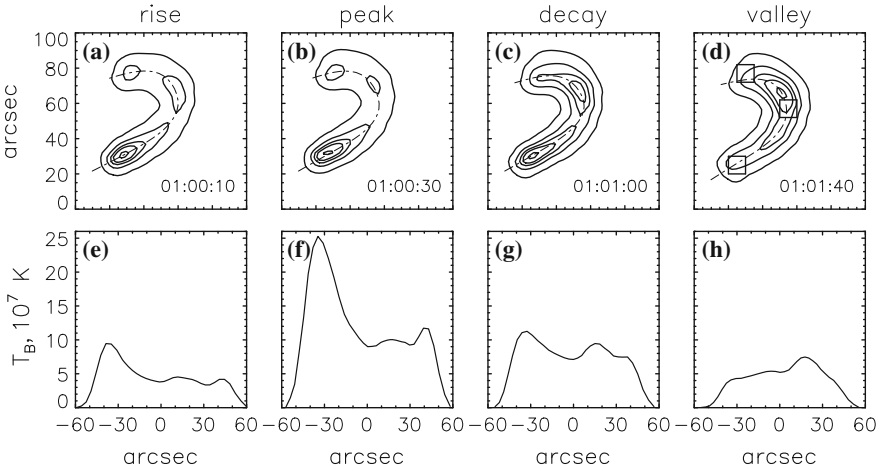

Fig. 6.41 **a**–**d**: 34 GHz contour images of the radio source at four different moments taken in the rise, peak and decay phases as well as at the end of the decay phase of the main peak just before the start of the second peak. Contours show 0.1, 0.4, 0.6, 0.75, 0.95 levels of the maximum brightness temperature. Dot-dashed line shows the visible flaring loop axis. **e**–**h**: spatial distributions of radio brightness temperature at 34 GHz along a visible flaring loop axes shown on the top panel at the corresponding moments of time. Abscissa is the distance along the loop, negative values correspond to southern FP and zero position to the LT

Interestingly, the sources of all major temporal peaks 1–6 are located at the same radio loop and the similar evolution of brightness distribution repeats itself for all these sub-bursts. Figure 6.42 shows 34 GHz images of the flare for peaks 2–6 (left column) and valleys following each peak (third column from left). We can see that at peak times 34 GHz brightness maximum is located in southern FP with additional brightening in the northern leg, while valleys are accompanied by brightening of the loop central part with the brightness maximum slightly shifted to the northern leg. Second and fourth columns are the corresponding spatial profiles of T_B^{34} along a visible flaring loop axes. Zero position of the ordinate axis corresponds to the loop top. We can see that absolute brightness temperature of the loop top at the valley times is not reduced compared to the corresponding previous peaks of the flux time profile. It remains 50 MK for peaks 2 and 3; 40 MK for peak 4; 20 MK for peak 5 and it even increases from 10 MK to 20 MK for peak 6. At the same time the brightness T_B in the southern FP drops down significantly.

6.6.3.2 Dynamics of Brightness Distribution at 17 GHz

At the second frequency, 17 GHz, the similar tendency of brightness distribution evolution is found in Fig. 6.39 for peaks 4–6. However, unlikely to 34 GHz, for the peaks 1–3, the upper part of the loop was most bright already by the time of peak's

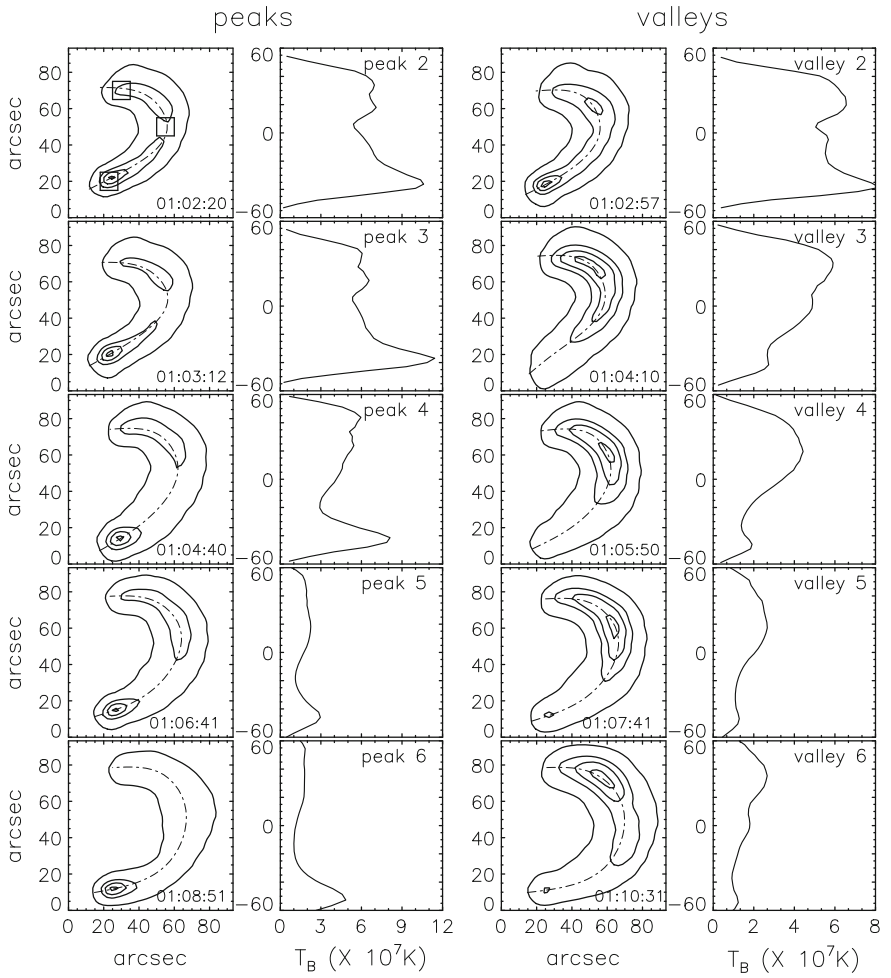

Fig. 6.42 34 GHz contour images of the radio source taken at the times of peaks 2–6 (left column) as well as at the of following valleys (third column from left). Contours show 0.1, 0.5, 0.75, 0.95 levels of the maximum brightness temperature. Dot-dashed line shows the visible flaring loop axis. Second and fourth columns: spatial distributions of radio brightness temperature along a visible axes of flaring loop shown on the image at the left at the corresponding moment of time. Ordinate axis is the distance along the loop, negative values correspond to southern FP and zero position to the LT

maximum. A comparison of Figs. 6.41 and 6.43 clearly show that the most bright regions of the loop at 17 GHz are definitely shifted from the most bright regions at 34 GHz toward the middle part of the loop. It is well seen even in the rise phase of peak 1.

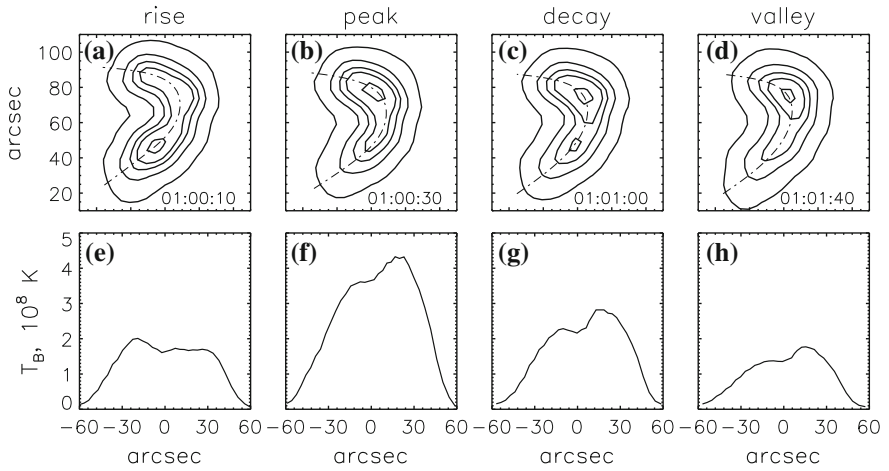

Fig. 6.43 The same as in Fig. 6.41, but for frequency 17 GHz

More quantitative information about the redistribution of the MW brightness along the flaring loops can be obtained from the comparative analysis of the emission time profiles generated in different parts of the loop.

6.6.3.3 MW Emission Time Profiles from the Upper and Lower Parts of the Loop

In Fig. 6.44 we show the flux time profiles from the regions corresponding to different parts of the MW loop. Flux densities F_{17} and F_{34} at two frequencies were calculated from NoRH images by integration of brightness temperature over areas of the size $10'' \times 10''$. The location of boxes is shown in Fig. 6.41d. Time profiles of fluxes from boxes, located near southern FP (SFP), in the loop top (LT) and near northern FP (NFP) are shown in Fig. 6.44a, b, and c, respectively. The time resolution is 1 s, the time interval is limited by the main peak. The dotted and solid lines correspond to the 17 and 34 GHz emission, respectively.

A very interesting feature of these time profiles is time delays. We can see that the emission maximum from the loop top is delayed against maxima from the FP sources for both frequencies. These delays are more pronounced at 34 GHz (6 ± 1 s for NFP and 9 ± 1 s SFP) than at 17 GHz (4 ± 1 s for NFP and 8 ± 1 s SFP). Furthermore, the time profile of 34 GHz emission from the loop top is wider and its decay is slower than those from the FPs. Another type of time delay is the delay of the burst maxima at higher frequency, 34 GHz, against that at 17 GHz.

Time profiles of spectral index $\alpha = ln(F_{34}/F_{17})/ln(34/17)$ are shown in Fig. 6.44d. The dotted, solid and dashed lines correspond to SFP, LT and NFP sources, respectively. Spectral index, α is negative and increasing for the LT and NFP sources

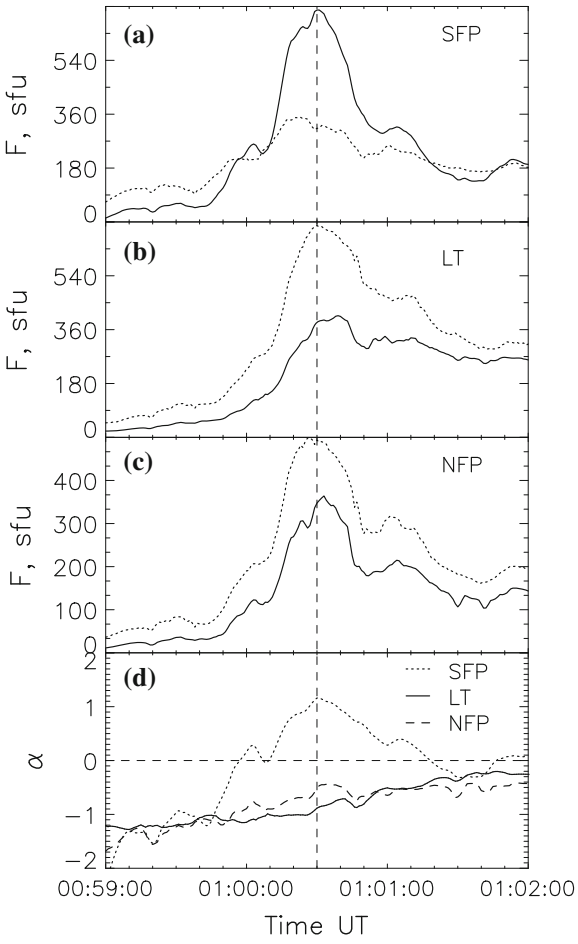

Fig. 6.44 Flux density time profiles averaged over 2 s from three boxes shown in Fig. 6.39d and located at **a** southern FP (SFP), **b** loop top (LT), and **c** northern foot point (NFP). The dotted and solid lines correspond to the 17 and 34 GHz emission, respectively. **d** Spectral indexes time profiles averaged over 5 s. The dotted, solid and dashed lines correspond to the SFP, LT and NFP sources, respectively

during the main temporal peak. It remains almost constant (between -0.5 and -0.3) during other subpeaks. Therefore, these parts of the loop are optically thin at least at 34 GHz. However, α is positive for the southern FP source during three first major peaks. It is seen from Fig. 6.44a that the flux density at 34 GHz well exceeds the flux at 17 GHz from this source. Since the brightness temperature in SFP reaches very high values $T_B \geq 10^8$ K, such fact implies that the southern part of the loop at 17 GHz is the optically thick NT GS source. This conclusion is confirmed by the evolution of spectral index: it increases on the rising phase and decreases just after the burst peak when the number density of accelerated electrons falls down resulting in subsequent optical thickness diminution. If the Razin effect is responsible for positive α, the evolution of spectral index would be different [41].

6.6.4 Discussions

6.6.4.1 Explanation for the Main Observational Features

It is interesting, that together with some similarity of the brightness distribution evolutions at 34 and 17 GHz, there is quite a strong difference between them. At frequency 34 GHz the brightness has its maximum in the middle part of the loop only on the late decay phase, whereas at 17 GHz this occurs much earlier: already on the maximum and initial decay phases of the major burst peaks.

We believe that the different time evolution of the 17 GHz source can be easily explained by enhanced optical thickness ($\tau \geq 1$) of the MW loop at this frequency. A strong evidence of this fact for the southern part of the loop is presented at the end of the previous section from the analysis of the frequency spectral index. A simple comparison of Figs. 6.41 and 6.43 show that at 17 GHz the brightness in the middle part of the loop at all the main peak phases is several times higher than at positions of its southern and northern feet (that is at positions of 34 GHz brightness peaks in SFP and NFP on the rise and maximum phases).

This feature is a well-known property of the brightness distribution along an optically thick MW loop [106–108]. The brightness temperature in the middle part is higher because the emission at a fixed frequency in the optically thick source with weaker magnetic field is generated at higher harmonic numbers by higher-energy electrons. Further in the paper we will mostly discuss images at 34 GHz because of two reasons: (1) better spatial resolution; (2) smaller optical thickness (usually $\tau < 1$) that allows us to avoid the influence of self-absorption on the brightness distribution.

The most interesting result obtained from the analysis in Sect. 6.6.2 is that the brightness distribution at 34 GHz along the loop is changed for all major temporal peaks of the burst with the same tendency. Namely, the rise phase of every next major peak results in the redistribution of brightness toward FPs (mostly toward the SFP). And, on the contrary, after the peak maximum (in the decay phase) the emission in the upper part of the loop gradually becomes dominant, and the FP sources almost disappear.

Our observation of the brightness peaks in the loop feet on the rise and maximum phases agrees with the well-known model simulations [106, 107] that predict the brightness peaks of optically thin GS emission to be near the FPs of extended loops with a nonuniform magnetic field, $B(s)$, under the assumption of homogeneous distribution of NT electrons, $N(s) = const$, along the loop. The increase of the brightness temperature occurs due to strong dependence of GS intensity on the magnetic field strength, that is expected to be larger near the feet of an extended loop. However, the observed gradual appearance of the brightness maximum near the loop top in the decay phase is not possible to explain in the frame of the accepted model assumption, especially for the analyzed limb loop whose plane is almost perpendicular to the line of sight.

In our opinion, the most probable explanation for the observed relative enhancement of brightness in the upper part of the loop is a strong relative increase of electron number density near the loop top, similar to the explanation proposed for the famous LT optically thin MW sources [105]. There may be at least two reasons for that. One of them could be the appearance of a new source of accelerated electrons in the top part of the loop in the decay phase. Such an assumption, however, looks unlikely because in this case we should expect such a wonderful appearance in the decay phase of each major peak. Another one is the influence of transport effects, namely, faster scattering of NT electrons into a loss-cone in the lower part of the loop and, on the contrary, their better accumulation in its upper part [112]. The effects naturally act after each new electron injection resulting in the observed sequence of the oscillatory redistribution of brightness in the loop.

There are strong observational evidences for this quite natural idea. The first evidence is the fact that the absolute brightness temperature at 34 GHz in the loop top at the majority of valleys is not reduced compared to corresponding previous peaks of flux densities (Sect. 6.6.3). This fact denotes a process of the accumulation of accelerated electrons in the upper part of the loop. The existence of delays between MW and HXR intensity time profiles, as well as between emission maxima at the higher and lower frequencies is another evident indication of electron trapping in MW sources [90, 125]. Furthermore, the delays between MW emissions from the upper and lower parts of the loop as well as longer decay of the emission from the loop top are also a strong evidence of the preferable trapping of high-energy electrons in the upper part of the flaring loop.

The proposed idea will be tested quantitatively in Sect. 6.6.4.2 by means of numerical simulations of dynamics of NT electrons and their GS emission in different parts of a magnetic loop (trap). But before starting the simulations, we need to know some parameters of plasma, magnetic field, and NT electrons in the observed flaring loop.

6.6.4.2 Diagnostics of Magnetic Field Strength and High-Energy Electrons Number Density in the Upper and Lower Parts of the Loop

Let us estimate the ratio of electron number densities in the upper and lower parts of the loop N_{LT}/N_{SFP} for the moments of time corresponding to the maximum and decay phases of major peak 1 in Fig. 6.39. Estimations can be done by fitting observed fluxes at 17 and 34 GHz by the spectrum for both sources using exact formulas [17] for the GS emissivity and absorption coefficient. Note that for the estimations we need to know the electron energy spectrum, electron pitch-angle distribution, the sizes of the MW source. We also should know the magnetic field strength B and plasma density n_0 in a source, since in the case of high ratio of n_0/B the Razin effect may strongly influence on the GS intensity and frequency spectrum [46]. For our crude estimations, most of the information was obtained from observations, and some from simple realistic assumptions.

For spectra calculations we assumed that non-thermal electrons have an isotropic pitch-angle distribution and double power-law energy dependence with the *high-energy* power-law index δ_h derived from HXR emission and low-energy index derived from relation $\delta_l = \delta_h - 1.5$ with the break energy $E_{break} = 1$ MeV determined from the relation between the energy dependent life time of electrons and time scale of the observed peak 1 [46, 94]. The ambient plasma density was derived from GOES/SXT data at the time of peak 1: $n_0 = 8 \times 10^{10}$ cm^{-3}. The source depth was taken as $L \approx 3.6 \times 10^8$ cm, to be equal to the width of the MW loop $10''$ divided by filling factor $k = 2$.

To evaluate the magnetic field strength we used the fact, that the SFP source was optically thick at 17 GHz at the moment of peak 1 (see Sect. 6.6.3). Assuming that the viewing angle $\theta \sim 80$–$85°$ and taking power-law index $\delta = 3.6$ derived from HXR emission in the thick-target approach (Sect. 6.6.2), we estimated magnetic field strength in the southern FP as $B_{SFP} \approx 1000$ G. For this estimation we took into account the filling factor of MW loop $k = 2$ obtained from EUV observation (see Sect. 6.6.2), multiplying observed T_B by this factor. Using the derived B, we calculated the number density of accelerated electrons in SFP source as $N_{SFP}(E > 0.5\ \text{MeV}) = 3 \times 10^4$ cm^{-3} at the maximum of peak 1. At the valley time we have $\delta = 4.1$ (see Fig. 6.39c) and $N_{SFP}(E > 0.5\ \text{MeV}) = 3 \times 10^3$ cm^{-3}. For estimations of electron number densities we chose the energies of emitting electrons as $E > 0.5$ MeV because it is consistent with the observed frequencies, 17 and 34 GHz, estimated values of magnetic field, plasma number density, and the values of observed time delays between MW and HXR peaks [125].

As it follows from Fig. 6.44, the LT and northern foot sources should be optically thin. Therefore, in this case we used a different procedure for evaluating the magnetic field strength, namely the spectral forward fitting. The best spectral fit for the looptop (LT) source was obtained with magnetic field strength $B_{LT} \approx 200$ G and electron number density $N_{LT}(E > 0.5\,\text{MeV}) = 9 \times 10^5$ cm^{-3} at the peak time, and $N_{LT}(E > 0.5\ \text{MeV}) = 6 \times 10^5$ cm^{-3} at the valley time.

A similar spectral fitting carried out for the northern FP source gave the magnetic field strength $B_{NFP} \approx 800$ G. The lower (than in the SFP) value of B_{NFP} agrees well with weaker MW emission from the NFP (compared to the SFP). It also agrees with the existence of HXR-source in this FP with the lack of HXR emission in the SFP on the initial stage of the flare (around 00:54 UT) [118].

From the obtained numbers we can conclude that the number of mildly relativistic electrons in the LT is much higher than near the southern FP. This is true even in the maximum phase of peak 1 ($N_{LT}/N_{SFP} \sim 30$), that is quite unexpected because the brightness temperature in the loop top is by 2.5 times lower than near the FP. During the decay phase the number density of electrons N_{SFP} dropped down by order of magnitude, while N_{LT} only by 1.5 times. As a result the ratio N_{LT}/N_{SFP} has grown about 7 times and reached 200. So, the results of our diagnostics confirm the guess about a relative enhancement of electron number density in the upper part of the loop in the decay phase.

6.6.4.3 Dynamics of Electron and MW Distributions in a Magnetic Loop

To understand the origin of the observed MW brightness distribution and its dynamics we do modeling of the time evolution of spatial distribution of NT electrons and GS emission along a magnetic loop. The distribution of energetic electrons along a magnetic loop can be obtained by solving the kinetic Fokker–Planck equation. We consider the non-stationary Fokker–Planck equation in the form [126], which takes into account Coulomb collisions and magnetic mirroring:

$$\frac{\partial f}{\partial t} = -c\beta\mu\frac{\partial f}{\partial s} + c\beta\frac{d\,ln B}{ds}\frac{\partial}{\partial\mu}\left[\frac{1-\mu^2}{2}f\right]$$

$$+\frac{c}{\lambda_0}\frac{\partial}{\partial E}\left(\frac{f}{\beta}\right) + \frac{c}{\lambda_0\beta^3\gamma^2}\frac{\partial}{\partial\mu}\left[\left(1-\mu^2\right)\frac{\partial f}{\partial\mu}\right] + S\,, \qquad (6.6.1)$$

where $f = f(E, \mu, s, t)$ is electron distribution function of kinetic energy $E = \gamma - 1$ (in units of mc^2), pitch-angle cosine $\mu = cos\ \alpha$, distance from the flaring loop center s, and time t, $S = S(E, \mu, s, t)$ is injection rate, $\beta = v/c$, v and c are electron velocity and speed of light, $\gamma = 1/\sqrt{1-\beta^2}$ is Lorentz factor, $B = B(s)$ is magnetic field distribution along the loop, $\lambda_0 = 10^{24}/n(s)\ln\ \Lambda$, $n(s)$ is plasma density distribution, $\ln\Lambda$ is Coulomb logarithm.

For simplicity, just to show most important effects of spatial dynamics of electron distribution in a trap, the assumptions are followed by the Ref. [114]. Some of model parameters are taken to be close to ones obtained in Sect. 6.6.4. The magnetic trap (loop) is symmetrical and its half-length is $s_{max} = 3 \times 10^9$ cm. Plasma density is homogeneous along the loop and $n_0 = 5 \times 10^{10}$ cm^{-3}. Magnetic field is inhomogeneous: $B(s) = B_0\ \exp(s^2/s_B^2)$, where $s_B = 2.37 \times 10^9$ cm. The injection function $S(E, \mu, s, t)$ is supposed to be a product of functions dependent only on one variable (energy E, cosine of pitch-angle μ, position s, and time t):

$$S(E, \mu, s, t) = S_1(E)S_2(\mu)S_3(s)S_4(t)\,, \qquad (6.6.2)$$

where the energy dependence is a power-law $S_1(E) = (E/E_{min})^{-\delta}$, $E_{min} = 30$ keV, with constant spectral index $\delta = 3.6$ that is equal to one derived from HXR spectrum; pitch-angle distribution is Gaussian: longitudinal to magnetic field lines (or beam-like) $S_2(\mu) = \exp[-(1-\mu^2)/\mu_0^2]$, or transverse to magnetic field lines (or pancake-like) $S_2(\mu) = \exp[-\mu^2/\mu_0^2]$; spatial distribution is also Gaussian, $S_3(s) = \exp[-(s-s_1)^2/s_0^2]$; time dependence is $S_4(t) = \exp[-(t-t_m)^2/t_0^2]$, $t_m = 25$ s, $t_0 = 14$ s, injection duration is 50 s, similar to single peak duration of the flare under study.

Distributions $f = f(E, \mu, s, t)$ were obtained for different combinations of parameters. We changed three parameters of injection function to have various models to study: (1) s_1, location of the source of energetic electrons (loop top, $s_1 = 0$; close to a FP, $s_1 = 2.4 \times 10^9$ cm); (2) s_0, its extension along the loop (compact

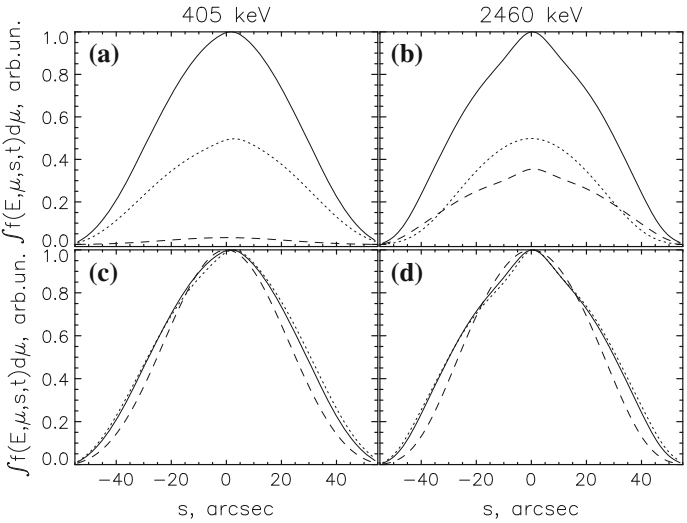

Fig. 6.45 Results of the model simulations using the Fokker–Planck equation. Electron number density along the loop is shown by dotted lines at the rising phase ($t = 18.2$ s), by solid lines near the peak time ($t = 31.8$ s), and by dashed lines at the decay phase ($t = 99$ s) for energy of electrons (**a**, **c**) $E = 405$ keV and (**b**, **d**) $E = 2460$ keV. On plots (**c**, **d**) distribution function for each time is normalized to its maximum. Injection is located in the loop top, $s = 0$ cm, pitch-angle distribution of injection function is longitudinal along the loop toward to right foot

source, $s_0 = 3 \times 10^8$ cm; extended, $s_0 = 2 \times 10^9$ cm; and continuous along the trap, $s_0 \gg s_{max} = 3 \times 10^9$ cm); (3) the type of pitch-angle distribution (isotropic, $\mu_0 \gg 1$; longitudinal; and transverse to magnetic field lines).

The obtained electron distributions show quite strong anisotropies of different types ('pancake' or 'beam-like') in different parts of the magnetic loop. It is known [51] that GS emission is very sensitive to the anisotropies of emitting mildly relativistic electrons. So, the corresponding GS emission distributions along the model loop were calculated using the exact formalism [17]. For the calculations we took viewing angle $\theta = 78.5$ deg because the flaring loop was observed on the solar limb, and its plane was seen almost perpendicular to the line of sight (see Fig. 6.45). We assumed that the principal spatial sizes of the model loop were coincident with ones used in Sect. 6.6.4.2.

As a result of our simulations we were able to compare the dynamics of GS emission distribution for various models with the observed dynamics of MW brightness along loops at 34 and 17 GHz. Most of the considered models are shown to be inconsistent with the observations. For example, the models with a compact isotropic (or pancake type of anisotropy) source located at the loop top give a GS brightness distribution at 34 GHz with the single maximum at the loop top during all the injection period. So, they are not consistent with the MW brightness peaks near the FPs observed during the rise and maximum phases. The models with a compact source of electrons with any type of anisotropy located near a loop FP can not provide the

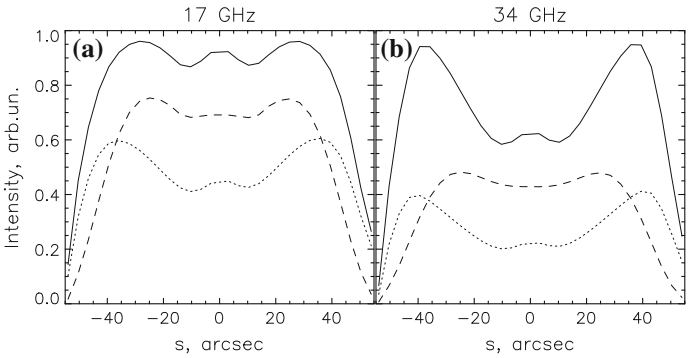

Fig. 6.46 Evolution of GS intensity distribution along the model loop **a** at 17 GHz and **b** at 34 GHz calculated for the same moments of time as in Fig. 6.45

peak of energetic electrons number density at the upper part of the loop during the rise and maximum phases. Therefore, they are not consistent with the results of MW diagnostics (Sect. 6.6.4) showing that the electron number density at the loop top is much greater than near the southern FP.

Only two models have shown the GS emission spatial dynamics similar to the observed brightness dynamics at 34 and 17 GHz. Both of them are characterized by the source of electrons located at the loop top. One of them has an extended electron source of Gaussian type $S_3(s) = \exp[-s^2/s_0^2]$, $s_0 = 2 \times 10^9$ cm, with the isotropic injection $S_2(\mu) = const$. In Figs. 6.45 and 6.46 we present the results of the simulation for another model which describes our observation in the best way. In this model a compact source of electrons $S_3(s) = \exp[-s^2/s_0^2]$, $s_0 = 3 \times 10^8$ cm, is located in the center of the trap ($s = 0$) with the pitch-angle distribution slightly anisotropic along magnetic field lines $S_2(\mu) = \exp[-(1-\mu^2)/\mu_0^2]$, with the wide beam ($\mu_0 = 0.6$) directed toward the right foot.

In Fig. 6.45 one can see the time evolution of normalized electron number density along the loop for energies of electrons $E = 405$ keV and $E = 2460$ keV. On plots (c, d) distribution function for each time is normalized to its maximum. A single peak of the electron distribution at the trap center is seen at the rising (dotted line), peak (solid line), and decay (dashed) phases of the flare. It is very well seen that, in the decay phase, the number density of electrons with higher energy, $E = 2460$ keV decreases much slower than at energy $E = 405$ keV. Note also that on the late decay phase, the distributions at each energy become narrower, the relative number density of mildly relativistic electrons gradually increases in the LT region. This happens due to faster precipitation of electrons having their mirror points near the ends of the magnetic trap. In general, the precipitation and loss of energy due to Coulomb collisions goes faster for lower-energy electrons.

The evolution of GS emission distribution along the model loop for corresponding moments of time is shown in Fig. 6.46a at 17 GHz and in Fig. 6.46b at 34 GHz. In the rise phase of electron injection, the shape of the spatial distribution of 34 GHz

intensity has two well pronounced peaks near FPs with separation about 80″. The small hump at the center of the trap (produced due to the electron number density peak) is also seen, but its intensity is two times smaller. It is clear that the brightness peaks near the FPs are produced due to the strong dependence of GS intensity on the magnetic field strength that is several times higher there than in the LT.

On the injection maximum phase, the GS intensity distribution has the same shape, but the distance between two brightness peaks becomes smaller, 75″. In the decay phase, it is much more narrow (50″) and flat, two strong brightness peaks almost disappear, and now most of emission comes from the upper part of the loop. Our analysis shows that such a brightness redistribution has occurred due to two reasons. The main one is associated with a relatively faster decay of the lower-energy electrons (compare Fig. 6.43a and b). GS emission at a given frequency is generated at lower gyro-harmonic number in the region of stronger magnetic field and, thus, mostly by lower-energy electrons than in the region of weaker field. Therefore, the emission from regions close to FPs decreases faster than the intensity from the loop top. The second reason is the above mentioned relative enhancement of emitting electrons in the top part of the loop.

A comparison of this simulation with our observational results shows that the observed spatial profile at 34 GHz (see Fig. 6.41e–h) has a very similar dynamics. Two brightness maxima are separated by about 80″ in the rise phase, 75″ at peak time, and they disappear at the decay (valley) phase. At the same time, the model doesn't explain (1) the difference in intensity between two FP sources, and (2) the hump in the loop center on the late decay phase as it is observed.

In Fig. 6.46a one can see that, in the rise phase, the emission distribution at 17 GHz looks very alike to that at 34 GHz. However, unlike to the distribution at 34 GHz, it is more narrow and concentrated in the upper part of the loop already on the maximum phase of the burst. Our analysis shows that the emission concentrates in the loop center because the source at 17 GHz becomes optically thick on the maximum phase, especially near the loop FPs. This behavior at all burst phases is very well consistent with the observations (see Fig. 6.41e–h) and the ideas considered in the beginning of Sect. 6.6.1.

6.6.5 Conclusions

We have used high-resolution radio observations of NoRH at 17 and 34 GHz to study dynamics of brightness distribution along a giant flaring loop during the event 2002 August 24. This flare had the time profile with 6 major emission peaks. We have found the similar tendency in dynamics of emission distribution for all temporal peaks: redistribution of the radio brightness from the FPs to the upper part of the loop during each peak. Together with similarity of the brightness distribution evolutions at 34 and 17 GHz, there is quite a strong difference between them. At frequency 34 GHz the brightness has its maximum in the middle part of the loop only on the late decay

phase, whereas at 17 GHz this occurs much earlier: already on the maximum and initial decay phases of the major burst peaks.

Analysis of time profiles from the different parts of the loop shows that the emission maxima from the LT are delayed against the maxima from the FP sources for both frequencies, delays are more pronounced at 34 GHz (6 s ± 1 s for northern FP and 9 s ± 1 s for southern FP). We also found a delay of the burst maximum at higher frequency, 34 GHz, against that at 17 GHz and time delays between corresponding peaks of MW and HXR emission in channel 53–150 keV (6 s ± 2 s for 17 GHz and 8 s ± 2 s for 35 GHz).

Since this event was a limb flare with the viewing angle almost equal for all parts of the loop, we had a chance to make an easier diagnostics of plasma parameters in the loop. We did our estimations by fitting GS emission to the observed brightness temperatures and frequency spectrum slope between 17 and 34 GHz, as well as by making use of soft and HXR, EUV and optical data. As a result, we have obtained the magnetic field strength in the southern FP source $B_{SFP} \approx 1000$ G, and in the loop top $B_{LT} \approx 200$ G; number densities of accelerated electrons with energies more than 500 keV $N_{SFP} = 3 \times 10^4$ cm^{-3} and $N_{LT} = 9 \times 10^5$ cm^{-3} at the maximum of peak 1 and $N_{SFP} = 3 \times 10^3$ cm^{-3}, $N_{LT} = 6 \times 10^5$ cm^{-3} at the valley time. The results show two important properties: (1) the number density of mildly relativistic electrons in the loop top is much higher than near the FPs during rise, maximum and decay of each major peak, and (2) the ratio of the electron number densities in the loop top and a FP increases considerably from the maximum to decay phase.

We consider these observational facts and results of diagnostics as a reliable evidence of effective trapping of mildly relativistic electrons in the upper part of the flaring loop, as well as their redistribution along the loop. To illustrate this idea more quantitatively, we have modeled the time evolution of electron spatial distribution along a magnetic loop by solving the non-stationary Fokker–Planck equation for plasma and loop parameters obtained from our diagnostics. The results of our model simulations show that a brightness dynamics similar to the observed one can be obtained in two models. Both of them are characterized by the source of electrons located at the loop top. One of them has an extended electron source of Gaussian type with the isotropic injection. Another one has a compact source of electrons with slightly anisotropic (longitudinal) injection. Our model simulation shows that in the late decay phase we can clearly see a gradual redistribution of electrons in the loop. The distribution becomes narrower, the relative number density of mildly relativistic electrons gradually increases in the LT region. Such a brightness redistribution has occurred due to two reasons: (1) relatively faster decay of the lower energy electrons, responsible for the GS emission near the FPs with higher magnetic field; (2) faster precipitation of electrons having their mirror points near the ends of the magnetic trap.

The observed difference between the emission distribution at 17 and 34 GHz is also displayed well in our simulations. At 17 GHz the emission concentrates in the loop center earlier, already on the maximum phase, because the source at 17 GHz becomes optically thick at that time, especially near the loop FPs. Besides of this success in modeling and explaining the major properties of the dynamics of brightness

distribution, we should say that some observed phenomena are still not explained. For example, among them are: the presence of a hump in the loop center on the late decay phase and the difference in intensity between two FP sources. Therefore, further development of the model is needed.

6.7 Inversion of NT Electron Spectral Index

6.7.1 Overview

Solar flares are basically the process to transform the magnetic energy into the non-thermal (NT), thermal and other energies. The bulk of the flare energy has been stored in the thermal plasma and the NT electrons. The emissions radiated from the thermal plasma include the SXRs, violet, optics (H_α), and white lights, while the NT electrons can radiate the HXR, MW (above 1 GHz) emissions, and solar type *III* bursts.

According to the emission mechanism, it is a general way in the astronomy to invert the physical parameters and processes from the observational emission intensity. For example, we can invert the parameters of the NT electrons from the MW and HXR emissions. Much more observations have proved that the solar flares can accelerate the NT electrons with a power-law spectrum, which radiates the MW emission through the GS mechanism and the HXRs through the thin- or thick-target bremsstrahlung mechanism.

Solar flares exhibit an inverted-V shape spectrum at the MW emissions, i.e. between 3 and 80 GHz. Figure 6.47 shows the MW spectra of an event observed by NoRP at six distinct frequencies, including 1, 2, 3.75, 9.4, 17, and 35 GHz respectively [127], where the frequency with the maximum intensity is around the inverted frequency, at which the optical depth is united. The part less than the inverted frequency is optically thick due to the self and atmosphere absorption, while the other

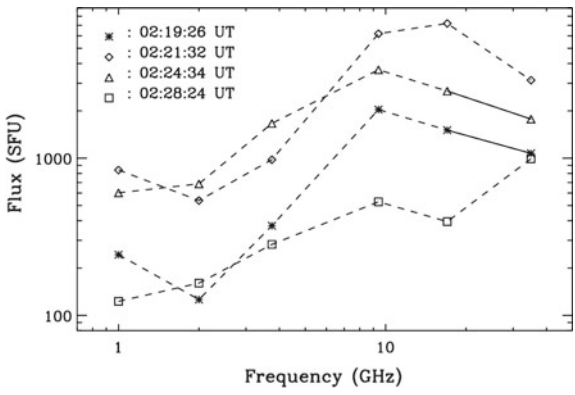

Fig. 6.47 Microwave spectra at six discrete times of the 2003 May 13 flare observed by NoRP. Two frequencies of 17 and 35 GHz are used to invert the microwave spectral index [127]

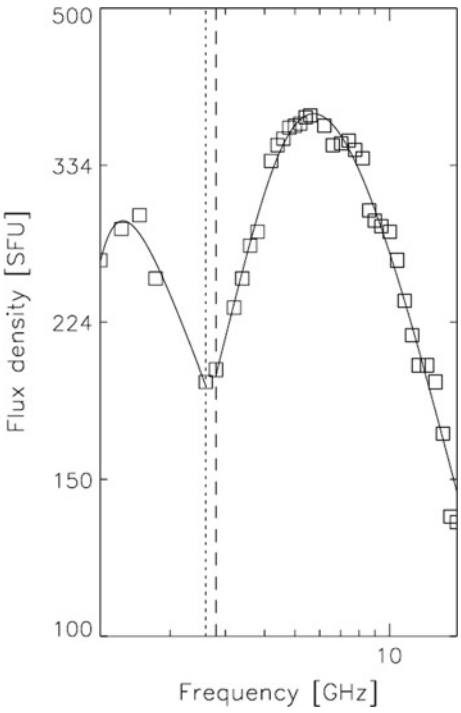

Fig. 6.48 Two components with the inverted-V spectral shape detected by OVSA at the decimeter and centimeter ranges [128]

side above the inverted frequency is optically thin, which is only related the NT electrons. This is similar to the power-law spectra of HXR photons. With high spectral-resolution observations from OVSA, some events exhibit the microwave spectra with not a single but two inverted-V shapes. One is located at the decimeter, and another is at the centimeter, as shown in Fig. 6.48 [128].

Figures 6.47 and 6.48 show the MW emission decreasing with the frequency increasing at the centimeter range after the solar flare onset. This is because the high-energy electrons of power-law spectra would become few, and their radiation could be little as well. However, the interesting things are found at the submillimeter (THz) range. Some events do not decrease the radio emissions, but increase with the frequency increasing at this range. In other words, there is a new radio component appearance at the submillimeter. Figure 6.49 shows the MW spectra from 1 to 1000 GHz of a solar flare observed by OVSA and SST (Solar Submillimeter Telescope) [129]. There are two frequencies at the submillimeter, and their radio fluxes increase with the frequency. Based on the GS mechanism [130], there would be another inverted-V spectral shape at the submillimeter. It is possible to detect three inverted-V shapes on the broad spectra from the decimeter through the centimeter to the submillimeter in the solar flares. And the submillimeter observations give a new window for the solar radio study.

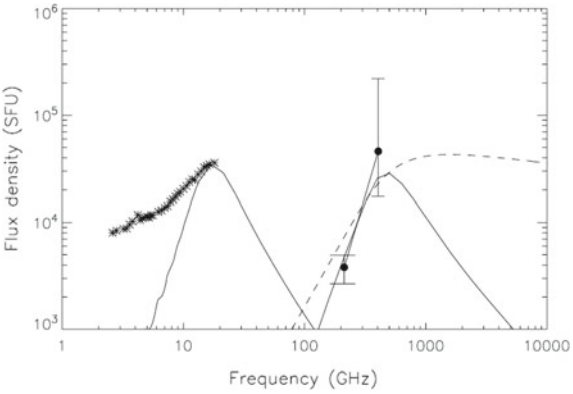

Fig. 6.49 Microwave (star) and THz (solid) spectra detected by OVSA and SST (Solar Submillimeter Telescope). Two solid lines are computation results from the synchrotron mechanism and the dashed line is from thermal mechanism [129]

As mentioned before, the HXR photons usually display the power-law spectra same as the optically thin part of the MW emissions during solar flares. To study the spectral index and its time evolution detected from the MW and HXR emissions is helpful for completely understanding the acceleration mechanism in solar flares. As an earlier note, the electron spectral index is the HXR photon spectral index plus or minus one dependence on the thin- or thick-target models, while the MW intensity spectral index (δ) is related with the NT electron spectral index (γ), i.e., $\gamma = 1.1(\delta + 1.2)$. Therefore, the time evolution of both the HXR photon spectra and the MW intensity spectra is same as that of the NT electron spectra during solar flares, but their values are different. We will study the NT electron spectra detected from the HXR and MW intensity spectra.

6.7.2 Comparison of NT Spectral Indices of MW and X-Ray Emissions in Solar Flares

According to the thick-target model, the NT electron spectra are well studied from the HXR observations. Based on the previous results, the solar flares are divided into three catalogs, i.e. types A, B, and C from the various spectral characteristics. Type A is called thermal flare, whose thermal component is dominated, or the MW and HXR emissions are quiet. It has a steep X-ray spectrum with a soft index above 7 at the 40 keV. Type B is an impulsive flare, who has a soft-hard-soft (SHS) spectral evolution pattern corresponding to the HXR intensity with the rise-peak-decay phases. In other words, the spectral index is decreasing with the HXT intensity rising after the flare onset, and the index reaches the minimum value at the flare peak, then returns to the initial values in the intensity decay. Therefore, the spectral index is anti-correlated with the HXR intensity, which is used to determine whether an event is the type-B flare. From RHESSI observations with the high time resolution, the solar flares exhibit the SHS spectral pattern for the whole flare, and so do for each HXR peak,

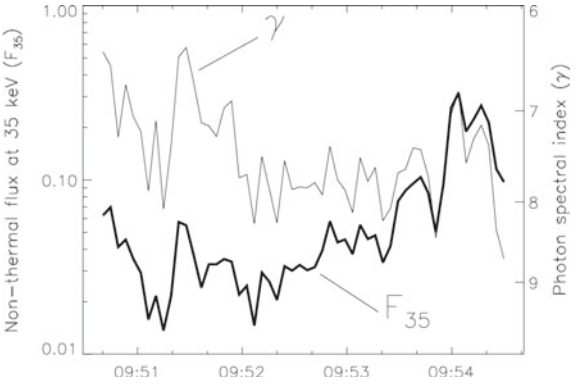

Fig. 6.50 Time evolutions of the hard X-ray spikes (F_{35}) and their spectral indexes (γ) [131]

as shown in Fig. 6.50 [131]. Type C is a gradual event, which often exhibits the soft-hard-harder (SHH) spectral pattern corresponding to the HXR rise-peak-decay phases. Namely, the spectral index is monotonously decreased from the flare onset to the end. RHESSI observations give a new spectral evolution, such as hard-soft-hard (HSH) pattern during some solar flares, as mentioned in Sect. 5.4.

The MW spectral index is also able to be detected from the observations. In solar physics, NoRP is an unique instrument to detect for about two solar cycles. It works on seven discrete frequencies, such as 1, 2, 3.75, 9.4, 17, 35, and 80 GHz. The last channel (at 80 GHz) is often ruled out to do research due to the heavy effects from the earth atmosphere. There are about 500 solar flares observed by NoRP from 1998 to 2005. These events are enough to statistically study the time evolution of the MW spectral index.

As noted before, the solar flares exhibit the inverted-V shapes of the MW spectra, which are well consistent with the theoretic expectation of GS mechanism. Observationally, most solar flares display their inverted frequencies between 10 and 20 GHz, not rule out the values less than 10 GHz or greater 20 GHz. As an earlier note, the NT electron spectral index is derived from the optically thin part (i.e. above the inverted frequency). For the observations of NoRP, the frequency with the maximum flux is usually at 9.4 or 17 GHz for the different solar flares or the different periods of the same event. It is possible that the solar flares have an inverted frequency around 9.4 or 17 GHz due to the large gaps among these frequencies. In this case, the optically thin frequencies possibly include 9.4, 17, and 35 GHz or just last two channels.

In order to calculate the MW spectral index in the optically thin part, the solar flares are chosen as follows. First, the event has a frequency with the maximum flux less than 9.4 GHz, which ensures that both 17 and 35 GHz would be the optically thin. Therefore, the events with the maximum frequency at 9.4 GHz are ruled out. Second, the fluxes at 35 GHz should have a maximum value not less than 50 sfu in order to have a good SNR. If the channel of 35 GHz has a small flux, the noise would affect the spectral index. According to these two rules, 103 solar flares are chosen from about 500 NoRP events.

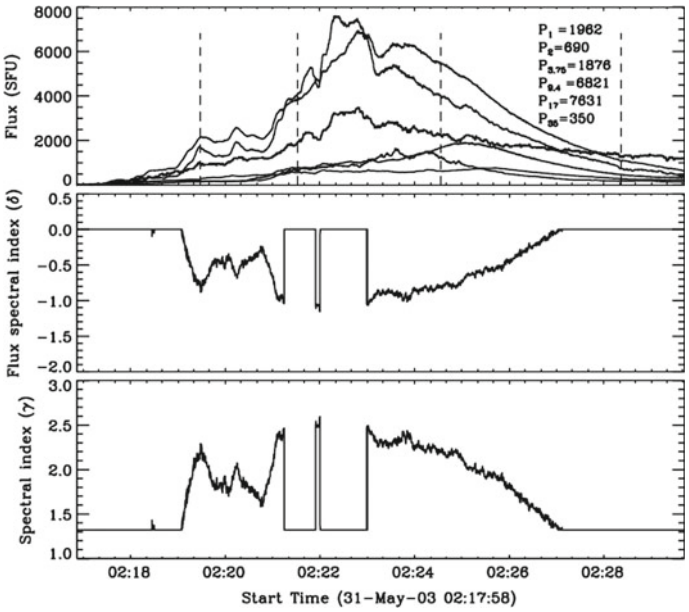

Fig. 6.51 Time evolution of the microwave fluxes (top), the microwave spectral index (middle) and the non-thermal electron spectral index (bottom) [132]

We have the formula to compute the NT electron spectral index from NoRP observations in the details [127]. Based on the GS mechanism, the MW emission has a power-low dependence on the frequency at the optically thin part, such as $S(\mu, t) = F_0\mu^{\delta(t)}$, where μ, S, and δ are the frequency, flux, and spectral index, respectively. According to the NoRP observations, μ has two values as 17 and 35 GHz. In this case, the time evolution of microwave flux spectral index is calculated as follows:

$$\delta(t) = \frac{log(S_1(t)/S_2(t))}{log(\mu_1/\mu_2)} = \frac{log(S_{17}(t)/S_{35}(t))}{log(17/35)}. \tag{6.7.1}$$

The spectral index $\gamma(t)$ of NT electrons to radiate the MW emissions is calculated with a simple formula of $\gamma(t) = -1.1(\delta(t) - 1.32)$ detected from the GS mechanism. In some events, it is possible that the frequency with the maximum flux is changed between 9.4 and 17 GHz during the flare. According to the previous rules, $\delta(t)$ is not calculated at the period with a maximum frequency at 17 GHz, as shown in Fig. 6.51 [132]. The intervals with the flat of both $\delta(t)$ and $\gamma(t)$ indicate the maximum frequency at 17 GHz. In this case, the inverted frequency could be around 17 GHz, and it is possible that the inverted frequency is greater than 17 GHz, which is optically thick. Thus, 17 GHz can not be used to calculate the spectral index.

Using the method as mentioned before, the time evolution of the MW spectral index in each events of 103 observed by NoRP is statistically studied. Different from

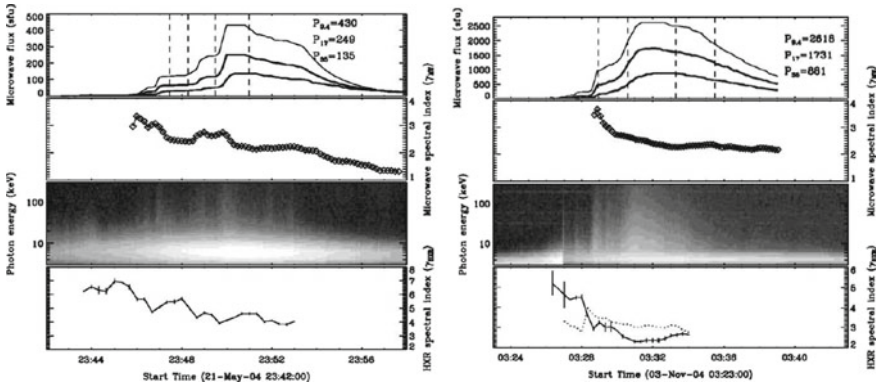

Fig. 6.52 Time evolution of the microwave and hard X-ray spectra of two solar flares at 2004 May 21 and 2004 November 3 [132]

the three types in the X-rays, two types of spectral patterns are found in the MW emissions. Type I is the SHS spectral evolution with the rise-peak-decay phases, which is similar to the type B of X-rays. Like type-C flares, Type II is the SHH spectral evolution in the MW emissions. No events similar as the thermal flares in the X-rays found in the MW emissions. This is because the MW emissions are radiated by the NT electrons. The MW emissions of thermal plasma are very weak. However, the X-rays are radiated by both the thermal and NT electrons. If there are no NT electrons, the thermal plasma also can radiate the strong soft X-rays. In this case, the spectra detected from the X-rays are flat and soft, but few MW emissions. Therefore, the thermal flares can not be observed at the MW wavelength.

For the same event which radiates both the MW and X-ray emissions, the MW spectral index could show the similar evolution pattern as that of the X-rays. Theoretically, the NT electrons of the MWs should be same as that of HXRs. Using the observations of NoRP and RHESSI, Fig. 6.52 shows the time evolution of the spectral indices detected from the MW and HXR emissions for two solar flares. Both events exhibit the similar evolution patterns as the SHS or SHH patterns at both the MW and HXR emissions. Thus, the positive correlations are found between the MW and HXR spectral indices, as shown in Fig. 6.53. Based on the linear relationship between the intensity and NT electron spectral indexes, whatever at the MW or HXR emissions, the electron spectral indices detected from the MW emission are different from the that detected from the HXRs, but they have a similar evolution during the flare lifetime, which indicates that both the MW and HXR emissions have the same origination. The spectral indices of NT electrons are related to the inversion method, the radiation mechanism, and the calibration of instruments. It is reasonable to choose the MW or X-ray spectral indices as the spectra of a solar flare.

The statistics results show that the type II events (91) are dominated in the MW observations (103 solar flares in total). This fact is different from the HXR observations, which shows that type-B events are dominated. Therefore, it is possible for a

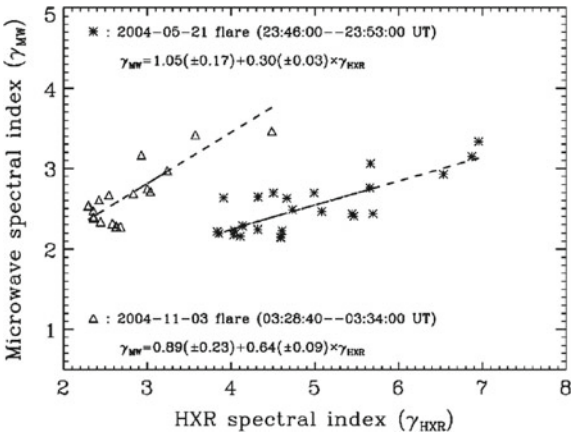

Fig. 6.53 The positive correlation of the microwave spectral index dependence on the hard X-ray spectral index in two solar flares [132]

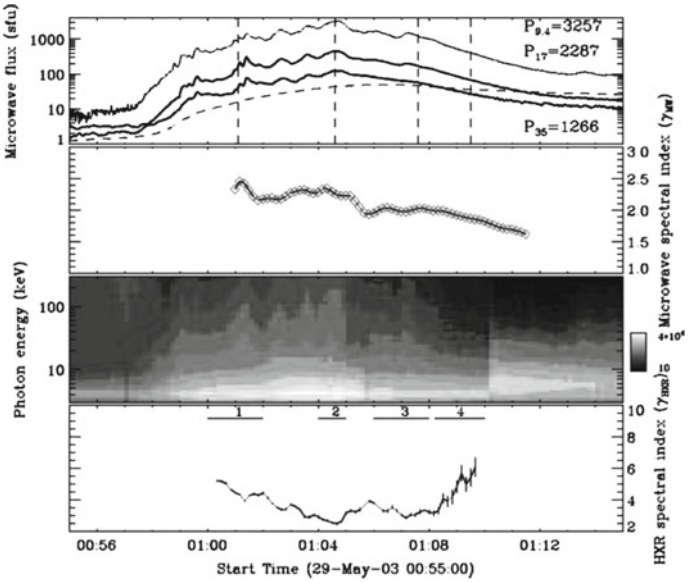

Fig. 6.54 Time evolution of the microwave spectra (soft-hard-harder) and the hard X-ray spectra (soft-hard-soft) of the 2003 May 29 flare [133]

solar flare to display different spectral evolutions in the MW and HXR emissions, such as the SHH pattern in the MW emissions, and the SHS pattern in the HXRs. Figure 6.54 shows a typical example of such events detected by NoRP and RHESSI on 2003 May 29 [133].

For the events as shown in Fig. 6.54, what is time evolution of the NT electron spectra? Based on the mechanism, the spectral pattern detected from the HXRs is able to represent the information of NT electrons. This is because the HXRs are well explained by thick-target bremsstrahlung mechanism. Otherwise, the MW emission mechanism is complicated and related to several physics parameters of the radiation region. Firstly, the MW emission is produced by the NT electrons with an energy as higher as MeV, which is three orders bigger than the electrons to radiate the HXRs. Secondly, the trapped electrons would contribute the MW emission, especially in the decay phase. Because the electrons with the higher energy would be trapped for a longer time, and these electrons can radiate the MW emissions and affect the spectral evolution. Thirdly, the plasma temperature would increase with the time during the solar flare, and the thermal plasma can contribute the MW emissions, except for the GS mechanism. These three facts would contribute the MW emissions, especially on the optically thin frequency range. The results are the MW spectral index decreasing slowly, and possibly increasing with the time. That is reason that most of solar flares display the SHH spectral pattern in the MW observations.

6.7.3 Summary

The NT electrons can radiate both the HXR and MW emissions through the thick-target bremsstrahlung and GS mechanisms respectively. It is a general way to detect the physics information, such as spectral index and its evolution of NT electrons from the HXR and MW observations. The solar flares show the spectral index between 2 and 8, and their values change with the flare flux, such as the SHS or the SHH spectral pattern, whatever in the HXR or the MW observations. Theoretically, the HXR and MW emissions are thought to be radiated by the same electrons accelerated during solar flares. Therefore, the spectral indices detected from the HXRs are correlated with those detected from the MW emissions. However, some events exhibit different spectral patterns at the HXRs and MWs. The physical reason is due the complication of the MW emissions. At the flare onset, the MW emissions are radiated by the GS mechanism. After the maximum phase, the plasmas increase its temperature due the chromospheric evaporation. Thus, these thermal plasmas also radiate the MW emissions, especially on the high frequency. Observationally, most of solar flares exhibit the SHS spectral pattern in the HXRs, but the SHH pattern in the MW emissions. This results that the MW spectral evolution is different from the HXR spectra in the same event.

6.8 Radio Diagnostics of the Solar Flaring Loop Parameters

The work is devoted to the development of a method for determining flaring loop parameters and accelerated NT electrons based on the observed spectrum and polarization degree of their MW emission [134]. The radio diagnostics can theoretically be used to recover the following parameters in a radio source: the magnetic field strength and direction, the background plasma density and temperature, and the variables characterizing the accelerated electron density, energy and pitch-angle distributions.

Fleishman and Kuznetsov [135] developed a program package that makes it possible to rapidly calculate the intensity of ordinary and extraordinary waves from a homogeneous GS emission source for different values of the input parameters such as the accelerated electron number density, energy spectral index, and pitch-angle distribution type, background plasma number density, magnetic field value and field line direction relative to an observer, etc. Thus, flaring loop parameters can be determined for loop quasi-homogeneous regions.

6.8.1 Method for Recovering Flaring Loop Parameters

The method for fitting the theoretically calculated GS radio emission characteristics to the observed characteristics is reduced to solving the following system of equations for each region of the studied source:

$$J_{fi}(x_1,\ x_2,\ \ldots\ x_n) = J_{fi}^{observ}\ (i = 1, 2, \ldots m). \tag{6.8.1}$$

where the right- and left-hand sides of each equation includes the characteristics of the radio emission received from a source (J_{observ}) and the theoretically calculated emission characteristics, respectively; ($x_1,\ x_2, \ldots,\ x_k$) are the determined radio source parameters; and ($x_{k+1},\ x_{k+2}, \ldots,\ x_n$) are the known fixed radio source parameters. The solution of this system is reduced to finding the minimum of a certain functional that includes the right- and left-hand sides of the solved equation system. For example, this functional can take the following form:

$$\begin{aligned} K(x_1, x_2, \ldots x_n) = a_1[|\ J_{f1}(x_1, x_2, \ldots x_n) - J_{observ}(f1)\ |]^{\lambda} + \\ + a_2[|\ J_{f2}(x_1, x_2, \ldots x_n) - J_{observ}(f2)\ |]^{\lambda} + \\ \ldots a_n[|\ J_{fn}(x_1, x_2, \ldots x_n) - J_{observ}(fn)\ |]^{\lambda}\ , \end{aligned} \tag{6.8.2}$$

where $a_1,\ a_2, \ldots,\ a_n$ are the weight coefficients and $\lambda = 2$. A fast calculation program [135] was used in this work in order to calculate the GS emission characteristics

(the left-hand side of Eq. (6.8.1)). In the Ref. [136], the problem of recovering radio source parameters was applied for the first time to the solar flare radio emission based on forward fitting. For this purpose, the authors used the functional minimization simplex-method. In the present work, we applied the method of genetic algorithm for finding the global minimum [137], which was not used previously in flaring loop radio diagnostics, in order to solve this problem. The main idea of this method is that new point generations or candidate solutions of equation system (1) (the sets of the program input parameters $(x_1, x_2, \ldots, x_k)$ are successively formed. New generations are formed by selecting the best points in the previous iteration according to the minimal difference between the characteristics of the observed radio emission and the radio emission calculated at these points, which should approach the true required parameter values.

6.8.2 Determination of Model Radio Source Parameters

A model radio source was represented as a set of homogeneous three-dimensional regions (boxes), and the geometric dimensions, the magnetic field value, and the parameters of NT electrons and background plasma were determined for each. The program presented in the Ref. [135] was used to calculate the fluxes and degree of circular polarization at several specified frequencies for each region. Subsequently, a certain number of parameters for each source region are assumed to be unknown, and the remaining parameters are recovered by the method in above.

The distribution of the recovered parameters, which depend on a certain coordinate S along a radio source, is presented in Fig. 6.55. The box number can be taken as coordinate S. The source thickness was assumed to be identical for each box (10^8 cm). It was specified that the electron pitch-angle distribution is isotropic for the entire radio source. The values of the flux and modulus of the circular polarization degree at 12, 17, 25, and 40 GHz frequencies were calculated for each box.

The real and recovered values are shown by a solid line and diamonds in Fig. 6.55. The accuracy of the determination of the background plasma number density is decreased at its relatively small values, because the Razin influence is low at the frequencies for which the radio emission was calculated. The average determination accuracy for the accelerated electron number density is 80% for this model. The coincidence between true and recovered values of the energy spectrum index and viewing angle is more than 98% for the entire source. The magnetic field determination relative error is not more than 8%. The computation time is about 3 h.

6.8.3 Recovering Physical Parameters of Solar Flaring Loops

To recover the physical parameters of solar flaring loops, we used data on the radio emission obtained with the NoRH. We constructed radio images of the flare region

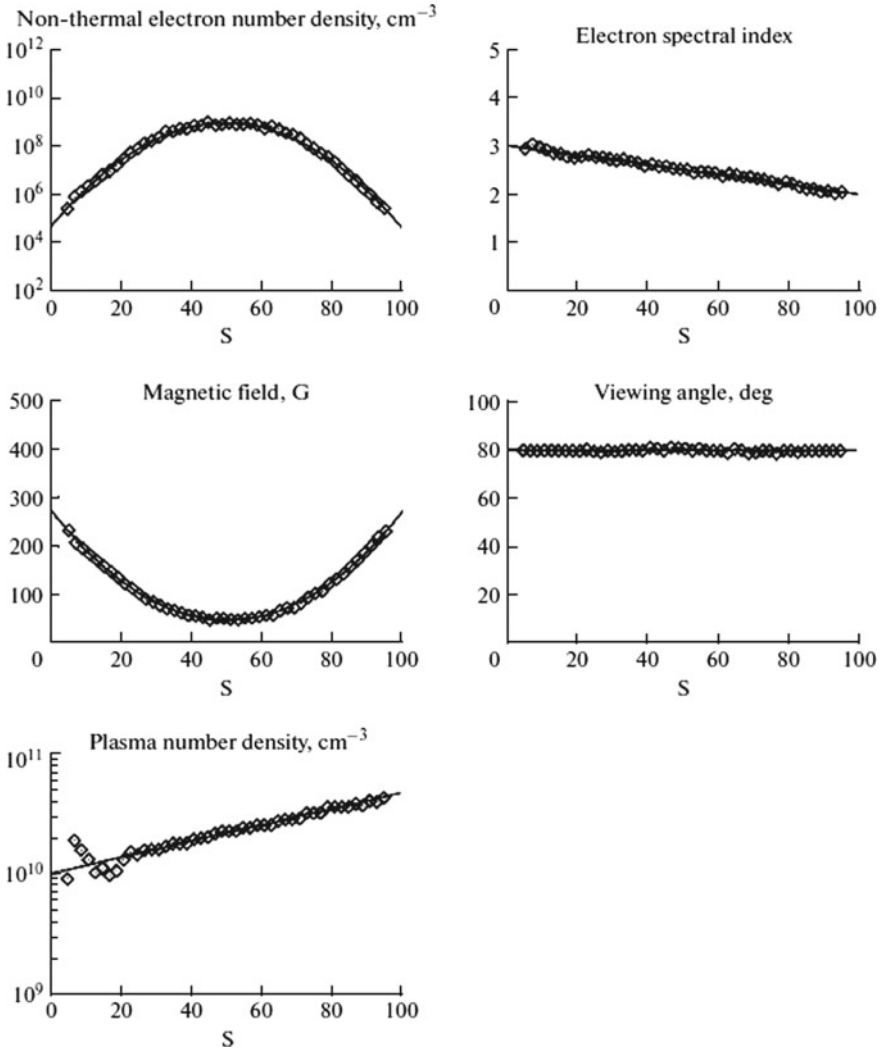

Fig. 6.55 Recovering the physical parameters of the model radio source. The recovered and real values are shown by diamonds and a solid line, respectively

for the event of July 19, 2012, at the 17 and 34 GHz frequencies based on the NoRH data with the 10" and 5" spatial resolution, respectively, and a 1 s time resolution. The radio brightness distribution maps make it possible to determine the loop structure and geometrical dimensions. The radio brightness distribution maps at a frequency of 34 GHz for four instants of time are presented in Fig. 6.56. Figure 6.56 also shows the location and dimension of the boxes where the flaring loop parameters were recovered. Two boxes are located at the loop FPs (UFP, LFP), and two boxes are

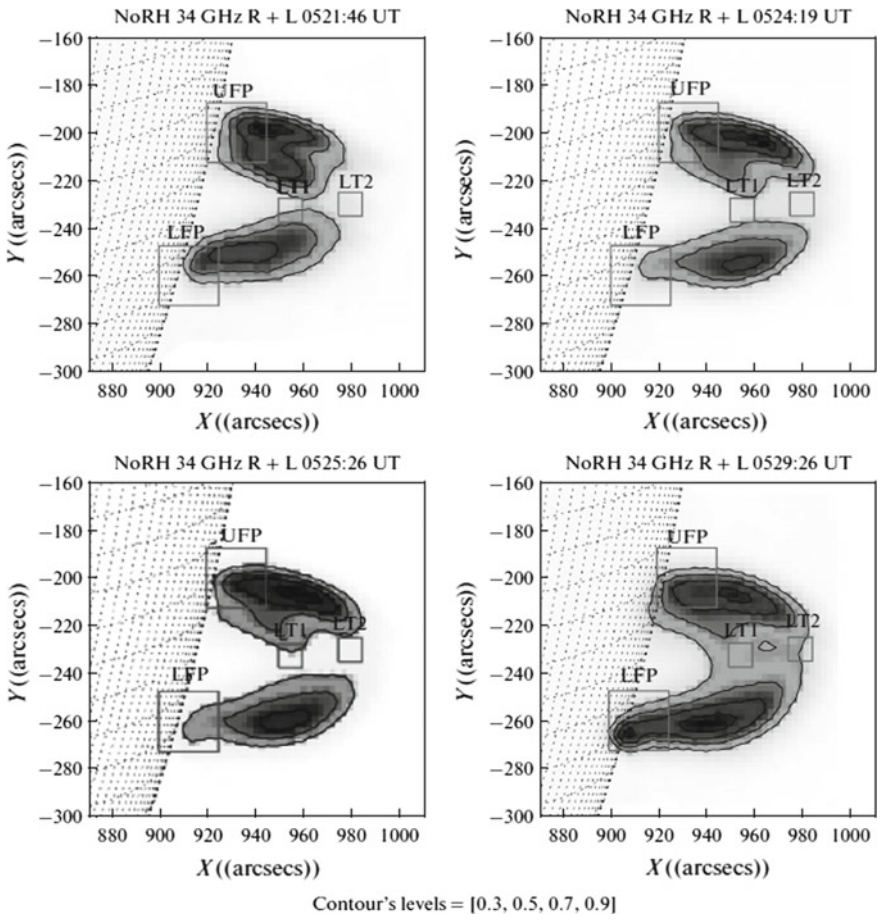

Fig. 6.56 Radio brightness maps for the event of July 19, 2012, at frequency of 34 GHz (the NoRH data) for four instants of time. The analyzed source regions are marked by boxes. Two (UFP, LFP) and two (LT1, LT2) boxes are located at the loop FPs and tops, respectively

located at the loop tops (LT1, LT2). Figures 6.57 and 6.58 present the time profiles of the observed radio emission fluxes at 17 and 34 GHz and the degree of circular polarization at 17 GHz for these boxes.

We assumed that the electron distribution depends on energy E and pitch-angle cosine $\mu = \cos(\alpha)$ and is the multiplication of two independent functions:

$$U(E,\ \mu,\ t)) = k(t)U_1(E,\ t)U_2(\mu)\ , \tag{6.8.3}$$

where k is the time-dependent coefficient. The NT electron energy distribution was assumed to be a double power-law in the range from 10 to 10 MeV with a break at an energy of 100 keV. The energy spectral index was 2.5 before the break and

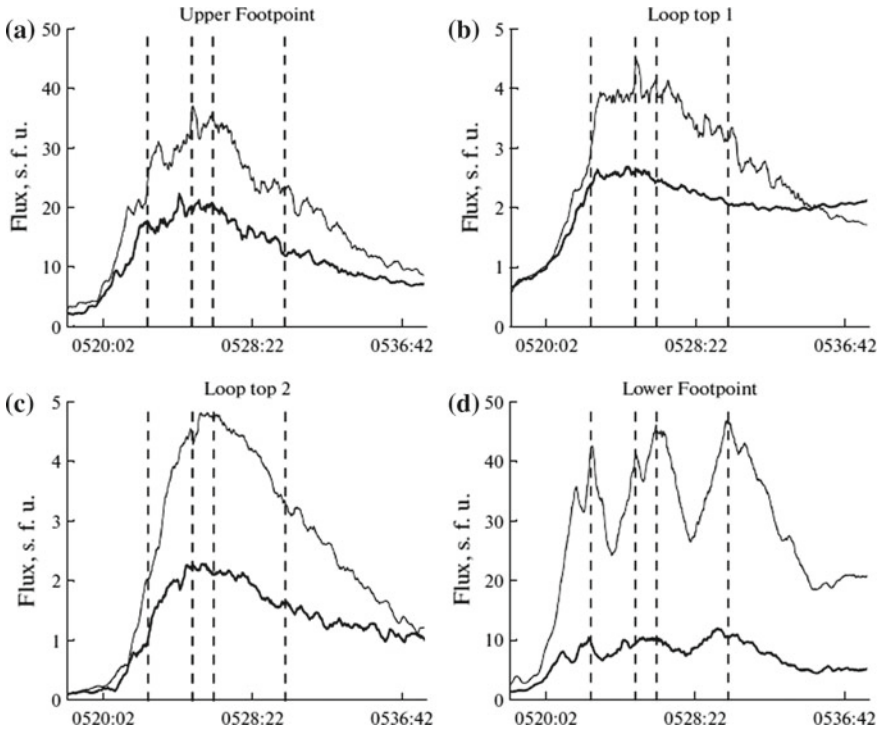

Fig. 6.57 Time profiles of emission fluxes at frequencies of 17 and 34 GHz (thin and thick lines, respectively) in the studied flaring loop regions: **a** the upper FP, **b** top 1, **c** top 2, and **d** the lower FP. The instants of time for which the maps of the radio brightness and degree of circular polarization are presented are shown by vertical lines

was considered as a recovered parameter after the break. The thickness of each local source was taken equal to a loop thickness of $h = 2\times10^9\text{cm}^3$, which was determined from the radio brightness distribution maps at the 34 GHz frequency at a level that accounted for 0.5 of the maximal brightness temperature. The transverse dimension depended on the box size, the integral emission from which was used in fitting. The parameter recovering procedure was performed under the assumption on two types of electron pitch-angle distributions (1) isotropic ($U_2(\mu) = 1$) and (2) anisotropic with electrons mostly directed along the magnetic loop axis:

$$U_2(\mu) = \exp((\mu - \mu_0)^2/\Delta\mu^2)\ , \tag{6.8.4}$$

where $\mu_0 = 1$ ($\alpha_0 = 0$) and $\Delta\mu$ characterizes the width of an anisotropic electron beam. We accepted that $\Delta\mu = 1$. Figures 6.59 and 6.60 show the time profiles of the recovered parameters for the lower FP, on the assumption that the pitch-angle distributions are (a) isotropic and (b) anisotropic, respectively. The time profiles of the number density of NT electrons and the index of their energy spectrum are

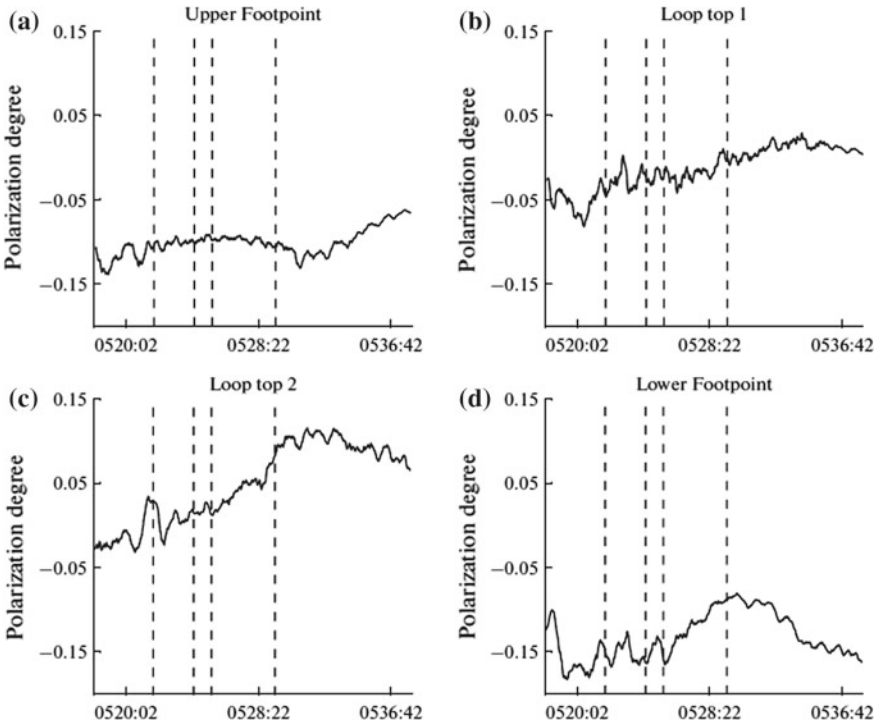

Fig. 6.58 Time profiles of the polarization degree of the emission at 17 GHz in the studied flaring loop regions: **a** the upper FP, **b** top 1, **c** top 2, and **d** the lower FP. The instants of time for which the maps of the radio brightness and degree of circular polarization are presented are shown by vertical lines

presented on the top panel. The profiles of the magnetic field and viewing angle are shown on the bottom panel. In both cases recovering the parameters performed using the genetic algorithm gave a viewing angle about 70°–75°, which agrees with the flaring loop position on the solar limb (see Fig. 6.56). Similar numerical values of the electron energy spectral index and the index dynamics were obtained for each FP.

The dynamics of the NT electron number density for both isotropic and anisotropic pitch-angle distribution is similar, but the numerical values differ by approximately an order of magnitude. Higher values of number densities for the quasi-longitudinal pitch-angle distribution are quite natural, since the GS emission effectiveness in the quasi-transverse direction strongly decreases in this case (70°–75°) as compared to the case of isotropic distribution (see the Ref. [51]). If the pitch-angle distribution is isotropic, the average magnetic field value is approximately 120 G for the northern and southern FPs. On the assumption that the pitch-angle distribution is anisotropic, the magnetic field values are about 300 and 400 G for the southern and northern FPs, respectively.

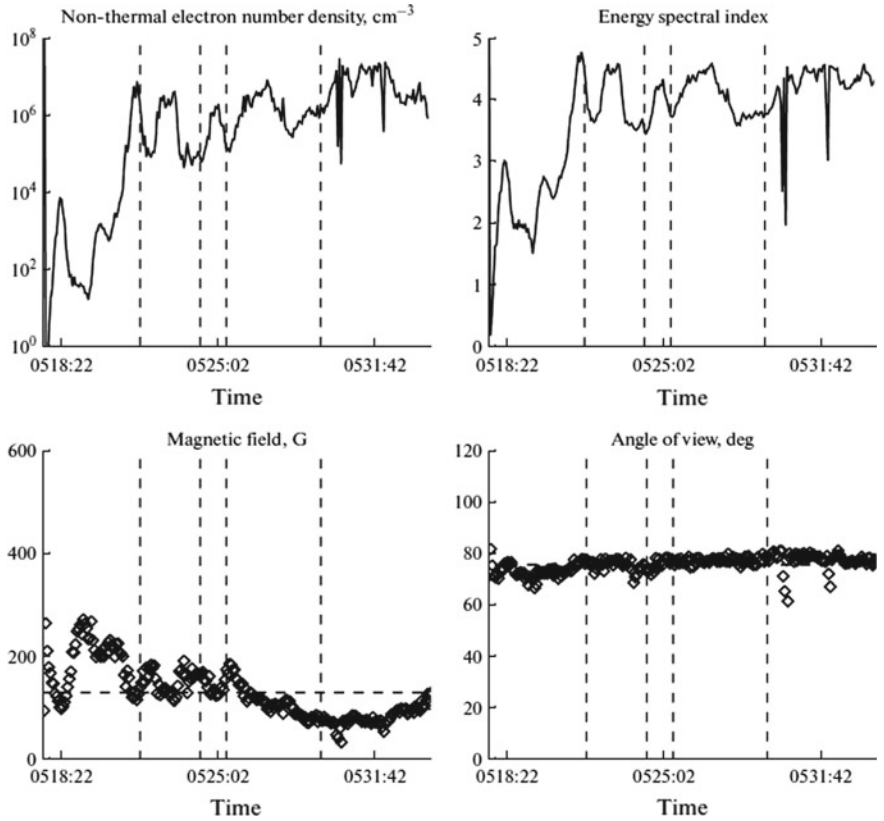

Fig. 6.59 Time profiles of the recovered values of the NT electron number density, magnetic field, energy spectral index, and viewing angle for the flaring loop lower FP on the assumption that the pitch-angle distribution is isotropic

No solution was found for the LT1 and LT2 regions when the parameters were recovered for the case of the isotropic electron pitch-angle distribution. That is, it was impossible to find the set of accelerated electron number density and energy spectral index and the magnetic field magnitude and direction in a source so that the theoretically calculated fluxes and degree of circular polarization would coincide with the values observed at the loop top. At the same time, the parameters were recovered successfully at the flaring loop top for the case of an anisotropic pitch-angle distribution. Recovering results for the LT2 box are shown in Fig. 6.61. It was found that the time profiles of the accelerated electron number density and energy spectral index are characterized by the main maximum at an instant of time close to the radio burst maximum time moment, which agrees with the time profiles of the microwave emission. The viewing angle is about 80°. The magnetic field value varies from 500 to 100 G. Such considerable magnetic field variations are hardly realistic. This is most probably caused by an insufficient number of independent

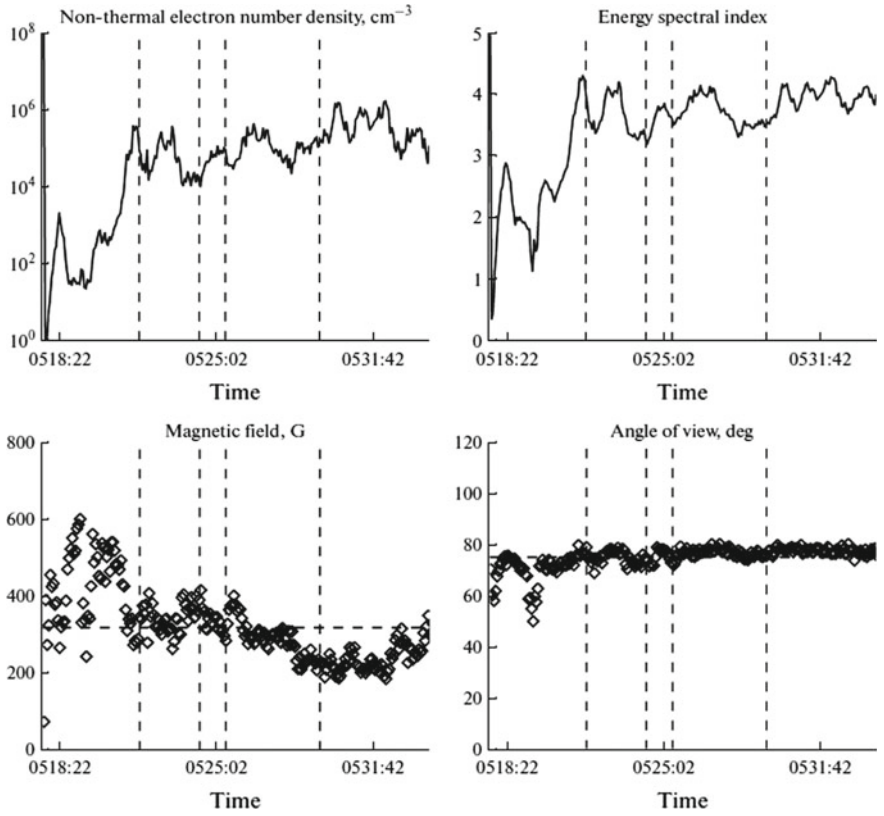

Fig. 6.60 Time profiles of the recovered values of the NT electron number density, magnetic field, energy spectral index, and viewing angle for the flaring loop lower FP on the assumption that the pitch-angle distribution is anisotropic

input parameters (the intensity at 17 and 34 GHz and the polarization degree at 17 GHz); i.e., three observed characteristics were used to recover four parameters. It is evidently necessary to have data on the intensity and polarization at a larger number of frequencies in order to recover parameters more reliably. Therefore, it is very promising to perform observations at five frequencies, and they are to be done in the nearest future at the modernized Siberian Solar Radio Telescope and at the Chinese Spectral Radioheliograph (MUSER).

6.8.4 Conclusions

During the performed study, we developed a method for determining radio source parameters based on the solution of a system of equations for the intensity and circular

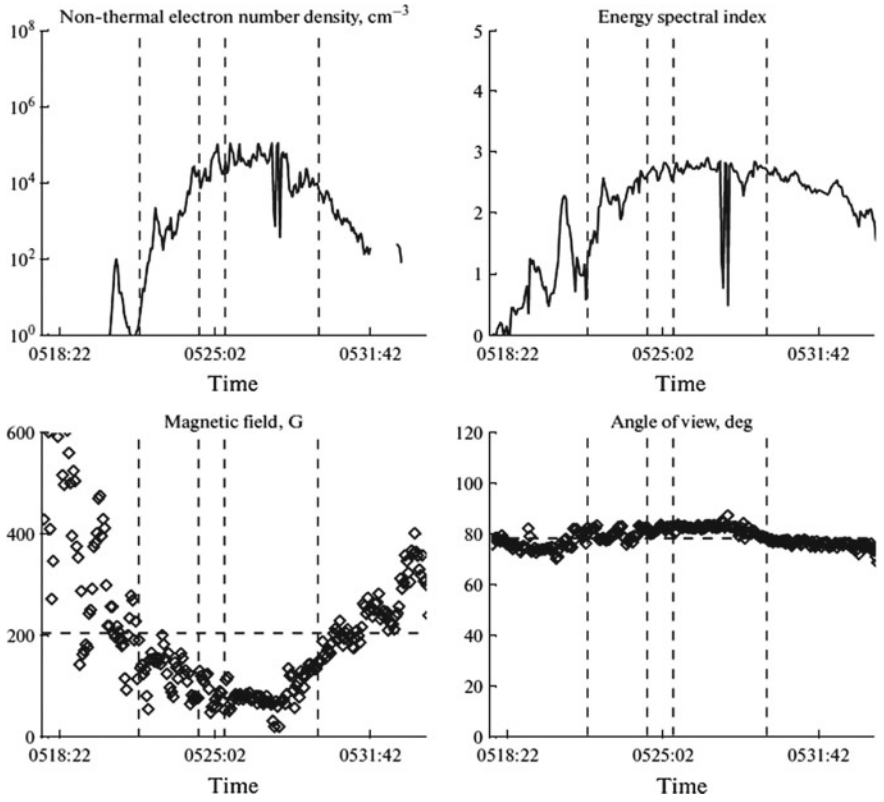

Fig. 6.61 Time profiles of the recovered values of the **a** NT electron number density, **b** magnetic field, **c** energy spectral index, and **d** viewing angle at the flaring loop top on the assumption that the longitudinal pitch-angle distribution is anisotropic

polarization degree for the theoretical and observed GS emissions. The application of the genetic algorithm strategy for recovering five model radio source parameters (accelerated electron number density and energy spectral index, magnetic field magnitude, angle between magnetic field lines and line of sight, and background plasma number density) based on data on the microwave emission at four frequencies showed that the method accuracy is good and the computation time is acceptable.

The developed method was adapted for determination of the above parameters for real flaring loops based on the NoRH observations at frequencies of 17 and 34 GHz. For the event of July 19, 2012, we successfully recovered four loop parameters for the loop FPs under the assumption that the pitch-angle distribution is isotropic or anisotropic. We indicated that parameters at the loop top can be recovered only when the pitch-angle distribution of energetic electrons is anisotropic (longitudinal).

References

1. Kundu, M.R.: Measurement of solar magnetic fields from radio observations. Societá Astronomica Italiana, Memorie **61**, 431–455 (1990)
2. Preka-Papadema, P., Alissandrakis, C.E., Dennis, B.R., et al.: Modeling of a microwave burst emission. Sol. Phys. **172**, 233–238 (1997)
3. Nindos, A., White, S.M., Kundu, M.R., et al.: Observations and models of a flaring loop. Astrophys. J. **533**, 1053–1062 (2000)
4. Kundu, M.R., Nindos, A., Grechnev, V.V.: The configuration of simple short-duration solar microwave bursts. Astron. Astrophys. **420**, 351–359 (2004)
5. Grebinskij, A., Bogod, V., Gelfreikh, G., et al.: Microwave tomography of solar magnetic fields. Astron. Astrophys. Suppl. **144**, 169–180 (2000)
6. Ryabov, B.I., Maksimov, V.P., Lesovoi, S.V., et al.: Coronal magnetography of solar active region 8365 with the SSRT and NoRH radio heliographs. Sol. Phys. **226**, 223–237 (2005)
7. Gary, D.E., Keller, C.U. (eds.): Solar and Space Weather Radiophysics-Current Status and Future Developments. Astrophysics and Space Science Library, p. 314. Kluwer Academic Publishers, Dordrecht (2004)
8. Zhou, A.H., Karlický, M.: Magnetic field estimation in microwave radio sources. Sol. Phys. **153**, 441–444 (1994)
9. Dulk, G.A., Marsh, K.A.: Simplified expressions for the gyrosynchrotron radiation from mildly relativistic, nonthermal and thermal electrons. Astrophys. J. **259**, 350–358 (1982)
10. Huang, G.L.: Calculations of coronal magnetic field parallel and perpendicular to line-of-sight in microwave bursts. Sol. Phys. **237**, 173–183 (2006)
11. Huang, G.L., Ji, H.S., Wu, G.P.: The radio signature of magnetic reconnection for the M-class flare of 2004 November 1. Astrophys. J. **672**, L131–L134 (2008)
12. Kosugi, T., Dennis, B.R., Kai, K.: Energetic electrons in impulsive and extended solar flares as deduced from flux correlations between hard X-rays and microwaves. Astrophys. J. **324**, 1118–1131 (1988)
13. Huang, G.L., Zhou, A.H., Su, Y.N., Zhang, J.: Calculations of the low-cutoff energy of nonthermal electrons in solar microwave and hard X-ray bursts. New Astron. **10**, 219–236 (2005)
14. Takakura, T., Scalise, E.: Gyro-synchrotron emission in a magnetic dipole field for the application to the center-to-limb variation of microwave impulsive bursts. Sol. Phys. **11**, 434–455 (1970)
15. Huang, G.L.: Diagnostics of the low-cutoff energy of nonthermal electrons in solar microwave and hard X-ray bursts. Sol. Phys. **257**, 323–334 (2009)
16. Huang, G., Song, Q., Li, J.: Determination of intrinsic mode and linear mode coupling in solar microwave bursts. Astrophys. Space Sci. **345**, 41–47 (2013)
17. Ramaty, R.: Gyrosynchrotron emission and absorption in a magnetoactive plasma. Astrophys. J. **158**, 753–770 (1969)
18. Ji, H.S., Huang, G.L., Wang, H.M.: The relaxation of sheared magnetic fields: a contracting process. Astrophys. J. **660**, 893–900 (2007)
19. Wang, S., Liu, C., Liu, R., Deng, N., Liu, Y., Wang, H.: Response of the photospheric magnetic field to the X2.2 flare on 2011 February 15. Astrophys. J. **745**, L17–L21 (2012)
20. Hudson, H.S., Fisher, G.H., Welsch, B.T.: Flare energy and magnetic field variations. In: Howe, R., Komm, R.W., Balasubramaniam, K.S., Petrie, G.J.D. (eds.) Subsurface and Atmospheric Influences on Solar Activity. ASP Conference Series 383, p. 221. ASP, San Francisco (2008)
21. Fisher, G.H., Bercik, D.J., Welsch, B.T., Hudson, H.S.: Global forces in eruptive solar flares: the lorentz force acting on the solar atmosphere and the solar interior. Sol. Phys. **277**, 59–76 (2012)
22. Wang, H., Liu, C.: Observational evidence of back reaction on the solar surface associated with coronal magnetic restructuring in solar eruption. Astrophys. J. **716**, L195–L199 (2010)
23. Huang, G., Li, J., Song, Q., Tan, B., Huang, Y., Wu, Z.: Attenuation of coronal magnetic field in solar microwave bursts. Astrophys. J. **806**, 12–18 (2015)

24. Huang, G.L., Nakajima, H.: Diagnosis of coronal magnetic field with data of Nobeyama Radio Heliograph. New Astron. **7**, 135–145 (2002)
25. Ji, H.S., Huang, G.L., Wang, H.M., et al.: Converging motion of H conjugate Kernels: the signature of fast relaxation of a sheared magnetic field. Astrophys. J. **636**, L173–L174 (2006)
26. Hachenberg, O., Wallis, G.: Das Spektrum der Bursts der Radiofrequenzstrahlung der Sonne im cm-Wellenbereich. Mit 21 Textabbildungen, Zeitschrift für Astrophysik **52**, 42 (1961)
27. Lee, J.W., Gary, D.E., Zirin, H.: Flat microwave spectra seen at X-class flares. Sol. Phys. **152**, 409–428 (1994)
28. Klein, K.-L., Trotett, G.: 1984: gyrosynchrotron radiation from a source with spatially varying field and density. Astron. Astrophys. **141**, 67–76 (1984)
29. Ramaty, R., Petrosian, V.: Free-free absorption of gyrosynchrotron radiation in solar microwave bursts. Astrophys. J. **178**, 241–250 (1972)
30. White, S.M., Kundu, M.R., Bastian, T.S., Gary, D.E., Hurford, G.J., Kucera, T., Bieging, J.H.: Multifrequency observations of a remarkable solar radio burst. Astrophys. J. **384**, 656–664 (1992)
31. Croom, D.L.: 71 GHz (4.2 mm) Solar radio bursts in the period July 1967 to December 1969. Sol. Phys. **15**, 414–423 (1970)
32. Shimabukuro, F.I.: On the temperature and emission measure of thermal radio bursts. Sol. Phys. **23**, 169–177 (1972)
33. Zirin, H., Tanaka, K.: The flares of August 1972. Sol. Phys. **32**, 173–207 (1973)
34. Correia, E., Kaufmann, P., Magun, A.: The observed spectrum of solar burst continuum emission in the submillimeter spectral range infrared solar physics. In: Rabin, D.M., Jefferies, J.T., Lindsey, C. (eds.) International Astronomical Union Symposium on Proceedings of the 154th Symposium of the International Astronomical Union held in Tucson, Arizona, USA, 2-6 March 1992, vol. 154, p. 125. Kluwer Academic Publishers, Dordrecht (1994)
35. Kaufmann, P., Raulin, J.-P., Melo, A.M., Correia, E., Costa, J.E.R., Giménez de Castro, C.G., Silva, A.V.R., Yoshimori, M., Hudson, H.S., Gan, W.Q., Gary, D.E., Gallagher, P.T., Levato, H., Marun, A., Rovira, M.: Solar submillimeter and Gamma-Ray burst emission. Astrophys. J. **574**, 1059–1065 (2002)
36. Kaufmann, P., Levato, H., Cassiano, M.M., Correia, E., Costa, J.E.R., Giménez de Castro, C.G., Godoy, R., Kingsley, R.K., Kingsley, J.S., Kudaka, A. S., Marcon, R., Martin, R., Marun, A., Melo, A.M., Pereyra, P., Raulin, J., Rose, T., Silva Valio, A., Walber, A., Wallace, P., Yakubovich, A., Zakia, M.B.: New telescopes for ground-based solar observations at submillimeter and mid-infrared. Proc. SPIE **7012**, 70120L (2008)
37. Raulin, J.-P., Makhmutov, V.S., Kaufmann, P., Pacini, A.A., Lüthi, T., Hudson, H.S., Gary, D.E.: Analysis of the impulsive phase of a solar flare at submillimeter wavelengths. Sol Phys. **223**, 181–199 (2004)
38. Trottet, G., Raulin, J.-P., Giménez de Castro, C.G., Lüthi, T., Caspi, A., Mandrini, C.H., Luoni, M.L., Kaufmann, P.: Origin of the submillimeter radio emission during the time-extended phase of a solar flare. Sol. Phys. **273**, 339–361 (2011)
39. Giménez de Castro, C.G., Cristiani, G.D., Simües, P.J.A., Mandrini, C.H., Correia, E., Kaufmann, P.: A burst with double radio spectrum observed up to 212 GHz. Sol. Phys. **284**, 541–558 (2013)
40. Kaufmann, P., Raulin, J.-P., Giménez de Castro, C.G., Levato, H., Gary, D.E., Costa, J.E.R., Marun, A., Pereyra, P., Silva, A.V.R., Correia, E.: A new solar burst spectral component emitting only in the terahertz range. Astrophys. J. **603**, L121–L124 (2004)
41. Melnikov, V.F., Gary, D.E., Nita, G.M.: Peak frequency dynamics in solar microwave bursts. Sol. Phys. **253**, 43–73 (2008)
42. Torii, C., Tsukiji, Y., Kobayashi, S., Yoshimi, N., Tanaka, H., Enome, S.: Full-automatic radiopolarimeters for solar patrol at microwave frequencies. Proc. Nagoya Univ. Res. Inst. Atmos. **26**, 129–132 (1979)
43. Nakajima, H., Sekiguchi, H., Sawa, M., Kai, K., Kawashima, S., Kosugi, T., Shibuya, N., Shinohara, N., Shiomi, Y.: The radiometer and polarimeters at 80, 35, and 17 GHz for solar observations at Nobeyama. Publ. Astron. Soc. Japan **37**, 163–170 (1985)

44. Song, Q., Nakajima, H., Huang, G., Tan, B., Huang, Y., Wu, Z.: Turnover frequency in solar microwave bursts with an extremely flat optically-thin spectrum. Sol. Phys. **291**, 3619–3635 (2016)
45. Ramaty, R., Schwartz, R.A., Enome, S., Nakajima, H.: Gamma-ray and millimeter-wave emissions from the 1991 June X-class solar flares. Astrophys. J. **436**, 941–949 (1994)
46. Razin, V.A.: Izv. Vyssh. Uchebn. Zaved. Radiofiz. **3**, 584 (1960)
47. Newkirk Jr, G.: Coronal magnetic fields and the solar wind, solar wind. In: Charles, P.S., Paul, J.C., John, M.W. (eds.), p. 11, Scientific and Technical Information Office, National Aeronautics and Space Administration, Washington (1972)
48. Dulk, G.A., McLean, D.J.: Coronal magnetic fields. Sol. Phys. **57**, 279–295 (1978)
49. Krüger, A., Hildebrandt, J.: Corona magnetic fields deduced from radio methods (invited), The magnetic and velocity fields of solar active regions. In: Zirin, H., Ai, G., Wang, H. (eds.) Proceedings of the International Astronomical Union (IAU) Colloquium no. 141, held in Beijing, China, 6-12 September 1992. Astronomical Society of the Pacific Conference Series, vol. 46, p. 249. Astronomical Society of the Pacific (ASP), San Francisco (1993)
50. Mandrini, C.H., Démoulin, P., Klimchuk, J.A.: Magnetic field and plasma scaling laws: their implications for coronal heating models. Astrophys. J. **530**, 999–1015 (2000)
51. Fleishman, G.D., Melnikov, V.F.: Gyrosynchrotron emission from anisotropic electron distributions. Astrophys. J. **587**, 823–835 (2003)
52. Fu, Q., Ji, H., Lao, D., Liu, Y., Chen, Z., Cheng, C., Wang, S., Xie, R., Guo, Y.: A separatrix frequency of microwave type III burst found in microwave range in corona. Acta Astrophys. Sin. **17**, 441–444 (1997)
53. Huang, G.L., Li, J.P., Song, Q.W.: The calculation of coronal magnetic field and density of nonthermal electrons in the 2003 October 27 microwave burst. Res. Astron. Astrophys. **13**, 215–225 (2013)
54. Maurya, R.A., Vemareddy, P., Ambastha, A.: Velocity and magnetic transients driven by the X2.2 white-light flare of 2011 February 15 in NOAA 11158. Astrophys. J. **747**, 134–145 (2012)
55. Sakurai, T., Hiei, E.: New observational facts about solar flares from ground-based observations. Adv. Space Res. **17**, 91–100 (1996)
56. Ding, M.D., Qiu, J., Wang, H.: Non-LTE calculation of the Ni I 676.8 Nanometer line in a flaring atmosphere. Astrophys. J. **576**, L83–L86 (2002)
57. Qiu, J., Gary, D.: Flare-related magnetic anomaly with a sign reversal. Astrophys. J. **599**, 615–625 (2003)
58. Seehafer, N.: Determination of constant alpha force-free solar magnetic fields from magnetograph data. Sol. Phys. **58**, 215–223 (1978)
59. Gan, W.Q., Li, Y.P., Chang, J.: Energy shortage of nonthermal electrons in powering a solar flare. Astrophys. J. **552**, 858–862 (2001)
60. Kontar, E.P., Brown, J.C., McArthur, G.: Nonuniform target ionization and fitting thick target electron injection spectra to RHESSI data. Sol. Phys. **210**, 419–429 (2002)
61. Kontar, E.P., Brown, J.C., Emslie, A.G., Schwartz, R.A., Smith, D.M., Alexander, R.C.: An explanation for non-power-law behavior in the hard X-ray spectrum of the 2002 July 23 solar flare. Astrophys. J. **598**, L123–L126 (2003)
62. Holman, G.D.: The effects of low- and high-energy cutoffs on solar flare microwave and hard X-Ray spectra. Astrophys. J. **586**, 606–616 (2003)
63. Zhang, J., Huang, G.L.: The effect of the compton backscattering component on the photon spectra of three Yohkoh/Hard X-ray telescope flare. Astrophys. J. **592**, L49–L52 (2003)
64. Zhang, J., Huang, G.L.: Joint effects of compton backscattering and low-energy cutoff on the flattening of solar hard X-ray spectra at lower energies. Sol. Phys. **219**, 135–148 (2004)
65. Kašparová, J., Karlický, M., Kontar, E.P., Schwartz, R.A., Dennis, B.R.: Multi-wavelength analysis of high-energy electrons in solar flares: a case study of the August 20, 2002 flare. Sol. Phys. **232**, 63–86 (2005)
66. Kontar, E.P., MacKinnon, A.L., Schwartz, R.A., Brown, J.C.: Compton backscattered and primary X-rays from solar flares: angle dependent Green's function correction for photospheric albedo. Astron. Astrophys. **446**, 1157–1163 (2006)

67. Kašparová, J., Kontar, E.P., Brown, J.C.: Hard X-ray spectra and positions of solar flares observed by RHESSI: photospheric albedo, directivity and electron spectra. Astron. Astrophys. **466**, 705–712 (2007)
68. Han, G., Li, Y.P., Gan, W.Q.: A study of the low energy cutoff of nonthermal electrons in RHESSI flares. Chin. Astron. Astrophys. **33**, 168–178 (2009)
69. Miyamoto, K.: Fundamentals of Plasma Physics and Controlled Fusion, pp. 88–89. Science Press, Beijing (1981)
70. Gan, W.Q.: A comparison between the spectral parameters of both electron and proton dominated events. Astrophys. Space Sci. **274**, 481–488 (2000)
71. Huang, G.L.: The common cutoff energy of non-thermal electrons with power law distribution. Astrophys. Space Sci. **272**, 325–332 (2000a)
72. Huang, G.L.: Energy cutoff, energy index, and density of nonthermal electrons responsible for solar microwave and HXR bursts. Sol. Phys. **196**, 395–402 (2000)
73. Bai, T., Ramaty, R.: Backscatter, anisotropy, and polarization of solar hard X-rays. Astrophys. J. **219**, 705–726 (1978)
74. Tandberg-Hanssen, E., Emslie, A.G.: The Physics of Solar Flares. Cambridge University Press, Cambridge (1988)
75. Huang, G.L.: Initial pitch-angle of narrowly beamed electrons injected into a magnetic mirror, formation of trapped and precipitating electron distribution, and asymmetry of hard X-ray and microwave footpoint emissions. New Astron. **12**, 483–489 (2007)
76. Huang, G.L., Nakajima, H.: Statistical analysis of flaring loops observed by nobeyama radioheliograph. I. Comparison of looptop and footpoints. Astrophys. J. **696**, 136–142 (2009)
77. Huang, G.L., Song, Q.W., Huang, Y.: Statistics of flaring loops observed by the nobeyama radioheliograph. III. Asymmetry of two footpoint emissions. Astrophys. J. **723**, 1806–1816 (2010)
78. Marsh, K.A., Hurford, G.J., Zirin, H., Dulk, G.A., Dennis, B.R., et al.: Properties of solar flare electrons, deduced from hard X-ray and spatially resolved microwave observations. Astrophys. J. **251**, 797–804 (1981)
79. Alissandrakis, C.E.: Gyrosynchrotron emission of solar flares. Sol. Phys. **104**, 207–221 (1986)
80. Nitta, N., White, S.M., Schmahl, E.J., Kundu, M.R.: On the reconciliation of simultaneous microwave imaging and hard X-ray observations of a solar flare. Sol. Phys. **132**, 125–136 (1991)
81. Silva, A.V.R., Wang, H., Gary, D.E.: Correlation of microwave and hard X-ray spectral parameters. Astrophys. J. **545**, 1116–1123 (2000)
82. White, S.M., Kundu, M.R.: Solar observations with a millimeter-wavelength array. Sol. Phys. **141**, 347–369 (1992)
83. Kundu, M.R., White, S.M., Gopalswamy, N., Lim, J.: Millimeter, microwave, hard X-ray, and soft X-ray observations of energetic electron populations in solar flares. Astrophys. J. Supplement Ser. **90**, 599–610 (1994)
84. Silva, A.V.R., Gary, D.E., White, S.M., Lin, R.P., de Pater, I.: First images of impulsive millimeter emission and spectral analysis of the 1994 August 18 solar flare. Sol. Phys. **175**, 157–173 (1997)
85. Raulin, J.-P., White, S.M., Kundu, M.R., Silva, A.V.R., Shibasaki, K.: Multiple components in the millimeter emission of a solar flare. Astrophys. J. **522**, 547–558 (1999)
86. Hildebrandt, J., Krüger, A., Chertok, I.M., Fomichev, V.V., Gorgutsa, R.V.: Solar microwave bursts from electron populations with a 'Broken' energy spectrum. Sol. Phys. **181**, 337–349 (1998)
87. Melrose, D.B., Brown, J.C.: Precipitation in trap models for solar hard X-ray bursts. Mon. Not. R. Astron. Soc. **176**, 15–30 (1976)
88. Vilmer, N., Kane, S.R., Trottet, G.: Impulsive and gradual hard X-ray sources in a solar flare. Astron. Astrophys. **108**, 306–313 (1982)
89. Melnikov, V.F., Magun, A.: Dynamics of energetic electrons in a solar flare loop and the flattening of its millimeter-wavelength radio emission spectrum. Radiophys. Quantum Electron. **39**, 971–977 (1996)

90. Melnikov, V.F., Magun, A.: Spectral flattening during solar radio bursts at Cm-mm wavelengths and the dynamics of energetic electrons in a flare loop. Sol. Phys. **178**, 153–171 (1998)
91. Yoshimori, M., Suga, K., Morimoto, K., Hiraoka, T., Sato, J., et al.: Gamma-ray spectral observations with YOHKOH. Astrophys. J. Supplement Ser. **90**, 639–643 (1994)
92. Trottet, G., Vilmer, N., Barat, C., Benz, A., Magun, A., et al.: A multiwavelength analysis of an electron-dominated gamma-ray event associated with a disk solar flare. Astron. Astrophys. **334**, 1099–1111 (1998)
93. Vilmer, N., Trottet, G., Barat, C., Schwartz, R.A., Enome, S., et al.: Hard X-ray and gamma-ray observations of an electron dominated event associated with an occulted solar flare. Astron. Astrophys. **342**, 575–582 (1999)
94. Melnikov, V.F., Silva, A.V.R.: Dynamics of solar flare microwave and hard X-ray spectra. In: Wilson, A (ed.) Magnetic Fields and Solar Processes. The 9th European Meeting on Solar Physics, held 12-18 September 1999, Florence, Italy. European Space Agency, ESA SP-448, p. 1053 (1999)
95. Stahli, M., Gary, D.E., Hurford, G.J.: High-resolution microwave spectra of solar bursts. Sol. Phys. **120**, 351–368 (1989)
96. Dulk, G.A., Kiplinger, A.L., Winglee, R.M.: Characteristics of hard X-ray spectra of impulsive solar flares. Astrophys. J. **389**, 756–763 (1992)
97. Marsh, K.A., Hurford, G.J.: Two-dimensional VLA maps of solar bursts at 15 and 23 GHz with arcsec resolution. Astrophys. J. **240**, L111–L114 (1980)
98. Kundu, M.R., Schmahl, E.J., Velusamy, T., Vlahos, L.: Radio imaging of solar flares using the very large array - new insights into flare process. Astron. Astrophys. **108**, 188–194 (1982)
99. Kawabata, K., Ogawa, H., Takakura, T., Tsuneta, S., Ohki, K., et al.: Fan-beam observations of millimeter wave burst associated with X-Ray and Gamma-Ray events detected from HINOTORI. In: Proceedings of the Hinotori Symposium held Solar Flares, p. 168 (1981)
100. Nakajima, H.: Particle acceleration in the 1981 April 1 flare. Sol. Phys. **86**, 427–432 (1983)
101. Hanaoka, Y.: Double-loop configuration of solar flares. Sol. Phys. **173**, 319–346 (1997)
102. Nishio, M., Yaji, K., Kosugi, T., Nakajima, H., Sakurai, T.: Magnetic field configuration in impulsive solar flares inferred from coaligned microwave/X-ray images. Astrophys. J. **489**, 976–991 (1997)
103. Hanaoka, Y.: High-energy electrons in double-loop flares. Publ. Astron. Soc. Japan **51**, 483–496 (1999)
104. Kundu, M.R., Nindos, A., White, S.M., Grechnev, V.V.: A multiwavelength study of three solar flares. Astrophys. J. **557**, 880–890 (2001)
105. Melnikov, V.F., Shibasaki, K., Reznikova, V.E.: Loop-top nonthermal microwave source in extended solar flaring loops. Astrophys. J. **580**, L185–L188 (2002)
106. Alissandrakis, C.E., Preka-Papadema, P.: Microwave emission and polarization of a flaring loop. Astron. Astrophys. **139**, 507–511 (1984)
107. Klein, K.-L., Trottet, G.: Gyrosynchrotron radiation from a source with spatially varying field and density. Astron. Astrophys. **141**, 67–76 (1984)
108. Bastian, T.S., Benz, A.O., Gary, D.E.: Radio emission from solar flares. Annu. Rev. Astron. Astrophys. **36**, 131–188 (1998)
109. Tzatzakis, V., Nindos, A., Alissandrakis, C.E., Shibasaki, K.: A statistical study of microwave flare morphologies. In: Recent Advances in Astronomy and Astrophysics: 7th International Conference of the Hellenic Astronomical Society, AIP Conference Proceedings, vol. 848, pp. 248–252 (2006)
110. Martynova, O.V., Melnikov, V.F., Reznikova, V.E.: Proceedings of 11th Pulkovo International Conference on Solar Physics, Saint-Peterburg, p. 241 (2007)
111. White, S.M., Kundu, M.R., Garaimov, V.I., Yokoyama, T., Sato, J.: The physical properties of a flaring loop. Astrophys. J. **576**, 505–518 (2002)
112. Melnikov, V. F.: Electron Acceleration and Transport in Microwave Flaring Loops. Proc. Nobeyama Symposium (Kiosato, 26-29 October 2004), Ed. K.Shibasaki, NSRO Report, **1**, 11–22 (2006)

113. Melnikov, V.F., Gorbikov, S.P., Reznikova, V.E., Shibasaki, K.: Bull. Russ. Acad. Sci. Phys. **70**, 1684 (2006)
114. Yokoyama, T., Nakajima, H., Shibasaki, K., Melnikov, V.F., Stepanov, A.V.: Microwave observations of the rapid propagation of nonthermal sources in a solar flare by the nobeyama radioheliograph. Astrophys. J. **576**, L87–L90 (2002)
115. Stepanov, A.V., Yokoyama, T., Shibasaki, K., Melnikov, V.F.: Turbulent propagation of high-energy electrons in a solar coronal loop. Astron. Astrophys. **465**, 613–619 (2007)
116. Su, Y.N., Huang, G.L.: Polarization of loop-top and footpoint sources in microwave bursts. Sol. Phys. **219**, 159–168 (2004)
117. Karlicky, M.: Loop-top gyro-synchrotron source in post-maximum phase of the August 24, 2002 flare. New Astron. **9**, 383–389 (2004)
118. Li, Y.P., Gan, W.Q.: The shrinkage of flare radio loops. Astrophys. J. **629**, L137–L139 (2005)
119. Nakajima, H., Nishio, M., Enome, S., Shibasaki, K., Takano, T., et al.: The nobeyama radioheliograph. Proc. IEEE **82**, 705–713 (1994)
120. Domingo, V., Fleck, B., Poland, A.I.: The SOHO mission: an overview. Sol. Phys. **162**, 1–37 (1995)
121. Handy, B.N., Acton, L.W., Kankelborg, C.C., Wolfson, C.J., Akin, D.J., et al.: The transition region and coronal explorer. Sol. Phys. **187**, 229–260 (1999)
122. Kuznetzov, S.N., Kudela, K., Myagkova, I.N., et al.: Indian J. Radio Space. Physics **33**, 353 (2004)
123. Oraevsky, V.N., Sobelman, I.I., Zitnik, I.A., Kuznetsov, V.D., Stepanov, A.I.: CORONAS-F observations of active phenomena on the sun. Adv. Space Res. **32**, 2567–2572 (2003)
124. Bai, T.: Two classes of gamma-ray/proton flares - impulsive and gradual. Astrophys. J. **308**, 912–928 (1986)
125. Melnikov, V.F.: Electron acceleration and capture in impulsive and gradual bursts: results of analysis of microwave and hard x-ray emissions. Radiophys. Quantum Electron. **37**, 557–568 (1994)
126. Hamilton, R.J., Lu, E.T., Petrosian, V.: Numerical solution of the time-dependent kinetic equation for electrons in magnetized plasma. Astrophys. J. **354**, 726–734 (1990)
127. Ning, Z., Ding, M.: Microwave spectral evolution of solar flares. Publ. Astron. Soc. Japan **59**, 373–379 (2007)
128. Nita, G., Gary, D., Lee, J.: Statistical study of two years of solar flare radio spectra obtained with the owens valley solar array. Astrophys. J. **605**, 528–545 (2004)
129. Silva, A., Share, G., Murphy, R., Costa, J., de Castro, C., Raulin, J., Kaufmann, P.: Evidence that synchrotron emission from nonthermal electrons produces the increasing submillimeter spectral component in solar flares. Sol. Phys. **245**, 311–326 (2007)
130. Zhou, A., Huang, G., Li, J.: New explanations for some observation phenomena of the peak frequency of solar radio bursts. Astrophys. J. **708**, 445–449 (2010)
131. Grigis, P., Benz, A.: The spectral evolution of impulsive solar X-ray flares. Astron. Astrophys. **426**, 1093–1101 (2004)
132. Ning, Z.: Microwave and hard X-ray spectral evolution in two solar flares. Astrophys. J. **659**, L69–L72 (2007a)
133. Ning, Z.: Different behaviors between microwave and hard X-ray spectral hardness in two solar flares. Astrophys. J. **671**, L197–L200 (2007b)
134. Morgachev, A.S., Kuznetsov, S.A., Melnikov, V.F.: Radio diagnostics of the solar flaring loop parameters by the forward fitting method. Geomagn. Aeron. **54**, 933–942 (2014)
135. Fleishman, G.D., Kuznetsov, A.A.: Fast gyrosynchrotron codes. Astrophys. J. **721**, 1127–1141 (2010)
136. Fleishman, G.D., Nita, G.M., Gary, D.E.: Dynamic magnetography of solar flaring loops. Astrophys. J. Lett. **698**, L183–L187 (2009)
137. Gladkov, L.A., Kureichik, V.V., Kureichik, V.M.: Geneticheskie algoritmy: Uchebnoe posobie. 2-e izd. (Genetic Algorithms: A Textbook). Fizmatlit, Moscow (2006)

Chapter 7
Global Behaviors for Dynamics of Flaring Loops

7.1 Global Behaviors Revealed by Observations at Multi-wavebands

7.1.1 Contraction of Flaring Loops prior to Their Expansion

Solar flares are explosive phenomena produced by sudden release of free magnetic energy. It is generally believed that flare loops, especially those of two-ribbon flares, show continuous expansion motions during their eruption. Meanwhile, flare ribbons separate continuously in space from each other. Such observational phenomena are interpreted in theory by continuously rising of the magnetic reconnection site, which closely follows erupting magnetic flux ropes (or filaments). However, results based on a statistical study with Yohkoh HXR Telescope data indicate that FPs in only 13% of the flares show standard separation motion [1], while in more flares they show motions parallel to bright flare ribbons, even with tendency to converge. Using high-cadence time sequence of observations for the M1.2 class flare on September 9, 2002, at Big Bear Solar Observatory (BBSO), Ji et al. [2] found that the distance between H_α kernels decreases at the rising phase of the flare, it increases only after the peak time. At the same time, the height of the LT X-ray source of the flare decreases at first, and increases after the maximum phase. From Fig. A.12 in Appendix A, we can see that the time profiles of the flare emission, the distance between bright kernels, and the height of the loop top X-ray source show a good correlation or anti-correlation not only as a whole but also in some details.

By analyzing the same flare, Shen et al. [3] found that during the period of the descending motion of the LT source, i.e., the rising phase of the flare, the HXR sources in different energies are mixed; only during the period that the LT source ascends, i.e., the decay phase of the flare, their positions can be distinguished. During the whole period of decay phase, the LT source at higher energies is always higher in altitude than that at lower energies. In present 2D framework of flare models, upward and downward jets are produced after magnetic reconnection. The downward jet collides

G. Huang et al., *Solar Flare Loops: Observations and Interpretations*,
https://doi.org/10.1007/978-981-10-2869-4_7

with the plasma on the top of a flaring arcade, producing a HXR LT source. Due to heat conduction and cooling effects, the lower part of the LT source is a little far away from the collision site. Thus, we can expect that the HXR LT source at higher energy bands will be higher in altitude. The quite different temperature structures give that magnetic reconnection processes in the rising and decay phases of solar flares are different. Using a high-cadence imaging observation of an M1.1 class solar flare made with the H_α Fine Structure Telescope at GanYu solar station, Ji et al. [4] further found that the converging and separation motions are a kind of unshearing process of magnetic fields. This result indicates that magnetic reconnection during the flaring periods occurs in a sheared magnetic field. The most convincing event is the X10 class flare that occurred on October 29, 2003 (one of the famous "Halloween storms of 2003"). The whole process of this flare can be divided into a sigmoid phase and an arcade phase [5]. The unshearing and converging motion of the FPs and the descending of the LT source occur in the sigmoid phase, while the expansion period of the flare loop corresponds to the arcade phase in the later stage of the flare. It is equally important that this is the first time the sigmoid structure of magnetic field being observed in HXR bands, see Fig. A.13 in Appendix A.

Due to the projection effect, flares on the solar disk show more clearly the motion of FPs, while those limb events show more clearly the motion of LT sources or the flare loops. Therefore, most studies deal with the motions of FPs or LT sources separately, few studies discuss the relationship between them in the same event. With observations for an M1.2 limb flare on 2002 April 15 made by RHESSI, for the first time, Sui et al. discovered descending motion of the loop top source [6, 7]. Meanwhile, in literature, there are some flares with their FPs having a kind of converging motion [8, 9]. It can be seen from the beginning of this chapter that flare loops have a contracting behavior as a whole. The contraction of a radio loop for a limb flare during its early impulsive phase clearly illustrates this point of view [10].

The dynamic evolution of flare loops can be summarized as following conclusions. Flare loops show early contraction and later expansion motions; the contraction motion appears as converging motion of FPs, descending of whole loops or descending of LT sources, while the expansion motion appears as separation motion of FPs, expansion of whole loops or ascending of LT sources. During the periods of contraction and expansion, flare shearing decreases continuously. The best observational example supporting this picture has been given by an X7.1 flare that occurred on 2005 January 20 [11] (see Fig. A.14 in Appendix A). It is worth mentioning that the contraction of flare loops here is different from the shrinkage of flare loops reported by Švestka et al. [12], in which an apparent shrinking occurs when X-ray emitting loops cool down to H_α emitting loops.

In fact, the process of contraction and expansion is not always along the solar radial direction. For example, the trajectory of coronal source is almost parallel to the solar disk for the M1.6 FP-occulted flare that occurred on 2002 April 4 (Fig. A.15 in Appendix A). Such kind of trajectories can be defined as U-shaped motion trajectories. The turning point of the U-shaped trajectories always corresponds to the peak time of flares. The distance between the coronal source and the turning point can be defined as the "height" of coronal source. According to this definition, it can be

frequently seen that X-ray sources in different energy bands are mixed in the rising phase of the flare, after the peak time, the coronal source at higher energy bands is located higher than lower energy bands.

7.1.2 The Relaxation of Sheared Magnetic Field

How to interpret the contraction phenomenon of flare loops makes a challenge to the present theories and simulations of flares. Based on observations, Sui et al. interpreted the descending of the loop top source as the formation of the current sheet in the framework of 2D standard flare models [6, 7]. For the M1.2 flare that occurred on 2002 April 15, they simultaneously observed an X-ray coronal source, which moves upward as one LT source moves downward. The observational phenomenon supporting this interpretation is the temperature structure existing between the coronal source and the LT source. However, such a phenomenon is quite uncommon. Veronig et al. presented simulations for the collapse of magnetic loops in a standard 2D magnetic reconnection model, by the way, they explained the acceleration of electrons based on this model [13]. But all the above pictures cannot explain the unshearing and converging motion of flare FPs. Hudson proposed the concept of implosion, the key idea is that the magnetic pressure will decrease due to release of free magnetic energy, which will give rise to the descending of magnetic loops in observations [14].

The Lorentz force plays a dominant role in the magnetized plasma of the solar corona. Thus, the magnetic field is force-free in nature. The above mentioned "implosion" concept can be understood by a linear force-free model of a magnetic loop [15]:

$$\mathbf{B}(x, y, z) = \mathbf{B}_0(x, y)e^{-\gamma z} , \tag{7.1.1}$$

where $B_0(x, y)$ has three components, γ denotes the decrease of magnetic field in space, therefore, in some way it can be used to indicate the height of the magnetic loop ($H \propto 1/\gamma$). We assume that γ and the force-free parameter are only the functions of time. Using the force-free equation

$$\nabla \times \mathbf{B} = \alpha \mathbf{B} , \tag{7.1.2}$$

and the divergence-free equation

$$\nabla \cdot \mathbf{B} = 0 , \tag{7.1.3}$$

we have the Helmholtz equation which should be satisfied by each magnetic field component:

$$\nabla^2 \mathbf{B} = \alpha^2 \mathbf{B} \,. \tag{7.1.4}$$

Substituting Eqs. (7.1.1)–(7.1.4), we have the following conditions for the three components of $B_0(x, y)$:

$$B_{0x} = -k^{-2}\left(-\gamma \frac{\partial B_{0z}}{\partial x} + \alpha \frac{\partial B_{0z}}{\partial y}\right) , \tag{7.1.5}$$

$$B_{0y} = -k^{-2}\left(-\alpha \frac{\partial B_{0z}}{\partial x} - \gamma \frac{\partial B_{0z}}{\partial y}\right) , \tag{7.1.6}$$

$$B_{0z} = -k^{-2}\left(\frac{\partial^2 B_{0z}}{\partial x^2} + \frac{\partial^2 B_{0z}}{\partial y^2}\right) , \tag{7.1.7}$$

where $k^2 = \alpha^2 + \gamma^2$. Making an assumption that the magnetic field at the photosphere does not change during flares, i.e., k remains constant, this is equal to that B_{0z} remains almost fixed throughout the flaring processes. Thus, we get

$$B_z \propto e^{-\gamma z}, \;\; B_\perp \propto e^{-\gamma z} \,, \tag{7.1.8}$$

where $B_\perp = \sqrt{B_x^2 + B_y^2}$. In addition, the total magnetic energy integrated over the entire flare region must decrease during a flare, i.e.,

$$\frac{d}{dt} E = \frac{d}{dt} \int \frac{\mathbf{B}^2}{8\pi} dV < 0 \,, \tag{7.1.9}$$

where $dV = dxdydz$, and

$$\int \mathbf{B}^2 dV = \frac{1}{2\gamma}(1 - e^{-2\gamma H_U}) \int (B_{0\perp}^2 + B_{0z}^2) dxdy = \frac{1}{2\gamma} \int (B_{0\perp}^2 + B_{0z}^2) dxdy \,, \tag{7.1.10}$$

where H_U is the height of the upper boundary of the boxed flare region. Let $H_U \to \infty$, we see that the value of γ must increase in order to let the integrated magnetic energy decrease. This is to say, the scale height of the coronal magnetic field decreases. Therefore, we prove that the span (proportional to $B_\perp$) and the height (proportional to B_z) of the magnetic arcade will decrease simultaneously during a flare. Magnetic shear is related to the value of B_{0y}/B_{0x}, we have

$$\frac{B_{0y}}{B_{0x}} = \left(\frac{\alpha}{\gamma}\frac{\partial B_0 z}{\partial x} + \frac{\partial B_0 z}{\partial y}\right)\left(\frac{\partial B_0 z}{\partial x} - \frac{\alpha}{\gamma}\frac{\partial B_0 z}{\partial y}\right)^{-1} . \tag{7.1.11}$$

Additionally, by the above assumptions, k is roughly a constant, and α must decrease. Thus, it is not difficult to find that the flare shear continues to decrease during the flaring process.

In the process of deducing the above equations, the essence is force-free fields with different energies under the same boundary condition. Strong shear is related to magnetic configuration with bigger spans and heights, correspondingly, weak shear is related to magnetic configuration with smaller spans and heights. Therefore, after a flare (release of free magnetic energy), the magnetic loop will become smaller in 3D space, which is related to contraction of flare loops. In other words, contraction of flare loops is the natural result after the release of free magnetic energy. Here, we must neglect the so-called "line-tying effect" of magnetic field lines, i.e., the magnetic loop is anchored in the photosphere. Our results indicate that the field line starting from one site will no longer be able to reach the original site after the energy release (see Fig. 7.1 and the illustration in the caption).

The recently high-resolution observations by SDO/AIA show that non-flaring loops at the edge of the active region also have a contraction process during flares. A number of non-flaring loops experience contraction motions in sequence with lower loops contracting first and upper loops contracting later. The studies by Shen et al. show that such a contraction is caused by magnetic pressure drop left by the eruption of the filament (flux rope), making the peripheral magnetic loops contract continually [16]. The analyses of several events in another literature [17] show that the propagation speed of the pressure drop is about 300 km/s, corresponding to the speed of fast mode Alfvén waves.

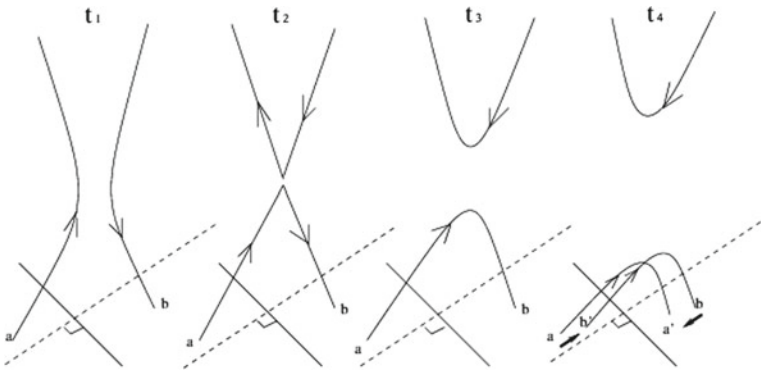

Fig. 7.1 Contraction of a magnetic loop during the energy release. The magnetic loop initially connecting from **a** to **b** can only connect to other locations, resulting in the decrease of the magnetic shear and the size of the whole magnetic loop as well

7.1.3 Possible Impact on the Lower Atmosphere

It is well known that the release of flare energy originates from magnetic energy stored in the solar corona. Therefore, general views hold that the photospheric magnetic field does not change during flares. More than two decades ago, BBSO group discovered that the vector magnetic field at the solar flaring site shows a rapid and permanent change [18, 19]. Later, it was found that penumbra filaments also have a rapid and permanent change after flares. The result from a preliminary study shows that the penumbra filaments disappear, while granulations change into plages [20]. This means that the magnetic field restructuring caused by release of the magnetic energy extends to the lower layer of the solar atmosphere. During the restructuring of the magnetic field, the eruption of the sigmoid magnetic structure makes the local coronal magnetic field collapse downward, the height distribution of the magnetic free energy thereby is pushed lower and the magnetic loops become lower and more horizontal. Therefore, the horizontal magnetic field near the flaring polarity inversion line (PIL) shows a rapid and irreversible change after the impulsive phase of the flare, the enhancement of the field is about 10–30% of the pre-flare magnitude. Meanwhile, the photospheric magnetic field also becomes more sheared and inclined. The work by Jing et al. also supports this inference [21]. Their study shows that though the magnetic shear (representing the non-potentiality of the magnetic field) becomes weaker and weaker in the high solar corona, it becomes stronger in the lower solar corona. The work by Sun et al. more clearly shows that near the flaring PIL, the electric current density does increase near the photosphere, but decreases more quickly at higher atmospheric layers [22]. Maybe it can be explained by that the total magnetic free energy decreases, but, meanwhile, the local magnetic free energy in the lower layer of solar corona increases after flares.

Hudson et al. and Fisher et al. considered that, after flares, the magnetic tension force has a change in the direction pointing to the photosphere [23, 24]. Solar flares, especially large ones, are often associated with upward mass motions, such as the eruption of CMEs. Thus, the magnetic field restructuring during flares will transport momentum downwards as the result of momentum conservation. Assuming that the photospheric magnetic field change is δB and the magnetic field decreases fast enough with height, the Lorentz force acting on per unit area of the photospheric surface is estimated to be

$$\delta f_z = (B_z \delta B_z - \delta B_x B_x - B_y \delta B_y)/4\pi \ . \tag{7.1.12}$$

Due to the contraction of flare loops, the magnetic field becomes more horizontal. Thus, the direction of the force given by Eq. (7.1.12) is pointing downward, i.e., the rapid enhancement of the transverse magnetic field may cause the sudden increase of the Lorentz force pointing downward. Such force could be the driving force for observed “sun-quakes”.

7.1.4 Sigmoid Magnetic Ropes

Hudson et al. [25] analyzed a list of halo CMEs over the time range from 1996 to 1997, they picked out seven events with identifiable surface features in soft X-rays. These events have a characteristic pattern of sigmoid to arcade development. The pre-flare structure disrupted during the flare, leaving the appearance of compact transient coronal holes. During the eruption of CMEs, the bright sigmoidstructure erupts outwards, leaving a series of brightening magnetic arcades. Many researchers have ever noticed such a phenomenon [26, 27], which now is generally regarded as a key element for eruptive flares. Considering that the contraction of the flare loops occurs at this stage, so it should be related with the magnetic reconnection or instabilities in flux ropes.

In cylindrical coordinates, from the Helmholtz equation (7.1.4) satisfied by the linear force-free field, it is not difficult to find that the solution of the linear force-free field is the sum of a series of "Bessel function". Taylor et al. [28] gave the general solution of the linear force-free field in cylindrical coordinates as

$$B_r^{mk}(r,\theta,z) = \frac{-1}{\sqrt{\alpha^2-k^2}}\left[kJ_m'(\rho)+\frac{m\alpha}{\rho}J_m(\rho)\right]\sin(m\theta+kz)\ , \tag{7.1.13}$$

$$B_\theta^{mk}(r,\theta,z) = \frac{-1}{\sqrt{\alpha^2-k^2}}\left[\alpha J_m'(\rho)+\frac{mk}{\rho}J_m(\rho)\right]\cos(m\theta+kz)\ , \tag{7.1.14}$$

$$B_z^{mk}(r,\theta,z) = J_m(\rho)\cos(m\theta+kz)\ , \tag{7.1.15}$$

where $\rho = (\sqrt{\alpha^2-k^2})r$. The simplest form the helical force-free field is the axial-symmetric case for $m=0$ and $k=0$:

$$B_r = 0 \quad B_\theta = AJ_1(\alpha r) \quad B_z = AJ_0(\alpha r)\ , \tag{7.1.16}$$

which yields the Lundquist solution. Rust and Kumar [29] gave an analytical form of the S-shaped flux tube by using the sum of solutions for $m=0$ and $m=1$:

$$\mathbf{B} = C_1 B^{00}(r) + C_2 B^{1k}(r,\theta,z)\ . \tag{7.1.17}$$

Figure A.16 in Appendix A shows the configuration of the simplest helical force-free field and an S-shaped flux tube plotted using Eq. (7.1.17). Using the boundary condition at infinity ($|b| < r^{-1}$) and the first zero position of the zeroth order Bessel function, they provide the values of the radius for the configuration of the simplest helical force-free field and the S-shaped force-free field, which are $R \sim 0.8/\alpha$ and $R \sim 2.405/\alpha$, respectively.

Kink instability exists in magnetic flux ropes. Assuming that the magnetic field of flux ropes is force free, the energy variation can be derived for a small perturbation ξ from basic MHD equations. Assuming the small perturbation vector is ξ, we have the energy variation as

$$\delta W = \frac{1}{2}\int_V [(\nabla \times \mathbf{A})^2 - \alpha \mathbf{A} \cdot (\nabla \times \mathbf{A})] d\tau \ , \tag{7.1.18}$$

where $\mathbf{A} = \xi \times \mathbf{B}$. The first term of Eq. (7.1.18) is always positive. According to the energy principle, the first term is an absolute stable term, while the second term could be an unstable term in some situations, the value, and sign which depend on the form of the perturbation vector ξ and are directly related to the value of the force-free factor α. For example, the potential field ($\alpha = 0$) is stable. In fact, the value of α determines the degree of kink. When analyzing the instability of a system using the energy principle, the general way is to find the minimum value of δW. If the minimum value of δW is negative, the system must be unstable.

It is worth mentioning that Voslamber and Callebaut [30] presented the instability conditions for a cylindrically symmetric force-free field as

$$m = \pm 1 \quad |\frac{k}{\alpha}| \leq 0.272 \ , \tag{7.1.19}$$

the minimum value of k can be estimated to be the reciprocal value of the flux rope length ($1/L$). Thus, it can be found that the stable condition for a flux rope with length L is

$$|\alpha| \leq \frac{1}{0.272L} \ , \tag{7.1.20}$$

or, for a certain value of α the stable condition of the flux rope is

$$L \leq \frac{1}{0.272|\alpha|} \ . \tag{7.1.21}$$

Rust and Kumar [29] proposed that the magnetic configuration of flux ropes is basically helical, extending along the axial direction, with only two feet rooted in the photosphere. This result can be used to estimate the maximum length for a stable flux rope. Similarly, using the stable condition in Eq. (7.1.19), Rust and Kumar [27] explained the observational result that the parameter $2\pi R/L$ of the soft X-ray sigmoid structures is statistically concentrated around 0.7.

Using the Eq. (7.1.18) for energy, Anzer [31] analyzed the stability of a flux rope with infinite length. He assumed

$$\xi = f(r) \exp[i(m\theta + kz)] \ , \tag{7.1.22}$$

and found that kink instability is always existed in the flux rope with an infinite length. Thus, it is a problem that energy can't be effectively stored in the flux rope. Therefore, why the magnetic loops are stable for a long time in the corona cannot be explained. In order to resolve the energy accumulation problem, Raadu [32] considered an axial-symmetric flux rope with a finite length, this flux rope roots in the dense photosphere. Thus, for all perturbations, the magnetic field lines at two sides are stationary, which is the so-called "line-tying effect". With the perturbations form of ξ originally used by Anzer [31], Raddu [32] assumed the form as

$$\xi_1 = f(z) \cdot \xi \ , \tag{7.1.23}$$

If the length of the flux rope is L, and $f(0) = f(L) = 0$, this is the mathematical expression of the line-tying effect. Tedious mathematical deductions are acquired to understand the line-tying effect. But, in simple, the line-tying effect makes the form of δW add one term, which can be expressed as

$$\delta W_{min} = (\pi/L)^2 A + C \ . \tag{7.1.24}$$

The first term of Eq. (7.1.24) is the newly added one, the value of which is always positive. Therefore, it can be seen that the line-tying effect makes the flux tube more stable. In addition, this term is proportional to L^{-2}, so the shorter the flux is, the more stable it is. The value of term A depends on the size of the cross section of the flux rope. To sum up, the reason why the coronal loops are especially stable is the line tying of the feet of the loops. When the twist exceeds a certain value, the coronal loops become unstable. This value depends on the aspect ratio of the loops. In analyzing a flux rope using theories or observations, a useful quantity is the number of turns that a field line wraps around the flux rope. Using the equation for the magnetic field line

$$d\theta = \frac{B_\theta}{r B_z} dz \ , \tag{7.1.25}$$

the number of turns from one end to another end of the flux rope with a length $2L$ is derived:

$$\Phi(r) = \frac{2L B_\theta}{r B_z} \ . \tag{7.1.26}$$

For a uniformly twisted force-free field, the critical value is 3.3π; for other fields, the value is located between 2π and 6π.

Observationally, a sigmoidal shape in hot EUV or SXR emissions actually is composed of two sheared J-shaped features. It is believed that once the sheared loops become unstable for some reasons reconnection will occur. A most recent study given by Shen et al. shows that the reconnection sometimes plays a key role in initiating the X 1.7 class flare on May 13, 2013 [33]. The reconnection between two

J-shaped magnetic loops was activated after occurrence of an X-ray precursor that started ∼9 min before onset of the flare, and it produced a hot magnetic flux rope that expands outward and a flare loop that contracts inward. The observation again shows that contraction of flare loops and the eruption of a sigmoid structure are associated and they both are key phenomena in initiating solar flares.

7.2 Failed Eruption of Filaments

CMEs are a large amount of magnetized plasma being ejected from the Sun and are transported into the interplanetary space. The ejected materials exist initially in the form of filaments, SXR sigmoid structures or magnetic loops that connect active regions or even cross the solar equator. Observations show little the photospheric magnetic field changes during the eruption of CMEs, therefore, the energy required by the eruption must be stored in the solar corona. The storage of large amounts of energy before eruption will certainly cause the coronal magnetic field to be twisted or highly sheared. The former corresponds to a field that has the axial flux with two feet anchored in the photosphere, which is called as a flux rope. The latter refers to sheared magnetic arcades. Numerical simulation shows that the shearing arcades will eventually evolve into a flux rope that erupts outward [34].

The eruption of a filament shows a slow rise and a fast rise processes, physically corresponding to two different stages, magnetic energy accumulation, and release, respectively. It has been introduced that magnetic energy (manifested as current) is accumulated in the solar corona, which corresponds to the accumulation of the magnetic twist or shear. The kink instability only occurs during the eruption and is not the driving force of the eruption. The driving force comes from the magnetic pressure, at the same time, the magnetic tension force produced by the magnetic field overlying on the flux rope acts as a restraining force. When the magnetic tension force is bigger than the magnetic pressure, the flux rope fails to erupt, forming the so-called "failed eruption" [35]. In addition, the strength of the magnetic field overlying on the flux rope determines the final speed of the CMEs [36].

Figure 7.2 shows the "failed filament eruption" observed by Ji et al. [35] at BBSO. In cooperation with the space observations by RHESSI, this project carried out high-cadence flare observations (25 fps) in H_α blue wing (−1.3 Å). The blue wing is chosen in order to avoid the strong thermal effects near the H_α line center and the downflow effects in the H_α red wing. Therefore, the blue wing is suitable to study the bombardment of NT electrons [37, 38], thus the observation can be used to distinguish between the thermal and non-thermal chromospheric heating, verify the heating model of the chromosphere. High-cadence observations are hopefully to show the fine temporal structures on a sub-second scale. NOAA Active Region 9957 was selected because of the existence of a small filament in this active region. By reducing the field of view, the TRACE satellite carried out joint observations of this active region with high time resolution. For the first time, Ji et al. observed the eruption of the filament with such a high cadence [35]. A lot of interesting processes

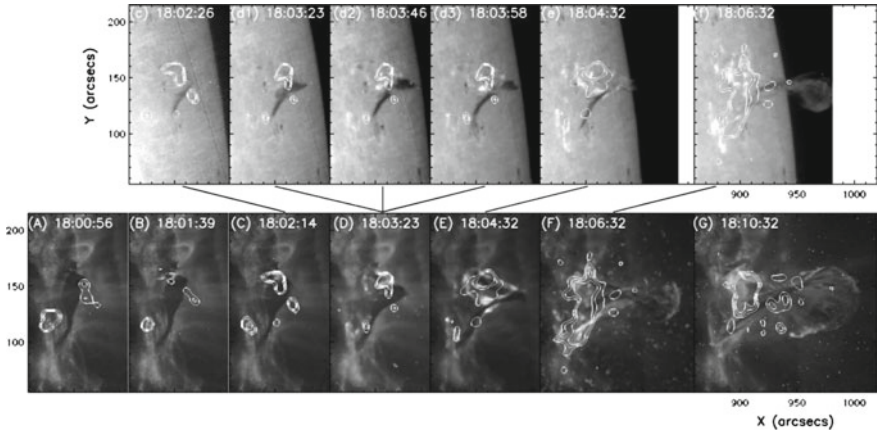

Fig. 7.2 Bottom panels (**a**–**g**): Trace Fe xii 195 Å images of the "failed filament eruption" that occurred at the west solar limb on 2002 May 27 and the associated M2.0 class flare. Top panels (**c**, **d1**–**d3**, and **e**–**f**): Joint observations of the filament eruption in H_α blue wing at BBSO. The contours are from RHESSI maps in the energy range of 12–25 keV. The RHESSI maps for panels **d2** and **d3** are the same as that for **d1** (18:03:46 and 18:03:58 UT are very near the RHESSI attenuator switching interval)

could be missed with normal low-cadence mode observations. For example, when the filament rose to the magnetic reconnection site (HXR loop top source), it began to rupture. The rupturing process lasted only for less than 10 s.

Generally, three physical processes can be clearly observed from this eruptive event: (1) The deceleration process of the filament. The negative acceleration is about 10 times greater than the solar gravitational constant, which strongly shows that the magnetic tension force produced by the overlying magnetic field of the flux rope plays a strong role in pulling back the eruptive filament. (2) The kink instability process during the filament eruption. From the H_α blue wing observations in Fig. 7.2, the south leg shows blue asymmetries (appearing as enhanced absorption), the north leg does not have any blue asymmetric component. We speculate that the north leg is redshifted during the eruptive process. Such a motion pattern is typical during the process that the twist changes into writhe. For clarity, we describe the process in the cartoon in Fig. A.17 of Appendix A. (3) The solar atmosphere is heated after the falling back of the filament materials. As shown in Fig. 7.3, in the decay phase of the flare (appearing as the decrease of the X-ray flux), the H_α emission has a sudden increase. This indicates that the falling back of the filament heats the solar atmosphere, in which the magnetic energy release may play an essential role.

Models for flux rope eruption are generally constructed from two aspects, one is by (for example, kinematic flux emergence) increasing the magnetic pressure in the flux rope [39, 40], such a kind of model has to make use of torus instability finally [41]. Aulannier et al. [42] simulated the driving of the sheared magnetic arcade by the flux-cancellation-driven photospheric reconnection. The results show that the

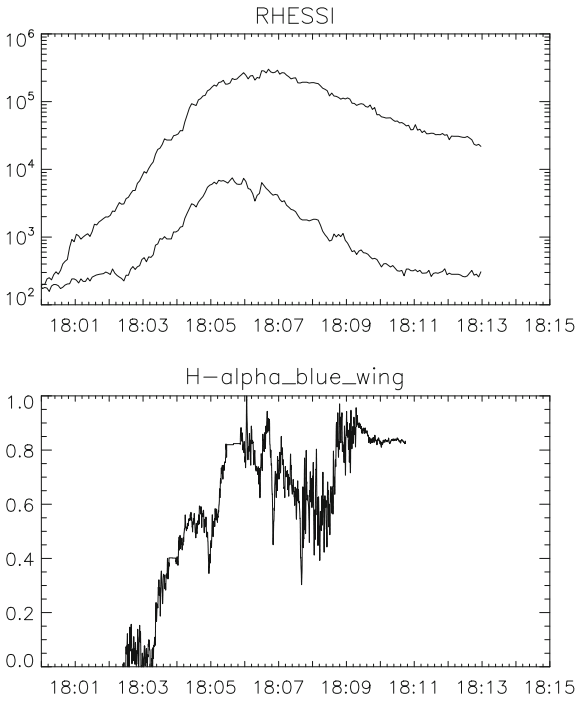

Fig. 7.3 Upper: RHESSI Light curves at the energy bands of 3–6 and 6–12keV for the "failed filament eruption" associated with an M2.0 flare. Lower: the light curve of the H_α blue wing emission. It can be seen that in the decay phase of the flare (appearing as the decrease of the X-ray flux), the H_α emission has a sudden increase

sheared arcades evolve into a slowly rising and stable flux rope at last. As the flux rope reaches the altitude at which the decay index $-\partial \ln B / \partial \ln z$ of the background field exceeds 3/2, torus instability occurs and the flux rope rapidly accelerates upward. Another aspect is by decreasing the magnetic tension force overlying on the flux rope, the typical models of which are the break-out model and the emerging flux model proposed by Chen et al. [43]. The tether-cutting model has both aspects, in which the tether-cutting reconnection not only speeds up the formation of the flux rope, but also decreases the overlying magnetic tension.

In this "failed filament eruption" event, the formation of the magnetic pressure force that drives and especially triggers the eruption of the flux rope has not been observed. However, it can be seen from Fig. 7.2 that before the rising of the filament, X-ray emissions are produced above the filament. The X-ray emissions are probably the signatures of the magnetic field reconnection above the filament. The magnetic reconnection reduces the magnetic tension force over the filament and thereby the filament erupts, which coincides with the results predicted by break-out model.

7.3 Dynamics of MW and HXR Flaring Loop System

7.3.1 Introduction

Large two-ribbon flares are a complex phenomenon, which may be accompanied by coronal mass ejections (CME's) and prominence eruptions (see a review 44). The basic model for such flares is the standard reconnection model, known as the "CSHKP" [45–48]. In this model, a flare occurs in the coronal arcade containing a prominence presumably due to the onset of reconnection below the rising arcade. A rapid eruption at the flare onset leads to the stretching of arcade field lines and formation of vertical current sheet above the magnetic inversion line where a production of high energy particles and flare loops via reconnection occurs. This picture has been developed by many people [49–54]. This model predicts such morphological features as an expansion of the flare ribbons/FP distance and growth of a flare loop system.

In the past decade, a special attention was paid to the new observational phenomenon: the contraction of flaring loops on the flare rising phase which is not predicted by the standard model. The usual expansion motion of flaring loops occurs only after the contraction. This loop contraction consists of three different observational factors: converging motion of FPs measured using HXR emission data [2, 4, 15, 55, 56], downward motion of the loop top observed in soft X-rays [3, 6, 7, 57] and shrinkage of the loop length [10, 58]. The phenomenon challenges the standard flare model and triggered a model improvement and development.

MW emission is generated through the GS mechanism by mildly relativistic electrons rotating around magnetic field lines. So it is a good tracer of a flaring loop. In some flares, the whole MW flaring loop is observed. Therefore, in these cases MW observations with high spatial resolution allow us to study the loop length and LT height evolution, FP motion as well as the loop's orientation during the flare process. The combination of both X-rays and MWs is even more powerful for this type of study. Moreover, an opportunity to study a radio brightness distribution along the flaring loop gives an additional information about an acceleration site location in a loop and mildly relativistic electrons' pitch angle distribution [59–61]. Obtained information can be used for the comparison with existing flare models and acceleration mechanisms. In this section (see also paper [62]) we have used this opportunity for the large two-ribbon flare 2005 August 22 well resolved with NoRH and partly observed with RHESSI.

7.3.2 Observations

The intense solar flare occurred 2005 August 22 at 00:54 UT with heliographic coordinates $S12°$, $W49°$. It was one from the serious of flares connected with active region (AR) NOAA 10798 and was accompanied by a high-speed CME. Figure A.18

in Appendix A shows the emission time profiles in soft X-Rays, MWs, and HXRs. GOES fluxes in channels 1–8 Å (thick line) and 0.5–4 Å (thin line) are shown in Fig. A.18a. The flare was M2.6 class on the GOES scale and related to the long duration events. The corresponding MW burst was observed by NoRH [63] at two frequencies 17 and 34 GHz with spatial resolution $10''$ and $5''$, respectively. Figure A.18b shows NoRH time profiles of total fluxes integrated over the partial images, the size of $313'' \times 313''$, which includes the whole AR. They display multiple emission peaks with durations from 3 to 8 min at both frequencies, 17 GHz (thick line) and 34 GHz (thin line). The Ramaty High Energy Solar Spectroscopic Imager (RHESSI) was in the shadow of the Earth until 01:02 UT, therefore, observations of the X-ray burst started only after the main peak on the NoRP time profiles. RHESSI count rate in the channel 25–50 keV is shown in Fig. A.18c.

7.3.3 Morphological Feature of AR10798 at H-Alpha and EUV in Pre-flare Phase

Evolution of AR structure prior to the flare was examined [64] and shown in Fig. A.19 in Appendix A. According to their study, AR NOAA 10798 emerged on 18 August 2005 and rapidly evolved. The arch-filament system seen in the Hα images on 18 August with potential magnetic field connecting the sunspots of opposite polarity (Fig. A.19a). During 18–19 of August the counterclockwise rotating motion of the sunspots pair was seen on magnetograms obtained by SOHO/MDI. We also found clockwise rotation of preceding (positive polarity) sunspot after August 19. This rotation is particularly well seen during August 21. Due to this complex rotation motion, the Hα arch system was abruptly changed on 21 August: clear oblique structure appeared (Fig. A.19b) and then a large filament evolved. The filament lays near the magnetic neutral line between the sunspots. This filament is seen as a bright J-shaped structure on the EUV pre-flare images in Fig. A.20 of Appendix A. The images were obtained about 20 min prior to the MW flare onset with Trace 171 Å, Fig. A.20a and SOHO/EIT 195 Å, Fig. A.20b. The Trace 171 Å spectral line is mainly sensitive to plasmas at a temperature around 1 MK (Fe IX) and SOHO/EIT 195 Å 1.5 MK (Fe XII). This J-shapeD structure consists of two parts: northern and southern ones with no connectivity between them. The high spatial resolution ($\sim 1''$) of Trace images allows to see more details: multiple small loop system at the left of filament's northern part. A superposed 17 GHz Nobeyama loops are shown by white contours on levels 0.04 and 0.1 levels of maximum brightness temperature, T_b^{max}, at the flare onset time, *a*. 00:52 UT and *b*. 00:53 UT. At the latter time $T_b^{max} = 7.4 \times 10^5$ K. The outer contour of loop FPs includes a corresponding part of the filament. RHESSI HXR sources observed at the time of flare 01:03:20 UT are shown by the dotted contour on plot b. Southern HXR source coincides with the lower end of the J-shape structure. This bright EUV filament disappeared after the flare and corresponding CME. There were no Hα and EUV observations during the MW flare period.

7.3.4 Radio, Optical, and X-Ray Images of Flaring Loops

MW flare morphology and its evolution are shown in Fig. A.21 of Appendix A. Images of the source at 17 GHz (Stokes I) and 34 GHz, with black thin contours at levels 0.1, 0.3, 0.5, 0.7, 0.9 of maximum brightness temperature T_b^{max} are presented in the left and in the right columns, respectively. At the first emission peak time 00:56:34 UT, $T_b^{max} = 2.3 \times 10^7$ K at 17 GHz and $T_b^{max} = 3.6 \times 10^6$ K at 34 GHz. On Fig. A.21a the level 0.05 of T_b^{max} is also presented. White dot-dashed lines show visible flaring loop axes. They were drawn using a spline approximation through the brightest points along the loop and used for measuring apparent loop length. In the middle column, SOHO/MDI magnetograms (grayscale) are overlaid by black contours of polarization maps at 17 GHz (Stokes V) at 0.2, 0.4, 0.6, 0.8, 0.95 levels of the minimum brightness temperature T_b^{min}. Only negative brightness temperatures were observed in polarization during the flare with typical values of polarization degree 30%. The magnetogram shows the negative (black color) and the positive (white color) magnetic structures. The white contour line shows the magnetic reversal line. All images are adjusted to the time of magnetogram 00:53:00 UT.

On the rise phase of the flare well-defined round-shaped FP sources of the loop are seen in intensity at both frequencies (Fig. A.21a–m). They correspond to the magnetic field of opposite polarity on the SOHO MDI magnetogram (Fig. A.21g). Magnetic field strength is $B_{min} \approx -1300$ G and $B_{max} \approx +1800$ G in the areas of the southern and northern polarization sources between levels 0.1 and 0.4 of T_b^{min}.

Note, that two FP sources have the same negative sign of circular polarization (Stokes V) at 17 GHz. This is quite unusual. Mostly we see positive Stokes V over the positive polarity of photospheric magnetic field, and negative Stokes V over the negative one. This happens in the case of optically thin GS emission generated in magnetic loop located close to the solar disk center [65]. The polarization reversal in the case of our flaring loop happens for the northern source which is expected to have positive V. A well known simple explanation of the reversal could be the optical thickness of the northern source. However, the spectral slope between 17 and 34 GHz derived from NoRH image data is always negative everywhere in the loop including the northern source. Therefore, the northern source is optically thin and this explanation of the reversal is not valid.

There are two other possible reasons for the polarization reversal, but both of them do not have robust observational basis to be proved. One of them is the mode decoupling for the emission coming from the northern source. This mechanism may work if the LOS is perpendicular to the magnetic field in the northern source. The second reason may be a specific orientation of the flaring loop. The flaring loop under consideration is located far from the solar disk center and turned to the E-W direction. In this case, it may happen that it is oriented such that at its magnetic axes, the magnetic field vector everywhere in the loop has an obtuse angle with the direction of the line of site. Therefore, the sign of polarization should be the same everywhere in the loop as it is observed. Note that this interpretation also suffers from the lack of observational evidence. In fact, it is found by a recent statistics of

NoRH that an identical polarization sign in both two FPs occupies about 80% of selected events [66], which shows that the linear mode coupling happens generally [67], and above two explanations are both related to the linear mode coupling (when the angle between the magnetic field and LOS varies from an acute one to an obtuse one) [68].

Then an almost similar evolution was observed in intensity (Stokes I) at both frequencies, 17 and 34 GHz: the entire loop structure was well seen during the whole of burst, but its orientation, length and size changed with time. We used these images to measure apparent loop length and LT height. In the period between 00:58:50 and 01:01:00 UT, the radio brightness gradually concentrated to the loop top, FPs faded and then reverse process started. About 01:15 UT, a new bright loop appeared at the higher altitude (Fig. A.21e). The top of this new loop is indicated as LT_2. In the same time the lower loop remains to be seen. After 01:23 UT, strong changes in the loop structure occurred, which is not discussed further.

RHESSI HXR maps at energy 25–50 keV are superimposed on plots Fig. A.21p–r by dot-dashed contour at 0.4, 0.6, 0.8, and 0.95 levels of maximum count rates. We use the CLEAN method [69] with natural weighting with grids 3–8 to construct HXR maps. In this way, RHESSI HXR maps have an FWHM spatial resolution of ≈10 arc s. From figures, we can see that the centers of two HXR sources approximately correspond to the 0.1 level of T_b^{max} 34 GHz loop. It should be mentioned that the northern HXR source may not be detected when it becomes weak, while the southern source is always present during the flare. The fainter HXR northern FP (NFP) is in a good agreement with the stronger magnetic field here.

Note, that in several time moments the HXR emission is also detectable over the radio loop apex at levels 0.4–0.5 of peak flux. These over the loop top sources are well seen in Fig. A.22 of Appendix A, which represents SOHO/EIT 195 Å images obtained at 02:32:44 UT, about 1 h after the flare. Images show post-flare arcade visible side. We superimposed 17 GHz loop by white contour lines and RHESSI HXR sources by dotted lines for each temporal emission peak. Only those RHESSI maps were selected which contain the HXR source near the radio loop apex. Analysis of the RHESSI SXR images at energies 6–12 keV showed that soft X-ray loop system is located lower than HXR coronal source at 01:12 and 01:19:40 UT. Moreover, Fig. A.22 shows that the flare was developing along elongated arcade, from its northern part to southern. The radio loop together with HXR sources is following the direction and orientation of the EUV arcade.

7.3.5 Time Profiles

In Fig. A.23a–c of Appendix A we show the flux time profiles from the regions corresponding to different parts of the MW loop. Flux densities are calculated from NoRH images by integration of brightness temperature over areas of the size $25'' \times 25''$, so, that area includes changing location of FPs and LT during the flare process. The time resolution is 2 s. Dashed vertical lines are drawn to divide different emission

peaks which are numbered on the top of plot a. It is interesting that the time profiles from both southern FP (SFP) and northern FP (NFP) consist of six emission peaks while there is only one (first) temporal peak in the LT_1 source which is much smoother. We limited LT_1 flux evolution by 01:15 UT since after that the loop top rises higher and reaches the level LT_2, the northern leg occupies the area of LT_1. Emission in the LT_2 source gradually grows during peaks 4–6.

Surprisingly, SFP is brighter than NFP in MW intensity at both frequencies 17 and 34 GHz during first three peaks and it remains brighter in polarization during all the flare. Taking into account that magnetic field is stronger in NFP, this fact contradicts to the usual concept that the FP with the stronger magnetic field should have stronger radio emission and weaker X-ray emission. We suppose that possible reason for this contradiction is a difference in viewing angles for the two conjugate FP sources, the viewing angle for the SFP source should be higher.

Even we can see time delays between NFP and SFP emission maxima, these delays are caused by kinetic effects inside the big loop. In the same time, we have found good temporal correlation between fluxes from two FPs on the smaller timescale (15 s) variations, which are in phase with peak to peak correspondence. These small-scale peaks rather connected with acceleration process inside each fine magnetic tube which are not resolved with NoRH.

Figure A.23d demonstrates time profiles of HXR emission in energy band 25–50 keV for both NFP and SFP. RHESSI flux is calculated from RHESSI images by integration of counts over areas of the size $33'' \times 33''$ to improve signal-to-noise ratio. The time resolution is 20 s. A comparison of MW and HXR emission profiles shows one to one correspondence of their peaks with the delay of radio emission up to 1 min.

7.3.6 Evolution of Spatial Characteristic Parameters

Figures A.24a and b in Appendix A represent time profiles of the apparent loop length and height, respectively. The loop length is measured along the visible loop axis shown in Fig. A.21 between two foots on the level 0.1 of maximum T_b. This level corresponds to centers of HXR-sources and, therefore, to the level of Sun's chromosphere where the loop ends are anchored. The LT altitude is measured as a distance from the middle of the loop axis and the middle of the span between two FPs as it is shown inreal time profiles shown Fig. A.21f.

It is clear that the brightness redistribution along the loop that occurred during the decay of the first peak and the rise period of the second peak have to influence on the location of 0.1 level of T_b^{max}. This level is rising and descending together with the relocation of the brightness peak. To find out the time period of this influence we modeled the loop and changed the brightness of FPs and LT according to real-time profiles shown on Fig. A.23a. As a result, we found that brightness redistribution affects location of 0.1 level of T_b^{max} between 00:56:30 UT and 01:02:00 UT, in the period when the ratio of fluxes from FP to LT $F_{FP}/F_{LT} < 1$ for both FPs.

Both parameters, the loop length and LT height are decreasing at the rising phase (12% in the length and 8% in the altitude) and increasing during peak 3. During the fifth emission peak, we again observe the radio loop shrinkage in the length (12%) and height (8%) simultaneously with formation of the new loop at higher altitude. The descending loop top is observed for 4 min and it moves down with an average speed 16 km s^{-1} at both periods. About 01:15 UT a new bright loop appeared on the altitude 45 mm, about 10 mm higher than the previous loop. A detailed consideration of MW images show that at the same time several other loops at different height levels with the lengths between 80 and 120 mm exist simultaneously. The average speed of the loop top raising during 3^d to 5^{th} emission peaks is 21 km s^{-1}. The increase in the altitude is 38%, and in the loop length is 28%. In Fig. A.24b of Appendix A we also show by diamonds the altitude of the HXR source observed over the radio loop. It is clearly seen that the HXR source altitude grows faster than the altitude of the MW LT source. Its average speed is 31 km s^{-1}.

The time profiles of the projected distance between two radio FPs (crosses) is given in Fig. A.24c. It is measured between two ends of the loop axis on the level 0.1 of maximum T_b. The evolution of the perpendicular and parallel to the magnetic neutral line (NL) components of the FPs distance is shown in Fig. A.24d and e, respectively. To calculate it we drew the simplified magnetic NL on the photosphere using SOHO MDI magnetogram. The FP distance is decreasing during the rising phase with the speed $v \approx 16$ km s^{-1}. This contraction is caused by the decrease of both components, parallel and perpendicular. Apparent FP distance again falls into contraction after the second peak. But the last contraction is mostly due to unshearing motion.

Figure A.24f represents the evolution of the flare shear angle. The shear angle is defined as angle formed by the line connecting two conjugate FPs and the line perpendicular to the magnetic NL. Therefore, this is analogue of parallel component of FP distance. It was shown by the Ref. [69], that a flare shear is basically consistent with the magnetic shear computed from vector magnetograms and, therefore, is important for evaluating of magnetic non-potentiality of a loop structure: the higher the angle, the larger magnetic non-potentiality. The shear angle decreases from 45° to 25° monotonically in the course of the flare. The evolution of parameters at 34 GHz show the same tendencies. So, we don't present it here.

On Fig. A.24c–f parameters measured with RHESSI at energy 25–50 keV are shown by diamonds. To determine the centroid positions of sources we use the center-of-mass method. Sometimes, there are two HXR sources associated with the northern foot point. We take them as one and use their weighted average position. We can see that polynomial approximation of time dependence for all four parameters obtained from HXRs have the same trends as time profiles obtained from MWs. At the same time, vertical shifts between them are seen. To analyze the reason of these shifts we have measured the time evolution of distances between HXR and MW sources for each FP. We found that the distance for southern FP is systematically larger (3″) relatively to northern FP. This asymmetry gives smaller parallel component of FPs distance and shearing angle and larger perpendicular FPs distance measured from HXRs as compared to MWs.

An important issue here is the measurement accuracy. It is well known from the theory of interferometry (see the Ref. [70]) that the error of the determination of the contour level location or brightness center position is significantly less than the interferometer beam size, which is about $10''$ for 17 GHz. The accuracy increases significantly with the increasing signal-to-noise ratio. Because of NoRH has high sensitivity, 5×10^{-3} sfu in flux density, the signal-to-noise ratio is very high during the flare (not less than 5). In this paper we use detectors 3–7 to reconstruct RHESSI clean maps, in this way RHESSI HXR maps have an FWHM spatial resolution of about $10''$. Even with detectors 3–7 RHESSI can determine source centroid to better than $1''$ on condition that both sources are well defined. However, due to low signal-to-noise ratio, especially for the NFP, we have a significant dispersion of measured parameters. Standard deviation obtained from fitting is 2 mm for distance and $3.7^{(\circ)}$ for shearing angle. The corresponding standard errors for measurements with NoRH are 1 mm and 1.4°.

7.3.7 Trajectories of Flaring Loop Top and Feet

In Fig. A.25 in Appendix A we drew the simplified magnetic NL on the photosphere (white line) and plotted FPs and LT sources positions. Each color corresponds to different temporal emission peaks, which are depicted on the plot. The SOHO MDI magnetogram obtained at 00:50 UT is superimposed by contour lines, red for positive and blue for negative polarities. Contours show magnetic field on levels 150 G, 400 G, 600 G, 800 G for both positive and negative polarities. We can see that the northern FP of the apparent bright loop moves predominantly along the magnetic neutral line in the south-west direction, and the position of the southern FP is almost invariable. On the rising phase, the LT moves from south to north (black diamonds). Then the entire loop was gradually stretching upward. After the fourth peak the simultaneous descending of the most bright loop and formation of a new MW loop at higher altitude were observed.

7.3.8 Discussions

Let us discuss the most interesting findings discovered from observations which are able to help in a reconstruction of the flare scenario.

7.3.8.1 Pre-flare Development

As we have shown above, due to the counterclockwise rotating motion of the sunspots pair and clockwise rotation of leading sunspot prior to the flare the Hα arch system evolved from the state with potential magnetic field to the sheared state with clear

oblique magnetic loop structures. According to Fig. A.21, the overall neutral line has a reverse S shape, which is the other indirect evidence of a sheared magnetic field. In the past, a development of shear before flares was observed in the chromosphere from Hα (see the Ref. [71] and others) and also in the photosphere in magnetograms (see the Ref. [47] and others). It was considered as a signature of a storage of free energy in overlying corona via creation of non-potential magnetic field. Existence of the magnetic shear, therefore, is an important indicator of initiation of a big solar flare.

It is clear from the Fig. A.20 that the flare onset is associated with J-shaped hot structure crossing the NL and seen in EUV. This kind of structures as well as S-shaped or sigmoidal configurations are often observed in SXR and EUV before and at the beginning of large flares/CME (see the Ref. [27] and the subsequent studies). They signify a highly sheared magnetic flux ropes or so-called sheared "core fields" which harbor enhanced coronal heating [72]. In the recent numerical simulation [34], a magnetic flux rope is heated through the slow photospheric bald-patch reconnection during the early formation of the sigmoid. Note here, that for the AR understudy, the Ref. [64] reported a new flux emergence around the magnetic neutral line and filaments formation at about 09:00 UT on August, 21. An eruption of sigmoidal, S-shaped or J-shaped structures is believed to play an important role in large flare/CME events. This eruption may be initiated by some kind of instability (kink, torus) or by reconnection between two flux ropes [34, 72, 73].

7.3.8.2 Unshearing Motion of Flare Loops

The motions of loops from a strongly sheared to a less sheared structure are often observed in Hα, HXR and EUV [4, 15, 74–77]. In this paper, such kind of unshearing motion is found for the first time also from MW observations. Indeed, as we reported in Sect. 7.3.7, during the flare process the shear angle of the loop steadily decreases. In the flare under study this reduction is due to the northern FP motion along the magnetic neutral line from the northern part to the southern part of the arcade. Therefore, reduction of flare shear has to be considered as an important component for the flare scenario/model.

7.3.8.3 Propagation of Flaring Process Along an Arcade of Loops

It is interesting that though we observe one single MW loop during almost all the flare process, the tracing of the loop's FPs and LT motion in this flare show that the energy release and acceleration of electrons up to relativistic energies occur in sequence along the extensive arcade of loops. This arcade is well seen on Hα images prior to the flare and on EUV images after the flare. The bright well visible radio loop as well as HXR FPs of the loop follow the direction and orientation of the EUV arcade, from its northern part to the southern. It means that successive emission peaks on the time profile occur in different parts of the arcade, not in the same magnetic loop.

Particles are accelerated in a sequence of magnetic field lines along the arcade, and not in a single loop. Simultaneous existence of several loop tops at different height levels at 01:15 UT (see Figs. A.21e and A.24a, b) indicates that at least several loops become involved into the process.

7.3.8.4 Shrinkage and Stretching of the Flaring Loop

We have found the loop length contraction and LT descending motion with a speed $v \approx 16\,\mathrm{km\,s^{-1}}$ during the first peak of the MW burst (see Fig. A.24a, b). On the second stage, after the first peak, since 01:02 UT the entire loop was gradually stretching upward with an average speed $v \approx 21\,\mathrm{km\,s^{-1}}$. After the fourth peak the simultaneous descending of the most bright loop and formation of a new MW loop at a higher altitude were observed. A similar behavior was found for the multicomponent time profile flare of 2002 August 24 observed with NoRH, and it was supposed that the expansion of the observed MW loop is caused by a chromospheric evaporation induced by the intense energy injection during the first burst peak [10]. In the case of the flare 2005 August 22 we would not say that the expansion (stretching up) of the MW loop is due to the high pressure caused by such an evaporation. We rather explain it by the appearance of new tiny flaring loops at higher and higher levels in the corona. This interpretation is clearly confirmed by the existence of several emission peaks (caused by several repeated injections) and by the observed changes of the loop FP locations (Fig. A.25).

The descending motion of the coronal source is typical for the initial phase of many other flares [3, 4, 6, 7, 10, 14, 15, 57, 58, 77]. The derived shrinkage velocity of the radio loops agrees with the result of observations of loop tops in HXR emission [6, 7, 77]: 8–45 $\mathrm{km\,s^{-1}}$ and in EUV observations [57, 58]: 15 $\mathrm{km\,s^{-1}}$. The shrinkage of the loop length in the case of 2005 August 22 flare is accompanied by converging motion of FPs both on the rising phase (first peak) and during the fifth peak. These two temporally associated phenomena were found in some other events [4, 15, 77].

There are several theoretical models that try to explain the considered two stages in the spatial development of flares. Most of them propose very similar explanation for the second (expansion) stage of eruptive flares. The general idea is that during this stage a reconnection is going in a way similar to the reconnection in the standard model of large eruptive flares: new reconnected field lines appear higher and higher along a vertical current sheet. This process is followed by a gradual increase of the height of new flaring loops and increase of their FPs separation transverse to the magnetic neutral line (NL). The models by Somov [78] and Bogachev et al. [1] generalized this consideration taking into account the relaxation of sheared magnetic field near the NL. This allowed them to explain not only the transverse FP's separation, but also a directed (unshearing) movement of FPs along the NL.

Our observation well agree with both above predictions. In the event under study the separation motion is found to occur during the second - third emission peaks, the separation reaches $\approx 2\,\mathrm{mm}$ (Fig. A.24d). Since the loop is located far from the central meridian (heliographic coordinates $S12°$, $W49°$), projection effects there

forbid precise measurements of distances along the view angle, i.e., perpendicular to the NL component of the FP distance. However, we can confidently measure the FPs separation component parallel to the magnetic neutral line.

The dynamic shrinkage has various explanations. Within the magnetic reconnection process in solar flares, it is expected that newly reconnected field lines relax by "shrinking" down to form a system of closed loops [13, 79–81]. In the numerical simulation of magnetic reconnection with heat conduction [82–84], the downward jet collides with the line-tied magnetic loops, and a termination shock appears at the loop top. The height of the bright loop decreases rapidly at the beginning until the loop top reaches its minimum height. Thereafter it rises almost uniformly with time with its two FPs separation. Depending on the model parameters, the loop top height may show temporal variations, that is sometimes it drops down against a rising background [84].

The Ref. [14] gives an interpretation of the LT altitude decrease in the frame of a collapsing magnetic trap model [85, 86] embedded in a standard 2D reconnection flare model. The Ref. [5] suggested that the observed altitude decrease of the LT source might be also related to the change from slow X-point to fast Petscheck-type reconnection which would not only increase the energy release rate but also push the lower bound of the current sheet downward. However, this scenarios cannot explain converging motion of FPs. As well in 2D models the observed propagation of flaring process along an arcade and unshearing motion are not possible to explain.

The explanation of the FPs converging simultaneously with the descending and unshearing motion of flaring loops is possible in the frame of three-dimensional models. In the "rainbow reconnection model" [78] these phenomena is a consequence of three-dimensional magnetic reconnection at a separator in the corona. The separator is located above the photospheric neutral line like a rainbow above a river. During the first stage of the flare, the reconnection releases an excess of magnetic energy related to the magnetic tensions generated before a flare by the shear flows in the photosphere. The collapsing magnetic trap formed in a downflow after the reconnection at the separator explains the descending motion of the LT source. During the second phase, the ordinary reconnection process dominates describing the energy release in terms of the standard model of large eruptive flares with increasing FP separation and upward motion of the LT source. The observed propagation of flaring process along an arcade also can be understood in this unshearing process [1].

Note that the above model does not take into account a possible role of the activation of the J- or S-shaped filament located close to the NL. However, such a filament and a corresponding CME are important properties of the flare 2005 August 22 as well as of other powerful eruptive flares. According to SOHO/LASCO CME on line catalog, an halo-type CME was first observed at 01:31 UT on the height $h = 3.92\ R_{SUN}$ with Large Angle Spectrometric Coronograph (LASCO) aboard SOHO. Extrapolation shows that it started from 1 R_{SUN} between 01:02–01:05 UT, that is just after the first temporal peak. This is a strong evidence of the eruption of the filament observed in the pre-flare period.

Recently, many authors exploit the idea that different kinds of instabilities or loss of equilibrium can produce a dense plasma eruption and accompanying flare

process [34, 72, 73, 87, 88]. An explanation of the first (shrinkage) and second (expansion) stages based on the idea of the erupting flux rope, is considered in the Ref. [5]. They assume that magnetic field lines in the arcade are distributed in such a way that the magnetic field that is close to the NL has a significant shear, and field lines are less sheared at longer distances from the NL. A flare is triggered by the magnetic reconnection in the middle of the sigmoid that produces a single long unstable twisted loop (flux rope) which moves upward. It first meets inner field lines with significant shear and then the outer magnetic field lines which are little sheared. Based on magnetic explosion conjecture [15], it is showed that the release of magnetic energy will reduce magnetic shear and that the less sheared arcade will have smaller height and span [15]. The moving upward flux rope stretches the overlying magnetic field to form a vertical current sheet. In the second stage, the magnetic reconnection occurs in the current sheet at increasing altitude, producing two separating FPs/flare ribbons. We consider that this scenario is the most satisfying to our observations including pre-flare and second stages.

7.3.8.5 Two Stages in the Development of MW Emission

Two different stages can be clearly distinguished from the flux time profiles (Fig. A.23) in the development of MW emission. The first stage corresponds to the first temporal peak on the MW time profiles. This peak is well pronounced in emission at 17 and 34 GHz from both FPs and from the loop top. The second stage corresponds to the period of 2nd to 6th peaks. On this stage, the temporal behaviors of the emission from the two FP regions and the LT region are completely different. Temporal peaks 2–6 are well pronounced in emission from the FP regions, their intensities are comparable with the intensity of peak 1. At the same time, the loop top source emission is much weaker than during peak 1, looks very gradual and does not show any emission peaks, except gradual increase during the sixth peak in the LT_2 source.

Both GS and free–free emission can contribute to the 17 and 34 GHz radio emission. However, our estimates show that GS is much more efficient for this flare. To evaluate the contribution of the free–free radiation to the total flux we calculated the flux density of thermal radio emission from the whole of radio loop using plasma temperature and Emission Measure obtained from GOES data. The evaluation shows that it is less than 1% at the first peak time and only 4% at 01:23 UT. Therefore, contribution of the free–free radiation is very small. As well, the flare frequency spectra reconstructed with NoRP data show a typical GS shape with the peak frequency $f_{peak} \leq 10$ GHz and negative slope over f_{peak} during the flare period. A calculation of the power law spectral index α using flux densities at 17 and 34 GHz shown in Fig. A.23a and c indicate that this is true for all parts of the loop: $\alpha = -3$ on the rise phase and then grows to $\alpha = -1$ in the average for both FPs and loop top. In the case of optically thin free–free emission, one would expect flat spectrum with $\alpha \approx 0$.

Model simulations with making use of the non-stationary Fokker–Planck equation and calculation of GS emission [59, 61, 89] show that absence of secondary emission peaks in the loop top is possible in the case of anisotropic injection of accelerated

electrons into the loop predominantly along magnetic field lines. In this case, injected electrons pass quickly through the loop apex generating emission of very small intensity and then are reflected close to the ends of magnetic trap where they generate emission of much higher intensity due to the stronger magnetic field and high pitch-angles. The observed picture can happen if the acceleration process occurs in a wide range of pitch-angles on the first stage and then changes to the beam-like acceleration along the loop axes on the second stage of the flare.

We consider that the abovementioned MW emission properties on the second stage of the flare can be explained in the frame of electron acceleration model in collapsing magnetic field [1, 78]. The collapsing magnetic trap is a system of contracting magnetic field lines and the flowing plasma in the cusp magnetic field below the current sheet and above the relatively dense soft X-ray flare loop with a quasi-stationary magnetic field. The Refs. [1, 78] have shown that the contracting local trap exists during 1–10 s and can serve as an efficient electron accelerator to relativistic energies via the first-order Fermi and betatron acceleration mechanisms.

The betatron electric field always increases the momentum perpendicular to the magnetic field. Therefore, it contradicts to our conclusion about anisotropic injection of high energy electrons along magnetic field lines on the second stage. The first-order Fermi acceleration gives an increase in the longitudinal particle momentum with decreasing separation between the magnetic mirrors of the local trap. Even if the initial particle distribution is isotropic, under the action of the Fermi acceleration the electron pitch angles decrease and the pitch-angle distribution is elongated along the large trap axis, which is in agreement with our conclusion. On the second stage of the flare, the Fermi acceleration may become more efficient than the betatron one due to, for example, a higher location of the current sheet over the flaring arcade (in other words, due to a longer local trap) and, therefore, result in a more beamed injection along the loop axes.

7.3.8.6 Relative Positions of HXR Coronal Source and MW Loop Apex

It is interesting that HXR coronal sources seen on several images (Fig. A.22) are located higher than MW loop apex and show faster upward motion. The sources above the SXR LT are usually called as Masuda sources. They are found in flares during the impulsive peak and were interpreted as evidence of magnetic reconnection above the SXR flaring loop [74]. However, in Masuda flares as well as in cases reported later (e.g., the Ref. [14]) the HXR LT source at higher photon energies is located at higher altitudes. According to the standard model, the reconnection progressively occurs at higher and higher altitude and, therefore, lower energy electrons are expected to situate at lower altitude where reconnection process has occurred earlier. In the event under study, we observe opposite situation: the MW loop whose emission is generated by electrons of hundreds keV is located lower than 25–50 keV HXR coronal source.

We consider that this situation again can be understood in the frame of the collapsing magnetic trap model. A large number of low energy (tens of keV) electrons produced in the reconnection region and trapped locally in the collapsing field lines

above the quasi-stationary magnetic loop can survive there for a fraction of second and generate the above the loop HXR-source. It is clear that at the same time a fraction of accelerated relativistic electrons can survive on the contracting field line of the large trap (flaring loop) for much longer time than the lifetime of the local trap. They should generate microwave GS emission even when the contracting line reaches its minimum height.

7.3.9 Conclusions

We have studied the spatial dynamics of the flaring loop in the large flare/CME event 2005 August 22. It has been found that the pre-flare morphology of the AR exhibits a strongly sheared arcade seen in Hα and accompanied with the J-shaped filament bright in EUV. Two parts of the bright EUV filament spatially coincide with two 17 GHz FP sources at the time of the flare onset. During the whole burst, the entire loop structure was well seen at 17 and 34 GHz, but the loop's orientation, length and size were changing with time. RHESSI observations showed two FP sources at 25–50 keV, as well as coronal sources which were appeared sometimes over the radio loop apex.

The tracing of FPs and LT motion shows that energy release and high energy electron acceleration occur in sequence along the extensive arcade that is well seen on Hα images prior to the flare and on EUV images after the flare. The motion of magnetic loops goes from the highly sheared to the less sheared state. The northern FP of the apparent bright loop moves along the magnetic neutral line, and the position of southern FP is almost invariable so that the shear angle of the loop steadily decreases during the flare process.

We have found the loop length contraction and LT descending during the first emission peak accompanied by converging motion of FPs on the rising phase. Then the entire loop was gradually stretching upward. After the fourth peak, the simultaneous descending of the most bright loop and formation of a new MW loop at higher altitude were observed. The analysis of HXRs has shown a good correlation with results obtained from MWs for the period of RHESSI observations.

We didn't find one single flare model which could explain all observational findings. We consider the flare scenario similar to the proposed by the Ref. [47] and reported by the Ref. [5]. The flare might be triggered by the activation of the J-shaped flux rope and its interaction with the highly sheared arcade. The moving upward flux rope stretches the overlying magnetic field to form a vertical current sheet. In the second stage, the magnetic reconnection occurs in the current sheet at increasing altitude, producing rising LT and stretching loop length. Additional evidence for such scenario is SOHO/LASCO observations, which give extrapolated rising start time of the filament just after the first temporal peak.

The revealed properties of time profiles of MW emission confirm the existence of two stages in the development of the flare. On the first stage, which corresponds to the first temporal peak on MW time profiles, the emission peaks are present

simultaneously in the LT and FP regions at both frequencies, 17 and 34 GHz. On the second stage, after the first emission peak, repeated emission peaks are present only in the FP regions. We conclude that these two different stages are connected with differences in the acceleration process: on the first stage, an injection of high energy particles occurs in a wide range of pitch-angles while on the second stage it changes to the beam-like acceleration along the loop axes and takes place over the flaring arcade. This situation can be explained in the frame of collapsing magnetic trap [1, 78], in which Fermi acceleration may become more efficient on the second stage of the flare. Note that the collapsing trap model is also able to explain the found relative displacement of the MW loop and HXR coronal source, the latter being above the first.

7.4 Quasi-periodic Pulsations (QPPs) in Microwave Band

As it was already mentioned in the book's Introduction chapter, the discovery of spatially resolved MHD wave and oscillatory activity of the corona is one of the most remarkable achievements of solar physics in the last decade. Now there are abundant evidences of MHD waves of various kinds in the corona. Several theoretically predicted wave modes (transverse kink and sausage, and longitudinal) have been identified in the imaging and spectral data with high temporal and spatial resolution in the visible light, EUV, soft X-ray, and microwave bands [90].

The periods of QPPs can be split into several bands, from sub-seconds up to tens of minutes. Short-QPPs (sub-second) in the m-dm-cm radio emission are likely to be associated with kinetic processes caused by the dynamic interaction of electromagnetic, plasma or whistler waves with energetic particles trapped in closed magnetic fields during solar radio bursts. Long-QPPs, with periods from several to tens of minutes, are usually associated with active region dynamics and global oscillations of the Sun. Medium period- QPPs (seconds to several minutes) detected in microwave, white light, EUV and X-ray emissions are likely to be associated with magnetohydrodynamic (MHD) processes in solar flaring loops. Recently, they have attracted strong attention because of the newly opened possibility of observing such QPPs directly using instruments with high spatial resolution. In particular, the Nobeyama Radioheliograph (NoRH) has sufficiently high angular (5″) and (10″) at 34 and 17 GHz, respectively and temporal (100 ms) resolutions, allowing the determination of the spatial structure of the pulsating regions, their phase relations and the fine temporal and spectral structure of the QPPs. Also, medium QPPs are interesting due to their possible association with the fundamental physical processes operating in flares: spontaneous and triggered energy releases, magnetic reconnection, thermodynamics, MHD oscillations, particle acceleration and other kinetic effects (see review [90]).

7.4.1 Types of QPPs in Microwave Band

In this book section, we concentrate our attention on the medium-QPPs, following the results of paper [91].

7.4.1.1 Observations and Data Reduction

Our selection criteria for the analysis of flaring sources are as follows. The microwave source should: (i) be well resolved by NoRH, that is, its length should be larger than the beam size at 17 GHz; (ii) have a single loop shape; (iii) be located near the solar disk center, or have relatively small intensity if located near the limb, reducing the influence of positional ambiguity in the image synthesis. Specific features of the radio emission time profiles, i.e., the visible presence or absence of QPPs, are not accounted for in the selection. In other words, events without a pronounced QPP pattern are not excluded from our consideration. As a result, we have chosen 12 single flaring loops observed in the period 2002–2005. The evolution of the selected events is analyzed with two independent instruments, NoRP and NoRH. This gives us the opportunity to exclude spectral components of instrumental origin.

There is an extensive literature on methods of detection of QPPs and identification of oscillatory components of solar emissions [91–95]. In the current study, we use several of them. Our procedure for a spectral analysis of signals is as follows. The flux density time profiles of the events, $F_f(t)$, are smoothed over an interval τ that is usually greater than the expected period of the QPP. This gives us the slowly varying component $F_f^{sm}(t)$. The high-frequency component is obtained by subtraction of the slowly varying component from the original time series,

$$F_f^{hf}(t) = F_f(t) - F_f^{sm}(t) \; . \tag{7.4.1}$$

Then, we obtain the modulation signal,

$$\Delta_f(t) = F_f^{hf}(t)/F_f^{sm}(t) \; . \tag{7.4.2}$$

This was done for a broad range of smoothing intervals: $\tau = 5$, 7, 10, 13, 15, 20, 25, 30, and 40 s, allowing us to understand whether the spectral peak found is real or produced by the smoothing (filtering) procedure. The suitability of this method for determining the reliability of the spectral components was verified by numerical simulations. For this we used the model function

$$f_1(t_i) = f_b(t_i)[1 + f_s(t_i)] + f_n(t_i) \; . \tag{7.4.3}$$

where t_i is the time of the measurement in seconds, $t_i = i$, where $i = 1, 2, 3, \ldots$, N s; $f_b(t_i) = \sin(2\pi t_i/P_b)$ is a function defining the slowly varying background, with period $P_b = 3N$; $f_s(t_i) = \sum_{j=0}^{m} \tilde{A}_{sj} \sin(2\pi t_i/\tilde{P}_j)$ is a periodic component

(signal) defined as the sum of m harmonic functions with different periods $\tilde{P}_j$ and amplitudes $\tilde{A}_{sj}$, $j = 0, \ldots, m$. The noise component $f_n(t_i)$ is defined as a numerical series of normally distributed random values with a mean value of zero and a standard deviation A_n which is either equal to the signal amplitude ($A_s/A_n = 1$) or twice larger than it ($A_s/A_n = 0.5$).

Our data analysis method was tested for different signal and noise functions given by Eq. (7.4.3). We varied the number of periodic components, and their periods, amplitudes, and SNR ratio. For each fixed set of these parameters, a noise function was tried 100 times in order to calculate deviations of values of a period estimated by our method from that obtained by Eq. (7.4.3). We have found that despite the appearance of some spectral peaks caused by the noise function $f_n(t_i)$, the periodic component $f_s(t_i)$ is well distinguished in all cases. Moreover, errors in the period estimations are relatively small.

For the preliminary spectral analysis, the time profiles $\Delta_f(t)$ were studied using wavelet (Morlet) analysis, in particular, the routines developed by Torrence and Compo [94]. Wavelet spectra give us the general spectral-time evolution of the analyzed signal, and allow us to identify the candidate spectral-time intervals which may contain QPPs. Then, the candidate intervals are studied using autocorrelation, cross-correlation and Fourier methods, with the aim of determining the characteristic periods and their evolution, and the duration of phase conservation in the oscillations.

For the final analysis and classification, we have chosen only those oscillatory patterns which satisfy the following criteria. First, the oscillations should be well pronounced in the data from both instruments (NoRH and NoRP) and have similar frequency–time behavior of the wavelet spectra. Second, they should be seen in periodograms of auto-correlation and cross-correlation functions at 17 and 34 GHz. Third, the value of their period should not depend upon the selected low-frequency filter (the specific value of τ), at least inside the corresponding error bar. Fourth, their quality $Q = \pi N$ should exceed nine (that is, the number N of observed periods should be at least three).

7.4.1.2 Results of Data Analysis

The properties of the QPPs found in this study are rather different. According to the time evolution, we divide the QPPs into four types: (i) those with stable mean periods in the range 5–20 s (eight events); (ii) those with spectral drift to shorter periods in the rise phase of the burst (two events); (iii) those with drift to longer periods in the decay phase (two events); (iv) those with an X-shaped drift between periods of 20–40 s (one event).

The events illustrating each of these types are described in the following subsections and are shown in Figs. A.26–29 of Appendix A. For each event, the color panel demonstrates the wavelet power spectrum of the modulation signal $\Delta_f(t)$ for the NoRH data at 17 GHz. Six colors correspond to six power levels ranging from zero to the maximum value. Thin solid contours show 95% significance level, estimated

according to the Ref. [96]. For better visualization, the normalized time profile of the radio emission intensity $F_f(t)$ is superimposed onto the wavelet spectrum by the thick solid line. Cross-hatched regions on either end of the wavelet spectra indicate the cone of influence. The small panel on the right of the wavelet spectrum represents the global wavelet power spectrum of the modulation signal. The dashed line on this plot defines the 95% significance level. Each figure also shows the auto-correlation function of the modulation signal $\Delta_f(t)$ at 17 GHz and a set of periodograms (in units of spectral power normalized to the total variance), which correspond to different smoothing intervals τ. The dashed line in the panel with periodogram plots shows the 99% significance level estimated according to Horne and Baliunas [97].

Pulsations with a Stable Mean Period

In our analysis, we consider a QPP as having a stable mean period P if the drift rate is $dP/dt < 3\,\mathrm{s\,min^{-1}}$. Figure A.26 shows a typical example of a QPP of the first type. A single spectral component with a stable period $P \approx 8$–$9\,\mathrm{s}$ dominates in the wavelet power spectrum, especially during the rise phase of the flare (Fig. A.26a). The QPPs become fainter during the maximum phase of the flare and regain the strength in the decay phase of the flare, while not reaching the power level they have in the rise phase. The period of the pulsations stays stable over 100 s, reaching a quality $Q \approx 35$. The autocorrelation function of the QPP (Fig. A.26b) has a very pronounced oscillatory pattern over the time interval that includes several cycles. Hence, the pulsations keep the phase during a sufficiently long time. The periodogram of the autocorrelation function has an obvious peak at 8–9 s, which is consistent with the wavelet analysis. Reliability of the spectral peak is proved by coincidence of its position for periodograms taken for different smoothing times: $\tau = 10\,\mathrm{s}$ (black line), 15 s (red line), 20 s (orange line), 25 s (green line), and 30 s (blue line). Sometimes two different non-overlapping periodicities occur in this type of QPPs [90].

Pulsations with Spectral Drift to Shorter Periods

The flare on 31 May 2002 illustrates the second type of pulsations (Fig. A.27). Figure A.27a and b show the wavelet spectra of the modulation signals obtained with NoRH and NoRP at 17 GHz, respectively. The spectra contain a pronounced component with a positive frequency drift during the rise and maximum phases of the flare. Five cycles of QPP are observed in a time interval of about one minute. The period of the pulsations decreases from $P \approx 17\,\mathrm{s}$ in the rise phase to $P \approx 9\,\mathrm{s}$ in the maximum, with a mean drift rate $dP/dt \approx -14\,\mathrm{s\,min^{-1}}$. The spectral analysis reveals two periods corresponding to the final and start values of the drifting component (Fig. A.27d). The first (left) peak on the periodogram at $P \approx 9\,\mathrm{s}$ is narrow. The second (right) one looks wider. Note that the next lower frequency component is an artefact, it appears due to the main flux peak.

Pulsations with Spectral Drift to Longer Periods

The variation of the microwave emission of the flare on 03 July 2002 has an interesting spectral behavior. According to Fig. A.28a, the MW burst consists of three peaks. The first one occurs from 02:10:20 to 02:11:00 UT (40–80 s), the second one

from 02:11:00 to 02:13:00 UT (80–240 s) and a subsequent smooth weak peak from 02:13:00 to 02:16:00 UT (240–420 s). Note that the source of all peaks is the same single flaring loop. Two types of pulsations are seen in the wavelet power spectrum. The first and the second peaks contain stable period QPPs (e.g., with a period of about 15 s and a quality $Q \approx 12$ during the decay of the first impulsive peak, see Fig. A.28a). This part of the burst, shown by the two vertical dashed lines in Fig. A.28a, is zoomed in Fig. A.28b for a more detailed view. These QPPs belong to the pulsations of the first type, discussed above and illustrated in Fig. A.26.

In the decay phase of the flare, shown in Fig. A.28a from the dotted line to the end, there is clear evidence of a QPP with a negative frequency drift (see Fig. A.28c). The period of this QPP increases from 22 to 30 s in four to five cycles with a mean drift rate $dP/dt \approx 11\,\mathrm{s\,min^{-1}}$. The periodogram of the auto-correlation function of this QPP has two peaks, similar to the previous example (Fig. A.27d). Their values correspond to the starting and final values of the drifting component (Fig. A.28d).

Pulsations with an X-shaped Drift

The flare on 21 May 2004 (see Fig. A.29) has a peculiar QPP, which we refer to as the fourth type. Wavelet power spectra of this event show X-shaped structures drifting between the periods of 20 and 40 s (Fig. A.29a, b). Two drifting spectral branches start at the beginning of the rise phase; initially, they have different periods, of about 40 and 25 s. With time, the periods converge with a drift rate $|dP/dt| \approx 10\,\mathrm{s\,min^{-1}}$. In about 100 s, the branches merge into one with a period of about 30 s and then bifurcate again with a mean drift rate $|dP/dt| \geq 10\,\mathrm{s\,min^{-1}}$. Both branches last for about 180 s and fade away at the flare maximum. Similar wavelet spectral signatures are present in both NoRH and NoRP signals. To illustrate the reliability of the observed QPPs, here we also show results of our spectral analysis of the signal at 34 GHz. As we can see in Fig. A29c and d, periodograms of the auto-correlation functions of the pulsations at 17 and 34 GHz both have two well-pronounced spectral peaks at periods of about 38 and 26 s. The ratio of the periods is 0.68, indicating that these periodicities are not simple harmonics caused by a temporal nonlinearity of the signal (which would give a period ratio of 0.5). Moreover, as is evident in the wavelet spectra, the ratio changes with time from 0.68 up to one and then comes down to the initial value.

7.4.1.3 Discussion and Conclusions

In this section, we have studied the temporal evolution of MW QPPs from a set of twelve flares, observed simultaneously with both NoRH and NoRP. The MW sources of all the analyzed flares have a well-resolved single loop shape. The signals were detrended and analyzed using the wavelet, correlation and periodogram techniques. All the flares were processed in a similar way, resembling the approach proposed in De Moortel and McAteer [98]. The main result of our study is the clear evidence that the presence of an oscillatory component in flaring light curves is a widespread phenomenon, independent of the event selection criterion. This result indicates that

oscillations are an intrinsic feature of flaring energy release. Thus, our understanding of solar flares cannot be complete without revealing the physical mechanisms responsible for the generation of the periodicity.

The ranges of the detected periods coincide with the expected transverse and longitudinal fast magnetoacoustic and Alfvén transit times (for Alfvén speeds in the range of several hundreds to a few thousands km s^{-1}). This suggests that the QPPs are likely to be associated with MHD oscillations in either the flaring loops or in their nearest neighborhood. Periods P of standing fast magnetoacoustic and Alfén modes are linked with the length L of the oscillating structure as

$$P \approx \frac{2L}{C_{ph}n}\ , \tag{7.4.4}$$

where n is an integer corresponding to the number of the longitudinal harmonics and C_{ph} is the phase speed of the mode. The value of C_{ph} is in the range from the Alfvén speed inside the structure, C_{Ai}, to the external Alfvén speed, C_{Ae}. In particular, for the torsional mode we get $C_{ph} = C_{Ai}$, for the long-wavelength sausage mode $C_{ph} \approx C_{Ae}$ and for ballooning modes $C_ph \approx \sqrt{2}C_{Ai}$ (e.g., see the Ref. [90]). Also, the simultaneous presence of two or more periodicities in the data (multi-periodicity) found in this study supports the interpretation of the QPPs in terms of MHD oscillations. Indeed, different periods and their ratios can be easily obtained from Eq. (7.4.4) if there are several different MHD modes, with different mode numbers n and phase speeds C_{ph}, excited simultaneously in the same flaring loop. On the other hand, it does not seem to be simple to explain the multi-periodicity in terms of repetitive reconnection [99]. In the LCR-circuit model the multi-periodicity could be obtained in the case of several interacting flaring loops, which is not consistent with our observations.

Moreover, the detected period modulation or drift can also be easily explained with the use of Eq. (7.4.4). Indeed, the variation of the loop length, the magnetic field strength and of the plasma density caused by the evolution of the flaring structure and its neighborhood, in response to the energy release, modifies the period of MHD oscillations. Thus, we conclude that the most likely interpretation of the periodicities detected in our study is connected with MHD oscillations.

7.4.2 Theoretical Explanations of QPPs

7.4.2.1 Global Sausage Mode [99]

The analyzed flare occurred on the January 12, 2000, at the eastern limb (N13E80) and was observed with both NoRH and NoRP. Also, the flare was detected with SXT, HXT, and WBS instruments onboard Yohkoh. The pulsations are observed to be synchronous at both the frequencies analyzed. Moreover, it is worth to note that the MW pulsations coincide in time with the quasi-periodic pulses detected at the HXR

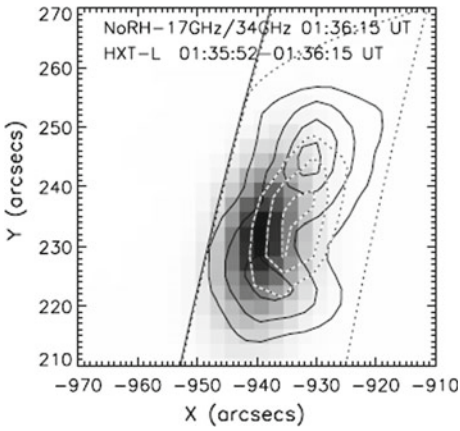

Fig. 7.4 Radio images made at the flare maximum at 01:36:15 UT at 34 GHz (filled pixels) and 17 GHz (dotted contour curves, the contour levels are 0.7, 0.85, and 0.98 of the maximum brightness temperature T_{B17}). The black contour shows the positioning of the HXR sources, obtained in the channel L (13.9–22.7 keV) of Yohkoh/HXT. The HXR signal had been integrated over the time interval 01:35:52–01:36:15 UT, the contours correspond to the levels 0.2, 0.4, 0.6, and 0.9 of the maximum value

time profiles in the 25–85 and 85–826 keV channels of Yohkoh/WBS. Similar to the MW emission (see Figs. 3–4 of Ref. [100]), the Fourier spectra of the HXR total flux oscillations show the presence of two well pronounced spectral components: with the periods 15–17 and 8–9 s in the 25–85 keV channel and with the periods 13–15 and 6–9 s in the 85–826 keV channel.

Figure 7.4 shows the radio images taken at the flare maximum at 01:36:15 UT at 34 GHz (filled pixels) and 17 GHz (the dotted contour curves), the contour levels are 0.7, 0.85, and 0.98 of the maximum brightness temperature T_{B17}. The brightness temperatures reached values 5.7×10^7 K at 17 GHz and 3.7×10^7 K at 34 GHz. The black contours show the positioning of the elongated HXR source, obtained in the channel L (13.9–22.7 keV) of Yohkoh/HXT, and correspond to the levels 0.2, 0.4, 0.6, and 0.9 of the maximum value. The HXR signal had been integrated over the time interval 01:35:52–01:36:15 UT. The source's double peak structure shows the places of strong electron precipitation.

As the flaring loop observed was well resolved with NoRH, it made possible to study the properties of the radio pulsations at different parts of the loop. To improve the SNR, the signal was integrated over a 10"×10" box. Then, for each box, we calculated the flux density $F(t)$, integrating the values of the radio brightness T_B over the box in an NoRH image. In addition, the relative variations of the flux $\Delta F/F$ were calculated for each box. Such an analysis revealed that the pulsations were present in the loop wherever we placed the box. Similarly to the integrated flux, the pulsations observed at 17 and 34 GHz are synchronous with each other. And, most interestingly, they are correlated at any part of the loop. The time profiles $\Delta F/F$ measured at 17 GHz are shown in Fig. 7.5, for the Southern (panel a) and Northern

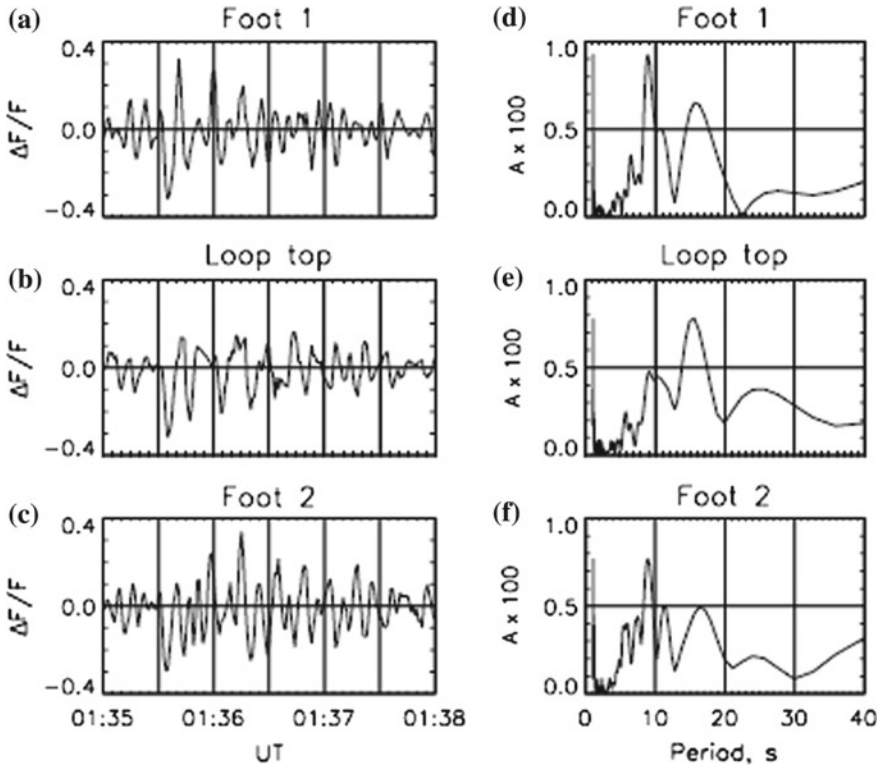

Fig. 7.5 The time profiles $\Delta F/F$ measured at 17 GHz for the three different regions of the size 10"×10": the Southern (panel **a**) and Northern **c** legs of the loop, and the loop apex **b** determined as the center of the radio source detected at 34 GHz. The Fourier spectra of these time profiles are shown in plots **d**–**f**, respectively. The spectra show that there are both the 8–11 and 14–17 s spectral components everywhere in the loop, the shorter period component dominates at the legs **d** and **f**, while the longer period component – at the apex **e**

(c) legs of the loop near the FPs, and for the loop apex (panel b). The loop apex was determined as the center of the radio source detected at 34 GHz, and the positions of the FPs—as HXR brightness maxima. The Fourier spectra of those time profiles are shown in Fig. 7.5d–f, respectively. The pulsations at the loop legs are observed to be well correlated with each other. However, the pulsations observed at the legs do not correlate very well with the pulsations recorded near the apex. Indeed, if some peaks at the leg and apex time profiles coincide with each other, there are certainly more peaks at the leg time profiles than at the apex. The Fourier analysis demonstrates that despite there being both the 8–11 and 14–17 s spectral components everywhere in the loop, the shorter period component dominates at the legs (Fig. 7.5d and f), while the longer period component–at the apex (Fig. 7.5e). The last result coincides with the result of the Fourier analysis of the correlation curves (see Figs. 3 and 4 in the Ref. [100]). This is connected with the fact that the contribution of the apex signal

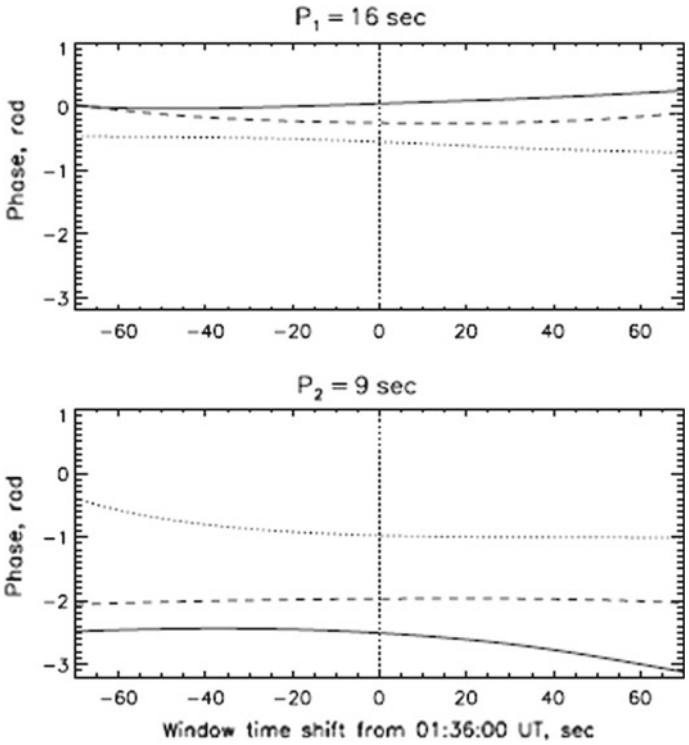

Fig. 7.6 The phase evolution near the burst maximum at 01:36:00 UT for the two spectral peaks of oscillations: $P_1 = 16\,\mathrm{s}$ and $P_2 = 9\,\mathrm{s}$. The phase of oscillations for the loop top source is shown by the solid line, and for the northern (Foot 2) and southern (Foot 1) leg sources by the dotted and dashed lines, respectively. The phase shift between oscillations from the loop top and foot sources is well pronounced for the P_2 spectral component and is very small for the P_1 component

to the correlation flux is strongest, as the apex is seen to be the brightest part of the loop.

A search for a phase shift between oscillations in different parts of coronal loops is very important for selection between different MHD modes and their harmonics. In Fig. 7.6 we compare phases of oscillations for the peak periods of the two spectral components, $P_1 = 16\,\mathrm{s}$ and $P_2 = 9\,\mathrm{s}$. The phases in the interval $\pm 70\,\mathrm{s}$ around the burst maximum 01:36:00 UT were calculated using imaginary and real parts of the Fast Fourier Transform of the oscillating signal in the running window of the Gaussian shape

$$g(t,\ t_0) = \exp[-(t - t_0)^2/\tau^2]\,, \tag{7.4.5}$$

with the width $\tau = 90\,\mathrm{s}$ that is comparable with the burst half amplitude duration. The phase of the oscillations for the loop top source is shown by solid line, and for

the northern (Foot 2) and southern (Foot 1) leg sources by dotted and dashed lines, respectively. Phases of both spectral components are quite stable in the time interval ±70 s around 01:36:00 UT. As one can see, the phase shift between oscillations from the LT and legs sources is very small for the P_1 component, less than 0.5 rad or $1/12 \times P_1 \approx 1.3$ s, and two times less for the opposite leg sources. However it is well pronounced for the P_2 spectral component. The value of the phase shift between P_2-oscillations from the loop top and the northern leg sources is ≈1.5 rad or $\approx 1/4 \times P_2 = 2.2$ s. For the southern leg source the phase difference has the same sign, but the value is three times smaller, only ≈0.5 rad or $1/12 \times P_2 \approx 0.7$ s. The small phase difference for this source is possibly connected with its proximity to the loop top source.

According to the theory developed by Edwin and Roberts [101, 102] linear MHD perturbations of a straight plasma cylinder with the radius $r = a$ are described by dispersion relation

$$\rho_c(\omega^2 - k_z^2 C_{Ae}^2) m_0 \frac{I_m'(m_0 a)}{I_m(m_0 a)} + \rho_0(k_z^2 C_{A0}^2 - \omega^2) m_e \frac{K_m(m_e a)'}{K_m(m_e a)} , \tag{7.4.6}$$

where $I_m(x)$ and $K_m(x)$ are modified Bessel functions of order m, and the prime denotes the derivative with respect to argument x. The functions m_0 and m_e which may be considered as radial wave numbers of the perturbations inside and outside the cylinder, respectively, are defined through

$$m_i^2 = \frac{(k_z^2 C_{si}^2 - \omega^2)(k_z^2 C_{Ai}^2 - \omega^2)}{(C_{si}^2 + C_{Ai}^2)(k_z^2 C_{Ti}^2 - \omega^2)} , \tag{7.4.7}$$

where $i = 0,\ e$. In the internal and external media, the sound speeds are C_{s0} and C_{se}, the Alfvén speeds are C_{A0} and C_{Ae}, and the tube speeds are C_{T0} and C_{Te}, respectively. (The definitions of the speeds are standard, see, e.g., the Ref. [103].) Relations between those characteristic speeds determine properties of MHD modes guided by the cylinder. For modes that are confined to the tube (evanescent outside, in $r > a$), the condition $m_e > 0$ has to be fulfilled. The integer m is the azimuthal mode number. It determines the azimuthal modal structure: waves with $m = 0$ are sausage modes, waves with $m = 1$ are kink modes, waves with higher m are referred to as flute or ballooning modes. The existence and properties of the modes are determined by the equilibrium physical quantities. In particular, for $m_0^2 < 0$, the internal radial structure of the modes is described by the Bessel functions $J_m(x)$, and the radial dependence of the oscillation is quasi-periodic.

Figure 7.7 shows dispersive curves of MHD modes guided by a magnetic cylinder with the characteristic speeds $C_{A0} = 600\,\mathrm{km\,s^{-1}}$, $C_{Ae} = 3300\,\mathrm{km\,s^{-1}}$, $C_{s0} = 340\,\mathrm{km\,s^{-1}}$, and $C_{se} = 200\,\mathrm{km\,s^{-1}}$ that are obtained using the loop parameters derived from microwave and X-ray diagnostics in Sect. 3 of Ref. [100]. There is an infinite number of modes with a given azimuthal number m, corresponding to different radial numbers, l. The modes with higher radial numbers l have higher phase speeds along the loop and exist for higher values of the longitudinal wave number k.

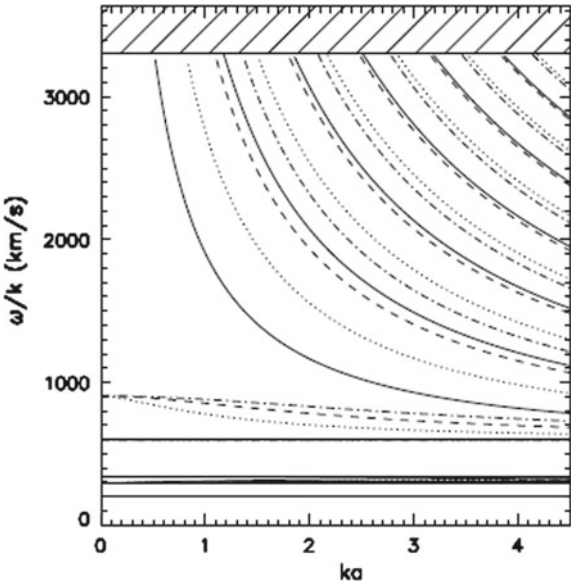

Fig. 7.7 Phase speeds of MHD modes of a straight magnetic cylinder as function of the longitudinal wave number normalized by the cylinder radius a, for $C_{A0} = 600\,\mathrm{km\ s^{-1}}$, $C_{Ae} = 3300\,\mathrm{km\ s^{-1}}$, $C_{s0} = 340\,\mathrm{km\ s^{-1}}$, and $C_{se} = 200\,\mathrm{km\ s^{-1}}$. Solid curves correspond to sausage ($m = 0$) modes of different radial numbers ($l = 1, 2, 3,\ldots$), dotted curves to kink ($m = 1$) modes, dashed and dashed-dotted curves—to the ballooning modes $m = 2$ and $m = 3$, respectively. For fast modes, the lowest phase speed curves of each line style correspond to the $l = 1$ mode. Horizontal straight lines show the characteristic speeds mentioned above. The hatched region shows where no trapped mode can exist

The horizontal axis of Fig. 7.11 shows the normalized longitudinal wave number, which may be rewritten through the longitudinal wave length $ka = 2\pi a/\lambda$. As fast modes of a coronal loop should have nodes of the transverse velocity perturbations at the loop FPs, the wavelengths of the modes are quantized, $\lambda = 2L/n$, where n is an integer corresponding to the mode number (or the number of maxima of the transverse velocity perturbations along the loop) and L is the length of the loop. Identification of a particular mode should be based upon the analysis of the mode period and the mode radial and longitudinal numbers. The radial mode number l is perhaps the most difficult to measure, as the loop width is usually either unresolved or resolved very poorly. The lowest $n = 1$ mode is a fundamental or global mode. Global kink ($n = 1$, $m = 1$) modes have been discovered with Trace EUV imaging telescope [104, 105].

The length of the analyzed loop is estimated as $L = 25\,\mathrm{mm}$. The observationally determined distribution of the oscillation power along the loop has one maximum, near the loop apex, suggesting that the observed mode is global. In the loop of the observed length, the global (n = 1) mode with the period of 16 s should have the phase speed about $3130\,\mathrm{km\ s^{-1}}$. According to Fig. 7.7 the longest wavelength mode

which can have such a speed is the sausage mode. The corresponding normalized longitudinal wave number $ka \approx 0.54$, which gives us $a \approx L/6 \approx 4.3$ mm. As the observed loop is sufficiently thick, this estimation is realistic. The next longest wavelength global mode, the kink $l = 2$ mode, requires $ka = 0.85$, which does not seem to be realistic as the loop would be too thick in this case. All other global modes require the loop to be even thicker and should be ruled out on those grounds. Similarly, the longitudinal modes are excluded because they cannot reach the required phase speed. In addition, according to Fig. 7.6 (upper panel) all parts of the loop analyzed are observed to oscillate in phase with each other. This confirms the identification of the observed mode as the global sausage $l = 1$ mode, as suggested in Nakariakov et al. [103].

7.4.2.2 Kink Mode Standing Waves [106]

In Fig. A.28 of Appendix A we already show the main temporal and spectral properties of the spatially unresolved signal of the flare on 3 July 2002 observed by NoRH in the period 02:09:12–02:17:12 UT, Kupriyanova et al. [91] noticed an interesting drifting feature on the wavelet spectrum of QPPs during the final phase of this flare. To be sure that the periods found from microwave data have solar origin, we carried out a spectral analysis of the intensity variations of the HXR emission obtained with RHESSI, and applied the same procedure of spectral analysis, as for microwave data, to all RHESSI energy channels (see Fig. 1d of the Ref. [106]). One can see that the spectral components in the periodograms are split into three groups with periods close to 30, 20, and 10 s, which are similar to those found for the microwave emission (see Fig. 1c of the Ref. [106]) obtained using a completely independent instrument. We believe this is a strong evidence of the solar origin of the periodicities.

To increase the SNR, we merged areas with similar profiles of the wavelet spectra into three large boxes: 8×8 pixels ≈20"×20" (Fig. A.30a of Appendix A). Time profiles of modulation depth $\Delta\tau(t_i)$ from these boxes for $\tau = 25$ s are shown in Fig. A.30b. They present a good quality of oscillatory patterns through the whole time interval. The periodic structure of these time profiles is much better seen in its autocorrelation functions (Fig. A.30c). Hence, pulsations keep the phase during a sufficiently long time and have rather good quality: $Q = \pi n \approx 20$ (n is the number of periods) for QPPs with $P \approx 30$ s and $Q \geq 30$ for QPPs with $P \approx 20$ s. Note that the emission intensity oscillates in anti-phase in the northern and southern sources (Fig. A.30b). Wavelet spectra of $\Delta\tau(t_i)$ from the selected three large boxes are shown in Fig. A.30d for the smoothing filter width $\tau = 25$ s.

Results of the Fourier analysis for the large boxes confirm the results of the wavelet analysis. Periodograms of autocorrelation functions R of modulation depth $\Delta\tau(t_i)$ for the set of τs are shown in Fig. A.30e by solid lines. The periodograms for boxes 0 and 2 have similar profiles. They indicate the following set of mean periods: $P_1^I \approx 32.6 \pm 3.0$ s, $P_1^{II} \approx 22.6 \pm 1.5$ s, $P_2^{II} \approx 18.8 \pm 1.0$ s, $P_1^{III} \approx 11.5 \pm 0.4$ s, and $P_2^{III} \approx 9.8 \pm 0.3$ s. Periodograms for box 1 show a dominant spectral peak with period $P_1^I \approx 30.3 \pm 3.0$ s. Also, there are three very weak peaks with periods from

13.1 to 17.7 s, which are slightly higher than the significance level only for $\tau \leq$ 15 s. The periodogram analysis in Sect. 4.3 of the Ref. [105] shows that the set of three pairs of strong spectral components is observed throughout the analyzed time interval (02:13:40–02:17:10 UT): $\langle P\rangle_1^I \approx 34.9$ s and $\langle P\rangle_2^I \approx 31.2$ s, $\langle P\rangle_1^{II} \approx 21.3$ s and $\langle P\rangle_2^{II} \approx 18.7$ s, $\langle P\rangle_1^{III} \approx 11.5$ s and $\langle P\rangle_2^{III} \approx 9.8$ s.

Based on Eqs. (7.4.6) and (7.4.7), the calculations for $B_0 = 180$ G, $T_0 = 5\times10^6$ K, and $n_0 = 5\times10^{10}\text{cm}^{-3}$ show that the kink mode provides values of the periods and their ratios $P_{kink}^I/P_{kink}^{II} \approx 31.1\,\text{s}/18.7\,\text{s} \approx 1.66$ and $P_{kink}^{II}/P_{kink}^{III} \approx 18.7\,\text{s}/11.4\,\text{s} \approx 1.64$ much closer to those observed: $P_{obs}^I/P_{obs}^{II} \approx 31.1\,\text{s}/18.7\,\text{s} \approx 1.66$ and $P_{obs}^{II}/P_{obs}^{III} \approx 18.7\,\text{s}/11.4\,\text{s} \approx 1.64$.

Let us consider now possible mechanisms of the microwave emission modulation by the kink mode oscillations of the flare loop. A well-known mechanism is the GS emission modulation produced by horizontal kink mode oscillations. During this type of oscillation, the magnetic field strength is almost unchanged, but the direction of the field lines can change remarkably. The modulation occurs due to the dependence of the emissivity of the NT GS radiation on the angle θ between the magnetic field direction in the source and the LOS [107]

$$I(\theta) \propto (\sin\theta)^{-1.43+0.65\delta} B^{0.90\delta-0.22}\,. \tag{7.4.8}$$

Here δ is the spectral index of accelerated electrons, $2 < \delta < 7$, and B is the magnetic field strength. In our case the flaring loop is oriented in the north-south direction and its heliographic coordinates are S19W48. Thus, field lines near the FPs are probably inclined by more than 48° to the line of sight for the northern FP and less than 48° for the southern FP. The LT field lines are inclined at an angle of the order of 70°. This means that in order to produce the observed oscillations of 2–5% of the MW intensities near the FPs and LT (see Fig. A.30), the amplitude of the angle should be around $\Delta\theta = 1.5{-}3.0°$, assuming $\delta = 4.7$. Such angle variations look rather reasonable.

It follows from Eq. (7.4.8) and properties of the horizontal kink mode that the modulation of the GS emission by the fundamental (global) kink mode with period $P \approx 30$ s can be significant throughout the loop. The QPPs are expected to be in phase everywhere in the loop. The QPPs with period $P \approx 20$ s caused by the second harmonic of the kink mode are expected to have larger amplitudes at the position between the LT and FPs, but closer to the FPs. These oscillations of the emission intensity should be in anti-phase in the northern and southern sources because of the anti-phase displacements of the opposite loop legs (see the Ref. [108]). In general, this behavior of the predicted microwave emission is in agreement with the observed properties of QPPs discussed in Sect. 4 of the Ref. [106]. Especially good agreement is found for the FPs of the flaring loop where viewing angle variations are expected to be maximal both for $P \approx 30$ s and $P \approx 20$ s oscillations (Fig. A.30).

Another mechanism of GS modulation by kink oscillations can be provided by the vertical oscillations of a magnetic loop. The first observations of this oscillatory mode by the Trace spacecraft in the 195 Å bandpass were reported by Wang and Solanki [109]. Theoretical studies of the mode were reported in a number of papers [88, 110,

111]. Recently, using data from the AIA and HMI on board of SDO together with the STEREO/EUVI-A, Aschwanden and Schrijver [112] found that vertical kink oscillations of a magnetic loop with curvature radius variations $R(t) = R_0 + A(t)$ can modulate the plasma density and magnetic field strength in the oscillating loop more or less similarly to the sausage mode oscillations, but with a different period. When the loop stretches up or shrinks down, its cross-sectional radius $a(t)$ varies proportionally to the oscillating amplitude $A(t)$ (see Eq. (7) in the Ref. [112]). In our notation,

$$a(t) = a_0 \left(1 + \frac{A(t)}{R_0}\right) . \tag{7.4.9}$$

This results in periodic changes of the loop volume and provides plasma density variations inversely to $a(t)$. On the other hand, from the law of magnetic flux conservation, it follows that the magnetic field strength should also vary inversely to $a(t)$. The strongest variations of the magnetic field $B(t)$ are expected in the loop top for the case of the global vertical kink mode. As follows from Eq. (7.4.8), the intensity of GS emission is proportional to the magnetic field to the power of four, $I \propto B^4$, for $\delta = 4.7$. Obviously, this effect can lead to a strong modulation of the GS emission in the upper part of the loop, which is exactly what we observe for the 30 s spectral component (see Fig. 5a of the Ref. [105]). A calculation of the modulation depth using Eqs. (7.4.1) and (7.4.2) gives its value in the loop top: $\Delta I/I < 5\%$. Therefore, the variations of the magnetic field should be as low as $\Delta B/B = \Delta I/4I < 1.25\%$.

From the law of magnetic flux conservation $B(t) \times S(t) = \text{const}$, where $S(t) = \pi a(t)^2$, we conclude that variations of the loop cross-sectional radius $a(t)$ are twice less than variations of the magnetic field and anti-correlate with them; $\Delta a/a_0 = \Delta B/2B$, that is $\Delta a/a_0 < 0.6\%$. From Eq. (7.4.9) one gets $\Delta a/a = A/R_0$. For the fundamental kink mode, variations of a have maximum amplitude in the loop top. An analysis of the loop spatial structure (Sect. 4.1 of the Ref. [105]) gives the following estimations for the loop cross-sectional radius and for the loop curvature radius, respectively: $a \approx 4$ pixels and $R = d/2 \approx 7.5$ pixels. This means that the variations of these sizes are very small, $\Delta a < 0.024$ pixels and $A < 0.045$ pixels. These changes are considerably less than the NoRH beam size, and cannot be observed directly. But they are high enough to produce observable changes in fluxes from different sites of the flaring region. Similar considerations of the second and third harmonics of the vertical kink mode oscillations lead to the following predictions. The second harmonic should provide anti-phase oscillations of the magnetic field strength in the opposite ends of the flaring loop and, consequently, the anti-phase oscillations of the GS emission. The third harmonic has three regions of high-amplitude variations of the magnetic field and corresponding regions of microwave emission variations: one in the middle and two near the ends of the magnetic loop. These predictions are in good agreement with our results of spatially resolved observations as shown in Fig. 5 of the Ref. [106]. However, note that the theory of the vertical kink mode oscillations is still in the initial stage of its development, and more efforts by MHD theoreticians are needed to achieve more reliable conclusions.

7.4.2.3 Slow Magnetoacoustic Waves [113]

Quasi-periodic pulsations (QPPs) of the microwave emission with periods P from several to several tens of seconds have been observed in solar flares, and have been widely discussed in the literature [90, 91, 100, 106]. Only recently the oscillations with $P \approx 1$–15 min have also been detected in flares in the microwave band [114–119]. We have detected in the gradual component of the MW emission of a class M2.5 GOES flare that occurred close to the limb on June 2, 2007, to study the amplitude and phase characteristics of minute QPPs in various sections of the flare loop, as tools for identifying their origin.

The flare was associated with a coronal loop with the coordinates S06 E74, visible in the Stokes I map for time $t_{300} = 05{:}41{:}43$ UT shown by the grayscale in Fig. 7.8a. The distance between the loop FPs, $d \approx 40$", provides an estimate of the length of the semicircular loop, $L \approx 44$ mm. Note that the thickness of the loop is not uniform. The radius of the loop (half-thickness) at its apex is $a \approx 18$", while the radius at the base is $a \approx 12$". This yields the estimate for the ratio of the loop radius to its length $a/L \approx 0.2$–0.3. Figure 7.8b shows the temporal profiles of the flux (input signal) in the Stokes I and V channels, obtained by integrating over three selected boxes (squares in Fig. 7.8a): at the apex (box1) and either end (box0 and box2). During the interval when the smooth component existed, delineated by the vertical dotted

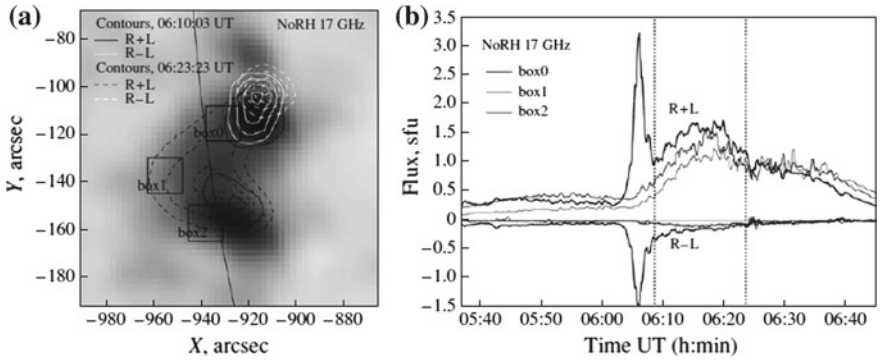

Fig. 7.8 **a** Radio map of the flare region. The grayscale shows the intensity in the I channel of the 17 GHz MW emission in the initial phase of the flare (at time $t_{300} = 05{:}41{:}43$ UT). The dark contours show the position of the source in the I channel ($I = R + L$), and the white contours its position in the V channel ($V = R - L$). The solid and dashed contours correspond to times $t_{2000} = 06{:}10{:}03$ UT and $t_{2800} = 06{:}23{:}23$ UT—the beginning and end of the smooth component. The contours correspond to 0.96, 0.8, 0.6, and 0.4 of the peak brightness in the I and V channels. **b** Temporal profiles of the flux in the intensity channel, obtained by integrating over the areas inside the squares in the left panel. The upper family of curves corresponds to the I channel and the lower family to the V channel. In each set of curves, the bold curve shows the flux from the northern source (box0), the medium curve the flux from the southern source (box2), and the thin curve the flux from the loop apex (box1). The vertical dotted curves delineate the smooth component (from t_{2000} to t_{2800})

lines in Fig. 7.8b, there was a redistribution of the radio brightness toward higher layers in the corona in the Stokes I channel. This is shown by a comparison of the solid and dashed dark contours depicting the distribution of radio brightness at times t_{2000} = 06:10:03 UT and t_{2800} = 06:23:23 UT. The polarized source (Stokes V channel)remained stationary in space, making it possible to stabilize the image relative to its brightness center and avoid the effect of jitter.

QPPs with periods of several minutes can be seen in the temporal profiles of the gradual component of the microwave emission in the three selected boxes (Fig. 7.8b). Note that the long duration of this gradual component (15 min) enabled us to confidently distinguish and study QPPs with periods up to four minutes. The QPPs are more clearly visible in plots of the high-frequency signal $F_{\tau I}^{hf}$ (Fig. 7.9a). The pulsation amplitude is $\Delta I/I < 4\%$. Wavelet spectra of the high-frequency signal are shown in Fig. 7.9b. Several spectral components with constant periods of $P \approx 55$–65, 110–120, and 220–250 s are present in the various boxes. A spectral component with period $P \approx 110$–120 s is visible during the entire time interval. Consequently, its quality is $Q = \pi n \approx 25$ (n is the number of pulsation periods observed). This spectral component also possesses the highest spectral power, which is especially clearly visible in the global wavelet spectra (far-right plots in Fig. 7.9b).

The quasi-periodic character of the MW emission is also demonstrated by the autocorrelation functions of the high-frequency signal, $R(F_{\tau I}^{hf})$ (Fig. 7.10a). Periodograms for τ = 100, 150, 200, and 250 s are shown in Fig. 7.10b. QPPs with

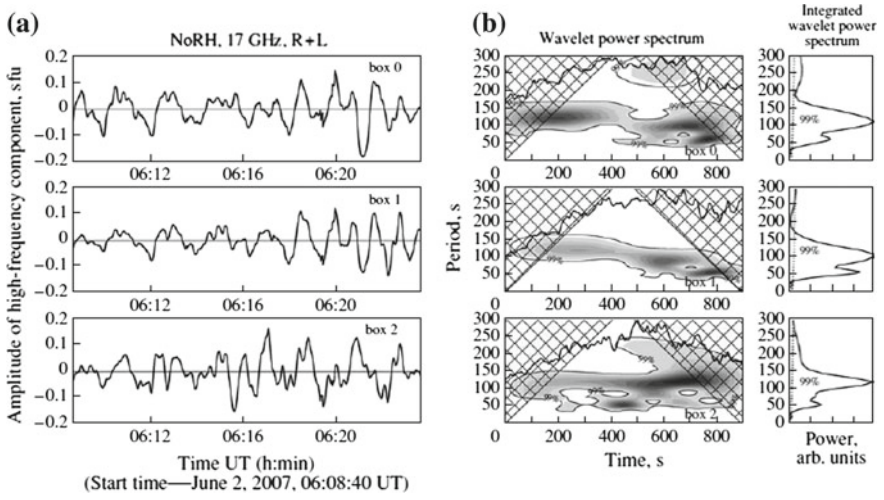

Fig. 7.9 **a** Temporal profiles of the high-frequency signal $F_{\tau I}^{hf}$ of the smooth component in the areas indicated by squares in Fig. 7.8a during the time interval from t_{2000} to t_{2800}. **b** Wavelet spectra of the high-frequency signal $F_{\tau I}^{hf}$ in the I channel for the three boxes for τ = 100 s. The bold curve in the wavelet spectrum for each box shows the normalized temporal profile of the flux from the corresponding box. The thin, solid contour shows the 99% confidence level. The far-right plots present the global wavelet spectra. The dashed lines show the 99% confidence levels

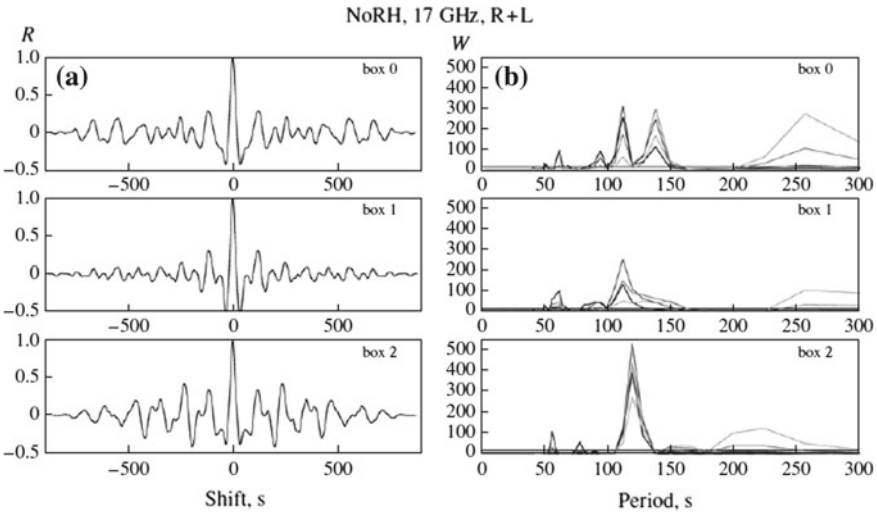

Fig. 7.10 **a** Autocorrelation function of the high-frequency signal of the temporal profiles in the intensity channel ($R(F_{\tau I}^{hf})$) for $\tau = 100$ s. **b** Periodograms of the autocorrelation functions $R(F_{\tau I}^{hf})$. Decreasing thickness of the curves corresponds to $\tau = 100, 150, 200,$ and 250 s. The horizontal line shows the 99% confidence level

periods $P \approx 55$–65, 110–120, and 220–250 s are present in various sections of the flare region. Figure 7.10b shows that the periods of the spectral components remain constant for the different τ values. This testifies that the QPPs are associated with the signal, and are not filtration artefacts. The observed periods agree with the periods found using a wavelet analysis. Note that there is also a peak in the periodograms with $P \approx 140$ s in box0, that is not present in the wavelet spectrum. The highest spectral power W is displayed by the peak with period $P \approx 110$–120 s, which also agrees with the results of the wavelet analysis.

Note that the uncertainty in the periods worsens with increasing period. This is due to the inhomogeneity of the period grid in the discrete Fourier transform. For the duration of the time series considered here, $N = 901$ s, the periods of 55–65 s have uncertainties $\pm$ (2–2.5) s, periods of 110–120 s have uncertainties $\pm$ (6–8) s, and periods of 220–250 s have uncertainties $\pm$ (22–32) s. Analysis of the phase relations between the temporal profiles of the pulsations in various sections of the flare loop shows that they are fairly ambiguous for the spectral components with periods $P \approx$ 55–65 s and $P \approx$ 220–250 s. However, oscillations of the intensity in the spatially separated boxes were essentially in-phase for the component with $P \approx$ 110–120 s when the boxes were arranged along the loop (Fig. 7.9a).

The oscillation periods we have found for the thermal MW emission lie in the range 55–250 s. These correspond to the periods of standing MHD waves captured in coronal magnetic tubes [96]. Since the observed QPPs represent oscillations of the thermal radio flux [119], this modulation could be produced by modes characterized by an appreciable compression of the plasma; i.e., radial fast magnetoa-

coustic ("sausage") and slow magnetoacoustic (SMA) modes. The periods of standing MHD waves trapped in a magnetic tube with enhanced plasma density are given by Eq. (7.4.4). To estimate the periods of the sausage and SMA modes, we adopted the typical parameters of flare loops obtained for previously studied solar flares [90, 100, 114]: a temperature for the radiating plasma $T = 23$ MK, a number density of thermal particles $N = 10^{11}\text{cm}^{-3}$, and a loop-average magnetic field $B = 300$ G. We also used the loop length, $L \approx 44$ mm, and the ratio of the loop radius (half-thickness) and its length, $a/L \approx 0.2$–0.3, estimated from the radio maps. The phase velocity of the sausage mode was found using the solution of the dispersion Eq. (7.4.6). Our analysis showed that, for the chosen values of the loop parameters, the sausage mode of the fundamental tone does not exist, even in the case of a thick loop. The periods of the second and third harmonic are $P_{FMA2} \approx 12$ s and $P_{FMA3} \approx 10$ s. Note that the observed periods exceed these values by nearly an order of magnitude. Therefore, the sausage mode was excluded from further consideration. The phase velocity of the SMA mode is $v_{ph} = C_T$, where C_T is the so-called tube velocity, which is given by [90]

$$C_T = C_s C_A / \sqrt{C_S^2 + C_A^2}\,, \tag{7.4.10}$$

where C_A and C_s are the Alfvén speed and the sound speed, respectively. The phase velocity of the SMA mode is an order of magnitude lower than the phase velocity of the sausage mode. Consequently, the periods of the SMA mode correspond better to the observed periods. We accordingly considered this mode in more detail to check for consistency with the observed characteristics of the flare loop and the derived spectral and phase relations of the oscillations.

In the Ref. [118], periods of the order of several minutes and the presence of several spectral peaks simultaneously were explained as an effect of a parametric resonance of standing acoustic waves, which are a special case of SMA waves. According to the Ref. [117], spectral peaks should appear at the frequencies $\omega_n = n\omega/2$, where $n = 1,\ 2,\ 3, \ldots$, ω is the frequency of the external excitation, and $\omega_1 = \omega/2$ is the frequency of the fundamental standing-acoustic-wave mode in the magnetic loop. The set of periods obtained $P \approx 220$–250, 110–120, and 55–65 s can be explained by parametric resonance if the period $P \approx 110$–120 s is the period of the external excitation. In such a case the spectral component with $P \approx 110$–120 s should be the second harmonic of the acoustic mode. This means that the phase of the wave should vary appreciably along the loop axis. However, in the observations, this spectral component is distinguished by the co-phased nature of the intensity oscillations along the entire loop length. Therefore, parametric resonance does not provide a suitable explanation for the observed phases and the spectral features in the observed pulsations.

The fact that the observed pulsations with $P \approx 110$–120 s are co-phased along the loop suggests we are dealing with the fundamental tone of a SMA oscillation. With the plasma parameters in the magnetic tube adopted above and the measured length $L \approx 44$ mm, the period of the fundamental of the SMA mode calculated using

Eqs. (7.4.9), (7.4.6), and (7.4.10), $P_{SMA1} \approx 118$ s, corresponds to the observations. The periods of the second and third harmonics are $P_{SMA2} \approx 59$ s and $P_{SMA3} \approx 40$ s. The period P_{SMA2} is also observed in the periodograms (Fig. 7.10b).

Our conclusion that the pulsations in the coronal loop are associated with the SMA mode is in agreement with the recently published results [119, 121]. Note also that it is not possible to obtain the entire set of observed periods, for example, $P \approx 220$–250 s, using SMA oscillations in a single magnetic tube. However, if we allow for the possibility that several magnetically unrelated plasma tubes with different parameters filling the observed flare loop [114] could simultaneously fall within the NoRH beam, this could, in principle, explain the observed set of periods. For example, for a loop with a lower temperature of $T = 5$ MK and with $B = 300$ G and $N = 10^{11}\text{cm}^{-3}$, we obtain the periods $P_{SMA1} \approx 241$ s, $P_{SMA2} \approx 120$ s, and $P_{SMA3}80$ s. Thus, the observed QPPs are most likely associated with SMA oscillations in a filamentary flare loop.

7.4.2.4 Summary

Three typical events of spatially and temporally resolvable QPPs observed by NoRH are studied intensively with methods of correlation and Fourier analysis of the integrated signal (correlation amplitudes) as well as wavelet analysis to obtain the periods and spectral components in different parts of flaring loops. Comparison of spatial and spectral properties of the observed QPPs with the solution of dispersion equation for MHD oscillations of a magnetic tube allowed us to choose the most appropriate MHD mode among potentially possible modes of standing MHD waves, which respectively support the global sausage, kink, and SMA modes in the three events. A further development of these methods to use for other flares opens new possibilities for studying QPP processes in solar flares.

7.4.3 Relation of Repetition Rate and Burst Flux in QPPs

7.4.3.1 Overview

Based on a statistical study on the sub-second pulsations of the flux at 22∼90 GHz, Kaufmann et al. found a positive correlation between the repetition rate R of pulsations and corresponding background (averaged) flux S in bursts, which was defined as $R - S$ relation: $S = UR + b$, here U represents the energy emitted in an individual pulse, and the mean value of U at 22∼90 GHz equals 5 sfu·s, and it is considered as "the quasi-quantized energy release" [122, 123]. Afterward, a similar $R - S$ relation was also found in another statistical study on the bursts at 10 ∼15 GHz with pulsations of seconds, but the mean value of U increases to 1443 sfu·s, while an inverse correlation was found between the modulation depth of pulsations and background flux in bursts [124].

It was proposed from the above observations that the flare energy release process may be composed of a series of elementary flares with different timescales, which are excited by the plasma instabilities occurred in the magnetic elements or elementary magnetic tubes with different spatial scales in solar atmosphere [125], and thus to cause the quasi-periodic acceleration and injection of energetic electrons in flaring loops as well as the modulation of radio emission. It is assumed that the energy conservation is satisfied in the process of wave-particle interaction (plasma instabilities), it can be proven that the saturated time of instabilities is inversely proportional to the initial intensity of radio emission, but directly proportional to the modulation depth of the intensity of radio emission, which can naturally explain the statistical relations as mentioned above in the case of a series of continuous pulses [126].

However, the quite different periods and values U (the quasi-quantized energy release) at different frequencies are not studied and explained, which may be related to the distribution of flare energy release in different coronal heights, and something like the frequency dependence in the avalanche model discussed in Sect. 3.1.3.

7.4.3.2 Data Process

In order to statistically compare the radio pulsations at different frequencies, it is necessary to select the observations of one instrument that covers the full MW band, such as the data of NoRP at 6 frequencies in 1∼35 GHz. In the 24 events of NoRH with a loop-like structure or three separated sources [127], we selected 14 events evidently with second or sub-second pulsations, which are listed in Table 7.1.

Table 7.1 Date, start, end, and peak times, central coordinates, and GOES class of the 14 selected events

No	Date	Start (UT)	Peak (UT)	End (UT)	Center	Class
1	19990216	02:52:32	02:57:50	05:37:20	S26W16	M3.2
2	19990828	00:52:28	00:56:42	01:05:07	S25W11	M2.8
3	20010325	04:15:15	04:17:26	04:21:45	N17E49	M2.5
4	20010925	04:25:09	04:34:01	04:51:42	S21E01	M7.6
5	20011023	00:13:50	00:16:14	00:20:59	S18E12	M1.3
6	20030613	04:33:59	04:34:30	04:35:10	N12W72	M1.7
7	20031024	05:06:48	05:07:47	05:11:47	S21E70	M4.2
8	20031029	00:26:14	00:29:31	00:44:12	S19E07	M1.1
9	20031104	05:35:42	05:49:23	06:17:07	S16W71	M2.6
10	20040105	02:37:37	03:20:34	06:12:41	S11E35	M6.9
11	20040521	23:41:39	23:50:15	00:06:44	S10E53	-
12	20040722	23:51:35	00:31:15	01:28:05	N05E16	M9.1
13	20050115	05:55:38	06:07:44	06:30:05	N14E02	M8.6
14	20070603	01:57:07	01:57:32	02:42:56	S07E66	-

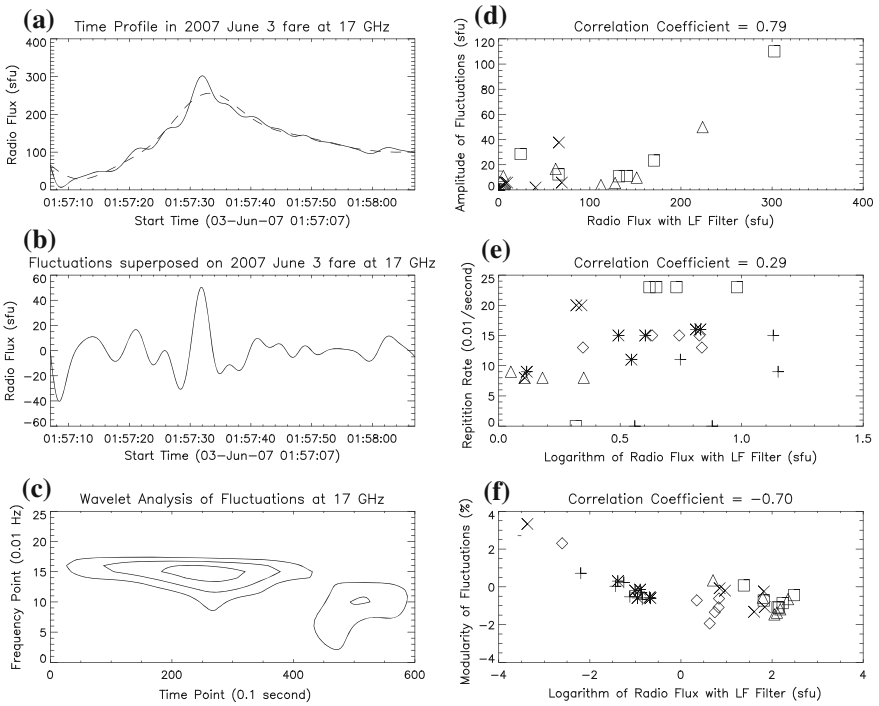

Fig. 7.11 **a** 17 GHz flux (solid) of NoRP in the 2007 June 3 event overlain by the background flux (dashed), **b** the pulsations after high-pass filter, **c** the wavelet analysis of pulsations, and the correlation of background flux with **d** the amplitude, **e** repetition rate, and **f** modulation depth of pulsations, in which the symbols of plus, asterisk, diamond, triangle, box, and cross correspond to the data of NoRP at 1.0, 2.9, 3.75, 9.4, 17, and 35 GHz, respectively

The criterion of data selection is that the amplitude of pulsations should be much larger than the sensitivity of receiver (5∼10 sfu) and signal-to-noise ratio, with the data process as follows [128]:

(1) A digital filter is used to separate the slowly varied background flux in bursts and fast varied pulsations, which are respectively shown by the dashed curve in Fig. 7.11a and solid curve in Fig. 7.11b, as an example at 17 GHz in the event on 2007 June 3.

(2) The wavelet analysis has been made for the pulses, it is noticed that the definitions of time and frequency in wavelet analysis are different from those in the Fourier transformation, which should be transformed to the same as the Fourier definitions [129]. Here, the frequency of wavelet analysis just means the repetition rate of pulsations, as shown by Fig. 7.11c.

(3) The correlation analysis is made respectively among he the background flux in bursts, the amplitude, repetition rate, and modulation depth of pulsations, as shown

by Fig. 7.11d–f. The linear correlation coefficient in Fig. 7.11 is just given for 17 GHz as one example.

7.4.3.3 Variation of Various Statistical Relations with Frequencies

According to the data analysis, all the correlations background flux with the amplitude, repetition rate, and modulation depth of pulsations are satisfied by the confidence level of 0.95 in the 14 events at 6 frequencies, as shown by the 2007 June 3 event in Fig. 7.11. The frequency dependence of the averaged correlation coefficients in the 14 events with an error bar is given in Fig. 7.12.

It can be seen from Fig. 7.12a that the correlation coefficient between the background flux and the amplitude of pulsations decreases monotonously with increasing of frequency in a range of 0.4∼0.8, which means that the amplitude of pulsations strong depends on the burst flux, especially in lower frequencies. On the other hand, the correlation coefficients between the background flux and repetition rate of pulsations and anti-correlation between the background flux and modulation depth of pulsations are respectively 0.4∼0.6, and –0.5∼–0.8, which are all reliable statistical

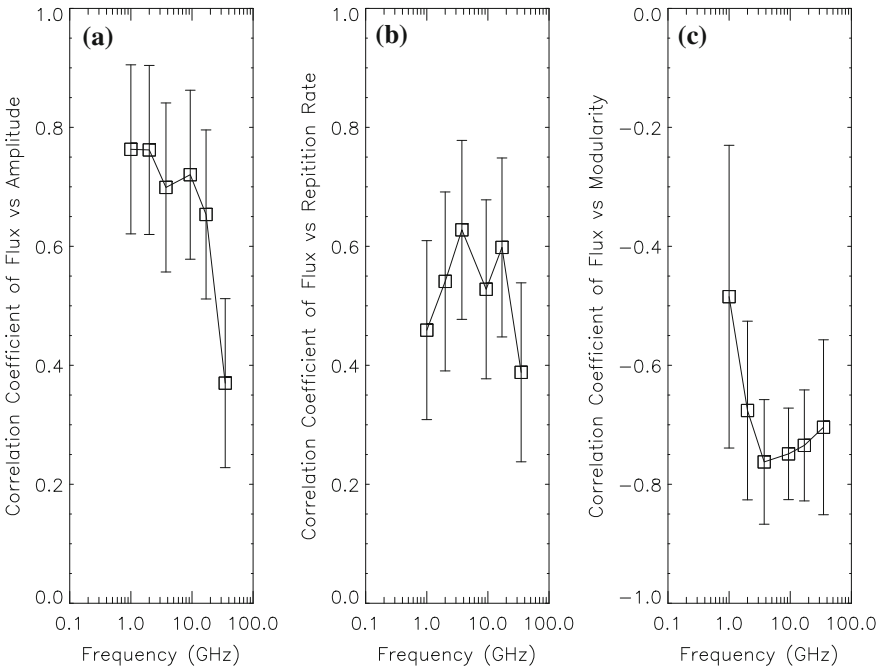

Fig. 7.12 The frequency dependence of the averaged correlation coefficients of the background flux with **a** the amplitude, **b** repetition rate, and **c** modulation depth of pulsations in the 14 selected events of NoRP

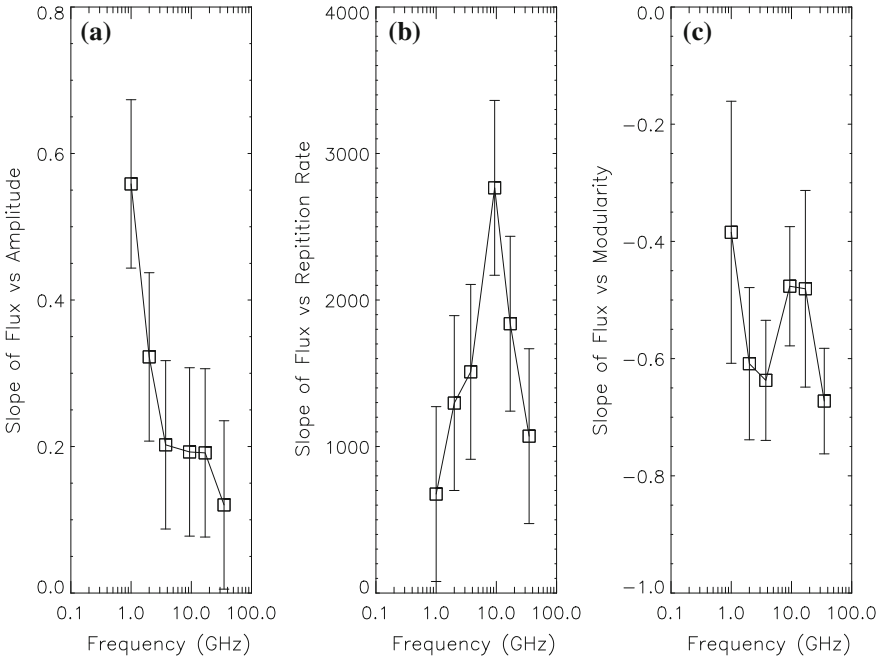

Fig. 7.13 The frequency dependence of the averaged slopes of the background flux with **a** the amplitude, **b** repetition rate, and **c** modulation depth of pulsations in the 14 selected events of NoRP

results, but frequency dependence is not meaningful due to the error bar comparable with the total variation in Fig. 7.12b–c.

Furthermore, Fig. 7.13 gives the frequency dependence of the averaged slopes of the background flux with the amplitude, repetition rate, and modulation depth of pulsations in the 14 selected events of NoRP. Figure 7.13a shows that the increasing rate of the amplitude of pulsations with the burst flux decreases with increasing of frequency. It is interesting that the averaged slope of the background flux with the repetition rate of pulsations in Fig. 7.13b has the maximum at a middle frequency (around 10 GHz), in respect to the energy released in an individual pulse U, it is about 2700 sfu·s, and rapidly decreases with increasing of frequency, up to zero around 100 GHz, which is well consistent with the previous statistical results as mentioned in the overview. In addition, the frequency dependence of the averaged slopes of the background flux with the modulation depth of pulsations is meaningless due to the comparable error bars and total variation in Fig. 7.13c.

7.4.3.4 Discussions

The statistical results in Figs. 7.11, 7.12 and 7.13 support the general existence of a strong correlation of the background flux with the amplitude, repetition rate, and

modulation depth of second and sub-second pulsations overlaid on the MW bursts at different frequencies. Especially, the maximum U around 10 GHz, which implies that the flare energy release may be the most violent in the coronal height corresponding to this frequency, and it is consistent with the prediction of avalanche model [130].

7.5 Motion of X-Ray Sources Along Flaring Loops

7.5.1 Overview

Much more observations show that there are three HXR sources during the flare eruption, double FPs, and one LT. Generally, the FP sources exhibit a high energy above 25 keV while the LT source is around 10 keV. As mentioned before, another HXR source above the LT is observed with high sensitivity. Both the LT and above the LT sources are called double coronal sources in the documents, which are thought to be the observational evidence of the current sheet located between them. With a high energy resolution, RHESSI observations show the gradient spatial distributions of the different energy sources, such as the more closer the higher energy for both coronal sources, which further prove the current sheet between them (see Fig. A.31 in Appendix A) [6, 7, 131]. Both coronal sources appear at the lower energy band than the FP sources. For the disk event, it is very hard to distinguish the LT and the above-the-LT source without the observations at other wavelength. However, it is easy to do for the limb event. In this case, double FP sources are located on the disk, while both coronal sources are off the limb, and the above-the-LT source does be above the LT source. The four HXR sources can outline the magnetic topology in the space. Form the photospheric magnetic diagram, one FP source is around the positive field, while another is around the negative field. This is consistent with the standard flare model. There is a current sheet between the LT and above-the-LT sources, and magnetic reconnection takes place there to accelerate the NT electrons with the bidirections. Thus, both coronal HXR sources are radiated. The electrons propagate along the magnetic legs downward to the FPs, and radiate double FP source there. Therefore, the shape, location, and scale of the flare loop can be measured from the HXR observations.

7.5.2 Motion of X-Ray Sources Along Flaring Loops

To study the HXR source motions along the flaring loops, it is first to detect the spatial shape of the loop. As noted before, the flare loop topology is able to be outlined based on the three or four HXR source positions for the disk event. Observationally, most of the solar flares take place on the disk. It is still to outline the loop shape according to the HXR sources, but there are some difficulties due to the projection effects.

Meanwhile, the loop shape can also be outlined from the SXR emissions, which are usually bright the whole loop.

The soft and hard X-ray source distributions in the flare loops are related to the radiation mechanism. As mentioned in Sect. 4.1, the SXRs are radiated by the thermal emission mechanism, and the HXRs are radiated by the thin- or thick-target bremsstrahlung. The HXR sources at different energy bands are related to the plasma density. In the solar atmosphere, the plasma density changes with the flare loop, which results in the dependence of HXR source positions on the energies. Observationally, the HXRs change their positions along the flare loop, indicating that the plasma density changing with the flare loop. Therefore, the rules of the HXR source motions reflect the plasma movements during the flare eruptions. However, these plasmas who can move have a density limit. From the observations, only the HXRs at the middle energy (i.e., around 25 keV) exhibit their source motions. In other words, the plasmas with the high energy do not move at all during the flare. From observations, the HXR sources at high energy (i.e., above 50 keV) do not show their source motions along the loops. Previous studies show that the HXR (FP) sources above 50 keV display the perpendicular, parallel or antiparallel motions to the magnetic neutral lines [1, 56, 132, 133]. This is because the NT electrons propagate along the various magnetic lines with different FPs. Observationally, the HXRs changes their source positions with the time, which looks like the source motions, but they are not real motions. Therefore, these HXR source motions are basically different from the motions along the flare loops studied here.

In order to study the HXR source motions along the flare loop, the flare loop shape has to be first outlined from the observations. Figure A.32 in Appendix A shows the flare images detected by RHESSI on 2002 Sept. 10 [134]. The whole flare loop is bright at 3–6 keV, and two FP sources appear at 45–60 keV. This event is on the disk, and the flare loop is not an ideal circular, but a curved shape as shown by the dashed lines with a fixes width of 12 arc s (about 9000 km), which is thought to be the flare loop. During the flare development, this loop coves the all X-ray emissions, whatever the soft or hard X-rays.

Second, the X-ray fluxes are integrated between the two dashed lines. They are the one dimension distributions of X-ray sources along the flare loop. The X-ray source positions are determined by the maximum peaks. Third is to repeat the second step to obtain the one dimension distributions at different times. Fourthly, to repeat these steps at various energy bands. The RHESSI X-ray images are reconstructed in the uninterrupted time interval with a time binning equal to 8 s and an energy binning of 2–15 keV from 3 to 60 keV, i.e., 3–6, 6–8, 8–10, 10–12, 12–14, 14–16, 16–18, 18–20, 20–22, 22–25, 25–28, 28–31, 31–37, 37–45, and 45–60 keV. Figure A.33 in Appendix A shows the time evolution of X-ray brightness distribution along the flare loop from X_1 to X_2 at 14 energy bands. Thus, the LT source could be located at the middle of Y-axis, while the double FPs are at the two ends. The local brightness maxima are traced by two lines (marked by asterisks and pluses) corresponding to the location changes of FP_1 (green curve) and FP_2 (blue curve). For the X-ray emissions at 6–8 keV, the X-ray sources show the upward (to the LT) and downward motions on the rising and decay phases. At the flare beginning with the X-ray fluxes

increasing, the X-ray source separates into two and move towards the FPs along the loop legs. The distance between them reaches the maximum value around the X-ray peak. These two sources then move closer gradually (towards the LT) on the decay phase and merge together at the position same as before. Meanwhile, there are double FP sources at the high energy (i.e., above 25 keV) and stay at the original positions during the rising-decay phases. For the X-rays at the middle energy bands, i.e., from 10 keV to 20 keV, the X-rays show a complicated motion. Some of them display the separation motions without the mergence. The X-rays at the high energy tend to stay around the FPs. The separation and mergence motions are very clearly seen at 3–6 keV.

Figure A.34 in Appendix A shows RHESSI light curves at five energy bands and a GOES SXR light curve at 1–8 Å (top), RHESSI 3–300 keV X-ray emissions as a function of time (middle), and the HXR source motions at 20–22 keV (bottom) for the 2002 Sept. 10 flare. Using the same method as before, Fig. A.34 (bottom) gives the time evolution of the X-ray brightness distribution along the flare loop. The flare perfectly exhibits the FP_2 source movement upward firstly to the loop top then downward with the rising-decay phases. The source speed is roughly measured from the source positions, and its maximum value is about 1000 km s^{-1} at the rising or decay phases. These motions last for about one minute. The same motion was also found in the 2002 Nov. 28 flare [135]

Figure A.35 in Appendix A shows 20–30 keV HXR source motions along the flare loop after the chromospheric evaporation for the 2004 Oct. 30 solar flare. The similar examples can also found in other papers [136–138]. The source speed is about 300–400 km $s^{[-1]}$. On the other hand, it is an interesting topic to study the relationship between the X-ray source motions along the flare loops and the loop shrinkage (in Sect. 5.1.1) at the present time.

7.5.3 Summary

In order to study the X-ray source motions along the flare loop, it is first to determine the flare loop shape from the X-ray observations. Most of solar flares display a simple loop structure from the X-ray emissions, but maybe a complicated loop systems in the optic and EUV wavelengths. In fact, the mass motions along the loops are very complicated from the optic and EUV observations.

RHESSI observations show the X-ray source motions related with the X-ray flux, for example, the X-ray source exhibits the downward-upward motions along the flare loop top corresponding to the X-ray rising-decay phases. The flare displays a single source around the LT at the beginning, then this source separates into two movements downward to the FPs. These two sources reach the maximum distance at the time same as that of the X-ray peak. After that, the double sources are not stopped, but continuously move upward to the flare loop top again on the X-ray decay phase, and merge into a single source again as the position same as that of the original one at the beginning. These motions are possibly related to the plasma density change around

the LT. At the flare onset, the NT electrons inject into the LT to heat the local plasma through the collisions. Thus, the temperature would increase and the high pressure drives the local plasma expansion. The plasma density around the flare LT would decrease. And the pressure continuously drives the plasma front movement downward along the loop legs. The plasma front would move quickly at the beginning, and gradually become slowly due to the resistance from the surrounding materials. The resistance would increase along the loop legs. When the X-rays reach the maximum, the NT electrons could be the maximum as well. The driven pressure arrive the maximum too. There is a balance between the driven pressure and resistance. The plasma front arrives the maximum distance around the FPs where has more dense plasma. On the other hand, the NT electrons also reach FPs to heat the local plasma there to drive the chromospheric evaporation. The evaporation should increase the resistance continuous around the FPs. The increasing resistance would drive the plasma front backward to the flare LT. These result the plasma density changing from rare to dense around flare LT. Observationally, the X-ray sources merge together and stay the LT. Such motions are well seen at the low energy of 3–6 keV. For the X-ray sources do not show any motions at the high energy above 25 keV. The X-rays at the middle energy also display such motions, and the lower energy the more clearly.

7.6 Interaction of Flaring Loops

The collision of two or multiple flaring loops is an important style to excite the magnetic reconnection and flare energy release. The interaction due to the collision of flaring loops is also called as coalescence instability with an electric current along the flaring loop [139–147]. With the enhanced spatial resolution of space and ground-based telescopes, the interaction of two pr multiple flaring loops has been observed frequently in optical, radio, EUV, and X-ray wavebands [148–162]. Most studies pay attention to the spatial structure and configuration of interacted loops, but only less attention was paid to the relevant dynamic spectrum and time profile. Hence, we plan to discuss some examples with spatial, temporal, and (dynamic) spectral observations, as well as a statistical result about coronal loop interaction.

7.6.1 Typical Examples of Loop Interaction

7.6.1.1 Event 1: 2002 April 21 [160]

An X-class flare occurred in the 2002 April 21 event was accompanied with the CME observed by SOHO, Trace, and RHESSI satellites, as well as the ground-based telescope like NoRH, to which has been paid particular attention by a series of studies as one typical solar erupted event. The feature of interacted loop system is this event is that a multiple-loop system expanded outside from solar limb with a speed of

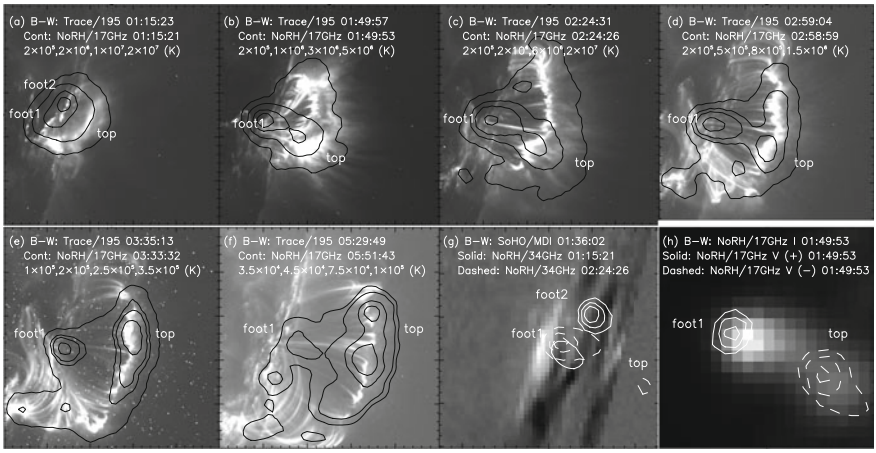

Fig. 7.14 **a**–**f** Trace images overlaid by NoRH 17 GHz contours in the 2002 April 21 flare, **g** one SOHO/MDI image overlaid by the NoRH 34 GHz contours, and **h** One NoRH 17 GHzGHz Stokes I image overlaid by Stokes V contours in the top and bottom of loop system on 2002 April 21

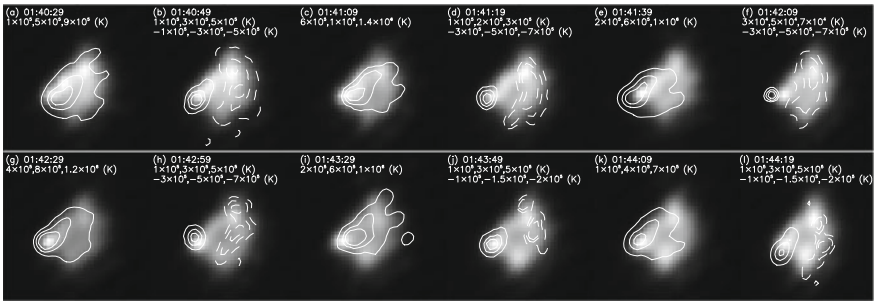

Fig. 7.15 Evolving NoRH 17 GHz Stokes I images overlaid by Stokes V contours in the initial stage of the 2002 April 21 event

10 km/s, while the loop interaction occurred in the top of loop system to cause a locally brightened limb of the expanded loop system as shown by Fig. 7.14a–f, in which the Trace images overlaid by NoRH 17 GHz contours.

It can be seen from Fig. 7.14g that the initial strong emission in foot 1 than that in foot 2 (solid contours) gradually turned to a single foot 2 and loop top emission (dashed contours), while Fig. 7.14h shows that the polarization sense is opposite in foot 2 and loop top, and the evolving polarization is an important feature in this event. It is interesting that the polarization sense in loop top was quasi-periodically reversed in 5 min before the loop system expanded with a period of 10∼20 s, and finally the polarization in the loop top became the LCP sense (dashed contours), while the polarization in foot 2 kept the RCP sense (solid contour) as shown by Fig. 7.15.

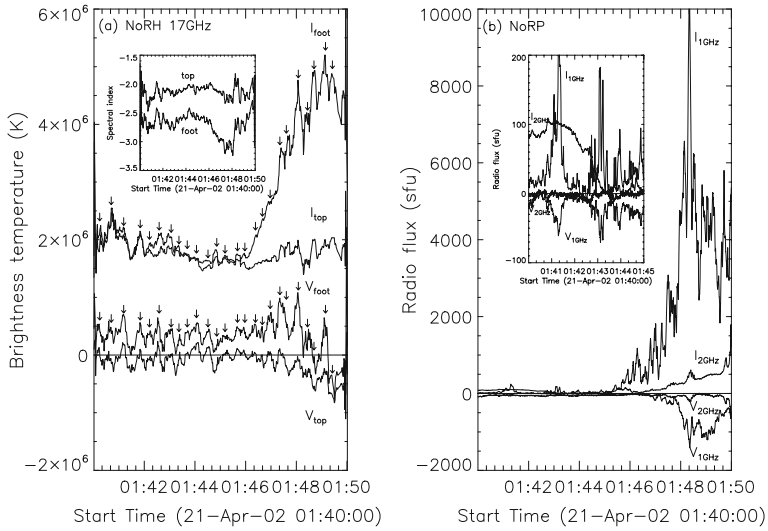

Fig. 7.16 **a** Evolving NoRH 17 GHz Stokes I and V in the loop top and foot of the 2002 April 21 event in comparison with **b** that observed by NoRP

The quasi-periodically variation is actually an important feature in the magnetic reconnection excited by coronal loop interaction, as well as a precursor before the occurrence of flare-CME events as mentioned in the previous examples, which may be associated with some plasma waves or instabilities, and this process frequently occurs in the loop top as shown by this event. For further analyzing this periodically reversion of polarization sense, Fig. 7.16a gives the time evolutions of NoRH 17 GHz intensity and polarization on the LT and foot 2 in the event, which clearly shows that the polarization in the LT was oscillated around zero point and finally turned to the LCP sense, while the RCP sense was always kept in the foot.

The spectral evolutions in the loop top and foot are given in an embedded panel of Fig. 7.16a, with the HSH pattern as mentioned in Sect. 3.3.3 for the MW burst with multiple peaks. If the periodical variations of intensity and polarization are modulated by the oscillated magnetic field due to some plasma waves, they should be anti-correlated, because the intensity and polarization are positively and negatively correlated with the local magnetic field, respectively [107, 163]. However, the observed result is opposite to the above prediction, thus we proposed a reasonable explanation is that the quasi-periodic variation is caused by a periodic acceleration and injection of NT electrons into the flaring loops. Figure 7.16b also gives the full-disk observation of NoRP in this event for both intensity and polarization (see the embedded panel), which shows the periodic feature for both of them. In addition, the overall variation of intensity was inversely proportional to that of polarization in the observations of both NoRH and NoRP (see Fig. 7.16), which can be explained by the relevant variation of local magnetic field as mentioned in Sect. 6.2.

7.6.1.2 Event 2: 2002 September 9 [160, 161]

The time resolution of optical observations is commonly lower than that of radio and X-ray. A high-cadence observation of Big Bear Solar Observatory is compared with the simultaneous observations of OVSA, SOHO, and RHESSI in the 2002 September 9 event for analyzing the spatial and temporal feature of loop interaction in this event. Figure 7.17a gives a SOHO/EIT image with the collision of a double loop system overlaid by OVSA 4.8 GHz contours, which is just located in the joint part of the double loop system, a_1, a_2 and b_1, b_2 are respectively two groups of optical conjugated bright points in respect to the feet of the double loop system (see Fig. 7.17d). Figure 7.17b gives an image of OVSA 6.2 GHz overlaid by RHESSI 12–25 keV contours, which are all located nearby the loop top or joint part of the double loop system. Figure 7.17c gives an image of SOHO/MDI overlaid by the OVSA 7.8 GHz contours, which shows that the two groups of optical conjugated bright points

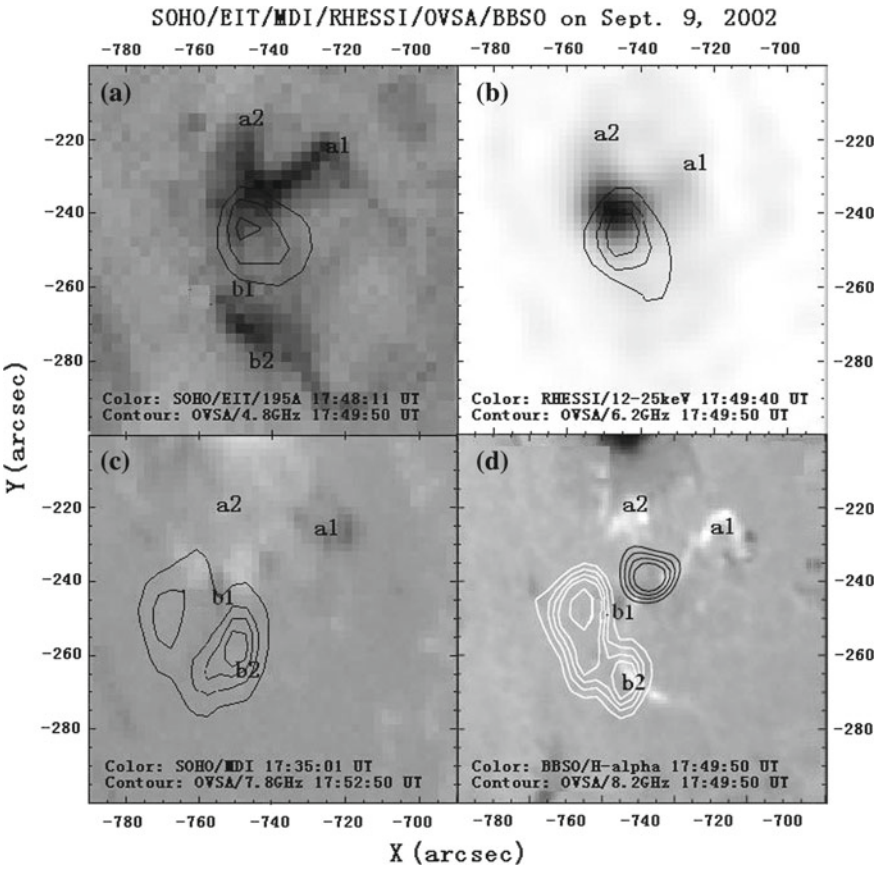

Fig. 7.17 Observations of BBSO, OVSA, SOHO, and RHESSI in the 2002 September 9 event

correspond to two group of diploe magnetic fields with opposite polarities, while the high-frequency radio emission moved to the feet of lower loop. The background of Fig. 7.17d is an image of BBSO overlaid by the OVSA 8.2 GHz (white) contours and RHESSI 12–25 keV (black) contours, which are respectively located in the feet of lower loop and the common loop top of the double loop system.

Figure 7.18 gives the time profiles of OVSA 5.0 and 8.2 GHz, RHESSI 12–25 and 25–50 keV, BBSO a_1, a_2 and b_1, b_2, which clearly show a common periodic structure with 10 sub-peaks (marked by 10 vertical lines) at different wavebands, and caused by a common effect of loop interaction. It is obvious that the correlation between optical and X-ray data, while two strong peaks appeared in radio data after the optical and X-ray flares decayed, which just corresponds to the maximum phases of optical emission at b_1 and b_2, thus there were possibly two regions in the flare energy release of this event [158].

Furthermore, we process a correlation analysis in Fig. 7.19 for the OVSA data at different frequencies around the duration (17:44:20–7:44:24 UT) of the first peak in Fig. 7.18.

It is interesting that there are two groups of opposite time delays toward the lower and higher frequencies, respectively appeared at 7.8 and 9.4 GHz (with the order of magnitude of 1 s, and in respect to the speed of 10^4 km/s), which means that the radio source (NT electrons) may be accelerated from the positions corresponding to 7.8 and 9.4 GHz, and propagate upward and downward simultaneously.

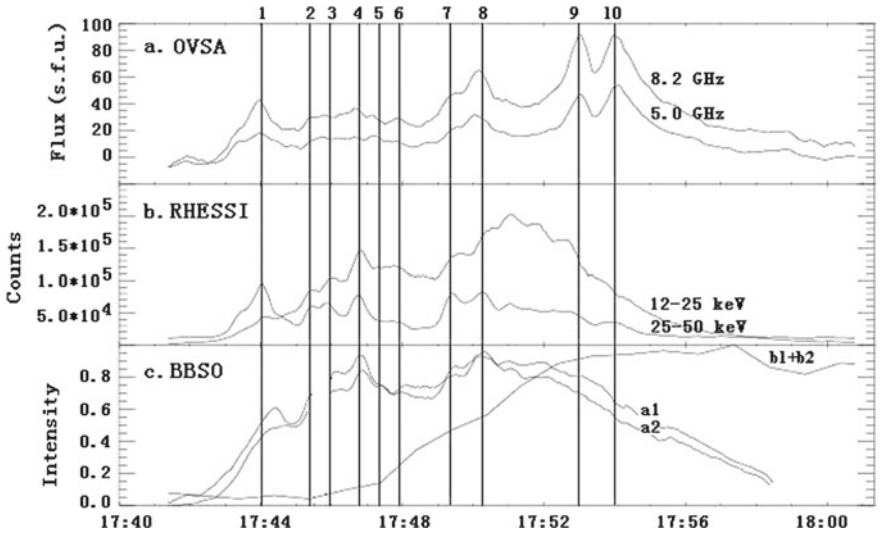

Fig. 7.18 Time profiles of BBSO, OVSA, and RHESSI in the 2002 September 9 event

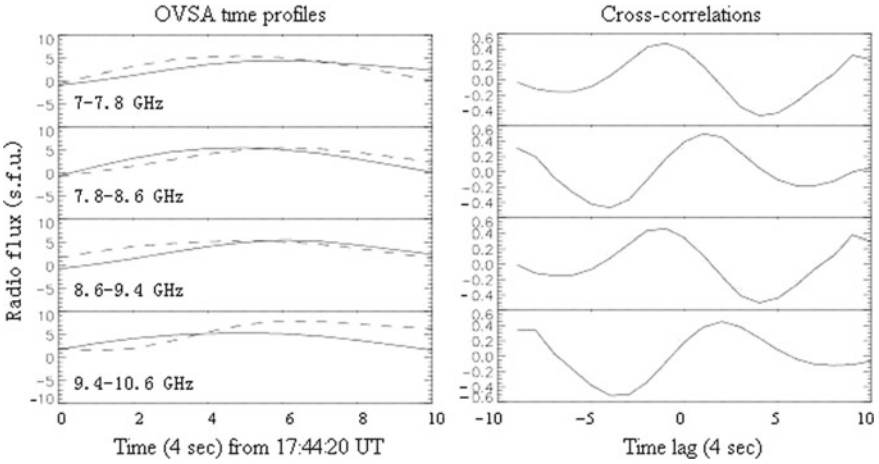

Fig. 7.19 Correlation analysis of OVSA data in the 2002 September 9 event

7.6.1.3 Event 3: 2003 October 24 [164]

The effect of loop interaction on the spectral evolution is rarely considered in previous studies. A new pattern of hard-soft-hard (HSH) has been found in the MW and HXR bursts with multiple sub-peaks, which is commonly originated from the periodical acceleration of NT electrons from the magnetic reconnection site excited by loop interaction. Moreover, a theoretical study shows an evident time delay between the HXR spectra in lower and higher energies, and with increasing of energies, the HXR spectrum becomes gradually synchronous with the MW one, due to the increasing trapping effect on the MW and HXR at higher energies [165], while the spectrum by trapped electrons will be harder that of originally injected electrons [166], thus to explain the HSH pattern naturally (see Sects. 3.3.3 and 5.4 for detail).

In a typical coronal loop, the magnetic field in loop top is weaker than that in the feet, to form a magnetic mirror, which implies that the trapping effect will be stronger in the loop top, and thus the HSH pattern in MW and HXR bursts is more easier to appear in the loop top. One limb flare occurred in 2003 October 24 as shown by Fig. A.3 in Appendix A with one SOHO/EIT image overlaid by the SOHO/MDI magnetogram, NoRH 17 GHz, RHESSI 15–20, and 35–40 keV contours, there is a loop-like structure with one top and two feet appeared in MW and HXR data, which are coincident basically with the SOHO/EIT image. Figure 3.56 shows the time profiles, spectral evolution, and the correlation between them in the loop top and feet, it is a little surprising that the HSH pattern appeared in the loop top and one foot (with an anti-correlation), while the common SHH pattern appeared in another foot (with a positive correlation), which can be well explained by the loop interaction as shown by the Trace image in Fig. A.4 of Appendix A, there was a compact loop interacted with a huge loop in the foot with HSH pattern, which is actually the top of the compact loop.

7.6.2 Statistical Evidence of Loop Interaction

A statistical study has been performed in 24 loop-like events of NoRH [167], which are divided into two groups, one with the LT spectrum always harder than that in the feet, and another with the LT spectrum at least softer than that in one foot (see Fig. 3.34), and these two groups just correspond to the standard model of a single flaring loop and the commonly observed interaction between a compact loop and a huge loop [148], respectively (see Fig. 3.35).

All the statistical results in Fig. 3.45 strong support that the asymmetry in two feet is more obvious in the second group with loop interaction, which cannot be simply explained by the relatively weaker asymmetry of magnetic mirror ratios in two feet (see Fig. 3.39), but well consistent with the stronger asymmetry of initial pith-angle distributions in two feet, and this also a statistical evidence for the loop interaction in the second group.

7.6.3 Conclusions

Some conclusions can be summarized from the above individual and statistical studies:

(1) The periodic variation with a period of seconds is an important feature in the magnetic reconnection caused by loop interaction, which commonly occurs in the initial phase of flares to be considered as a signature or precursor of flare-CME events.

(2) The altitude of magnetic reconnection or particle acceleration site can be evaluated from the analysis of the frequency drift and time delay among different radio frequencies.

(3) Due to the quasi-periodically injections of NT electrons caused by loop interaction, the HSH pattern may appear in each sub-peak of MW and HXR (at higher energies) bursts.

(4) The statistical study on the asymmetry of two feet shows that the double loop interaction may occupy 50% of total MW bursts.

7.7 Numerical Models and Observations of Chromosphere Evaporation

7.7.1 Introduction

In the strongly coupled solar atmosphere where the temperature and density change by several orders of magnitude from the chromosphere to the corona, chromospheric evaporation is one of the most important processes in solar flares and plays a key role

in the flare dynamics. Many processes are involved, such as the release, transport, and deposition of energy. Chromospheric evaporation is characterized by high-speed plasma upflows (blueshifts) in the spectroscopic observations. They are sometimes accompanied by chromospheric condensation, which is characterized by plasma downflows (redshifts). The study of chromospheric evaporation from the theoretical and observational perspectives has achieved great progress and is still one of the hot topics in modern solar physics. The numerical models and results of observations from ground-based and space-borne solar telescopes are described briefly as follows.

7.7.2 Numerical Models

Since the 1980s, a large number of numerical models have been proposed to simulate the hydrodynamics of the flare atmosphere responds to the energy input. For the sake of simplicity, most of the models are one-dimensional (1D), i.e., the plasmas are constrained within a flare loop and can move only along the loop. According to the energy source, the models are generally divided into two types: thermal and non-thermal (NT) models.

7.7.2.1 NT Models

In the NT models, the flare occurs with a beam of accelerated electrons. The upper atmosphere is heated to ~10 MK through Coulomb collisions of the electrons with the ambient dense plasmas. Meanwhile, HXR emissions are produced by the energetic electrons through Bremsstrahlung. It is also called thick-target model [168].

One of the most successful models of flare loop dynamics is proposed [169–171], which solves the 1D hydrodynamics of the flare atmosphere heated by a beam of energetic electrons. It also takes the thermal conduction and radiative losses into account. The optically thick radiative loss rate is treated by solving a simplified radiative transfer equation. This model clearly reveals the physical nature of chromospheric evaporation, a consequence of energy imbalance at the upper chromosphere, where a substantial portion of the beam energy is deposited. However, the heating is counteracted by radiative losses. If the heating timescale is shorter than the radiative timescale, the injected energy cannot be radiated away and the local temperature should be increased rapidly to several MK. The overpressure drives the heated plasma upward into the corona, a process termed chromospheric evaporation. If the heating is strong enough, the overpressure can at the same time drive a condensed downward moving front, which is called chromospheric condensation. According to the injected NT energy flux, the chromospheric evaporation is divided into two types [170]. If the energy flux exceeds a critical value of $\sim 10^{10}$ erg cm^{-2} s^{-1}, then explosive evaporation takes place accompanied by blueshift at speeds of hundreds of km s^{-1} in the emission lines formed in the coronal temperature and redshifts at speeds of tens of km s^{-1} in the emission lines formed in the transition regions and chro-

mosphere. The upper limit of evaporation velocity is $\sim 2.35 c_s$, where c_s denotes the sound speed. If the energy flux is less than the threshold, gentle evaporation takes place accompanied by blueshifts at speeds of tens of km s^{-1} in all emission lines. Moreover, an analytical expression of the condensation lifetime was derived [172], $\tau = \pi\sqrt{H/g}$, where H and g stand for the gravitational scale height and acceleration of gravity in the chromosphere. The typical value of τ is ~ 1 min. Similar flare models heated by non-thermal electrons have also been proposed [173–175], which successfully reproduced the dynamic phenomena of chromospheric evaporation and condensation.

In the electron-heated model, the dynamic feature of chromospheric evaporation, characterized by the Doppler shifts and broadening of emission line profiles, depends essentially on the parameters of the beam as well as the initial atmosphere. A detailed investigation on the role of total energy flux ($10^{10} - 10^{11}$ erg cm^{-2} s^{-1}), spectral index (4−6), and low-energy cutoff (10−20 keV) in the Ca XIX line profiles was performed [176, 177]. It is concluded that higher peak electron beam flux, lower low-energy cutoff, and larger spectral indices all move the atmospheric response toward larger enhancements of the parameters of the corona. In a unified computational model, it was also found that atmospheric response to a beam of charged particles is strongly dependent on the accelerated particle cutoff energy and spectral index [177]. In addition, the effect of a nonuniform (tapered) loop geometry and preheating of the atmosphere was explored [178]. The upward velocity of evaporation is faster than the case of uniform loop geometry, while the upward velocity is greatly reduced and close to the observational results when the corona is preheated. After a detailed comparison with the Ca XIX line observed by Yohkoh/BCS, it was argued that none of the models can exactly reproduce all the observational features [179]. That is to say, a model with a lower initial density produces a too large evaporation velocity, while a model with a higher initial density yields too narrow line profiles. Recently, the importance of electron energy on the two types of evaporation was investigated [180]. It is revealed that the threshold between explosive and gentle evaporations is not fixed at a given beam energy flux. Instead, it strongly depends on the electron energy and duration of heating. A relation between the threshold energy flux (F) and the electron energy (E_*) is derived:

$$\log F = 6.99 + 2.43 \log E_* \,. \tag{7.7.1}$$

So far, the most sophisticated 1D flare model is the radiative hydrodynamic model [177, 181, 182], which is mostly based on the RADYN code [183]. The model solves the equations of mass conservation, momentum conservation, and internal energy conservation, which are coupled with equations of radiative transfer and statistical equilibrium. That means the radiative transfer within some strong lines, at least for H, He, and Ca II, are treated in detail. This model shows similar dynamics in the flare loop as the previous models. However, some new features appear owing to the inclusion of the ionization effect. There are two phases of dynamic responses, a gentle phase and an explosive phase. In the gentle phase, the energy deposited by the electron

beam is mostly consumed in ionizing the neutral atoms in the lower atmosphere and the temperature does not increase significantly. So, the atmosphere remains to be in quasi-equilibrium. Once the atmosphere is fully ionized, the input energy can no longer be radiated away. Hence, the temperature increases rapidly, resulting in a dynamic evolution of the atmosphere characterized by evaporation, condensation, waves, and shocks. The duration of gentle phase decreases with increasing flare class or non-thermal energy flux. Recently, the model is improved by including stochastic particle acceleration by turbulence or plasma waves [184]. The acceleration model can yield an electron distribution with a thermal component and a non-thermal one. The former tends to deposit energy in the corona rather than in the chromosphere. Thermal conduction front propagates downward and carries the bulk of the thermal energy to heat the transition region, where radiative loss is less efficient than in the chromosphere. Therefore, an energy flux much lower than 10^{10} erg cm^{-2} s^{-1} can also generate explosive evaporation and the velocity of chromospheric evaporation is higher than the case of power-law injection of electrons with a low-energy cutoff [185].

7.7.2.2 Thermal Models

1D Models

If the energy release results in a bulk heating of the plasma near the reconnection site instead of accelerating the electrons (protons), the lower atmosphere is heated by thermal conduction front propagating downward, which has been extensively simulated [186–188]. The hydrodynamic response of the lower atmosphere is similar to that in the non-thermal models. Upflows of heated plasma (evaporation) with a velocity of hundreds of km s^{-1} and downflows of compressed region (condensation) are well reproduced [186]. It was found that evaporation continues in the gradual phase [187]. In particular, they considered the soft X-ray (SXR) heating of the chromosphere by adopting a point source in addition to a plane source that was usually adopted. It was found that the importance of SXR heating depends on the coronal density. Conduction-driven models in the flare impulsive phase have also been proposed [189–191].

To resolve the discrepancies between observed SXR line properties and model results, a pseudo two-dimensional model was proposed [192], which is composed a series of 1D hydrodynamic loops with a semicircular shape but increasing radii. These 1D loops are heated successively and evolve independently to mimic the successive reconnection and formation of post flare loops. The spatial integrated emission feature can then be derived and compare with observations. The SXR brightening starts from the FPs and expands into the upper corona as a result of chromospheric evaporation. By adjusting the heating time duration in a single loop, such a pseudo 2D model is able to reproduce some typical observed feature that 1D models cannot explain, such as a dominant stationary component plus a blueshifted component in the SXR

lines. Besides, it can produce relatively slow but long-lasting evaporation that more favorably agrees with observations.

In principle, the evaporation velocity should be dependent on the energy released during the flare and the pre-flare condition. A quantitative relationship between these parameters is quite useful in spectral analysis and diagnostics of the flare energy release. Recently, in the framework of 1D gas dynamics, numerical experiments were performed to study the conduction-driven evaporation [193]. By assuming that the transition region can be represented by an isothermal density jump if the heating timescale is short, the maximum evaporation velocity can be expressed as $0.38(F/\rho)^{1/3}$, where F and ρ denote the energy flux and pre-flare coronal density. The condensation velocity is expressed as $10^{-4}(F/\rho)^{1/2}$. In a follow-up work, the effect of two different flare loop parameters (post-shock temperature and transition region temperature ratio) on the properties of the flow reversal point between evaporation and condensation was investigated [194]. The authors found that both of the evaporation characteristics (temperature and velocity–temperature derivative) have scaling-law relationships to the flare parameters.

2D MHD Models

Despite of the significant progress that 1D hydrodynamic models have achieved, they do not include details of the energy release via magnetic reconnection. The combination of magnetic reconnection and subsequent evaporation/condensation can only be accomplished in two-dimensional (2D) or three-dimensional (3D) MHD simulations. Hitherto, only a few works have been dedicated to such a combination [83, 195]. In their simulations, the magnetic energy released through magnetic reconnection is consistently converted into the thermal energy near the reconnection site and then conducted downward along the field lines. An adiabatic shock is initially formed at the reconnection site and separated into a conduction front and an isothermal slow-mode shock. Chromospheric evaporation is clearly revealed in such a 2D MHD simulation. A scaling law is discovered between the flare loop apex temperature (T_A) and the coronal magnetic field strength (B), i.e., $T_A \propto B^{6/7}$. The velocity of evaporation is slower than that in 1D models, which is explained by the lack of non-thermal electron beams [195].

Combination of the radiative hydrodynamic modeling and observations of flares is worthwhile to perform diagnostics of the energy release [196]. It is noted that Alfvénic waves propagating from the corona to the chromosphere, may also play a role in heating the upper chromosphere and driving explosive evaporation [197].

7.7.3 Observations of Chromospheric Evaporation

7.7.3.1 Explosive Evaporation

As mentioned above, explosive chromospheric evaporation features high-speed upflows in the emission lines formed in the corona and downflow in the emission lines

formed in the transition region and chromosphere. The multiwavelength observations of explosive evaporations are abundant, especially in the typical two-ribbon flares, compact flares, and even in microflares. Recently, the investigations on circular-flare ribbons have unveiled some interesting results.

Two-Ribbon and Compact Flares

In the context of 2D standard flare model [45, 47, 48, 198], the accelerated non-thermal electrons propagate downward along the newly reconnected magnetic field lines. The chromosphere is heated up to 10^7 K [199] and two bright flare ribbons form at the FPs of the flare loops observed in Hα, Ca II H, He I 10830 Å, UV, and EUV wavelengths.

In the 1980s, instruments for solar observations were mostly ground-based with lower resolutions and cadences. However, important and fundamental discoveries have been made in some of the pioneering works. In the flare of 1980 May 7 observed by SMM and the Sacramento Peak Observatory (SPO) in Hα wavelength, it was found that chromospheric evaporation has taken place concurrently with the appearance of SXR [200]. The authors further estimated the total emission measure and number of electrons of the evaporated material in the coronal loops. It is concluded that evaporation is driven by two mechanisms. Flare-accelerated electrons and thermal conduction play a major role during the impulsive phase and thermal (gradual) phase, respectively. NT velocity of $\geq 100\,\mathrm{km\ s^{-1}}$ and upward velocity of $300-400\,\mathrm{km\ s^{-1}}$ are detected in the Ca XIX and Fe XXV spectral lines [200]. In a followup work [201], it was found that the evaporation velocity is correlated with the spectral index of the HXR flux and with the rise time of the thermal emission measure of the coronal plasma. In addition, the emission measure of the evaporated material is correlated with the total energy deposited by the non-thermal electrons in the chromosphere. Later on, correlation between the blueshifted velocity and the HXR intensity (flux) was discovered [202]. Using the observations of four flares, it was discovered [203] that the total momentum of upflows of evaporation plasma in SXR equal to that of the downflows of condensation plasma in Hα (see Fig. 7.20). The momentum balance of explosive evaporation is proved by quantitative calculations based on observations from the state-of-the-art space telescopes [204, 205].

Before the launch of SOHO, the BCS aboard Yohkoh spacecraft is the most important instrument for spectroscopic observations of the Sun, thanks to its high resolution and wide temperature coverage [206]. An X1.5 flare observed by Yohkoh and Mees Solar Observatory in Hα was studied [207]. It is demonstrated that the upflowing and downflowing plasma originate in the same locations. The Ca XIX SXR spectra of four flares was analyzed [208] and found that the upflows last for $4-10$ min with velocities ranging from 180 and $320\,\mathrm{km\ s^{-1}}$. A correlation between the NT turbulent velocity and upflow velocity is discovered and justified by the observations from more sophisticated telescopes [209].

The CDS aboard SOHO contributed remarkably to our understanding of chromospheric evaporation, though the spatial resolution is not so high [210]. During the gradual phase of an M6.8 flare on 1998 April 29, it was found [211] both upflows and downflows in transition region and coronal lines, indicating explosive evaporation as

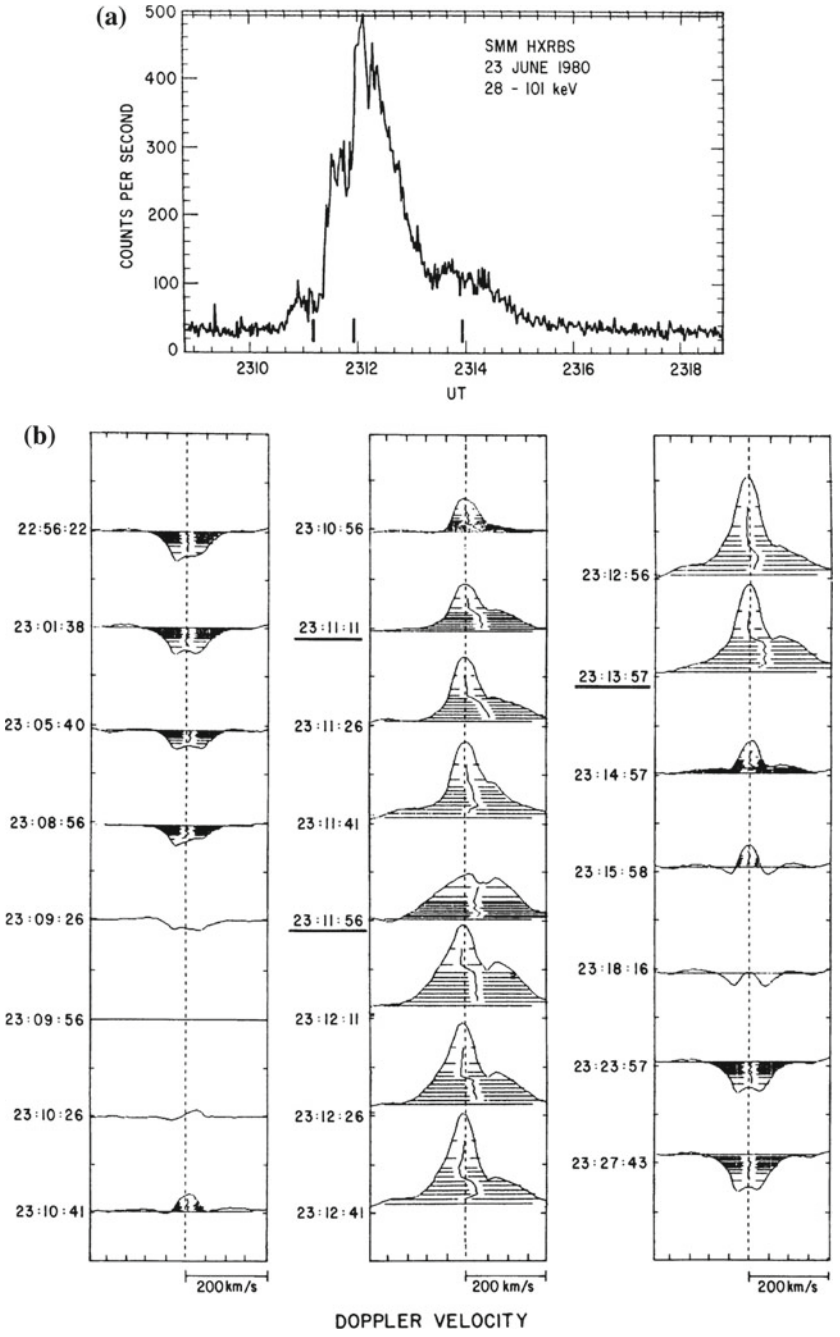

Fig. 7.20 Upper panel: HXR count rate observed by SMM on 1980 June 23. Lower panel: Hα line profiles observed by SPO, with bisectors drawn at the intensity levels indicated by the horizontal striations centered within the most intense emission. Adapted from the Ref. [203]

a result of ongoing magnetic reconnection. The blueshifted regions are located at the outer edge of flare ribbons observed in both EUV and Hα wavelengths (see Fig. A.36 in Appendix A). The momentum of the upflows and downflows balance each other, which agrees with the numerical models [212]. During the impulsive phase of an M2.2 flare, upflows at a speed of $\sim$230 km s^{-1} in Fe XIX and downflows at speeds of 36 and 43 km s^{-1} at chromospheric and transition region lines are observed [213]. Using the observed values of spectral index of electron spectrum and a low-energy cutoff, a quantitative estimation of the electron energy flux ($\geq 4 \times 10^{10}$ ergs cm^{-2} s^{-1}) based on the thick-target flare model suggests that the explosive evaporation is driven by non-thermal electron beam. Interestingly, flare-like explosive evaporation is detected at a location remote from the primary region of particle acceleration [214]. The remote region and the primary region are probably connected by a large-scale, closed coronal loop that guides the accelerated electrons.

Despite of substantial investigations on chromospheric evaporation, detailed analysis of the cooling of the evaporated material are rare. An M6.3 flare on 2001 June 15 observed by CDS was studied [215]. The O III, O V, and Mg X lines exhibit multiple components and downflows. The downflows at speeds of $\leq$ 100 km s^{-1} are considered as the "warm rain" falling back to the Sun due to cooling and condensing coronal flare plasma following chromospheric evaporation during the impulsive phase.

Although the CDS aboard SOHO achieved a big success, the EIS aboard Hinode had better performance and more exciting outcomes [216]. In a C1.1 flare on 2007 December 14, simultaneous blushifts in the hot emission lines (Fe XIV–Fe XXIV) and redshifts in the relatively cool lines (O VI–Fe VIII) are observed by Hinode/EIS [217]. The upflow velocity (v_{up} [km s^{-1}]) of evaporation scales with temperature (T [MK]) as $v_{up} \approx 8 - 18T$ in the range of 2–16 MK. The downflow velocity (v_{down} [km s^{-1}]) of condensation scales with T as $v_{down} \approx 60 - 17T$ in the range of 0.5–1.5 MK. The conversion temperature between the upflow and downflow is $\sim$1.5 MK (see Fig. 7.21). Since chromospheric evaporation is accompanied by line broadenings due to a superposition of flows (turbulence), there is a strong correlation between the Doppler velocity and NT velocity [218–221]. The electron number density at the flare FPs can increase up to a few 10^{10} cm^{-3} [222–224]. A significant correlation is discovered between the electron density and NT velocity [220, 225].

On 27 June 2013, IRIS was successfully launched. It obtains spectra of emission lines in FUV and NUV passbands formed in the chromosphere and transition region. Slit-jaw imager is used to obtain images in four passbands [226]. Covering a great temperature range from 0.5 to 10 MK, IRIS has unprecedented spatial, temporal, and spectral resolutions to study the solar activities more clearly, though the FOV ($130'' \times 175''$) is limited. Hitherto, there has been extensive studies on solar flares using the observations of IRIS, most of which combine the spectral data with the full-disk images of SDO/AIA [227]. In a C1.6 flare on 2014 April 19, it was reported [228] the detection of upflows of $\sim$260 km s^{-1} in Fe XXI line and downflows in the cool emission lines (Si IV, O IV, C II, and Mg II) at the FPs of the flare loop. The results are consistent with the theory of electron-driven explosive evaporation. Additional evidence of such scenario come from the correlation between the HXR fluxes and the

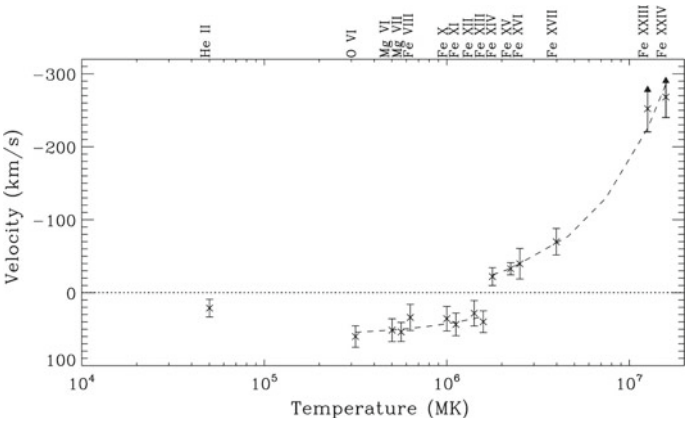

Fig. 7.21 Plasma velocity from a flare footprint as a function of T for each of the emission lines. Adapted from the Ref. [217]

Doppler velocities of explosive evaporations [209, 229], see Fig. A.37 in Appendix A. During the decay phase of flares when the flare loops are filled with hot plasmas, thermal conduction from the corona to the chromosphere plays a dominant role in driving continuous evaporation [230]. Interestingly, the Doppler velocities and line widths at the flare ribbons show quasi-periodic pulsations (QPPs) with periods of several minutes [231, 232], which is explained by periodic particle accelerations from the magnetic reconnection site and precipitations in the chromosphere.

The IRIS "sit-and-stare" observation model enables scientists to investigate the temporal evolution of the flare more accurately. For the X1.6 flare on 2014 September 10, the velocity of upflows in Fe XXI line decreases from ∼300 km s^{-1} to zero within ∼720 s, while the velocity of downflows in Mg II line decreases from ∼40 km s^{-1} to a few km s^{-1} within ∼60 s (see Fig. 7.22), which is consistent with the 1D hydrodynamic simulations [172, 233]. In a C6.5 flare, the velocity of upflows in Fe XXI line decreases from ∼82 km s^{-1} to ∼15 km s^{-1} within 720 s, and the non-thermal line width decreases [234] from ∼130 km s^{-1} to ∼50 km s^{-1}. The timescale of evaporation is comparable to the values obtained by EIS [235]. It is noticed that the starting times of downflows (condensation) and upflows (evaporation) are not coincident, but have a delay of tens of seconds, probably due to the weak Fe XXI emission at the earliest initiation of flare [233, 236].

Circular-Ribbon Flares

Occasionally, circular flare ribbons appear accompanied by remote brightening, which is believed to be associated with a magnetic null point where the magnetic field vanishes ($\boldsymbol{B} = \boldsymbol{0}$) and the dome-like fan-spine topology [237–239]. Such a 3D magnetic topology usually corresponds to a parasitic polarity surrounded by the main opposite polarity in the photosphere [240, 241]. So far, chromospheric evaporation and condensation in circular-ribbon flares have rarely been investigated. In a pio-

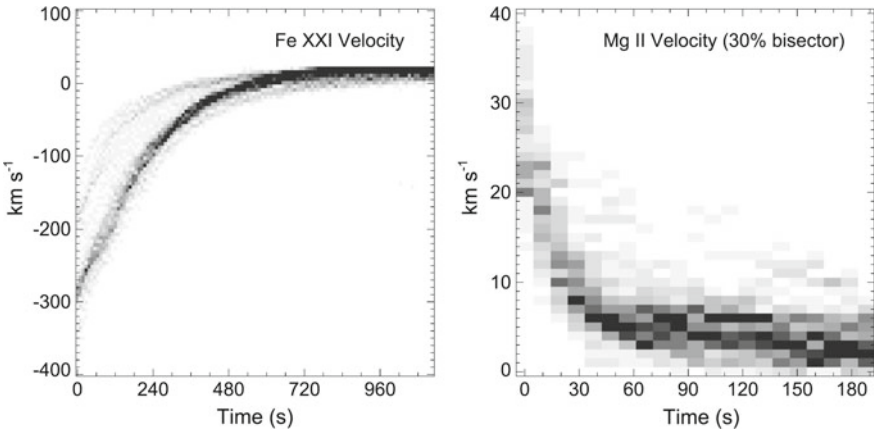

Fig. 7.22 Superposed epoch analysis of Fe XXI and Mg II flows. The grayscale darkens with increasing occurrence within a given velocity interval. Adapted from the Ref. [223]

neering work [242], it was studied the red asymmetry of Hα line profiles of 4 flares, two of which occurring on June 20 and June 21 in 1982 were indeed circular-ribbon flares. It is concluded that the redshifted emission streaks of Hα line are due to the continuous downward motion in the flare chromospheric region with velocities of $40-100\,\mathrm{km\ s^{-1}}$. However, the cadence of observation was relatively lower.

The spectroscopic observations of IRIS with high cadence and high resolution provide a good opportunity to study circular-ribbon flares. Using the combined observations from SDO, IRIS, and RHESSI [243] on 2015 October 16, it was discovered explosive chromospheric evaporations in a GOES C4.2 circular-ribbon flare that was located in AR 12434 [244]. The impulsive phase of the flare was characterized by plasma upflow ($35-120\,\mathrm{km\ s^{-1}}$) observed in the high-temperature Fe XXI λ1354.09 line. At the same time, downflow ($10-60\,\mathrm{km\ s^{-1}}$) was observed in the low-temperature Si IV λ 1393.77 line. The inner flare ribbon (IFR) where chromospheric evaporation occurred was cospatial with the single HXR source at $12-25\,\mathrm{keV}$. A quantitative estimation based on the thick-target model shows that the electron energy flux exceeds the threshold value for explosive evaporation [172]. Therefore, it is concluded that the explosive chromospheric evaporation in the circular-ribbon flare was most likely driven by the NT electrons accelerated by magnetic reconnection (see Fig. A.38 in Appendix A).

Using the "two-step" raster observations of IRIS with a cadence of 6 s in a follow-up work [245], another one of homologous circular-ribbon flares on 2015 October 16 was studied. During the impulsive phase of the flare, plasma downflow was observed at the CFR in the Si IV λ1402.77 line, suggesting explosive chromospheric condensation. The downflow Doppler velocity of the CFR increased rapidly from a few $\mathrm{km\ s^{-1}}$ to the peak values of $45-52\,\mathrm{km\ s^{-1}}$. Afterwards, it decreased gradually to the initial level within 3−4 min, indicating ongoing magnetic reconnection. Some interesting results are also revealed thanks to the high cadence of IRIS. The downflow speeds

are positively correlated with logarithm of the Si IV line intensity and time derivative of the SXR flux. For the C3.1 flare in this study, RHESSI data was unavailable. So, there were no HXR images and light curves. However, radio dynamic spectra were characterized by a type *III* radio burst associated with the flare, implying that the chromospheric condensation was most probably driven by non-thermal electrons. Based on the results of 1D numerical simulation [246] and the observed peak Doppler velocity of condensation, a lower limit of energy flux of the precipitating electrons is estimated. Since the slit positions were located at the western part of the CFR far from the IFR, the intensity of Fe XXI line was too weak to derive convincing upward Doppler velocities.

Microflares

Explosive chromospheric evaporation exists not only in typical flares, but also in microflares, where the total energy budget is lower by six orders of magnitude. Three microflares observed by SOHO/CDS and RHESSI were studied [247]. The three events present different dynamics in the chromosphere and transition region. There are downflows of $\leq 40\,\mathrm{km\ s^{-1}}$ in the first one, upflows of $\leq 40\,\mathrm{km\ s^{-1}}$ in the second one, and coexisting upflows and downflows of $\leq 20\,\mathrm{km\ s^{-1}}$ in the third one. NT electron beams are believed to drive the evaporations in the microflares. A B-class flare with temperature of $\sim$15 MK was studied [248]. Weak upflow velocities ($\sim 14\,\mathrm{km\ s^{-1}}$) in emission lines and downflow velocities ($\sim 14\,\mathrm{km\ s^{-1}}$) in hot Fe XV line ($T \approx 2$ MK) are observed by Hinode/EIS, which is a surprising result that could not be well explained by current flare models. During the precursor of a microflare on 2009 July 5, redshifted O V emission is detected, implying explosive evaporation. However, the blushifts in Fe XIX and Si XII lines are absent [249]. The authors concluded that explosive evaporation occurs at either low temperature ($T < 2$ MK) or high temperature ($2 < T < 8$ MK) where CDS observations are not sensitive. The most direct evidence of explosive evaporation in a microflare come from the observation by Hinode/EIS on 2007 December 7 [250]. Temperature-dependent upflows and downflows in the impulsive phase are found. The conversion temperature between upflows to downflows is < 1 MK (see Fig. 7.23).

As mentioned above, the threshold value of energy flux is dependent on the electron energy [180], indicating that a lower energy flux is sufficient for driving evaporation for the low-energy electrons. This could explain why explosive evaporations can also take place in microflares.

7.7.3.2 Gentle Evaporation

Contrary to the explosive evaporation, gentle evaporation features upflows in all the emission lines [251]. Direct evidence of gentle evaporation during the impulsive phase of a C9.1 flare is reported [252]. Plasma upflows of $10-110\,\mathrm{km\ s^{-1}}$ are observed in transition region and coronal lines, which results from low flux of non-thermal electrons rather than thermal conduction (see Fig. 7.24). Gentle evaporation during the gradual phase of an X17 flare is reported [253]. In the EUV lines, upflows

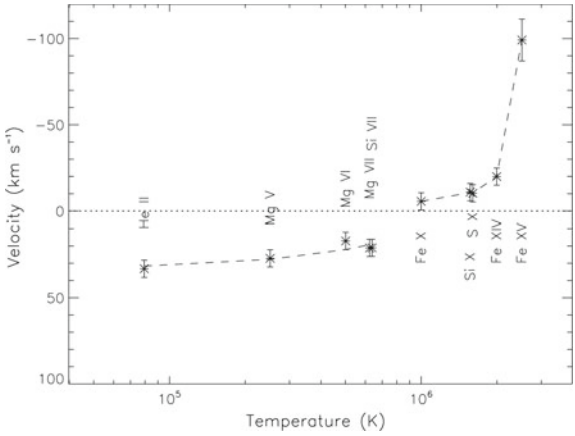

Fig. 7.23 Velocities of evaporated plasma as a function of the formation temperature. Adapted from the Ref. [250]

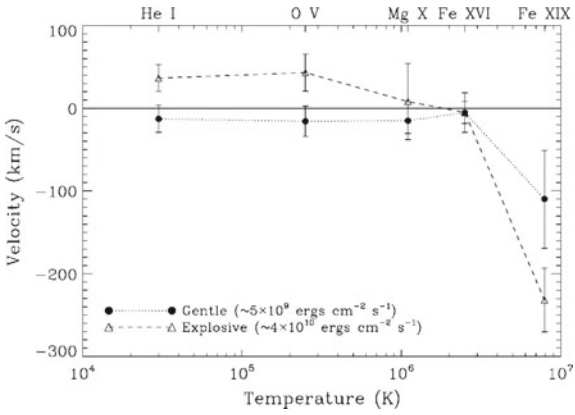

Fig. 7.24 Plasma velocity as a function of temperature for each of the CDS lines. Adapted from the Ref. [252]

at speeds of $\leq 60\,\mathrm{km\ s^{-1}}$ are observed in the outer edges of the ribbons of the two-ribbon flare, which is considered to be caused by heating near the top of the flare loop arcade. It was presented [254] the first detection of gentle evaporation during the cooling phase of a flare in the SXR Mg XI line. It is found that the upward flux of enthalpy transported by the evaporating plasma has a linear correlation with the downward flux of thermal energy conducted from the corona, indicating conduction-driven evaporation. Gentle evaporation can also take place in microflares at speeds of $\leq 20\,\mathrm{km\ s^{-1}}$, which is likely caused by NT electrons [255]. Using the IRIS observations of an M-class flare, a subsonic blueshift of $\sim 50\,\mathrm{km\ s^{-1}}$ that lasted for several minutes in the hot Fe XXI line was observed [256]. The authors concluded that the gentle evaporation was driven by heating of the chromosphere by non-thermal electrons and by a heat flux from the energy release site.

7.7.3.3 Coexisting Gentle and Explosive Evaporations

During the whole evolution of a flare, the origin and amount of energy for heating the flare loops should change with time. Therefore, conversion from one type to the other type of evaporation is expected. In an M1.5 flare observed by SOHO/CDS, explosive and gentle evaporation take place during the first and second rapid intensity increase in Fe XIX, respectively. There are two possibilities to account for the conversion. One is an increased absorption of beam energy during the gentle event since the beam passed through an atmosphere modified by the explosive event. The other is a decreased acceleration of non-thermal electron beams via magnetic reconnection [257]. In an M2 flare on 2001 April 24, gentle evaporation takes place during both precursor events observed in O III, O IV, O V, Ne VI, and He II lines. Explosive evaporation occurs during the impulsive phase, which is characterized by downflows at speeds of $\sim$40 km s^{-1} in the above cool lines and upflows at speeds of 60$-$80 km s^{-1} in the hotlines. In another C-class flare, gentle evaporation with upflows of $\sim$90 km s^{-1} in Fe XIX line take place at the flare onset. Explosive evaporations with upflows of $\sim$80 km s^{-1} in Fe XIX line and downflows of $\sim$20 km s^{-1} in He I and O V lines take place during the impulsive phase [258]. 0-dimensional hydrodynamic simulation using the EBTEL model [259], it is indicated that both thermal conduction and NT beam heating play important roles in heating the flare plasma. In the X1.0 flare on 2014 March 29, gentle and explosive evaporation occur at different locations in the impulsive phase and flare peak, respectively [260]. More importantly, dominant blueshifts in Fe XXI were detected, which is in agreement with theoretical predictions. Owing to the relatively lower resolutions, previous spectroscopic observations show a dominant stationary component plus a blueshifted component in hot emission lines, contrary to the evaporation model. Careful analysis of a C4.2 flare on 2007 January 16 shows that different patterns of evaporation at different locations of the flare, implying different heating mechanisms in the flare region [261].

7.7.4 X-Ray and Radio Imaging Observations

Apart from the spectroscopic observations of chromospheric evaporation, direct imaging observations in SXR, HXR, and radio wavelengths are also reported. The flare on 1994 June 30 was studied [262]. During the impulsive phase, displacement of footprint sources in HXR and SXR are observed, which is interpreted to be the images of the evaporating front projected onto the solar disk. Using the high-resolution observations of 13 transient brightening by Hinode/XRT [263], it was found that all of them have a pair of evaporation upflows moving symmetrically from the FPs of a magnetic loop at speeds of 100$-$500 km s^{-1}. In two sympathetic coronal bright points observed by Hinode/XRT, which are connected with the primary bright point, a possible signature of gentle evaporation at speeds of $\sim$76 and $\sim$47 km s^{-1} was identified [264]. However, the possibility of reflecting slow-mode wave cannot be excluded.

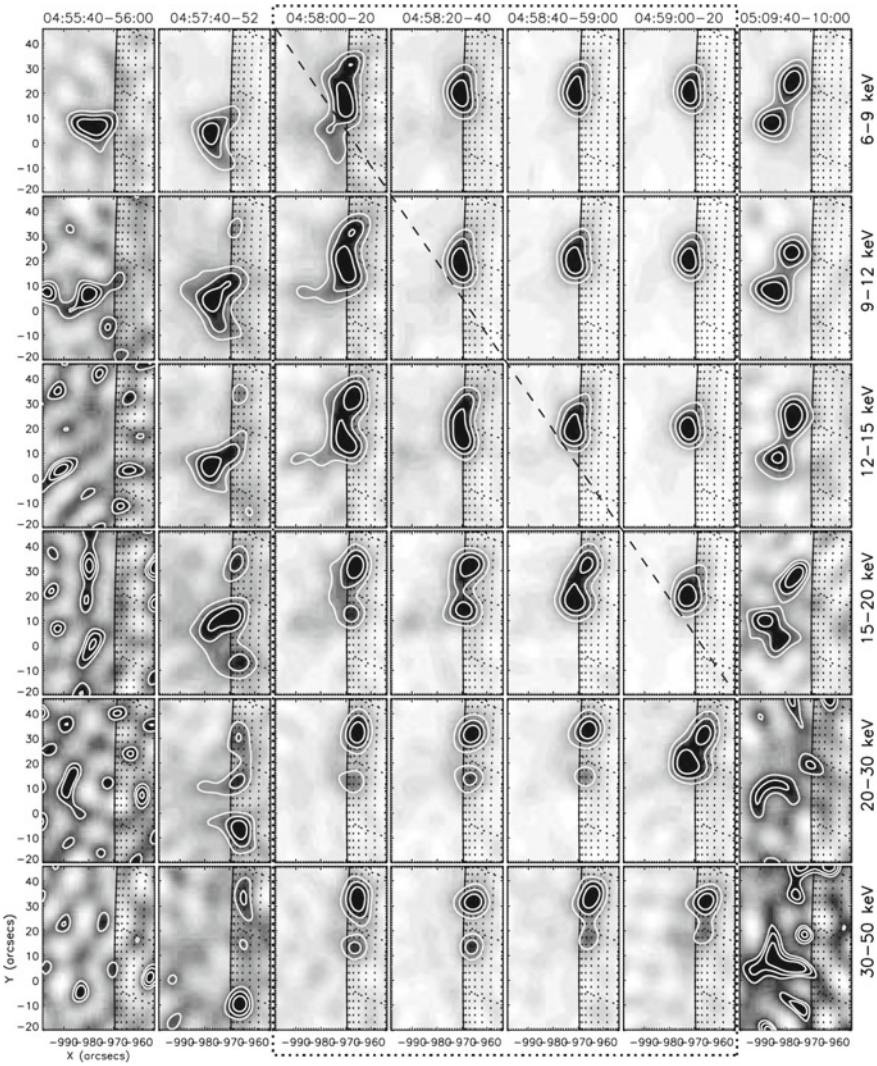

Fig. 7.25 Mosaic of CLEAN images at different energies (rows) and times (columns). Contour levels are set at 40, 60, and 80% of the maximum brightness of each image. Adapted from the Ref. [265]

The evolution of the HXR sources during the impulsive phase of an M1.7 flare on 2003 November 13 was investigated [265]. It is found that the HXR emission moves above the FPs and finally merge into a single LT source at speeds of hundreds of km s^{-1}. The merging of HXR sources starts at low energies and proceeds to higher energies, which is explained by continuous electron-driven chromospheric evaporation (see Fig. 7.25). In an M1.0 flare on 2004 December 1, a similar merging

process of HXR emission from the FPs to the LT in the energy band of 10−15 keV was observed [137]. Interestingly, the authors also noticed two groups of parallel-drifting structures in the radio spectra, which is explained by chromospheric evaporation. The radio dynamic spectra (0.1−3 GHz) of 21 flare episodes and detected slowly drifting high-frequency cutoffs with drift rates of -41 ± 32 MHz s^{-1} was analyzed [266]. Based on a coronal loop density model, the velocity of evaporation upflow is estimated to be 236 km s^{-1}. In the context of standard flare model based on magnetic reconnection, the converging motions of the HXR sources seem to be ubiquitous [134, 138, 267].

7.7.5 Summary

In the past four decades, the research on chromospheric evaporation has made enormous strides both theoretically and observationally, thanks to the scientific instruments aboard the ground-based (e.g., BBSO) and space-borne solar telescopes (e.g., SMM/BCS, Yohkoh/BCS, SOHO/CDS, Hinode/EIS, IRIS, RHESSI, Trace, STEREO, SDO, etc.). The progresses are briefly summarized as follows:

1. There are mainly two numerical models to account the heating of flare atmosphere and driving chromospheric evaporation. In the non-thermal flare model, electron beams accelerated via magnetic reconnection transport along the reconnected magnetic field lines and precipitate downward into the chromosphere, resulting heating of the cool and dense plasma. In the thermal model, the energy is conducted downward into the chromosphere by heat flux. Both electron beams and thermal conduction can drive upward evaporation into the coronal loops and downward condensation. The momentum of evaporation and condensation balance each other.
2. If the energy flux for heating the chromosphere exceeds a critical value, explosive evaporation occurs at the flare ribbons, which is characterized by upflow observed in the hot emission lines formed in the corona and downflow observed in the cooler lines formed in the chromosphere and transition region. Otherwise, gentle evaporation occurs, which is characterized by upflows observed in all emission lines.
3. Both kinds of evaporations exist in two-ribbon flares, compact flares, circular-ribbon flares, and even microflares, indicating the same process happens at various scales. Evaporation could appear at the pre-flare (precursor) phase, impulsive (rise) phase, and gradual (decline) phase of flares. Generally speaking, thermal conduction and/or electron beams with lower energy flux play a role in the pre-flare phase, electron beams with higher energy flux play a key role in the impulsive phase, and thermal conduction plays a dominant role in the gradual phase [231, 268]. Conversions from one type to the other type have been reported. Besides, different patterns of flows could exist at different locations of the same flare.

4. In the future, comprehensive and self-consistent numerical modeling, including the whole process of magnetic reconnection, particle acceleration, energy precipitation, and evaporation, is required. More telescopes using advanced techniques are expected. Higher resolutions, faster cadences, and better performances of the telescopes will undoubtedly unveil new phenomenon in the solar atmosphere and deepen our understanding on the flare dynamics.

References

1. Bogachev, S.A., Somov, B.V., Kosugi, T., Sakao, T.: The motions of the hard X-Ray sources in solar flares: images and statistics. Astrophys. J. **630**, 561–572 (2005)
2. Ji, H., Wang, H., Goode, P.R., Jiang, Y., Yurchyshyn, V.: Traces of the dynamic current sheet during a solar flare. Astrophys. J. **607**, L55–L58 (2004)
3. Shen, J., Zhou, T., Ji, H., Wang, N., Cao, W., Wang, H.: Early abnormal temperature structure of X-Ray loop-top source of solar flares. Astrophys. J. **686**, L37–L40 (2008)
4. Ji, H., Huang, G., Wang, H., Zhou, T., Li, Y., Zhang, Y., Song, M.: Converging motion of Hα conjugate Kernels: the signature of fast relaxation of a sheared magnetic field. Astrophys. J. **636**, L173–L174 (2006)
5. Ji, H., Wang, H., Liu, C., Dennis, B.R.: A hard X-Ray sigmoidal structure during the initial phase of the 2003 October 29 X10 flare. Astrophys. J. **680**, 734–739 (2008)
6. Sui, L., Holman, G.D.: Evidence for the formation of a large-scale current sheet in a solar flare. Astrophys. J. **596**, L251–L254 (2003)
7. Sui, L., Holman, G.D., Dennis, B.R.: Evidence for magnetic reconnection in three homologous solar flares observed by RHESSI. Astrophys. J. **612**, 546–556 (2004)
8. Fletcher, L., Hudson, H.S.: Spectral and spatial variations of flare hard X-ray footpoints. Sol. Phys. **210**, 307–321 (2002)
9. Krucker, S., Hurford, G.J., Lin, R.P.: Hard X-Ray source motions in the 2002 July 23 Gamma-Ray flare. Astrophys. J. **595**, L103–L106 (2003)
10. Li, Y.P., Gan, W.Q.: The oscillatory shrinkage in TRACE 195 Å loops during a flare impulsive phase. Astrophys. J. **644**, L97–L100 (2006)
11. Zhou, T.-H., Wang, J.-F., Li, D., Song, Q.-W., Melnikov, V., Ji, H.-S.: The contracting and unshearing motion of flare loops in the X 7.1 flare on 2005 January 20 during its rising phase. Res. Astron. Astrophys. **13**, 526–536 (2013)
12. Svestka, Z.F., Fontenla, J.M., Machado, M.E., Martin, S.F., Neidig, D.F.: Multi-thermal observations of newly formed loops in a dynamic flare. Sol. Phys. **108**, 237–250 (1987)
13. Veronig, A.M., Karlický, M., Vršnak, B., Temmer, M., Magdalenić, J., Dennis, B.R., Otruba, W., Pötzi, W.: X-ray sources and magnetic reconnection in the X3.9 flare of 2003 November 3. Astron. Astrophys. **446**, 675–690 (2006)
14. Hudson, H.S.: Implosions in coronal transients. Astrophys. J. **531**, L75–L77 (2000)
15. Ji, H., Huang, G., Wang, H.: The relaxation of sheared magnetic fields: a contracting process. Astrophys. J. **660**, 893–900 (2007)
16. Shen, J., Zhou, T., Ji, H., Wiegelmann, T., Inhester, B., Feng, L.: Well-observed dynamics of flaring and peripheral coronal magnetic loops during an M-class limb flare. Astrophys. J. **791**, 83–91 (2014)
17. Liu, R., Liu, C., Török, T., Wang, Y., Wang, H.: Contracting and erupting components of sigmoidal active regions. Astrophys. J. **757**, 150–162 (2012)
18. Wang, H.: Evolution of vector magnetic fields and the August 27 1990 X-3 flare. Sol. Phys. **140**, 85–98 (1992)
19. Wang, H., Ewell Jr., M.W., Zirin, H., Ai, G.: Vector magnetic field changes associated with X-class flares. Astrophys. J. **424**, 436–443 (1994)

20. Wang, S., Liu, C., Liu, R., Deng, N., Liu, Y., Wang, H.: Response of the photospheric magnetic field to the X2.2 flare on 2011 February 15. Astrophys. J. **745**, L17–L22 (2012)
21. Jing, J., Song, H., Abramenko, V., Tan, C., Wang, H.: The statistical relationship between the photospheric magnetic parameters and the flare productivity of active regions. Astrophys. J. **644**, 1273–1277 (2006)
22. Sun, X., Hoeksema, J.T., Liu, Y., Wiegelmann, T., Hayashi, K., Chen, Q., Thalmann, J.: Evolution of magnetic field and energy in a major eruptive active region based on SDO/HMI observation. Astrophys. J. **748**, 77–93 (2012)
23. Hudson, H.S., Fisher, G.H., Welsch, B.T.: Flare Energy and magnetic field variations. In: Howe, R., Komm, R.W., Balasubramaniam, K.S., Petrie, G.J.D. (eds.) Subsurface and Atmospheric Influences on Solar Activity. ASP Conference Series, vol. 383, pp. 221–226 (2008)
24. Fisher, G.H., Bercik, D.J., Welsch, B.T., Hudson, H.S.: Global forces in eruptive solar flares: the lorentz force acting on the solar atmosphere and the solar interior. Sol. Phys. **277**, 59–76 (2012)
25. Hudson, H.S., Lemen, J.R., St. Cyr, O.C., Sterling, A.C., Webb, D.F.: X-ray coronal changes during Halo CMEs. Geophys. Res. Lett. **25**, 2481–2484 (1998)
26. Sakurai, T., Shibata, K., Ichimoto, K., Tsuneta, S., Acton, L.W.: Flare-related relaxation of magnetic shear as observed with the Soft X-ray telescope of YOHKOH and with vector magnetographs. Publ. Astron. Soc. Japan **44**, L123–L127 (1992)
27. Rust, D.M., Kumar, A.: Evidence for helically kinked magnetic flux ropes in solar eruptions. Astrophys. J. **464**, L199–L202 (1996)
28. Taylor, J.B.: Relaxation and magnetic reconnection in plasmas. Rev. Mod. Phys. **58**, 741–763 (1986)
29. Rust, D.M., Kumar, A.: Helical magnetic fields in filaments. Sol. Phys. **155**, 69–97 (1994)
30. Voslamber, D., Callebaut, D.K.: Stability of force-free magnetic fields. Phys. Rev. **128**, 2016–2021 (1962)
31. Anzer, U.: The stability of force-free magnetic fields with cylindrical symmetry in the context of solar flares. Sol. Phys. **3**, 298–315 (1968)
32. Raadu, M.A.: Suppression of the kink instability for magnetic flux ropes in the chromosphere. Sol. Phys. **22**, 425–433 (1972)
33. Shen, J., Wang, Y., Zhou, T., Ji, H.: Initiation processes for the 2013 May 13 X1.7 limb flare. Astrophys. J. (2017). in press
34. Török, T., Chandra, R., Pariat, E., Démoulin, P., Schmieder, B., Aulanier, G., Linton, M.G., Mandrini, C.H.: Filament interaction modeled by flux rope reconnection. Astrophys. J. **728**, 65–70 (2011)
35. Ji, H., Wang, H., Schmahl, E.J., Moon, Y.-J., Jiang, Y.: Observations of the failed eruption of a filament. Astrophys. J. **595**, L135–L138 (2003)
36. Liu, Y.: Halo coronal mass ejections and configuration of the ambient magnetic fields. Astrophys. J. **654**, L171–L174 (2007)
37. Fang, C., Henoux, J.C., Gan, W.Q.: Diagnostics of non-thermal processes in chromospheric flares. 1. Hoe and Call K line profiles of an atmosphere bombarded by 10–500 keV electrons. Astron. Astrophys. **274**, 917–922 (1993)
38. Ding, M.D., Qiu, J., Wang, H., Goode, P.R.: On the fast fluctuations in solar flare Hα blue wing emission. Astrophys. J. **552**, 340–347 (2001)
39. Fan, Y., Gibson, S.E.: On the nature of the X-Ray bright core in a stable filament channel. Astrophys. J. **641**, L149–L152 (2006)
40. Amari, T., Luciani, J.F., Aly, J.J.: Coronal magnetohydrodynamic evolution driven by subphotospheric conditions. Astrophys. J. **615**, L165–L168 (2004)
41. Fan, Y., Gibson, S.E.: Onset of coronal mass ejections due to loss of confinement of coronal flux ropes. Astrophys. J. **668**, 1232–1245 (2007)
42. Aulanier, G., Török, T., Démoulin, P., DeLuca, E.E.: Formation of torus-unstable flux ropes and electric currents in erupting sigmoids. Astrophys. J. **708**, 314–333 (2010)

43. Chen, P.F., Shibata, K.: An emerging flux trigger mechanism for coronal mass ejections. Astrophys. J. **545**, 524–531 (2000)
44. Priest, E.R., Forbes, T.G.: The magnetic nature of solar flares. Astron. Astrophys. Rev. **10**, 313–377 (2002)
45. Carmichael, H.: A process for flares. In: Wilmot, N.H (ed.) The Physics of Solar Flares, Proceedings of the AAS-NASA Symposium held 28–30 October, 1963 at the Goddard Space Flight Center, Greenbelt MD, Washington, DC: National Aeronautics and Space Administration, Science and Technical Information Division, p. 451 (1964)
46. Sturrock, P.A.: Model of the high-energy phase of solar flares. Nature **211**, 695–697 (1996)
47. Hirayama, T.: Theoretical model of flares and prominences. I: evaporating flare model. Sol. Phys. **34**, 323–338 (1974)
48. Kopp, R.A., Pneuman, G.W.: Magnetic reconnection in the corona and the loop prominence phenomenon. Sol. Phys. **50**, 85–98 (1976)
49. Priest, E.R.: Book-Review - solar flare magnetohydrodynamics. Science **214**, 356 (1981)
50. Moore, R.L.: Evidence that magnetic energy shedding in solar filament eruptions is the drive in accompanying flares and coronal mass ejections. Astrophys. J. **324**, 1132–1137 (1988)
51. Moore, R.L., Roumeliotis, G.: Triggering of eruptive flares - destabilization of the preflare magnetic field configuration. In: Svestka, Z., Jackson, B.V., Machado, M.E (eds.) Eruptive Solar Flares. Proceedings of Colloquium 133 of the International Astronomical Union, held at Iguazu, Argentina, 2–6 August, 1991, p. 69. Springer, New York (1992)
52. Shibata, K.: New observational facts about solar flares from YOHKOH studies - evidence of magnetic reconnection and a unified model of flares. Adv. Space Res. **17**, 9–18 (1996)
53. Shibata, K.: A unified model of solar flares. In: Watanabe, T., Kosugi, T., Sterling, A.C (eds.) Observational Plasma Astrophysics: Five Years of Yohkoh and Beyond, vol. 229, p. 187. Kluwer Academic Publishers, Boston (1998)
54. Shibata, K.: Evidence of magnetic reconnection in solar flares and a unified model of flares. In: Structure Formation and Function of Gaseous, Biological and Strongly Coupled Plasmas, p. 74 (1999)
55. Liu, R., Wang, H., Alexander, D.: Implosion in a coronal eruption. Astrophys. J. **696**, 121–135 (2009)
56. Yang, Y.H., Cheng, C.Z., Krucker, S., Lin, R.P., Ip, W.H.: A statistical study of hard X-Ray footpoint motions in large solar flares. Astrophys. J. **693**, 132–139 (2009)
57. Li, Y.P., Gan, W.Q.: On the peak times of thermal and nontheral emissions in solar flares. Astrophys. J. **652**, L61–L63 (2006)
58. Joshi, B., Veronig, A., Cho, K.-S., Bong, S.-C., Somov, B.V., et al.: Magnetic reconnection during the two-phase evolution of a solar eruptive flare. Astrophys. J. **706**, 1438–1450 (2009)
59. Melnikov, V.F., Shibasaki, K., Reznikova, V.E.: Loop-top nonthermal microwave source in extended solar flaring loops. Astrophys. J. **580**, L185–L188 (2002)
60. Altyntsev, A.T., Fleishman, G.D., Huang, G.L., Melnikov, V.F.: A broadband microwave burst produced by electron beams. Astrophys. J. **677**, 1367–1377 (2008)
61. Reznikova, V.E., Melnikov, V.F., Shibasaki, K., Gorbikov, S.P., Pyatakov, N.P., Myagkova, I.N., Ji, H.: 2002 August 24 limb flare loop: dynamics of microwave brightness distribution. Astrophys. J. **697**, 735–746 (2009)
62. Reznikova, V.E., Melnikov, V.F., Ji, H., Shibasaki, K.: Dynamics of the flaring loop system of 2005 August 22 observed in microwaves and hard X-rays. Astrophys. J. **724**, 171–181 (2010)
63. Nakajima, H., Nishio, M., Enome, S., Shibasaki, K., Takano, T., et al.: The nobeyama radioheliograph. Proc. IEEE **82**, 705–713 (1994)
64. Asai, A., Shibata, K., Ishii, T.T., Oka, M., Kataoka, R., et al.: Evolution of the anemone AR NOAA 10798 and the related geo-effective flares and CMEs. J. Geophys. Res. **114**, A00A21 (2009)
65. Bastian, T.S., Benz, A.O., Gary, D.E.: Radio emission from solar flares. Annu. Rev. Astron. Astrophys. **36**, 131–188 (1998)
66. Huang, G.L., Nakajima, H.: Statistical analysis of flaring loops observed by nobeyama radioheliograph. I. Comparison of looptop and footpoints. Astrophys. J. **696**, 136–142 (2009)

67. Melrose, D.B., Robinson, P.A.: Reversal of the sense of polarization in solar and steller flares. Astron. Soc. Aust. Proc. **11**, 16–20 (1994)
68. Huang, G.L., Song, Q.W., Li, J.P.: Determination of intrinsic mode and linear mode coupling in solar microwave bursts. Astrophys. Space Sci. **345**, 41–47 (2013)
69. Zhou, T., Ji, H.: A comparison between magnetic shear and flare shear in a well-observed M-class flare. Res. Astron. Astrophys. **9**, 323–332 (2009)
70. Thomson, A.R., Moran, J.M., Swenson Jr., G.W.: Interferometry and Synthesis in Radio Astronomy. Wiley-Interscience, New York (1986)
71. Tanaka, K., Nakagawa, Y.: Force-free magnetic fields and flares of August 1972. Sol. Phys. **33**, 187–204 (1973)
72. Moore, R.L., Sterling, A.C., Hudson, H.S., Lemen, J.R.: Onset of the magnetic explosion in solar flares and coronal mass ejections. Astrophys. J. **552**, 833–848 (2001)
73. Kliem, B., Titov, V.S., Török, T.: Formation of current sheets and sigmoidal structure by the kink instability of a magnetic loop. Astron. Astrophys. **413**, L23–L26 (2004)
74. Masuda, S., Kosugi, T., Hudson, H.S.: A hard X-ray two-ribbon flare observed with Yohkoh/HXT. Sol. Phys. **204**, 55–67 (2001)
75. Asai, A., Ishii, T.T., Kurokawa, H., Yokoyama, T., Shimojo, M.: Evolution of conjugate footpoints inside flare ribbons during a great two-ribbon flare on 2001 April 10. Astrophys. J. **586**, 624–629 (2003)
76. Su, Y., Golub, L., Van Ballegooijen, A.A.: A statistical study of shear motion of the footpoints in two-ribbon flares. Astrophys. J. **655**, 606–614 (2007)
77. Liu, W., Petrosian, V., Dennis, B., Holman, G.: Conjugate hard X-Ray footpoints in the 2003 October 29 X10 flare: unshearing motions, correlations, and asymmetries. Astrophys. J. **693**, 847–867 (2009)
78. Somov, B.V.: Non-neutral current sheets and solar flare energetics. Astron. Astrophys. **163**, 210–218 (1986)
79. Lin, J., Forbes, T.G., Priest, E.R., Bungey, T.N.: Models for the motions of flare loops and ribbons. Sol. Phys. **159**, 275–299 (1995)
80. Forbes, T.G., Acton, L.W.: Reconnection and field line shrinkage in solar flares. Astrophys. J. **459**, 330–341 (1996)
81. Lin, J.: Motions of flare ribbons and loops in various magnetic configurations. Sol. Phys. **222**, 115–136 (2004)
82. Yokoyama, T., Shibata, K.: Magnetic reconnection coupled with heat conduction. Astrophys. J. **474**, L61–L64 (1997)
83. Yokoyama, T., Shibata, K.: A two-dimensional magnetohydrodynamic simulation of chromospheric evaporation in a solar flare based on a magnetic reconnection model. Astrophys. J. **494**, L113–L116 (1998)
84. Chen, P.F., Fang, C., Tang, Y.H., Ding, M.D.: Flaring loop motion and a unified model for solar flares. Astrophys. J. **520**, 853–858 (1999)
85. Somov, B.V., Kosugi, T.: Collisionless reconnection and high-energy particle acceleration in solar flares. Astrophys. J. **485**, 859–868 (1997)
86. Karlický, M., Kosugi, T.: Acceleration and heating processes in a collapsing magnetic trap. Astron. Astrophys. **419**, 1159–1168 (2004)
87. Shibasaki, K.: High-beta disruption in the solar atmosphere. Astrophys. J. **557**, 326–331 (2001)
88. Tsap, Y.T., Kopylova, Y.G., Stepanov, A.V., Melnikov, V.F., Shibasaki, K.: Ballooning instability in coronal flare loops. Sol. Phys. **253**, 161–172 (2008)
89. Gorbikov, S.P., Melnikov, V.F.: Math. Model. **19**, 112 (2007)
90. Nakariakov, V.M., Melnikov, V.F.: Quasi-periodic pulsations in solar flares. Space Sci. Rev. **149**, 119–151 (2009)
91. Kupriyanova, E.G., Melnikov, V.F., Nakariakov, V.M., Shibasaki, K.: Types of microwave quasi-periodic pulsations in single flaring loops. Sol. Phys. **267**, 329–342 (2010)
92. O'Shea, E., Banerjee, D., Doyle, J.G., Fleck, B., Murtagh, F.: Active region oscillations. Astron. Astrophys. **368**, 1095–1107 (2001)

93. McAteer, R.T.J., Gallagher, P.T., Bloomfield, D.S., Williams, D.R., Mathioudakis, M., Keenan, F.P.: Ultraviolet oscillations in the chromosphere of the quiet sun. Astrophys. J. **602**, 436–445 (2004)
94. Dmitriev, P.B., Kudryavtsev, I.V., Lazutkov, V.P., Matveev, G.A., Savchenko, M.I., Skorodumov, D.V., Charikov, Yu.E: Solar flares registered by the IRIS spectrometer onboard the CORONAS-F satellite: peculiarities of the X-ray emission. Sol. Syst. Res. **40**, 142–152 (2006)
95. Reznikova, V.E., Melnikov, V.F., Su, Y., Huang, G.: Pulsations of microwave flaring emission at low and high frequencies. Astron. Rep. **51**, 588–596 (2007)
96. Torrence, C., Compo, G.P.: A practical guide to wavelet analysis. Bull. Am. Meteorol. Soc. **79**, 61–78 (1998)
97. Horne, J.H., Baliunas, S.L.: A prescription for period analysis of unevenly sampled time series. Astrophys. J. **302**, 757–763 (1986)
98. De Moortel, I., McAteer, R.T.J.: Waves and wavelets: an automated detection technique for solar oscillations. Sol. Phys. **223**, 1–11 (2004)
99. Inglis, A.R., Nakariakov, V.M.: A multi-periodic oscillatory event in a solar flare. Astron. Astrophys. **493**, 259–266 (2009)
100. Melnikov, V.F., Reznikova, V.E., Shibasaki, K., Nakariakov, V.M.: Spatially resolved microwave pulsations of a flare loop. Astron. Astrophys. **439**, 727–736 (2005)
101. Edwin, P.M., Roberts, B.: Wave propagation in a magnetically structured atmosphere. III - the slab in a magnetic environment. Sol. Phys. **76**, 239–259 (1982)
102. Edwin, P.M., Roberts, B.: Wave propagation in a magnetic cylinder. Sol. Phys. **88**, 179–191 (1983)
103. Nakariakov, V.M.: In: Dwivedi, B.N. (ed.) Dynamic Sun, pp. 314–334. Cambridge University Press, Cambridge (2003)
104. Aschwanden, M.J., Fletcher, L., Schrijver, C.J., Alexander, D.: Coronal loop oscillations observed with the transition region and coronal explorer. Astrophys. J. **520**, 880–894 (1999)
105. Nakariakov, V.M., Ofman, L., Deluca, E.E., Roberts, B., Davila, J.M.: TRACE observation of damped coronal loop oscillations: implications for coronal heating. Science **285**, 862–864 (1999)
106. Kupriyanova, E.G., Melnikov, V.F., Shibasaki, K.: Spatially resolved microwave observations of multiple periodicities in a flaring loop. Sol. Phys. **284**, 559–578 (2013)
107. Dulk, G.A., Marsh, K.A.: Simplified expressions for the gyrosynchrotron radiation from mildly relativistic, nonthermal and thermal electrons. Astrophys. J. **259**, 350–358 (1982)
108. Nakariakov, V.M., Verwichte, E.: Coronal waves and oscillations. Living Rev. Sol. Phys. **2**(3) (2005)
109. Wang, T.J., Solanki, S.K.: Vertical oscillations of a coronal loop observed by TRACE. Astron. Astrophys. **421**, L33–L36 (2004)
110. Verwichte, E., Foullon, C., Nakariakov, V.M.: Seismology of curved coronal loops with vertically polarised transverse oscillations. Astron. Astrophys. **452**, 615–622 (2006)
111. Díaz, A.J.: Fast magnetohydrodynamic oscillations in an elliptical coronal arcade. Astron. Astrophys. **456**, 737–746 (2006)
112. Aschwanden, M.J., Schrijver, C.J.: Coronal loop oscillations observed with atmospheric imaging assemblyłkink mode with cross-sectional and density oscillations. Astrophys. J. **736**, 102–122 (2011)
113. Kupriyanova, E.G., Melnikov, V.F., Puzynya, V.M., Shibasaki, K., Ji, H.S.: Long-period pulsations of the thermal microwave emission of the solar flare of June 2, 2007 from data with high spatial resolution. Astron. Rep. **58**, 573–577 (2014)
114. Zaitsev, Valerii V., Stepanov, Alexander V.: Reviews of topical problems: coronal magnetic loops. Phys. Uspekhi **51**, 1123–1160 (2008)
115. Mészárosová, H., Karlický, M., Ryb?, J., Jiricka, K.: Tadpoles in wavelet spectra of a solar decimetric radio burst. Astrophys. J. Lett. **697**, L108–L110 (2009)
116. Sych, R., Nakariakov, V.M., Karlicky, M., Anfinogentov, S.: Relationship between wave processes in sunspots and quasi-periodic pulsations in active region flares. Astron. Astrophys. **505**, 791–799 (2009)

117. Reznikova, V.E., Shibasaki, K.: Flare quasi-periodic pulsations with growing periodicity. Astron. Astrophys. **525**, 112–118 (2011)
118. Kislyakova, K.G., Zaitsev, V.V., Urpo, S., Riehokainen, A.: Long-period oscillations of the solar microwave emission. Astron. Rep. **55**, 275–283 (2011)
119. Kim, S., Nakariakov, V.M., Shibasaki, K.: Slow magnetoacoustic oscillations in the microwave emission of solar flares. Astrophys. J. Lett. **756**, L36–L40 (2012)
120. Puzynya, V.M., Melnikov, V.F.: In: Stepanov, A.V., Nagovitsyn, YuA (eds.) Proceedings of the Conference on Solar and Solar-Earth Physics-2010 (Glavn. Astron. Observ. RAN, St.-Petersburg), p. 335 (2010)
121. Wang, T.: Standing slow-mode waves in hot coronal loops: observations, modeling, and coronal seismology. Space Sci. Rev. **158**, 397–419 (2011)
122. Kaufmann, P., Strauss, F.M., Laporte, C., Opher, R.: Evidence for quasi-quantization of solar flare mm-wave radiation. Astron. Astrophys. **87**, 58–62 (1980)
123. Sturrock, P.A., Kaufmann, P., Moore, R.L., Smith, D.F.: Energy release in solar flares. Sol. Phys. **94**, 341–357 (1984)
124. Qin, Z., Huang, G.: Some characteristics of pulsations in radio bursts at 9.375 GHz. Astrophys. Space Sci. **218**, 213–222 (1994)
125. Aschwanden, M.J.: Theory of radio pulsations in coronal loops. Sol. Phys. **111**, 113–136 (1987)
126. Huang, G., Qin, Z., Yao, Q.: A model for solar radio pulsations at short centimetric band. Astrophys. Space Sci. **243**, 401–412 (1996)
127. Huang, G., Nakajima, H.: Statistical analysis of flaring loops observed by nobeyama radioheliograph. I. Comparison of looptop and footpoints. Astrophys. J. **696**, 136–142 (2009)
128. Huang, G., Song, Q.: Frequency dependence of the relation between repetition rate and burst flux in solar radio pulsations. Sol. Phys. **264**, 345–351 (2010)
129. Huang, G., Wang, D., Song, Q.: Whistler waves in Freja observations. J. Geophys. Res. **109**, A02307 (2003)
130. Song, Q., Huang, G.: A tentative statistical analysis of flare events observed by NoRH and NoRP. Adv. Space Res. **41**, 1188–1190 (2008)
131. Liu, W., Petrosian, V., Dennis, B., Jiang, Y.: Double coronal hard and soft X-Ray source observed by RHESSI: evidence for magnetic reconnection and particle acceleration in solar flares. Astrophys. J. **676**, 704–716 (2008)
132. Sakao, T., Kosugi, T., Masuda, S.: Energy release and particle acceleration in solar flares with respect to flaring magnetic loops. Obs. Plasma Astrophys. Five Years YOHKOH Beyond **229**, 273 (1998)
133. Gan, W., Li, Y., Miroshnichenko, L.: On the motions of RHESSI flare footpoints. Adv. Space Res. **41**, 908–913 (2008)
134. Ning, Z., Cao, W.: Hard X-ray source distributions on EUV bright Kernels in a solar flare. Sol. Phys. **269**, 283–293 (2011)
135. Ning, Z.: X-ray source motion along the loop in two solar flares. Astrophys. Space Sci. **346**, 307–318 (2013)
136. Liu, W., Liu, S., Jiang, Y., Petrosian, V.: RHESSI observation of chromospheric evaporation. Astrophys. J. **649**, 1124–1139 (2006)
137. Ning, Z., Cao, W., Huang, J., Huang, G., Yan, Y., Feng, H.: Evidence of chromospheric evaporation in the 2004 December 1 solar flare. Astrophys. J. **699**, 15–22 (2009)
138. Ning, Z., Cao, W.: Investigation of chromospheric evaporation in a neupert-type solar flare. Astrophys. J. **717**, 1232–1242 (2010)
139. Tajima, T., Brunel, F., Sakai, J.-I., Vlahos, L., Kundu, M.R.: The coalescence instability in solar flares. In: Proceedings of the 107th IAU Symposium. D. Reidel Publishing Co., Dordrecht, pp. 197–208 (1985)
140. Sakai, J.-I., Ohsawa, Y.: Particle acceleration by magnetic reconnection and shocks during current loop coalescence in solar flares. Space Sci. Rev. **46**, 113–198 (1987)
141. Sakai, J.-I., de Jager, C.: Coronal explosions as a signature of current loop coalescence in solar flares. Sol. Phys. **123**, 393–396 (1989)

142. Sakai, J.-I., Koide, S.: Classification of magnetic reconnection during two current-loop coalescence. Sol. Phys. **142**, 399–402 (1992)
143. Chargeishvili, B., Zhao, J., Sakai, J.-I.: Dynamics of the physical state during two-current-loop collisions. Sol. Phys. **145**, 297–315 (1993)
144. Zhao, J., Chargeishvili, B., Sakai, J.-I.: Prompt high-energy particle acceleration during two-current-loop collisions. Sol. Phys. **146**, 331–341 (1993)
145. Zhao, J., Chargeishvili, B., Sakai, J.-I.: Characteristics of plasma temperature variation during two-current-loop collisions. Sol. Phys. **147**, 131–136 (1993)
146. Sakai, J.-I., de Jager, C.: Solar flares and collisions between current-carrying loops types and mechanisms of solar flares and coronal loop heating. Space Sci. Rev. **77**, 1–192 (1996)
147. Smith, P.D., Sakai, J.-I.: Chromospheric magnetic reconnection: two-fluid simulations of coalescing current loops. Astron. Astrophys. **486**, 569–575 (2008)
148. Hanaoka, Y.A.: Flare caused by interacting coronal loops. Astrophys. J. **420**, L37–L40 (1994)
149. Hanaoka, Y.A.: Flares and plasma flow caused by interacting coronal loops. Sol. Phys. **165**, 275–301 (1996)
150. Hanaoka, Y.A.: Double-loop configuration of solar flares. Sol. Phys. **173**, 319–346 (1997)
151. Inda-Koide, M., Sakai, J.-I., Koide, S., Kosugi, T., Sakao, T., Shimizu, T.: Publ. Astron. Soc. Japan **47**, 323–330 (1995)
152. Aschwanden, M.J., Benz, A.O.: Electron densities in solar flare loops, chromospheric evaporation upflows, and acceleration sites. Astrophys. J. **480**, 825–835 (1997)
153. Kundu, M.R., Grechnev, V.V., Garaimov, V.I., White, S.M.: Double loop configuration of a flaring region from microwave, extreme-ultraviolet, and X-ray imaging data. Astrophys. J. **563**, 389–402 (2001)
154. Pohjolainen, S.: Repeated flaring from LoopCLoop interaction. Sol. Phys. **2003**, 319–339 (2003)
155. Huang, G.L., Wu, H.A., Grechnev, V.V., Sych, R.A., Altyntsev, A.T.: The radio signature of twisted magnetic ropes and reconnection site in the low corona. Sol. Phys. **213**, 341–358 (2003)
156. Huang, G.L.: Radio and multiwavelength evidence of coronal loop eruption in a flare-coronal mass ejection event on 15 April 1998. J. Geophys. Res. **109**, A02105 (2004)
157. Wu, G.P., Huang, G.L., Tang, Y.H., Xu, A.A.: The observational evidence on the loop loop interaction in a flare CME event on April 15, 1998. Sol. Phys. **2005**(227), 327–337 (2005)
158. Huang, G.L., Ji, H.S.: Microwave, optical, EUV, and hard X-ray signature of possible coronal loop interaction. Sol. Phys. **2005**(229), 227–236 (2005)
159. Huang, G.L., Ji, H.S.: Radio, Hard X-ray, EUV and optical study of September 9, 2002 solar flare. Astrophys. Space Sci. **2006**(301), 65–71 (2006)
160. Huang, G.L., Lin, J.: Quasi-periodic reversals of radio polarization at 17 GHz observed in the 2002 April 21 solar event. Astrophys. J. **639**, L99–L102 (2006)
161. Kolomański, S., Karlický, M.: The interaction of a plasmoid with a loop-top Kernel. Astron. Astrophys. **475**, 685–693 (2007)
162. Kumar, P., Srivastava, A.K., Somov, B.V., Manoharan, P.K., Erdélyi, R., Uddin, W.: Evidence of solar flare triggering due to loop-loop interaction caused by footpoint shear motion. Astrophys. J. **723**, 1651–1664 (2010)
163. Zhou, A.H., Karlický, M.: Magnetic field estimation in microwave radio sources. Sol. Phys. **153**, 441–444 (1994)
164. Huang, G.L., Li, J.P.: Co-analysis of solar microwave and hard X-ray spectral evolutions. II. In three sources of a flaring loop. Astrophys. J. **740**, 46–56 (2011)
165. Minoshima, T., Yokoyama, T., Mitani, N.: Comparative analysis of nonthermal emissions and electron transport in a solar flare. Astrophys. J. **673**, 598–610 (2008)
166. Metcalf, T.R., Alexander, D.: Coronal trapping of energetic flare particles: Yohkoh/HXT observations. Astrophys. J. **522**, 1108–1116 (1999)
167. Huang, G.L., Song, Q.W., Huang, Y.: Statistics of flaring loops observed by the Nobeyama Radioheliograph. III. Asymmetry of two footpoint emissions. Astrophys. J. **723**, 1806–1816 (2010)

168. Brown, J.C.: The deduction of energy spectra of non-thermal electrons in flares from the observed dynamic spectra of hard X-ray bursts. Sol. Phys. **18**, 489–502 (1971)
169. Fisher, G.H., Canfield, R.C., McClymont, A.N.: Flare loop radiative hydrodynamics. V - response to thick-target heating. VI - chromospheric evaporation due to heating by nonthermal electrons. VII - dynamics of the thick-target heated chromosphere. Astrophys. J. **289**, 414–441 (1985a)
170. Fisher, G.H., Canfield, R.C., McClymont, A.N.: Flare loop radiative hydrodynamics - part six - chromospheric evaporation due to heating by nonthermal electrons. Astrophys. J. **289**, 425–433 (1985b)
171. Fisher, G.H., Canfield, R.C., McClymont, A.N.: Flare loop radiative hydrodynamics - part seven - dynamics of the thick target heated chromosphere. Astrophys. J. **289**, 434–441 (1985c)
172. Fisher, G.H.: IAU Colloq. 89: radiation hydrodynamics in stars and compact objects **255**, 53–74 (1986)
173. Nagai, F., Emslie, A.G.: Gas dynamics in the impulsive phase of solar flares. I. Thick-target heating by nonthermal electrons. Astrophys. J. **279**, 896–908 (1984)
174. Emslie, A.G., Nagai, F.: Gas dynamics in the impulsive phase of solar flares. II - the structure of the transition region - a diagnostic of energy transport processes. Astrophys. J. **288**, 779–788 (1985)
175. Mariska, J.T., Emslie, A.G., Li, P.: Numerical simulations of impulsively heated solar flares. Astrophys. J. **341**, 1067–1074 (1989)
176. Li, P., Emslie, A.G., Mariska, J.T.: Soft X-ray diagnostics of electron-heated solar flare atmospheres. Astrophys. J. **341**, 1075–1081 (1989)
177. Allred, J.C., Kowalski, A.F., Carlsson, M.: A unified computational model for solar and stellar flares. Astrophys. J. **809**, 104–117 (2015)
178. Emslie, A.G., Li, P., Mariska, J.T.: Diagnostics of electron-heated solar flare models. III - effects of tapered loop geometry and preheating. Astrophys. J. **399**, 714–723 (1992)
179. Mariska, J.T.: Flare plasma dynamics obseved with the YOHKOH Bragg crystal spectrometer. III. Spectral signatures of electron-beam-heated atmospheres. Astrophys. J. **444**, 478–486 (1995)
180. Reep, J.W., Bradshaw, S.J., Alexander, D.: Optimal electron energies for driving chromospheric evaporation in solar flares. Astrophys. J. **808**, 177–188 (2015)
181. Abbett, W.P., Hawley, S.L.: Dynamic models of optical emission in impulsive solar flares. Astrophys. J. **521**, 906–919 (1999)
182. Allred, J.C., Hawley, S.L., Abbett, W.P., Carlsson, M.: Radiative hydrodynamic models of the optical and ultraviolet emission from solar flares. Astrophys. J. **630**, 573–586 (2005)
183. Carlsson, M., Stein, R.F.: Formation of solar calcium H and K bright grains. Astrophys. J. **481**, 500–514 (1997)
184. Rubio da Costa, F., Liu, W., Petrosian, V., Carlsson, M.: Combined modeling of acceleration, transport, and hydrodynamic response in solar flares. II. Inclusion of radiative transfer with RADYN. Astrophys. J. **813**, 133–149 (2015)
185. Liu, W., Petrosian, V., Mariska, J.T.: Combined modeling of acceleration, transport, and hydrodynamic response in solar flares. I. The numerical model. Astrophys. J. **702**, 1553–1566 (2009)
186. Cheng, C.-C., Oran, E.S., Doschek, G.A., Boris, J.P., Mariska, J.T.: Numerical simulations of loops heated to solar flare temperatures. I. Astrophys. J. **265**, 1090–1119 (1983)
187. MacNeice, P.: A numerical hydrodynamic model of a heated coronal loop. Sol. Phys. **103**, 47–66 (1986)
188. Gan, W.Q., Fang, C.: A hydrodynamic model of the gradual phase of the solar flare loop. Astrophys. J. **358**, 328–337 (1990)
189. Pallavicini, R., Peres, G., Serio, S., et al.: Closed coronal structures. V - gasdynamic models of flaring loops and comparison with SMM observations. Astrophys. J. **270**, 270–287 (1983)
190. Peres, G., Reale, F., Serio, S., Pallavicini, R.: Hydrodynamic flare modeling - comparison of numerical calculations with SMM observations of the 1980 November 12 17:00 UT flare. Astrophys. J. **312**, 895–908 (1987)

191. Gan, W.Q., Zhang, H.Q., Fang, C.: A hydrodynamic model of the impulsive phase of a solar flare loop. Astron. Astrophys. **241**, 618–624 (1991)
192. Hori, K., Yokoyama, T., Kosugi, T., Shibata, K.: Pseudo-two-dimensional hydrodynamic modeling of solar flare loops. Astrophys. J. **489**, 426–441 (1997)
193. Longcope, D.W.: A simple model of chromospheric evaporation and condensation driven conductively in a solar flare. Astrophys. J. **795**, 10–25 (2014)
194. Brannon, S., Longcope, D.: Modeling properties of chromospheric evaporation driven by thermal conduction fronts from reconnection shocks. Astrophys. J. **792**, 50–64 (2014)
195. Yokoyama, T., Shibata, K.: Magnetohydrodynamic simulation of a solar flare with chromospheric evaporation effect based on the magnetic reconnection model. Astrophys. J. **549**, 1160–1174 (2001)
196. Kennedy, M.B., Milligan, R.O., Allred, J.C., Mathioudakis, M., Keenan, F.P.: Radiative hydrodynamic modelling and observations of the X-class solar flare on 2011 March 9. Astron. Astrophys. **578**, A72–A83 (2015)
197. Reep, J.W., Russell, A.J.B.: Alfvénic wave heating of the upper chromosphere in flares. Astrophys. J. Lett. **818**, L20–L24 (2016)
198. Sturrock, P.A.: A model of quasi-stellar radio sources. Nature **211**, 697–700 (1966)
199. Antonucci, E., Gabriel, A.H., Acton, L.W., et al.: Impulsive phase of flares in soft X-ray emission. Sol. Phys. **78**, 107–123 (1982)
200. Acton, L.W., Leibacher, J.W., Canfield, R.C., et al.: Chromospheric evaporation in a well-observed compact flare. Astrophys. J. **263**, 409–422 (1982)
201. Antonucci, E., Dennis, B.R.: Observation of chromospheric evaporation during the solar maximum mission. Sol. Phys. **86**, 67–76 (1983)
202. Zarro, D.M., Slater, G.L., Freeland, S.L.: Impulsive phase soft X-ray blueshifts at a loop footpoint. Astrophys. J. **333**, L99–L101 (1988)
203. Canfield, R.C., Metcalf, T.R., Zarro, D.M., Lemen, J.R.: Momentum balance in four solar flares. Astrophys. J. **348**, 333–340 (1990)
204. Teriaca, L., Falchi, A., Cauzzi, G., et al.: Solar and heliospheric observatory/coronal diagnostic spectrograph and ground-based observations of a two-ribbon flare: spatially resolved signatures of chromospheric evaporation. Astrophys. J. **588**, 596–605 (2003)
205. Teriaca, L., Falchi, A., Falciani, R., Cauzzi, G., Maltagliati, L.: Dynamics and evolution of an eruptive flare. Astron. Astrophys. **455**, 1123–1133 (2006)
206. Ogawara, Y., Takano, T., Kato, T., et al.: The SOLAR-A mission - an overview. Sol. Phys. **136**, 1–16 (1991)
207. Wuelser, J.-P., Canfield, R.C., Acton, L.W., et al.: Multispectral observations of chromospheric evaporation in the 1991 November 15 X-class solar flare. Astrophys. J. **424**, 459–465 (1994)
208. Ding, M.D., Watanabe, T., Shibata, K., et al.: Chromospheric evaporation in four solar flares observed by YOHKOH. Astrophys. J. **458**, 391–396 (1996)
209. Li, D., Ning, Z.J., Zhang, Q.M.: Imaging and spectral observations of quasi-periodic pulsations in a solar flare. Astrophys. J. **813**, 59–71 (2015a)
210. Harrison, R.A., Sawyer, E.C., Carter, M.K., et al.: The coronal diagnostic spectrometer for the solar and heliospheric observatory. Sol. Phys. **162**, 233–290 (1995)
211. Czaykowska, A., De Pontieu, B., Alexander, D., Rank, G.: Evidence for chromospheric evaporation in the late gradual flare phase from SOHO/CDS observations. Astrophys. J. **521**, L75–78 (1999)
212. Brosius, J.W., Phillips, K.J.H.: Extreme-ultraviolet and X-ray spectroscopy of a solar flare loop observed at high time resolution: a case study in chromospheric evaporation. Astrophys. J. **613**, 580–591 (2004)
213. Milligan, R.O., Gallagher, P.T., Mathioudakis, M., et al.: RHESSI and SOHO CDS observations of explosive chromospheric evaporation. Astrophys. J. **638**, L117–120 (2006b)
214. Brosius, J.W., Holman, G.D.: Chromospheric evaporation in a remote solar flare-like transient observed at high time resolution with SOHO's CDS and RHESSI. Astrophys. J. **659**, L73–76 (2007)

215. Brosius, J.W.: Chromospheric evaporation and warm rain during a solar flare observed in high time resolution with the coronal diagnostic spectrometer aboard the solar and heliospheric observatory. Astrophys. J. **586**, 1417–1429 (2003)
216. Culhane, J.L., Harra, L.K., James, A.M., et al.: The EUV imaging spectrometer for Hinode. Sol. Phys. **243**, 19–61 (2007)
217. Milligan, R.O., Dennis, B.R.: Velocity characteristics of evaporated plasma using Hinode/EUV imaging spectrometer. Astrophys. J. **699**, 968–975 (2009)
218. Mariska, J.T., Doschek, G.A., Bentley, R.D.: Flare plasma dynamics observed with the YOHKOH bragg crystal spectrometer. I. Properties of the CA XIX resonance line. Astrophys. J. **419**, 418–425 (1993)
219. Mariska, J.T.: Flare plasma dynamics observed with the YOHKOH bragg crystal spectrometer. 2: properties of the Fe XXV, CA XIX. Astrophys. J. **434**, 756–765 (1994)
220. Milligan, R.O.: Spatially resolved nonthermal line broadening during the impulsive phase of a solar flare. Astrophys. J. **740**, 70–80 (2011)
221. Young, P.R., Doschek, G.A., Warren, H.P., Hara, H.: Properties of a solar flare Kernel observed by Hinode and SDO. Astrophys. J. **766**, 127–142 (2013)
222. Graham, D.R., Fletcher, L., Hannah, I.G.: Hinode/EIS plasma diagnostics in the flaring solar chromosphere. Astron. Astrophys. **532**, A27–A39 (2011)
223. Polito, V., Reep, J.W., Reeves, K.K., et al.: Simultaneous IRIS and Hinode/EIS observations and modelling of the 2014 October 27 X2.0 class flare. Astrophys. J. **816**, 89–108 (2016)
224. Gömöry, P., Veronig, A.M., Su, Y., Temmer, M., Thalmann, J.K.: Chromospheric evaporation flows and density changes deduced from Hinode/EIS during an M1.6 flare. Astron. Astrophys. **588**, A6–A17 (2016)
225. Doschek, G.A., Warren, H.P., Young, P.R.: Chromospheric evaporation in an M1.8 flare observed by the extreme-ultraviolet imaging spectrometer on Hinode. Astrophys. J. **767**, 55–67 (2013)
226. De Pontieu, B., Title, A.M., Lemen, J.R., et al.: The interface region imaging spectrograph (IRIS). Sol. Phys. **289**, 2733–2779 (2014)
227. Lemen, J.R., Title, A.M., Akin, D.J., et al.: The atmospheric imaging assembly (AIA) on the solar dynamics observatory (SDO). Sol. Phys. **275**, 17–40 (2012)
228. Tian, H., Li, G., Reeves, K.K., et al.: Imaging and spectroscopic observations of magnetic reconnection and chromospheric evaporation in a solar flare. Astrophys. J. **797**, L14–L20 (2014)
229. Tian, H., Young, P.R., Reeves, K.K., et al.: Temporal evolution of chromospheric evaporation: case studies of the M1.1 flare on 2014 September 6 and X1.6 flare on 2014 September 10. Astrophys. J. **811**, 139–155 (2015)
230. Battaglia, M., Kleint, L., Krucker, S., Graham, D.: How important are electron beams in driving chromospheric evaporation in the 2014 March 29 flare? Astrophys. J. **813**, 113–120 (2015)
231. Li, D., Ning, Z.J., Zhang, Q.M.: Imaging and spectral observations of quasi-periodic pulsations in a solar flare. Astrophys. J. **807**, 72–83 (2015b)
232. Brosius, J.W., Daw, A.N.: Quasi-periodic fluctuations and chromospheric evaporation in a solar flare ribbon observed by IRIS. Astrophys. J. **810**, 45–57 (2015)
233. Graham, D.R., Cauzzi, G.: Temporal evolution of multiple evaporating ribbon sources in a solar flare. Astrophys. J. **807**, L22–L26 (2015)
234. Polito, V., Reeves, K.K., Del Zanna, G., Golub, L., Mason, H.E.: Joint high temperature observation of a small C6.5 solar flare with Iris/Eis/Aia. Astrophys. J. **803**, 84–96 (2015)
235. Brosius, J.W.: Chromospheric evaporation in solar flare loop strands observed with the extreme-ultraviolet imaging spectrometer on board Hinode. Astrophys. J. **762**, 133–139 (2013)
236. Young, P.R., Tian, H., Jaeggli, S.: The 2014 March 29 X-flare: subarcsecond resolution observations of Fe XXI λ1354.1. Astrophys. J. **799**, 218–230 (2015)
237. Masson, S., Pariat, E., Aulanier, G., Schrijver, C.J.: The nature of flare ribbons in coronal null-point topology. Astrophys. J. **700**, 559–578 (2009)

238. Wang, H., Liu, C.: Circular ribbon flares and homologous jets. Astrophys. J. **760**, 101–109 (2012)
239. Zhang, Q.M., Ning, Z.J., Guo, Y., et al.: Multiwavelength observations of a partially eruptive filament on 2011 September 8. Astrophys. J. **805**, 4–21 (2015)
240. Pariat, E., Antiochos, S.K., DeVore, C.R.: A model for solar polar jets. Astrophys. J. **691**, 61–74 (2009)
241. Zhang, Q.M., Chen, P.F., Guo, Y., Fang, C., Ding, M.D.: Two types of magnetic reconnection in coronal bright points and the corresponding magnetic configuration. Astrophys. J. **746**, 19–27 (2012)
242. Ichimoto, K., Kurokawa, H.: H-alpha red asymmetry of solar flares. Sol. Phys. **93**, 105–121 (1984)
243. Lin, R.P., Dennis, B.R., Hurford, G.J., et al.: The reuven ramaty high-energy solar spectroscopic imager (RHESSI). Sol. Phys. **210**, 3–32 (2002)
244. Zhang, Q.M., Li, D., Ning, Z.J., et al.: Explosive chromospheric evaporation in a circular-ribbon flare. Astrophys. J. **827**, 27–37 (2016a)
245. Zhang, Q.M., Li, D., Ning, Z.J.: Chromospheric condensation and quasi-periodic pulsations in a circular-ribbon flare, Astrophys. J. (2016b). submitted
246. Fisher, G.H.: Dynamics of flare-driven chromospheric condensations. Astrophys. J. **346**, 1019–1029 (1989)
247. Berkebile-Stoiser, S., Gömöry, P., Veronig, A.M., Rybák, J., Sütterlin, P.: Multi-wavelength fine structure and mass flows in solar microflares. Astron. Astrophys. **505**, 811–823 (2009)
248. Milligan, R.O.: A hot microflare observed with RHESSI and Hinode. Astrophys. J. **680**, L157–L160 (2008)
249. Brosius, J.W., Holman, G.D.: Early chromospheric response during a solar microflare observed with SOHO's CDS and RHESSI. Astrophys. J. **720**, 1472–1482 (2010)
250. Chen, F., Ding, M.D.: Evidence of explosive evaporation in a microflare observed by Hinode/EIS. Astrophys. J. **724**, 640–648 (2010)
251. Berlicki, A., Heinzel, P., Schmieder, B., Mein, P., Mein, N.: Non-LTE diagnostics of velocity fields during the gradual phase of a solar flare. Astron. Astrophys. **430**, 679–689 (2005)
252. Milligan, R.O., Gallagher, P.T., Mathioudakis, M., Keenan, F.P.: Observational evidence of gentle chromospheric evaporation during the impulsive phase of a solar flare. Astrophys. J. **642**, L169–L171 (2006a)
253. del Zanna, G., Schmieder, B., Mason, H., Berlicki, A., Bradshaw, S.: The gradual phase of the X17 flare on October 28, 2003. Sol. Phys. **239**, 173–191 (2006)
254. Zarro, D.M., Lemen, J.R.: Conduction-driven chromospheric evaporation in a solar flare. Astrophys. J. **329**, 456–463 (1988)
255. Brosius, J.W., Holman, G.D.: Observations of the thermal and dynamic evolution of a solar microflare. Astrophys. J. **692**, 492–501 (2009)
256. Sadykov, V.M., Vargas Dominguez, S., Kosovichev, A.G., et al.: Properties of chromospheric evaporation and plasma dynamics of a solar flare from iris. Astrophys. J. **805**, 167–181 (2015)
257. Brosius, J.W.: Conversion from explosive to gentle chromospheric evaporation during a solar flare. Astrophys. J. **701**, 1209–1218 (2009)
258. Raftery, C.L., Gallagher, P.T., Milligan, R.O., Klimchuk, J.A.: Multi-wavelength observations and modelling of a canonical solar flare. Astron. Astrophys. **494**, 1127–1136 (2009)
259. Klimchuk, J.A., Patsourakos, S., Cargill, P.J.: Highly efficient modeling of dynamic coronal loops. Astrophys. J. **682**, 1351–1362 (2008)
260. Li, Y., Ding, M.D., Qiu, J., Cheng, J.X.: Chromospheric evaporation in an X1.0 flare on 2014 March 29 observed with IRIS and EIS. Astrophys. J. **811**, 7–20 (2015)
261. Li, Y., Ding, M.D.: Different patterns of chromospheric evaporation in a flaring region observed with Hinode/EIS. Astrophys. J. **727**, 98–104 (2011)
262. Silva, A.V.R., Wang, H., Gary, D.E., Nitta, N., Zirin, H.: Imaging the chromospheric evaporation of the 1994 June 30 solar flare. Astrophys. J. **481**, 978–987 (1997)
263. Nitta, S., Imada, S., Yamamoto, T.T.: Clear detection of chromospheric evaporation upflows with high spatial/temporal resolution by Hinode XRT. Sol. Phys. **276**, 183–197 (2012)

264. Zhang, Q.M., Ji, H.S.: Chromospheric evaporation in sympathetic coronal bright points. Astron. Astrophys. **557**, L5–L8 (2013)
265. Liu, W., Liu, S., Jiang, Y.W., Petrosian, V.: RHESSI observation of chromospheric evaporation. Astrophys. J. **649**, 1124–1139 (2006)
266. Aschwanden, M.J., Benz, A.O.: Chromospheric evaporation and decimetric radio emission in solar flares. Astrophys. J. **438**, 997–1012 (1995)
267. Ning, Z., Cao, W.: Hard X-ray source distributions on EUV bright kernels in a solar flare. Sol. Phys. **269**, 283–293 (2011b)
268. Battaglia, M., Fletcher, L., Benz, A.O.: Observations of conduction driven evaporation in the early rise phase of solar flares. Astron. Astrophys. **498**, 891–900 (2009)

Appendix
Color Figures

A.1 Chapter 3 (from Fig. A.1)

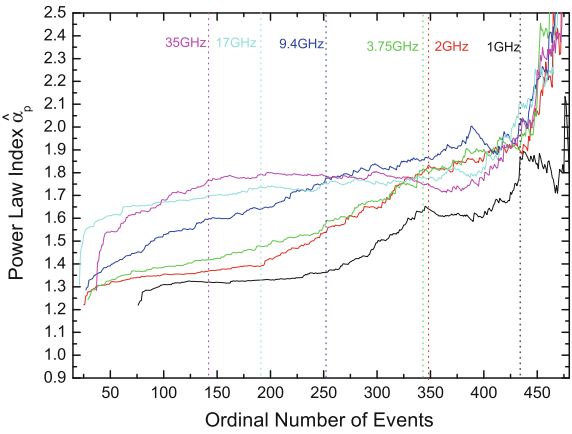

Fig. A.1 The curves with six different colors represent the power-law indices varied with lower cutoffs at six frequencies of NoRP

G. Huang et al., *Solar Flare Loops: Observations and Interpretations*,
https://doi.org/10.1007/978-981-10-2869-4

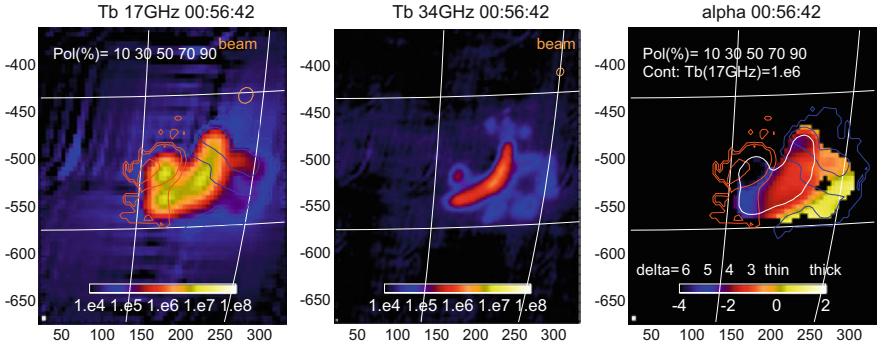

Fig. A.2 Intensity and spectral slope distributions along the extended flaring loop in the event August 28, 1999[85]. Left and middle panels: MW intensity (brightness temperature) map at 17 and 34 GHz obtained by NoRH in unit of Kelvin (color bar for the levels). Red and blue contours on the left panel indicate the polarization degree at levels of 10, 30, 50, 70, and 90%. Beam size at half level of the peak intensity is shown as a brown circle at the right upper corner. Right panel: Map of MW spectral slope α. The levels for each color are shown in the color bar, which is indexed below the bar with the values of α and is indexed above the bar with the power-law index of the electron distribution function δ derived in the Ref. 39 of Chap. 3. White contour indicates the level of the intensity of $T_b = 1$ MK at 17 GHz. Blue and red contours are the same as those in the left panel

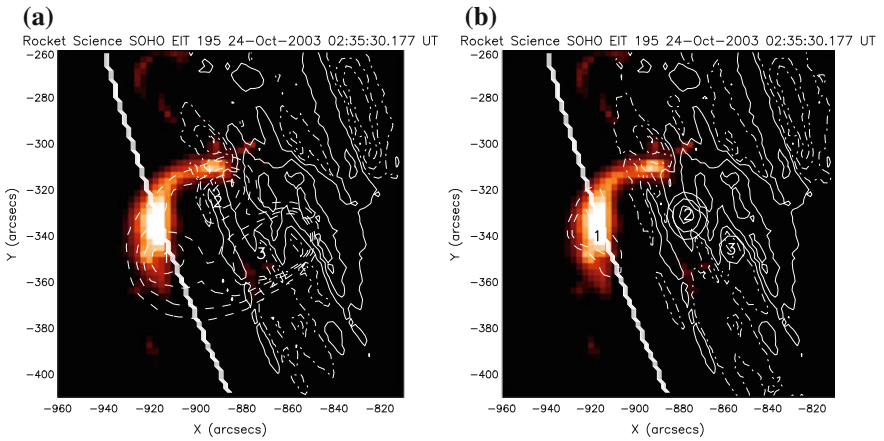

Fig. A.3 Simultaneous observations of SOHO, RHESSI, and NoRH in the 2003 October 24 flare

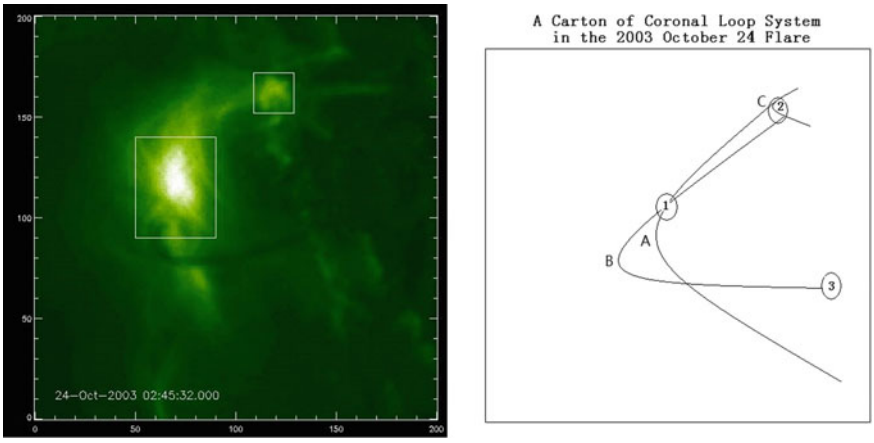

Fig. A.4 Left panel: Trace image, and right panel: carton in the 2003 October 24 event

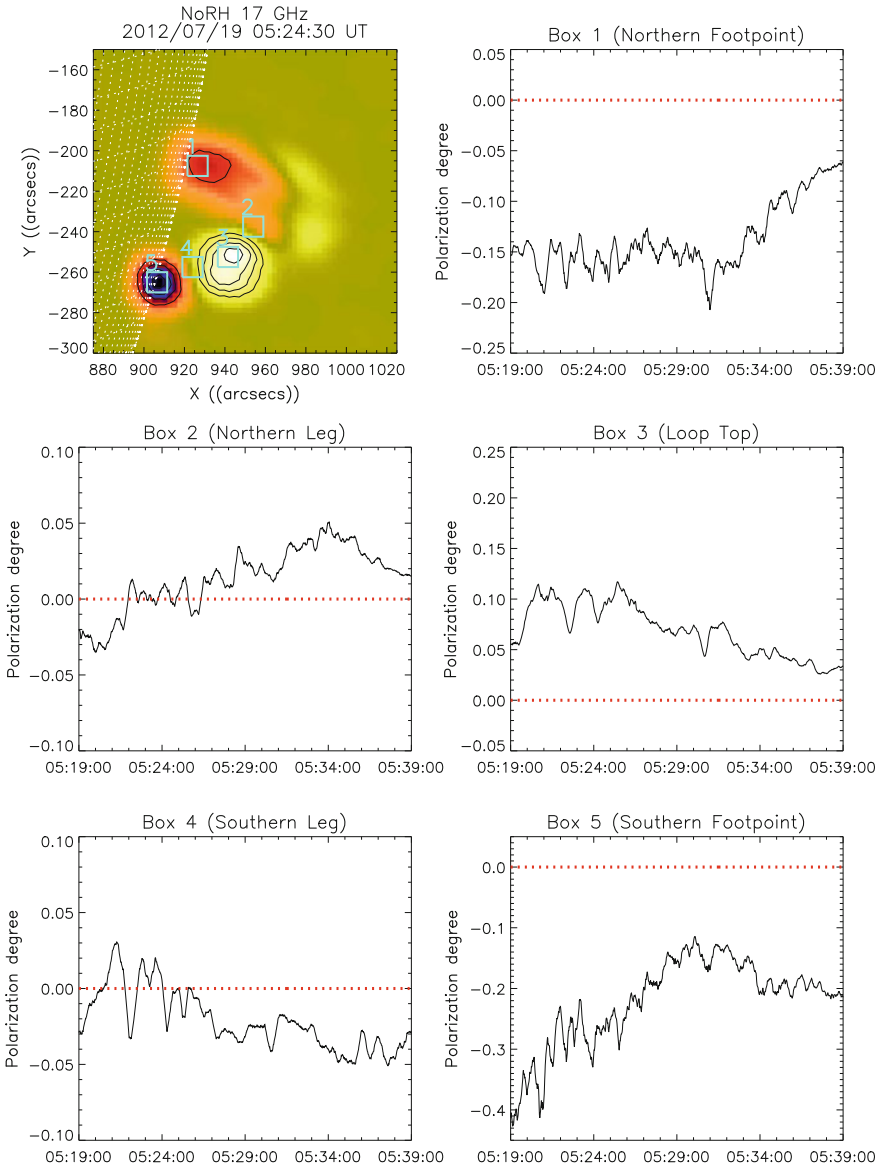

Fig. A.5 Maps of the polarization degree distribution at a frequency of 17 GHz for the event on July 19, 2012, at 0524:30 UT. Squares indicate boxes with dimensions of 10×10 arc s, for which the polarization degree dynamics was analyzed. The graphs show the time profiles of the polarization degree of the northern FP, the northern leg, the LT, the southern leg, and the southern FP. The horizontal dotted line represents a zero value of the polarization degree

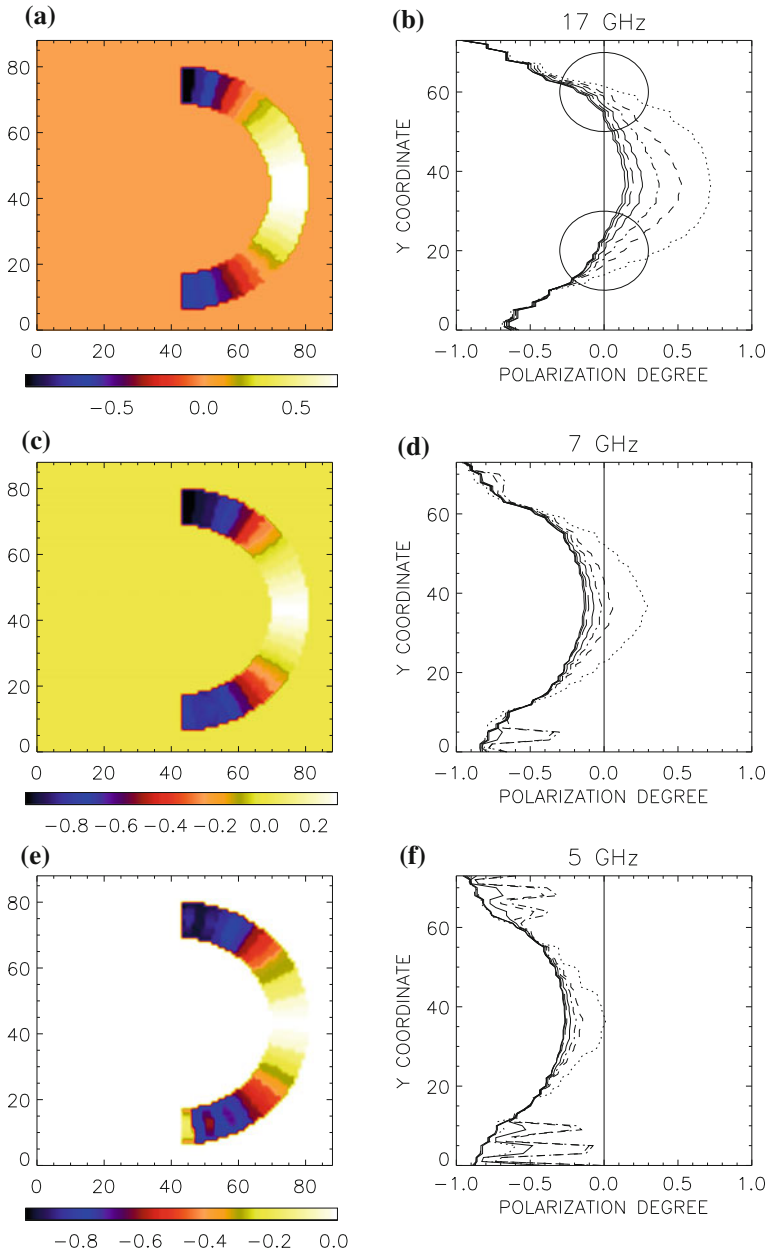

Fig. A.6 In the left column, the distribution map of the circular polarization degree is given for the model loop for the moment $t = 9$ s at frequencies of 17, 7, and 5 GHz (**a**, **c**, **e**). The right column shows the spatial distribution profiles of the polarization degree along the loop at different times on frequencies 17, 7, and 5 GHz (**b**, **d**, **f**). Time moments $t = 3$, 12, 21, 30, 39, 48, and 57 s correspond to the dotted, dashed, dash-dotted, three dots dashed, long dashed, and two solid lines. Circles indicate the field of the change of the polarization sign in time

A.2 Chapter 4 (from Fig. A.7)

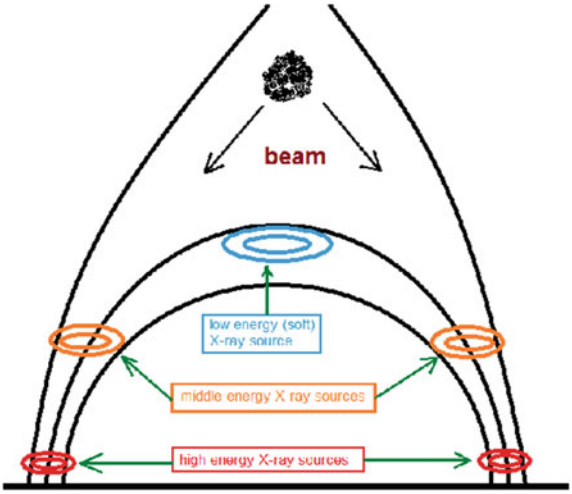

Fig. A.7 HXR source distribution along the flare loop for the plasma with an idea stratification: the lower energy source and the closer LT, the higher energy source and the faster LT (see the Ref. 9 in Chap. 4)

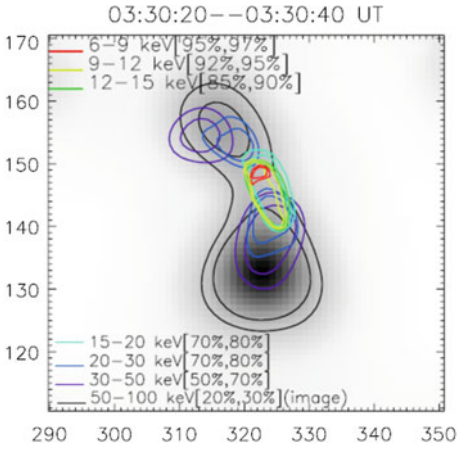

Fig. A.8 Time evolution of the HXR sources at 20–30 keV for the 2003 October 30 flare detected by RHESSI (see the Ref. 10 in Chap. 4)

A.3 Chapter 6 (from Fig. A.9)

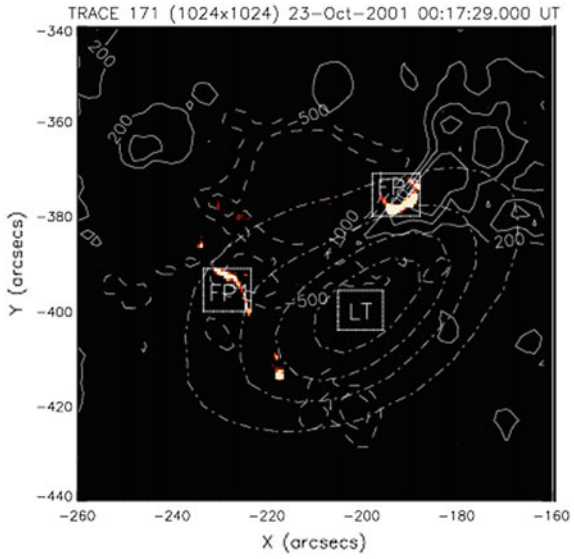

Fig. A.9 Simultaneous observations of TRACE, SOHO/MDI, and NoRH in October 23, 2001

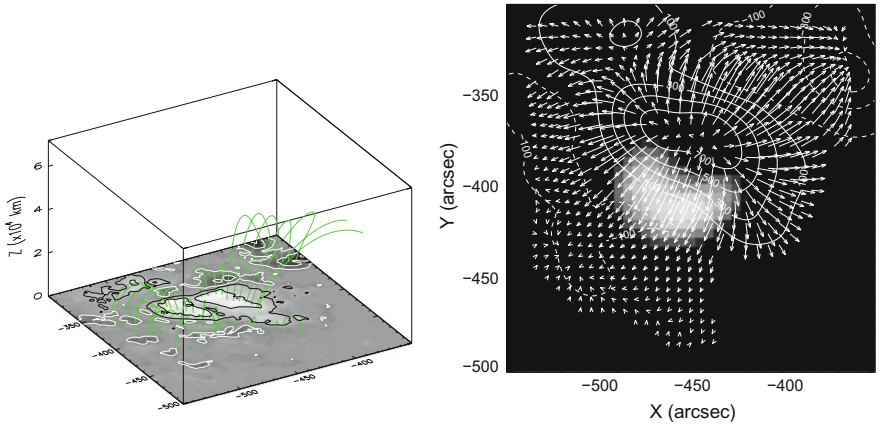

Fig. A.10 Left panel: the 3D extrapolation of SOHO/MDI magnetogram, and right: the contours of extrapolated magnetogram at 10^4 km overlaid on the 17 GHz image of brightness temperature at the peak time of 2003 October 27 flare, in which the solid and dashed contours represent the positive and negative magnetic poles, respectively, the symbols of arrows refer to the direction of extrapolated magnetic field

A.4 Chapter 7 (from Fig. A.12)

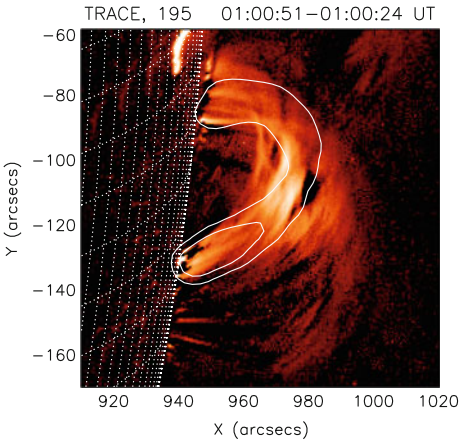

Fig. A.11 Differential TRACE (195 Å) images (color) obtained by subtracting of the earlier (01:00:24 UT) image from the later (01:00:51 UT) one and superimposed 34 GHz Nobeyama loop (white contour). Contours correspond to 0.25 and 0.5 levels of maximum brightness temperature

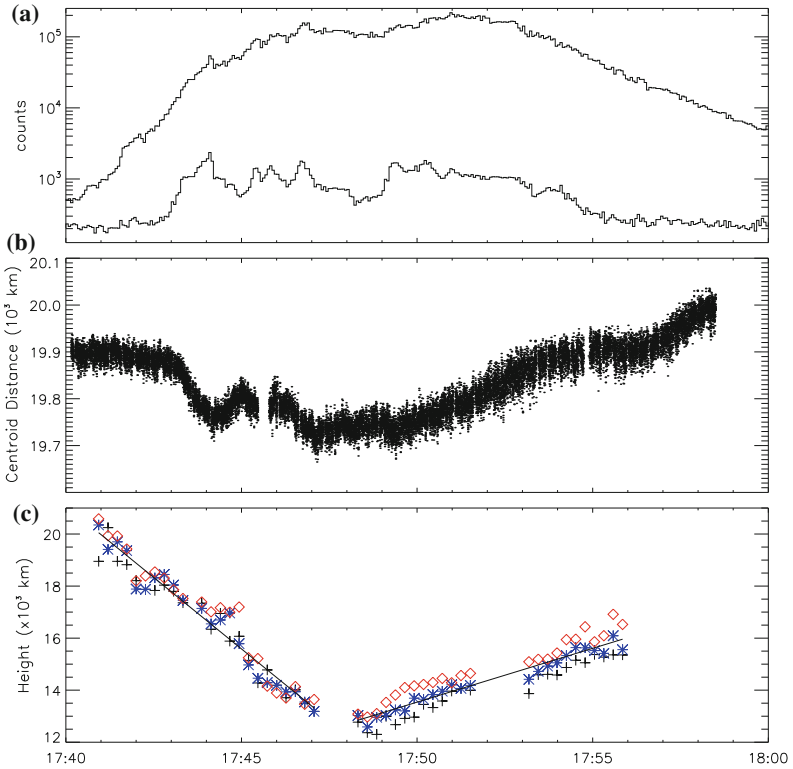

Fig. A.12 **a** Light curves of HXR emissions in the 12–25 and 25–50 keV energy bands of the 2002 September 9 flare; **b** Time profiles of the distance between H bright kernels of the flare; **c** Time profiles of the height of the loop-top source of the flare at three different energies: 8–10 keV (cross), 10–13 keV (diamond), and 13–16 keV (asterisk)

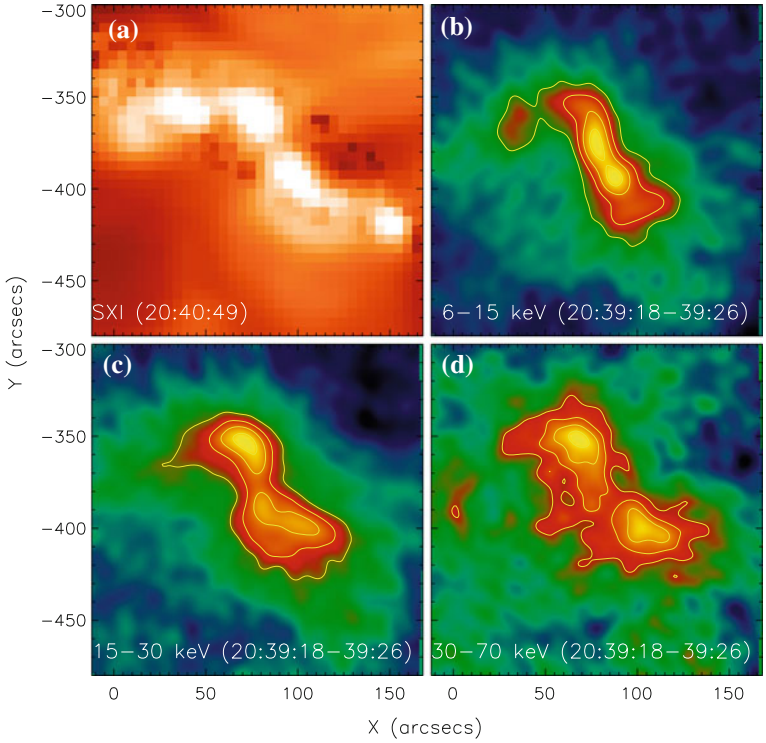

Fig. A.13 Sigmoid structure in the 2003 October 29 flare in hard X-ray bands

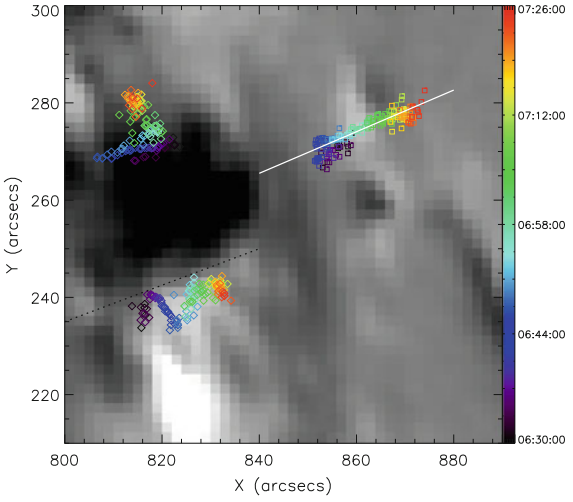

Fig. A.14 The X7.1 flare that occurred on January 20, 2005. The background is an MDI longitudinal magnetogram (black: negative polarity, white: positive polarity). The dotted line is the magnetic polarity inversion line (PIL). The two sides of the magnetic PIL show the trajectories of the FPs, the white line shows the trajectory of the LT X-ray source. Colors indicate different times

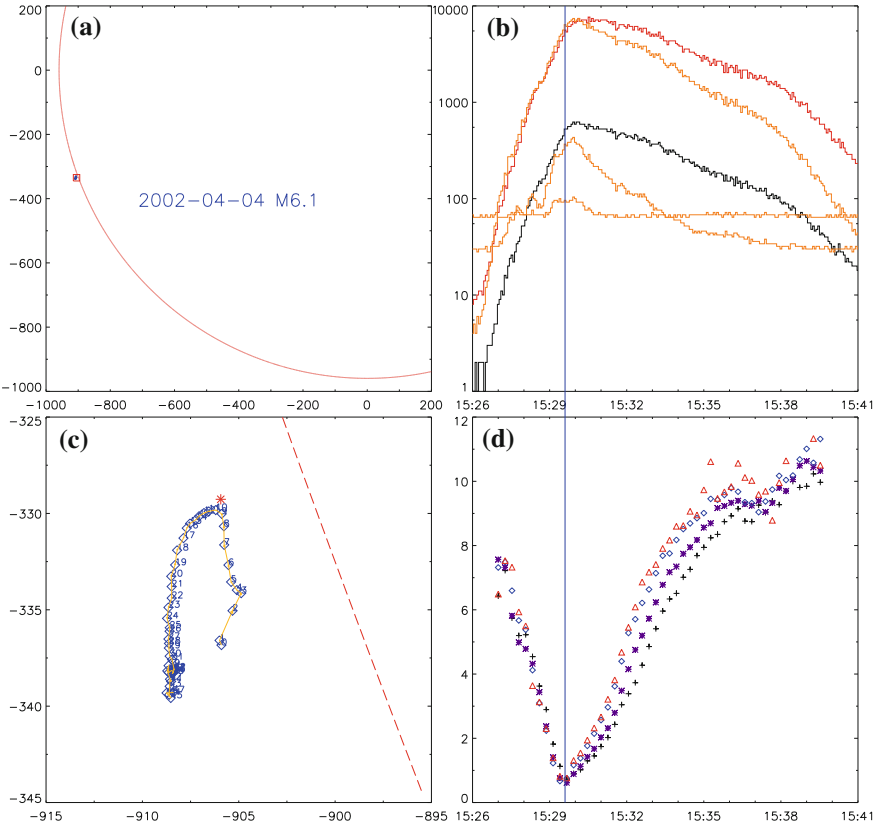

Fig. A.15 The M6.1 FP-occulted flare that occurred on April 4, 2002 observed by RHESSI. Panel **a** shows the position of the HXR emission (coronal source) relative to the solar disk; Panel **c** shows the trajectory of the coronal source at 12–25 keV energy band during the flare, the X-ray light curves of the flare are shown in panel **b** in the energy ranges of 3–6, 6–12, 12–25, 25–50, and 50–100 keV; Panel **d** shows the time profiles of the "heights" of the LT source in the energy ranges of 6–9, 9–12, 12–16, and 16–20 keV

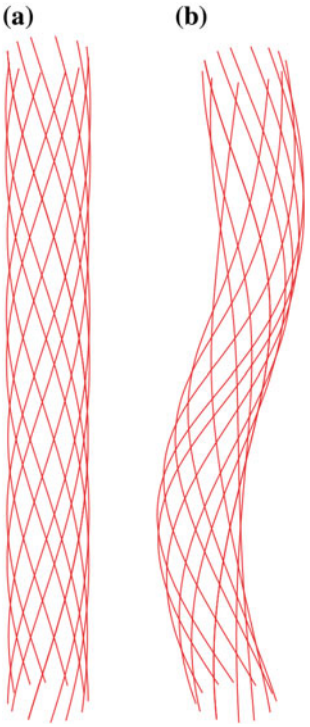

Fig. A.16 **a** Take parameters $C_1 = 1$ and $C_2 = 0$, corresponding to the simplest form of the helical force-free field; **b** Take parameters $C_1 = 0.75$ and $C_2 = 0.25$, corresponding to the S-shaped force-free field

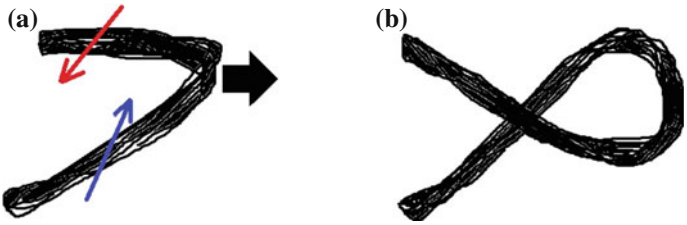

Fig. A.17 **a** Motions during the filament eruption (the black arrow indicates the upward motion) when the kink instability occurs, the red arrow indicates the redshift and the blue one indicates the blueshift. **b** the configuration produced by the kink instability

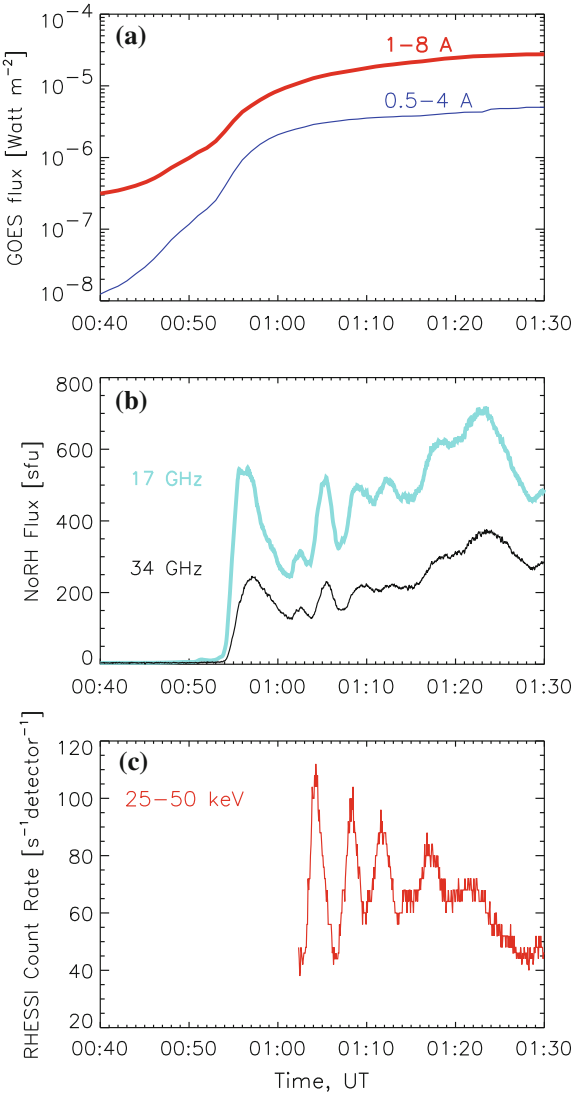

Fig. A.18 Light curves of the flare. **a** Soft X-ray in the GOES 1–8 Å (thick line) and 0.5–4 Å (thin line) channels; **b** NoRH fluxes integrated over the AR at 17 GHz (thick line) and 34 GHz (thin line), and **c** HXR count rate measured in RHESSI 25–50 keV channel

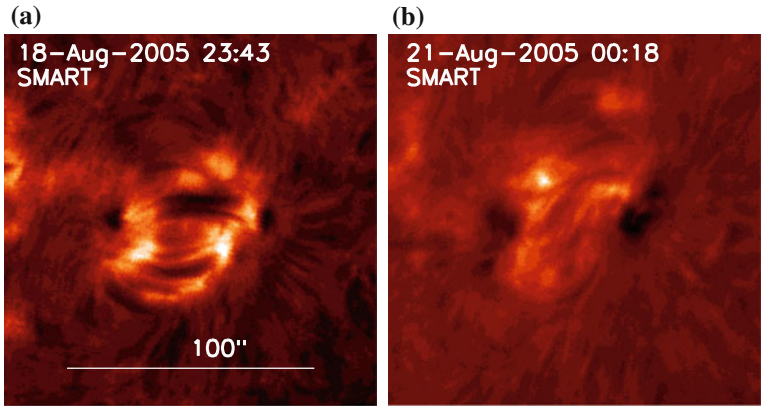

Fig. A.19 Evolution of AR: Hα images obtained with SMART at Hida observatory. This figure created on the basis of Fig. 4 from the Ref. 64 in Chap. 7

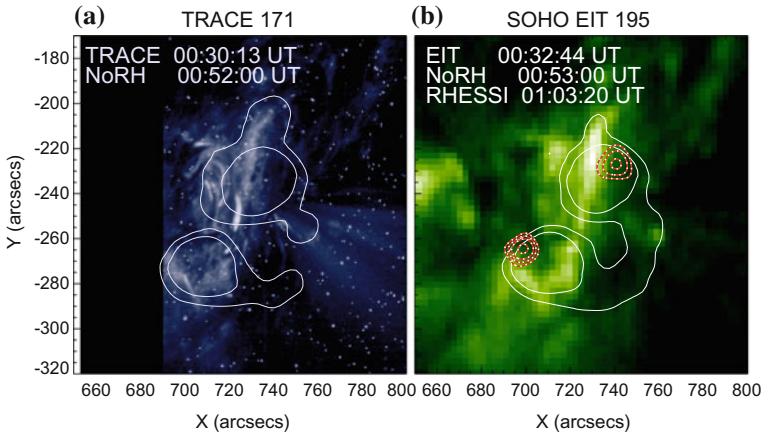

Fig. A.20 The EUV images (gray scale) obtained with **a** TRACE 171 Å and **b** SOHO/EIT 195 Å prior to the flare. 17 GHz loop is superimposed by white contour lines at levels 0.04 and 0.1 of T_b^{max} at the time of flare onset. RHESSI HXR sources at levels 0.6, 0.7, 0.8, and 0.95 of maximum counts are shown by dotted line on plot **b**. Times are depicted on each plot. All images are rotated to the time 00:53:00 UT. Black part of TRACE map is out of FOV

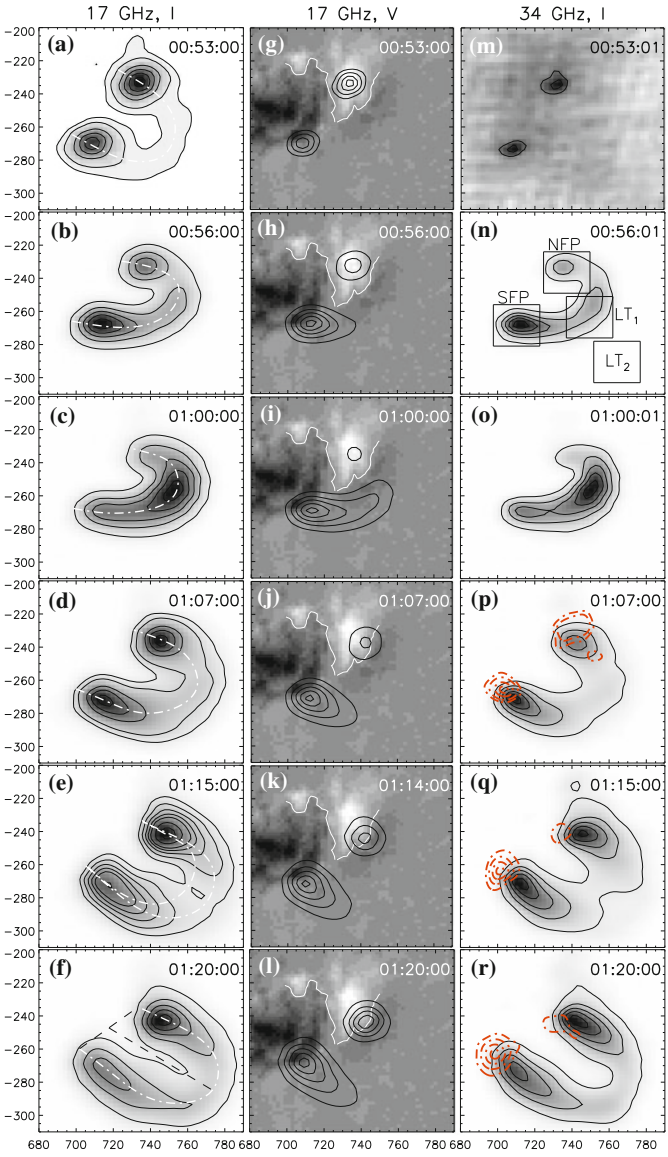

Fig. A.21 Evolution of the flare source morphology. Left column: NoRH images at 17 GHz, Stokes I. Contours correspond to 0.1, 0.3, 0.5, 0.7, and 0.9 levels of T_b^{max}. White dot-dashed lines show visible flaring loop axes, black dashed lines on f are loop span and height. Middle column: SOHO/MDI magnetogram (grayscale) taken at 00:53:00 UT overlaid by black contours of polarization images at 17 GHz (Stokes V) at 0.2, 0.4, 0.6, 0.8, and 0.95 levels of the T_b^{min}, all V values are negative. White contour line shows the magnetic reversal line. Right column: 34 GHz images (grayscale and thin black contours at the same levels as at 17 GH, I). On plots **p**, **q**, and **r** HXR sources with energy 25–50 keV are superimposed by dot-dashed contour at 0.4, 0.6, 0.8, and 0.95 levels of maximum count rates. Units of X- and Y-axis are arcsec from disk center. All images are rotated to the time of magnetogram

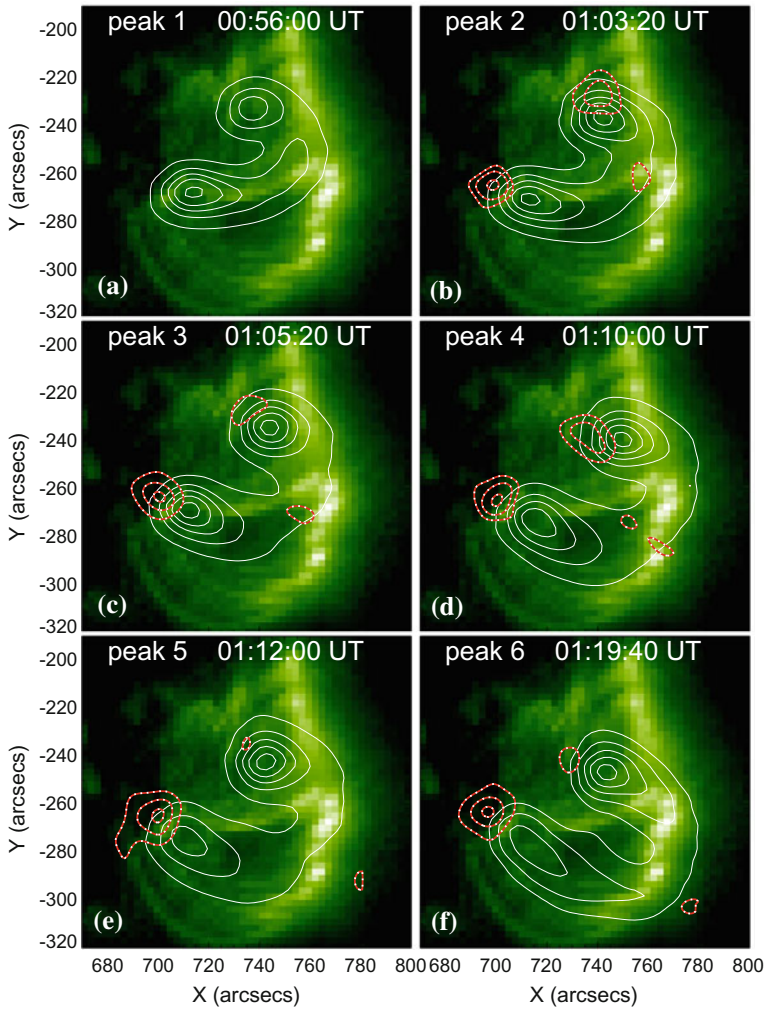

Fig. A.22 The EUV images (gray logarithmic scale) of post-flare arcade obtained with SOHO/EIT 195 Å at 02:32:44 UT. 17 GHz loop are superimposed by white contour lines at levels 0.1, 0.3, 0.5, 0.7, and 0.95 of T_b^{max} at the time of each temporal peak. RHESSI HXR sources with energy 25–50 keV at levels 0.4, 0.7, and 0.95 of maximum counts are shown by dotted line on plots **b**–**f** obtained at the same time as NoRH images. Times are depicted on each plot. All images are rotated to the time 00:53:00 UT

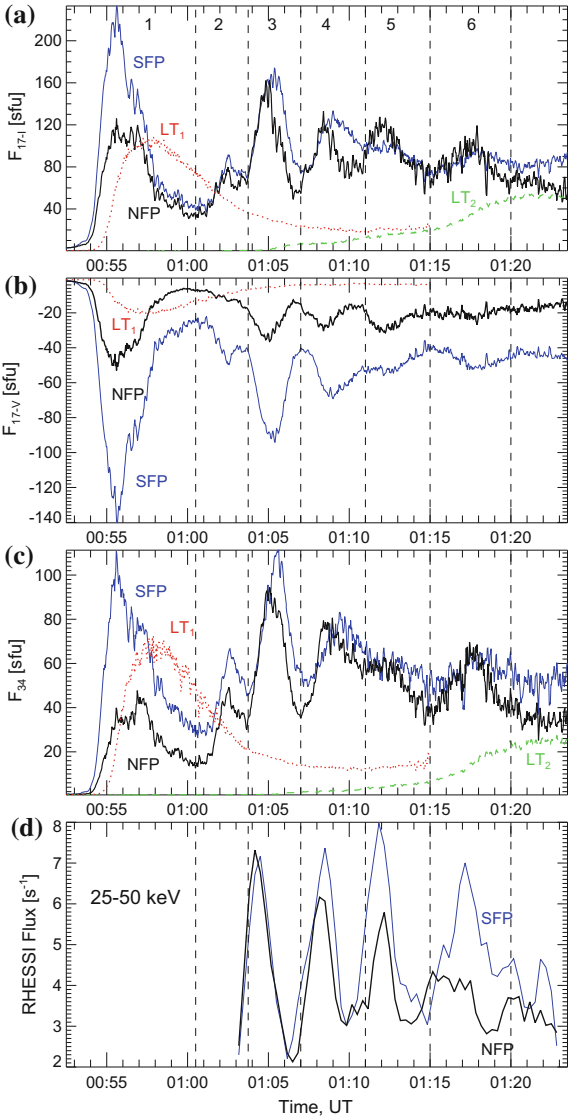

Fig. A.23 Time profiles measured with NoRH at **a** 17 GHz (Stokes I), **b** 17 GHz (Stokes V), **c** 34 GHz, and **d** with RHESSI at energy 25–50 keV. Flux densities from south FP (thin line), north FP (thick line), LT_1 (dotted line), and LT_2 (dashed line) are obtained by integration over areas of the size $25'' \times 25''$. Locations of areas are shown in Fig. A.19

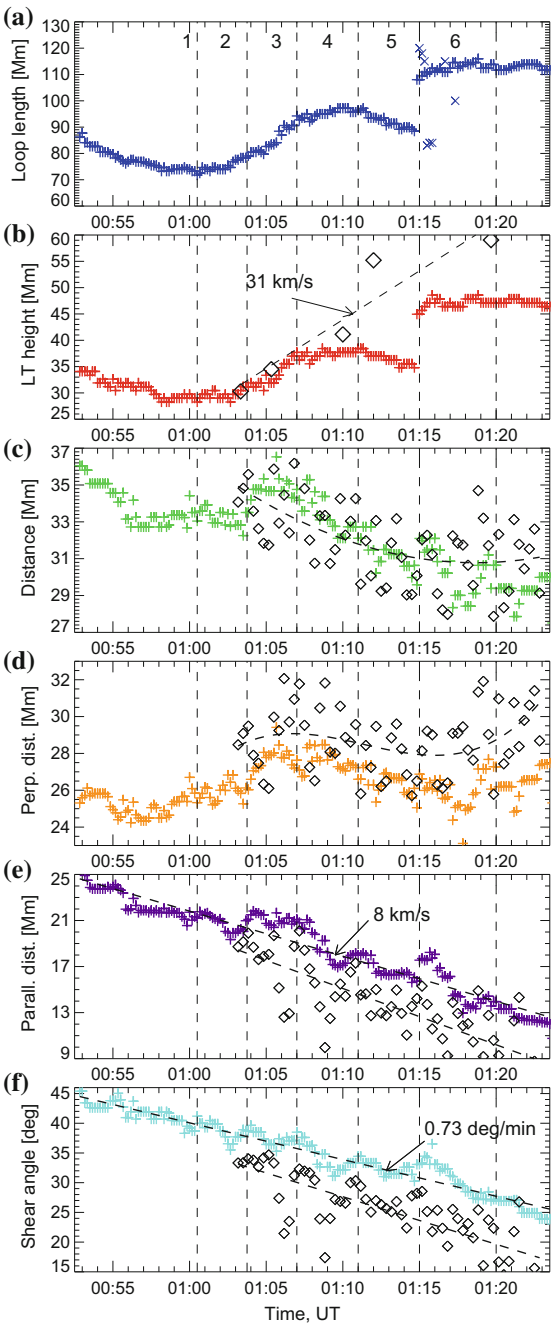

Fig. A.24 Time profiles for a number of quantities measured with NoRH at 17 GHz (crosses), and with RHESSI at energy 25–50 keV (diamonds): **a** apparent loop length and **b** altitude; **c** projected footpoint distance, its components (**d**) perpendicular and (**e**) parallel to the magnetic inverse line; **f** shear angle. Dashed lines are (**c**, **d**) polynomial or (**e**, **f**) linear fitting of HXR time profiles

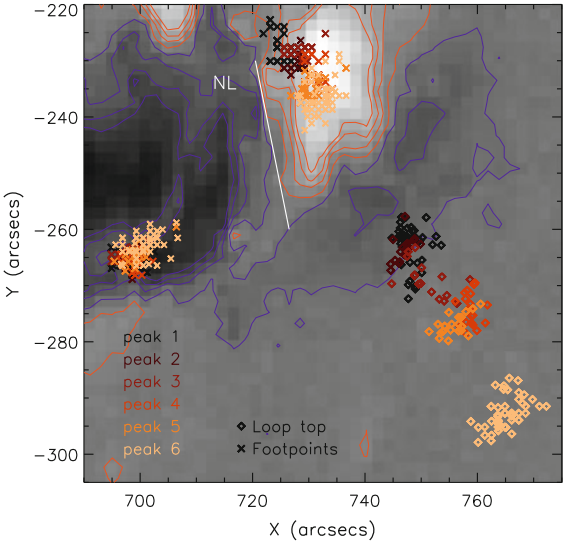

Fig. A.25 FPs (crosses) and LT (diamonds) trajectories during the flare process obtained at 17 GHz, I on an MDI magnetogram. The evolution in time is coded from dark to light colors. SOHO MDI magnetogram is superimposed by contour lines, red for positive and blue for negative polarities. Simplified magnetic NL on the photosphere is shown by white line

Color Figures in Chap. 7 (continued)

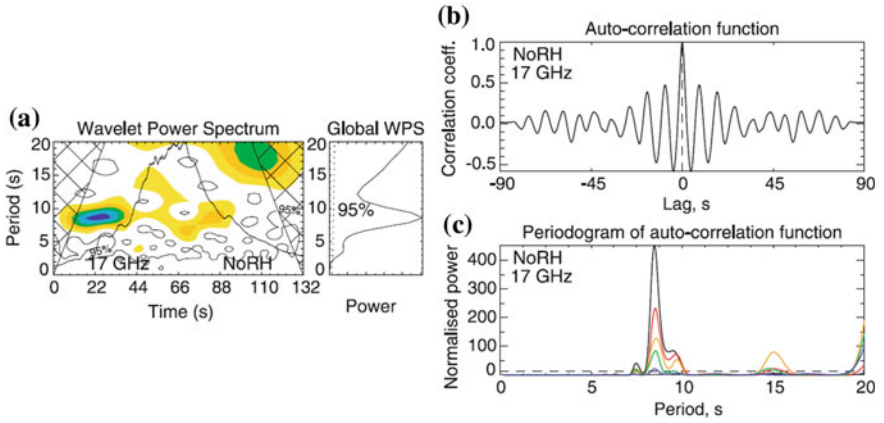

Fig. A.26 Wavelet and autocorrelation analyses of the flare on July 28, 2002, 23:00:20C23:02:32 UT, recorded with NoRH at 17 GHz. **a** Wavelet power spectrum of the modulation amplitude $\Delta_f(t)$, $\tau = 10$ s, with the superimposed normalized time profile $F_f(t)$ of the radio emission, both obtained with NoRH at 17 GHz. Thin solid contours show 95% significance level. The right plot is the global wavelet power spectrum of $\Delta_f(t)$. Dashed line shows the 95% significance level. **b** Autocorrelation function of the modulation amplitude $\Delta_f(t)$, $\tau = 10$ s. **c** Periodograms (in units of spectral power normalized to the total variance), of an autocorrelation function: black solid line for $\tau = 10$ s, red for $\tau = 15$ s, orange for $\tau = 20$ s, green for $\tau = 25$ s, and blue for $\tau = 30$ s. The spectral power for $\tau = 20$, 25, and 30 s is multiplied by four to see details. The black color periodogram corresponds to the autocorrelation function displayed in the upper panel. Black dashed line corresponds to the 99% significance level

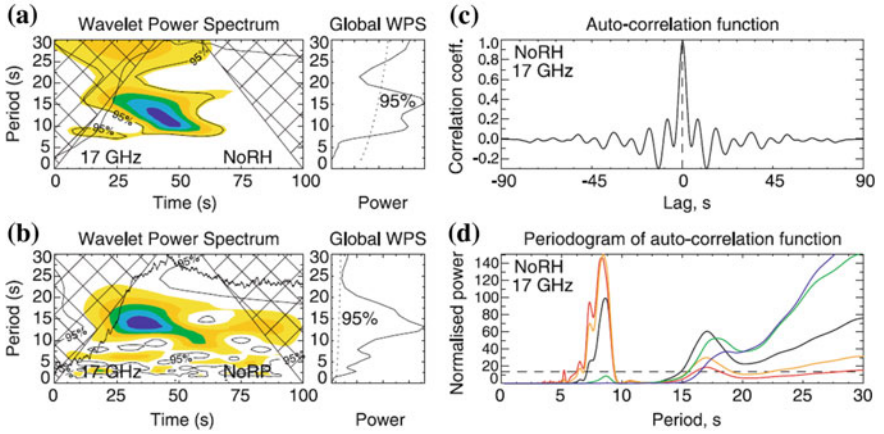

Fig. A.27 The same as Fig. A.24, but for the flare on July 18, 2002, 03:32:13C03:33:43 UT. Periodograms: black solid line for $\tau = 15$ s, red for $\tau = 10$ s, orange for $\tau = 20$ s, green for $\tau = 25$ s, and blue for $\tau = 30$ s. The black color periodogram corresponds to the autocorrelation function displayed in the upper panel

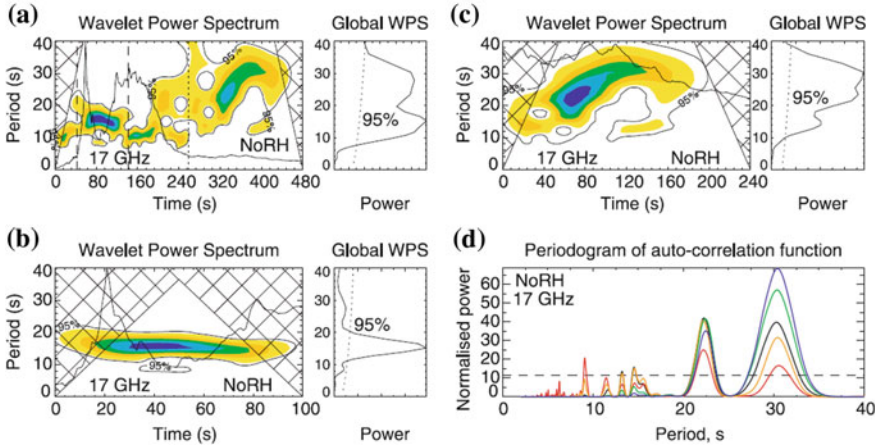

Fig. A.28 Analysis of the flare on July 03, 2002, 02:09:12C02:17:12 UT observed at 17 GHz. **a** Wavelet power spectrum of the modulation signal ($\tau = 15$ s) with superimposed normalized profile of the radio emission, both obtained with NoRH. Time interval between two vertical dashed lines indicates the occurrence of the first QPP. The time interval between the vertical dotted line to the end of the event indicates the occurrence of the second QPP. The right plot is the global wavelet power spectrum. The dashed line shows the 95% significance level. **b** Zoomed wavelet spectrum of the first QPP, from 02:09:50 to 02:11:30 UT. **c** Zoomed wavelet spectrum of the second QPP, from 02:13:30 to 02:17:30 UT. **d** Periodograms of the autocorrelation functions constructed for the modulation signal of the second QPP. Black solid line is for $\tau = 15$ s, red for $\tau = 7$ s, orange for $\tau = 10$ s, green for $\tau = 20$ s, and blue for $\tau = 25$ s. The dashed line corresponds to the 99% significance level

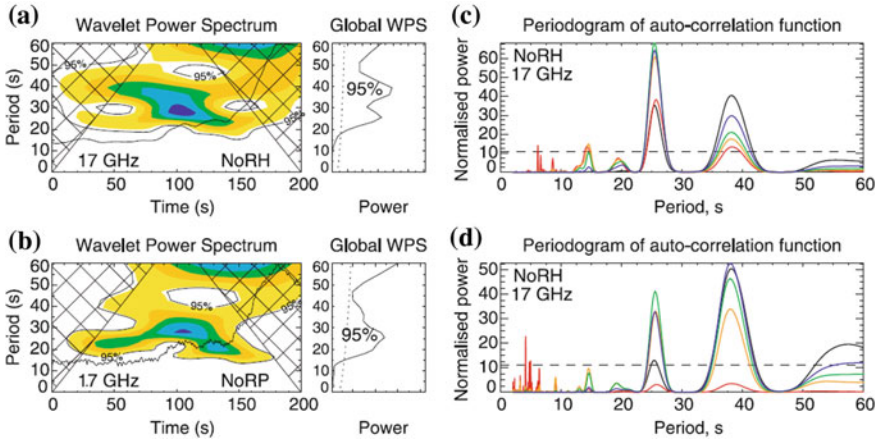

Fig. A.29 Analysis of the flare on May 21, 2004, 23:47:10C23:50:30 UT. **a** Wavelet power spectrum of the modulation signal ($\tau = 30$ s), with superimposed normalized profile of the radio emission, both obtained with NoRH at 17 GHz. The right plot is the global wavelet power spectrum. The dashed line shows the 95% significance level. **b** The same as on panel **a** but for the NoRP data. **c** Periodograms of the autocorrelation function constructed for the modulation signal obtained with NoRH at 17 GHz. **d** The same as **c** but at 34 GHz. On plots **c**, **d** the black line is for $\tau = 30$ s, red for $\tau = 7$ s, orange for $\tau = 10$ s, green for $\tau = 15$ s, and blue for $\tau = 20$ s; the dashed line corresponds to the 99% significance level

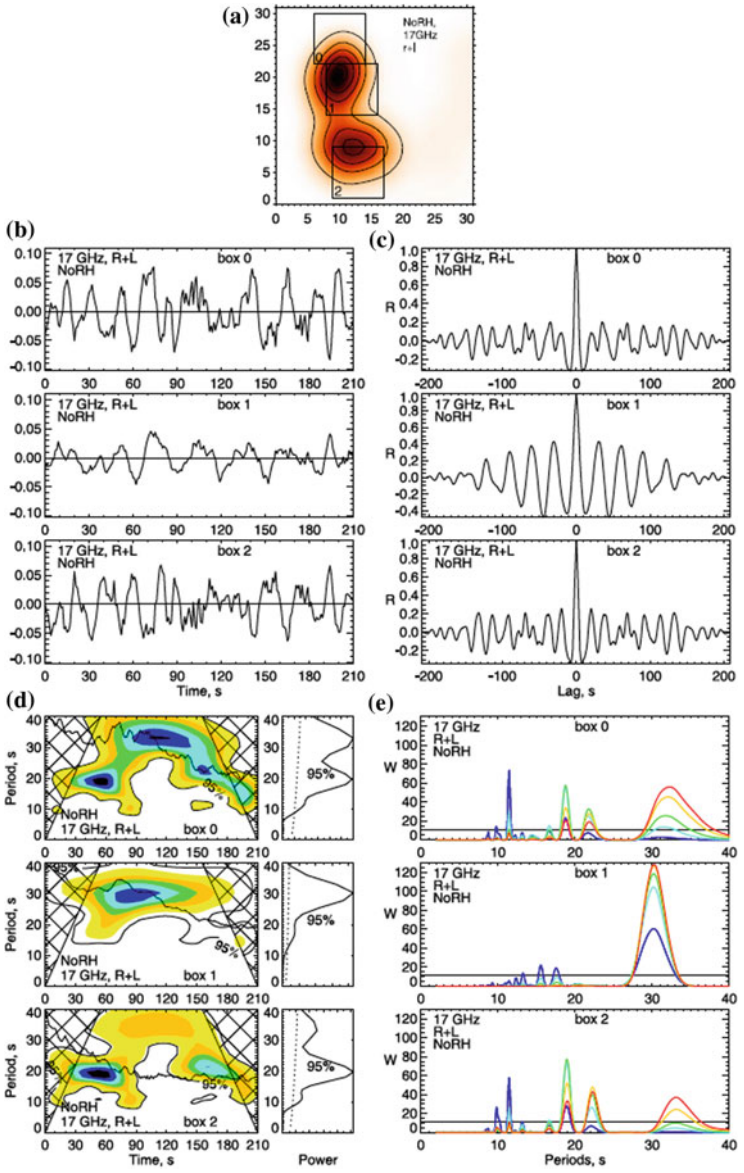

Fig. A.30 **a** The distribution of radio brightness at $t_{73} = 02{:}14{:}53$ UT. Contours show the levels 0.1, 0.3, 0.5, 0.7, 0.9, and 0.97 of F^{max}. Numbered squares show the positions of three large boxes of 20"×20". Panels **b**, **c**, **d** are for $\tau = 25$ s. **b** Time profiles of modulation depth $\Delta_\tau(t_i)$ from these boxes (02:13:40 to 02:17:10 UT). **c** Autocorrelation functions R of $\Delta_\tau(t_i)$. **d** Wavelet power spectra (WPS) of $\Delta_\tau(t_i)$. Thick black curve shows the normalized temporal profiles of the fluxes from each box. Cross-hatched regions on the ends of the WPS indicate the cone of influence. The small panel on the right of the WPS represents the global WPS. **e** Periodograms of autocorrelation functions R of $\Delta_\tau(t_i)$. The blue, pale blue, green, orange, and red solid lines correspond to the set of smoothing times $\tau = 15, 20, 25, 30$, and 35 s. The horizontal line marks the significance level $W_{sign} \approx 11.4$

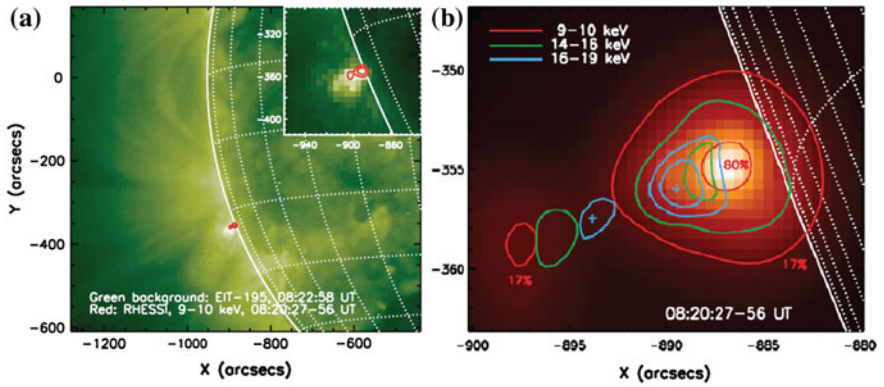

Fig. A.31 Double coronal sources of the 2002 April 30 solar flare. **a** is 195 Åimage detected by SOHO/EIT with RHESSI contours at 9–10 keV, **b** is RHESSI image with the contours at 9–10, 14–16 and 16–19 keV (from the Ref. 134 of Chap. 7)

Fig. A.32 RHESSI image of the 2002 September 10 solar flare. Thin and thick contours are set at 3–6 and 45–60 keV. FP_1 and FP_2 are two FP sources and the dashed lines outline the flare loop (from the Ref. 137 of Chap. 7)

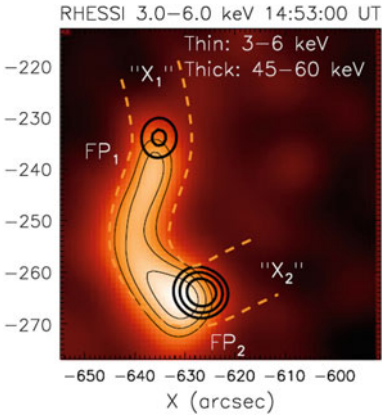

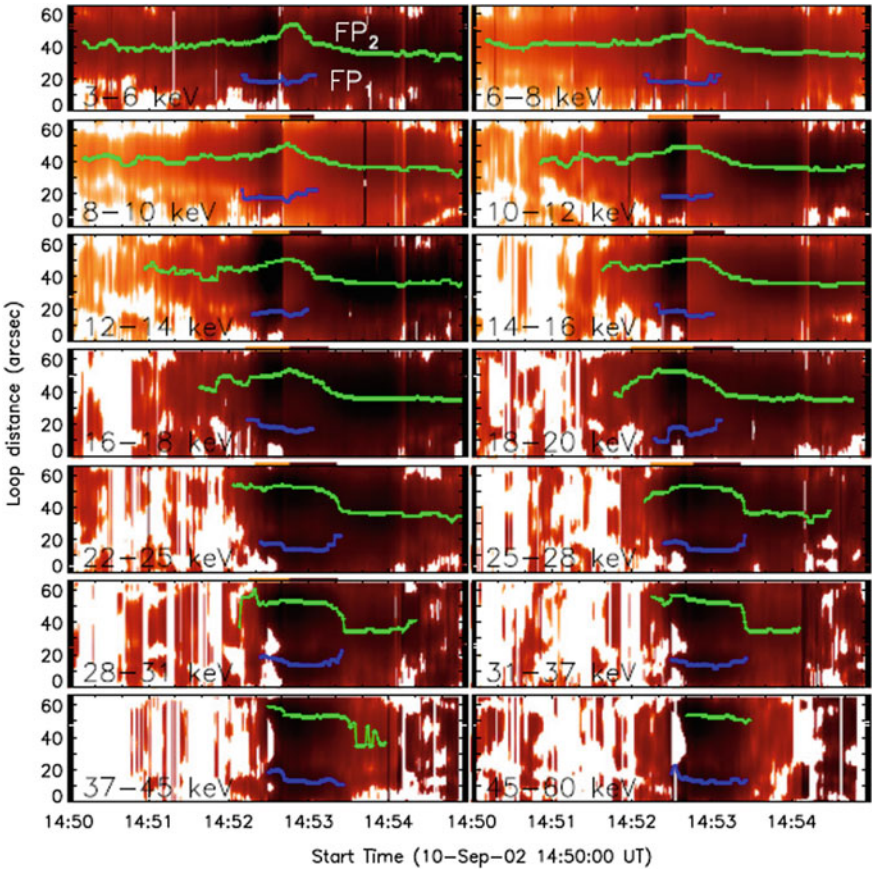

Fig. A.33 Time evolution of the X-ray fluxes along the flare loop at 14 energy bands for the 2002 September 10 solar flare. The positions of two X-ray source are marked by stars and plus (from the Ref. 137 of Chap. 7)

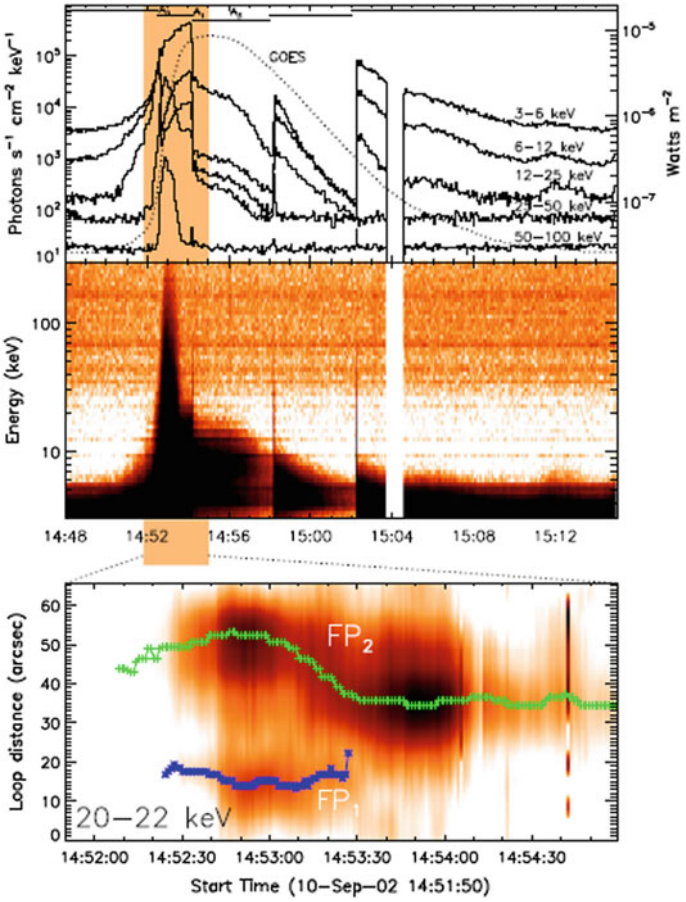

Fig. A.34 The 2002 September 10 solar flare detected by RHESSI. Top: RHESSI (solid) at five energy bands and GOES 1–8 Å (dotted) light curves. The shaded interval indicates the period of source motions in bottom. Middle: RHESSI 3–300 keV X-ray dynamic spectra; Bottom: time evolution of the 20–22 keV brightness along the flare loop. The pluses and asterisks correspond to two FPs (from the Ref. 137 of Chap. 7)

Fig. A.35 X-ray source distribution dependence on the energies from 6 to 100 keV in the 2004 October 30 flare. The background image is the 20–30 keV intensity when the chromosphere evaporation started (from the Ref. 141 of Chap. 7)

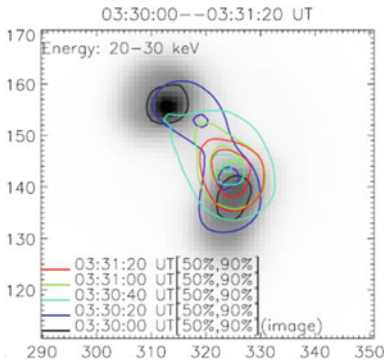

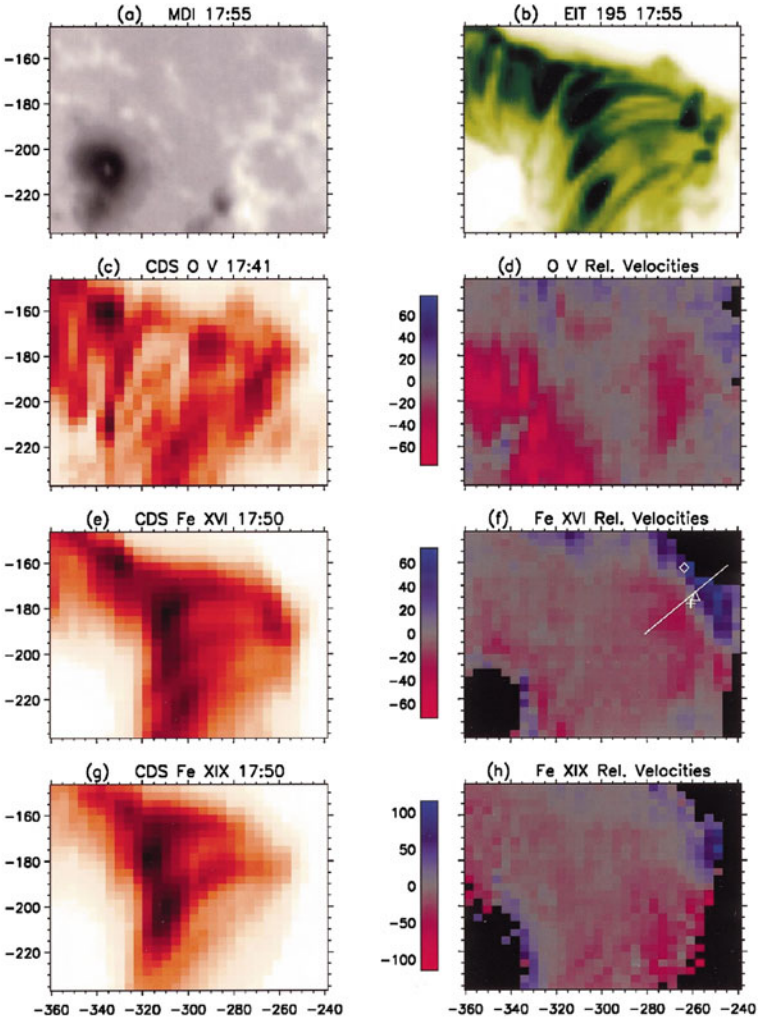

Fig. A.36 Flare region in different wavelengths at the beginning of the CDS observations. Adapted from the Ref. 214 of Chap. 7

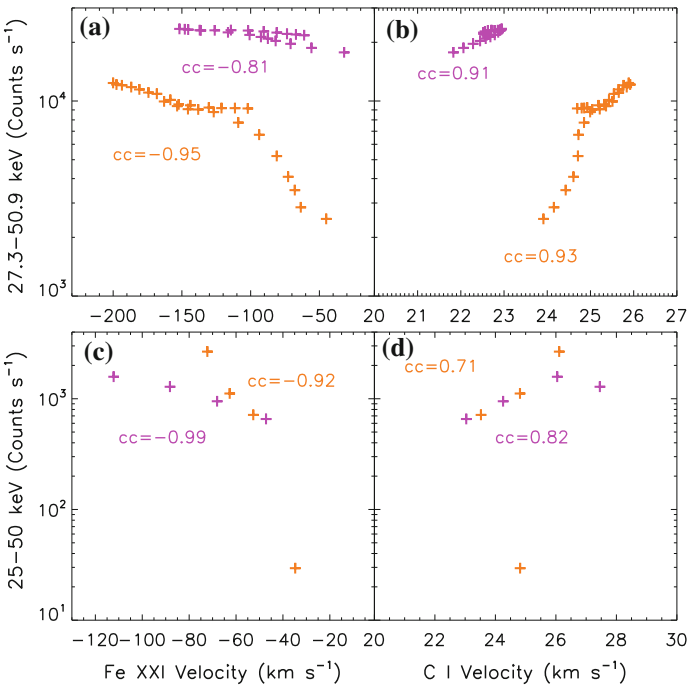

Fig. A.37 Scatter plots of two HXR peaks (orange and purple) dependence on Doppler velocities of Fe XXI and C I for the 2014 September 10 flare (upper panels) and October 22 flare (lower panels). Adapted from the Ref. 212 of Chap. 7

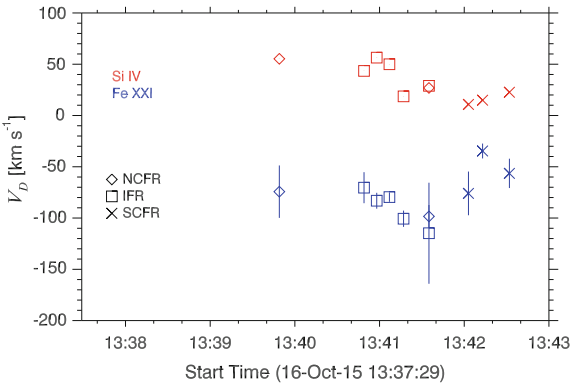

Fig. A.38 Doppler velocities of the downflow and upflow for the northern CFR (diamonds), IFR (boxes), and southern CFR (crosses). Adapted from the Ref. 215 of Chap. 7

Index

G. Huang et al., *Solar Flare Loops: Observations and Interpretations*,
https://doi.org/10.1007/978-981-10-2869-4